polymers

Nanoparticle-Reinforced Polymers

Edited by
Ana María Díez-Pascual

Printed Edition of the Special Issue Published in *Polymers*

www.mdpi.com/journal/polymers

MDPI

Nanoparticle-Reinforced Polymers

Nanoparticle-Reinforced Polymers

Special Issue Editor

Ana María Díez-Pascual

MDPI • Basel • Beijing • Wuhan • Barcelona • Belgrade

Special Issue Editor
Ana María Díez-Pascual
Alcalá University
Spain

Editorial Office
MDPI
St. Alban-Anlage 66
4052 Basel, Switzerland

This is a reprint of articles from the Special Issue published online in the open access journal *Polymers* (ISSN 2073-4360) from 2018 to 2019 (available at: https://www.mdpi.com/journal/polymers/special_issues/nanoparticle_reinforced_polymers)

For citation purposes, cite each article independently as indicated on the article page online and as indicated below:

LastName, A.A.; LastName, B.B.; LastName, C.C. Article Title. *Journal Name* **Year**, *Article Number*, Page Range.

ISBN 978-3-03921-283-5 (Pbk)
ISBN 978-3-03921-284-2 (PDF)

Contents

About the Special Issue Editor

Ana María Díez-Pascual graduated with a degree in Chemistry in 2001 (awarded Extraordinary Prize) from the Complutense University (Madrid, Spain), where she carried out her Ph.D. (2002–2005) on dynamic and equilibrium properties of fluid interfaces under the supervision of Prof. Rubio. In 2005, she worked together with Prof. Miller at the Max Planck Institute of Colloids and Interfaces (Germany) conducting the rheological characterization of water-soluble polymers. During 2006–2008, she was a Postdoctoral Researcher at the Physical Chemistry Institute of the RWTH Aachen University (Germany), where she worked on the layer-by-layer assembly of polyelectrolyte multilayers onto thermoresponsive microgels. Then she moved to the Institute of Polymer Science and Technology (Madrid, Spain) and participated in a Canada-Spain joint project to develop carbon nanotube (CNT)-reinforced epoxy and polyetheretherketone composites for transport applications. Currently, Dr. Diez-Pascual is a Postdoctoral Researcher at Alcala University (Madrid, Spain) focused on the development of polymer/nanofiller systems for biomedical applications. She has participated in 22 research projects (11 international, 10 national, of which 3 have been with private companies, and she was the principal investigator for 6 projects). She has published **102 SCI articles** (97% in Q1 journals). She has an **h-index of 39** and **more than 3000 total citations**. More than 50% of her articles are in journals with an impact factor $\geq$4.8, such as *J. Mater. Chem, Carbon*, and *J. Phys. Chem. C*. She is the first and corresponding author of 2 invited reviews in *Prog. Mater. Sci.* and is a frequent reviewer for ACS, MDPI, and Elsevier journals. She has published 19 book chapters and 2 monographies and edited 1 book, and is the first author of an international patent. She has contributed to 61 international conferences (45 oral communications, including 6 by invitation) and has been a member of the organizing committee in 3 workshops and 1 national meeting. She was invited to impart seminars at prestigious international research centers, such as Max Planck in Germany, NRC in Canada, and School of Materials in Manchester, UK. She was awarded the **TR35 2012 Prize** by the Massachusetts Institute of Technology (MIT) for her innovative work in the field of nanotechnology.

Preface to "Nanoparticle-Reinforced Polymers"

This book, a collection of 12 original contributions and 4 reviews, provides a selection of the most recent advances in the preparation, characterization, and applications of polymeric nanocomposites comprising nanoparticles. The concept of nanoparticle-reinforced polymers came about three decades ago, following the outstanding discovery of fullerenes and carbon nanotubes. One of the main ideas behind this approach is to improve the matrix mechanical performance. The nanoparticles exhibit higher specific surface area, surface energy, and density compared to microparticles and, hence, lower nanofiller concentrations are needed to attain properties comparable to, or even better than, those obtained by conventional microfiller loadings, which facilitates processing and minimizes the increase in composite weight. The addition of nanoparticles into different polymer matrices opens up an important research area in the field of composite materials. Moreover, many different types of inorganic nanoparticles, such as quantum dots, metal oxides, and ceramic and metallic nanoparticles, have been incorporated into polymers for their application in a wide range of fields, ranging from medicine to photovoltaics, packaging, and structural applications.

Ana María Díez-Pascual
Special Issue Editor

polymers

MDPI

Editorial

Nanoparticle Reinforced Polymers

Ana María Díez-Pascual

Department of Analytical Chemistry, Physical Chemistry and Chemical Engineering, Faculty of Sciences, Institute of Chemistry Research "Andrés M. del Río" (IQAR), University of Alcalá, Ctra. Madrid-Barcelona, Km. 33.6, 28871 Madrid, Spain; am.diez@uah.es; Tel.: +34-918-856-430

Received: 24 March 2019; Accepted: 1 April 2019; Published: 4 April 2019

The beginning of nanomaterials and nanoscience dates back to 1959 when the Nobel laureate in Physics Richard Feynman gave the famous lecture entitled "There's Plenty of Room at the Bottom." Nonetheless, the concept of nanoparticle-reinforced polymers came about three decades ago after the outstanding discovery of fullerenes and carbon nanotubes. The addition of these nanoparticles into different polymer matrices opened up an important research area in the field of composite materials. Furthermore, many different types of inorganic nanoparticles, such as quantum dots, metal oxides, and ceramic and metallic nanoparticles, have been incorporated into polymers for application in a wide range of fields, such as medicine, photovoltaics, packaging and structural applications, etc. One of the main ideas behind this approach is to improve the matrix mechanical performance. The nanoparticles exhibit higher specific surface area, surface energy, and density compared to microparticles, hence lower nanofiller concentrations are needed to attain properties comparable to or even better than those obtained by conventional microfiller loadings, which facilitate processing and minimizes the increase in composite weight. Nonetheless, a number of challenges have to be faced. Nanoparticle agglomeration within the polymer matrix and poor interfacial adhesion between the nanofillers and the matrix frequently hinder property improvements, demanding modification of the surface chemistry to promote physical or chemical interactions with the polymer chains. Furthermore, the fabrication procedure of the nanoparticle-modified polymers leads to different morphologies that have a strong influence on the final properties of the materials. This Special Issue, with a collection of 12 original contributions and four reviews, provides selected examples of the most recent advances in the preparation, characterization, and application of polymeric nanocomposites comprising nanoparticles.

Recently, inorganic fullerenes, nanotubes, and 2D nanomaterials based on layered metal dichalcogenides such as WS_2 and MoS_2, have emerged as being among the most promising polymer reinforcements. These types of nanoparticles are currently the subject of intense research, summarized in different literature reviews [1–3]. In particular, the incorporation of environmentally-friendly tungsten disulfide (WS_2) nanoparticles has been shown to improve the thermal, mechanical, and tribological properties of a series of thermoplastic polymers, including isotactic polypropylene (iPP) [4], polyphenylene sulfide (PPS) [5], and poly(ether ether ketone) (PEEK) [6]. Efficient dispersion of WS_2 was achieved through simple melt-blending without using modifiers or surfactants. Continuing progress in the field, WS_2-based nanotubes have been used to prepare poly(3-hydroxybutyrate-co-3-hydroxyvalerate) (PHBV) nanocomposites by blending in solution [7], and the effects of the nanotubes on the isothermal crystallization behavior and kinetics of PHBV were investigated by differential scanning calorimetry (DSC) and polarized optical microscopy (POM). Results revealed that very low nanotube loadings (0.1–1.0 wt %) raised the crystallization rate of the matrix due to the heterogeneous nucleation effect and provided understanding of the structure-property relationships in PHBV-based nanocomposites that are useful for their practical applications. Hybrids comprising reduced graphene oxide (rGO) and WS_2 nanoparticles grafted with active amino groups were used to develop bismaleimide (BMI) nanocomposites (NH_2-rGO/WS_2/BMI) via the casting method [8]. Results demonstrated unprecedented enhancements in the mechanical properties of the BMI resin with

trace amounts of nanofillers. In particular, only 0.6 wt % NH_2-rGO/WS_2 increased the impact and flexural strength of the matrix by 91.3% and 62.6%, respectively, ascribed to the layered structure of the hybrid nanoparticles, strong interfacial adhesion, and uniform dispersion of the NH_2-rGO/WS_2 within the resin. Besides, the thermal stability significantly improved with the addition of the nanoparticles.

Monolayers of molybdenum disulfide (MoS_2) are of great interest to tailor the mechanical and gas barrier properties of polymeric materials. In this regard, Tsai et al. [9] exfoliated MoS_2 via modification with ethanethiol and nonanethiol to obtain monolayers with thicknesses in the range of 0.7–1.1 nm, which were then added to chlorobutyl rubber to prepare MoS_2-butyl rubber nanocomposites with loadings of 0.5, 1, 3, and 5 wt %. The tensile stress and oxygen transmission rate of the matrix showed maximum augments of 30.7% and 49.6%, respectively, making these nanocomposites highly suitable to be applied as pharmaceutical stoppers. Another field of application of rubber-based nanocomposites is tire manufacturing. Thus, the development of silica/rubber composites with low rolling resistance in an energy-saving method is of great interest. Zheng and coworkers [10] proposed a novel strategy in which alcohol polyoxyethylene ether (AEO) and a silane coupling agent (K-MEPTS) were grafted onto the surface of silica nanoparticles and subsequently incorporated into a rubber matrix using the latex compounding technique. The characteristics of the resulting nanocomposites were studied by a rubber process analyzer (RPA), transmission electron microscopy (TEM), and tensile tests. Results revealed that AEO forms a physical interface between the nanoparticles and the matrix that reduces silica aggregation, while K-MEPTS forms a chemical interface that enhances the reinforcing effect of the nanoparticles and minimizes the joint friction between them. Overall, AEO and K-MEPTS acted synergistically to improve the mechanical and dynamic performances of silica/rubber nanocomposites.

Noble metal nanoparticles (NPs) are very attractive catalysts due to their highly active surface atoms [11]. Nonetheless, owed to their high surface-to-volume ratio and surface energy, they can easily agglomerate during the catalytic reaction process. To overcome this issue, NPs are commonly stabilized by polymers, complex ligands, or surfactants [12], albeit the catalytic reactivity of the resulting blends is low. To solve this drawback, Wang and coworkers [13] developed a composite membrane with SiO_2 microspheres coated by Ag NPs on a PVDF substrate. The membrane displayed high catalytic reactivity when catalyzing the reduction of p-nitrophenol to p-aminophenol, an important fine chemical intermediate, under a cross-flow. The reaction followed a first-order kinetics, and its speed raised with increasing the Ag concentration in the membrane, the reaction temperature, and the operating pressure. Therefore, the developed reaction system will be of great interest for the chemical industry.

On the other hand, AuNPs can be used as colorimetric sensors for Ag+ detection. However, AuNPs-based sensors generally suffer from poor selectivity and low sensitivity, owed to the nanoparticle tendency to aggregate during their synthesis and sensing process. To address this issue, Liu et al. [14] functionalized the nanoparticles with a thermoresponsive polymer that acted as both a reducing and stabilizing agent: hyperbranched polyethylenimine-terminal isobutyramide (HPEI-IBAm). The modified nanoparticles showed outstanding thermal stability up to 200 °C, high tolerance of a wide range of pH, and high salt resistance. The developed colorimetric sensor exhibited high stability, selectivity, and sensitivity, with an extremely low detection limit of 7.22 nM. More importantly, due to the thermoresponsivity of HPEI-IBAm, the AuNPs/Ag composites could be separated by heating the system above the cloud point of the polymer solution followed by centrifugation, thereby preventing and controlling Ag+ pollution to the environment.

AuNPs have also been successfully used for the colorimetric detection of melamine ($C_3H_6N_6$), a white heterocycle compound extensively applied in the manufacturing of plastics, laminates, dyes, and fertilizers that can cause health problems or even death [15]. However, the current methods for melamine detection involve time-consuming steps, complicated procedures, and expensive equipments. Zhang et al. [16] developed a fluorescence resonance energy transfer (FRET) system for melamine detection based on AuNPs and conjugated polymer nanoparticles (CPNs), which led to a maximum energy transfer efficiency of 82.1%. The system was found to be highly selective and sensitive to melamine detection, with a detection limit of 1.7 nmol/L. Results revealed that the fluorescence of

CPNs was initially quenched by AuNPs and then restored after melamine addition since it reduced the FRET between CPNs and AuNPs. Moreover, the proposed method was tested in powdered infant formula with very good results. A FRET mechanism was also designed for ratiometric fluorescent temperature sensing based on two thermo-responsive polymers, poly(*N*-isopropylacrylamide) and poly(N-isopropylmethacrylamide), which present lower critical solution temperatures (LCSTs) of 31.1 and 48.6 °C, respectively [17]. The fluorescent intensity of each polymer (with maxima at 436 and 628 nm, respectively) decreased upon heating the polymer aqueous solution. When the two polymer aqueous solutions were mixed, the fluorescent intensity at 436 nm decreased while that at 628 nm increased with increasing temperature owed to the FRET effect. This temperature sensing system displayed good stability and biocompatibility, and could be very interesting for biomedical applications, such as bioimaging of biological processes at specific organelles.

The FRET mechanism also influences the power conversion efficiency in polymeric organic light-emitting diodes (OLEDs). The energy emission may be reduced or even eliminated when the nonradiative energy transfer processes is very efficient [18]. This drawback can be addressed by the incorporation of nanostructured materials such as SiO_2/TiO_2 nanocomposites. Thus, the performance of OLEDs based on hybrids of poly(9,9-di-*n*-octylfluorenyl-2,7-diyl) (PFO), which acts as a donor material, and poly(2-methoxy-5-(2-ethyl-hexyloxy)-1,4-phenylene-vinylene) (MEH-PPV), which acts as an acceptor material, was significantly improved upon addition of SiO_2/TiO_2 nanoparticle blends [19]. An improved charge carrier injection and an important reduction in the turn-on voltage of the devices was observed in the presence of the nanocomposites, as well as an enhancement of the MEH-PPV electroluminescence peaks, not only due to the reduction of the FRET effect but also to a hole-electron recombination.

It should be noted that SiO_2 and TiO_2 are among the most common inorganic oxide nanofillers used in polymer-based nanocomposites. An effective approach to achieve their homogeneous dispersion within the matrix is in situ synthesis using techniques such as the sol–gel, microemulsion, or hydrothermal/solvothermal methods [20]. These methods typically involve the mixing of precursors with a non-reactive solvent and the monomer, and the reaction of the precursors starts the nanoparticle synthesis either before or during monomer polymerization. This bottom–up approach allows better control over the structure and properties of the nanocomposites; given that the nanoparticles are grown inside the polymer matrix, the passivating effect of the polymer chain functional groups on the nanoparticles can control particle size and decrease agglomeration. However, the unreacted precursors or byproducts of the in situ reactions frequently modify the properties of the nanocomposite. Considering the large number of studies published on the in situ synthesis of SiO_2 and TiO_2 nanofillers, Adnan et al. [21] collected the most relevant results in the field, focusing on the sol-gel method and thermoset matrices like epoxy resins and poly(dimethylsiloxane) (PDMS). In addition to the preparation techniques and strategies, the properties and most relevant applications of such nanocomposites are discussed, including laminates, structural composites, electrical insulation, coatings for epoxy and optical devices, and coatings and bioactive materials for PDMS.

Carbon based nanoparticles such as graphite carbon nanoparticles (CNPs) have also been used as reinforcing materials of different matrices including epoxy resins. In this regard, Nezhad and Thakur [22] reported on the preparation and mechanical characterization of epoxy/CNPs nanocomposites with nanoparticle loadings in the range of 1–5 wt%. Embedment conditions and timing were optimized, and the failure strain, hardness, strength, and modulus of the different samples were measured. A worsening in properties was found upon addition of the highest CNPs loading, attributed to a morphological change, including re-agglomeration of the nanoparticles. On the other hand, graphene and its derivatives, graphene oxide (GO) and reduced graphene oxide (rGO), have huge potential for energy applications due to their 2D structure, large specific surface area, high thermal conductivity, optical transparency, and enormous mechanical strength combined with intrinsic flexibility. The combination of graphene-based nanomaterials with polymers opens up an interesting research field, leading to novel nanocomposites with improved structural and functional properties

due to synergistic effects. In this regard, a brief review [23] that summarizes the most recent progress in the development of graphene/polymer nanocomposites for use in polymer solar cells is timely. These nanocomposites have already been used as transparent conducting electrodes, active layers, and interfacial layers of such type of cells. Characteristic photovoltaic parameters including the open-circuit voltage, short-circuit current density, fill factor, and power-conversion efficiency are comparatively described for the different device structures, and future perspectives in the field are discussed.

Incorporating a small amount of nanofillers into polymers is an effective approach to enhance their electrical breakdown strength [24]. However, nanoparticle surface modification and/or chemical grafting to the matrix are generally required to attain strong nanofiller-matrix interfacial adhesion and homogeneous nanoparticle dispersion. Accordingly, surface modified MgO, TiO_2, Al_2O_3, and ZnO nanoparticles have been modified by a silane coupling agent and then incorporated into dielectric polymers such as polypropylene (PP), polyester, and polyimide (PI) to fabricate nanocomposite dielectric materials [25]. In this regard, Min et al. [26] fabricated PP/Al_2O_3 nanocomposites with silane-modified Al_2O_3 contents in the range of 0.5–2 wt % via ultrasonication followed by melt blending, and their trap distribution and dc electrical breakdown properties were measured. It was found that the nanocomposites with the lowest loading displayed the best electrical breakdown strength, attributed to the formation of isolated interfacial regions that reduced the effective carrier mobility and strengthened the interaction between molecular chains, thereby hindering the charge transport and the displacement of molecular chains with occupied deep traps. Nanocomposites based on other commodity thermoplastic polymers such as polyethylene congeners (i.e., LDPE, HDPE, and XLPE) are widely used as dielectric materials, in particular for power cable insulation. Continuing progress in this topic, Pleşa et al. [27] reviewed the structure-property relationships of these nanocomposites and their electrical performance. In particular, their electrical conductivity, relative permittivity, dielectric losses, partial discharges, space charge, electrical and water tree resistance behavior, and electric breakdown are discussed in detail.

Besides the investigation on the nanoparticle dispersion and nanofiller-matrix interfacial adhesion, other parameters such as the polymer conformation, packing, and dynamics of adsorption at the matrix-nanoparticle interface have been investigated by several authors [28,29]. Continuing progress in this topic, Song et al. [30] analyzed the effect of the polymer chain topology structure on the adsorption behavior at the polymer-nanoparticle interface by coarse-grained molecular dynamics simulations. For weak polymer-nanoparticle interactions, ring chains with a closed topology structure prevail at the interfacial region, whereas for strong interactions, linear chain preferential adsorption takes place. These results are interesting for the design of high-performance nanocomposites with tailored morphology.

Another current interesting topic is the incorporation of nanoparticles into hydrogels, which leads to multifunctional nanocomposite polymers widely used in a number of applications, ranging from drug delivery to bioimaging and tissue engineering. Dannert et al. [31] reviewed different reported methods to integrate nanoparticles into hydrogels, the interactions in these composites, and how these support the enhanced mechanical and optical properties of the hydrogels, including their self-healing ability. Furthermore, the ability of the nanofillers to tailor the equilibrium swelling and elasticity of the hydrogels is discussed, as well as the use of this type of polymers as dispersing agents for nanomaterials, consequently enabling an improved performance in catalytic and sensor applications.

Acknowledgments: Ana M. Díez-Pascual wishes to acknowledge the Ministerio de Economía y Competitividad (MINECO) for a "Ramón y Cajal" Research Fellowship co-financed by the EU.

Conflicts of Interest: The authors declare no conflict of interest.

References

1. Naffakh, M.; Díez-Pascual, A.M. Thermoplastic polymer nanocomposites based on inorganic fullerene-like nanoparticles and inorganic nanotubes. *Inorganics* **2014**, *2*, 291–312. [CrossRef]

2. Tenne, R.; Rosentsveig, R.; Zak, A. Inorganic nanotubes and fullerene-like nanoparticles: Synthesis, mechanical properties, and applications. *Phys. Stat. Sol. A* **2013**, *210*, 2253–2258. [CrossRef]
3. Naffakh, M.; Díez-Pascual, A.M.; Marco, C.; Ellis, G.; Gómez-Fatou, M.A. Opportunities and challenges in the use of inorganic fullerene-like nanoparticles to produce advanced polymer nanocomposites. *Prog. Polym. Sci.* **2013**, *38*, 1163–1231. [CrossRef]
4. Díez-Pascual, A.M.; Naffakh, M. Polypropylene/glass fiber hierarchical composites incorporating inorganic fullerene-like nanoparticles for advanced technological applications. *ACS Appl. Mater. Interfaces* **2013**, *5*, 9691–9700. [CrossRef] [PubMed]
5. Díez-Pascual, A.M.; Naffakh, M. Tuning the properties of carbon fiber-reinforced poly(phenylene sulphide) laminates via incorporation of inorganic nanoparticles. *Polymer* **2012**, *53*, 2369–2378. [CrossRef]
6. Naffakh, M.; Díez-Pascual, A.M.; Marco, C.; Gómez, M.A.; Jiménez, I. Novel melt-processable poly(ether ether ketone) (PEEK)/inorganic fullerene-like WS2 nanoparticles for critical applications. *J. Phys. Chem. B* **2010**, *114*, 11444–11453. [CrossRef]
7. Silverman, T.; Naffakh, M.; Marco, C.; Ellis, G. Effect of WS_2 inorganic nanotubes on isothermal crystallization behavior and kinetics of poly(3-hydroxybutyrate-*co*-3-hydroxyvalerate). *Polymers* **2018**, *10*, 166. [CrossRef]
8. Guo, L.; Yan, H.; Chen, Z.; Liu, Q.; Feng, Y.; Ding, F.; Nie, Y. Amino Functionalization of reduced graphene oxide/tungsten disulfide hybrids and their bismaleimide composites with enhanced mechanical properties. *Polymers* **2018**, *10*, 1199. [CrossRef]
9. Tsai, C.-Y.; Lin, S.-Y.; Tsai, H.-C. butyl rubber nanocomposites with monolayer mos_2 additives: structural characteristics, enhanced mechanical, and gas barrier properties. *Polymers* **2018**, *10*, 238. [CrossRef]
10. Zheng, J.; Ye, X.; Han, D.; Zhao, S.; Wu, X.; Wu, Y.; Dong, D.; Wang, Y.; Zhang, L. Silica modified by alcohol polyoxyethylene ether and silane coupling agent together to achieve high performance rubber composites using the latex compounding method. *Polymers* **2018**, *10*, 1. [CrossRef]
11. Li, K.; Chen, X.; Wang, Z.; Xu, L.; Fu, W.; Zhao, L.; Chen, L. Temperature-responsive catalytic performance of Ag nanoparticles endowed by poly (N-isopropylacrylamide-co-acrylic acid) microgels. *Polym. Compos.* **2017**, *38*, 708–718. [CrossRef]
12. Herves, P.; Perez-Lorenzo, M.; Liz-Marzan, L.M.; Dzubiella, J.; Lu, Y.; Ballauff, M. Catalysis by metallic nanoparticles in aqueous solution: Model reactions. *Chem. Soc. Rev.* **2012**, *41*, 5577–5587. [CrossRef] [PubMed]
13. Wang, W.; Chen, X.; Zhao, C.; Zhao, B.; Dong, H.; Ma, S.; Li, L.; Chen, L.; Zhang, B. Cross-flow catalysis behavior of a PVDF/SiO_2@Ag nanoparticles composite membrane. *Polymers* **2018**, *10*, 59. [CrossRef]
14. Liu, X.; Zhu, C.; Xu, L.; Dai, Y.; Liu, Y.; Liu, Y. Green and facile synthesis of highly stable gold nanoparticles via hyperbranched polymer in-situ reduction and their application in Ag^+ detection and separation. *Polymers* **2018**, *10*, 42. [CrossRef]
15. Zhao, J.; Wu, H.; Jiang, J.; Zhao, S. Label-free fluorescence turn-on sensing for melamine based on fluorescence resonance energy transfer between CdTe/CdS quantum dots and gold nanoparticles. *RSC Adv.* **2014**, *4*, 61667–61672. [CrossRef]
16. Zhang, C.-J.; Gao, Z.-Y.; Wang, Q.-B.; Zhang, X.; Yao, J.-S.; Qiao, C.-D.; Liu, Q.-Z. highly sensitive detection of melamine based on the fluorescence resonance energy transfer between conjugated polymer nanoparticles and gold nanoparticles. *Polymers* **2018**, *10*, 873. [CrossRef]
17. Ding, Z.; Wang, C.; Feng, G.; Zhang, X. Thermo-responsive fluorescent polymers with diverse LCSTs for ratiometric temperature sensing through FRET. *Polymers* **2018**, *10*, 283. [CrossRef]
18. Gupta, V.; Bharti, V.; Kumar, M.; Chand, S.; Heeger, A.J. Polymer–polymer Förster resonance energy transfer significantly boosts the power conversion efficiency of bulk-heterojunction solar cells. *Adv. Mater.* **2015**, *27*, 4398–4404. [CrossRef]
19. Al-Asbahi, B.A. Influence of SiO_2/TiO_2 Nanocomposite on the optoelectronic properties of PFO/MEH-PPV-based OLED devices. *Polymers* **2018**, *10*, 800. [CrossRef]
20. Schottner, G. Hybrid sol-gel-derived polymers: Applications of multifunctional materials. *Chem. Mater.* **2001**, *13*, 3422–3435. [CrossRef]
21. Adnan, M.M.; Dalod, A.R.M.; Balci, M.H.; Glaum, J.; Einarsrud, M.-A. In situ synthesis of hybrid inorganic-polymer nanocomposites. *Polymers* **2018**, *10*, 1129. [CrossRef]
22. Nezhad, H.Y.; Thakur, V.K. Effect of morphological changes due to increasing carbon nanoparticles content on the quasi-static mechanical response of epoxy resin. *Polymers* **2018**, *10*, 1106. [CrossRef]

23. Díez-Pascual, A.M.; Luceño Sánchez, J.A.; Peña Capilla, R.; García Díaz, P. recent developments in graphene/polymer nanocomposites for application in polymer solar cells. *Polymers* **2018**, *10*, 217. [CrossRef]
24. Huang, X.Y.; Zhi, C.Y. *Polymer Nanocomposites: Electrical and Thermal Properties*; Springer: Basel, Switzerland, 2016; pp. 1–346.
25. Zhou, Y.; Hu, J.; Dang, B.; He, J.L. Effect of different nanoparticles on tuning electrical properites of polypropylene nanocomposites. *IEEE Trans. Dielectr. Electr. Insul.* **2017**, *24*, 1380–1389. [CrossRef]
26. Min, D.; Yan, C.; Mi, R.; Ma, C.; Huang, Y.; Li, S.; Wu, Q.; Xing, Z. Carrier Transport and molecular displacement modulated dc electrical breakdown of polypropylene nanocomposites. *Polymers* **2018**, *10*, 1207. [CrossRef]
27. Pleşa, I.; Noţingher, P.V.; Stancu, C.; Wiesbrock, F.; Schlögl, S. Polyethylene nanocomposites for power cable insulations. *Polymers* **2019**, *11*, 24. [CrossRef]
28. Crawford, M.K.; Smalley, R.J.; Cohen, G.; Hogan, B.; Wood, B.; Kumar, S.K.; Melnichenko, Y.B.; He, L.; Guise, W.; Hammouda, B. Chain conformation in polymer nanocomposites with uniformly dispersed nanoparticles. *Phys. Rev. Lett.* **2013**, *110*, 196001. [CrossRef] [PubMed]
29. Wang, Y.; Shu, X.; Liu, J.; Ran, Q. Conformational properties and the entropic barrier in the "head-on" adsorption of a single polymer chain towards a flat surface. *Soft Matter.* **2018**, *14*, 2077–2083. [CrossRef] [PubMed]
30. Song, Q.; Ji, Y.; Li, S.; Wang, X.; He, L. adsorption behavior of polymer chain with different topology structure at the polymer-nanoparticle interface. *Polymers* **2018**, *10*, 590. [CrossRef]
31. Dannert, C.; Stokke, B.T.; Dias, R.S. Nanoparticle-hydrogel composites: from molecular interactions to macroscopic behavior. *Polymers* **2019**, *11*, 275. [CrossRef]

polymers

MDPI

Article

Effect of WS_2 Inorganic Nanotubes on Isothermal Crystallization Behavior and Kinetics of Poly(3-Hydroxybutyrate-*co*-3-hydroxyvalerate)

Tyler Silverman [1], Mohammed Naffakh [1,*], Carlos Marco [2] and Gary Ellis [2]

[1] Escuela Técnica Superior de Ingenieros Industriales, Universidad Politécnica de Madrid (ETSII-UPM), José Gutiérrez Abascal 2, 28006 Madrid, Spain; tsilverman1@gmail.com

[2] Instituto de Ciencia y Tecnología de Polímeros (ICTP-CSIC), Juan de la Cierva 3, 28006 Madrid, Spain; cmarco@ictp.csic.es (C.M.); gary@ictp.csic.es (G.E.)

* Correspondence: mohammed.naffakh@upm.es; Tel.: +34-913-363-164

Received: 15 December 2017; Accepted: 6 February 2018; Published: 9 February 2018

Abstract: Nanocomposites of poly(3-hydroxybutyrate-*co*-3-hydroxyvalerate) (PHBV) and tungsten disulfide inorganic nanotubes (INT-WS_2) were prepared by blending in solution, and the effects of INT-WS_2 on the isothermal crystallization behavior and kinetics of PHBV were investigated for the first time. The isothermal crystallization process was studied in detail using various techniques, with emphasis on the role of INT-WS_2 concentration. Differential scanning calorimetry (DSC) and polarized optical microscopy (POM) showed that, in the nucleation-controlled regime, crystallization rates of PHBV in the nanocomposites are influenced by the INT-WS_2 loading. Our results demonstrated that low loadings of INT-WS_2 (0.1–1.0 wt %) increased the crystallization rates of PHBV, reducing the fold surface free energy by up to 24%. This is ascribed to the high nucleation efficiency of INT-WS_2 on the crystallization of PHBV. These observations facilitate a deeper understanding of the structure-property relationships in PHBV biopolymer nanocomposites and are useful for their practical applications.

Keywords: inorganic nanotubes; PHBV; nanomaterials; morphology; crystallization kinetics

1. Introduction

Over recent years, bio-based products have attracted increasing interest due to escalating environmental concerns and diminishing fossil resources [1]. Consequently, there is and has been a growing demand and interest, in both academic and industrial realms, to investigate biopolymers (i.e., polymeric material of non-fossil, biological origin) and develop strategies that can implement them for societal needs. Biopolymers can be broadly classified into two main categories: agropolymers, such as starch and other carbohydrates, proteins, etc., and biodegradable polymers, such as polyhydroxyalkanoates (PHAs), poly(lactic acid), etc. Biosynthetic polymers such as PHAs are linear, aliphatic polyesters that are produced by a microbial process in a sugar-based medium, where in certain bacteria they act as carbon (energy) storage banks [2]. A family of these materials from over 150 different monomers can be obtained with incredibly diverse properties [3]. Of these, polyhydroxybutyrate (PHB), polyhydroxyvalerate (PHV), and their copolymers poly(hydroxybutyrate-*co*-hydroxyvalerate) (PHBV), are commonly used matrices in bio and eco-composites [4]. Whilst PHB exhibits high stiffness and crystallinity, the incorporation of 3-hydroxyvalerate (HV) groups in a random copolymer with 3-hydroxybutyrate (HB) is a strategy used to increase the flexibility and processing capabilities of the polymer, reducing stiffness, melting point and crystallinity of the copolymer on increasing the HV content [3]. Despite improved thermal and mechanical properties, PHBV still presents some disadvantages, which include a narrow processing

window, a slow crystallization rate, and low values of strain-at-break, along with a higher cost when compared with petroleum-based synthetic polymers [5]. To solve the aforementioned limitations, methods such as physical blending or chemical structure design combined with processing conditions can be applied to improve the performance of PHA products [3,6].

Nanocomposite strategies have been suggested to overcome the inherent shortcomings of biopolymer-based materials, and nano-biocomposites obtained by introducing nanofillers into biopolymers result in very promising materials, manifesting improved thermal and mechanical properties whilst maintaining material biodegradability, without introducing toxicity [6]. These find applications mainly in packaging, agriculture, and biomedical or hygiene devices, and represent an emerging alternative towards environmentally benign and economically viable chemical production [7]. Depending on the processing conditions from the melt into the solid state, biopolymeric materials may partially crystallize into a semicrystalline morphology that affects the aforementioned relevant properties. For this reason, numerous studies have been undertaken to characterize the crystallization behavior and to control the crystallinity, the crystallization kinetics, the spherulitic superstructure, or the crystal polymorphism, employing calorimetry and optical microscopy techniques [3,8]. In particular, calorimetry enables quantification of transition temperatures and enthalpies in isothermal and non-isothermal modes. Lorenzo et al. [8] have suggested a methodology for the minimization of possible errors associated with data manipulation in the measurement and analysis of conventional experimental DSC data. Isothermal crystallization experiments performed by DSC showed an increase in the crystallization kinetics of polycaprolactone (PCL) with increases in carbon nanotubes content as a consequence of the supernucleation effect [9]. Making use of fast scanning chip calorimeters and combining both approaches allowed them to shed further light on fundamental details of the polymer-crystallization process [10]. Furthermore, systematic studies of nucleation, crystallization, melting, and reorganization are made possible for a large number of polymers. In particular, promising research serving as a conceptual study to quantitatively approach the link between the condition of cooling the melt of crystallizable polymers, the formation of crystal nuclei and the cold-crystallization behavior have been successfully developed [11].

The enhancement of biodegradability, biocompatibility, thermal conductivity and mechanical proprieties of biopolymeric materials can be achieved by adding nanofillers [12–15]. On the other hand, the use of layered transition metal dichalcogenide nanofillers such as tungsten and molybdenum disulfide (WS_2, MoS_2) inorganic fullerenes (IFs) and inorganic nanotubes (INTs) [16,17] is expected to produce advanced nanocomposite materials [18,19]. As well as unique electronic and mechanochemical behavior, these novel nanomaterials show remarkable properties like high impact resistance and flexibility under tensile stress, excellent tribological behavior, superior fracture resistance to shockwaves, and simple and relatively inexpensive fabrication methods [20]. Recently, the incorporation of WS_2 in polymer systems has demonstrated a range opportunities for many new applications. For example, IF-WS_2 nanoparticles were used to produce advanced nylon-6 nanocomposites [21]. In particular, it was shown that introducing IF-WS_2 nanoparticles into nylon-6 provoked a strong nucleation effect which induced changes in the crystal growth process. In the same way, the addition of low WS_2 loadings strongly increased the crystallization rate of PHBV [22]. For these systems, drawing induced during melt crystallization process has been shown to vary the crystalline structure (i.e., from α to β) leading to improved mechanical properties in melt-spun bio-based PHBV fibers [23]. Similarly, WS_2 nanotubes (INT-WS_2) have been shown to improve the thermal, mechanical and tribological properties of biopolymers like poly(3-hydroxybutyrate) (PHB) [24] and poly(L-lactic acid) (PLLA) [25], and the bio-applied polymer poly(ether ether ketone) (PEEK) [26]. Additionally, from an environmental viewpoint, INT-WS_2 have demonstrated much lower cytotoxicity than other nanoparticle fillers, such as silica or carbon black [27] and have shown promise with respect to biocompatibility in the case of salivary gland cells [28].

The present work continues progress in this field and is centered on the incorporation of INT-WS_2 as nanoreinforcements to improve the processability and performance of PHBV. Scanning electron

microscopy (SEM) observations revealed that an excellent dispersion of highly efficient INT-WS_2 nucleating agents was achieved, leading to composites with substantially enhanced thermal and mechanical properties [29]. However, to date the influence of the nanofiller on the crystallization behavior and kinetics of PHBV under isothermal conditions has not been investigated. Here, this process is studied in detail using differential scanning calorimetry (DSC) and polarized optical microscopy (POM) techniques, with particular emphasis on the role of INT-WS_2 concentration. The research reported provides a better understanding of the structure-property relationship of PHBV biopolymer nanocomposites, with an outlook towards extending their practical applications.

2. Experimental Section

2.1. Materials and Processing

The PHBV biopolymer employed, containing 2.0 wt % hydroxyvalerate (HV) with a reported Mw = 410 kg mol^{-1}, was obtained in powder form from Goodfellow Cambridge, Ltd. (Huntingdon, UK) and used as received. The tungsten disulfide inorganic nanotubes (INT-WS_2) were provided by NanoMaterials, Ltd. (Yavne, Israel) and used without chemical modification. Several formulations of PHBV/INT-WS_2 (0.1, 0.5 and 1.0 wt %) nanocomposites were prepared [29]. The nanofiller was dispersed in a solution of PHBV in chloroform (HPLC grade, Sigma-Aldrich Química SL, Madrid, Spain), which was subsequently precipitated in methanol (HPLC grade, Sigma-Aldrich Química SL, Madrid, Spain), then filtered and dried in a vacuum oven at 50 °C for 24 h.

2.2. Characterization Techniques

2.2.1. Differential Scanning Calorimetry (DSC)

The isothermal crystallization and melting behavior of the new nanocomposites were studied using a Perkin Elmer DSC7/Pyris differential scanning calorimeter (Perkin-Elmer España SL, Madrid, Spain). The instrument was calibrated for temperature and heat flow using high purity indium and zinc standard. A tau lag calibration of the instrument for different heating rates was performed using indium. The experimental and theoretical procedures used in this study are similar to those employed in our previous publications for PLLA/INT-WS_2 [25] and nylon-6/IF-WS_2 [21]. In this case, samples of 6–11 mg were placed in sealed 40 μL aluminum pans under a flowing nitrogen atmosphere. Before cooling, the samples were maintained for 5 min at 180 °C to erase any prior thermo-mechanical history and to assure maximum thermal stability of the components as well as the reproducibility of the results. Then the molten samples were cooled at fastest achievable rate of 64 °C min^{-1} to specific isothermal crystallization temperatures (T_c) and maintained until crystallization was completed (i.e., complete return to baseline), and the heat evolved during crystallization was recorded as a function of time at selected T_c. Pyris DSC7 kinetic software was used to obtain partial areas from the data points of the exotherm, corresponding to a given degree of the total crystalline transformation. The crystallinity of PHBV in the samples was determined, after normalizing for filler content, using a value of ΔH_m for 100% crystalline PHBV (low HV content) of 146 J g^{-1} [3,30]. The isothermal crystallization step was followed by a heating step up to 180 °C at a rate of 5 °C min^{-1}, and melting temperatures (T_m) were taken as the peak maxima of the melting endotherms.

2.2.2. Polarized Optical Microscopy (POM)

Polarized optical microscopy (POM) was used to investigate the spherulitic morphology of neat PHBV and the PHBV/INT-WS_2 nanocomposites employing a Mettler FP-80HT (Mettler-Toledo SAE, Barcelona, Spain) hot stage on a Reichert Zetopan Pol polarizing microscope equipped with a Nikon FX35A 35 mm SLR camera. The isothermal crystallization cycles consisted in a 5-min hold period at 180 °C followed by rapid cooling at 20 °C min^{-1} to specific crystallization temperatures, T_c = 110 °C,

112 °C and 122 °C. Samples were maintained at T_c for enough time to allow the monitorization of the spherulitic growth process.

3. Results

3.1. Isothermal Crystallization

The physical and mechanical properties of semicrystalline polymers depend on the morphology, the crystalline structure and the degree of crystallinity. Much effort has been devoted to study the isothermal crystallization kinetics of new PHBV/INT-WS_2 bionanocomposites, with a view to control the crystallization rate, degree of crystallinity and, consequently, its morphology and properties. In this respect, the isothermal melt crystallization kinetics of neat PHBV and its nanocomposites was investigated with DSC over a wide range of crystallization temperatures from 94 °C to 130 °C. The curves in Figure 1 indicate the total time for the complete crystallization process at the above-mentioned temperatures and are truncated at the time when no further crystallization was evident by DSC. Figure 1a shows that at higher T_c more time is required to fully crystallize the pure PHBV sample. At lower T_c the curves shifted to shorter times, indicating increased crystallization rates directly proportional to the isothermal crystallization temperature employed. The crystallization behavior of the nanocomposites with temperature was similar, Figure 1b–d. These results are consistent with the theory of crystallization kinetics, implying that as the supercooling (i.e., the difference between the melting and crystallization temperatures) increases, the crystallization rate accelerates and the crystallization exotherm becomes sharper, controlled in turn by the evolution of the number of crystal nuclei formed during crystallization process of the biopolymer matrix. In previous studies on the nucleation behavior of PLLA reported by Androsch et al. [11], it was shown that isothermal formation of crystal nuclei at high supercooling of the melt can be quantified by the analysis of crystallization at elevated temperature.

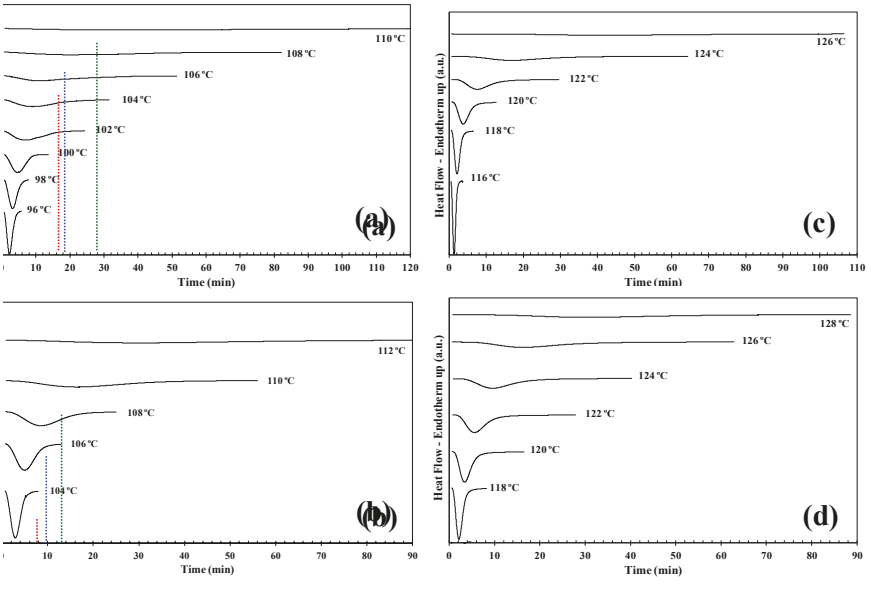

Figure 1. Differential scanning calorimetry (DSC) thermograms of isothermal crystallization of (**a**) PHBV; (**b**) poly(3-hydroxybutyrate-*co*-3-hydroxyvalerate)/ tungsten disulfide inorganic nanotubes (PHBV/INT-WS_2) (0.1 wt %); (**c**) PHBV/INT-WS_2 (0.5 wt %) and (**d**) PHBV/INT-WS_2 (1.0 wt %) obtained at the indicated crystallization temperatures.

By comparing Figure 1a with Figure 1b–d, it is clear that at the T_c the exothermic peaks for the nanocomposites are in all cases sharper than those for pure PHBV indicating that the INT-WS_2 accelerates the crystallization process of the polymer in the nanocomposites. The reduction in the time to reach overall crystallization can be employed to describe this acceleration process. For example, the PHBV copolymer without INT-WS_2 fully crystallized after approximately 120 min at T_c = 110 °C, whereas for the 0.5 wt % nanocomposite material it took less than 4 min at T_c = 116 °C (i.e., at a temperature of 4 °C higher than that of the pure polymer). From the data it can be seen that the incorporation of low INT-WS_2 weight-fractions in PHBV nanocomposite allows the crystallization to take place at higher temperatures and over larger intervals (96–110 °C for PHBV, 116–126 °C for PHBV/INT-WS_2 (0.1 wt %), 104–112 °C PHBV/INT-WS_2 (0.5 wt %) and 118–128 °C for PHBV/INT-WS_2 (1.0 wt %).

The relative crystallinity, $X(t)$, can be defined by the following expression:

$$X(t) = \frac{\int_0^t \frac{dH(t)}{dt} dt}{\int_0^{t\infty} \frac{dH(t)}{dt} dt} = \frac{\Delta H_t}{\Delta H_\infty} \quad (1)$$

where dH/dt is the heat flow rate; ΔH_t is the heat generated at time t; ΔH_∞ is the total heat generated to the end of the crystallization process. The classical Avrami Equation (2) was employed to describe the isothermal crystallization kinetics:

$$X(t) = 1 - \exp(-kt^n) \quad (2)$$

where n is the Avrami exponent, which is a constant that depends on the nucleation mechanism and type of crystal growth, and k is the Avrami rate constant associated with nucleation and growth rate parameters. Equation (2) can be rewritten as:

$$\log[-\ln(1 - X(t))] = \log k + n \log t \quad (3)$$

and the values of log $[-\ln(1 - X(t))]$ plotted versus log t, allowing the Avrami exponent n and the crystallization rate constant k to be calculated from the slope and intercept of the linear fit, respectively. It is rare that the Avarmi equation can be used to describe the entire crystallization process, but is widely accepted as valid at the early stage of crystallization, as previously reported in our studies for nylon-6/IF-WS_2 [21] and PLLA/INT-WS_2 [25]. Linear regressions of these straight lines at low levels of crystalline transformation (5–40%) yielded the Avrami exponents (n) shown in Table 1. As an example, Figure 2 illustrates the Avrami plots for both neat PHBV and PHBV/INT-WS_2 (1.0 wt %) at different crystallization temperatures and the data are represented in Table 1. The average values obtained for n varied with the INT-WS_2 concentration: $n \approx 3.0$ for neat PHBV, $n \approx 3.3$ for PHBV/INT-WS_2 (0.1 wt %), $n \approx 4.2$ for PHBV/INT-WS_2 (0.5 wt %) and $n \approx 4.4$ for PHBV/INT-WS_2 (1.0 wt %). According to the ideal case of the Avrami equation for nucleated crystallization with three-dimensional crystal growth, the value of the exponent should be n = 3 [31]. A value of n = 4 indicates ideal three-dimensional growth with a linear increase in nucleation sites over time due to heterogeneous nucleation, which was expected for the binary composite materials with the addition of nanoparticles. However, the ideal state was not achieved during the crystallization process probably due to athermal crystallization and/or imperfections within the polymer network (entanglements, single chains transversing multiple lamellae, etc.) as well as secondary crystallization processes, mixed nucleation modes and the change in material density [3]. Moreover, even some experimental factors such as an error introduced in the determination of the onset of crystallization or induction time, the establishment of the baseline and incomplete isothermal crystallization data, the effect of the cooling rate from the melt to the isothermal crystallization temperature and the conversion range employed for the fitting can lead to non-integer values of n [8]. In addition, the supernucleation effect of the nanotubes could also be connected to the variation of the n exponents [9]. The values of n reported in the literature for PHBV systems are

dispersed, ranging from 1.7 to 4 [3]. Liu et al. [32] also obtained n values of 2.0–2.2 for P(3HB-*co*-3HV) (6.6 mol % HV). Chan et al. [33], however, obtained n values across a range of HV contents of 2.35–2.7, and Saad et al. [34] obtained an exponent of 3.8 for thin P(3HB) films. Meanwhile, Xu et al. [35] applied the Avrami equation to IR data for isothermal crystallization of P(3HB) and Nodax (P(3HB-*co*-3HHx)) and obtained an n value of 1.72 and 2.08 respectively, indicating that a heterogeneous nucleation mechanism exists in this case. Nonetheless, the increase of the Avrami exponent compared to the neat sample did justify the fact that the initial nucleation stage was enhanced by the nanoparticles. With the linearized Avrami plots, the intercept value is ln(k) and the overall rate constant (k) is easily determined.

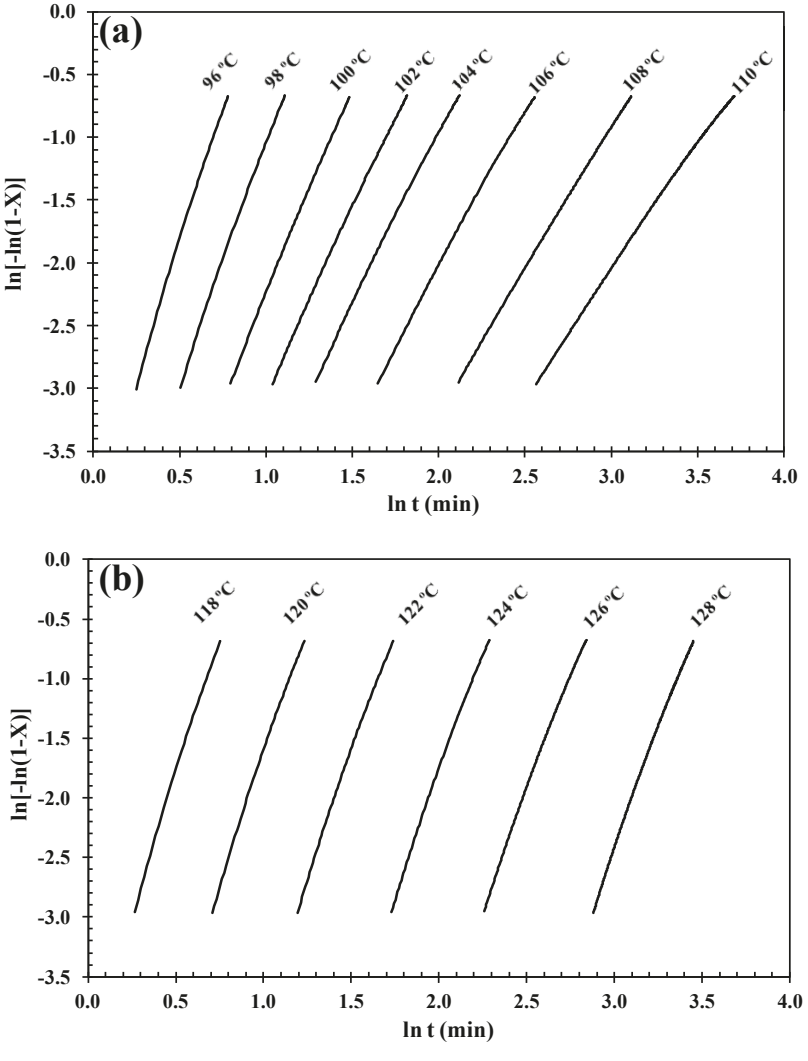

Figure 2. Avrami plots of the crystallization of (**a**) PHBV and (**b**) PHBV/INT-WS_2 (1.0 wt %) as a function of the crystallization temperature (T_c).

Table 1. Isothermal crystallization parameters of PHBV and PHBV/INT-WS_2 nanocomposites. T_c = crystallization temperature, $\tau_{0.5}$ = the time needed to reach 50% crystalline transformation, n = Avrami exponent, k_n = overall rate constant, T_m = melting temperature and σ_e = fold surface free energy. (*) The main error arises from baseline selection during data processing. We estimate the following errors: ±1 J/g for (ΔHt) and ±100 for $\Delta(\tau_{0.5})$.

INT-WS_2 Content (wt %)	T_c (°C)	$\tau_{0.5}$ (min)	n	$k_n \times 10^5$	T_{m1}/T_{m2} (°C)	σ_e (erg cm^{-2})
0	96	2.4	4.4 ± 0.1	15.65	149.6/160.0	75 ± 3
	98	3.3	3.8 ± 0.1	7.31	148.5/159.5	
	100	4.9	3.3 ± 0.1	3.71	147.5/158.0	
	102	6.9	2.9 ± 0.2	2.51	147.1/157.3	
	104	9.5	2.7 ± 0.1	1.5	146.9/156.8	
	106	15.1	2.5 ± 0.1	0.77	145.7/154.9	
	108	26.3	2.3 ± 0.1	0.42	144.7/153.6	
	110	49.3	2.0 ± 0.2	0.28	145.2/155.8	
0.1	104	3	4.0 ± 0.1	8.49	145.2/155.8	57 ± 2
	106	5.2	3.6 ± 0.1	1.83	144.2/154.4	
	108	9.3	3.3 ± 0.2	0.43	144.1/153.7	
	110	19	3.0 ± 0.1	0.1	144.4/153.0	
	112	37.2	2.7 ± 0.1	0.05	144.8/152.3	
0.5	116	1.4	5.2 ± 0.1	145.23	156.7/165.2	71 ± 3
	118	2.2	4.6 ± 0.2	17.5	154.6/165.2	
	120	4.1	4.2 ± 0.1	1.84	153.6/161.2	
	122	8.6	3.9 ± 0.1	0.16	153.3/160.0	
	124	19.5	3.7 ± 0.2	0.01	153	
	126	47.6	3.8 ± 0.2	0.003	152.5	
1	118	2.3	4.6 ± 0.1	14.37	152.4/160.8	58 ± 2
	120	3.8	4.3 ± 0.1	2.29	152.7/160.3	
	122	6.3	4.1 ± 0.1	0.34	153.1/160.0	
	124	10.8	4.1 ± 0.2	0.04	153.8/160.3	
	126	19	3.9 ± 0.2	0.01	154	
	128	34.9	4.0 ± 0.2	0.005	154.7	

Another common way to estimate the overall rate constant, also k, is by the well-fitting logarithmic representation of the following expression [36]:

$$k_n = \frac{\ln 2}{(\tau_{0.5})^n} \quad (4)$$

where $\tau_{0.5}$ is the time needed to reach 50% crystalline transformation. Values of k_n obtained for both neat PHBV and its nanocomposites are represented in Figure 3, where the effect of the crystallization temperature (T_c) and INT-WS_2 concentration on the overall crystallization rate can be observed (Table 1). By increasing T_c from 96 °C to 110 °C, the crystallization of neat PHBV becomes hindered and k_n decreases due to the excessive mobility of the polymer chains that reduces the development of nucleation sites at the higher temperature. A similar phenomenon takes place for PHBV/INT-WS_2 (1.0 wt %) in the range of 118–128 °C. The values of k_n for the nanocomposites were found to be higher in all cases than those for PHBV. Whilst PHBV presented a value of $k_n \approx 2.51 \times 10^{-5}$ at T_c = 102 °C, in the case of the nanocomposites, the values of k_n of around the same order were obtained at 120 °C for a concentration of 1.0 wt % of INT-WS_2. The results show that INT-WS_2 nanoparticles are effective nucleating agents for PHBV, promoting the nucleation of the crystallization of the polymer chains at small nanofiller loadings, without altering its crystal structure [29]. Additionally, the presence of increasing content of INT-WS_2 also improves the crystallinity of PHBV, as can be seen in Figure 4.

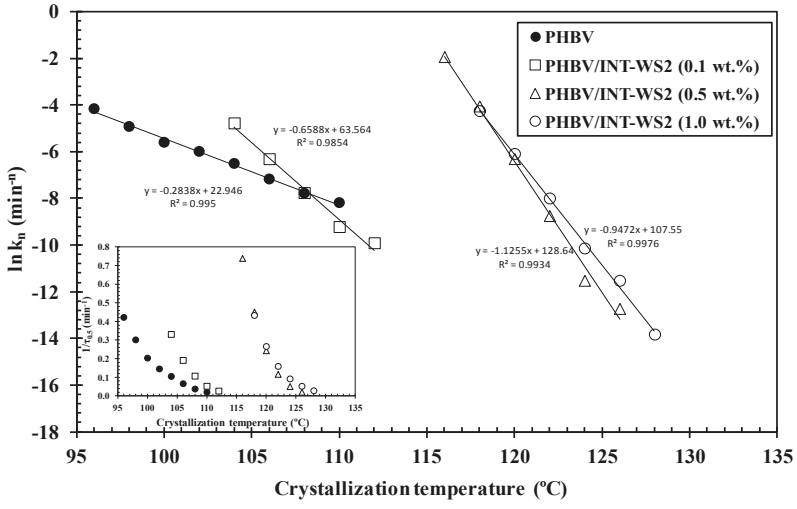

Figure 3. Logarithmic plots of the global rate constant (k) of PHBV/INT-WS_2 nanocomposites as a function of the crystallization temperature (T_c); the inset represents the inverse of crystallization half-time ($1/\tau_{0.5}$) as a function of T_c.

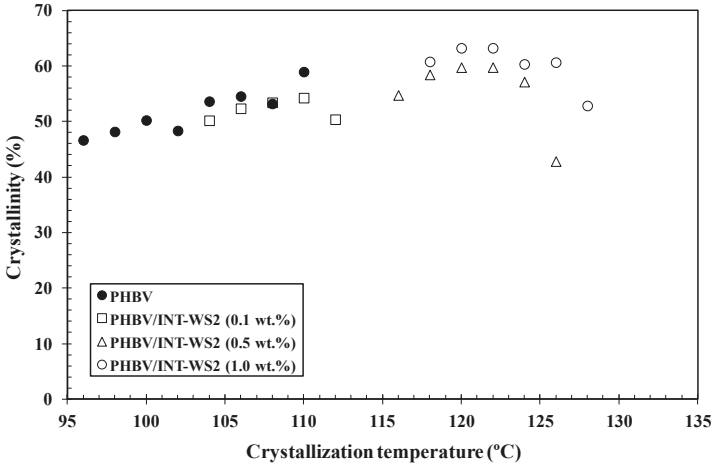

Figure 4. Variation of the crystallinity of isothermal crystallization of PHBV/INT-WS_2 nanocomposites as a function of the crystallization temperature (T_c).

Hereafter, the melting behavior of PHBV/INT-WS_2 will be presented in order to understand the dependence of the double melting temperatures of PHBV with composition. Figure 5 shows the DSC melting curves obtained in this study after isothermal crystallization at different T_c for PHBV/INT-WS_2 (1.0 wt %), where a clear double melting behavior was observed and the results for all samples are summarized in Table 1. No clear difference was observed in the evolution of the double melting temperature with INT-WS_2 due the large shift of the crystallization interval of PHBV to higher temperature and direct temperature comparisons were not feasible (i.e., the measurable temperature range for neat PHBV was 96–110 °C, whereas for the 1.0 wt % nanocomposite, the measurable temperature range was 118–128 °C).

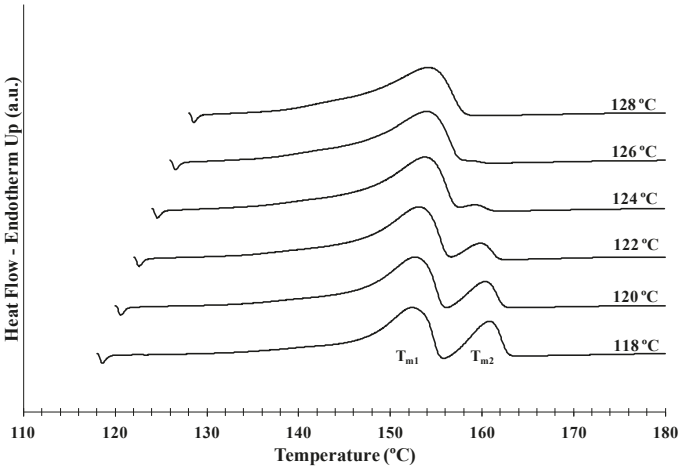

Figure 5. Melting DSC thermograms of PHBV/INT-WS_2 (1.0 wt %) nanocomposite obtained at a heating rate of 5 °C min^{-1} after isothermal crystallization at the indicated temperatures.

3.2. Crystallization Activation Energy

For further insight into the crystallization behavior of PHBV and its nanocomposites, the free energy of folding (σ_e) was calculated using the Lauritzen and Hoffman (L–H) model [37,38], previously adopted to calculate the isothermal crystallization activation energy of nylon-6/IF-WS_2 [21] and PLLA/INT-WS_2 [25]. In this approximation, σ_e represents the energy required to fold the polymer chains during crystallization. In agreement with the kinetic theory of crystallization and independent regime type, the crystallization rate (G) can be expressed as:

$$G = G_0 \exp[-\frac{U^*}{R(T_c - T_0)}] \exp[-\frac{K_{g(III)}}{fT_c\Delta T}] \quad (5)$$

where G_0 is a temperature independent pre-exponential term, U^* is the activation energy required for chain movement (2.45×10^6 cal $kmol^{-1}$), T_0 is the temperature at which there is no chain motion (usually $T_0 = T_g - 51.6$ K), R is the universal gas constant, ΔT is the undercooling, or $T_m^0 - T_c$ where T_m^0 is the equilibrium melting temperature, f is a correction factor that accounts for the variation of the equilibrium melting enthalpy (ΔH_m^0) with temperature, defined as $2T_c/(T_c + T_m^0)$, and K_g is the nucleation constant for Regime III [3,39], which can be expressed by:

$$K_{g(III)} = \frac{4b_0\sigma_u\sigma_e T_m^0}{k_B\Delta H_m^0} \quad (6)$$

where k is the Boltzmann constant, 1.38×10^{-26} kJ K^{-1}, b_0 = 7.2 nm and corresponds to the thickness of a single crystalline monolayer added during growth [3], and σ_e and σ_u are the basal and lateral interfacial free energies of the crystallite, respectively. The logarithmic representation of the first term of Equation (5) versus $1/fT_c\Delta T$ is presented in Figure 6 for all the samples analyzed, and the linear fits observed support unique regime behavior. The values of $K_{g(III)}$ were calculated from the slopes of these plots.

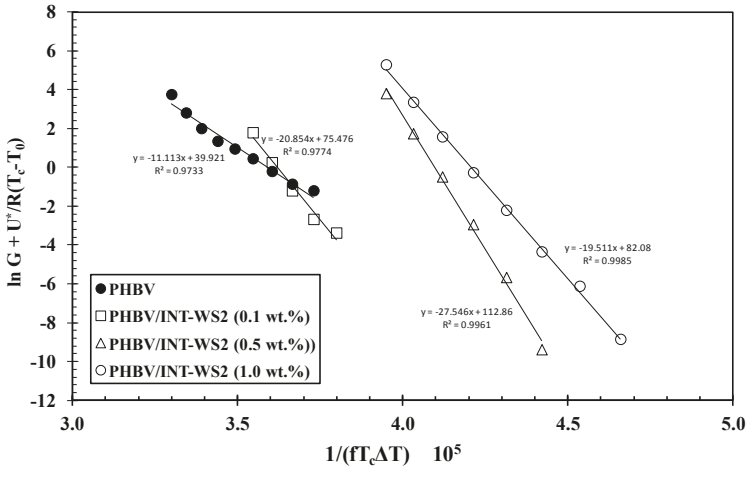

Figure 6. Logarithmic plots of Lauritzen and Hoffman (L–H) equation for PHBV/INT-WS_2 nanocomposites.

Although the literature values found for ΔH_m vary considerable since they are fundamentally conditioned by the determination method [3], the influence of this experimental variability in the comparative analysis of the values of the interfacial free energies can be eliminated by applying the Hoffman approximation [38], which determines the interfacial free energy using the following expression:

$$\sigma_u = \alpha \Delta H_m^0 \sqrt{a_0 b_0} \quad (7)$$

where α = 0.24 (for high melting polyesters) and $a_0 b_0$ = 38.01 Å [40] that corresponds to the chain cross-section in the PHBV crystal. Thus, the basal interfacial free energy can be derived from the following equation:

$$\sigma_e = \frac{k_B K_{g(III)}}{4 b_0 T_m^0 \alpha \sqrt{a_0 b_0}} \quad (8)$$

Under these considerations and based on our previous studies of the isothermal crystallization of polymer/WS_2 systems [21,25], the values of σ_e obtained for PHBV, PHBV/INT-WS_2 (0.1 wt %), PHBV/INT-WS_2 (0.5 wt %) and PHBV/INT-WS_2 (1.0 wt %) are around 75, 57, 71 and 58 erg cm^{-2}, respectively. There is a clear trend for decreasing values of σ_e as the INT-WS_2 content is increased. From these results, we can conclude that between around 6–24% lower energy is required to generate crystalline nuclei of PHBV, which in turn also promotes the formation of new PHBV crystal surfaces. This excellent matching suggests that PHBV crystals might grow on the INT-WS_2 surface by an epitaxial mechanism in absence of the chemical interaction between the INT-WS_2 and PHBV. More in-depth experiments will be conducted to verify this proposal in a future study.

3.3. Spherulitic Growth Analysis from POM Observation

Optical light microscopy images of crystals produced during the isothermal crystallization of PHBV and its nanocomposite containing INT-WS_2 were obtained. As an example, Figures 7 and 8 shows the spherulitic morphology of neat PHBV and PHBV/INT-WS_2 (1.0 wt %) isothermally crystallized at 100 °C and 122 °C, respectively.

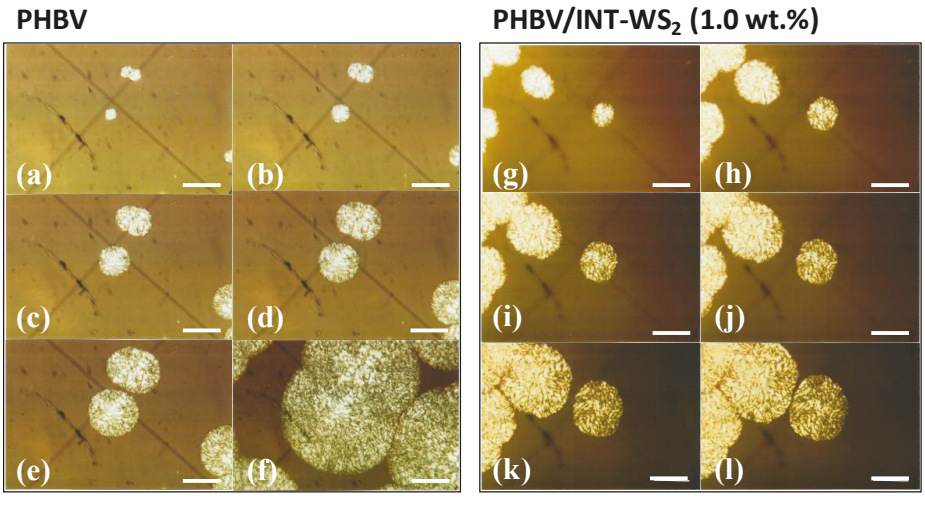

Figure 7. POM images of PHBV/INT-WS_2 nanocomposites. PHBV: (**a**–**f**) are images taken at 8 min; 12 min; 23 min; 30 min; 37 min and after 60 min rapidly cooled to 80 °C, respectively; and PHBV/INT-WS_2 (1.0 wt %): (**g**–**l**) are images taken at 4 min; 5 min; 6 min; 7 min, 8 min and 10 min, respectively. Scale bar 100 μm.

The mainly circular superstructures are indicative of the formation of a central nucleus followed by radial, outward growth, as expected. In Figure 7e crystal diameters of approximately 130 μm were observed after 37 min and in Figure 7k crystal diameters of 140 μm were seen after only 8 min. This observation further confirms the acceleration of the crystallization process of PHBV by incorporation of INT-WS_2. Another effect observed in the nucleated systems was an average decrease in crystal diameters of the neighboring spherulites before impingement. This was due to a higher density of nucleation sites and faster crystal formation compared to the neat copolymer. Assuming linear, constant growth rates, a linear slope of the growth diameter with respect to time for the four samples clearly indicated that crystal growth is faster in the samples containing INT-WS_2 than in the pure PHBV sample (Figure 8). The crystal growth rates for neat PHBV are 0.54 and 0.92 μm min^{-1} at T_c = 110 °C and 112 °C, respectively. The crystal growth rates for the 0.1, 0.5 and 1.0 wt % nanocomposites are 2.61, 4.48, and 8.62 μm min^{-1}, which is sixteen times faster for the 1.0 wt % sample compared to the neat polymer at the two different T_c values. Another way to interpret this figure is by comparing the time required for the spherulites to reach a certain diameter. To reach a diameter of, for example, 35 μm at T_c = 122 °C, inorganic nanotube fractions of 1.0 wt %, a 0.5 wt %, and 0.1 wt % in PHBV, needed approximately 4, 8, and 13 min, respectively. However, a neat PHBV sample requires around 38 and 65 min for T_c = 110 °C and 112 °C, respectively. This is another clear indication of the increase in the crystallization rate of PHBV due to the incorporation of the well-dispersed INT-WS_2 nanofiller. In particular, the increasing slope of the growth rate of the spherulite radii as a function of INT-WS_2 concentration may be due to the increased nucleation sites available thus facilitating accelerated growth in either case. More research would be required.

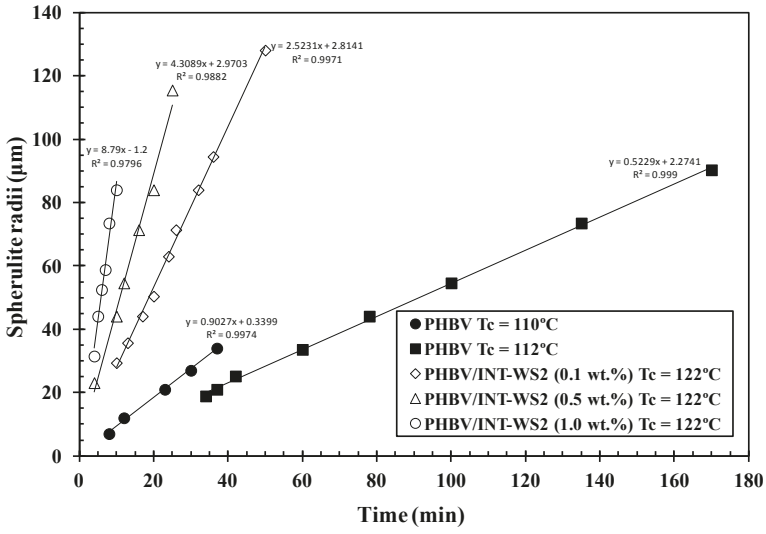

Figure 8. Isothermal spherulitic radii of PHBV/INT-WS_2 nanocomposites obtained at the indicated crystallization temperatures.

4. Conclusions

From the melt-crystallization measurements, it was shown that INT-WS_2 strongly affect the crystallization of PHBV polymer. INT-WS_2 accelerate the crystallization process of PHBV in the nanocomposites and shift the crystallization temperature/interval for PHBV to higher temperatures with increasing INT-WS_2 content. The experimental data fitted very well to the Avrami kinetic model. In particular, it was found that the value of the Avrami exponent n for PHBV/INT-WS_2 nanocomposites increased compared to that for neat PHBV, and the analysis of the activation energy of crystallization regime III using the Lauritzen and Hoffman (L–H) model showed that for the PHBV/INT-WS_2 nanocomposites, the fold surface free energy (σ_e) of PHBV chains decreased with increasing INT-WS_2 content. Similarly, the variation of the spherulitic radii of PHBV with crystallization time and concentration of nanofiller, calculated from the POM micrographs, also supports the spherulite growth-accelerating effect of PHBV. While the crystallization occurred at much higher temperatures with the incorporation of INT-WS_2, the direct comparisons of crystallization rates were not quantifiable at equivalent temperatures because of the acceleration effect of the doped materials. This new knowledge obtained from the crystallization kinetics of the PHBV biopolymer and its nanocomposites can provide an essential benchmark for optimizing the design and processing of PHBV-based thermoplastic materials with desirable properties.

Acknowledgments: This work was supported by the Spanish Ministry Economy and Competitivity (MINECO), Projects MAT2013-41021-P and MAT2017-84691-P. Mohammed Naffakh would also like to acknowledge the MINECO for a 'Ramón y Cajal' Senior Research Fellowship.

Author Contributions: Mohammed Naffakh conceived and designed the work; Tyler Silverman performed the DSC experiments; Carlos Marco performed the POM experiments; All authors contributed to the scientific discussion and Mohammed Naffakh, Tyler Silverman and Gary Ellis wrote the paper.

Conflicts of Interest: The authors declare no conflict of interest.

References

1. Gross, R.A.; Kalra, B. Biodegradable polymers for the environment. *Science* **2002**, *297*, 803–807. [CrossRef] [PubMed]
2. Keshavarz, T.; Roy, I. Polyhydroxyalkanoates: Bioplastics with a green agenda. *Curr. Opin. Microbiol.* **2010**, *13*, 321–326. [CrossRef] [PubMed]
3. Laycock, B.; Halley, P.; Pratt, S.; Werker, A.; Lant, P. The chemo-mechanical properties of microbial polyhydroxyalkanoates. *Prog. Polym. Sci.* **2014**, *39*, 397–442. [CrossRef]
4. Chen, G.Q. A microbial polyhydroxyalkanoates (PHA) based bio- and materials industry. *Chem. Soc. Rev.* **2009**, *38*, 2434–2446. [CrossRef] [PubMed]
5. Sudesh, K.; Abe, H.; Doi, Y. Synthesis, structure and properties of polyhydroxyalkanoates: Biological polyesters. *Prog. Polym. Sci.* **2000**, *25*, 1503–1555. [CrossRef]
6. Wang, S.; Chen, W.; Xiang, H.; Yang, J.; Zhou, Z.; Zhu, M. Modification and potential application of short-chain-length polyhydroxyalkanoate (SCL-PHA). *Polymers* **2016**, *8*, 273. [CrossRef]
7. Reddy, M.M.; Vivekanandhan, S.; Misra, M.; Bhati, S.K.; Mohanty, A.K. Biobased plastics and bionanocomposites: Current status and future opportunities. *Prog. Polym. Sci.* **2013**, *38*, 1653–1689. [CrossRef]
8. Arnaldo, T.L.; Arnal, M.L.; Albuerne, J.; Müller, A.J. DSC isothermal polymer crystallization kinetics measurements and the use of the Avrami equation to fit the data: Guidelines to avoid common problems. *Polym. Test.* **2007**, *26*, 222–231.
9. Trujillo, M.; Arnal, M.L.; Müller, A.J.; Mujica, M.A.; Urbina de Navarro, C.; Ruelle, B.; Dubois, P. Supernucleation and crystallization regime change provoked by MWNT addition to poly(ε-caprolactone). *Polymer* **2012**, *53*, 832–841. [CrossRef]
10. Toda, A.; Androsch, R.; Schick, C. Insights into polymer crystallization and melting from fast scanning chip calorimetry. *Polymer* **2016**, *91*, 239–263. [CrossRef]
11. Androsch, R.; Naeem Iqbal, H.M.; Schick, C. Non-isothermal crystal nucleation of poly (L-lactic acid). *Polymer* **2015**, *81*, 151–158. [CrossRef]
12. Wu, D.; Lin, D.; Zhang, J.; Zhou, W.; Zhang, M.; Zhang, Y.; Wang, D.; Lin, B. Selective localization of nanofillers: Effect on morphology and crystallization of PLA/PCL blends. *Macromol. Chem. Phys.* **2011**, *212*, 613–626. [CrossRef]
13. Armentano, I.; Marinucci, L.; Dottori, M.; Balloni, S.; Fortunati, E.; Pennacchi, M.; Becchetti, E.; Locci, P.; Kenny, J.M. Novel poly(L-lactide) PLLA/SWNTs nanocomposites for biomedical applications: Material characterization and biocompatibility evaluation. *J. Biomater. Sci. Polym. Ed.* **2011**, *22*, 541–556. [CrossRef] [PubMed]
14. Lizundia, E.; Oleaga, A.; Salazar, A.; Sarasua, J.R. Nano- and microstructural effects on thermal properties of poly (L-lactide)/multi-wall carbon nanotube composites. *Polymer* **2012**, *53*, 2412–2421. [CrossRef]
15. Terzopoulou, G.Z.; Bikiaris, D.; Triantafyllidis, K.S.; Diamanti, E.; Gournis, D.; Klonos, P.; Giannoulidis, E.; Pissis, P. Evaluation of the formed interface in biodegradable poly(L-lactic acid)/graphene oxide nanocomposites and the effect of nanofillers on mechanical and thermal properties. *Thermochim. Acta* **2014**, *597*, 48–57.
16. Naffakh, M.; Díez-Pascual, A.M.; Marco, C.; Ellis, G.; Gómez-Fatou, M.A. Opportunities and challenges in the use of inorganic fullerene-like nanoparticles to produce advanced polymer nanocomposites. *Prog. Polym. Sci.* **2013**, *38*, 1163–1231. [CrossRef]
17. Naffakh, M.; Díez-Pascual, A.M. Thermoplastic polymer nanocomposites based on inorganic fullerene-like nanoparticles and inorganic nanotubes. *Inorganics* **2014**, *2*, 291–312. [CrossRef]
18. Tenne, R.; Margulis, L.; Genut, M.; Hodes, G. Polyhedral and cylindrical structures of tungsten disulphide. *Nature* **1992**, *360*, 444–445. [CrossRef]
19. Margulis, L.; Salitra, G.; Tenne, R.; Talianker, M. Nested fullerene-like structures. *Nature* **1993**, *365*, 113–114. [CrossRef]
20. Zak, A.; Sallacan-Ecker, L.; Margolin, A.; Genut, M.; Tenne, R. Insight into the Growth Mechanism of WS_2 Nanotubes in the Scaled-up Fluidized-bed Reactor. *Nano* **2009**, *4*, 91–98. [CrossRef]
21. Naffakh, M.; Marco, C.; Gómez, M.A.; Jiménez, I. Novel melt-processable nylon-6/inorganic fullerene-like WS_2 nanocomposites: Complex isothermal crystallization kinetics and melting behaviour. *Mater. Chem. Phys.* **2011**, *128*, 265–273. [CrossRef]

22. Chen, Z.; Hu, Z.; Xiang, H.; Chen, W.; Ni, Z.; Zhu, M. Crystallization behavior of poly(3-hydroxybutyrate-*co*-3-hydroxyvalerate) with WS_2 as nucleating agent. *Mater. Sci. Forum* **2017**, *898*, 2239–2245. [CrossRef]
23. Chen, Z.; Xiang, H.X.; Hu, Z.; Ni, Z.; Zhu, M. Enhanced mechanical properties of melt-spun bio-based PHBV fibers: Effect of heterogeneous nucleation and drawing process. *Acta Polym. Sin.* **2017**, *7*, 1121–1129.
24. Naffakh, M.; Marco, C.; Ellis, G.; Cohen, S.R.; Laikhtman, A.; Rapoport, L.; Zak, A. Novel poly(3-hydroxybutyrate) nanocomposites containing WS_2 inorganic nanotubes with improved thermal, mechanical and tribological properties. *Mater. Chem. Phys.* **2014**, *147*, 273–284. [CrossRef]
25. Naffakh, M.; Marco, C. Isothermal crystallization kinetics and melting behavior of poly (L-lactic acid)/WS_2 inorganic nanotube nanocomposites. *J. Mater. Sci.* **2015**, *50*, 6066–6074. [CrossRef]
26. Naffakh, N.; Díez-Pascual, A.M. Nanocomposite biomaterials based on poly(etherether-ketone) (PEEK) and WS_2 inorganic nanotubes. *J. Mater. Chem. B* **2014**, *2*, 4509–4520. [CrossRef]
27. Pardo, M.; Shuster-Meiseles, T.; Levin-Zaidman, S.; Rudich, A.; Rudich, Y. Low cytotoxicity of inorganic nanotubes and fullerene-like nanostructures in human bronchial epithelial cells: Relation to inflammatory gene induction and antioxidant response. *Environ. Sci. Technol.* **2014**, *48*, 3457–3466. [CrossRef] [PubMed]
28. Goldman, E.B.; Zak, A.; Tenne, R.; Kartvelishvily, E.; Levin-Zaidman, S.; Neumann, Y.; Stiubea-Cohen, R.; Palmon, A.; Hovav, A.H.; Aframian, D.J. Biocompatibility of tungsten disulfide inorganic nanotubes and fullerene-like nanoparticles with salivary gland cells. *Tissue Eng. Part A* **2015**, *21*, 1013–1023. [CrossRef] [PubMed]
29. Silverman, T.; Naffakh, M.; Marco, C.; Ellis, G. Morphology and thermal properties of biodegradable poly(hydroxybutyrate-*co*-hydroxyvalerate)/tungsten disulphide inorganic nanotube nanocomposites. *Mater. Chem. Phys.* **2016**, *170*, 145–153. [CrossRef]
30. Branciforti, M.C.; Silveira Corrêa, M.C.; Pollet, E.; Marcondes Agnelli, J.A.; Nascente, P.A.; Avérous, L. Crystallinity study of nano-biocomposites based on plasticized poly (hydroxybutyrate-*co*-hydroxyvalerate) with organo-modified montmorillonite. *Polym. Test.* **2013**, *32*, 1253–1260. [CrossRef]
31. Avrami, M. Kinetics of phase change. II. Transformation-time relations for random distribution of nuclei. *J. Chem. Phys.* **1940**, *8*, 212–224. [CrossRef]
32. Liu, W.J.; Yang, H.L.; Wang, Z.; Dong, L.S.; Liu, J.J. Effect of nucleating agents on the crystallization of poly(3-hydroxybutyrateco-3-hydroxyvalerate). *J. Appl. Polym. Sci.* **2002**, *86*, 2145–2152. [CrossRef]
33. Chan, C.H.; Kummerlowe, C.; Kammer, H.W. Crystallization and melting behavior of poly(3-hydroxybutyrate)-based blends. *Macromol. Chem. Phys.* **2004**, *205*, 664–675. [CrossRef]
34. Saad, G.R.; Mansour, A.A.; Hamed, A.H. Dielectric investigation of cold crystallization of poly(3-hydroxybutyrate). *Polymer* **1997**, *38*, 4091–4096. [CrossRef]
35. Xu, J.; Guo, B.H.; Yang, R.; Wu, Q.; Chen, G.Q.; Zhang, Z.M. In situ FTIR study on melting and crystallization of polyhydroxyalkanoates. *Polymer* **2002**, *43*, 6893–6899. [CrossRef]
36. Hay, J.N. Application of the modified Avrami equations to polymer crystallisation kinetics. *Br. Polym. J.* **1971**, *3*, 74–82. [CrossRef]
37. Lauritzen, J.L.; Hoffman, J.D. Extension of theory of growth of chain-folded polymer crystals to large undercoolings. *J. Appl. Phys.* **1973**, *44*, 4340–4352. [CrossRef]
38. Hoffman, J.D.; Davies, G.T.; Lauritzen, J.J. *Treatise on Solid State Chemistry*; Hannay, N.B., Ed.; Plenum Press: New York, NY, USA, 1976; Volume 3.
39. Barham, P.J.; Keller, A.; Otun, E.L.; Holmes, P.A. Crystallization and morphology of a bacterial thermoplastic: Poly-3-hydroxybutyrate. *J. Mater. Sci.* **1984**, *19*, 2781–2794. [CrossRef]
40. Shan, G.F.; Gong, X.; Chen, W.P.; Chen, L.; Zhu, M.F. Effect of multi-walled carbon nanotubes on crystallization behavior of poly(3-hydroxybutyrate-*co*-3-hydroxyvalerate). *Colloid Polym. Sci.* **2011**, *289*, 1005–1014. [CrossRef]

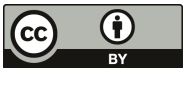

polymers

MDPI

Article

Amino Functionalization of Reduced Graphene Oxide/Tungsten Disulfide Hybrids and Their Bismaleimide Composites with Enhanced Mechanical Properties

Liulong Guo [1], Hongxia Yan [1,*], Zhengyan Chen [1], Qi Liu [1], Yuanbo Feng [1], Fan Ding [1] and Yufeng Nie [2]

[1] Department of Applied Chemistry, School of Natural and Applied Sciences, Northwestern Polytechnical University, Xi'an 710129, China; guo219823@mail.nwpu.edu.cn (L.G.); chenzhengyan@mail.nwpu.edu.cn (Z.C.); e0344066@u.nus.edu (Q.L.); fengyuanbo244@163.com (Y.F.); df276920255@163.com (F.D.)

[2] Department of Applied Mathematics, School of Natural and Applied Sciences, Northwestern Polytechnical University, Xi'an 710129, China; yfnie@nwpu.edu.cn

* Correspondence: hongxiayan@nwpu.edu.cn; Tel.: +86-029-8843-1657

Received: 2 October 2018; Accepted: 24 October 2018; Published: 27 October 2018

Abstract: A novel graphene-based nanocomposite particles (NH_2-rGO/WS_2), composed of reduced graphene oxide (rGO) and tungsten disulfide (WS_2) grafted with active amino groups (NH_2-rGO/WS_2), was successfully synthesized by an effective and facile method. NH_2-rGO/WS_2 nanoparticles were then used to fabricate new bismaleimide (BMI) composites (NH_2-rGO/WS_2/BMI) via a casting method. The results demonstrated that a suitable amount of NH_2-rGO/WS_2 nanoparticles significantly improved the mechanical properties of the BMI resin. When the loading of NH_2-rGO/WS_2 was only 0.6 wt %, the impact and flexural strength of the composites increased by 91.3% and 62.6%, respectively, compared to the neat BMI resin. Rare studies have reported such tremendous enhancements on the mechanical properties of the BMI resin with trace amounts of fillers. This is attributable to the unique layered structure of NH_2-rGO/WS_2 nanoparticles, fine interfacial adhesion, and uniform dispersion of NH_2-rGO/WS_2 in the BMI resin. Besides, the thermal gravimetrical analysis (TGA) revealed that the addition of NH_2-rGO/WS_2 could also improve the stability of the composites.

Keywords: reduced graphene oxide; graphene-like WS_2; bismaleimide; mechanical properties

1. Introduction

Bismaleimide (BMI) resins are a family of thermosetting polymers which have been leading contenders as matrix resins in many cutting-edge fields, especially in aerospace materials sector [1], due to the excellent thermal stability [2], good processability [3], remarkable mechanical properties [4], and prominent dielectric properties [5]. However, the biggest drawback of cured BMI resins is brittleness, which results from the high degree of crosslinking and multiple aromatic structure [6,7]. Consequently, unremitting efforts are made to modify BMI resins to reduce inherent brittleness and achieve elevated properties to satisfy various demands in advanced areas.

A series of studies has revealed that the incorporation of graphene and its derivatives into BMI resins can contribute to significant enhancements of mechanical properties [8]. Graphene oxide (GO) is found in a two-dimensional layered structure that consists of sp^2-hybridized carbon atoms in the form of hexagonal rings [9]. The presence of functional oxygen groups, like epoxy, hydroxyl, and carboxylic groups, on the basal and edge planes, enlarges the basal spacing of GO and makes the material

hydrophilic [10]. GO is a promising substitute for other nanofillers in composites considering the high specific surface area [11], excellent mechanical strength [12], thermal conductivity [13], and electrical properties [14]. In previous reports, functionalized graphene nanosheets with aniline groups on the surfaces (FGN), phosphorous-containing polyhedral oligomeric silsesquioxane-functionalized graphene oxide (P-POSS-GO), and magnetic GO nanosheets (GNS-Fe_3O_4@PZM), were synthesized and used to modify BMI resin in trace amounts [15–17]. The maximum flexural and impact strength among these studies were 163 MPa and 19.15 kJ/m^2, respectively. However, the percentage of increment of the flexural and impact strength were dissatisfactory. These results showed that graphene and its derivatives could only slightly improve the mechanical properties of BMI resins so that new particles should be prepared for further modification.

Numerous studies have pointed out that the critical defect of GO lay in the tendency of irreversible agglomeration during processing, due to the large specific surface area and strong van der Waals forces between GO sheets [18]. Recently, two-dimensional transition metal dichalcogenides (TMDs) have captured more attention since they can be fabricated into the graphene-like structure [19], presenting remarkable chemical, physical, and electrical properties [20]. As a member of TMDs, WS_2 is formed by hexagonally arranged sulfur atoms linked to a tungsten atom and separated by a weak van der Waals gap [21]. With similar morphology and layered structure, GO can be exploited as a buffer layer to form a three-dimensional structure with graphene-like WS_2. This structure exhibits pure graphene characteristics and prevents the aggregation of GO caused by van der Waals forces [22]. To the best of our knowledge, GO/WS_2 nanoparticles were widely used as electrocatalysts in electrochemistry [23]; few researchers have incorporated them into matrix resins to elevate mechanical properties.

It is worthy noting that interfacial interaction between graphene-based nanoparticles and the polymeric matrix plays a significant role in achieving the optimal enhancements of the mechanical properties of the composites [24]. One developed method to promote stronger interfacial bonds is to form covalent linkages between graphene-based nanoparticles and the supporting matrix, such as attaching functional groups to the surface of graphene [25], which also improves the dispersibility of graphene-based nanoparticles [26,27]. For example, γ-aminopropyltriethoxysilane (APS) is a kind of coupling agent with active amino groups. When APS is grafted on the surface of graphene-based nanoparticles, the terminal amino groups can covalently bond with the polymeric matrix, reinforcing the interfacial interaction and acquiring better mechanical properties.

In this article, a facile and scalable route to prepare NH_2-rGO/WS_2 hybrid nanoparticles from reduced graphene oxide and graphene-like WS_2 nanosheets was reported. A series of NH_2-rGO/WS_2/BMI composites with different loadings of NH_2-rGO/WS_2 were prepared, to investigate their structure and effect on properties systematically. Our study revealed that with the incorporation of suitable amounts of NH_2-rGO/WS_2 nanoparticles, the BMI composites produced comparatively higher impact and flexural strength than those of other graphene modified BMI resins with trace amount of fillers reported in the previous studies [15–17].

2. Materials and Methods

2.1. Reagents and Materials

WS_2 powders (<2 μm) were obtained from Macklin Chemistry Co., Ltd. *N*-methyl-2-pyrrolidone (NMP), tetrahydrofuran (THF), ethanol, ammonia water, acetone, and hydrazine hydrate were purchased from Tianjin Tianli Chemical Reagents Co. Ltd. Natural graphite flakes (325 mesh) were purchased from Qingdao Hensen Graphite Co. Ltd. The graphene oxide (GO) nanosheets were fabricated from natural graphite flakes via a modified Hummers' method [28]. γ-Aminopropyltriethoxysilane (APS) was provided by Jingzhou Jianghan Fine Chemical Co. Ltd. BMI was provided by Rongchang Ning research group at Northwestern Polytechnical University. Diallyl Bisphenol A (DBA) and 4,4′-bismaleimidodiphenylmethane (BDM) were purchased from Sigma-Aldrich. All reagents were of analytical grade, and used as received without further purification.

2.2. Experimental Section

2.2.1. Synthesis of Graphene Oxide/WS_2 Nanosheets (GO/WS_2)

Nanostructured WS_2 was prepared from commercial bulk WS_2 by a mechanochemical treatment method [29]. In a typical synthesis process, 0.5 g of WS_2 and 5.0 g of NaCl, with a ball feed ratio of 1:7, were added to the agate grinding bowl of a planetary ball mill, grinding for 2 h at a rotation rate of 560 rpm. The resulted solid was washed by deionized water repeatedly to remove NaCl, and was dried at 100 °C under vacuum for 8 h to obtain the exfoliated WS_2 nanosheets (exf-WS_2). Then exf-WS_2 was dissolved in NMP and stirred under ultrasound to disperse thoroughly. The obtained solution was centrifugated for 1.5 h at the rotation rate of 4000 rpm, after which the upper half of its volume was collected.

Subsequently, 500 mL of GO aqueous suspension was rotary-evaporated and dispersed in NMP under ultrasound for 30 min. Then exf-WS_2 was added and sonicated for 2 h. The hybrid solution was kept at 25 °C for 4 days, then 1 mL of concentrated hydrochloric acid was added into the solution with stirring. The mixture was further reacted at 80 °C for 1 day, after which it was cooled down to normal temperature and was transferred to absolute ethanol, filtered, and washed for several times. Finally, the product was dried at 60 °C in vacuum oven for more than 6 h.

2.2.2. Preparation of NH_2-rGO/WS_2 Hybrid Nanoparticles

The experimental procedures can be concluded as two steps: (1) the reaction to graft APS on the surface of GO/WS_2, and (2) the reducing reaction to obtain NH_2-rGO/WS_2 using hydrazine hydrate, and the reduction of GO is aimed at promoting the intercalation with WS_2 to prevent the agglomeration of nanoparticles.

In the first step, GO/WS_2 was dispersed in the mixture solution of 350 mL of ethanol and 16 mL of deionized water. After 30 min ultrasonication, 5 mL of APS, dissolved in 50 mL of ethanol and 4 mL of deionized water, was dropped into GO/WS_2 dispersion via a constant-pressure funnel. The dispersion was heated to 78 °C, and maintained for 4 h. Following washing with ethanol repeatedly, NH_2-GO/WS_2 nanoparticles were obtained after drying in a vacuum oven at 60 °C for 12 h.

In the second step, NH_2-GO/WS_2 was dispersed in 450 mL of deionized water under ultrasound for 30 min, and was transferred to a 500 mL three-necked flask holding a mechanical stirrer and reflux-condenser. Then, 10 mL of ammonia water and 4 mL of hydrazine hydrate were added. The mixture was heated in oil bath at 98 °C for 6 h. The product, abbreviated as NH_2-rGO/WS_2, was washed with deionized water several times, and dried in the vacuum oven at 60 °C for 8 h. The synthetic route of NH_2-rGO/WS_2 is shown in Scheme 1.

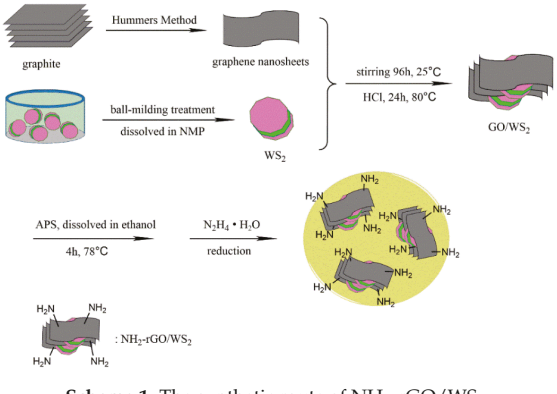

Scheme 1. The synthetic route of NH_2-rGO/WS_2.

2.2.3. Preparation of NH_2-rGO/WS_2/BMI Composites

The NH_2-rGO/WS_2/BMI composites were fabricated using a casting method. With a mass ratio of 3:4, DBA and BDM were blended in a beaker to prepare the pre-polymer, maintaining the temperature at 140 °C until thoroughly melted. Then, a suitable amount of NH_2-rGO/WS_2 was added to the pre-polymer and stirred for about 30 min to disperse homogeneously. Subsequently, the mixture was carefully poured into a pre-heated mold coated with release agent and degassed in the vacuum oven at 150 °C for 1 h. Afterwards, the mixture was cured and post-cured following the schedule of 150 °C/2 h, 180 °C/2 h, 220 °C/3 h and 250 °C/4h. Finally, the mold cooled down to room temperature, and was demolded to obtain the samples of NH_2-rGO/WS_2/BMI composites.

2.3. Characterization

Fourier transform infrared spectra (FT-IR) of the samples were tested from 4000 to 400 cm^{-1} with a Nicolet FT-IR 5700 spectrometer (USA), of which the resolution was 2 cm^{-1}. The X-ray diffraction (XRD) patterns of the samples were determined with a Bruker D8 ADVANCE X-ray diffractometer emitting Cu Kα radiation (λ = 0.15405 nm). X-ray photoelectron spectroscopy (XPS, Thermal Scientific K-Alpha XPS spectrometer) was adopted to investigate the elemental composition on the surface and analyze the valence state of the elements. The transmission electron microscopy (TEM) images were recorded on a JEOL JEM-200CX instrument.

Impact strength was measured based on GB/T 2567-2008 (Chinese Standard). Samples were divided into strips of (80 ± 0.2) × (10 ± 0.2) × (4 ± 0.2) mm^3 using a cutting machine. The impact speed towards the center of samples was 2.9 m/s, controlling the extreme deviation under ±10%. Flexural strength was determined based on GB/T 2567-2008 (Chinese Standard). Samples were cut into strips of (80 ± 0.2) × (15 ± 0.2) × (4 ± 0.2) mm^3. Scanning electron micrographs (SEM) were carried out on a Hitachi S-570 instrument (Tokyo, Japan) to observe the surface morphology of impact fracture. Thermal gravimetrical analysis (TGA) were obtained on Perkin Elmer TGA-7 (Waltham, MA, USA) at a heating rate of 10 °C min^{-1}, from 50 to 800 °C, in an argon atmosphere. Calorimetry studies were carried out on a TA Instruments DSC 2920 (TA Instrument, New Castle, DE, USA) under ultrahigh-purity nitrogen as inert atmosphere, from 30 to 300 °C, with a heating rate of 10 °C/min. Thermal conductivity of samples were measured at room temperature by a Hot Disk instrument (AB Co, Uppsala, Sweden).

3. Results and Discussion

3.1. Characterization of NH_2-rGO/WS_2 Nanoparticles

The FT-IR spectra of GO and NH_2-rGO/WS_2 are shown in Figure 1. In the spectrum of GO, the adsorption band at 3423 cm^{-1} is assigned to –OH, indicating that GO has been oxidized. The typical bands at 1643 and 1040 cm^{-1} are ascribed to C=C and C–O vibrations, respectively. By contrast, –OH and C–O vibrations at 3423 and 1040 cm^{-1} disappear in the spectrum of NH_2-rGO/WS_2, while the peak of C=C still exists, proving the reduction of GO. In addition, the adsorptions at 3450, 1380, and 1080 cm^{-1} are attributed to –NH_2, C–N, and Si–O–C, suggesting that APS has been successfully grafted to the surface of rGO/WS_2.

The crystallographic phases of bulk WS_2 and NH_2-rGO/WS_2 was investigated by XRD spectra, which is shown in Figure 2. The XRD spectrum of bulk WS_2 demonstrates highly crystalline hexagonal structure without any impurities. The strong (002) peak located at 2θ = 14.3° corresponded to a d-spacing of 0.62 nm, according to the Bragg equation, indicating a well-stacked layered structure along the c axis [30]. The XRD pattern of the bulk WS_2 shows sharper and more intense peaks as compared to NH_2-rGO/WS_2 nanoparticles, indicating both smaller lattice size and fewer layers of NH_2-rGO/WS_2 along the c axis. In the magnification spectrum of XRD, all the diffraction peaks of NH_2-rGO/WS_2 can be observed, as well as a new diffraction peak of rGO at 2θ ≈ 24.0°, confirming

the triumphant synthesis of NH_2-rGO/WS_2. The existence of rGO enables further decrease of WS_2 layers in NH_2-rGO/WS_2.

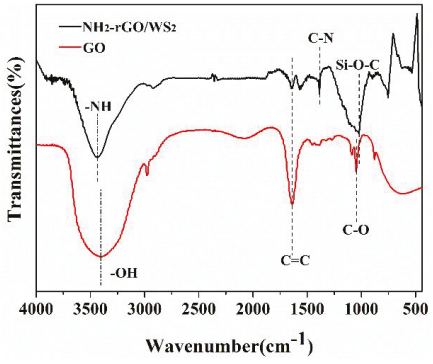

Figure 1. FT-IR spectra of as-prepared GO and NH_2-rGO/WS_2 nanoparticles.

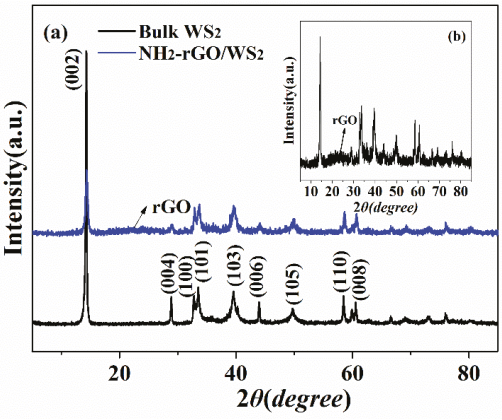

Figure 2. XRD patterns of bulk WS_2 and NH_2-rGO/WS_2 nanosheets.

XPS is employed to characterize the chemical composition and electronic structure of NH_2-rGO/WS_2 nanoparticles. Figure 3a shows the full-band XPS spectrum of NH_2-rGO/WS_2. Five obvious peaks can be observed at the binding energies of 285.0, 532.0, 102.0, 162.0, and 34.0 eV, which are ascribed to C 1s, O 1s, Si 2p, and W 4f, respectively. S atom and W atom come from WS_2, while Si atom derives from APS, which proves APS has been grafted to the surface of rGO/WS_2. There are five peaks (Figure 3b) at the binding energies of 284.4, 284.9, 285.8, 286.7, and 288.9 eV in the spectrum of C 1s, attributed to sp^2-hybridized C=C, sp^3-hybridized C–C, carbon in C–O bond, carbon in C=O bond, and a π–π^* peak [7]. The S 2p peak-fitting (Figure 3c) clearly reveals two resolved peaks at 162.3 eV and 163.5 eV, assigned to S $2p_{3/2}$ and S $2p_{1/2}$. The W 4f peak-fitting spectrum (Figure 3d) exhibits three peaks at 32.0, 34.1, and 37.3 eV, which are indexed to W $4f_{7/2}$, W $4f_{5/2}$, and W $5p_{3/2}$, respectively [22]. In the spectrum of Si 2p (Figure 3e), two peaks at 101.9 eV and 102.6 eV correspond to Si–O–C bond and Si–O–Si bond [31]. From the XPS spectra above, active –NH_2 functional groups are successfully grafted on the surface of rGO/WS_2.

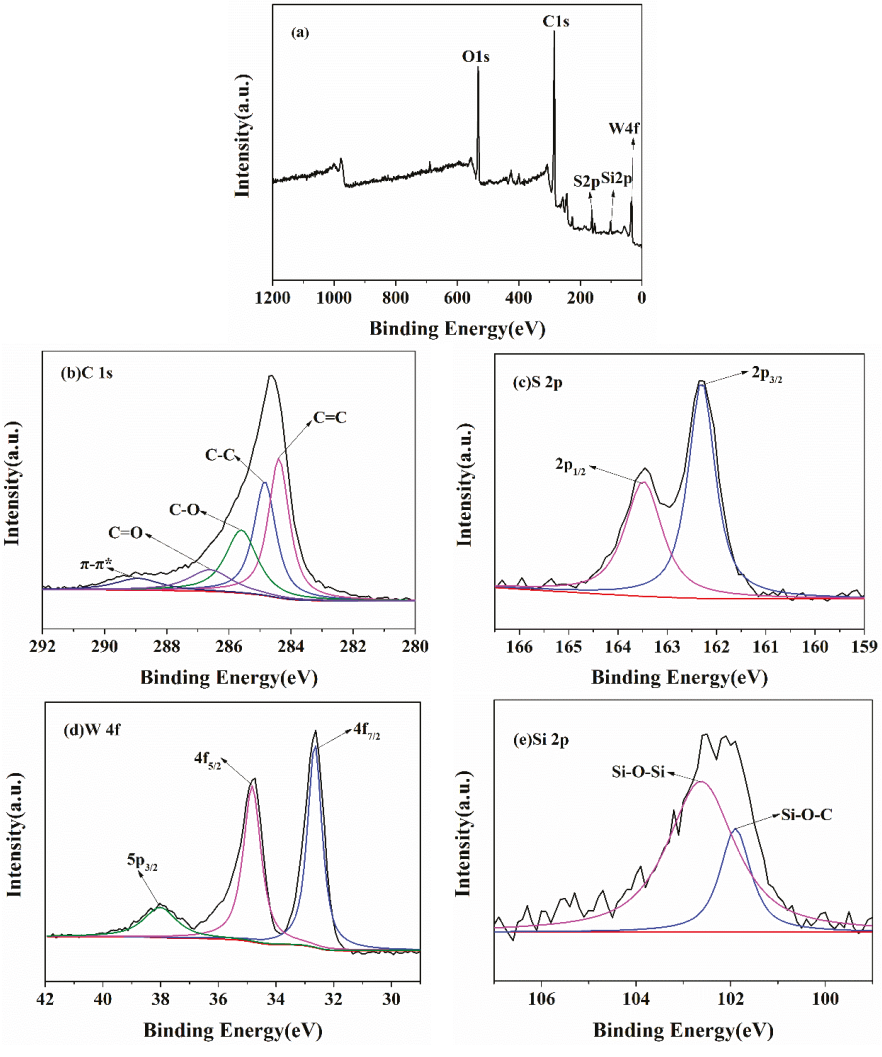

Figure 3. XPS spectra of (**a**) NH_2-rGO/WS_2, (**b**) C 1s, (**c**) S 2p, (**d**) W 4f and (**e**) Si 2p of NH_2-rGO/WS_2.

To better verify the microstructures of WS_2 and NH_2-rGO/WS_2, TEM and HRTEM studies were carried out. As is shown in Figure 4a,b, WS_2 demonstrates a well-layered structure with d(002) = 0.62 nm and periodic arrays of (100) planes with a W-S lattice spacing of 0.27 nm, which coincides with the result of XRD analysis and the hexagonal lattice of the WS_2 phase. It is labeled in Figure 4c that WS_2 has been anchored on GO nanosheets homogeneously, indicating the successful combination of WS_2 and GO nanosheets. The HRTEM image in Figure 4d explicitly exhibits that WS_2 and GO nanosheets appear alternatively, forming a multilayered hybrid structure.

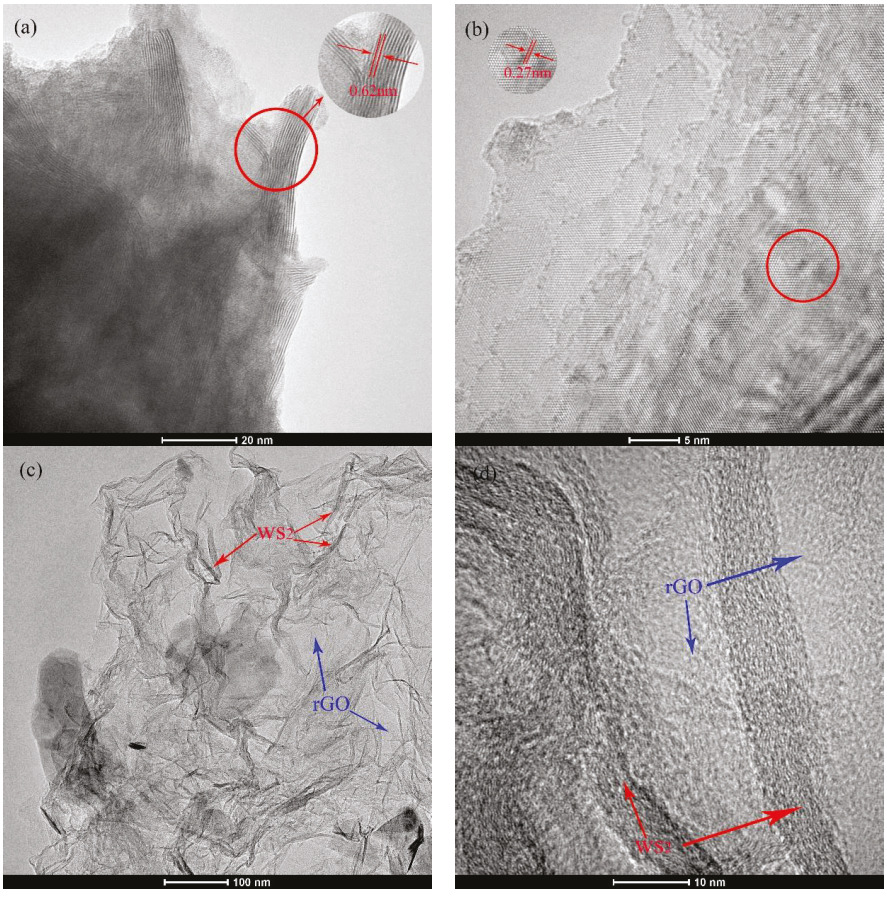

Figure 4. TEM and HRTEM images of (**a**,**b**) bulk WS_2; (**c**,**d**) WS_2/rGO.

3.2. Mechanical Properties of NH_2-rGO/WS_2/BMI Composites

In this work, it is investigated that the impact and flexural strength of NH_2-rGO/WS_2/BMI composites depend on the content of NH_2-rGO/WS_2 (from 0 to 1.0 wt %), shown in Figure 5a,b. An appropriate amount of NH_2-rGO/WS_2 can significantly improve the toughness and the ability to resist static bending moments. The impact and flexural strength increase continuously with the addition of NH_2-rGO/WS_2, peaking at 20.8 kJ/m^2 and 174 MPa when adding 0.6 wt % NH_2-rGO/WS_2, before taking a downward trend. Compared with the pure BMI resin (10.8 kJ/m^2 and 107 MPa), the impact and flexural strength of NH_2-rGO/WS_2/BMI increase by 91.3% and 62.6%, respectively. Rarely have previous studies achieved such remarkable improvements in the flexural and impact strength of graphene-based nanoparticle-modified BMI or other resins with trace amounts of fillers. Some previous works have been listed in Table 1; to the best of our knowledge, the comparatively optimal flexural and impact strength of graphene-based nanoparticle-modified BMI, or other resins among these studies, were 163 MPa and 19.15 kJ/m^2, respectively [4,15–17,32–34]. Thus, the results of the present work are comparable to that of previous works, indicating the NH_2-rGO/WS_2 nanoparticles play a vital role in elevating the mechanical properties of the BMI resin.

Table 1. Mechanical properties of bismaleimide and other polymer composite with different fillers.

Polymers	Fillers	Optimal Loading	Remarks	Reference
BMI	NH_2-rGO/WS_2	0.6 wt %	The flexural and impact strength of the composites increased by 62.6% and 91.3%, respectively, compared to the neat BMI	This paper
BMI	GO	0.15 wt %	The flexural and impact strength of the composites increased by 19.82% and 32.48%, respectively, compared to the neat BMI	[4]
BMI	MAH-GO	0.1 wt %	The flexural and impact strength of the composites increased by 37.48% and 77.28%, respectively, compared to the neat BMI	[4]
BMI	MPTS-GO	-	The tensile and impact strength of the composites increased by 22.17% and 66.64%, respectively, compared to the neat BMI	[8]
BMI	GNS-Fe_3O_4@PZM	0.4 wt %	The flexural and impact strength of the composites increased by 31.3% and 61.3%, respectively, compared to the neat BMI	[16]
BMI	P-POSS-GO	0.8 wt %	The flexural and impact strength of the composites increased by 24.6% and 100.8%, respectively, compared to the neat BMI	[17]
CE/BMI	FGONs	1.0 wt %	The flexural and impact strengths reached optimum values of 110 MPa and 10.98 kJ m^{-2}	[15]
Epoxy	WS_2-PEI	0.25 wt %	The fracture toughness increased by 82.98% and flexural strength increased by 65%, compared to the neat EP	[32]
Epoxy	IF-WS_2	0.5 wt %	The composite exhibited high shear and peel strength	[33]
Nylon 12	IF-WS_2	2 wt %	The tensile strength and bending strength of the composites increased by 27% and 28%, respectively	[34]

BMI, bismaleimide; MAH-GO, maleic anhydride-functionalized GO; MPTS-GO, γ-methacryloxypropyltrimethoxysilane-functionalized GO; GNS-Fe_3O_4@PZM, reduced graphene oxide-Fe_3O_4@polyphosphazene; P-POSS-GO, phosphorus-containing polyhedral oligomeric silsesquioxane-functionalized Graphene oxide; CE, cyanate ester; FGONs,γ-(2,3-epoxypropoxy)propyltrimethoxysilane-functionalized graphene oxide nanoflakes; WS_2-PEI, branched polyethyleneimine-functionalized WS_2; IF-WS_2, fullerene-like WS_2.

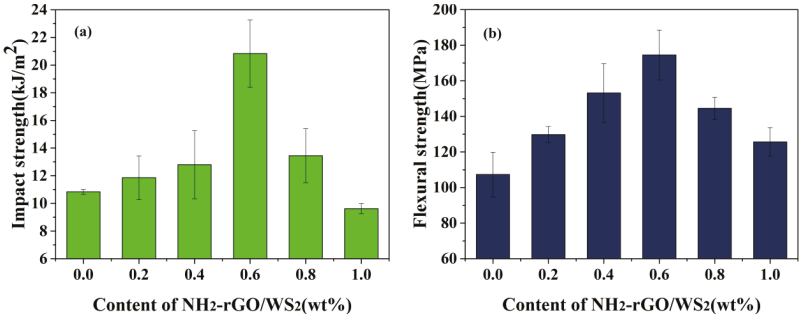

Figure 5. Impact strength (**a**) and flexural strength (**b**) of BMI composites with different contents of NH_2-rGO/WS_2 fillers.

Two reasons account for the enhancement of mechanical properties of NH_2-rGO/WS_2/BMI at a low content of fillers: (1) the fine dispersion of WS_2 and GO in BMI resin by sonication results in enhanced interactions between nanofillers and polymer matrix. Thus, when the distribution of the nanofiller is more homogenous without agglomeration, the interface can transfer load more effectively [35]; (2) there exists plenty of amine groups that can react with C=C bonds of BMI resin on the edge of NH_2-rGO/WS_2 nanoparticles, so that the bonding strength between fillers and BMI resin is reinforced [36]. However, the mechanical properties of the composites are deteriorated as the content of NH_2-rGO/WS_2 surpasses 0.6 wt %. This phenomenon can be explained by the fact that

excessive NH_2-rGO/WS_2 nanoparticles cannot be well dispersed in the BMI matrix. Instead, they are easy to agglomerate to cluster, contributing to stress concentration and weak interface adhesion [37]. Besides, at the procedure of curing, high concentration of NH_2-rGO/WS_2 thickens the BMI resin, not only impeding the volatilization of acetone in resin matrix, but also causing the generation of defects in the NH_2-rGO/WS_2/BMI composites [38]. Thus, only when the content of NH_2-rGO/WS_2 fillers is suitably added can the composites preform excellent mechanical properties.

To obtain more information concerning the toughening mechanism of NH_2-rGO/WS_2 in BMI matrix, the impact fracture surfaces were detected by SEM. Figure 6a–c demonstrate the impact fracture surfaces of pure BMI resin, NH_2-rGO/WS_2/BMI resin with 0.6 wt % fillers and NH_2-rGO/WS_2/BMI resin with 1.0 wt % fillers, respectively. Typical characteristics of brittle failure are explicitly presented in the fracture surface of neat BMI resin (Figure 6a). The fracture surface is relatively flat and smooth without interrupted crack propagation path, resulting in poor energy consumption during fracture. However, BMI composite containing 0.6 wt % NH_2-rGO/WS_2, shown in Figure 6b, has coarser surface with abundant ridges, ravine patterns, and dimples, presenting typical characteristics of ductile fracture. It also can be observed that a few NH_2-rGO/WS_2 nanoparticles appear around the dimples, implying that these dimples originated from NH_2-rGO/WS_2 nanoparticles [4]. Therefore, the highly dispersed NH_2-rGO/WS_2 contributes to the occurrence of dimples and dominant plastic deformation of BMI matrix, impeding further crack propagation and consuming much more energy, whereas the agglomerations of fillers can be seen on the fracture surface of the 1.0 wt % NH_2-rGO/WS_2/BMI composites (Figure 6c), leading to the deteriorated mechanical properties of the BMI composites.

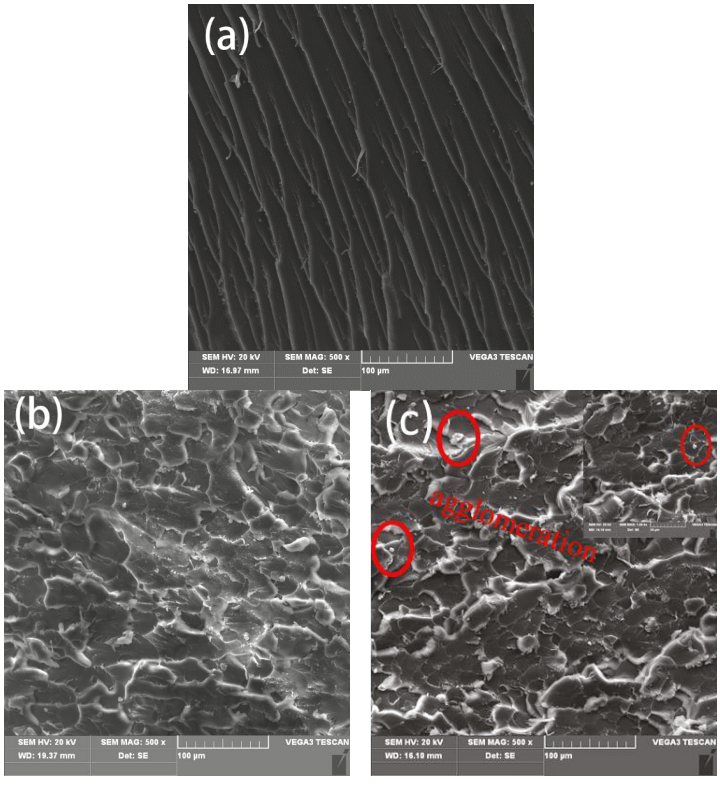

Figure 6. SEM images of the fracture surfaces of (**a**) the neat BMI (**b**) the composite with 0.6 wt % NH_2-rGO/WS_2 and (**c**) the composite with 1.0 wt % NH_2-rGO/WS_2.

3.3. Thermal Properties of NH_2-rGO/WS_2/BMI Composites

The curing behavior of a thermosetting system determines the structure, as well as the properties, of the cured resin. Figure 7 gives the DSC curves of the neat BMI resin and 0.6 wt % NH_2-rGO/WS_2/BMI composite. The neat BMI resin presents a sharp and strong exothermic peak at 257.4 °C, due to homopolymerization of BMI. By contrast, the exothermic peak of 0.6 wt % NH_2-rGO/WS_2/BMI composite shifts to the left with a peak temperature around 252.5 °C, and becomes broader. This is because that the amino groups on the edges of NH_2-rGO/WS_2 particles can react with imide rings through the Michael reaction [39]. The detailed reaction mechanism is shown in Scheme 2. It is notable that NH_2-rGO/WS_2/BMI resin shows better processability, since the whole exothermic peak of NH_2-rGO/WS_2/BMI composite appears at a lower temperature than that of the neat BMI resin.

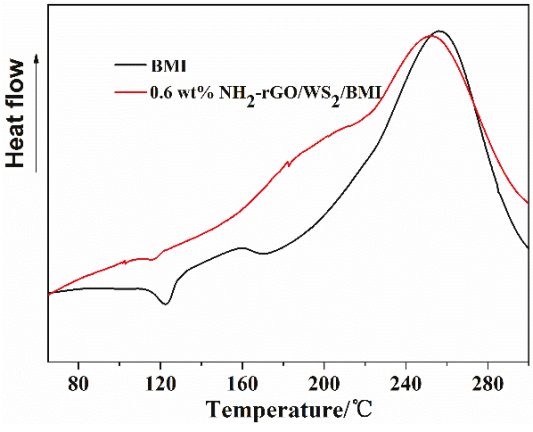

Figure 7. DSC curves of the neat BMI resin and 0.6 wt % NH_2-rGO/WS_2/BMI resin with a heating rate of 10 °C/min.

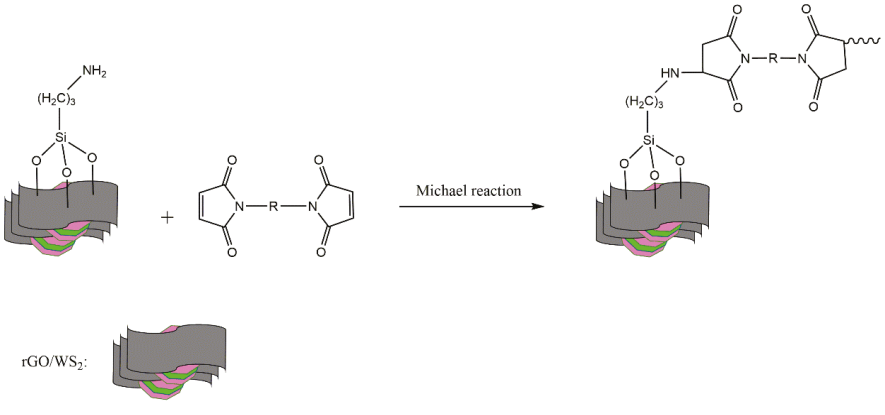

Scheme 2. The mechanism of Michael reaction of the amino groups on the NH_2-rGO/WS_2 particles to maleimide groups.

Figure 8 shows the overlay curves of weight loss of the cured neat BMI resin and BMI composite with 0.6 wt % of NH_2-rGO/WS_2 nanoparticles. As expected, BMI composite with 0.6 wt % of NH_2-rGO/WS_2 nanoparticles exhibit slightly higher decomposition temperature and a better thermal stability than the neat BMI resin. The char yield of the neat BMI resin at 800 °C is 27.6%. It is exciting

that the addition of 0.6 wt % of NH_2-rGO/WS_2 nanoparticles efficiently raises the char yield of the BMI composite at 800 °C to 29.6%, with an increase of 7.25%. The result indicates that NH_2-rGO/WS_2 fillers can improve the thermal property of the neat BMI resin. This can be explained by the barrier effect of modified GO nanosheets, uniform dispersion of NH_2-rGO/WS_2 fillers, and strong interfacial bonding between NH_2-rGO/WS_2 nanoparticles and BMI matrix [40].

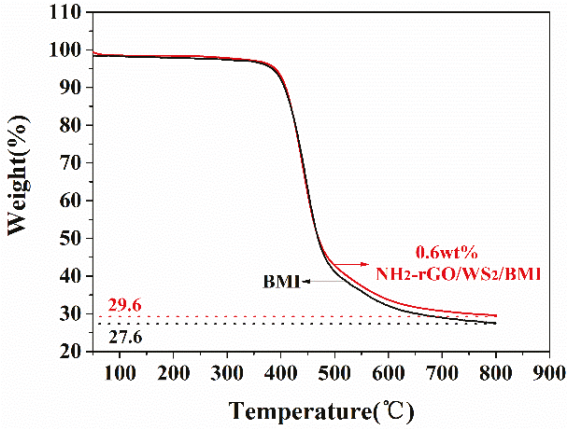

Figure 8. TGA curves of neat BMI and 0.6 wt % NH_2-rGO/WS_2/BMI composite.

4. Conclusions

In this study, reduced graphene oxide and WS_2 nanoparticles with active amino groups (NH_2-rGO/WS_2) were synthesized. BMI composites incorporated with NH_2-rGO/WS_2 nanoparticles at different loadings were prepared. The impacts of NH_2-rGO/WS_2 nanoparticles on the mechanical and thermal properties of the BMI resin were investigated and compared. Various characterizations, including FTIR, XPS, XRD, and TEM, demonstrated the successful preparation of NH_2-rGO/WS_2. Owing to the unique layered structure and the chemical interaction between amino groups on the surface of rGO/WS_2 nanoparticles and C=C bonds of BMI matrix, the dispersion and the interfacial adhesion were significantly enhanced, which further improved the mechanical properties of NH_2-rGO/WS_2/BMI composites considerably. The maximum increment of the impact and flexural strength of the composites (20.8 kJ/m^2 and 174 MPa) were 91.3% and 62.6%, respectively, compared with the neat BMI resin (10.8 kJ/m^2 and 107 MPa), at the loading of 0.6 wt % NH_2-rGO/WS_2 nanoparticles. In contrast with the optimal impact and flexural strength of graphene-modified BMI resins reported (19.15 kJ/m^2 and 163 MPa), trace amounts of NH_2-rGO/WS_2 nanoparticles promoted almost the best enhancements on mechanical properties of the BMI resin. In addition, the system showed a slight rise on the thermostability of the NH_2-rGO/WS_2/BMI composites.

Author Contributions: L.G. and Z.C. conceived and designed the experiment; L.G., Q.L. and F.D. performed the experiment; H.Y. and Y.N. supervised the project; L.G., Y.F. analyzed the data; L.G. wrote the paper; H.Y. and Y.N provided suggestions in the process of revising manuscripts. All the authors contributed to the realization of the manuscript.

Acknowledgments: This work is financially sponsored by the National Natural Science Foundation of China (Grant No. 21875188), the Natural Science Basic Research Plan in Shaanxi Province of China (2018JM2024).

Conflicts of Interest: The authors declare no conflict of interest.

References

1. Iredale, R.J.; Ward, C.; Hamerton, I. Modern advances in bismaleimide resin technology: A 21st century perspective on the chemistry of addition polyimides. *Prog. Polym. Sci.* **2017**, *69*, 1–21. [CrossRef]

2. Ren, Z.; Cheng, Y.; Li, Y.; Xiao, F. Preparation and characterization of soluble bismaleimide-triazine resins based on asymmetric bismaleimide. *J. Appl. Polym. Sci.* **2017**, *134*. [CrossRef]
3. Ren, Z.; Cheng, Y.; Kong, L.; Qi, T.; Xiao, F. High glass transition temperature bismaleimide-triazine resins based on soluble amorphous bismaleimide monomer. *J. Appl. Polym. Sci.* **2016**, *133*. [CrossRef]
4. Li, W.; Wang, M.; Yue, Y.; Ji, W.; Ren, R. Enhanced mechanical and thermal properties of bismaleimide composites with covalent functionalized graphene oxide. *RSC Adv.* **2016**, *6*, 54410–54417. [CrossRef]
5. Wang, Y.; Kou, K.; Zhuo, L.; Chen, H.; Zhang, Y.; Wu, G. Thermal, mechanical and dielectric properties of BMI modified by the Bis allyl benzoxazine. *J. Polym. Res.* **2015**, *22*, 51. [CrossRef]
6. Zhang, X.; Akram, R.; Zhang, S.; Ma, H.; Wu, Z.; Wu, D. Hexa(eugenol)cyclotriphosphazene modified bismaleimide resins with unique thermal stability and flame retardancy. *React. Funct. Polym.* **2017**, *113*, 77–84. [CrossRef]
7. Liu, Y.; Zhao, Y.; Jiao, L.; Chen, J. A graphene-like MoS_2/graphene nanocomposite as a high performance anode for lithium ion batteries. *J. Mater. Chem. A* **2014**, *2*, 13109–13115. [CrossRef]
8. Li, W.; Zhou, B.; Wang, M.; Li, Z.; Ren, R. Silane functionalization of graphene oxide and its use as a reinforcement in bismaleimide composites. *J. Mater. Sci.* **2015**, *50*, 5402–5410. [CrossRef]
9. Khobragade, P.S.; Hansora, D.P.; Naik, J.B.; Njuguna, J.; Mishra, S. Physico-mechanical properties of nano-polystyrene-decorated graphene oxide–epoxy composites. *Polym. Int.* **2017**, *66*, 1402–1409. [CrossRef]
10. Cobos, M.; González, B.; Fernández, M.J.; Fernández, M.D. Chitosan–graphene oxide nanocomposites: Effect of graphene oxide nanosheets and glycerol plasticizer on thermal and mechanical properties. *J. Appl. Polym. Sci.* **2017**, *134*. [CrossRef]
11. Zhou, L.; Yang, Z.; Yang, J.; Wu, Y.; Wei, D. Facile syntheses of 3-dimension graphene aerogel and nanowalls with high specific surface areas. *Chem. Phys. Lett.* **2017**, *677*, 7–12. [CrossRef]
12. Cygan, T.; Wozniak, J.; Kostecki, M.; Petrus, M.; Jastrzebska, A.; Ziemkowska, W.; Olszyna, A. Mechanical properties of graphene oxide reinforced alumina matrix composites. *Ceram. Int.* **2017**, *43*, 6180–6186. [CrossRef]
13. Bo, T.; Zhengwei, W.; Huang, W.; Sen, L.; Tingting, M.; Haogang, Y.; Xufei, L. RGO and Three-Dimensional Graphene Networks Co-modified TIMs with High Performances. *Nanoscale Res. Lett.* **2017**, *12*, 527. [CrossRef] [PubMed]
14. Zhong, J.; Zhou, G.; He, P.; Yang, Z.; Jia, D. 3D printing strong and conductive geo-polymer nanocomposite structures modified by graphene oxide. *Carbon* **2017**, *117*, 421–426. [CrossRef]
15. Ding, J.; Huang, Y.; Han, T.; Wang, Y. Synthesis of functionalized graphene oxide nanoflakes using silane coupling agents: Reinforcement of cyanate ester/bismaleimide nanocomposites. *High Perform. Polym.* **2016**, *28*, 147–155. [CrossRef]
16. Liu, C.; Yan, H.; Lv, Q.; Li, S.; Niu, S. Enhanced tribological properties of aligned reduced graphene oxide-Fe3O4@polyphosphazene/bismaleimides composites. *Carbon* **2016**, *102*, 145–153. [CrossRef]
17. Tang, C.; Yan, H.; Li, S.; Li, M.; Chen, Z. Novel phosphorus-containing polyhedral Oligomeric Silsesquioxane functionalized Graphene oxide: Preparation and its performance on the mechanical and flame-retardant properties of Bismaleimide composite. *J. Polym. Res.* **2017**, *24*, 1–12. [CrossRef]
18. McAllister, M.J.; Li, J.; Adamson, D.H.; Schniepp, H.C.; Abdala, A.A.; Liu, J.; Herrera-Alonso, M.; Milius, D.L.; Car, R.; Prud'Homme, R.K.; et al. Single sheet functionalized graphene by oxidation and thermal expansion of graphite. *Chem. Mater.* **2007**, *19*, 4396–4404. [CrossRef]
19. Ratha, S.; Rout, C.S. Supercapacitor Electrodes Based on Layered Tungsten Disulfide-Reduced Graphene Oxide Hybrids Synthesized by a Facile Hydrothermal Method. *ACS Appl. Mater. Interfaces* **2013**, *5*, 11427–11433. [CrossRef] [PubMed]
20. Kim, T.I.; Kwon, B.; Yoon, J.; Park, I.; Bang, G.S.; Park, Y.; Seo, Y.; Choi, S. Antibacterial Activities of Graphene Oxide Molybdenum Disulfide Nanocomposite Films. *ACS Appl. Mater. Interfaces* **2017**, *9*, 7908–7917. [CrossRef] [PubMed]
21. Tu, C.; Lin, L.; Xiao, B.; Chen, Y. Highly efficient supercapacitor electrode with two-dimensional tungsten disulfide and reduced graphene oxide hybrid nanosheets. *J. Power Sources* **2016**, *320*, 78–85. [CrossRef]
22. Choi, S.H.; Kang, Y.C. Sodium ion storage properties of WS_2-decorated three-dimensional reduced graphene oxide microspheres. *Nanoscale* **2015**, *7*, 3965–3970. [CrossRef] [PubMed]

23. Lee, H.J.; Lee, B.J.; Kang, D.; Jang, Y.J.; Lee, J.S.; Shin, H.S. 2D materials-based photoelectrochemical cells: Combination of transition metal dichalcogenides and reduced graphene oxide for efficient charge transfer. *FlatChem* **2017**, *4*, 54–60. [CrossRef]
24. Xu, L.Q.; Wang, L.; Zhang, B.; Lim, C.H.; Chen, Y.; Neoh, K.; Kang, E.; Fu, G.D. Functionalization of reduced graphene oxide nanosheets via stacking interactions with the fluorescent and water-soluble perylene bisimide-containing polymers. *Polymer* **2011**, *52*, 2376–2383. [CrossRef]
25. Kuilla, T.; Bhadra, S.; Yao, D.; Kim, N.H.; Bose, S.; Lee, J.H. Recent advances in graphene based polymer composites. *Prog. Polym. Sci.* **2010**, *35*, 1350–1375. [CrossRef]
26. Bao, C.; Guo, Y.; Song, L.; Kan, Y.; Qian, X.; Hu, Y. In situ preparation of functionalized graphene oxide/epoxy nanocomposites with effective reinforcements. *J. Mater. Chem.* **2011**, *21*, 13290–13298. [CrossRef]
27. Cano, M.; Khan, U.; Sainsbury, T.; O'Neill, A.; Wang, Z.; McGovern, I.T.; Maser, W.K.; Benito, A.M.; Coleman, J.N. Improving the mechanical properties of graphene oxide based materials by covalent attachment of polymer chains. *Carbon* **2013**, *52*, 363–371. [CrossRef]
28. Zhu, J.; Chen, M.; Qu, H.; Zhang, X.; Wei, H.; Luo, Z.; Colorado, H.A.; Wei, S.; Guo, Z. Interfacial polymerized polyaniline/graphite oxide nanocomposites toward electrochemical energy storage. *Polymer* **2012**, *53*, 5953–5964. [CrossRef]
29. Posudievsky, O.Y.; Khazieieva, O.A.; Cherepanov, V.V.; Dovbeshko, G.I.; Shkavro, A.G.; Koshechko, V.G.; Pokhodenko, V.D. Improved dispersant-free liquid exfoliation down to the graphene-like state of solvent-free mechanochemically delaminated bulk MoS_2. *J. Mater. Chem. C* **2013**, *1*, 6411–6415. [CrossRef]
30. Rout, C.S.; Joshi, P.D.; Kashid, R.V.; Joag, D.S.; More, M.A.; Simbeck, A.J.; Washington, M.; Nayak, S.K.; Late, D.J. Superior Field Emission Properties of Layered WS_2-RGO Nanocomposites. *Sci. Rep.* **2013**, *3*, 3282. [CrossRef] [PubMed]
31. Yan, H.; Li, S.; Jia, Y.; Ma, X.Y. Hyperbranched polysiloxane grafted graphene for improved tribological performance of bismaleimide composites. *RSC Adv.* **2015**, *5*, 12578–12582. [CrossRef]
32. Sahu, M.; Narashimhan, L.; Prakash, O.; Raichur, A.M. Noncovalently Functionalized Tungsten Disulfide Nanosheets for Enhanced Mechanical and Thermal Properties of Epoxy Nanocomposites. *ACS. Appl. Mater. Interfaces* **2017**, *16*, 14347–14357. [CrossRef] [PubMed]
33. Shneider, M.; Dodiuk, H.; Kenig, S.; Tenne, R. The Effect of Tungsten Sulfide Fullerene-Like Nanoparticles on the Toughness of Epoxy Adhesives. *J. Adhes. Sci. Technol.* **2010**, *24*, 1083–1095. [CrossRef]
34. Xu, F.; Yan, C.; Shyng, Y.T.; Chang, H.; Xia, Y.; Zhu, Y. Ultra-toughened nylon 12 nanocomposites reinforced with IF-WS_2. *Nanotechnology* **2014**, *25*, 325701–325710. [CrossRef] [PubMed]
35. Liu, P.; Yao, Z.; Zhou, J. Mechanical, thermal and dielectric properties of graphene oxide/polyimide resin composite. *High Perform. Polym.* **2016**, *28*, 1033–1042. [CrossRef]
36. Chen, Z.; Yan, H.; Liu, T.; Niu, S. Nanosheets of MoS_2 and reduced graphene oxide as hybrid fillers improved the mechanical and tribological properties of bismaleimide composites. *Compos. Sci. Technol.* **2016**, *125*, 47–54. [CrossRef]
37. Liu, C.; Yan, H.; Chen, Z.; Yuan, L.; Lv, Q. Effect of surface-functionalized reduced graphene oxide on mechanical and tribological properties of bismaleimide composites. *RSC Adv.* **2015**, *5*, 46632–46639. [CrossRef]
38. Wang, J.; Yang, S.; Huang, Y.; Tien, H.; Chin, W.; Ma, C.M. Preparation and properties of graphene oxide/polyimide composite films with low dielectric constant and ultrahigh strength via in situ polymerization. *J. Mater. Chem.* **2011**, *21*, 13569–13575. [CrossRef]
39. Gao, Y.; Gu, A.; Jiao, Y.; Yang, Y.; Liang, G.; Hu, J.; Yao, W.; Yuan, L. High-performance hexagonal boron nitride/bismaleimide composites with high thermal conductivity, low coefficient of thermal expansion, and low dielectric loss. *Polym. Adv. Technol.* **2012**, *23*, 919–928. [CrossRef]
40. Chen, H.; Ginzburg, V.V.; Yang, J.; Yang, Y.; Liu, W.; Huang, Y.; Du, L.; Chen, B. Thermal conductivity of polymer-based composites: Fundamentals and applications. *Prog. Polym. Sci.* **2016**, *59*, 41–85. [CrossRef]

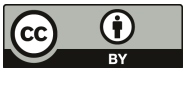

polymers

MDPI

Article

Butyl Rubber Nanocomposites with Monolayer MoS_2 Additives: Structural Characteristics, Enhanced Mechanical, and Gas Barrier Properties

Chi-Yang Tsai [1], Shuian-Yin Lin [2] and Hsieh-Chih Tsai [1,*]

[1] Graduate Institute of Applied Science and Technology, National Taiwan University of Science and Technology, Taipei 10607, Taiwan; charlie810903@gmail.com

[2] Industrial Technology Research Institute, Biomedical Technology and Device Research Laboratories, Hsinchu 31057, Taiwan; sylin@biip-mdcc.org

* Correspondence: h.c.tsai@mail.ntust.edu.tw; Tel.: +886-2-2730-3779; Fax: +886-2-2730-3733

Received: 31 January 2018; Accepted: 24 February 2018; Published: 27 February 2018

Abstract: Emerging two-dimensional (2D) materialsm, such as molybdenum disulfide (MoS_2), offer opportunities to tailor the mechanical and gas barrier properties of polymeric materials. In this study, MoS_2 was exfoliated to monolayers by modification with ethanethiol and nonanethiol. The thicknesses of resulting MoS_2 monolayers were 0.7 nm for MoS_2-ethanethiol and 1.1 nm for MoS_2-nonanethiol. MoS_2 monolayers were added to chlorobutyl rubber to prepare MoS_2-butyl rubber nanocomposites at concentrations of 0.5, 1, 3, and 5 phr. The tensile stress showed a maximum enhancement of about 30.7% for MoS_2-ethanethiol-butyl rubber and 34.8% for MoS_2-nonanethiol-butyl rubber when compared to pure chlorobutyl rubber. In addition, the gas barrier properties were increased by 53.5% in MoS_2-ethanethiol-butyl rubber and 49.6% in MoS_2-nonanethiol-butyl rubber. MoS_2 nanosheets thus enhanced the mechanical and gas barrier properties of chlorobutyl rubber. The nanocomposites that are presented here may be used to manufacture pharmaceutical stoppers with high mechanical and gas barrier properties.

Keywords: layered structures; polymer-matrix composites; mechanical properties; gas barrier properties

1. Introduction

Since the discovery of graphene, two-dimensional inorganic materials, such as MoS_2, have attracted great attention. MoS_2 has a structure similar to that of graphite; two layers of sulfur and one layer of molybdenum atoms in a sandwiched structure make up its hexagonal crystal lattice structure. MoS_2 is unreactive, unaffected by both acids and oxygen, and has a low coefficient of friction due to weak van der Waals interactions between the layers. As such, it is widely used as a dry lubricant. In addition, MoS_2 can be exfoliated into nanolayers without the need for complex methods. MoS_2 nanosheets have previously been utilized in transistors [1], biomaterials [2], and nanocomposites [3], and can also be added to polymers as a filler material; because of the high band gap of MoS_2, the electronic properties of the polymer matrices are not changed. A common reason to add fillers to polymers is to improve their mechanical properties. For example, polymer chains can interact with the nanosheet surfaces, resulting in reinforcements in all directions from the nanosheets. For the latter, it is important to fully exfoliate the two-dimensional inorganic materials to increase the surface area [4].

Many studies have reported the use of nanoscale fillers such as clay, reduced graphene oxide, and MoS_2 to improve the mechanical and gas barrier properties of polymer materials for a variety of applications. For example, the optimal mechanical or barrier properties were observed for exfoliated or intercalated polymer/clay nanocomposites, but using a high clay content of 5–10 wt % [5–7]. Clay

is difficult to exfoliate due to the many cations in the spacing between the layers of the material. In addition, clay is hydrophilic and cannot disperse well in hydrophobic polymers. However, quaternary ammonium cation salt can usually act as modifiers to enable exfoliation and dispersion of clay molecules in polymer matrices [8]. Graphene consists of two-dimensional sheets of sp^2-bonded carbon with a high specific surface area. Graphene-based nanocomposites play an important role because of their favorable mechanical, electrical, and barrier properties. Their barrier properties, for example, are much better than those of clay nanofillers [9–11]. Some applications require improvements in the mechanical properties and thermal stability of a polymer matrix, while maintaining the polymer's electrical insulation properties. Graphene, as a highly conductive material, does not appear to be a good filler material choice for such applications. In addition, fillers have to be uniformly dispersed in a polymer matrix. However, exfoliation of graphene is still unpractical, with the most common method involving the treatment of graphite with strong oxidizers to obtain exfoliated graphene oxide. MoS_2 exfoliation into nanosheets, on the other hand, can be achieved in a one-step, simple method at low MoS_2 loading rates, and is thus more economical. MoS_2 nanosheets are therefore an excellent alternative to clay and graphene-based materials for enhancing the properties of polymer matrices. MoS_2 has been reported as filler to manufacture photo-mechanical response material [12], gas selective membranes [13], and supercapacitor [14].

Due to weak van der Waals interactions between the layers of bulk MoS_2, MoS_2 nanosheets can easily be prepared by ultrasonication. A common method for the exfoliation of MoS_2 involves the use of lithium ions to intercalate the MoS_2 nanosheets. However, it is hard to disperse MoS_2 nanosheets in nonpolar polymers without modifying their surfaces with organic ligands. In previous works, ultrasonicating bulk MoS_2 powder produced a number of sulfur vacancies on the surface of a MoS_2 nanosheet, which were reported to act as targets for surface modification [15,16]. Here, thiol compounds were selected as modifiers of MoS_2 nanosheets to increase the affinity between the nanosheets and polymer matrix. With a greater degree of MoS_2 nanosheet dispersion, a greater degree of reinforcement would be expected in the nanocomposite.

Chlorobutyl rubber is often used in tires, gas masks, and chemical agent packaging because of its good mechanical and gas barrier properties. Unlike conventional butyl rubber, with a lack of double bond on the backbone of polymer chain, the vulcanization of chorobutyl rubber is more efficiently. The aim of this study was to enhance the mechanical and gas barrier properties of chemical agent packaging materials, which require enhanced gas barrier properties for the storage of chemical agents. For this reason, chlorobutyl rubber with added MoS_2 was studied as a suitable material. Exfoliated MoS_2 nanosheets surface-modified by ethanethiol and nonanethiol to enhance their affinity to polymers were expected to disperse well in chlorobutyl rubber and result in improved mechanical and gas barrier properties. Herein, the effects of ethanethiol- and nonanethiol-modified MoS_2 nanosheets are compared for various MoS_2 concentrations.

2. Materials and Methods

2.1. Materials

Chlorobutyl rubber (Mooney viscosity [ML_{1+8} 100 °C]: ~41–49) was obtain from ExxonMobil Chemical (Houston, TX, USA); MoS_2 from Alfa Aesar (Haverhill, MA, USA); hexane from Fisher Chemical (Hampton, NH, USA); ethanethiol from Sigma-Aldrich (St. Louis, MO, USA); nonanethiol from Acros (Hampton, NH, USA); ethylenethiourea(2-mercaptoimidazoline) from Kawaguchi Chemical Industry (Kawaguchi, Japan); and silicon dioxide (TOKUSIL 255, with surface area BET 177 m^2/g) was obtained from OSC Group (Miaoli, Taiwan).

2.2. Exfoliation of MoS_2

For the exfoliation of MoS_2, 400 mg MoS_2 powder and 20 mL hexane were mixed in 20-mL vials and ethanethiol and nonanethiol were added to each vial. Ultrasonication to exfoliate MoS_2 was

applied in a bath for 24 h. After ultrasonication, the contents of the vials were allowed to settle, and exfoliated MoS_2 was obtained as the suspension.

2.3. Preparation of MoS_2-butyl Rubber Nanocomposites

MoS_2-butyl rubber nanocomposites were prepared with various MoS_2 concentrations 0.5, 1, 3, and 5 parts per hundreds of rubber (phr). The previously obtained MoS_2 nanosheets were mixed with chlorobutyl rubber and were dissolved in hexane under mechanical stirring for 1 h to achieve a homogenous mixture. The hexane was then evaporated and the samples thus obtained were dried at 100 °C in a vacuum oven for 12 h to completely remove the solvent. The samples were compounded by two-roll-mill with 20 phr silicon dioxide as a widely used filler for rubber to improve the wear resistance and also acts as a reinforcing agent and using 0.5 phr ethylenethiourea(2-mercaptoimidazoline) as the curing reagent. After compression molding at 185 °C at a pressure of 50 kgf/cm^2 for 10 min, MoS_2-butyl rubber nanocomposite samples with dimensions of 15 cm × 15 cm and a 1-mm thickness were obtained.

2.4. Characterization

The morphologies of the MoS_2 nanosheets modified by ethanethiol and nonanethiol were observed using a Tecnai™ G2 F-20 (Philips, Amsterdam, Netherlands) transmission electron microscope (TEM). Raman spectra and Raman maps were obtained using an NRS5100 (JASCO, Tokyo, Japan) spectrometer. Cross-sectional images were obtained using a JSM-6500F (JEOL, Tokyo, Japan) scanning electron microscope (SEM); and, composite samples were cooled in liquid nitrogen and cut by a scalpel to prepare the samples for backscattered electron (BSE) imaging. Atomic force microscopy (AFM) was performed using a NX10 system (Park, Suwon, Korea). X-ray diffraction (XRD) was performed using a D8 SSS (Bruker, Billerica, MA, USA). UV-Vis spectra were obtained using a V-730 spectrometer (JASCO, Tokyo, Japan). Dynamic mechanical analysis was performed using a Q800 (TA Instruments, New Castle, DE, USA), while stress-strain curves were measured using a TS-2000 with a crosshead speed of 500 mm/min. The oxygen transmission rates were measured according to the ASTM D3985 standard using the OX-TRAN 2/61 (Mocon Inc., Minneapolis, MN, USA) at 23 °C and a relative humidity of 0%; film specimens of 5 cm in diameter and 1 mm in thickness were fixed between two chambers, and oxygen filled the upper chamber while nitrogen filled the lower chamber.

3. Results and Discussion

3.1. Exfoliation of MoS_2

Scheme 1 outlines the overall procedure for the preparation of the MoS_2 nanosheets and the production of MoS_2-butyl rubber nanocomposites. The exfoliation of MoS_2 was achieved by bath ultrasonication of bulk MoS_2 powder in hexane. It has previously been reported that this exfoliation process can produce a number of structural defects, such as S vacancy defects [17,18]. Then, MoS_2 nanosheets can be modified with thiol ligands. Ethanethiol and nonanethiol were used as the surface modifiers in this study. The carbon chains of these two thiols were hypothesized to modify the surface of MoS_2 to enhance its compatibility with chlorobutyl rubber. The organic modification of the surface and robust nature of the modifiers ensured good dispersion and a dramatically enhanced properties of the polymer materials.

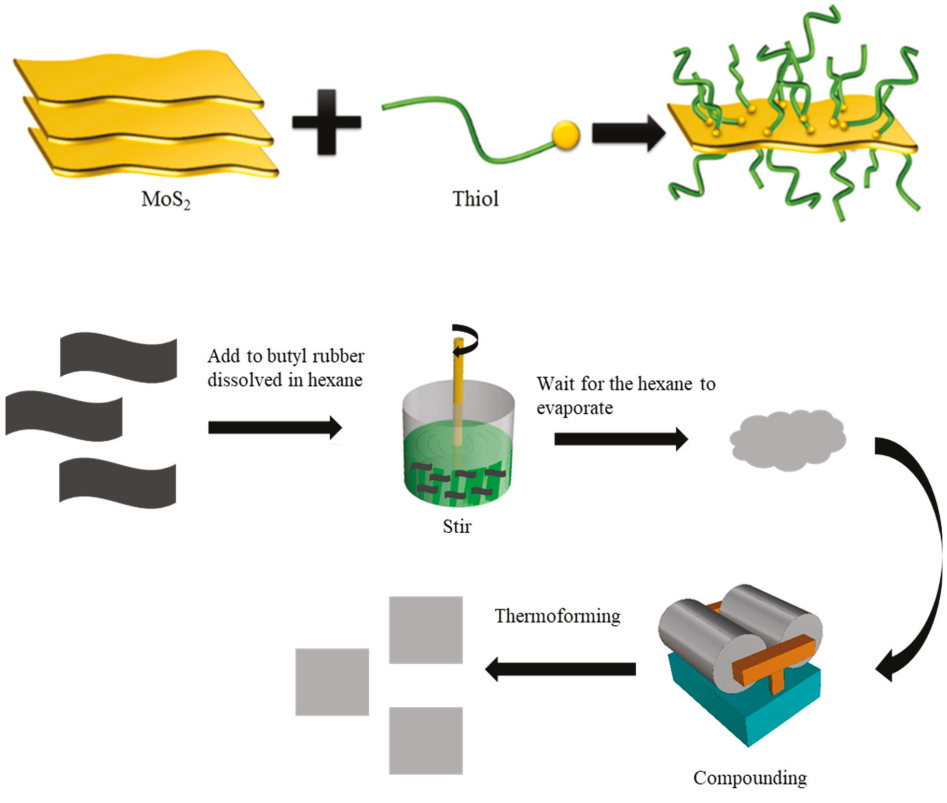

Scheme 1. Schematic illustration for exfoliation modification of MoS_2 and corresponding production of chlorobutyl rubber-based nanocomposites.

The morphologies of MoS_2 nanosheets modified by ethanethiol and nonanethiol are presented in TEM images (Figure 1a,b). The hexagonal structure of MoS_2 modified by ethanethiol and nonanethiol was clearly visible in high-resolution TEM images (Figure 1c,d). It can be inferred that these MoS_2 nanosheets were either several layers thick or monolayers, because the hexagonal lattice structure of MoS_2 was visible. The latter indicates that the crystal structures of MoS_2-ethanethiol and MoS_2-nonanethiol were retained during ultrasonication [19]. Raman spectra were used to confirm the modification of the MoS_2 nanosheet surfaces by ethanethiol and nonanethiol (Figure 2). Peaks were seen at ~380 cm^{-1} (E^1_{2g}, in-plane vibrations) and ~410 cm^{-1} (A_{1g}, out-of-plane vibrations), characteristic of the MoS_2 trigonal structure. Peaks at ~680 and ~1100 cm^{-1}, which indicate carbon-sulfur (ν_{cs}) [20] and carbon-carbon bonds (ν_{cc}) [21], respectively, were noted for the modified MoS_2. These results indicate that the surface of MoS_2 was successfully modified by ethanethiol and nonanethiol.

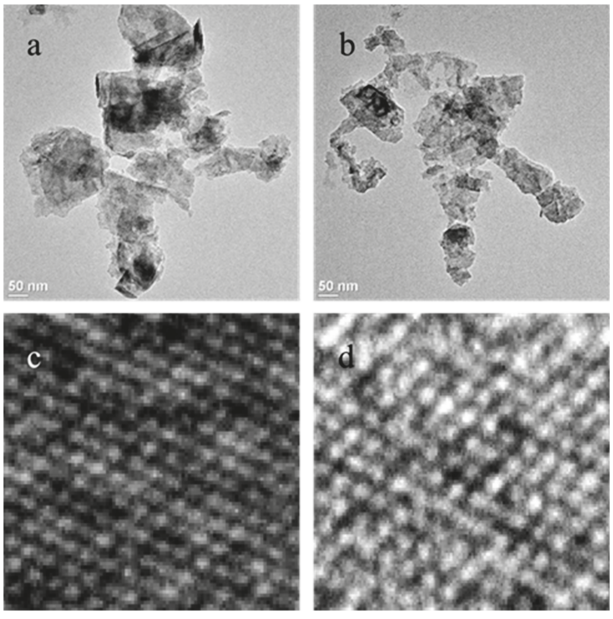

Figure 1. Transmission electron microscope (TEM) images of MoS_2 nanosheets. (**a**,**c**) Low- and high-resolution images of MoS_2-ethanethiol; (**b**,**d**) low- and high-resolution images of MoS_2-nonanethiol.

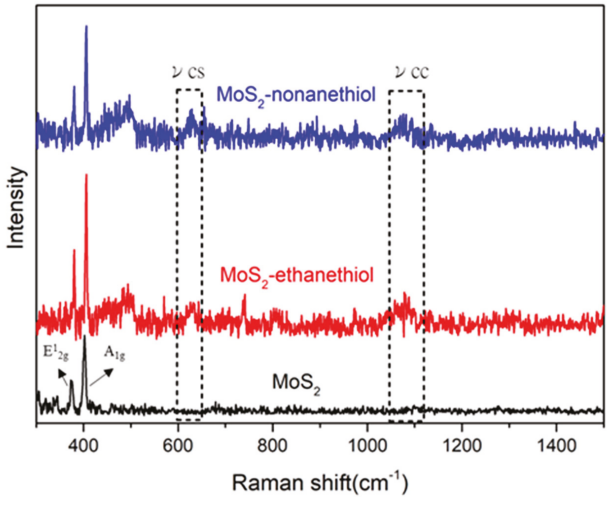

Figure 2. Raman spectra of MoS_2 and thiol-modified MoS_2.

The thicknesses of the exfoliated nanosheets were monitored through AFM examination of the exfoliated samples. The thickness of bulk MoS_2 was ~90–120 nm (Figure 3a), while that of MoS_2-ethanethiol was ~0.7 nm (Figure 3b) and that of MoS_2-nonanethiol was ~1.1 nm (Figure 3c), values that correspond to that of ~0.65 nm in previous reports on the thickness of MoS_2 monolayers [1]. The thicknesses obtained here being greater than the typical thickness of a single-layer MoS_2 sheet

may be attributed to thiol conjugation on the surface of MoS_2 [22]. Blue-shifts of UV-Vis spectra are dependent on changes in the band gap energy, which can be obtained from the wavelengths in UV-Vis spectra from the following equation:

$$\text{Band gap energy } (E) = (hc)/\lambda \quad (1)$$

where hc is Planck's constant and λ is the wavelength. Bulk MoS_2 is an indirect semiconductor with a band gap of ~1.2 eV, which increases to ~1.8 and ~1.9 eV for monolayers of MoS_2 [23,24]. To obtain the optimum parameters for exfoliation, the number of MoS_2 nanosheet layers was measured for various concentrations of ethanethiol and nonanethiol by UV-Vis spectra (Figure 4). The MoS_2-ethanethiol sample in Figure 4a shows a blue-shift from 697 to 688 nm. The latter wavelength of 688 nm corresponds to a band gap value of 1.80 eV. For MoS_2-nonanethiol in Figure 4b, a blue-shift from 697 to 685 nm can be observed. The latter wavelength of 685 nm corresponds to a band gap value of 1.81 eV. The conditions to exfoliate MoS_2 into monolayer involved the addition of 0.5 mL of either ethanethiol or nonanethiol with 400 mg bulk MoS_2 powder into 20 mL hexane. The exfoliation efficiency for MoS_2 that was treated with nonanethiol was greater than that of MoS_2 treated with ethanethiol.

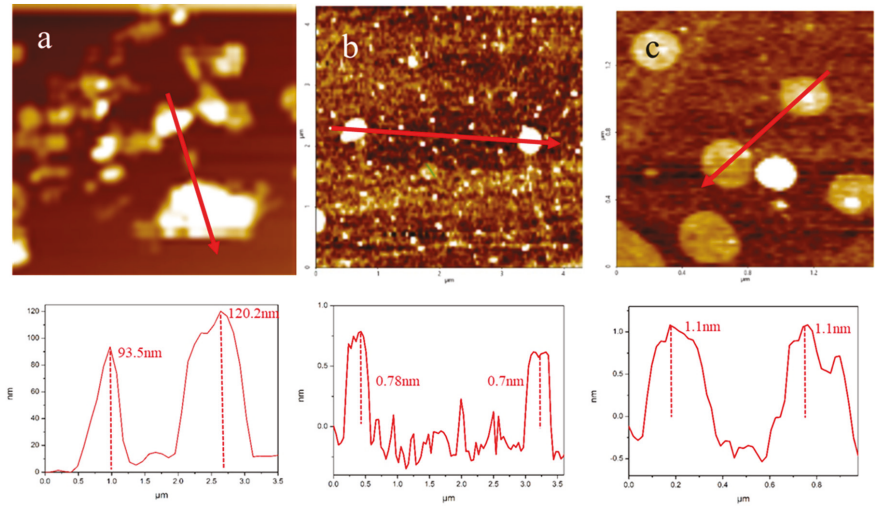

Figure 3. Atomic force microscope (AFM) images of: (**a**) bulk MoS_2, (**b**) MoS_2-ethanethiol, and (**c**) MoS_2-nonanethiol.

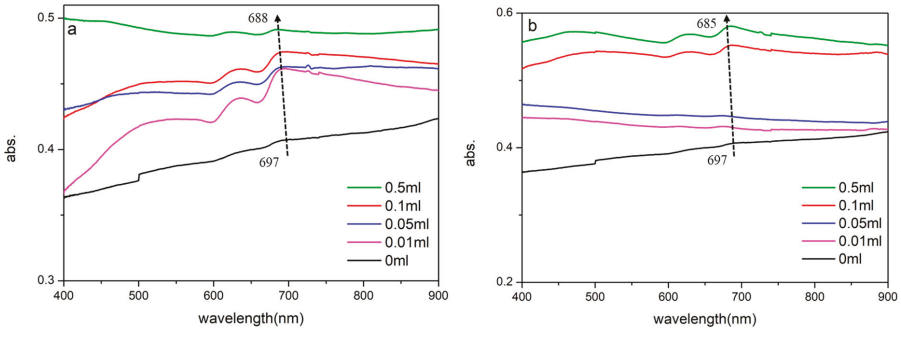

Figure 4. UV-Vis spectra: (**a**) MoS_2-ethanethiol and (**b**) MoS_2-nonanethiol.

3.2. Characterization of MoS_2-butyl rubber Nanocomposites

XRD was performed to characterize the obtained layered-structure materials and partially evaluate the dispersion state of layered nanofillers in the polymer composites. XRD scans of the polymer nanocomposites showed a nanofiller peak and a shift to a lower 2θ or larger d-spacing value when compared to bulk MoS_2. The peak shift indicates an expansion of the d-spacing of MoS_2 nanosheets; it was inferred that polymer chains had been intercalated in the MoS_2 nanosheets. For completely exfoliated layered nanofillers, no XRD peaks were expected for the nanocomposites, since they should not show regular spacing of the sheets [25].

The XRD patterns (Figure 5) of the MoS_2-butyl rubber nanocomposites confirm the intercalation of chlorobutyl rubber in the MoS_2 nanosheet interlayers by showing a decrease in 2θ value as the concentration of MoS_2 increased. The (002) peak of pure MoS_2 was at 2θ = 14.44°, corresponding to a d-spacing value of 0.3088 nm. After adding MoS_2 to chlorobutyl rubber, the 2θ peak of the (002) plane shifted to lower angles, associated with intercalation in nanocomposites. For MoS_2-ethanethiol-butyl rubber, the peak at 2θ = 14.44° (d = 0.3088 nm) for 0 phr shifted to 2θ = 14.40° (d = 0.3097 nm), and 2θ = 14.38° (d = 0.3102 nm) for the samples with 3 and 5 phr MoS_2, respectively. For MoS_2-nonanethiol-butyl rubber, the peak was at 2θ = 14.36° for the 0.5-phr sample, which indicates that the d-spacing of MoS_2 increased when MoS_2 nanosheets were inserted into the chlorobutyl rubber chains. The latter illustrates that, between the exfoliation and intercalation, the nanocomposites can be driven toward full exfoliation by decreasing the content of MoS_2 nanosheets. The greater shift at low concentrations indicates that nonanethiol is a more suitable modifier for MoS_2 exfoliation than ethanethiol.

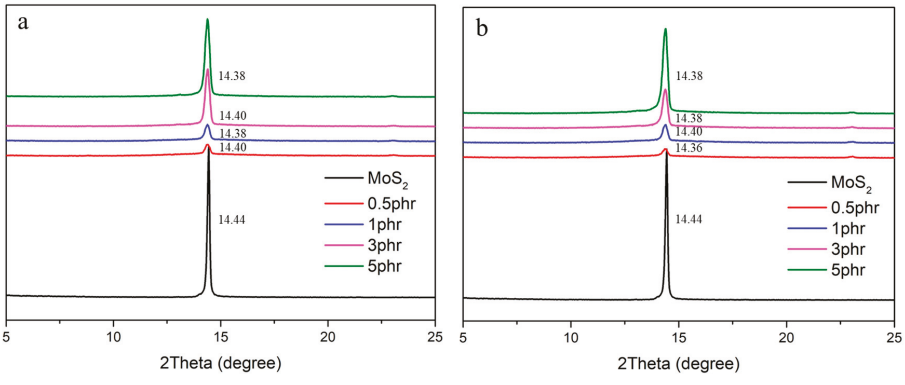

Figure 5. X-ray diffraction (XRD) patterns of MoS_2-butyl rubber nanocomposites: (**a**) MoS_2-ethanethiol-butyl rubber and (**b**) MoS_2-nonanethiol-butyl rubber.

The SEM-BSE images (Figure 6) of MoS_2-butyl rubber nanocomposite cross-sections demonstrate the dispersion of MoS_2 nanosheets in chlorobutyl rubber obtained at different concentrations. These micrographs confirm that, at higher concentrations, i.e., 3 and 5 phr, big clusters of agglomerated ethanethiol- and nonanethiol-modified MoS_2 were present. At lower concentrations, i.e., 0.5 and 1 phr, on the other hand, MoS_2 was homogeneously dispersed in chlorobutyl rubber.

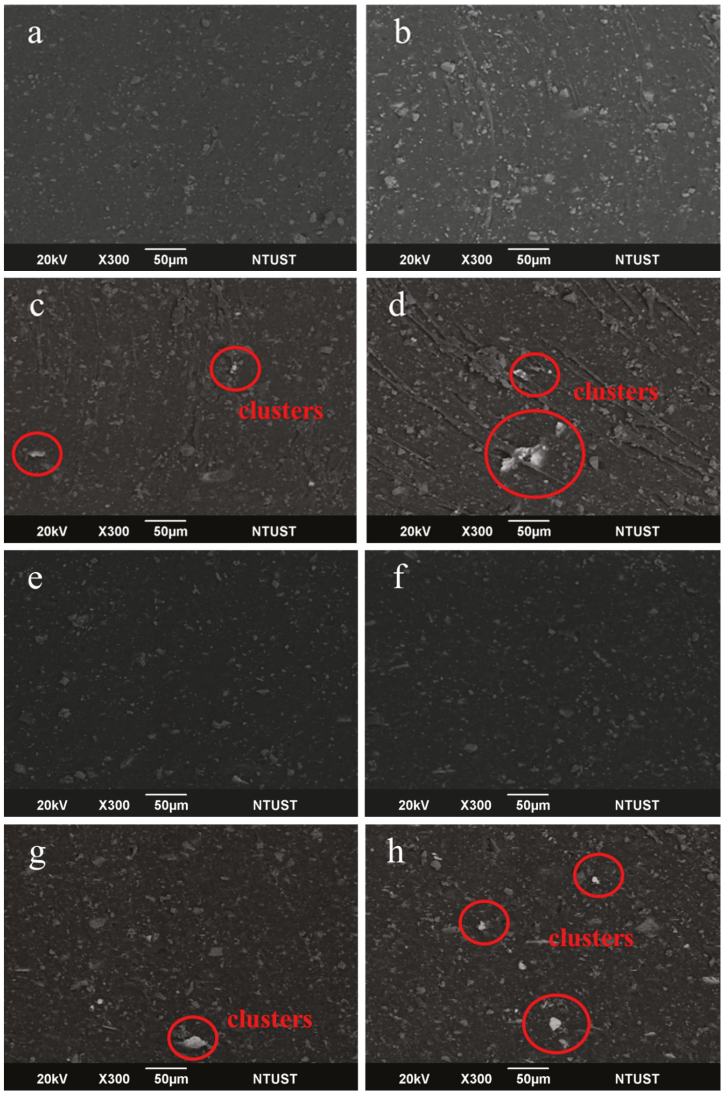

Figure 6. Scanning electron microscope backscattered electrons (SEM-BSE) cross-sectional images for MoS_2-butyl rubber with different concentrations of MoS_2 with either ethanethiol or nonanethiol: (**a**) 0.5 phr, ethanethiol; (**b**) 1 phr, ethanethiol; (**c**) 3 phr, ethanethiol; (**d**) 5 phr, ethanethiol; (**e**) 0.5 phr, nonanethiol; (**f**) 1 phr, nonanethiol; (**g**) 3 phr, nonanethiol; and, (**h**) 5 phr, nonanethiol.

The typical Raman peaks for MoS2-butyl rubber nanocomposites are shown in Figure 7. The peaks at ~380 and ~410 cm^{-1} correspond to MoS2, while the peaks at ~720, ~820, ~910, and ~1080 cm^{-1} correspond to chlorobutyl rubber. Raman mapping (Figure 8) was used to further confirm the dispersion state of MoS_2 nanosheets at different MoS_2 concentrations. Figure 8 shows the intensity maps of the A_{1g} peak (~410 cm^{-1}) of MoS_2 for nanocomposites with different concentrations of modified MoS_2 nanosheets. The Raman mapping images correspond well with the SEM-BSE images (Figure 6). At low concentrations of MoS_2 nanosheets, their distribution was uniform,

which implies homogeneous dispersion in chlorobutyl rubber. As the MoS_2 loading increased, however, agglomeration and clustering behavior of the MoS_2 was visible, illustrating poor dispersion. Nonetheless, due to their conjugation with ethanethiol or nonanethiol, MoS_2 nanosheets could disperse homogeneously in chlorobutyl rubber at low concentrations. As shown in Figure 6, MoS_2-nonanethiol-butyl rubber had a more uniform appearance than MoS_2-ethanethiol-butyl rubber; at 5 phr MoS_2, in particular, the clustering for MoS_2-ethanethiol-butyl rubber was more pronounced than for MoS_2-nonanethiol-butyl rubber.

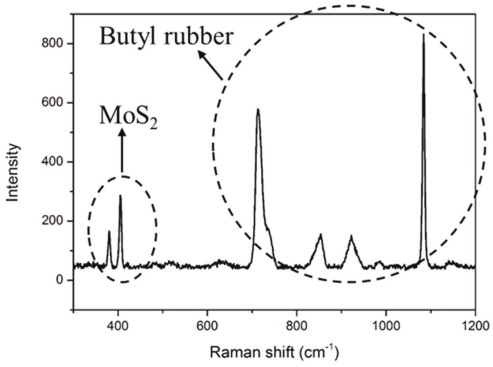

Figure 7. Typical Raman peaks for MoS_2-butyl nanocomposites.

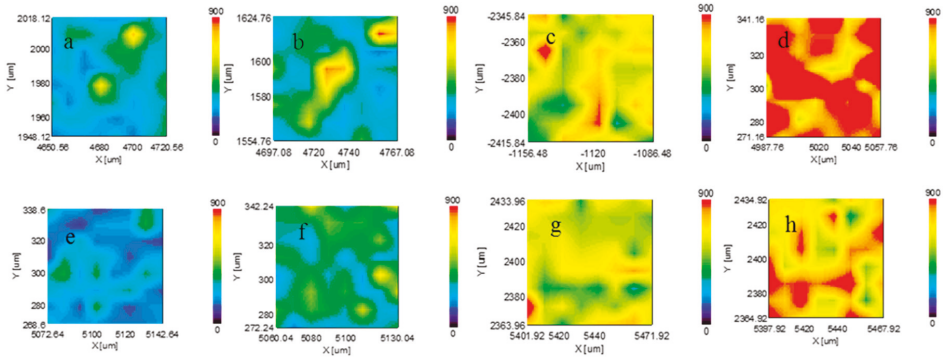

Figure 8. Raman mapping images for MoS_2-butyl rubber with different concentrations of MoS_2 with either ethanethiol or nonanethiol: (**a**) 0.5 phr, ethanethiol; (**b**) 1 phr, ethanethiol; (**c**) 3 phr, ethanethiol; (**d**) 5 phr, ethanethiol; (**e**) 0.5 phr, nonanethiol; (**f**) 1 phr, nonanethiol; (**g**) 3 phr, nonanethiol; and, (**h**) 5 phr, nonanethiol.

3.3. Tensile Properties of MoS_2-butyl Rubber Nanocomposites

The stress-strain curves (Figure 9) for neat chlorobutyl rubber and MoS_2-butyl rubber nanocomposites show that the tensile strength of the chlorobutyl rubber matrix increased upon MoS_2 nanosheet loading. Furthermore, the elongation at break of MoS_2-nonanethiol-butyl rubber was about 14.4% higher than that of MoS_2-ethanethiol-butyl rubber. The maximum increase in tensile strength for MoS_2-ethanethiol-butyl rubber was about 30.7% for a MoS_2 content of 3 phr. In MoS_2-nonanethiol-butyl rubber, likewise, the tensile strength was increased by about 34.8% for 1 phr MoS_2 as compared to that of the control sample. Therefore, the maximum increase in tensile strength was obtained for MoS_2-nonanethiol-butyl rubber instead of MoS_2-ethanethiol-butyl rubber. The significant increase

in tensile strength reached a peak at a loading of 3 phr for MoS_2-ethanethiol-butyl rubber and of 1 phr for MoS_2-nonanethiol-butyl rubber. At higher MoS_2 nanosheet contents, the tensile strength decreased again. The latter observations may be ascribed to the aggregation of MoS_2 nanosheets in the chlorobutyl rubber matrix, which is known to cause a decrease in tensile strength for rubber [26]. It is obvious from these results that MoS_2 nanosheets can significantly improve the strength of chlorobutyl rubber, possibly due to the high strength of MoS_2 nanosheets, better interactions between MoS_2 nanosheets and the polymer matrix, and/or a more uniform dispersion of MoS_2 nanosheets in the chlorobutyl rubber matrix due to abundant thiol groups on the MoS_2 nanosheet surfaces.

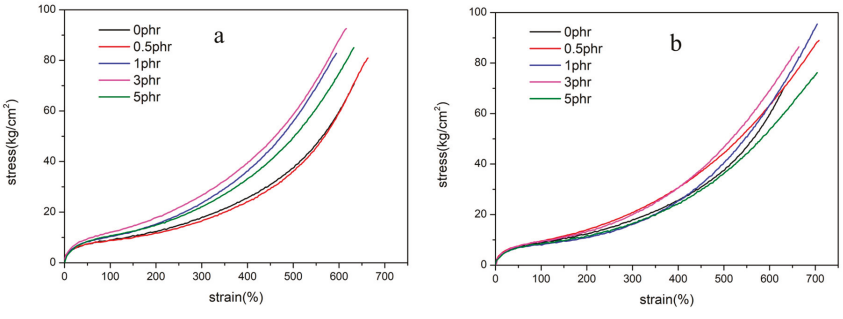

Figure 9. Stress-strain curves: (**a**) MoS_2-ethanethiol-butyl and (**b**) MoS_2-nonanethiol-butyl rubber.

3.4. Dynamic Mechanical Analysis of MoS_2-butyl Rubber Nanocomposites

For MoS_2-ethanethiol-butyl rubber, the storage modulus (Figure 10a) is a measure of its stiffness and the elastic of material that means the ability to recover pristine shape, and it a little increased for all the MoS_2-butyl rubber nanocomposites in rubbery region compared to pure chlorobutyl rubber but no significant increment in glassy region. In rubbery region, the nanocomposite containing 0.5 phr MoS_2 nanosheets exhibited the highest modulus value. MoS_2-nonanethiol-butyl rubber also showed an increase in the storage modulus (Figure 10b), with an increase in the content of MoS_2 nanosheets, except for 0.5 phr, and reached the highest modulus value for 3 phr. These results indicate that MoS_2 nanosheet incorporation into chlorobutyl rubber remarkably enhanced stiffness and had a significant reinforcing effect. This increase in storage modulus results from the intercalation of MoS_2 nanosheets in chlorobutyl rubber and strong interactions between the chlorobutyl rubber polymer chain and MoS_2 nanosheets. The mobility of the polymer chains in rubbery region was thus retarded by the MoS_2 nanosheets, resulting in the higher storage modulus.

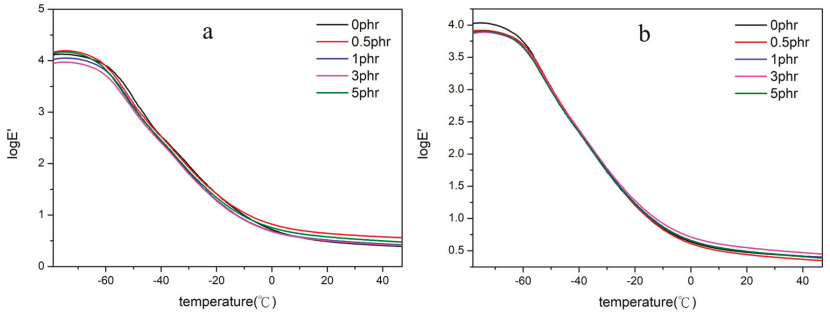

Figure 10. Storage modulus measurements: (**a**) MoS_2-ethanethiol-butyl and (**b**) MoS_2-nonanethiol-butyl rubber.

The tan(δ) values of MoS_2-ethanethiol-butyl rubber are shown in Figure 10a. For all of the samples of MoS_2-ethanethiol-butyl rubber, shifts to lower temperatures were observed when compared to the 0 phr sample. MoS_2 intercalated in chlorobutyl rubber may act as a lubricant, which leads to lowering of the glass transition temperature [27]. The tan(δ) values of MoS_2-nonanethiol-butyl rubber are shown in Figure 11b; similar shifts to lower temperatures can be seen, again indicating intercalation of MoS_2 nanosheets in the chlorobutyl rubber. The barrier effect of the nano-flakes restricting the motion of the polymer chains in the nanocomposites can be ascribed to the MoS_2 nanosheets.

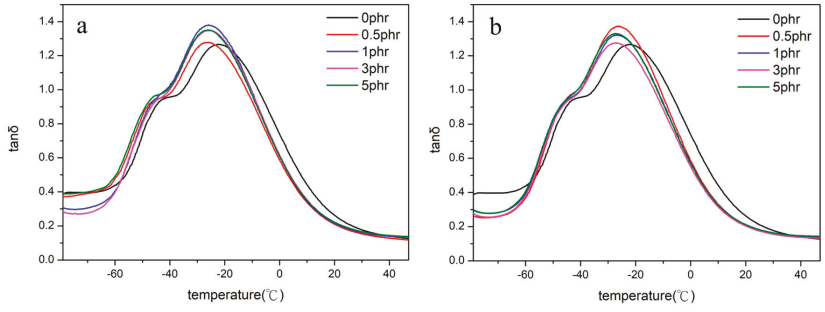

Figure 11. tan(*δ*) Measurements: (**a**) MoS_2-ethanethiol-butyl and (**b**) MoS_2-nonanethiol-butyl rubber.

3.5. Gas Barrier Properties of MoS_2-butyl Rubber Nanocomposites

The barrier properties of polymers can be significantly altered by including sufficient inorganic platelets to alter the path of gas molecules (Scheme 2) [4]. The oxygen transmission rate (OTR) (Table 1) of each MoS_2-butyl rubber nanocomposite was measured at 25 °C using the method outlined by ASTM D3985. When compared to that of pure chlorobutyl rubber, the OTR of MoS_2-ethanethiol-butyl rubber decreased dramatically to 42.3 cc/m^2-day at the MoS_2 nanosheet concentration of 0.5 phr. The OTR of MoS_2-nonanethiol-butyl rubber decreased to 47.2 cc/m^2-day at 0.5 phr, and thereafter decreased slowly at higher concentrations. The barrier performance for all MoS_2-butyl rubber nanocomposites could be improved markedly by the application of a small amount of organic-modified MoS_2. Moreover, there was little difference between the gas barriers of MoS_2-ethanethiol-butyl rubber and MoS_2-nonanethiol-butyl rubber, since the surface areas of MoS_2-ethanethiol and MoS_2-nonanethiol nanosheets were too small to retard the pathway of gas molecules. There are two reasons behind the enhancement of the gas barrier properties of the MoS_2-butyl rubber nanocomposites. First, MoS_2 nanosheets form tortuous pathways in chlorobutyl rubber, which retard the progress of gas molecules through the composite. Secondly, the diffusion coefficient of the gas molecules decreases because MoS_2 nanosheets strongly restrict the motion of the polymer chains [7].

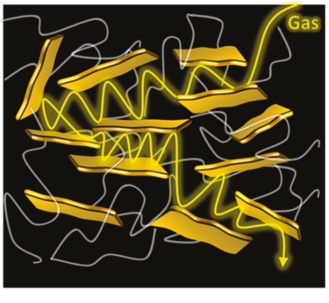

Scheme 2. Barrier to permeation imposed by nanoparticles embedded in a polymeric matrix.

Table 1. Oxygen transmission rates (OTRs) of MoS_2-butyl rubber nanocomposites.

	MoS_2-ethanethiol-butyl rubber (cc/m^2-day)	MoS_2-nonanethiol-butyl rubber (cc/m^2-day)
0 phr	90.9	90.9
0.5 phr	42.3	47.2
1 phr	48.2	46.8
3 phr	44.6	45.8
5 phr	43.7	46.5

4. Conclusions

In conclusion, we have demonstrated that MoS_2 nanosheets are an excellent filler material to enhance the tensile properties of chlorobutyl rubber. Ethanethiol and nonanethiol played an important role in modifying the surface of MoS_2 nanosheets. Using thiol modification of nanosheets helped to obtain MoS_2 monolayers with a thickness of ~0.8–1 nm, a key feature of MoS_2 nanosheets intercalated in chlorobutyl rubber. The obtained MoS_2 nanosheets were dispersed homogeneously in chlorobutyl rubber due to the thiol ligands modifying MoS_2 to enable greater affinity between MoS_2 and chlorobutyl rubber. Due to the high stiffness of the MoS_2 nanosheets, MoS_2 improved the mechanical properties of chlorobutyl rubber in tensile test, but not significantly in storage modulus. On the other hand, the gas barrier was improved dramatically, although similarly for MoS_2-ethanethiol- and MoS_2-nonanethiol-butyl rubber. These results offer new opportunities utilizing nanocomposites of polymers and MoS_2. Controlling the dimensions of MoS_2 nanosheets remains a challenge. Therefore, improved techniques are necessary to produce MoS_2 nanosheets of appropriate sizes, which can then achieve their full potential in polymer nanocomposites.

Acknowledgments: The authors would like to thank the Ministry of Science and Technology of the Republic of China (Taiwan) (grant number MOST 105-2622-E-011-009-CC2) for financially supporting this work.

Author Contributions: Chi-Yang Tsai, Shuian-Yin Lin and Hsieh-Chih Tsai conceived and designed the experiments; Chi-Yang Tsai performed the experiments; Chi-Yang Tsai and Hsieh-Chih Tsai analyzed the data; Chi-Yang Tsai wrote the paper.

Conflicts of Interest: The authors declare no conflict of interest.

References

1. Yoon, Y.; Ganapathi, K.; Salahuddin, S. How good can monolayer MoS_2 transistors be? *Nano Lett.* **2011**, *11*, 3768–3773. [CrossRef] [PubMed]
2. Anbazhagan, R.; Su, Y.-A.; Tsai, H.-C.; Jeng, R.-J. MoS_2-Gd chelate magnetic nanomaterials with core-shell structure used as contrast agents in in vivo magnetic resonance imaging. *ACS Appl. Mater. Interfaces* **2016**, *8*, 1827–1835. [CrossRef] [PubMed]
3. Feng, X.; Wen, P.; Cheng, Y.; Liu, L.; Tai, Q.; Hu, Y.; Liew, K.M. Defect-free MoS_2 nanosheets: Advanced nanofillers for polymer nanocomposites. *Compos. Part A* **2016**, *81*, 61–68. [CrossRef]
4. Paul, D.; Robeson, L.M. Polymer nanotechnology: Nanocomposites. *Polymer* **2008**, *49*, 3187–3204. [CrossRef]
5. Zachariah, A.K.; Geethamma, V.; Chandra, A.K.; Mohammed, P.; Thomas, S. Rheological behaviour of clay incorporated natural rubber and chlorobutyl rubber nanocomposites. *RSC Adv.* **2014**, *4*, 58047–58058. [CrossRef]
6. Liu, T.; Tjiu, W.C.; Tong, Y.; He, C.; Goh, S.S.; Chung, T.S. Morphology and fracture behavior of intercalated epoxy/clay nanocomposites. *J. Appl. Polym. Sci.* **2004**, *94*, 1236–1244. [CrossRef]
7. Liang, Y.; Cao, W.; Li, Z.; Wang, Y.; Wu, Y.; Zhang, L. A new strategy to improve the gas barrier property of isobutylene-isoprene rubber/clay nanocomposites. *Polym. Test.* **2008**, *27*, 270–276. [CrossRef]
8. Zheng, H.; Zhang, Y.; Peng, Z.; Zhang, Y. Influence of the clay modification and compatibilizer on the structure and mechanical properties of ethylene-propylene-diene rubber/montmorillonite composites. *J. Appl. Polym. Sci.* **2004**, *92*, 638–646. [CrossRef]
9. Galpaya, D.; Wang, M.; George, G.; Motta, N.; Waclawik, E.; Yan, C. Preparation of graphene oxide/epoxy nanocomposites with significantly improved mechanical properties. *J. Appl. Phys.* **2014**, *116*, 053518. [CrossRef]

10. Wu, J.; Huang, G.; Li, H.; Wu, S.; Liu, Y.; Zheng, J. Enhanced mechanical and gas barrier properties of rubber nanocomposites with surface functionalized graphene oxide at low content. *Polymer* **2013**, *54*, 1930–1937. [CrossRef]
11. Lian, H.; Li, S.; Liu, K.; Xu, L.; Wang, K.; Guo, W. Study on modified graphene/butyl rubber nanocomposites. I. Preparation and characterization. *Polym. Eng. Sci.* **2011**, *51*, 2254–2260. [CrossRef]
12. Fan, X.; Khosravi, F.; Rahneshin, V.; Shanmugam, M.; Loeian, M.; Jasinski, J.; Cohn, R.W.; Terentjev, E.; Panchapakesan, B. MoS_2 actuators: Reversible mechanical responses of MoS_2-polymer nanocomposites to photons. *Nanotechnology* **2015**, *26*, 261001. [CrossRef] [PubMed]
13. Patel, N.P.; Miller, A.C.; Spontak, R.J. Highly CO_2-permeable and selective polymer nanocomposite membranes. *Adv. Mater.* **2003**, *15*, 729–733. [CrossRef]
14. Ma, G.; Peng, H.; Mu, J.; Huang, H.; Zhou, X.; Lei, Z. In situ intercalative polymerization of pyrrole in graphene analogue of MoS_2 as advanced electrode material in supercapacitor. *J. Power Sources* **2013**, *229*, 72–78. [CrossRef]
15. Wang, T.; Zhu, R.; Zhuo, J.; Zhu, Z.; Shao, Y.; Li, M. Direct detection of DNA below ppb level based on thionin-functionalized layered MoS_2 electrochemical sensors. *Anal. Chem.* **2014**, *86*, 12064–12069. [CrossRef] [PubMed]
16. Chou, S.S.; De, M.; Kim, J.; Byun, S.; Dykstra, C.; Yu, J.; Huang, J.; Dravid, V.P. Ligand conjugation of chemically exfoliated MoS_2. *J. Am. Chem. Soc.* **2013**, *135*, 4584–4587. [CrossRef] [PubMed]
17. Zhou, W.; Zou, X.; Najmaei, S.; Liu, Z.; Shi, Y.; Kong, J.; Lou, J.; Ajayan, P.M.; Yakobson, B.I.; Idrobo, J.-C. Intrinsic structural defects in monolayer molybdenum disulfide. *Nano Lett.* **2013**, *13*, 2615–2622. [CrossRef] [PubMed]
18. Dungey, K.E.; Curtis, M.D.; Penner-Hahn, J.E. Structural characterization and thermal stability of MoS_2 intercalation compounds. *Chem. Mater.* **1998**, *10*, 2152–2161. [CrossRef]
19. Guan, G.; Zhang, S.; Liu, S.; Cai, Y.; Low, M.; Teng, C.P.; Phang, I.Y.; Cheng, Y.; Duei, K.L.; Srinivasan, B.M. Protein induces layer-by-layer exfoliation of transition metal dichalcogenides. *J. Am. Chem. Soc.* **2015**, *137*, 6152–6155. [CrossRef] [PubMed]
20. Bazylewski, P.; Divigalpitiya, R.; Fanchini, G. In situ raman spectroscopy distinguishes between reversible and irreversible thiol modifications in l-cysteine. *RSC Adv.* **2017**, *7*, 2964–2970. [CrossRef]
21. Marshall, C.P.; Marshall, A.O. The potential of raman spectroscopy for the analysis of diagenetically transformed carotenoids. *Philos. Trans. R. Soc. Lond. A Math. Phys. Eng. Sci.* **2010**, *368*, 3137–3144. [CrossRef] [PubMed]
22. Yin, W.; Yan, L.; Yu, J.; Tian, G.; Zhou, L.; Zheng, X.; Zhang, X.; Yong, Y.; Li, J.; Gu, Z. High-throughput synthesis of single-layer MoS_2 nanosheets as a near-infrared photothermal-triggered drug delivery for effective cancer therapy. *ACS Nano* **2014**, *8*, 6922–6933. [CrossRef] [PubMed]
23. Sim, D.M.; Kim, M.; Yim, S.; Choi, M.-J.; Choi, J.; Yoo, S.; Jung, Y.S. Controlled doping of vacancy-containing few-layer MoS_2 via highly stable thiol-based molecular chemisorption. *ACS Nano* **2015**, *9*, 12115–12123. [CrossRef] [PubMed]
24. Biswas, Y.; Dule, M.; Mandal, T.K. Poly(ionic liquid)-promoted solvent-borne efficient exfoliation of MoS_2/$MoSe_2$ nanosheets for dual-responsive dispersion and polymer nanocomposites. *J. Phys. Chem. C* **2017**, *121*, 4747–4759. [CrossRef]
25. Triantafillidis, C.S.; LeBaron, P.C.; Pinnavaia, T.J. Homostructured mixed inorganic-organic ion clays: A new approach to epoxy polymer-exfoliated clay nanocomposites with a reduced organic modifier content. *Chem. Mater.* **2002**, *14*, 4088–4095. [CrossRef]
26. Eksik, O.; Gao, J.; Shojaee, S.A.; Thomas, A.; Chow, P.; Bartolucci, S.F.; Lucca, D.A.; Koratkar, N. Epoxy nanocomposites with two-dimensional transition metal dichalcogenide additives. *ACS Nano* **2014**, *8*, 5282–5289. [CrossRef] [PubMed]
27. Choi, Y.S.; Choi, M.H.; Wang, K.H.; Kim, S.O.; Kim, Y.K.; Chung, I.J. Synthesis of exfoliated PMMA/Na-MMT nanocomposites via soap-free emulsion polymerization. *Macromolecules* **2001**, *34*, 8978–8985. [CrossRef]

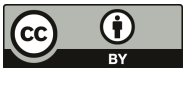

polymers

MDPI

Article

Silica Modified by Alcohol Polyoxyethylene Ether and Silane Coupling Agent Together to Achieve High Performance Rubber Composites Using the Latex Compounding Method

Junchi Zheng [1], Xin Ye [1,2], Dongli Han [1], Suhe Zhao [1,2], Xiaohui Wu [1], Youping Wu [1,2], Dong Dong [3], Yiqing Wang [1,2,*] and Liqun Zhang [1,2,*]

[1] Engineering Research Center of Elastomer Materials on Energy Conservation and Resources, Ministry of Education, Beijing 100029, China; 2015400076@mail.buct.edu.cn (J.Z.); yexin@mail.buct.edu.cn (X.Y.); handl@mail.buct.edu.cn (D.H.); zhaosh@mail.buct.edu.cn (S.Z.); wuxiaohui555@163.com (X.W.); wuyp@mail.buct.edu.cn (Y.W.)

[2] State Key Laboratory of Organic-Inorganic Composites, Beijing University of Chemical Technology, P.O. Box 57, Beisanhuan East Road, Beijing 100029, China

[3] Red Avenue New Materials Group Co., Ltd., Shanghai 200120, China; dondan68@163.com

* Correspondence: wangyq1@mail.buct.edu.cn (Y.W.); zhanglq@mail.buct.edu.cn (L.Z.); Tel.: +86-139-1021-5964 (L.Z.); Fax: +86-010-6444-3413 (L.Z.)

Received: 9 November 2017; Accepted: 18 December 2017; Published: 21 December 2017

Abstract: The study of preparing silica/rubber composites used in tires with low rolling resistance in an energy-saving method is fast-growing. In this study, a novel strategy is proposed, in which silica was modified by combing alcohol polyoxyethylene ether (AEO) and 3-mercaptopropyltriethoxysilane (K-MEPTS) for preparing silica/natural rubber (NR) master batches. A thermal gravimetric analyzer and Raman spectroscopy results indicated that both AEO and K-MEPTS could be grafted on to the silica surface, and AEO has a chance to shield the mercaptopropyl group on K-MEPTS. Silica modified by AEO and K-MEPTS together was completely co-coagulated with the rubber in preparing silica/NR composites using the latex compounding method with the help of the interaction between AEO and K-MEPTS. The performance of composites prepared by silica/NR master batches was investigated by a rubber process analyzer (RPA), transmission electron microscopy (TEM) and a tensile tester. These results demonstrate that AEO forms a physical interface between silica and rubber, resulting in good silica dispersion in the matrix. K-MEPTS forms a chemical interface between silica and rubber, enhancing the reinforcing effect of silica and reducing the mutual friction between silica particles. In summary, using a proper combination of AEO and K-MEPTS is a user-friendly approach for preparing silica/NR composites with excellent performance.

Keywords: chemical and physical interface; surface modification of silica; latex compounding method; silica/NR composite

1. Introduction

Silica is a non-carbon filler that is an extremely important reinforcing filler in the rubber industry [1]. Previous studies have confirmed that silica combines good mechanical performance [2], high wet grip resistance [3] and low rolling resistance [4] for silica/rubber composites. At present, silica/rubber composites are commonly used for producing "green tires" [5,6], which have low rolling resistance, resulting in reducing the vehicle's fuel consumption.

As an inorganic particle, silica has many hydroxyl groups (–OH) on its surface [7], causing the hydrophilic nature of the silica particle [8–10]. Therefore, the silica particle is less compatible with

a hydrophobic polymer, such as rubber [11]. However, the silica surface can be modified due to the numerous reactive hydroxyl groups [12,13]. Silica modification is an effective method for improving the compatibility between silica and rubber. Treatment with reactive silane coupling agent (SCA) is one of the major methods used in silica modification [14,15]. In principle, SCA possesses a readily hydrolyzable alkoxy group that reacts with the hydroxyl groups on the silica surface to form a stable siloxane linkage [16]. In addition, some surface active agents (SAA), such as poly ethylene glycol, triethanolamine and cetyltrimethylammonium bromide, are commonly used in silica modification. SAA can absorb on the silica surface, resulting in covering the silica surface and reducing the amount of the exposed hydroxyl groups.

Natural rubber (NR), which contains 93%–95% *cis*-1,4-polyisoprene, is an essential biosynthesized polymer [17]. It is naturally found in the form of a colloidal system known as NR latex, in which rubber particles are dispersed in an aqueous medium [18,19]. Therefore, the latex compounding method is used to prepare silica/NR composites to address the problems of low efficiency in the outdated mechanical blending method [20,21].

Preparing a silica/NR slurry with good silica dispersion and stable NR particles is key for the latex compounding method mentioned above. The silica in this slurry should be completely co-coagulated with the rubber when preparing silica/NR master batches, which is a floc containing silica and rubber. As these materials work at a high frequency of motion, silica/rubber composites should have excellent dynamic performance, which is not required in most kinds of polymer composites. Therefore, the silica in the master batches should have the potential to form a chemical interaction with NR, because the internal friction of silica/NR composites, which is the major factor in dynamic performance such as rolling resistance and wet grip of tires, can be reduced by a chemical interaction between silica and rubber. Preparing modified silica, using a proper strategy to achieve an ideal organic silica surface, is the most practical process to meet the above requirements.

In previous research, sulfide-containing SCAs were used for silica modification when preparing silica/rubber composites using the latex compounding method [21–24]. In principle, sulfide-containing SCAs react with silica as mentioned above, resulting in improving the dispersion of silica in a latex system and rubber matrices. Meanwhile, sulfide-containing SCAs can react with the double bonds in rubber molecules by their sulfide group. Therefore, the structure by which rubber molecules and silica particles are linked by the SCA is formed between silica and rubber by the help of the sulfide-containing SCAs through a "coupling bridge" [25]. Previous researchers indicated that the "coupling bridge", which is a typical chemical interface between silica and rubber, benefits the mechanical and dynamic properties of silica/rubber composites [26]. However, the hydroxyl groups on the silica react with the hydroxyl groups of hydrolyzed SCA in silica modified by SCA in the aqueous phase [27], meaning the hydrolysis of SCA is a precursor for silica modification. Polycondensation also occurs among the hydroxyl groups of hydrolyzed SCA, producing the polycondensates of SCA, resulting in the aggregation of several SCA molecules [25]. Therefore, using only SCA in silica modification is not adequately efficient. Only the chemical interface existing between silica and rubber is detrimental to the stretching of the rubber molecular chain under external force [28–30]. Moreover, the reaction between rubber and sulfide-containing SCA, known as "scorchy" behavior, is inevitable during the process [31], even though the mixing time and temperature are precisely controlled. Therefore, using sulfide-containing SCA only for silica modification is not an ideal method for preparing silica/rubber composites.

Parts of SAAs directly modify silica in the aqueous phase without polycondensation, and not all SAAs react with rubber under all conditions. Therefore, a physical interface between silica and rubber can only be formed with the help of SAA [32–34]. However, the dynamic performance of silica/rubber composites is very poor in the absence of a chemical interface between silica and rubber [8,28]. In our previous research, silica modified by SAA was not completely co-coagulated with the rubber when preparing silica rubber master batches using the latex compounding method.

For rubber composites prepared for "green tires", the dynamic performance is extremely important. Therefore, for this research, a chemical interface between silica and rubber was formed. Preparing high performance silica/rubber composites for "green tires" using the latex compounding method is a more complex and restrictive study than the preparation of other polymer composites. Using different modifiers to form chemical and physical interfaces between silica and rubber is a simple and feasible method to achieve this goal.

In this research, the silica/NR master batches were prepared using the latex compounding method. Alcohol polyoxyethylene ether (AEO) [35]), a widely-used nonionic SAA, and 3-mercaptopropyltriethoxysilane (K-MEPTS) [36], which was commercially developed and widely used in the rubber industry, were selected as modifiers to be used together in silica modification in the aqueous phase (as shown in Figure 1). This is a novel strategy proposed for silica modification for preparing silica/rubber master batches. The magnitude of the chemical and physical interface between silica and rubber is varied by adjusting the amount of AEO and K-MEPTS used in silica modification. In our research, pure and different modified silica were characterized by Fourier transform infrared spectroscopy (FT-IR), thermal gravimetric analysis (TGA), and Raman spectroscopy. The interaction between K-MEPTS and AEO was confirmed through the results of these characterizations. Pure and different modified silica were used in preparing silica/NR master batches by the latex compounding method. In this part of the research, the role played by K-MEPTS and AEO using the co-coagulation of silica and NR was confirmed. Finally, the properties of silica/NR composites containing different modified silica were compared. The effect of the chemical interface between silica and rubber, formed by K-MEPTS, and the physical interface between silica and rubber, formed by AEO, on the performance of silica/NR composites was investigated.

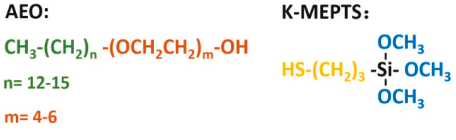

Figure 1. Chemical structure of alcohol polyoxyethylene ether (AEO) and 3-mercaptopropyltriethoxysilane (K-MEPTS).

2. Experimental Materials and Methods

2.1. Materials

High-ammonia NR latex with 60% total solid content was purchased from Hainan Rubber Industry Group Co., Ltd. (Hainan, China). Precipitated silica water slurry of K-160 (nanoparticle size: 20–30 nm, Brunauer-Emmett-Teller (BET) specific surface: 160.06 m^2/g) was produced by Wilmar China (Jiamusi, China). AEO (average molecular weight: 421 g/mol), which possesses a terminal hydroxyl group that can react with hydroxyl groups on the silica surface and possesses a long molecular chain that consists of polyolefin and polyether, was prepared by BASF SE. K-MEPTS (molecular weight: 196 g/mol) was obtained from Nanjing Capatue Chemical Co., Ltd. (Nanjing, China). The rest of the required materials were commercially available.

2.2. Preparation of Modified Silica

The silica slurry solid content was measured to dilute to a 10% concentration (e.g., 100 g dry weight of silica for every 1000 g silica slurry) by adding water into the raw precipitated silica slurry. The silica water slurry was subjected to high-speed stirring (800 rpm) for 30 min to obtain a stable suspension. Five beakers, numbered 1–5, were prepared, and 1000 g of silica slurry were transferred to each beaker. All silica slurries were heated to a temperature of 70 °C under high-speed stirring (800 rpm). K-MEPTS (6, 6, 4, and 2 g) was added into Beakers 1–4, and AEO (4, 6, 8 and 8 g) was

added into Beakers 2–5, respectively. The slurry was stirred for 0.5 h, and the modified silica slurry was then obtained. According to the amount of AEO and K-MEPTS added in the silica modification, we labelled the modified silica in Beakers 1–5 as A0K6-MS, A4K6-MS, A6K4-MS, A8K2-MS and A8K0-MS, respectively. The amounts of K-MEPTS and AEO used in the different modified silica are listed in Table 1.

Table 1. Formulation of modified silica and its label.

Material	A0K6-MS	A4K6-MS	A6K4-MS	A8K2-MS	A8K0-MS
Silica (dry weight)/g	100	100	100	100	100
3-mercaptopropyltriethoxysilane (K-MEPTS)/g	6	6	4	2	0
polyoxyethylene ether (AEO)/g	0	4	6	8	8

Part of the pure silica and modified silica powder was obtained by drying the corresponding modified silica slurry. Pure silica and modified silica powders were extracted in a Soxhlet extractor using ethanol for 24 h, 15 min for each reflux, to remove un-grafted AEO and K-MEPTS. Then, all extracted silica powders were dried in the same oven at 70 °C for 24 h. These silica powders were prepared for characterization using FT-IR, TGA and Raman spectroscopy.

2.3. Preparation of Master Batches

The modified silica slurry was cooled to room temperature and blended with the NR latex. The solid content of the NR latex was confirmed in advance, and the weight ratio of silica to NR was 50:100 (e.g., 50 g of silica nanoparticles for every 100 g solid content of NR). Then, the mixture of silica and NR latex was stirred for 0.5 h and coagulated with 3% formic acid solution. Finally, the flocs were washed with water 6 times and then dehydrated in a drying oven at 60 °C for 36 h to obtain silica/NR master batches. The master batches prepared with A0K6-MS, A4K6-MS, A6K4-MS, A8K2-MS and A8K0-MS were called A0K6-MB, A4K6-MB, A6K4-MB, A8K2-MB and A8K0-MB, respectively.

2.4. Preparation of Silica/NR Composites

The formulation of silica/NR compounds is shown in Table 2. Silica/NR compounds were obtained through three stages of mixing. First, the master batches were masticated for 2 min in an internal mixer equipped with an oil circulating system to maintain the processing temperature at 55 °C. Then, zinc oxide, stearic acid and *N*-1,3-dimethylbutyl-*N*′-phenyl-*p*-phenylenediamine were added to the master batches successively. Second, compounds were kneaded for 5 min in the same internal mixer at 150 °C to further promote the reaction between silica and modifier and then naturally cooled to room temperature. Finally, *N*-cyclohexyl-2-benzothiazole-sulfenamide, diphenyl guanidine and sulfur were uniformly blended in sequence with the cooled compound in a 6-inch mill (Shanghai Rubber Machinery Works No. 1, Shanghai, China) at room temperature. The total mixing time was no more than 15 min. The silica/NR compounds that contained A4K6-MB, A6K4-MB and A8K2-MB were denoted as A4K6-C, A6K4-C and A8K2-C, respectively.

Table 2. Formulation of silica/natural rubber (NR) compounds.

Material	Amount (phr [a])	Comment
Master batches	155	Filler and matrix
Stearic acid	2.0	Activator
Zinc oxide	5.0	Activator
N-1,3-dimethylbutyl-*N*′-phenyl-p-phenylenediamine	2.0	Antioxidant
N-Cyclohexyl-2-beozothiazole sulfenamide	2.0	Accelerator
1,3-Diphenylguanidine	1.0	Accelerator
Sulfur	2.0	Curing agent

[a] Parts per hundred of rubber.

The scorch time (T_{10}) and optimum cure time (T_{90}) of the compound were measured using a disc vulcameter. The compounds were vulcanized at 143 °C according to their optimum cure time (T_{90}) in a standard mold to produce the silica/NR vulcanizates, which were stored at room temperature for at least 24 h before determining the performance.

2.5. Characterizations

The groups of pure and modified silica were characterized by Fourier transform infrared spectroscopy (FT-IR; Bruker Optik GmbH Co., Tensor 27, Ettlingen, Germany), using the absorption mode under a wave ranging from 4000–400 cm^{-1} with a resolution of 4 cm^{-1}. The samples were pressed into pellets together with potassium bromide.

Raman spectra of pure and modified silica samples were recorded from 3200–2500 cm^{-1} on an inVia confocal Raman spectrometer (Renishaw PLC, Gloucestershire, UK) using a 514-nm laser beam. The power of a 514-nm argon ion excitation laser at the source is approximately 50 mW (highest power) and 20 mW at the surface of the sample. The Raman spectra of the samples were obtained from pressed solid samples in a sealed capillary tube.

Weight loss measurements of pure and modified silica and the master batches were performed on a thermal gravimetric analyzer (TGA) STARe system (Mettler-Toledo Co., Greifensee, Switzerland) in a nitrogen atmosphere. Samples for the TGA tests were heated at a heating rate of 10 °C/min. The residual weight of master batches, NR, silica, K-MEPTS and AEO were recorded as R_m, R_r, R_s, R_5 and R_A, respectively.

The filler dispersion in silica/NR master batches and silica/NR composites was observed under a Tecnai G2 20 transmission electron microscope (TEM, FEI Co., Hillsboro, OR, USA) with an accelerating voltage of 200 kV. Thin sections for TEM observations were cut by a microtome at −100 °C and collected on copper grids.

The dynamic rheological performances of silica/NR compounds and silica/NR composites were analyzed using RPA2000 (Alpha Technologies Co., Ltd., Akron, OH, USA) at 60 °C. For the rubber compounds, the strain varied from 0.1%–400% at the test frequency of 1 Hz. For the rubber vulcanizates, the strain varied from 0.1%–40% at the test frequency of 1 Hz. The test of each specimen was repeated 3 times.

The vulcanization characteristics of silica/NR compounds were measured at 143 °C using a P3555B2 disc vulkameter (Beijing Huanfeng Chemical Machinery Trial Plant, Beijing, China). The test of each specimen was repeated 3 times.

The mechanical performance of the silica/NR composites were investigated according to ASTM D638 specifications using a CMT4104 electrical tensile tester (Shenzhen SANS Test Machine Co., Shenzhen, China) with an across-head speed of 500 mm/min. The test of each specimen was repeated 5 times.

3. Results and Discussion

3.1. Characterization of Silica Modified by AEO and K-MEPTS

3.1.1. FT-IR of Pure and Modified Silica

As shown in Figure 2, compared to the FT-IR spectra of the pure silica, all curves of the modified silica had absorption peaks at 2930, 2970 and 2870 cm^{-1}, attributed to the vibrations of $–CH_2–$ and $–CH_3$ bonds [37]. The appearance of organic groups, such as $–CH_2–$ and $–CH_3$, on the modified silica surface shows that K-MEPTS and AEO exist on the silica surface.

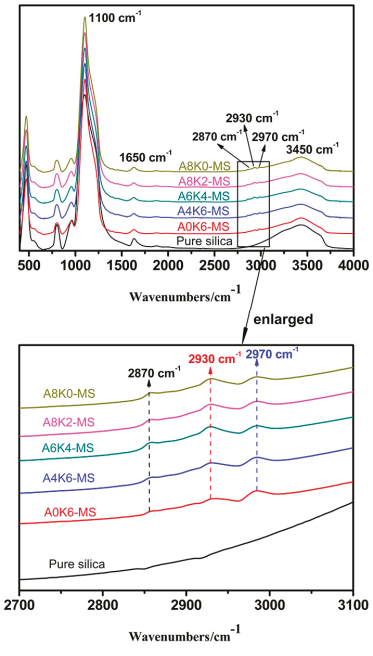

Figure 2. Fourier transform infrared (FT-IR) spectra of pure silica and all modified silica.

The absorption peaks at 3450 and 1650 cm^{-1} correspond to the stretching and deforming vibration modes of the –O–H bonds [38], respectively. The relative intensity (RI) of the peak at 3450 cm^{-1}, which is the difference between the intensity of the peak and the baseline, is determined by the number of –O–H bonds. Therefore, a high RI means a large number of hydroxyl groups is present on the silica surface. RI can be calculated using the normalized FT-IR data, and the RI of all samples are listed in Table 3. The RI of all silica modified by AEO and K-MEPTS together decreased with increasing the AEO used in silica modification, indicating that replacing K-MEPTS with AEO can more effectively reduce the amount of active –O–H bonds on the silica surface.

Table 3. Relative intensity (RI) of the peak at 3400 cm^{-1} for pure silica and all modified silica.

Sample	Pure silica	A0K6-MS	A4K6-MS	A6K4-MS	A8K2-MS	A8K0-MS
RI	0.318	0.211	0.189	0.184	0.178	0.196

3.1.2. Raman Spectroscopy of Pure and Modified Silica

No peak is shown on the curve of pure silica; therefore, no organic groups are present on the surface of pure silica (Figure 3). Meanwhile, one peak is found on the curve of A8KO-MS and two peaks on other curves. The peak at 2930 cm^{-1} corresponds to methylene bonds, demonstrating that the AEO and K-MEPTS were grafted on the silica surface. Another peak is recorded at 2570 cm^{-1}, which corresponds to –S–H bonds, indicating that K-MEPTS was grafted on the silica surface.

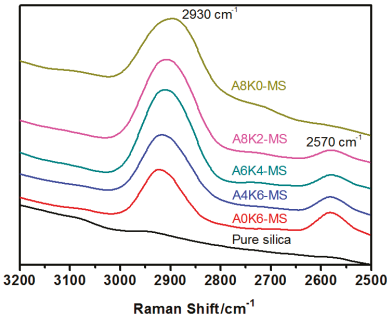

Figure 3. Raman spectra of pure silica and all modified silica.

The peak intensity around 2570 cm^{-1} for A4K6-MS is significantly weaker than that of A0K6-MS. The only difference for A0K6-MS and A4K6-MS was whether AEO was used in silica modification. The most probable reason for this result was that the AEO molecule had a chance to shield the mercaptopropyl group on K-MEPTS.

3.1.3. TGA Curves of Pure and Modified Silica

As illustrated in Figure 4 and Table 4, all the samples exhibited large weight losses in the first region between 35 and 120°C. The weight loss in this region was caused by the removal of the adsorbed water. The amount of adsorbed water on the silica surface shows the same tendency as the amount of hydroxyl groups on the silica surface.

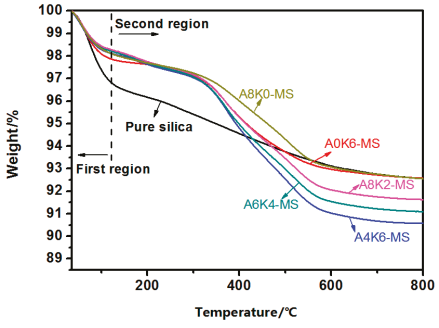

Figure 4. Thermal gravimetric analyzer (TGA) curves of pure silica and all modified silica.

Table 4. Weight losses of pure and modified silica in the first and second regions.

Sample	Weight loss in the first region (35–120 °C)/%	Weight loss in the second region (120–800 °C)/%
Pure silica	3.16	4.27
A0K6-MS	2.13	5.31
A4K6-MS	1.88	7.54
A6K4-MS	1.78	7.13
A8K2-MS	1.71	6.66
A8K0-MS	1.90	5.55

All of modified silica had a large weight loss in the second region between 120 and 800 °C. The weight loss of modified silica was due to the degradation of AEO and K-MEPTS, and the weight

loss of pure silica was due to the dehydroxylation of hydroxyl groups. All modified silica had a larger weight loss than pure silica in the second region; whereas A4K6-MS had a larger weight loss than A0K6-MS in the second region. This is a noteworthy finding that indicates that both K-MEPTS and AEO were grafted onto the silica surface.

For A4K6-MS, A6K4-MS and A8K2-MS, the total weight of AEO and K-MEPTS grafted on silica decreased, but the amount of adsorbed water decreased sequentially. Therefore, AEO is a more effective modifier than K-MEPTS in changing the hydrophilicity of silica. This result could be attributed to the structure of the AEO molecule, which likely covered multiple hydroxyl groups on the silica surface. In contrast, a K-MEPTS molecule could react with up to one hydroxyl group on the silica surface. The decrease in the hydrophilic nature of silica generally means that the compatibility between silica and the organic phase, such as rubber, is improved, which is crucial for preparing high performance silica/NR composites.

Based on the above results, the interaction between AEO and K-MEPTS is shown in Figure 5. The activity of the mercaptopropyl on K-MEPTS is affected by this interaction. Therefore, the chargeability and reactivity of silica modified with AEO and K-MEPTS together differ from that of silica modified with K-MEPTS alone.

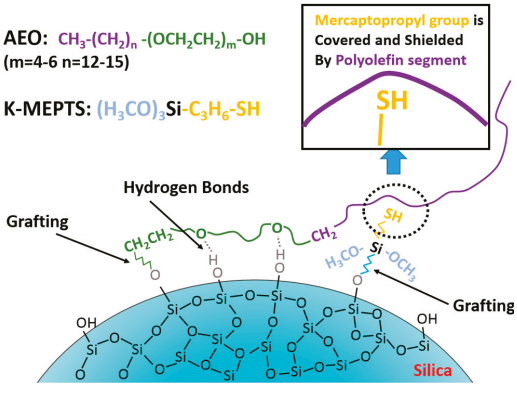

Figure 5. Schematic diagram of the interaction between AEO and K-MEPTS during silica modification.

3.2. Characterization of Silica/NR Master Batches Prepared with Pure and Modified Silica

3.2.1. Co-Coagulation of Silica/NR Mixture in Preparing the Master Batches

The co-coagulation of the silica/NR mixture used in preparing the master batches using several modified silica and pure silica (A0K0-MS) is shown in Figure 6. The images of the silica/NR mixtures, which were prepared by adding the NR latex into the silica slurries and stirring for 10 min, are shown in Figure 6a. Images of master batches, prepared by adding 3% formic acid solution into mixtures, are shown in Figure 6b. A6K4-MS was selected as the representative for silica modified with both AEO and K-MEPTS together, because the phenomenon of preparing silica/rubber master batches was almost the same for A4K6-MS, A6K4-MS and A8K2-MS.

As presented in Figure 6(a2), part of the mixture coagulated when NR was mixed with A0K6-MS, even if the formic acid solution was not added into this mixture. This phenomenon indicates that K-MEPTS promotes the coagulation of NR latex. As presented in Figure 6b, A0K6-MB, A8K0-MB and pure silica masterbatch were largely clustered, and the residual aqueous phase was white and turbid with abundant silica. Conversely, A6K4-MB coagulated as complete sediments, and the residual aqueous phase was clear.

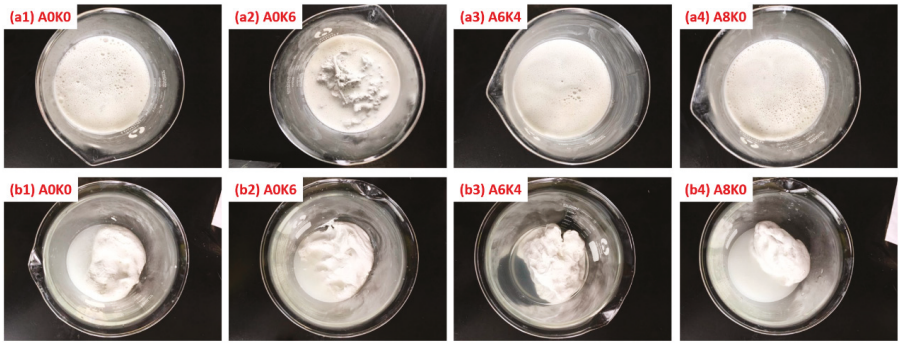

Figure 6. Preparation process of the master batches with pure and modified silica.

The difference in the coagulation phenomenon in different master batches was caused by electrostatic attractive or repulsive forces. An additional simple experiment was performed to confirm this inference. As presented in Figure 7, four kinds of pure and modified silica were added to a beaker with a 2 by 2.5-cm copper plate, as an electrode device. After two hours, the silica deposited on the electrode was weighed after drying. The results of silica deposition are also shown in Figure 7. The pure silica and A8K0-MS were deposited on the positive electrode, indicating that both were negatively charged. In contrast, A0K6-MS and A6K4-MS were deposited on the negative electrode; meanwhile, the amount of A0K6-MS deposited was more than the A6K4-MS deposited. This result indicates that A0K6-MS and A6K4-MS were positively charged, and the positive charge of A0K6-MS was more significant than that of A6K4-MS.

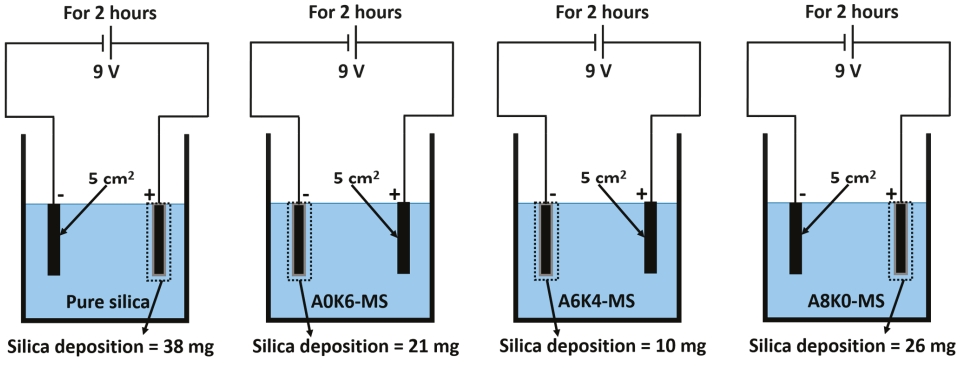

Figure 7. Schematic diagram of the silica deposition experiment.

Based on the above results, we made a schematic diagram of the electrostatic attractive or repulsive forces between silica and latex particles. The surface of both the silica particle and NR latex particle were negatively charged [39], causing an electrostatic repulsion in the system, as presented in Figure 8a. Therefore, pure silica/NR masterbatch had a large amount of silica loss in the aqueous phase. The changes in the silica surface charge contributed to the adsorption between rubber and silica. However, A0K6-MS had a significantly positive charge, resulting in a strong attractive force between A0K6-MS and rubber latex particles. This force would damage the electrical layer stability of the rubber latex particles, as shown in Figure 8b. Therefore, a mixture of A0K6-MS and NR latex was coagulated in the absence of formic acid solution.

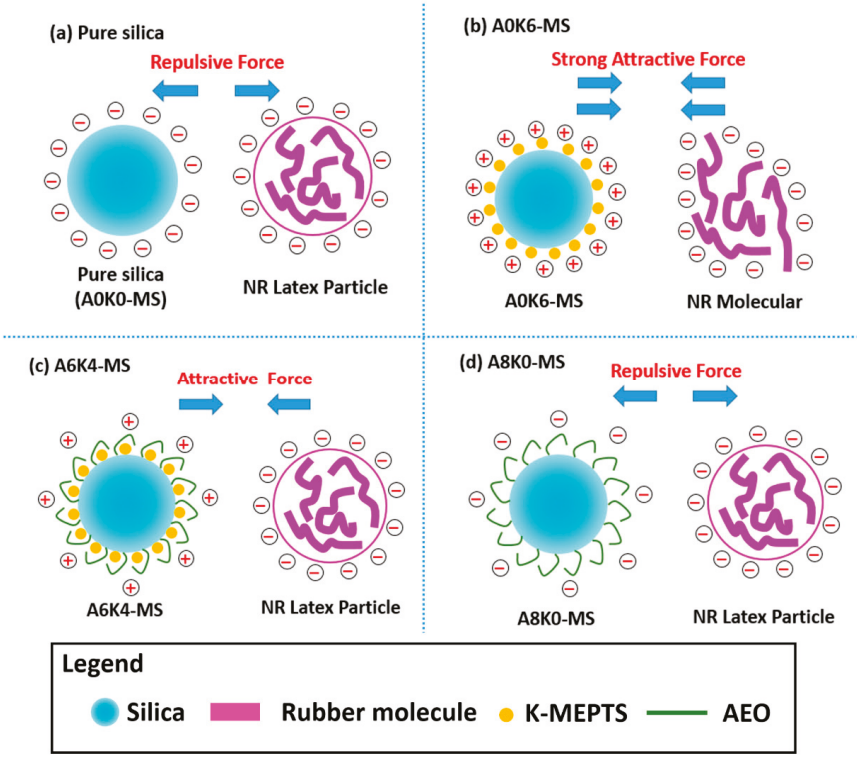

Figure 8. Schematic diagram of the electrostatic forces between pure or modified silica and NR.

The positive charge of A6K4-MS was weaker than that of A0K6-MS. The attractive force between the NR latex particles and modified silica was at an appropriate level, resulting in the successful preparation of A6K4-MB. However, AEO was a nonionic surfactant that had no effect on the electrical performance of the silica surface. Therefore, a repulsive force still existed between A8K0-MS and NR latex particles, as presented in Figure 8d. In this scenario, the co-coagulation of the mixture of latex, which included NR latex and A8K0-MS, was unsatisfactory.

3.2.2. Actual Amount of Silica in Silica/NR Master Batches

The actual amount of silica in the master batches was calculated using the following equation:

$$\text{Silica content (phr)} = \frac{100 \times (R_m - R_r)}{R_s + S_A \times R_A + S_5 \times R_5 - (1 + S_5 + S_A) \times R_\text{m}} \quad (1)$$

where R_m, R_r, R_s, R_5 and R_A are the 800 °C weight (%) of master batches, rubber, silica, K-MEPTS and AEO, respectively. S_5 is the weight ratio of K-MEPTS to modified silica, and S_A is the weight ratio of AEO to modified silica. The calculated results according to this equation are shown in Table 5. For all master batches that contained silica modified with K-MEPTS and AEO together, the actual amount of silica in the master batches is approximately equal to the additional amount of silica (50 parts per hundred of rubber (phr)). In contrast, the actual amount of silica in A0K6-MB, A8K0-MB and A0K0-MB is obviously lower than the 50 phr addition of silica. This result further indicates a huge loss of silica occurred during coagulation when K-MEPTS or AEO was used individually to modify silica. The results are consistent with the observed macroscopic phenomena in Section 3.2.1.

Table 5. Weight losses of six kinds of silica/NR master batches.

Samples	Weight residual/%	Theoretical amount of silica in masterbatches/phr	Actual amount of silica in masterbatches/phr
Pure NR	1.32	-	-
Pure silica	92.57	-	-
KH-590	9.13	-	-
AEO	3.27		
A0K6-MB	26.32	50	38.33
A4K6-MB	30.76	50	49.55
A6K4-MB	30.83	50	49.83
A8K2-MB	30.65	50	49.46
A8K0-MB	23.71	50	33.31
A0K0-MB	22.89	50	30.96

Because of the interaction between AEO and K-MEPTS, silica modified with AEO and K-MEPTS together had appropriate chargeability and completely co-coagulated with the rubber, which is another key factor for preparing high performance silica/NR composites using the latex compounding method.

3.2.3. Micromorphology of the Silica/NR Master Batches Observed by TEM

As shown in Figure 9, silica is uniformly dispersed in the matrix without serious aggregation in these master batches. The silica dispersion in A6K4-MB is somewhat more homogeneous than in other samples. This composite has fewer silica aggregates than the others. This result demonstrates that the electrostatic attractive force between A6K4-MS and rubber molecules is the most successful in the three master batches that were successfully prepared.

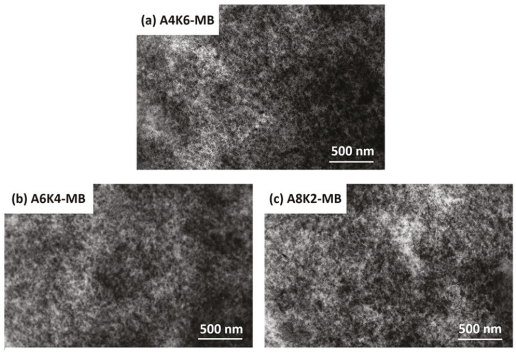

Figure 9. TEM images of (**a**) A4K6-MB; (**b**) A6K4-MB; and (**c**) A8K2-MB.

3.3. Characterization of the Preparation Process of Silica/NR Composites

The method of preparing A4K6-C, A6K4-C and A8K2-C is described in Section 2.4. A0K6-C cannot be prepared using master batches due to the huge silica loss in preparing A0K6-MB. Therefore, the mechanical blending method was used for preparing A0K6-C.

As shown in Table 6, A0K6-C had the shortest scorch time (T_{10}) in all the tested silica/rubber compounds. In increasing order, the scorch times of A4K6-C, A6K4-C and A8K2-C were longer than that of A0K6-C. The reactivity of the mercaptopropyl group decreases when AEO was used together with K-MEPTS. Therefore, AEO slowed the rate of reaction between K-MEPTS and rubber. The "scorchy: problem can be mitigated by using AEO and K-MEPTS together in silica modification. The ΔM of A0K6-C was a little bit higher than that of A4K6-C. The silica modified by K-MEPTS could function as a cross-linking point, resulting in the improved crosslinking density of the silica/rubber

composite, which is reflected by ΔM. Therefore, AEO has little effect on preventing the reaction between K-MEPTS and rubber.

Table 6. Vulcanization characteristics of four kinds of silica/NR compounds.

Samples	T_{10}/min	T_{90}/min	ΔM/dNm
A0K6-C	0.65	3.03	30.39
A4K6-C	2.05	5.28	28.72
A6K4-C	3.25	5.87	26.89
A8K2-C	3.72	7.33	24.95

3.4. Characterization of Silica Dispersion in Silica/NR Composites

3.4.1. Payne Effect of Silica/NR Compounds Investigated by RPA

At approximately 1% strain, the storage modulus (G') decreases rapidly with increasing strain and approaches 0 kPa with a sufficiently large strain as shown in Figure 10. The Payne effect is indicated by the $\Delta G'$, which is the difference between the minimum and maximum G' in the curve [40]. This effect can be attributed to deformation-induced changes in the microstructure of the material. The Payne effect is not significant when $\Delta G'$ is small. The low Payne effect indicates high uniformity of the filler dispersion.

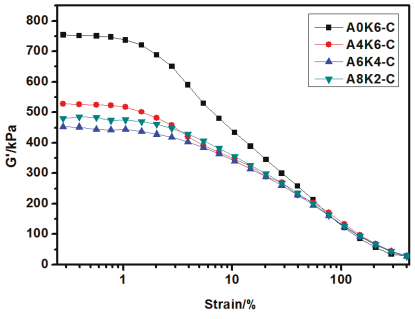

Figure 10. Strain amplitude dependence of the storage modulus (G') of four silica/NR compounds.

As shown in Figure 10, A0K6-C exhibits a more obvious Payne effect than the other silica/NR compounds. This finding indicates that the dispersion of silica modified by AEO and K-MEPTS together in silica/NR composites prepared in master batches is more homogeneous than that of silica modified by K-MEPTS alone in silica/NR composites prepared using mechanical blending. This result was caused by two reasons: AEO effectively reduces the hydrophilicity of silica, resulting in improving silica dispersion in NR matrix; and the silica dispersion in the rubber matrix is improved by the latex compounding method [22].

The Payne effect of the composite decreases with increasing AEO used in the silica modification and then reaches the lowest value when the weight ratio of AEO to silica is 6:100 and that of K-MEPTS to silica is 4:100 (A6K4-C). This result show the same tendency as the silica dispersion in silica/NR master batches. Therefore, the silica dispersion in master batches directly affects the dispersion of silica in silica/NR compounds, which further indicates the importance of preparing silica/NR master batches with a homogeneous silica dispersion.

3.4.2. Micromorphology of the Silica/NR Composites Observed by TEM

Figure 11 shows that the silica dispersion in the vulcanizates of A4K6-C, A6K4-C and A8K2-C is significantly more homogeneous than in the vulcanizate of A0K6-C, because the latter contains

more silica aggregates. AEO grafted onto the silica surface, but did not react with rubber, resulting in the formation of a physical interface between silica and rubber. This physical interface reduced the polarity of silica and improved the compatibility between silica and rubber, thus improving the dispersion of silica in rubber. In contrast, K-MEPTS grafted onto the silica surface and reacted with rubber, resulting in forming a chemical interface between silica and rubber. The silica particles could be connected with the rubber molecules with the help of K-MEPTS. Therefore, this chemical interface played a role in preventing the aggregation of primary silica particles. Silica modified by using both AEO and K-MEPTS together benefits from the chemical and physical interaction between silica and rubber. In this research, the silica/NR composites had the best silica dispersion when the weight ratio of AEO to K-MEPTS was 6:4 for silica modified by 10% weight modifiers.

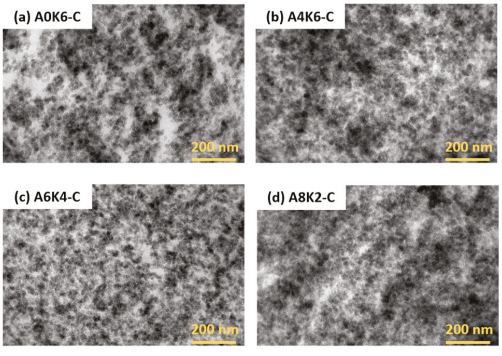

Figure 11. TEM images of four silica/NR composites.

3.5. Characterization of Silica/NR Composites

3.5.1. Mechanical Performances of Silica/NR Composites

As shown in Figure 12 A0K6-C vulcanizate exhibits a 50% higher modulus and a 40% lower elongation at break than A4K6-C vulcanizate. The tensile strength of A0K6-C vulcanizate is 40% lower than that of A4K6-C vulcanizate. The chemical interface formed by K-MEPTS functions as a "coupling bridge" to improve the reinforcing efficiency of silica on rubber, demonstrated by the high modulus. However, the excessive chemical interface between silica and rubber leads to stress-concentrated regions [31], resulting in a low elongation at the break. Because of the physical interface formed by AEO, the most elongated rubber chains slip along the surface of silica and equalize the high stress [41], resulting in a proper modulus and elongation at break of A4K6-C vulcanizate.

For vulcanizates of A4K6-C, A6K4-C and A8K2-C, with decreasing K-MEPTS used in silica modification, the modulus decreases, but the elongation at break increases. The chemical interface between silica and rubber becomes stronger with the increase in the amount of K-MEPTS used in silica modification. The physical interface between silica and rubber becomes stronger with the increase in AEO used in silica modification. As presented in Figure 12, the tensile strength of the composites peaked at a value of 28.9 MPa for the A6K4-C vulcanizate sample. The tensile strength of the silica/NR composite was affected by both the modulus and the elongation at break. Therefore, the mechanical performance of the silica/NR composites were the best when a proper combination of physical and chemical interface existed between silica and NR. In this research, the silica/NR composites had the best mechanical performance when the weight ratio of AEO to K-MEPTS was 6:4 with silica modified by 10% weight modifiers.

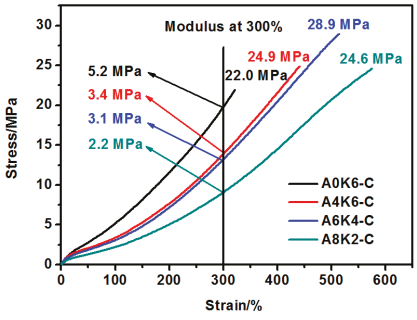

Figure 12. Mechanical performance of silica/NR composites.

3.5.2. Dynamic Performances of Silica/NR Composites

In tire applications, the tan δ values at 60 °C are typically used to predict rolling resistance. As presented in Figure 13, the tan δ values under large strain (>5%) are arranged from high to low in the following order: A0K6-C vulcanizate, A8K2-C vulcanizate, A4K6-C vulcanizate and A6K4-C vulcanizate. The rolling resistance of the A0K6-C vulcanizate was the highest of these four silica/NR composites due to the strong mutual friction between silica particles under cyclic reversed loading. In theory, the silica fixed with rubber molecules by a "coupling bridge" would barely enhance internal friction loss [4,27]. However, many silica aggregates were still present in the A0K6-C vulcanizate. The mutual friction remained strong between the silica particles that were tightly conglutinated under cyclic reversed loading. In contrast, silica modified with AEO and K-MEPTS together improved silica dispersion, with silica and rubber fixed together. Therefore, combining good silica dispersion and an appropriate interaction between silica and rubber by designing a proper interface were beneficial to improving the dynamic performance of silica/NR composites.

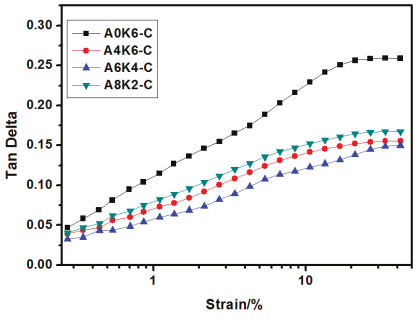

Figure 13. Strain-tan δ curve of four silica/NR composites (60 °C).

The relationship of the tan δ of silica/NR composites with increasing strain is also shown in Figure 13. The tan δ value of A0K6-C vulcanizate is the greatest and increases rapidly with increasing strain. The increase of the tan δ amplitude with strain increase in the curves of A4K6-C, A6K4-C and A8K2-C vulcanizates are lower than that of A0K6-C vulcanizate. A6K4-C vulcanizate has the lowest increase in tan δ value with strain in all samples, which means that when using A6K4-C composite as tire tread, the rolling resistance of the tire changes minimally with increasing vehicle load.

As shown in Figure 14, the heat build-up test, used to characterize the rolling resistance of silica/rubber composites in practical applications, was also performed to investigate the dynamic performance of different silica/NR vulcanizates. The heat build-up values are arranged from high

to low in the following order: A0K6-C vulcanizate, A8K2-C vulcanizate, A4K6-C vulcanizate and A6K4-C vulcanizate. This result aligns well with the loss factor (tan δ) measured by RPA. Therefore, using AEO and K-MEPTS together for silica modification is a novel strategy for preparing silica/NR composites used in "green tires" with low rolling resistance.

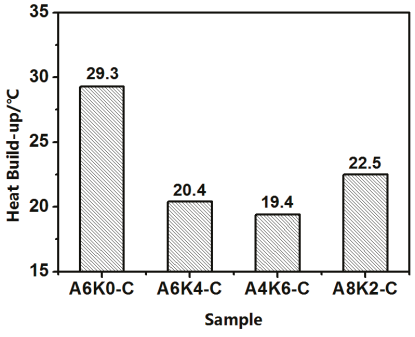

Figure 14. Heat build-up of four silica/NR composites.

4. Conclusions

In this research, we proposed an extremely effective strategy of using both AEO and K-MEPTS together for silica modification, by preparing silica/NR using the latex compounding method. As we designed, tailored silica was dispersed in the aqueous phase and completely co-coagulated with the NR. The silica/NR composites prepared by these master batches had ideal dynamic and mechanical performance, especially for A6K4-C, which was a composite containing silica modified with 6% AEO and 4% K-MEPTS (weight ratio of modifier to silica). This research provides a significant potential for preparing high performance silica/NR composites in a user-friendly method.

Furthermore, we investigated the effect of several interactions on the performance of silica/rubber composites. We confirmed that both AEO and K-MEPTS grafted onto the silica surface, and AEO shielded K-MEPTS, resulting in weakening the chargeability and activity of the mercaptopropyl group on K-MEPTS. This interaction between these two modifiers contributed to solving the problem of huge silica loss and "scorchy" behavior in the preparation of silica/rubber composites. This is a novel and practical interaction confirmed in this work. In silica/NR composites, AEO formed a physical interface between silica and rubber, resulting in reducing the aggregation of silica and improving the silica dispersion in the rubber matrix. Moreover, K-MEPTS formed a chemical interface between silica and rubber, resulting in strengthening the connection between silica and rubber and reducing the mutual friction between silica particles. Finally, AEO and K-MEPTS acted synergistically to improve the mechanical and dynamic performances of silica/NR composites.

Overall, the novel strategy outlined in this article provides a new strategy for the preparation of rubber materials with excellent performance. We hope that the preparation of silica/NR master batches using this strategy will present practical and profound applications in the rubber industry.

Acknowledgments: The authors acknowledge financial support from the National 973 Basic Research Program of China (2015CB654700), the Foundation for Innovative Research Groups of the National Nature Science Foundation of China (51221002 and 51521062) and the Major International Cooperation of the National Nature Science Foundation of China (51320105012).

Author Contributions: Liqun Zhang, Yiqing Wang and Junchi Zheng conceived and designed the experiments; Junchi Zheng and Dongli Han performed the experiments; Youping Wu, Xiaohui Wu and Xin Ye analyzed the data; Dong Dong contributed reagents/materials/analysis tools; Suhe Zhao and Junchi Zheng wrote the paper.

Conflicts of Interest: The authors declare no conflict of interest.

References

1. Miloskovska, E.; Nies, E.; Hristova-Bogaerds, D.; van Duin, M.; de With, G. Influence of reaction parameters on the structure of in situ rubber/silica compounds synthesized via sol-gel reaction. *J. Polym. Sci. B* **2014**, *52*, 967–978. [CrossRef]
2. Dong, B.; Liu, C.; Wu, Y.P. Fracture and fatigue of silica/carbon black/natural rubber composites. *Polym. Test.* **2014**, *38*, 40–45. [CrossRef]
3. Saeed, F.; Ansarifar, A.; Ellis, R.J.; Haile-Meskel, Y.; Irfan, M.S. Two advanced styrene-butadiene/polybutadiene rubber blends filled with a silanized silica nanofiller for potential use in passenger car tire tread compound. *J. Appl. Polym. Sci.* **2012**, *123*, 1518–1529. [CrossRef]
4. Liu, X.; Zhao, S.H.; Zhang, X.Y.; Li, X.L.; Bai, Y. Preparation, structure, and properties of solution-polymerized styrene-butadiene rubber with functionalized end-groups and its silica-filled composites. *Polymer* **2014**, *55*, 1964–1976. [CrossRef]
5. Hilonga, A.; Kim, J.K.; Sarawade, P.B.; Quang, D.V.; Shao, G.N.; Elineema, G.; Kim, H.T. Synthesis of mesoporous silica with superior properties suitable for green tire. *J. Ind. Eng. Chem.* **2012**, *18*, 1841–1844. [CrossRef]
6. Lin, Y.; Liu, S.Q.; Peng, J.; Liu, L. The filler-rubber interface and reinforcement in styrene butadiene rubber composites with graphene/silica hybrids: A quantitative correlation with the constrained region. *Compos. A* **2016**, *86*, 19–30. [CrossRef]
7. Toyonaga, M.; Chammingkwan, P.; Terano, M.; Taniike, T. Well-defined polypropylene/polypropylene-grafted silica nanocomposites: Roles of number and molecular weight of grafted chains on mechanistic reinforcement. *Polymers* **2016**, *8*, 300. [CrossRef]
8. Sarkawi, S.S.; Dierkes, W.K.; Noordermeer, J.W.M. Elucidation of filler-to-filler and filler-to-rubber interactions in silica-reinforced natural rubber by tem network visualization. *Eur. Polym. J.* **2014**, *54*, 118–127. [CrossRef]
9. Krysztafkiewicz, A.; Binkowski, S.; Jesionowski, T. Adsorption of dyes on a silica surface. *Appl. Surf. Sci.* **2002**, *199*, 31–39. [CrossRef]
10. Iacono, M.; Heise, A. Stable poly(methacrylic acid) brush decorated silica nano-particles by arget atrp for bioconjugation. *Polymers* **2015**, *7*, 1427–1443. [CrossRef]
11. Suzuki, N.; Ito, M.; Ono, S. Effects of rubber/filler interactions on the structural development and mechanical properties of nbr/silica composites. *J. Appl. Polym. Sci.* **2005**, *95*, 74–81. [CrossRef]
12. Ramier, J.; Chazeau, L.; Gauthier, C.; Guy, L.; Bouchereau, M.N. Grafting of silica during the processing of silica-filled sbr: Comparison between length and content of the silane. *J. Polym. Sci. B* **2006**, *44*, 143–152. [CrossRef]
13. Zhang, J.L.; Guo, Z.C.; Zhi, X.; Tang, H.Q. Surface modification of ultrafine precipitated silica with 3-methacryloxypropyltrimethoxysilane in carbonization process. *Colloids Surf. A* **2013**, *418*, 174–179. [CrossRef]
14. Kim, J.H.J.; You, Y.J.; Jeong, Y.J.; Choi, J.H. Stable failure-inducing micro-silica aqua epoxy bonding material for floating concrete module connection. *Polymers* **2015**, *7*, 2389–2409. [CrossRef]
15. Zhang, X.X.; Wen, H.; Wu, Y.J. Computational thermomechanical properties of silica-epoxy nanocomposites by molecular dynamic simulation. *Polymers* **2017**, *9*. [CrossRef]
16. Ridaoui, H.; Donnet, J.B.; Balard, H.; Kellou, H.; Hamdi, B.; Barthel, H.; Gottschalk-Gaudig, T.; Legrand, A.P. Silane modified fumed silicas and their behaviours in water: Influence of grafting ratio and temperature. *Colloids Surf. A* **2008**, *330*, 80–85. [CrossRef]
17. Kunioka, M.; Taguchi, K.; Ninomiya, F.; Nakajima, M.; Saito, A.; Araki, S. Biobased contents of natural rubber model compound and its separated constituents. *Polymers* **2014**, *6*, 423–442. [CrossRef]
18. Wadeesirisak, K.; Castano, S.; Berthelot, K.; Vaysse, L.; Bonfils, F.; Peruch, F.; Rattanaporn, K.; Liengprayoon, S.; Lecomte, S.; Bottier, C. Rubber particle proteins ref1 and srpp1 interact differently with native lipids extracted from hevea brasiliensis latex. *Biochim. Biophys. Acta* **2017**, *1859*, 201–210. [CrossRef] [PubMed]
19. Ibrahim, S.; Daik, R.; Abdullah, I. Functionalization of liquid natural rubber via oxidative degradation of natural rubber. *Polymers* **2014**, *6*, 2928–2941. [CrossRef]
20. Tangpasuthadol, V.; Intasiri, A.; Nuntivanich, D.; Niyompanich, N.; Kiatkamjornwong, S. Silica-reinforced natural rubber prepared by the sol-gel process of ethoxysilanes in rubber latex. *J. Appl. Polym. Sci.* **2008**, *109*, 424–433. [CrossRef]

21. Prasertsri, S.; Rattanasom, N. Mechanical and damping properties of silica/natural rubber composites prepared from latex system. *Polym. Test.* **2011**, *30*, 515–526. [CrossRef]
22. Gui, Y.; Zheng, J.; Ye, X.; Han, D.; Xi, M.; Zhang, L. Preparation and performance of silica/sbr masterbatches with high silica loading by latex compounding method. *Compos. B* **2016**, *85*, 130–139. [CrossRef]
23. Watanabe, M.; Tamaii, T. Acrylic polymer/silica organic-inorganic hybrid emulsions for coating materials: Role of the silane coupling agent. *J. Polym. Sci. A* **2006**, *44*, 4736–4742. [CrossRef]
24. Zhou, J.; Zhang, S.; Qiao, X.; Li, X.; Wu, L. Synthesis of sio2/poly(styrene-co-butyl acrylate) nanocomposite microspheres via miniemulsion polymerization. *J. Polym. Sci. A* **2006**, *44*, 3202–3209. [CrossRef]
25. Li, Y.; Han, B.; Wen, S.; Lu, Y.; Yang, H.; Zhang, L.; Liu, L. Effect of the temperature on surface modification of silica and properties of modified silica filled rubber composites. *Compos. A* **2014**, *62*, 52–59. [CrossRef]
26. Xie, Y.; Hill, C.A.S.; Xiao, Z.; Militz, H.; Mai, C. Silane coupling agents used for natural fiber/polymer composites: A review. *Compos. A* **2010**, *41*, 806–819. [CrossRef]
27. Li, Y.; Han, B.; Liu, L.; Zhang, F.; Zhang, L.; Wen, S.; Lu, Y.; Yang, H.; Shen, J. Surface modification of silica by two-step method and properties of solution styrene butadiene rubber (ssbr) nanocomposites filled with modified silica. *Compos. Sci. Technol.* **2013**, *88*, 69–75. [CrossRef]
28. Ostad-Movahed, S.; Yasin, K.A.; Ansarifar, A.; Song, M.; Hameed, S. Comparing effects of silanized silica nanofiller on the crosslinking and mechanical properties of natural rubber and synthetic polyisoprene. *J. Appl. Polym. Sci.* **2008**, *109*, 869–881. [CrossRef]
29. Ansarifar, A.; Wang, L.; Ellis, R.J.; Haile-Meskel, Y. Using a silanized silica nanofiller to reduce excessive amount of rubber curatives in styrene-butadiene rubber. *J. Appl. Polym. Sci.* **2011**, *119*, 922–928. [CrossRef]
30. Gao, Y.; Liu, J.; Shen, J.; Cao, D.; Zhang, L. Molecular dynamics simulation of the rupture mechanism in nanorod filled polymer nanocomposites. *Phys. Chem. Chem. Phys.* **2014**, *16*, 18483–18492. [CrossRef] [PubMed]
31. Zhang, P.; Zhao, F.; Yuan, Y.; Shi, X.; Zhao, S. Network evolution based on general-purpose diene rubbers/sulfur/tbbs system during vulcanization (i). *Polymer* **2010**, *51*, 257–263. [CrossRef]
32. Akbari, A.; Yegani, R.; Pourabbas, B. Synthesis of poly(ethylene glycol) (peg) grafted silica nanoparticles with a minimum adhesion of proteins via one-pot one-step method. *Colloids Surf. A* **2015**, *484*, 206–215. [CrossRef]
33. Cheng, Q.L.; Pavlinek, V.; He, Y.; Lengalova, A.; Li, C.Z.; Saha, P. Structural and electrorheological properties of mesoporous silica modified with triethanolamine. *Colloids Surf. A* **2008**, *318*, 169–174. [CrossRef]
34. Ma, X.K.; Lee, N.H.; Oh, H.J.; Kim, J.W.; Rhee, C.K.; Park, K.S.; Kim, S.J. Surface modification and characterization of highly dispersed silica nanoparticles by a cationic surfactant. *Colloids Surf. A* **2010**, *358*, 172–176. [CrossRef]
35. Wang, W.; Li, J.; Yang, X.; Li, P.; Guo, C.; Li, Q. Synthesis and properties of a branched short-alkyl polyoxyethylene ether alcohol sulfate surfactant. *J. Mol. Liq.* **2015**, *212*, 597–604. [CrossRef]
36. Debnath, N.; Mitra, S.; Das, S.; Goswami, A. Synthesis of surface functionalized silica nanoparticles and their use as entomotoxic nanocides. *Powder Technol.* **2012**, *221*, 252–256. [CrossRef]
37. Montenegro, L.M.P.; Griep, J.B.; Tavares, F.C.; de Oliveira, D.H.; Bianchini, D.; Jacob, R.G. Synthesis and characterization of imine-modified silicas obtained by the reaction of essential oil of eucalyptus citriodora, 3-aminopropyltriethoxysilane and tetraethylorthosilicate. *Vib. Spectrosc.* **2013**, *68*, 272–278. [CrossRef]
38. Yoshida, T.; Tanabe, T.; Hirano, M.; Muto, S. Ft-ir study on the effect of oh content on the damage process in silica glasses irradiated by hydrogen. *Nucl. Instrum. Methods Phys. Res.* **2004**, *218*, 202–208. [CrossRef]
39. Peng, Z.; Kong, L.X.; Li, S.D.; Chen, Y.; Huang, M.F. Self-assembled natural rubber/silica nanocomposites: Its preparation and characterization. *Compos. Sci. Technol.* **2007**, *67*, 3130–3139. [CrossRef]
40. Sajjayanukul, T.; Saeoui, P.; Sirisinha, C. Experimental analysis of viscoelastic properties in carbon black-filled natural rubber compounds. *J. Appl. Polym. Sci.* **2005**, *97*, 2197–2203. [CrossRef]
41. Boonstra, B.B. Mixing of carbon black and polymer: Interaction and reinforcement. *J. Appl. Polym. Sci.* **1967**, *11*, 389–406. [CrossRef]

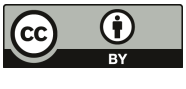

polymers

MDPI

Article

Cross-Flow Catalysis Behavior of a PVDF/SiO_2@Ag Nanoparticles Composite Membrane

Wenqiang Wang [1,2], Xi Chen [1,3,*], Chu Zhao [1,3], Bowu Zhao [1,3], Hualin Dong [1,3], Shengkui Ma [1,3], Liying Li [1,2,*], Li Chen [1,3] and Bin Zhang [4]

1 State Key Laboratory of Separation Membranes and Membrane Processes, Tianjin Polytechnic University, Tianjin 300387, China; wenqiang9109@163.com (W.W.); 18151308297@163.com (C.Z.); zbwnku@163.com (B.Z.); donghualin@tjpu.edu.cn (H.D.); mashengkui@tjpu.edu.cn (S.M.) chenli_tjpu@163.com (L.C.)
2 School of Environmental and Chemical Engineering, Tianjin Polytechnic University, Tianjin 300387, China
3 School of Materials Science and Engineering, Tianjin Polytechnic University, Tianjin 300387, China
4 Tianjin BeiAo Membrane Co., Ltd., Tianjin 300180, China; Tjzhangb@126.com
* Correspondence: polymerchenxi@163.com (X.C.); liliying_tjpu@163.com (L.L.); Tel.: +86-22-8395-5792 (X.C.); +86-22-8395-5931 (L.L.)

Received: 15 December 2017; Accepted: 6 January 2018; Published: 10 January 2018

Abstract: A blend of Polyvinylidene Fluoride (PVDF) and SiO_2 microspheres in *N*,*N*-Dimethylformamide (DMF) underwent phase inversion to form a PVDF/SiO_2 membrane with SiO_2 microspheres in the membrane's pores. Subsequently, the SiO_2 microspheres have been used as platforms for in site Ag nanoparticles (NPs) synthesis, forming a composite membrane. Benefitting from the full exposure of Ag NPs to the reactants, the composite membrane shows high catalytic reactivity when catalyzing the reduction of *p*-nitrophenol under a cross-flow. The catalytic reaction follows the first-order kinetics, and the reaction rate increases with an increase in the amount of Ag NPs in the membrane, the reaction temperature, and the operating pressure. What is more, highly purified products can be produced and separated from the reactants in a timely manner by using the composite membrane.

Keywords: Ag nanoparticles; catalysis; composite membrane; separation; SiO_2 microspheres

1. Introduction

Noble metal nanoparticles (NPs) are very attractive catalysts due to their highly active surface atoms [1–3]. However, they can easily agglomerate during the catalytic reaction process due to their high surface-to-volume ratio and surface energy [4]. In order to overcome this drawback in application, noble metal nanocatalysts are generally stabilized by stabilizers, such as polymers [2], complex ligands [5], and surfactants [4]. However, the catalytic reactivity of a metal nanocatalyst is low due to the restricted contact between the reactants and metal NPs resulting from the catalysts' surfaces covered by these stabilizers [6–8]. Fortunately, many studies have indicated that metal NPs loaded onto the surfaces of SiO_2 microspheres can fully expose their reactive points to reactants, and therefore have high reactivity [9–12]. However, the use and reuse of metal NPs is still difficult and inconvenient due to the aggregation of SiO_2 microspheres [9,10].

Membranes have been strongly suggested as supports for metal catalysts [13–16]. Membranes have large surface areas for loading metal NPs and many opened pores for reactants' passage. Furthermore, membranes with metal catalysts can be used continuously and repeatedly, without the need to separate the metal catalysts from the reaction system [13–17]. In addition, membranes as platforms can enhance the circular stability and longevity of the metal catalysts [13,17]. However, a tedious process is needed to introduce metal NPs into a membrane because the commonly used membrane material has no reactive groups for binding metal NPs [15,18]. Recently, we facilely

introduced noble metal NPs into a membrane by introducing polymeric spheres into the same one beforehand for loading metal NPs [13,17]. However, the functional polymers for binding metal NPs have been easily swollen, leading to a negative effect on catalysis [2,15,16,18]. Therefore, it is necessary to find a better strategy to load the noble metal NPs onto a membrane.

In addition, membranes have two external surfaces and many inner pores, which play different roles in a filtration process [19]. By the rejection of the membrane surface and the selective permeability of the membrane pore, different substances are separated from a mixture [19,20]. However, for too long, catalytic membranes have been only used as catalysts and their separation performance has not been focused on a catalysis process [15,16,18]. Even so, it is clear that the timely separation of products from reactants is still very important and necessary when a membrane is used as a catalyst because it can significantly decrease the operation's cost and avoid the undesired side reaction possible from the reactants and products [13,16,21]. Previous reports have provided many successful technologies to anchor metal NPs into a polymeric membrane, but the formed membrane cannot realize the desired timely separation of products due to the metal catalysts both on the membrane's surface and in the membrane's pores, which always leads to a mixture of reactants and products [15,16,18]. Obviously, a new membrane is needed to realize this special separation property [22]. Recently, we reported the successful separation of products from reactants by using a composite membrane with polymeric spheres and embedded metal NPs in the membrane's pores [13,17]. Since these polymeric spheres have the intrinsic drawbacks of wrapping the metal catalysts [2], they should be replaced by a better candidate.

Here, we report a composite membrane with SiO_2 microspheres coated by Ag NPs in the membrane pores and its catalytic property. The composite membrane was prepared from a first formation of a blend membrane with a PVDF substrate and SiO_2-NH_2 microspheres, and the subsequent growth of Ag NPs on the surfaces of the SiO_2-NH_2 microspheres. The catalysis and separation properties of the novel membrane were evaluated by the reduction of *p*-nitrophenol under a cross-flow model. The Ag NPs have high catalytic reactivity and a relatively low cost among the noble metal nanocatalysts, and the reduction of *p*-nitrophenol is a simple way for producing *p*-aminophenol, which is an important fine chemical intermediate [4,8,9]. Therefore, this reaction system will, no doubt, have significant value for the chemical industry.

2. Experimental Section

2.1. Materials and Reagents

Tetraethylorthosilicate (TEOS, 98%) and 3-(Aminopropyl)trimethoxysilane (APTMS, 97%) were purchased from Aladdin Chemistry Co., Ltd., Shanghai, China. Aqueous ammonia ($NH_3 \cdot H_2O$, 25%), anhydrous ethanol (99.7%), silver nitrate ($AgNO_3$, 99.8%), and *p*-nitrophenol, sodium borohydride ($NaBH_4$, 98%) were supplied by Kermel Reagent Co., Ltd., Tianjin, China. PVDF powders ($M_w = 3.52 \times 10^5$, $M_w/M_n = 2.3$, Solvay Company, Brussels, Belgium, Solef 1010) were used as received. *N*,*N*-Dimethylformamide (DMF, 99.5%) and polyvinylpyrrolidone (PVP K30, M_w = 58,000) were purchased from Guang Fu Fine Chemical Research Institute (Tianjin, China). All of the reagents were of analytical grade and used without further purification.

2.2. Synthesis of SiO_2-NH_2 Microspheres

SiO_2 microspheres were synthesized by the Stöber method [23] and then modified with -NH_2 groups through APTMS. In brief, a solution of ammonia (25.0 mL) and anhydrous ethanol (200.0 mL) was added into a three-neck round-bottom flask (500.0 mL) by vigorous stirring at 25 °C. After 0.5 h, TEOS (10.0 mL) was added to the flask. After another 12.0 h, APTMS (0.5 mL) was introduced into the solution. The mixture was retained at 80 °C for 2.0 h and then centrifuged. The SiO_2-NH_2 microspheres were obtained after the solid product underwent three cycles of centrifugation, re-suspension in anhydrous ethanol, and a final drying at 60 °C.

2.3. Preparation of the Composite Membrane

Preparation of the PVDF/SiO_2 blend membrane: the PVDF/SiO_2 blend membrane was prepared by immersion precipitation phase inversion [19,20]. PVDF powders (6.80 g), the synthesized SiO_2-NH_2 microspheres (1.20 g), and PVP (0.47 g) were dispersed in DMF (41.42 mL) by vigorous stirring until a clear homogeneous solution was obtained at 60 °C. After being degassed under vacuum, the casting solution was cast onto a glass plate, which was subsequently immersed in de-ionized water (25 °C). When the nascent membrane was separated from the substrate, it was rinsed with de-ionized water to remove the residual solvent thoroughly and then stored in de-ionized water.

Preparation of the composite membrane: in a dark environment, the as-prepared PVDF/SiO_2 membranes were immersed into different $AgNO_3$ solutions (2.18×10^{-3}, 2.18×10^{-4}, and 2.18×10^{-5} mM) for 24.0 h to load Ag^+ onto SiO_2-NH_2 microspheres of membranes. After the unbound Ag^+ in a membrane was washed by de-ionized water, fresh $NaBH_4$ solution was then used to reduce the Ag^+ of the membrane into Ag NPs. The obtained PVDF/SiO_2@Ag composite membranes were further rinsed with de-ionized water and then kept in de-ionized water until use. By changing the concentration of $AgNO_3$ solution, three composite membranes were prepared, named as MB-Ag-1, MB-Ag-2, and MB-Ag-3, respectively.

2.4. Characterization

2.4.1. Characterization of Composition, Structure, and Morphology

Fourier Transform Infrared Spectra (FTIR) of the SiO_2 microspheres and SiO_2-NH_2 microspheres were recorded using a Bruker VECTOR-22 IR spectrometer (Bruker Daltonic Inc., Karlsruhe, Germany). The chemical composition of a membrane was characterized using attenuated total reflectance Fourier Transform Infrared Spectra (ATR-FTIR) with Zinc Selenide (ZnSe) as an internal reflection element at an incident angle of 45°. The spectra were collected at 16 scans at a resolution of 4.0 cm^{-1} and recorded in a wave number range of 4000–400 cm^{-1}.

X-ray photoelectron spectroscopy (XPS) measurements of membrane surfaces were performed by using a Thermo Fisher K-alpha X-ray photoelectron spectrometer (Thermo Scientific, Waltham, MA, USA) with a monochromated Al Kα X-ray source (1486.6 eV photons) at a pass energy of 93.9 eV. The measurements were conducted at a take-off angle of 45° with respect to the sample surface. Survey XPS spectra were obtained by sweeping over 0–1350.0 eV electron binding energy with a resolution of 1.0 eV.

The membranes' morphologies were observed by field emission electron microscopy (FESEM, Hitachi S-4800, Tokyo, Japan). Dried samples were freeze-fractured using liquid nitrogen and then sputter-coated with a thin gold layer to increase the contrast and quality of the images. An energy dispersive X-ray analysis (EDX) was conducted to examine the cross-sectional compositions of the composite membranes.

2.4.2. Water Contact Angle Measurement

Water contact angle measurements were performed with the sessile drop method using a contact angle meter (JYSP-180, Jinshengxin, Testing Machine Co., Beijing, China) [24]. A syringe with a needle diameter of 0.525 mm was used to place a water droplet of 4.0 µL on the membrane surface. The contact angle was measured by generating tangent lines to both sides of the droplet static image with the Drop Shape Analysis software.

2.5. Measurements of a Membrane's Porosity and Pore Size

The porosity (ε) of a membrane was determined at 25 °C by the wet-dry weighting method [25]. The porosity was calculated as the pore's volume divided by the membrane's volume with Equation (1) [13]:

$$\varepsilon = \frac{W_1 - W_2}{\rho_w \times A \times l} \times 100\%, \quad (1)$$

where W_1 (g) is the weight of the wet membrane, W_2 (g) is the weight of the dry membrane, l (mm) is the membrane's thickness, A (cm^2) is the effective membrane surface area, and ρ_w ($g \cdot cm^{-3}$) is the water density. The average pore size (d) of the membrane was calculated according to the pure water flux by the Guerout-Elford-Ferry equation [20]:

$$d = \sqrt{\frac{(2.9 - 1.75\varepsilon) \times 8\eta l J}{\varepsilon \times A \times \Delta P}}, \quad (2)$$

where ε is the membrane's porosity, η (Pa·s) is the pure water viscosity, ΔP (MPa) is the operation pressure, and J ($L \cdot m^{-2} \cdot h^{-1}$) is the volume of pure water penetrating through the membrane during unit time.

2.6. Measurement of Metal Content

Metal contents were determined by measuring the concentrations of metal ions of a dilute nitric acid extract of the metal NPs of the composite membrane using inductively coupled plasma atomic emission spectrometry (ICP-AES, Varian 715-ES, Palo Alto, CA, USA). Before measurement, the composite membrane was immersed in nitric acid (10.0 mL, 5.0 M) for 0.5 h and then diluted to a final volume of 100.0 mL by de-ionized water.

2.7. Pure Water Flux through a Membrane

A membrane (17.9 cm^2) was firstly pre-pressured for 1.0 h under an operating pressure to maintain a steady state. Then, the pure water flux was measured under a cross-flow pattern [24,25]. The water flux (J) was obtained by an average of three measurements according to Equation (3) [24]:

$$J = \frac{Q}{A \times \Delta t}, \quad (3)$$

where Q (L) is the permeate volume and Δt (h) is the filtration time.

2.8. Catalytic Reduction of p-Nitrophenol by a Composite Membrane

The reactivity of the prepared PVDF/SiO_2@Ag composite membrane was investigated by the reduction of *p*-nitrophenol to *p*-aminophenol. The reaction was carried at pH 10.0. A feed solution was prepared by mixing a *p*-nitrophenol solution (0.144 mM, 490.0 mL) with a freshly prepared $NaBH_4$ aqueous solution (79.22 mM, 10.0 mL). The catalytic reaction was carried out under a cross-flow experiment apparatus as shown in Figure 1. Under a cross-flow, the feed solution circularly flowed through a composite membrane (A = 17.9 cm^2 and l = 0.16 mm) at 0.1 MPa and 25 °C. The concentration change of *p*-nitrophenol in the feed solution was studied by monitoring the absorbance maximum (λ_{max} = 400 nm) of *p*-nitrophenol with a UV-Vis spectrophotometer (TU-1810PC, Beijing Purkinje General Instrument Co., Ltd., Beijing, China) at an interval of 2.0 min.

2.9. Reusability Test

The catalytic recyclability was determined by repeating the measurement of *p*-nitrophenol reduction described in Section 2.8 with a composite membrane. After one measurement cycle, the membrane was washed thoroughly with water and the next catalytic run was then started. The aforementioned procedure was repeated eight times.

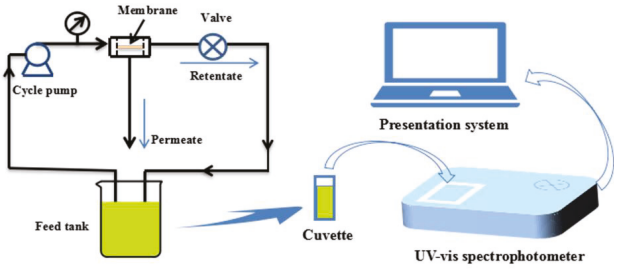

Figure 1. The diagram of experimental setup for catalysis.

3. Results and Discussion

3.1. Characterizations of SiO_2 and SiO_2-NH_2 Microspheres

The morphologies of the synthesized SiO_2 and SiO_2-NH_2 are observed by FESEM. As shown in Figure 2a, the as-prepared SiO_2 is a uniform microsphere. The average diameters of the SiO_2 microspheres are about 400.0 ± 20 nm. Meanwhile, the SiO_2-NH_2 also maintains a spherical shape, and does not show any difference to SiO_2 (Figure 2b). Figure 2c shows the FT-IR spectra of SiO_2 and SiO_2-NH_2 microspheres. All of the microspheres show peaks at around 1095 and 802 cm^{-1}, which are attributed to the Si–O–Si vibration [26]. The bands at 3500–3200 and 1630 cm^{-1} correspond to the Si–OH stretching [10,12,27]. Compared to the spectrum of the SiO_2 microsphere, the new peaks in the ranges of 3000~2850 and 730–650 cm^{-1} appearing in the spectrum of the SiO_2-NH_2 microsphere correspond to the C–H stretching vibration and N–H bending vibrations (APTMS), respectively [3]. The results demonstrate the presence of -NH_2 on the surfaces of SiO_2 microspheres, which can be used in the loading of Ag NPs for catalysis [9,10].

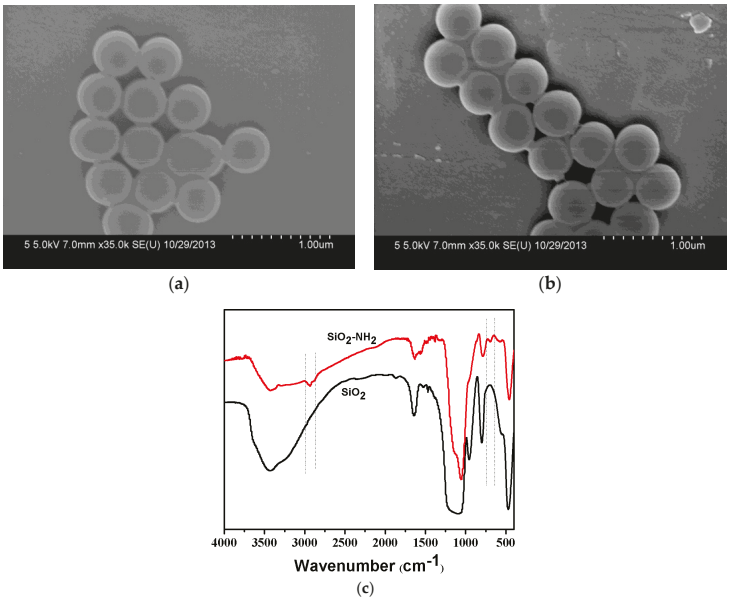

Figure 2. Field emission electron microscopy (FESEM) of synthesized SiO_2 microspheres (**a**) and SiO_2-NH_2 microspheres (**b**) and their FTIR spectra (**c**).

3.2. Chemical Composition of a Membrane

Figure 3 shows the ATR-FTIR spectra of the membranes. For all membranes, strong peaks at around 1280–1110 and 1461–1346 cm^{-1} are observed, which are assigned to the CF_2 and CH_2 of PVDF [20,24,25]. In comparison with the PVDF membrane, the PVDF/SiO_2 and PVDF/SiO_2@Ag membranes show distinct absorption bands of Si–O–Si at 1095 and 802 cm^{-1} (Figure 3) [9,10,12,26], confirming SiO_2-NH_2 microspheres in the blend membrane and composite membrane. Because of the very small content, the –NH_2 cannot be examined by the FTIR, but can be found by XPS measurement.

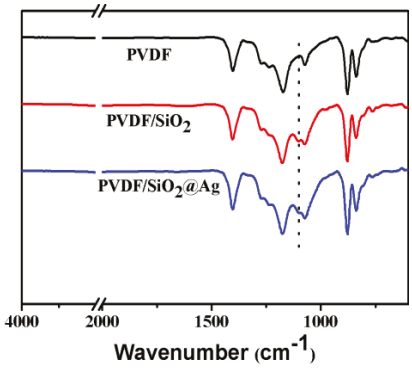

Figure 3. Transform Infrared Spectra (ATR-FTIR) spectra of the pure PVDF membrane, the PVDF/SiO_2 membrane, and the PVDF/SiO_2@Ag membrane: MB-Ag-1.

As shown in Figure 4, the PVDF/SiO_2 membrane shows all the binding energies that are ascribed to the PVDF membrane. Besides, the PVDF/SiO_2 membrane also shows a new binding energy (BE) at 100.5 eV that is assigned to Si–O–Si [28], and a new one at about 397.8 eV that is assigned to the -NH_2 groups of SiO_2-NH_2 [3]. Compared with the PVDF/SiO_2 membrane, the peaks corresponding to Ag 3d at BEs of 368.0 and 374.0 eV are also observed in the XPS spectra of the PVDF/SiO_2@Ag membrane, indicating that Ag^0 species have been loaded onto the composite membrane [29]. Thus, the XPS spectra confirm the presence of SiO_2-NH_2 microspheres and Ag^0 in the PVDF/SiO_2@Ag membrane.

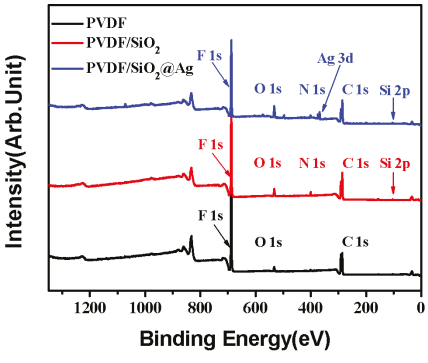

Figure 4. X-ray photoelectron spectroscopy (XPS) survey spectra of the pure PVDF membrane, the PVDF/SiO_2 membrane, and the PVDF/SiO_2@Ag membrane: MB-Ag-1.

3.3. Morphology and Structure of the Membrane

The morphologies of the composite membranes are observed by FESEM. As shown in Figure 5a, the composite membrane has a porous top surface with a pore size of about 20.0 nm. The small surface pores are formed by the instantaneous phase separation of the casting solution on the glass plate. Compared with the top surface, the bottom surface of the composite membrane shows rough and larger pores (Figure 5b), which are caused by the slow diffusion between the solvent and nonsolvent in the membrane formation process due to the bottom surface being closed to the glass plate [20].

The cross-section of the composite membrane shows a typical unsymmetrical structure, including a dense separation layer on the top surface of the membrane, a finger-like middle layer. And a sponge-like bottom layer (Figure 6a). The dense layer can resist protein or pollutants, and thereby reduce their pollution of the membrane inner in the filtration process. Due to the phase separation resulting from the poor interfacial compatibility between the SiO_2-NH_2 spheres and the PVDF in the membrane formation, the middle layer forms many pores with several thousand nanometers, which provide sufficient space for the SiO_2-NH_2 spheres used for binding metal catalysts [30]. The cross-section of the composite membrane (Figure 6b) shows that SiO_2-NH_2 microspheres are uniformly distributed in the membrane pores. A further amplified image (Figure 6c) shows that Ag NPs with a size of about 30.0 $\pm$ 5 nm are clearly stabilized on the surfaces of SiO_2-NH_2 microspheres. Because of the much larger sizes of the SiO_2-NH_2 microspheres than those of the surface pores, Ag NPs coated on the SiO_2-NH_2 microspheres can be long-term stained in the membrane pores, which is profitable for a catalysis application.

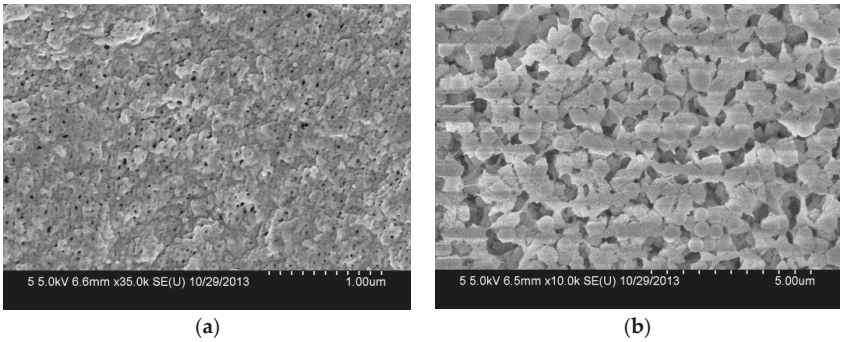

(**a**) (**b**)

Figure 5. FESEM images of the top surface (**a**) and the bottom surface (**b**) of PVDF/SiO_2@Ag membranes: MB-Ag-1.

Figure 7 shows the EDX spectrum of the cross-section of the composite membrane. As shown, the elements of C, N, O, F, Si, and Ag coexist, which is consistent with the XPS result (Figure 4). The content of the F and C elements is high, indicating that the main component of the composite membrane is PVDF [31], which will provide a good mechanical property for the composite membrane. The N and Si elements indicate the amino-functionalized SiO_2 microspheres in the membrane, which will account for the loading of Ag NPs [9,10,32]. The successful loading of Ag is confirmed by the Ag element in the EDX spectrum (Figure 7). The loaded Ag content is measured by ICP-AES. As shown in Table 1, the Ag loading content of the membrane increases from 0 to 5.32, 16.79, and 59.96 $\mu g/cm^2$ by increasing the concentration of $AgNO_3$ (2.18×10^{-5}, 2.18×10^{-4}, and 2.18×10^{-3} mM, respectively) in the preparation process.

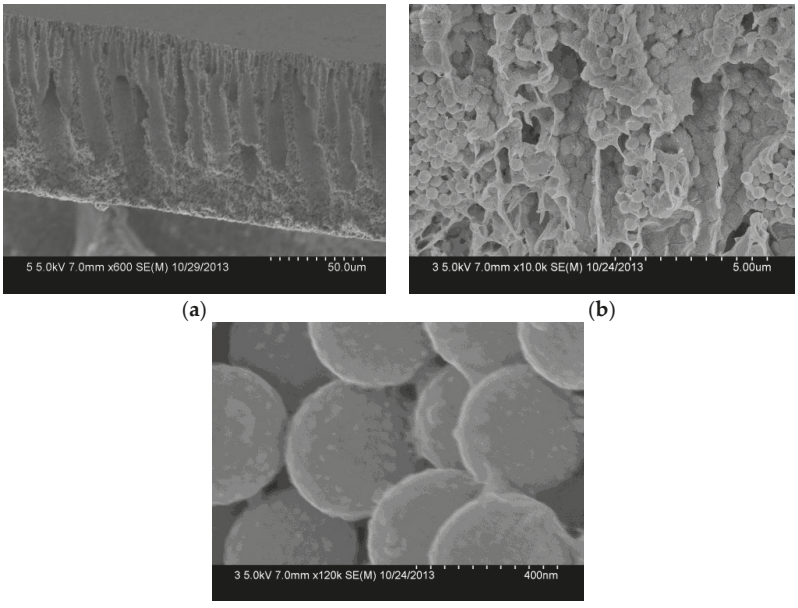

Figure 6. FESEM images of the cross-section (**a**), the further amplified cross-section (**b**) and the SiO_2 microspheres (**c**) of the PVDF/SiO_2@Ag membrane: MB-Ag-1.

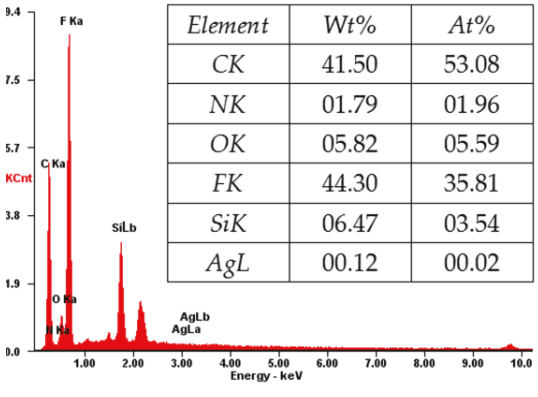

Element	*Wt%*	*At%*
CK	41.50	53.08
NK	01.79	01.96
OK	05.82	05.59
FK	44.30	35.81
SiK	06.47	03.54
AgL	00.12	00.02

Figure 7. X-ray analysis (EDX) of the PVDF/SiO_2@Ag membrane: MB-Ag-1.

Table 1. Structures and compositions of various composite membranes.

Sample	Average pore size (nm)	Porosity (%)	Ag loading (μg/cm^2)	Contact angle (°)
PVDF/SiO_2	120.0 ± 4	70.1	0	83.5
MB-Ag-1	125.0 ± 6	71.2	59.960	81.5
MB-Ag-2	125.0 ± 3	71.2	16.789	80.8
MB-Ag-3	125.0 ± 5	71.2	5.321	80.2

The porosity, average pore size, and water contact angle of various membranes are also shown in Table 1. As can be seen, the incorporation of Ag NPs hardly changes the porosity, pore size, and water contact angle of the PVDF/SiO_2@Ag composite membrane.

3.4. Catalytic Property

3.4.1. Catalytic Kinetics

Reduction of *p*-nitrophenol is catalyzed by the PVDF/SiO_2@Ag composite membrane. The process is monitored by continuously recording the UV-Vis absorption spectrum of the feed solution, and the result is shown in Figure 8. It can be seen that a strong absorption peak at 400 nm appears at first. This is because of the formation of *p*-nitrophenol ions in an alkaline condition [2,8,11]. The peak at 400 nm will remain unaltered in the absence of any catalyst [11,13,33]. However, when the feed solution circularly flows through the composite membrane, the peak at 400 nm gradually decreases with time. At the same time, the feed solution fades from the pale yellow color and ultimately becomes colorless. In this process, a new peak appears at 310 nm, which is ascribed to the absorption of the product of *p*-aminophenol [2,33]. The peak strength weakly increases with time, suggesting that *p*-nitrophenol is gradually converted to *p*-aminophenol. In the UV-Vis absorption spectrum, two isosbestic points are always seen at 280 and 314 nm, indicating that only *p*-aminophenol is formed during this reaction [2,8,11,13]. The reaction rapidly finishes at a short time of about 14.0 min due to large quantities of reactants accessing Ag NPs at unit time under the cross-flow model.

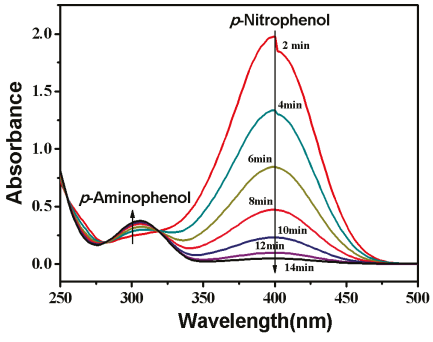

Figure 8. Change of UV-Vis absorption of the feed solution. Membrane: MB-Ag-1.

The composite membrane belongs to a heterogeneous catalyst [14–16,18,34]. It is well-known that the heterogeneous catalytic reaction model follows the Langmuir-Hinshelwood model, because the reaction is based on the adsorption of reactants on the catalyst surface [14–16,18,35]. The conversion of the reaction can be derived from the C_t/C_0, measured by the relative intensity of UV-Vis absorbance at 400 nm. Herein, C_t (mM) is the concentration of *p*-nitrophenol at the reaction time t and C_0 (mM) is the initial concentration. Since the dose of $NaBH_4$ is greatly excessive (see Section 2.8), the reaction process can be described by the following first-order kinetic equation [2,9,35].

$$-\ln(\frac{C_t}{C_0}) = k_{obs}t = K_{SA}a_s\rho_m t \quad (4)$$

Herein, k_{obs} is the apparent rate constant, reflecting the reaction rate, and K_{SA}, a_s, and ρ_m are the surface area-based rate constant ($L{\cdot}min^{-1}{\cdot}m^{-2}$), the specific surface area of Ag NPs ($m^2{\cdot}g^{-1}$), and the mass concentration of Ag NPs ($g{\cdot}L^{-1}$), respectively.

The plots of C_t/C_0 and $-\ln(C_t/C_0)$ versus time are shown in Figure 9. It is obvious that C_t/C_0 decreases with an increase of reaction time, revealing that the concentration of *p*-nitrophenol gradually

decreases [2,8,10,13,17]. Additionally, the plot of $-\ln(C_t/C_0)$ versus reaction time yields a good linear relation in the reaction, indicating that the reaction follows the first-order kinetics [2,12,13,17,18]. The reaction rate constant (K_{SA} = 33.2 L·min^{-1}·m^{-2}) is faster than that (K_{SA} = 27.9 L·min^{-1}·m^{-2}) of the reaction catalyzed by a composite membrane with Ag NPs coated on the surfaces of poly (methacrylic acid) (PMAA) microspheres in membrane pores [13]. The different reaction rates are ascribed to the different composite membrane structures. When Ag NPs are coated on the surfaces of PMAA spheres, the swelling of PMAA spheres by water could cause a wrap of Ag NPs by polymer chains, leading to a low reaction rate; in contrast, as Ag NPs are coated on the surfaces of SiO_2 spheres, the groups on the surfaces of SiO_2 spheres are so short that they cannot wrap the Ag NPs [9–12]. Thus, the as-prepared composite membrane exhibits a high reaction rate.

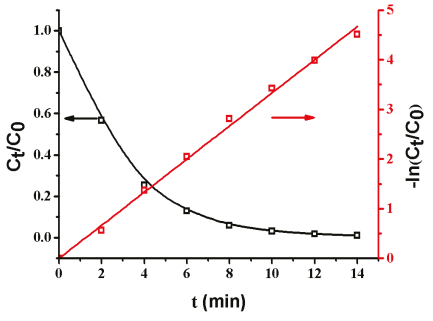

Figure 9. Changes of C_t/C_0 and $\ln(C_t/C_0)$ with time. Membrane: MB-Ag-1.

3.4.2. Effect of the Initial Concentration of *p*-Nitrophenol

Figure 10 shows the k_{obs} of the composite membrane under different *p*-nitrophenol concentrations. As can be seen, the k_{obs} decreases with an increase in the initial *p*-nitrophenol concentration in a concentration range of 0.036–0.108 mM. In such a concentration range, the increase of *p*-nitrophenol causes a slower decrease of C_t/C_0 with time, leading to the decline of k_{obs}. However, as the initial concentration of *p*-nitrophenol is higher than 0.1 mM (0.144–0.216 mM), the increase of *p*-nitrophenol only weakly affects the change of C_t/C_0 with time, and thus the k_{obs} tends to a low constant value. As is well-known, the reaction occurs on the Ag NPs' surfaces by transferring electrons from $NaBH_4$ to *p*-nitrophenol [4,14,35]. Therefore, the synergistic effects of the rate of electron transfer at the metal surface and the diffusion of *p*-nitrophenol to the metal surface, together with the rapid diffusion of *p*-aminophenol away from the surface, should be responsible for the catalytic rate.

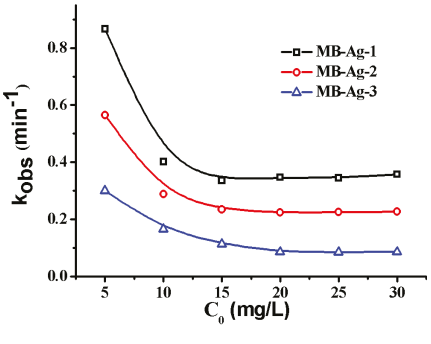

Figure 10. Effect of the initial concentration of *p*-nitrophenol on catalytic rate.

3.4.3. Effect of Operating Pressure

The catalytic reaction is directly related to the flow rate of reactants controlled by the operating pressure. Figure 11a shows the effect of the operating pressure on the catalytic reaction. As shown, when the operating pressure varies from 0.10–0.30 MPa, the k_{obs} increases. Under the present condition, the water flux linearly increases with an increase in the operating pressure, indicating that the composite membrane has good compression performance. The k_{obs} increase is due to the flow rate change resulting from the increase in the operating pressure. As shown in Figure 11a, the water flux increases with an increase in the operating pressure, leading to the shorter residence time of the feed solution inside of the membrane. Thus, the feed solution can quickly contact the Ag NPs in the membrane. At the same time, reaction product can also leave the membrane more rapidly. The two factors contribute to the increase of the catalytic reaction rate [13,17]. On the other hand, an increase in operating pressure will cause a decrease in the flow rate of the feed solution (Figure 11b) and an increase in the residue time of the feed solution on the membrane's surface. However, the flow rate of the feed solution on the membrane's surface is still very large (Figure 11b) and does not affect the rapid contact of reactants with Ag NPs in the mouths of the membrane pores. Thus, an increase in the operating pressure is also beneficial to the reaction in this case. Therefore, the catalytic rate shows an increase as a result of increasing the operating pressure.

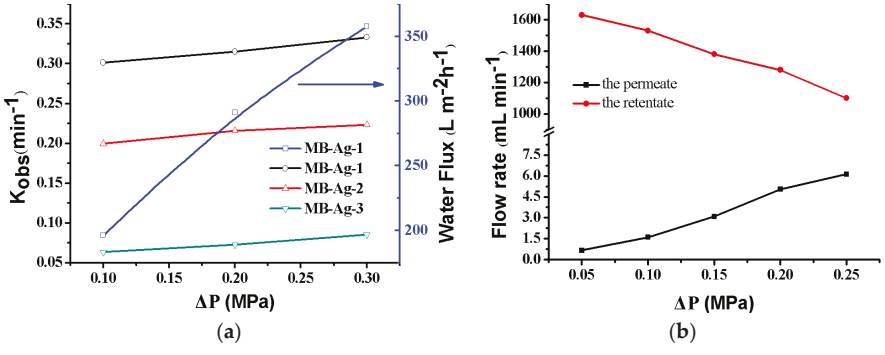

Figure 11. Effect of pressure on the catalytic rate, the water flux (**a**), and the flow rate (**b**) for the *p*-nitrophenol reduction with the MB-Ag-1 membrane.

3.4.4. Catalytic Activity as a Function of Ag Coating Content

Previous studies have shown that the contents and specific surface areas of noble metals in catalytic membranes have a great influence on the catalytic reaction [1,2,5,13,17]. In this study, the Ag coating content is also focused on. Figure 12 shows the reduction of *p*-nitrophenol with different composite membranes. A good linear relation of $-\ln(C_t/C_0)$ versus reaction time is observed in all reactions, revealing that the reduction of *p*-nitrophenol catalyzed by Ag NPs follows the first-order kinetics [2,13,17]. Furthermore, the reduction rate markedly increases with an increase in Ag content, which is consistent with other noble metal catalysts [2,17]. This is expected, because a greater Ag NP loading on the membrane results in an increase of the surface area of the catalysts, and thus provides more accessible active sites for reactants.

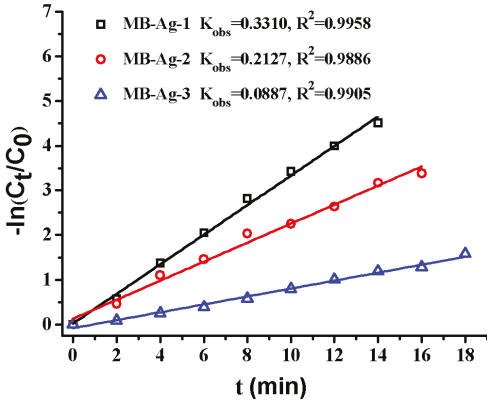

Figure 12. Effect of Ag loading content on catalytic rate.

3.4.5. Temperature Dependence and Activation Energy Calculation

The effect of temperature on the catalytic reduction of *p*-nitrophenol is shown in Figure 13. As can be seen from Figure 13a, the plot of $-\ln(C_t/C_0)$ versus reaction time at different temperatures presents linear relationships, and the reduction rate increases with increasing temperature. The specific relationship between the reaction rate constant and temperature can be described by the Arrhenius equation:

$$\ln(k_{obs}) = \ln A_0 - \frac{E_a}{RT}, \quad (5)$$

where T (K) is the thermodynamic temperature, E_a (kJ/mol) is the apparent activation energy, A_0 (min^{-1}) is the pre-exponential factor, and R is the ideal gas constant. According to the Arrhenius equation, the activation energy of the reaction could be calculated. Normally, the diffusion-controlled mechanism and the surface-controlled mechanism in a reaction are expressed with a lower activation energy (E_a: 8.0–21.0 kJ/mol) and a higher activation energy (E_a > 29.0 kJ/mol), respectively [2]. The activation energy values for different composite membranes are shown in Figure 13c. It is obvious that the activation energy value (E_a = 40.63 kJ/mol) is largest for the composite membrane with the lowest Ag content (MB-Ag-3); with an increase in Ag content, the E_a gradually decreases: the value of E_a is 27.58 kJ/mol (MB-Ag-2) and 19.89 kJ/mol (MB-Ag-1), respectively. Therefore, the reaction shows the diffusion-controlled mechanism for the composite membrane with a high Ag content and the surface-controlled mechanism for the composite membrane with a low Ag content.

3.5. Reusability of the Composite Membrane

Figure 14 shows the reusability of the composite membrane for the catalytic reduction of *p*-nitrophenol. The k_{obs} almost remains unchanged after reuse for four cycles, and only shows a slight decrease from the 5th to the 8th cycle, possibly caused by the passivation or the loss of a very few Ag NPs in the repeated washing process [2,13]. The result suggests that the PVDF/SiO_2@Ag membrane exhibits good stability and an antifouling property. Furthermore, since the general steps for the dispersion and separation of metal catalysts are omitted, the operations for using and recovering catalysts are very convenient [2,11].

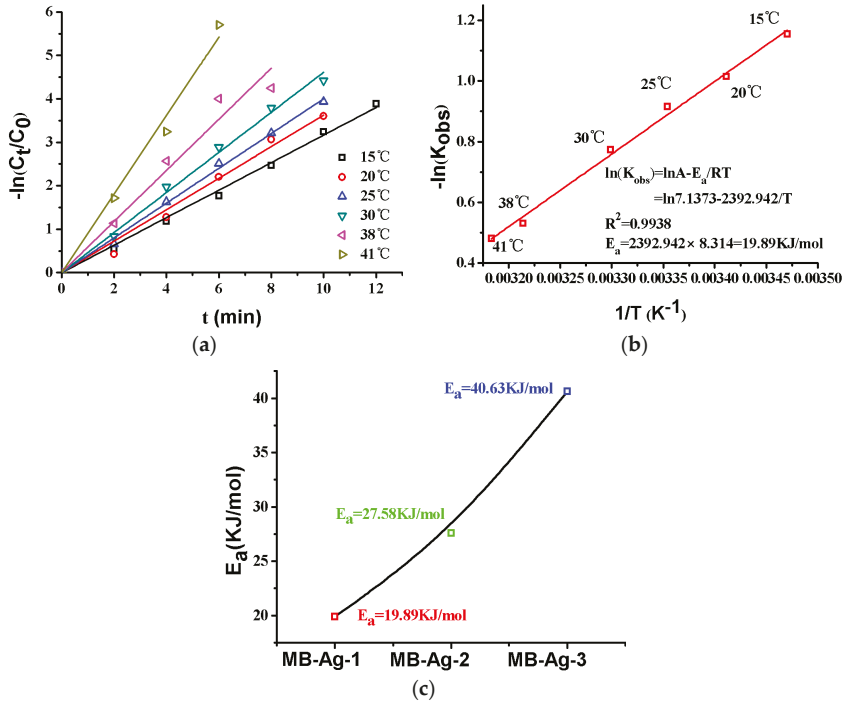

Figure 13. Reactions at different temperatures ((**a**), MB-Ag-1 membrane), E_a ((**b**), MB-Ag-1 membrane), E_a ((**c**), various membranes). RT: room temperature.

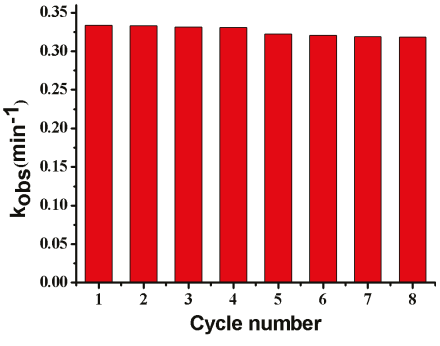

Figure 14. Reusability of the membrane: MB-Ag-1.

3.6. Separation of Products from Reactants

Under the cross-flow model, the feed solution passing through the composite membrane includes the retentate on the membrane's surface and the permeate in the membrane's pores. Therefore, the reactant's conversion comes from the retentate and the permeate, respectively. As the pressure increases, the conversion of reactant from the permeate decreases slightly, while the conversion rate of reactant from the retentate increases (Figure 15). The conversion of reactant is closely related to flow rate (Figure 11b). The fast flow rate of the reactant in the retentate and the few Ag NPs on the membrane's surface make the reactant to be rarely reduced (lower than 3.0%). On the contrary, the slow

flow rate of the reactant in the permeate and the abundant Ag NPs in the membrane pores make the reactant be reduced completely (more than 97.5%). Thus, it is possible to directly obtain a high-purity product by collecting the fluid of the permeate [13,17]. Therefore, the separation of the product from the reactant is achieved without the need for additional operating costs and energy consumption.

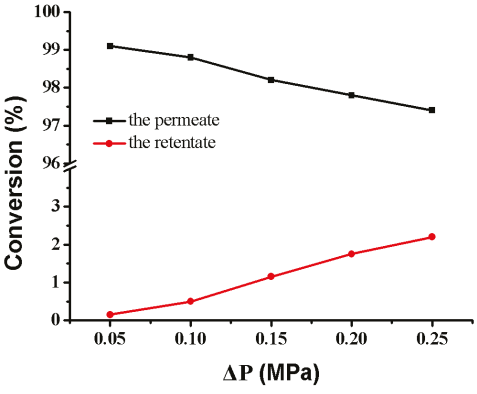

Figure 15. Conversion versus operating pressure in the reduction of *p*-nitrophenol membrane: MB-Ag-1.

4. Conclusions

This study reported a novel composite membrane with a SiO_2 microsphere-free porous surface and inner pores with immobilized SiO_2 microspheres decorated by Ag NPs. The composite membrane was used for the catalytic reduction of *p*-nitrophenol under a cross-flow operating model. It was surprising to find that very high conversion was obtained from the permeate while only very low conversion was obtained from the retentate. The high conversion corresponded to the enriched Ag NPs in the membrane pore, which provides an abundance of reactive sites for reactants, while the low conversion was related to the lack of catalysts on the membrane's surface. Thus, the products can be separated from the reactants flowing on the membrane's surface and directly obtained by collecting the fluid of the permeate by using the as-prepared composite membrane. The reaction obeys the first-order kinetics and the rate increases with an increase in temperature, Ag NPs content, and operating pressure. In addition, the composite membrane can be conveniently used and is very stable and therefore can hopefully be used in a wide range of applications.

Acknowledgments: The authors acknowledge the financial sponsorship of this work by the National Natural Science Foundation of China [No. 51003076], the Science and Technology Commission Foundation of Tianjin [No. 14JCZDJC38100], the University of Science and Technology Development Fund Planning Project of Tianjin [No. 2017ZD04], and Science and Technology Plants of Tianjin [No. 15PTSYJC00250].

Author Contributions: Xi Chen, Liying Li, Li Chen, and Bin Zhang conceived and designed the experiments; Wenqiang Wang, Chu Zhao, Bowu Zhao, Hualin Dong, and Shengkui Ma performed the experiments and analyzed the data; and Xi Chen and Wenqiang Wang wrote the paper.

Conflicts of Interest: The authors declare no conflict of interest.

References

1. Bi, C.; Cao, J.; Lina, H.; Wang, Y.; Chen, S. Enhanced photocatalytic activity of $Bi_{12}O_{17}Cl_2$ through loading Pt quantum dots as a highly efficient electron capturer. *Appl. Catal. B* **2016**, *195*, 132–140. [CrossRef]
2. Li, K.; Chen, X.; Wang, Z.; Xu, L.; Fu, W.; Zhao, L.; Chen, L. Temperature-responsive catalytic performance of Ag nanoparticles endowed by poly (*N*-isopropylacrylamide-*co*-acrylic acid) microgels. *Polym. Compos.* **2017**, *38*, 708–718. [CrossRef]

3. Celebi, M.; Yurderi, M.; Bulut, A.; Kaya, M.; Zahmakiran, M. Palladium nanoparticles supported on amine-functionalized SiO_2 for the catalytic hexavalent chromium reduction. *Appl. Catal. B* **2016**, *180*, 53–64. [CrossRef]
4. Herves, P.; Perez-Lorenzo, M.; Liz-Marzan, L.M.; Dzubiella, J.; Lu, Y.; Ballauff, M. Catalysis by metallic nanoparticles in aqueous solution: Model reactions. *Chem. Soc. Rev.* **2012**, *41*, 5577–5587. [CrossRef] [PubMed]
5. Zhan, P.; Wang, Z.-G.; Li, N.; Ding, B. Engineering Gold Nanoparticles with DNA Ligands for Selective Catalytic Oxidation of Chiral Substrates. *ACS Catal.* **2015**, *5*, 1489–1498. [CrossRef]
6. Gu, J.; Zhang, Y.W.; Tao, F.F. Shape control of bimetallic nanocatalysts through well-designed colloidal chemistry approaches. *Chem. Soc. Rev.* **2012**, *41*, 8050–8065. [CrossRef] [PubMed]
7. Linic, S.; Christopher, P.; Xin, H.; Marimuthu, A. Catalytic and Photocatalytic Transformations on Metal Nanoparticles with Targeted Geometric and Plasmonic Properties. *Acc. Chem. Res.* **2013**, *46*, 1890–1899. [CrossRef] [PubMed]
8. Dong, Z.; Le, X.; Dong, C.; Zhang, W.; Li, X.; Ma, J. Ni@Pd core-shell nanoparticles modified fibrous silica nanospheres as highly efficient and recoverable catalyst for reduction of 4-nitrophenol and hydrodechlorination of 4-chlorophenol. *Appl. Catal. B* **2015**, *162*, 372–380. [CrossRef]
9. Chi, Y.; Yuan, Q.; Li, Y.; Tu, J.; Zhao, L.; Li, N.; Li, X. Synthesis of Fe_3O_4@SiO_2-Ag magnetic nanocomposite based on small-sized and highly dispersed silver nanoparticles for catalytic reduction of 4-nitrophenol. *J. Colloid Interface Sci.* **2012**, *383*, 96–102. [CrossRef] [PubMed]
10. Du, X.; He, J.; Zhu, J.; Sun, L.; An, S. Ag-deposited silica-coated Fe_3O_4 magnetic nanoparticles catalyzed reduction of *p*-nitrophenol. *Appl. Surf. Sci.* **2012**, *258*, 2717–2723. [CrossRef]
11. Xiao, W.; Zhang, Y.; Liu, B. Raspberrylike SiO_2@reduced graphene oxide@AgNP composite microspheres with high aqueous dispersity and excellent catalytic activity. *ACS Appl. Mater. Interfaces* **2015**, *7*, 6041–6046. [CrossRef] [PubMed]
12. Tang, M.; Huang, G.; Li, X.; Pang, X.; Qiu, H. A facile approach to fabricate Au nanoparticles loaded SiO_2 microspheres for catalytic reduction of 4-nitrophenol. *Mater. Chem. Phys.* **2015**, *162*, 31–40. [CrossRef]
13. Chen, X.; Wang, Z.; Bi, S.; Li, K.; Du, R.; Wu, C.; Chen, L. Combining catalysis and separation on a PVDF/Ag composite membrane allows timely separation of products during reaction process. *Chem. Eng. J.* **2016**, *295*, 518–529. [CrossRef]
14. Fountoulaki, S.; Daikopoulou, V.; Gkizis, P.L.; Tamiolakis, I.; Armatas, G.S.; Lykakis, I.N. Mechanistic Studies of the Reduction of Nitroarenes by $NaBH_4$ or Hydrosilanes Catalyzed by Supported Gold Nanoparticles. *ACS Catal.* **2014**, *4*, 3504–3511. [CrossRef]
15. Gu, Y.; Favier, I.; Pradel, C.; Gin, D.L.; Lahitte, J.-F.; Noble, R.D.; Gómez, M.; Remigy, J.-C. High catalytic efficiency of palladium nanoparticles immobilized in a polymer membrane containing poly(ionic liquid) in Suzuki-Miyaura cross-coupling reaction. *J. Membr. Sci.* **2015**, *492*, 331–339. [CrossRef]
16. Prakash, S.; Charan, C.; Singh, A.K.; Shahi, V.K. Mixed metal nanoparticles loaded catalytic polymer membrane for solvent free selective oxidation of benzyl alcohol to benzaldehyde in a reactor. *Appl. Catal. B* **2013**, *132*, 62–69. [CrossRef]
17. Wang, Z.; Chen, X.; Li, K.; Bi, S.; Wu, C.; Chen, L. Preparation and catalytic property of PVDF composite membrane with polymeric spheres decorated by Pd nanoparticles in membrane pores. *J. Membr. Sci.* **2015**, *496*, 95–107. [CrossRef]
18. Emin, C.; Remigy, J.-C.; Lahitte, J.-F. Influence of UV grafting conditions and gel formation on the loading and stabilization of palladium nanoparticles in photografted polyethersulfone membrane for catalytic reactions. *J. Membr. Sci.* **2014**, *455*, 55–63. [CrossRef]
19. Chen, X.; He, Y.; Shi, C.; Fu, W.; Bi, S.; Wang, Z.; Chen, L. Temperature- and pH-responsive membranes based on poly(vinylidene fluoride) functionalized with microgels. *J. Membr. Sci.* **2014**, *469*, 447–457. [CrossRef]
20. He, Y.; Chen, X.; Bi, S.; Fu, W.; Shi, C.; Chen, L. Conferring pH-sensitivity on poly (vinylidene fluoride) membrane by poly(acrylic acid-*co*-butyl acrylate) microgels. *React. Funct. Polym.* **2014**, *74*, 58–66. [CrossRef]
21. Lau, W.N.; Yeung, K.L.; Martin-Aranda, R. Knoevenagel condensation reaction between benzaldehyde and ethyl acetoacetate in microreactor and membrane microreactor. *Microporous Mesoporous Mater.* **2008**, *115*, 156–163. [CrossRef]
22. Yang, H.C.; Zhong, W.; Hou, J.; Chen, V.; Xu, Z.K. Janus hollow fiber membrane with a mussel-inspired coating on the lumen surface for direct contact membrane distillation. *J. Membr. Sci.* **2017**, *523*, 1–7. [CrossRef]

23. Wong, Y.J.; Zhu, L.; Teo, W.S.; Tan, Y.W.; Yang, Y.; Wang, C.; Chen, H. Revisiting the Stöber method: Inhomogeneity in silica shells. *J. Am. Chem. Soc.* **2011**, *133*, 11422–11425. [CrossRef] [PubMed]
24. Chen, X.; Zhao, B.; Han, P.; Fu, W.; Chen, L. Temperature- and pH-sensitive membrane formed from blends of poly(vinylidene fluoride)-graft-poly(*N*-isopropylacrylamide) and poly(acrylic acid) microgels. *React. Funct. Polym.* **2014**, *84*, 10–20. [CrossRef]
25. Chen, X.; Zhao, B.; Zhao, L.; Bi, S.; Han, P.; Feng, X.; Chen, L. Temperature- and pH-responsive properties of poly(vinylidene fluoride) membranes functionalized by blending microgels. *RSC Adv.* **2014**, *4*, 29933. [CrossRef]
26. Kim, J.; Fu, Q.; Xie, K.; Scofield, J.M.P.; Kentish, S.E.; Qiao, G.G. CO_2 separation using surface-functionalized SiO_2 nanoparticles incorporated ultra-thin film composite mixed matrix membranes for post-combustion carbon capture. *J. Membr. Sci.* **2016**, *515*, 54–62. [CrossRef]
27. Choi, D.-W.; Chung, K.-B.; Park, J.-S. Rapid vapor deposition SiO_2 thin film deposited at a low temperature using tris(tert-pentoxy)silanol and trimethyl-aluminum. *Mater. Chem. Phys.* **2013**, *142*, 614–618. [CrossRef]
28. Ren, G.; Wang, W.; Shang, M.; Zou, H.; Cheng, S. Using a Macroporous Silver Shell to Coat Sulfonic Acid Group-Functionalized Silica Spheres and Their Applications in Catalysis and Surface-Enhanced Raman Scattering. *Langmuir ACS J. Surf. Colloids* **2015**, *31*, 10517–10523. [CrossRef] [PubMed]
29. Xu, H.; Yan, J.; Xu, Y.; Song, Y.; Li, H.; Xia, J.; Huang, C.; Wan, H. Novel visible-light-driven AgX/graphite-like C_3N_4 (X=Br, I) hybrid materials with synergistic photocatalytic activity. *Appl. Catal. B* **2013**, *129*, 182–193. [CrossRef]
30. Yang, H.C.; Hou, J.; Chen, V.; Xu, Z.K. Surface and interface engineering for organic-inorganic composite membranes. *J. Mater. Chem. A* **2016**, *4*. [CrossRef]
31. Zhang, F.; Zhang, W.; Yu, Y.; Deng, B.; Li, J.; Jin, J. Sol-gel preparation of PAA-g-PVDF/TiO_2 nanocomposite hollow fiber membranes with extremely high water flux and improved antifouling property. *J. Membr. Sci.* **2013**, *432*, 25–32. [CrossRef]
32. Oh, J.-S.; Luong, N.D.; Hwang, T.-S.; Hong, J.-P.; Lee, Y.K.; Nam, J.-D. In situ fabrication of platinum/graphene composite shell on polymer microspheres through reactive self-assembly and in situ reduction. *J. Mater. Sci.* **2012**, *48*, 1127–1133. [CrossRef]
33. Ibrahim, I.; Ali, I.O.; Salama, T.M.; Bahgat, A.A.; Mohamed, M.M. Synthesis of magnetically recyclable spinel ferrite (MFe_2O_4, M=Zn, Co, Mn) nanocrystals engineered by sol gel-hydrothermal technology: High catalytic performances for nitroarenes reduction. *Appl. Catal. B* **2016**, *181*, 389–402. [CrossRef]
34. Narayanan, K.B.; Park, H.H.; Han, S.S. Synthesis and characterization of biomatrixed-gold nanoparticles by the mushroom Flammulina velutipes and its heterogeneous catalytic potential. *Chemosphere* **2015**, *141*, 169–175. [CrossRef] [PubMed]
35. Armenise, S.; Garcia-Bordeje, E.; Valverde, J.L.; Romeo, E.; Monzon, A. A Langmuir-Hinshelwood approach to the kinetic modelling of catalytic ammonia decomposition in an integral reactor. *Phys. Chem. Chem. Phys. PCCP* **2013**, *15*, 12104–12117. [CrossRef] [PubMed]

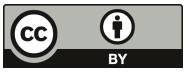

polymers

MDPI

Article

Green and Facile Synthesis of Highly Stable Gold Nanoparticles via Hyperbranched Polymer In-Situ Reduction and Their Application in Ag^+ Detection and Separation

Xunyong Liu [1,*], Chenxue Zhu [1], Li Xu [1], Yuqing Dai [1], Yanli Liu [2] and Yi Liu [1,*]

[1] School of Chemistry and Materials Science, Ludong University, Yantai 264025, Shandong Province, China; m13105202785@163.com (C.Z.); ldxuli@126.com (L.X.); daiyuqing1023@163.com (Y.D.)

[2] School of Information and Electronic Engineering, Shandong Technology and Business University, Yantai 264005, Shandong Province, China; yanliliu0727@163.com

* Correspondence: xunyongliu@ldu.edu.cn (X.L.); liuyi200541@ldu.edu.cn (Y.L.); Tel.: +86-535-667-2176 (X.L. & Y.L.)

Received: 26 November 2017; Accepted: 30 December 2017; Published: 3 January 2018

Abstract: The development of a green and facile strategy for synthesizing high stable gold nanoparticles (AuNPs) is still highly challenging. Additionally, the main problems regarding AuNPs based colorimetric sensors are their poor selectivity and low sensitivity, as well their tendency to aggregate during their synthesis and sensing process. Herein, we present an in-situ reduction strategy to synthesize thermoresponsive hyperbranched polymer (i.e., Hyperbranched polyethylenimine-terminal isobutyramide (HPEI-IBAm)) functionalized AuNPs. The HPEI-IBAm-AuNPs show excellent thermal stability up to 200 °C, high tolerance of a wide range of pH value (3–13), and high salt resistance. HPEI-IBAm acted as the template, the reducing agent, and the stabilizing agent for the preparation of AuNPs. The HPEI-IBAm-AuNPs can be used as colorimetric sensors for the detection of Ag^+. In the detecting process, HPEI-IBAm serves as a trigger agent to cause an unusual color change from red to brown. This new non-aggregation-based colorimetric sensor showed high stability (maintaining the color lasting without fading), high selectivity, and high sensitivity with an extremely low detection limit of 7.22 nM and a good linear relationship in a wide concentration range of 0–2.0 mM (R^2 = 0.9921). Significantly, based on the thermoresponsive property of the HPEI-IBAm, the AuNPs/Ag composites can be separated after sensing detection, which can avoid secondary pollutions. Therefore, the green preparation and the applications of the unusual colorimetric sensor truly embody the concepts of energy saving, environmental protection, and sustainable development.

Keywords: thermoresponsive hyperbranched polymer; gold nanoparticles; in-situ synthesis; colorimetric sensor; silver ions

1. Introduction

The phenomenal optical and chemical properties of gold nanoparticles (AuNPs) have drawn considerable attention for applications in the fields of chemical sensing [1,2], biomedicine [3,4], catalysis [5,6], and so on. In recent years, AuNPs are the most widely studied colorimetric sensors of Ag^+ detection due to their high extinction coefficients and sensitive surface plasmon resonance (SPR) sensing characteristics in the visible region [7–10]. Many methods using citrate reduction [11], hydrazine reduction [12], sodium borohydride reduction [13], and solvent extraction reduction [14] have been developed to prepare AuNPs. However, these small-molecule reducing agents are all highly

toxic or unsafe. Therefore, the use of green reducing agents can reduce waste and increase the safety of the sample preparation procedure.

As we all know, AuNPs can be used as colorimetric sensors of Ag^+ detection based on the color changes between red and blue (or purple) in the dispersion and aggregation of AuNPs [8,9,15], respectively. In the sensing system, AuNPs aggregation triggered only by interactions with a particular target is expected, which can greatly improve the specificity and selectivity of the colorimetric sensor. However, AuNPs prepared by traditional small-molecule reduction methods easily aggregate under the conditions of strong acid, solid state, or excess ion concentrations [16,17], which can interfere with the Ag^+ detection. Therefore, the stability of AuNPs is a major obstacle to practical applications. The design and preparation of AuNPs, which are stable over a broad range of conditions during storage and utilization, are meaningful and very essential.

Due to the limitations and disadvantages of small-molecule reducing agents, the utilization of hyperbranched polymers as multidentate ligands is an effective approach for preparing high stable AuNPs, because hyperbranched polymers have high steric hindrances and a great number of functional groups [18]. Hyperbranched polyethylenimine (HPEI) and its derivatives as typical hyperbranched polymers having a large amount of amino groups, and a specific spheroid-like shape can stabilize the AuNPs [7,10]. Meanwhile, we all know that the amino groups have good reducibility. Therefore, can HPEI derivatives be used as reductants to prepare AuNPs? If achieved, the green preparation of stabilized AuNPs by in-situ reduction of $HAuCl_4$ solution using HPEI derivatives as templates, reducing agents, and stabilizers without the additional step of introducing a toxic reducing agent will be significant. Moreover, it has been reported that the functionalized AuNPs can be used as colorimetric sensors to detect Ag^+ based on the reduction of Ag^+ by small-molecule reductant such as citrate, ascorbic acid, etc, to form Ag^0, which was deposited onto the surface of AuNPs with a color change [7,9,10]. Inspired by the above redox-modulated sensing mechanism, we want to use HPEI derivatives that existed in the AuNPs solution to replace these small-molecule reducing agents, which can simplify the detection process and avoid the use of some toxic reducing agents.

Thermoresponsive polymers-AuNPs composites have attracted much interest from both fundamental and applied research due to their sensitive response to external stimuli, such as temperature, pH, or salts [19,20]. Additionally, the composites can be used as colorimetric sensors for detecting the variation of external stimuli based on the thermo sensitive characters of polymers. Recently, we have reported that HPEI with terminal isobutyramide (IBAm) groups (HPEI-IBAm) showed better thermosensitivity than traditional thermoresponsive linear polymers [21]. However, whether and how we can utilize them as separation materials for enriching or separating AuNPs/analyte composites have not been studied systematically. As we all know, some sensor-Ag^+ assemblies are difficult to be separated from the sensing system, which can cause seriously secondary pollutions. Therefore, we propose a novel colorimetric sensor based on thermoresponsive HPEI-IBAm that can not only detect Ag^+ but also achieve the separation of sensor/Ag composites, which provides new ideas for the future design and research of environment-friendly multifunctional AuNPs.

Herein, we report that a kind of hyperbranched polymer, i.e., thermoresponsive HPEI-IBAm, can facilely induce the $HAuCl_4$ precursor to spontaneously form well-stabilized AuNPs via a thermal process without the additional step of introducing a reducing agents. Compared with the AuNPs prepared by classical small-molecule reduction as colorimetric sensors of Ag^+, this strategy had several advantages: (1) Thermoresponsive HPEI-IBAm not only serves as a green reductant and excellent stabilizer to prepare AuNPs via in-situ reduction, but it also serves as a trigger agent to induce an obvious color change due to the reduction of Ag^+ to Ag^0 deposited onto the surface of AuNPs, as well as serving as a separating agent to enrich and separate sensor/Ag composites; (2) HPEI-IBAm/AuNPs can realize the integration of the preparation, detection, and separation application, which serves the aims of energy saving, environmental protection, and sustainable development, and provides a basis to further develop multifunctional nano-composites; (3) In-situ formation of AuNPs by HPEI-IBAm with a large number of amino groups and high steric hindrances

can greatly improve the stability of AuNPs (even under the conditions of high temperature, acid medium, solid state, and excess ion concentrations), which can avoid the interferences from an acid medium, excess ion concentrations, and so on to improve the selectivity of Ag^+ detection; (4) The color change of AuNPs sensor from red to brown is more sensitive and selective than that from red to purple or blue (the color change from red to brown is unique and can easily be observed by naked eyes), and therefore this colorimetric sensor exhibits high sensitivity and excellent selectivity toward Ag^+; (5) The thermoresponsive HPEI-IBAm can separate AuNPs/Ag after the detection application by a simple precipitation or centrifugation process, which can avoid secondary pollutions. To the best of our knowledge, this is the first report to prepare AuNPs, detect Ag^+, and separate AuNPs/analyte composites simultaneously without the additional step of introducing a reductant and without secondary pollutions. This environment-friendly multifunctional colorimetric sensor really embodies energy saving, environment protection, and sustainable development.

2. Materials and Methods

2.1. Materials

Hyperbranched polyethylenimine (HPEI) with a number-average molecular weight of 10^4 g/mol was purchased from Aldrich and dried in a vacuum oven at 40 °C for 12 h prior to use. $AgNO_3$ and all other chemicals were analytical grade and purchased from Shanghai Sinopharm Chemical Reagent Corporation.

2.2. Characterization

^{1}H NMR spectra of the HPEI-IBAm were obtained on a Varian INOVA 500MHz spectrometer. Ultraviolet-visible (UV-vis) absorption spectra were performed using a T6 UV/Vis Spectrophotometer (Purkinje General, Beijing, China). Transmission electron microscopy (TEM) analysis was performed on a Philips (Amsterdam, Netherlands) TECNAI G2 F20 operating at 200 kV. The size of the nanoparticles was measured by dynamic light scattering on a Malvern Instruments (Malvern, UK) Zetasizer Nano-ZS90 at 25 °C. The concentration of Ag^+ was determined by an Inductively Coupled Plasma spectrometer (ICP-9000, Shimadzu, Kyoto, Japan).

2.3. Synthesis of Thermoresponsive HPEI-IBAm

The HPEI-IBAm is prepared using a simple amidation reaction between the amino groups of HPEI and isobutyric anhydride [22,23]. Under the atmosphere of nitrogen, 4.0 g isobutyric anhydride (0.025 mol) is added to 15 mL chloroform solution containing 2.0 g HPEI and 2.87 g triethylamine (0.028 mol). After stirring for 3 h at room temperature, the mixture is maintained at 65 °C for 24 h. The residues were obtained by vacuum distillation from reaction liquid, and their purification were carried out by dialysis against methanol using a benzoylated cellulose membrane with a molecular weight cut off 1000 for 3 days.

2.4. In-Situ Preparation of HPEI-IBAm Functionalized AuNPs

Five samples 1–5 were prepared as follows: briefly, 9 mL of $HAuCl_4$ (0.29 mM) was added into 6 mL of appropriate concentration of HPEI-IBAm aqueous solution (0.5, 1, 3, 9, and 18 mg/L) with initial molar ratio 0.06:1, 0.12:1, 0.36:1, 1.04:1, and 2.08:1 of HPEI-IBAm to gold (corresponding to samples 1–5, respectively). The reaction was carried out in a nitrogen atmosphere under continuous mechanical stirring at 80 °C for 20 min. The mixture was changed from pale yellow to wine red or pink, indicating the formation of HPEI-IBAm functionalized AuNPs.

2.5. Preparation of Citrate-Capped AuNPs

For the purpose of comparison, citrate-capped AuNPs were also synthesized according to the previous publications. Briefly, 5.0 mL of $HAuCl_4$ solution (5.34 mM) was added to 135 mL of Milli-Q

water in a three-necked flask, heated up to reflux. Then, 10 mL of sodium citrate solution (0.9%) was added to the boiling solution while stirring vigorously. After continuous boiling for 15 min, the reaction mixture was cooled to ambient temperature. The concentration of the AuNPs was estimated by Lambert-Beer's law (the extinction coefficient of ca. 13 nm AuNPs is 2.7×10^8 $M^{-1}\cdot cm^{-1}$ at 520 nm) [10,24].

2.6. Stability Testing of HPEI-IBAm Functionalized AuNPs

2.6.1. Thermal Stability Testing

For thermal stability testing, 4.8 mL of HPEI-IBAm functionalized AuNPs solution was dried into powder state in an oven at a given temperature. Three temperature levels of 110, 140, and 200 °C were applied to thermal stability tests. After drying, 4.8 mL of Milli-Q water was added to redisperse the HPEI-IBAm functionalized AuNPs solid powder for the DLS and UV-vis measurements. The previous drying and dissolving process was repeated to test the thermal stability of the HPEI-IBAm functionalized AuNPs. By contrast, the stability of citrate-capped AuNPs was also tested according to the same steps.

2.6.2. pH Stability Testing

For pH stability testing, 13 samples of 4.8 mL of HPEI-IBAm functionalized AuNPs or citrate-capped AuNPs solution were adjusted to different pH (range from 1.0 to 13.0). Then, the stability of HPEI-IBAm functionalized AuNPs and citrate-capped AuNPs solution under different pH can be evaluated by UV-Vis spectrometry, because the aggregation or dispersion of AuNPs is closely associated with the change of UV-Vis characteristic absorption spectrum. The UV-Vis absorption spectra of the AuNPs solution were recorded, respectively, after placing at room temperature for 1 and 7 days.

2.6.3. The Salt Tolerance Testing

10 samples of 4.8 mL of HPEI-IBAm functionalized AuNPs and citrate-capped AuNPs solution with mass concentration of NaCl from 0 to 12.5 g/L were used to evaluate the stability of the AuNPs solution for salt tolerance. The change in solution color and UV-Vis absorption spectra of two AuNPs systems were recorded to compare their difference in the salt tolerance and tolerant stability.

2.7. Colorimetric Sensing of Ag^+

The colorimetric sensing of Ag^+ was performed as follows. 0.9 mL of HPEI-IBAm solution (6.0 g/L) was added to the mixture of HPEI-IBAm functionalized AuNPs (3.0 mL) and Ag^+ (0.9 mL) at different concentrations (5.73 to 2 mM). After equilibrating at boiling temperature for 2 min, the color change and absorption spectra of the solution were recorded by a digital camera and a UV-vis spectrophotometer, respectively. All detecting experiments were performed in triplicate.

3. Results

3.1. Synthesis and Characterization of HPEI-IBAm

The thermoresponsive HPEI-IBAm was prepared according to the route in Scheme 1. Compared with HPEI, the HPEI-IBAm polymer possessed amide groups that were characterized by ^{1}H NMR (Figure S1) and FT-IR (Figure S2). As shown in Figure S1A, HPEI-IBAm exhibits a new signal located at 1.04 ppm that comes from the methyl protons of theisobutyramide groups (a′ in Figure S1A, –NH–CO–CH–$(CH_3)_2$, along with the disappearance of –NH_2 and NH peaks at 1.4–1.8 ppm (a and b in Figure S1B) of HPEI reactant. Meanwhile, the substitution degree of the amine groups of HPEI is about 83.1% calculated from the integral of the NMR data [22], which indicates that the HPEI-IBAm has not only a large number of isobutyramide groups (giving HPEI-IBAm thermosensitive character)

but also many unreacted amine groups (having reducing capacity). The successful synthesis of HPEI-IBAm was further confirmed according to the change of FTIR spectra of HPEI and HPEI-IBAm. In comparison to HPEI, HPEI-IBAm exhibits new bands at around 1633 and 2960 cm^{-1} corresponding to the characteristic C=O stretching vibrations of the –CONH– groups and $–CH_3$ stretching vibrations of the $–COCH(CH_3)_2$, respectively. These characterization results indicate that the HPEI-IBAm is successfully prepared by the reaction of HPEI and isobutyric anhydride.

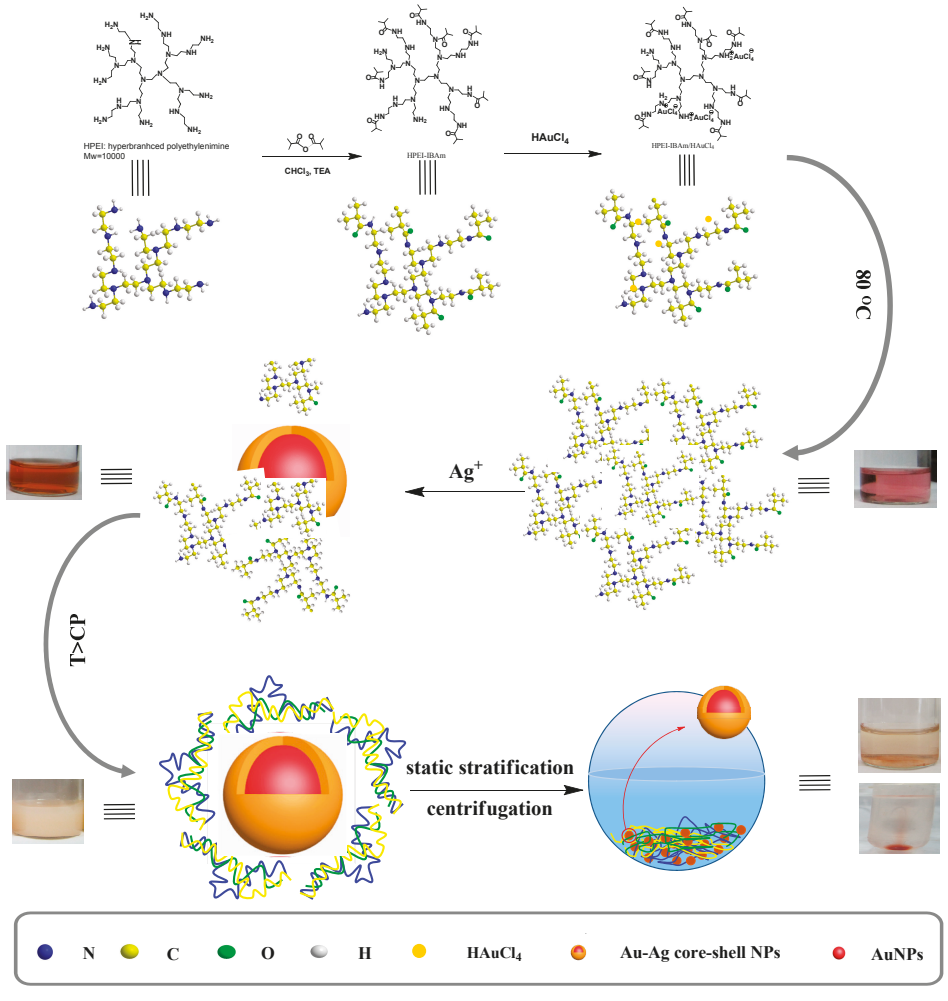

Scheme 1. Preparation of thermoresponsive HPEI-IBAm, HPEI-IBAm-AuNPs; the sensing and separating mechanism of HPEI-IBAm-AuNPs toward Ag^+.

3.2. In-Situ Preparation of HPEI-IBAm Functionalized AuNPs

To improve the stability of AuNPs and avoid the limitations and disadvantages of small-molecule reducing agents, the stabilization of AuNPs by polymers as multidentate ligands is one of the most important and effective methods. Over the last few decades, there has been growing interest in using dendritic polymers (especially dendrimers with perfect structure and hyperbranched polymers)

as stabilizers or templates to prepare functionalized AuNPs. For example, entrapped dendrimers or stabilized AuNPs can be prepared by the reduction of Au^{3+} inside the dendrimer core [25–29]. However, these AuNPs are very small in size (<5–9 nm in diameter) and difficult to visualize (especially at low concentration) and characterize (since they have no characteristic UV-Vis absorption), and are not applicable to colorimetric detection. The hyperbranched polymer with imperfect structure can prepare large-sized AuNPs due to its relatively weak steric repulsion compared to dendrimers [18].

We used a hyperbranched polymer derivative, i.e., thermoresponsive HPEI-IBAm, as reducing agent to prepare HPEI-IBAm functionalized AuNPs (Scheme 1). In the preparation process, no additional reducing agents were added. The formation of AuNPs depends on the amount of added HPEI-IBAm, because Au^{3+} can be reduced by the unreacted amine groups of HPEI-IBAm. As shown in Figure 1, the color and the maximum UV-vis absorption wavelength of AuNPs solution changed from purple red to red and shifted toward short wavelength (532 to 519 nm), respectively, as the increasing of HPEI-IBAm concentration in the experimental range (0.5 to 18 g/L). When the concentration of HPEI-IBAm was more than 3 g/L, the color and the maximum UV absorption wavelength of AuNPs solution did not significantly change, because all of the Au^{3+} had been reduced completely. Therefore, the concentration of HPEI-IBAm was fixed at 3 g/L (i.e., the initial molar ratio 0.36:1 of HPEI-IBAm to gold) for the preparation of HPEI-IBAm functionalized AuNPs.

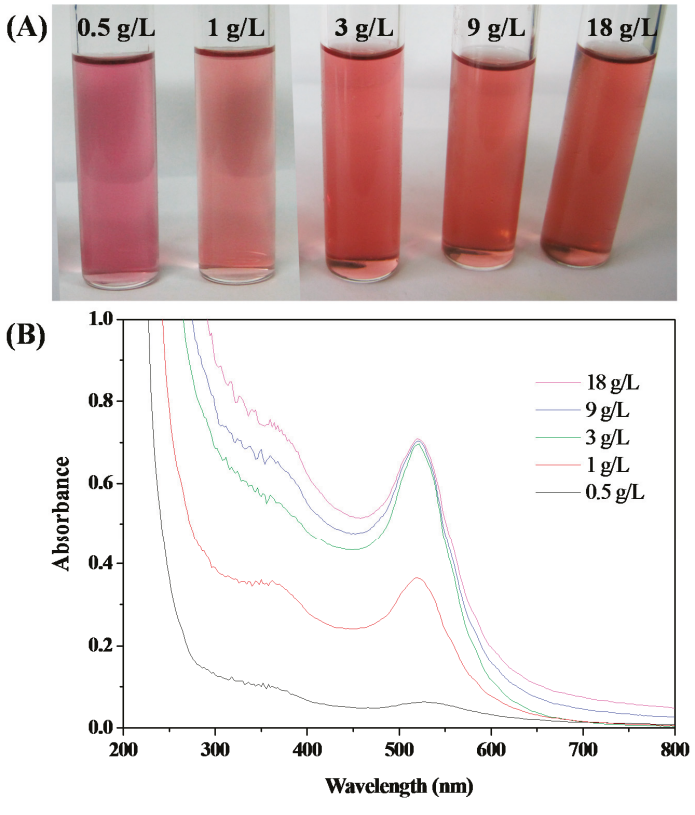

Figure 1. Effect of the concentration of HPEI-IBAm on synthesis of AuNPs: (**A**) the color and (**B**) the UV-Visible spectra.

As shown in Figure 2A, when the preparation temperature was set at 20, 40, 60, 80, and 100 °C, respectively, the products were purple (at 20 °C), purple red (at 40 °C) and red (above 60 °C). The AuNPs being purple or purple red are usually unstable and tend to aggregate, resulting in increased particle size and a shift to long wavelength of UV-vis absorption peak. It can be seen from Figure 2B,C that the maximum UV-Vis absorption wavelength and the particle size of AuNPs did not significantly change when the in-situ preparation temperature was higher than 80 °C. Therefore, we select 80 °C to prepare the HPEI-IBAm functionalized AuNPs.

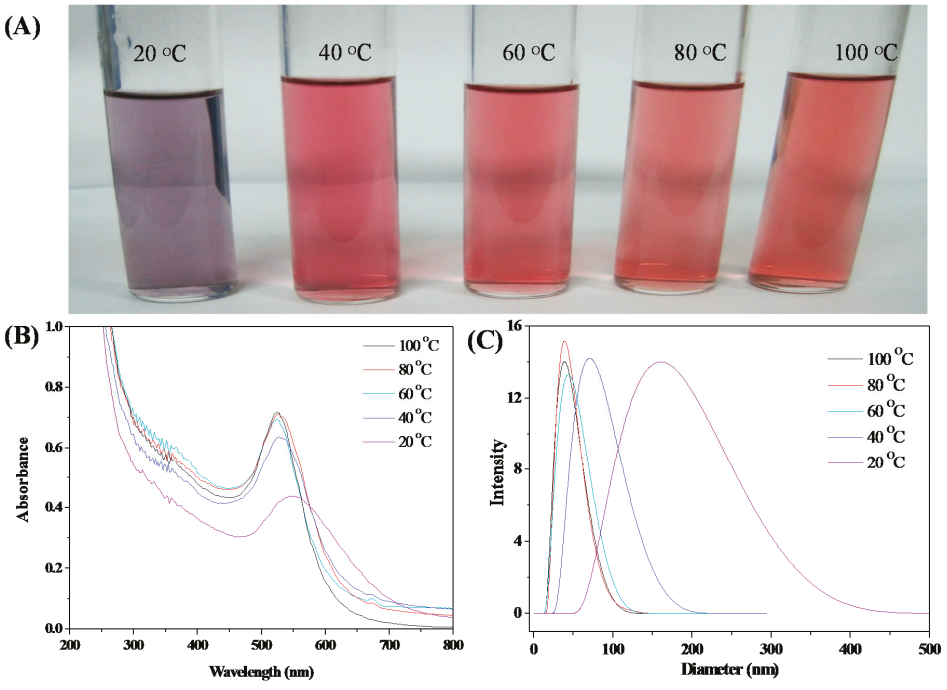

Figure 2. (**A**) Photographs, (**B**) UV-Visible spectra, and (**C**) DLS diagram of HPEI-IBAm functionalized AuNPs when the preparation temperature increased from 20 to 100 °C.

3.3. Stability of HPEI-IBAm Functionalized AuNPs

As we all know, noble metal nanoparticles are prone to aggregate due to the influence of Van der Waals force, temperature, pH, and other factors, reducing the stability of NPs, which is also a very challenging problem for all NPs in preparation and application [16]. In our present study, HPEI-IBAm functionalized AuNPs that have a special topology structure, where one gold NP is surrounded with multiple HPEI-IBAm molecules, are prepared by in-situ reaction of $HAuCl_4$ in HPEI-IBAm solution to improve their stability.

As shown in Figure 3 and Figure S3–S6, the HPEI-IBAm functionalized AuNPs showed higher thermal stability than citrate-capped AuNPs. After 10 times of evaporation at 110 or 130 °C and re-dispersion (Figure 3A and Figure S4A), a little red shift (Figure 3B) was shown in the UV-Visible spectra of the HPEI-IBAm functionalized AuNPs. The HPEI-IBAm functionalized AuNPs are stable even at 200 °C after 3 times of drying and re-dispersion as shown in Figure S6. Although the color of the HPEI-IBAm functionalized AuNPs solution changed from red to reddish brown (which was perhaps due to the partial oxidation of the amine groups of HPEI-IBAm) after 4 times of drying and re-dissolution, no aggregation or precipitation was observed. However, the citrate-capped AuNPs

showed obvious red shift (Figure 3C) and changed from red to blue (Figure 3A) after 1 time of evaporation at 110–200 °C and re-dispersion, indicating that the citrate-capped AuNPs are extremely unstable when they exist in solid form. Compared with the citrate-capped AuNPs, it can be seen that the HPEI-IBAm by means of its large steric hindrance effect and multi-site protection can significantly improve the thermal stability of AuNPs prepared by in-situ reduction reaction.

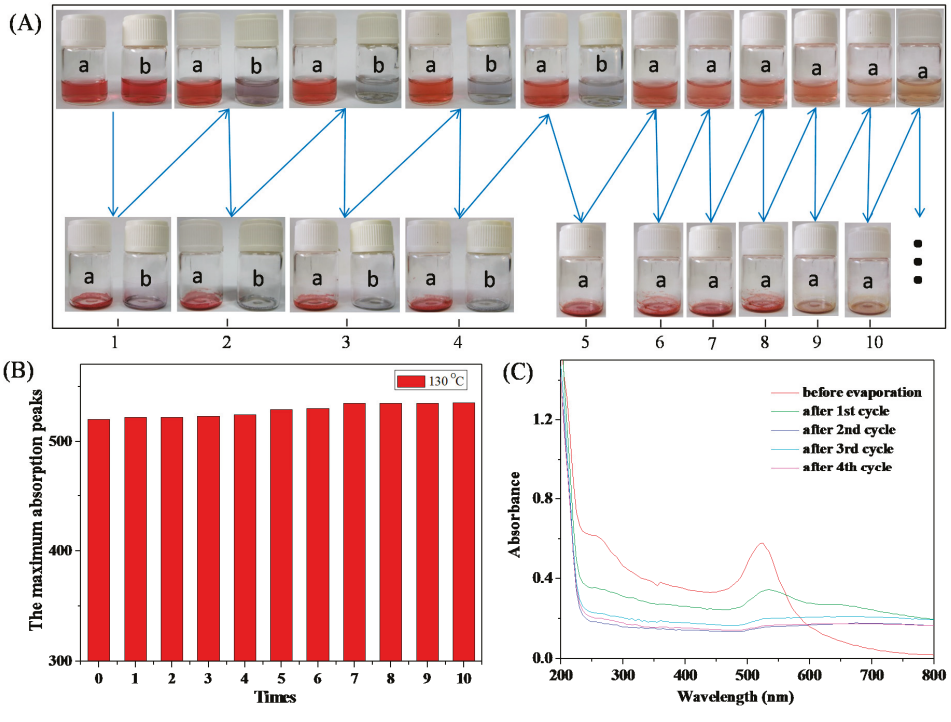

Figure 3. (**A**) Photographs of (a) the HPEI-IBAm functionalized AuNPs and (b) citrate-capped AuNPs after every evaporation at 130 °C and re-dispersion in Milli-Q water; (**B**) the maximum absorption peaks of the HPEI-IBAm functionalized AuNPs after each cycle's re-dispersion; (**C**) the UV-Vis spectra of the citrate-capped AuNPs after each cycle's re-dispersion.

It is well known that the pH of the different tested system may vary from acid to alkaline. Therefore, it is extremely important for the probe to remain stable in the widest possible range of pH. To demonstrate their potential applications in sensing, the pH stability of the HPEI-IBAm functionalized AuNPs and the citrate-capped AuNPs was also evaluated here. The HPEI-IBAm functionalized AuNPs can be stable after adjusting the pH 1–13 for 1 h (Figure 4A), and the citrate-capped AuNPs have shown a pronounced red shift after 1 h under the pH 1–2 (Figure 4D). After 24 h, the HPEI-IBAm functionalized AuNPs have a slight red shift only at pH = 1 (Figure 4B). However, the citrate-capped AuNPs have obvious red shift or precipitation at pH range of 1–5 (Figure 4E). After 5 d, the HPEI-IBAm functionalized AuNPs remain stable except for pH 1–2 (Figure 4C), which is mainly because HPEI-IBAm with a large number of amine groups can react with acid. The citrate-capped AuNPs not only precipitated completely at pH range of 1–5, but also decreased their absorption peak intensity at pH = 12 due to the influence of relatively high salt concentration (Figure 4F). Therefore, the HPEI-IBAm functionalized AuNPs have a wider range of acid-base usage than citrate-capped AuNPs, which is more conducive to the practical application of colorimetric detection.

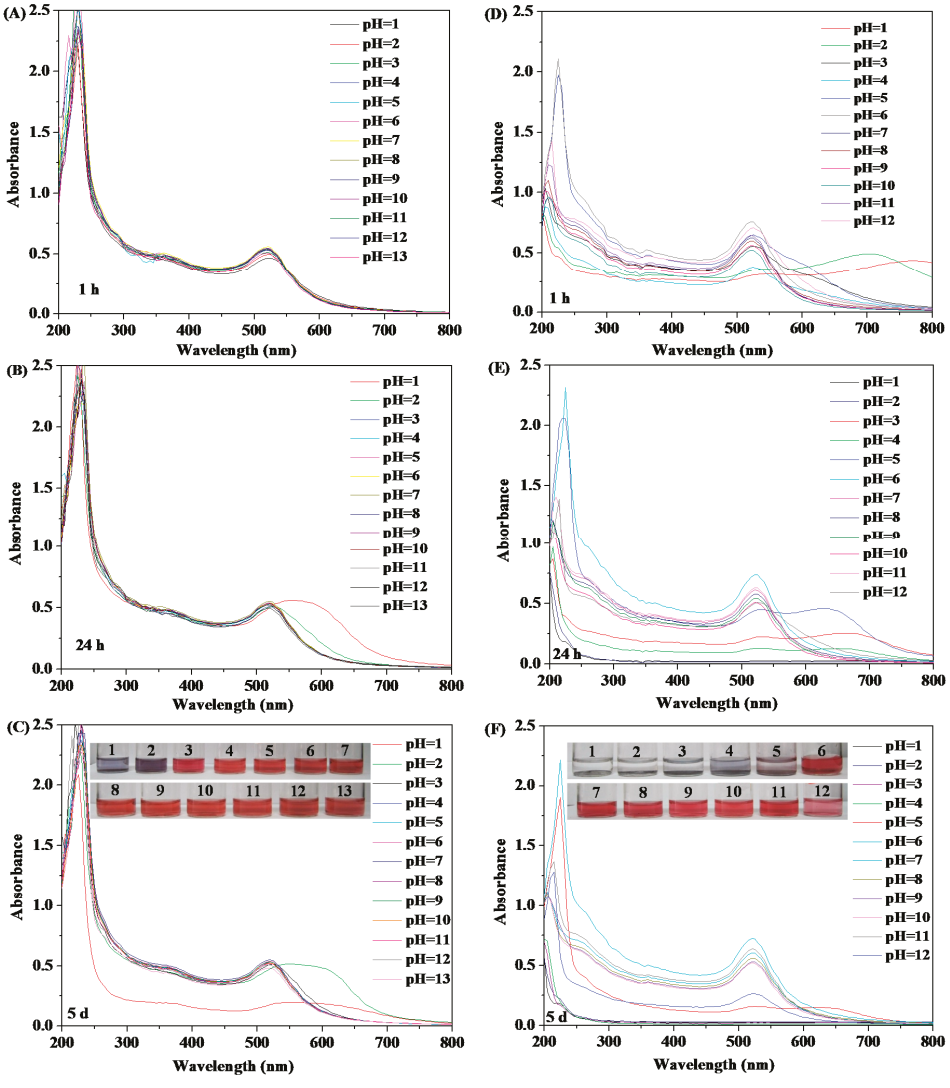

Figure 4. The UV-Vis spectra of the HPEI-IBAm functionalized AuNPs after (**A**) 1 h; (**B**) 24 h and (**C**, Inset shows the color of the HPEI-IBAm functionalized AuNPs) 5 d under different pH value; the UV-Vis spectra of the citrate-capped AuNPs after (**D**) 1 h; (**E**) 24 h; and (**F**, Inset shows the color of the citrate-capped AuNPs) 5 d under different pH value.

Besides the influence of temperature and pH on the stability of AuNPs, the salinity is also an important factor affecting the stability of AuNPs. If the effect of salt causes the aggregation and the color change of AuNPs, it will interfere with their colorimetric detection. Therefore, the AuNPs used for colorimetric detection require good salt tolerance. The salt tolerance of the HPEI-IBAm functionalized AuNPs, and the citrate-capped AuNPs was systematically studied. Experimental results demonstrate that no obvious changes in color (Figure 5A,B) and UV-Vis spectra (Figure 5C and Figure S7) before and after 24 h under different salt concentrations are observed for HPEI-IBAm

functionalized AuNPs, indicating that the HPEI-IBAm functionalized AuNPs are very stable against the variation of salinity. However, the citrate-capped AuNPs have obvious red shift (Figure 5D) in UV-Vis spectra, and the A_{650} values of the absorbance at 650 nm increase from 0.067 to 0.509 (Inset Figure of Figure 5D) with the increase of salt concentration, indicating that the citrate-capped AuNPs have aggregated and are unstable to salt. Meanwhile, the color of the citrate-capped AuNPs solution also changed from red to purple or blue (Figure 5E) and became lighter after 24 h (Figure 5F) due to the aggregation and precipitation of AuNPs with the decrease of the A_{650} values (Figure S8) relative to Figure 5D. The contrastive study proves that the HPEI-IBAm plays an important role in stabilizing the AuNPs.

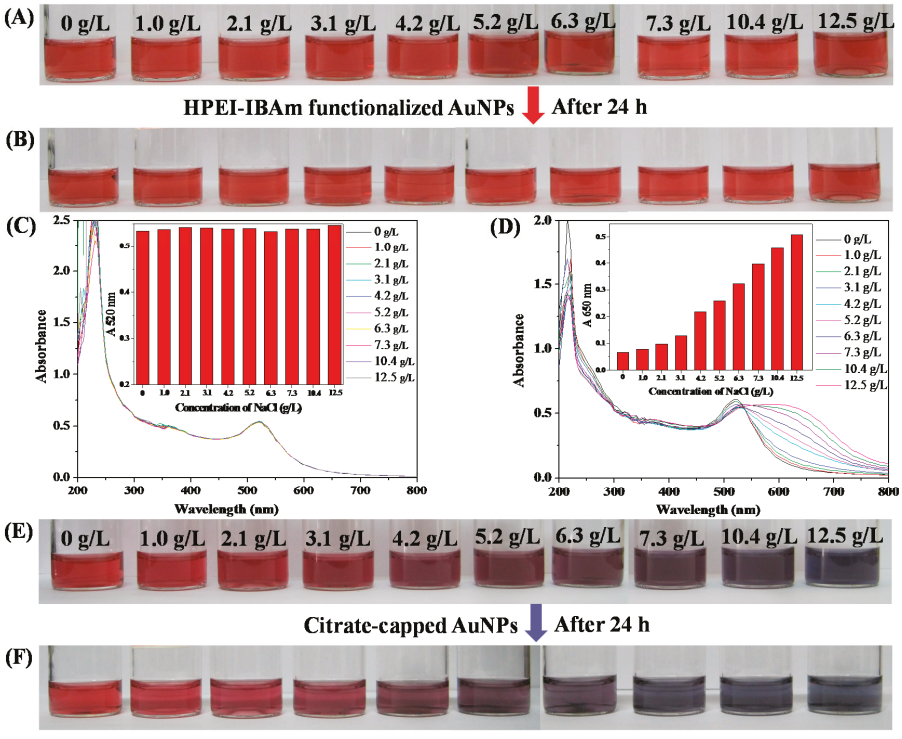

Figure 5. Photographs of the HPEI-IBAm functionalized AuNPs (**A**) before and (**B**) after 24 h under different salt concentrations; the UV-Vis spectra (**C**) of the HPEI-IBAm functionalized AuNPs after 24 h under different salt concentrations (Inset shows the A_{520} value of the absorbance at 520 nm versus the concentration of NaCl); the UV-Vis spectra (**D**) of the citrate-capped AuNPs under different salt concentrations (inset shows the A_{650} value of the absorbance at 650 nm versus the concentration of NaCl); photographs of the citrate-capped AuNPs (**E**) before and (**F**) after 24 h under different salt concentrations.

The above experiments show that the HPEI-IBAm functionalized AuNPs prepared by in-situ reaction have higher stability to temperature, pH, and salinity, which would greatly broaden their fields of application.

3.4. Colorimetric Sensing of Ag^+

The mechanisms of the conventional AuNPs-based colorimetric sensors for the detection of Ag^+ are mostly based on the aggregation of AuNPs with a red-to-blue or red-to-purple color change [9,15,30,31].

In our experiments, the citrate-capped AuNPs have slight (Figure 6B-b) and obvious (Figure S9B-c) red shift in UV-Vis spectra with a red (Figure 6A-a) to purple (Figure 6A-b) to blue (Figure S9A-c) color change after the addition of Ag^+ for 1 and 24 h, respectively. However, many factors, such as strong acid environment, high temperature, high salt, and so on, can also induce the aggregation of AuNPs with a red to blue (or purple) color change, which will interfere with the detection of Ag^+ and reduce the selectivity of colorimetric sensor. Therefore, developing a colorimetric sensor for Ag^+ detection based on the non-aggregation of AuNPs is of great significance. It has been reported that the citrate-capped AuNPs can be used as a colorimetric sensor for Ag^+ detection based on the reduction of Ag^+ by small-molecule reducing agents such as citrate, ascorbic acid, etc, to form Ag^0 deposited onto the surface of AuNPs [8–10]. Inspired by the redox-modulated sensing mechanism, we use HPEI-IBAm to replace these small-molecule reducing agents, which can avoid using some toxic reductants and stabilize the AuNPs/analyte composites to maintain the color lasting without fading. In this work, after the addition of HPEI-IBAm, the color of the HPEI-IBAm functionalized AuNPs solution changes from red (Figure 6A-c) to brown (Figure 6A-d) in the presence of Ag^+, which can realize the colorimetric detection of Ag^+. The brown color is similar to the color of the Au-Ag core-shell NPs (with Au as the core and Ag as the shell). Therefore, the sensing mechanism of this colorimetric sensor can be explained as follows: the reduced Ag^0 is directly deposited onto the AuNPs surface, forming the Au-Ag core-shell NPs because of the high affinity between Au and Ag and leading to a red to brown color change; meanwhile, the HPEI-IBAm with a high steric hindrance effect can protect Au-Ag core-shell NPs against aggregation (Scheme 1).

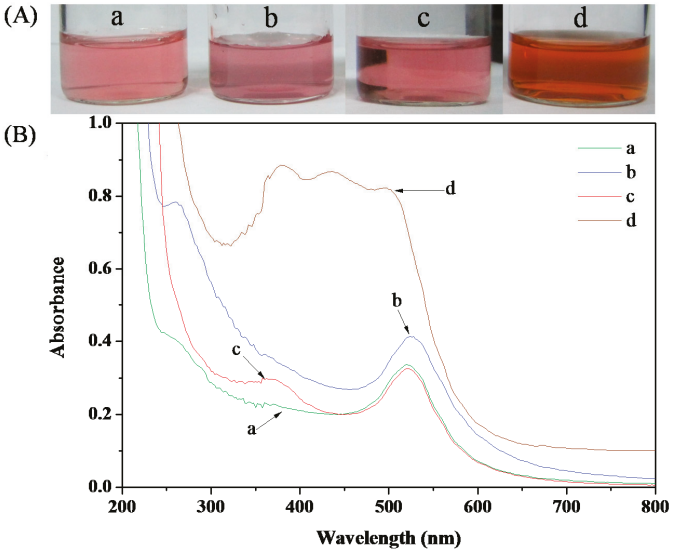

Figure 6. Colorimetric response of the sensor: (**A**) color changes and (**B**) absorption spectra of (a) 1.2 nM citrate-capped AuNPs; (b) 1.2 nM citrate-capped AuNPs with 0.573 mM Ag^+; (c) 1.2 nM HPEI-IBAm functionalized AuNPs; (d) 1.2 nM HPEI-IBAm functionalized AuNPswith 0.573 mM Ag^+.

From Curve c in Figure 6B, we can see that the surface plasmon resonance peak of the HPEI-IBAm functionalized AuNPs appears at about 520 nm. The UV-vis spectra of the Au-Ag core-shell NPs (Curve d in Figure 6B) showed a wide plasmon resonance bands, which was consistent with the other previous core-shell NPs. Therefore, from the change of the UV-vis absorption spectra, we could reasonably infer that Ag^0 was deposited on the preformed Au core surface, forming the Au-Ag core-shell NPs. These changes were further confirmed by the TEM images. It can be seen clearly from the TEM images

(Figure 7B) that most of the Au-Ag NPs had a darker central part (Au core) and a clearer outer part (Ag shell). Moreover, the HPEI-IBAm stabilized AuNPs and Au-Ag core-shell NPs shown in Figure 7 were all close to uniform dispersion, and no large aggregation was observed. Therefore, the new non-aggregation-based colorimetric sensor with a unique red-to-brown color change showed higher stability and anti-interference ability than that based on the aggregation of AuNPs with a red-to-blue (or purple) color change.

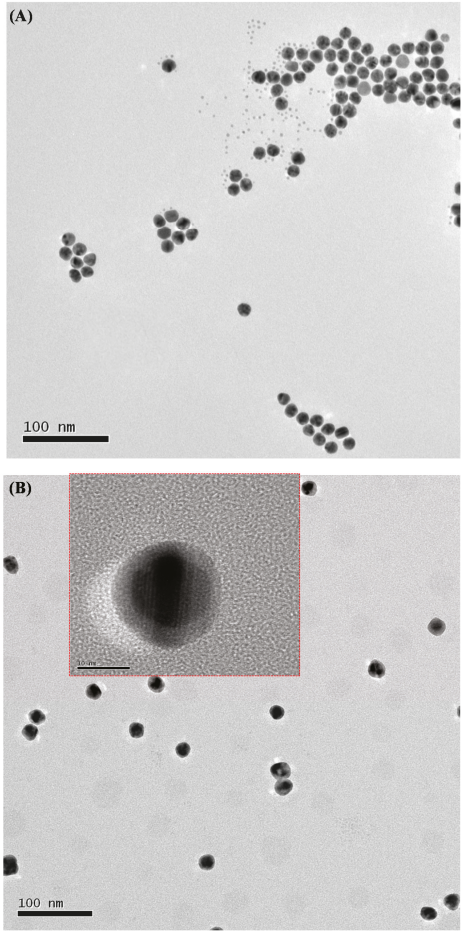

Figure 7. TEM images of (**A**) HPEI-IBAm functionalized AuNPs and (**B**) Au-Ag core-shell NPs (Inset shows a typical HR-TEM image of Au-Ag core-shell NP).

As is well known, the sensitivity of AuNPs based colorimetric sensor is highly dependent on the concentration of AuNPs [7,9,10]. Therefore, the effect of the dosage of HPEI-IBAm-AuNPs on the response of the sensor was examined. According to the sensing mechanism mentioned above, we can know that Ag^0 was directly deposited onto the surface of AuNPs, forming the Au-Ag core-shell NPs with a red to brown color change. Obviously, the higher concentration of AuNPs, the more Ag^0 is needed to cover the AuNPs and to cause the color change, making the sensor had low sensitivity. In the presence of Ag^+ at a given concentration, the lower concentration of AuNPs, the more Ag^0 will be deposited on the surface of each single AuNP, which is more conducive to cause the color

change and account for the lower detection limit (i.e., the higher sensitivity) but result in narrow linear range. Moreover, it can be seen from Figure 8 that the red of the sensor itself is not obvious at the concentration of AuNPs lower than 0.49 nM. When the concentration of AuNPs is higher than 0.49 nM, there are obvious differences in color (Figure 8A,B) and absorption spectra (Figure 8C,D) before and after the Ag^+ detection, which is beneficial to colorimetric observation. Hence, taking into account both the sensitivity and the linear range of the colorimetric sensor, the concentration of 0.49 nM was chosen as the optimal dosage of AuNPs for Ag^+ detection in our following experiments.

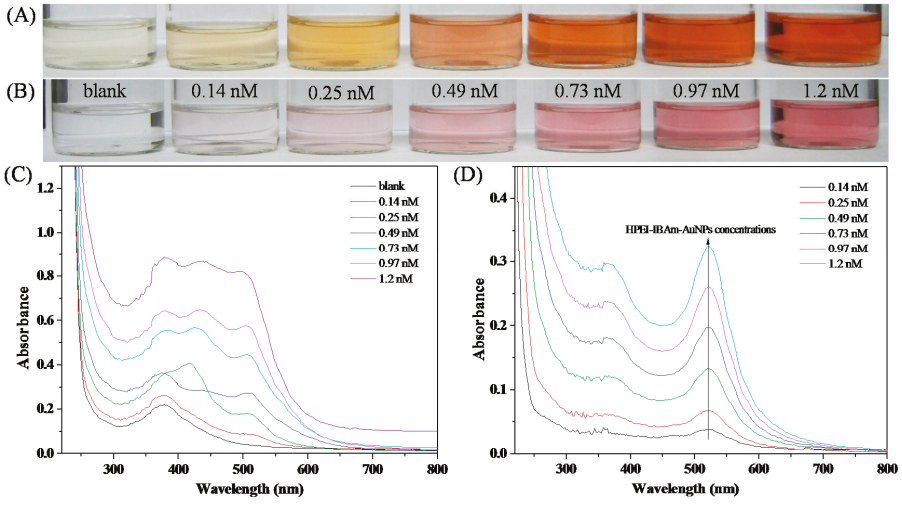

Figure 8. Photographs of HPEI-IBAm-AuNPs with different concentrations in the presence (**A**) and absence (**B**) of 0.573 mM Ag^+; UV-vis absorption spectra of HPEI-IBAm-AuNP solution with different concentrations in the presence (**C**) and absence (**D**) of 0.573 mM Ag^+.

The detection limit and detection range are the key factors that affect the practicability of colorimetric sensor. Figure 9 shows the responses of the color change and UV-vis absorption spectra of 0.49 nM HPEI-IBAm-AuNPs solution with different concentrations of Ag^+ (0–2 mM). Clearly, the color of HPEI-IBAm-AuNPs solution gradually changed from red through pale-brown to brown as the Ag^+ concentration increased (Figure 9A), enabling 57.3 μM of Ag^+ can be detected by the naked eye alone. With the increase of Ag^+ concentration, the ~520 nm plasmon peak of HPEI-IBAm-AuNPs gradually blue shifted to 380–450 nm (Figure 9B), which depends on the thickness of Ag shell [10,32]. Here, we can see that the maximum absorption is centered at about 414 nm from Figure 9B. Therefore, the sensor responses were expressed by the absorption value at 414 nm (that is $A_{414\,nm}$). A good linear relationship was obtained between $A_{414\,nm}$ and Ag^+ concentration in the range of 0–2.0 mM, with a correlation coefficient of R^2 = 0.9915 (Figure 9C). Especially, there is still a good linear relationship when the concentration of Ag^+ is as low as 5.73 nM to 5.73 μM with R^2 = 0.9957 (Figure S10). The limit of detection (LOD) for Ag^+ was calculated to be 7.22 nM (3σ, which was far below the guideline value of 0.1 mg/L ≈ 920 nM in drinking water defined by the EPA [33]). To the best of our knowledge, this non-aggregation based colorimetric sensor is one of the first reports on Ag^+ detection with the widest range of concentration and is one of the most sensitive methods for Ag^+ detection, compared with many other AuNPs-based sensors reported previously (Table S1). Therefore, this new colorimetric sensor based on the non-aggregation of AuNPs can be applied to the determination of Ag^+ in different environments.

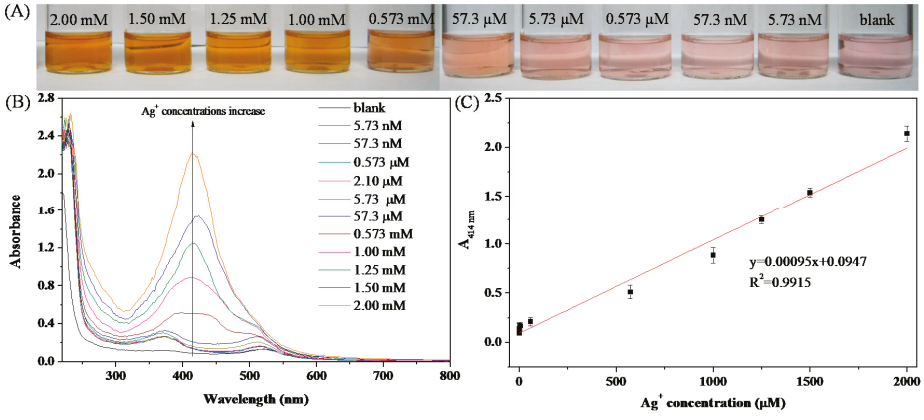

Figure 9. (**A**) Photographs and (**B**) UV-vis absorption spectra of 0.49 nM HPEI-IBAm-AuNPs solution in the presence of different Ag^+ concentration (0–2.0 mM); (**C**) linear response ($A_{414\ nm}$ value of the absorbance at 414 nm) of the colorimetric assay against the Ag^+ concentration range of 0–2.0 mM.

The selectivity of this colorimetric sensor for Ag^+ was evaluated by testing the response of the sensor to other metallic ions including Cd^{2+}, K^+, Na^+, Pb^{2+}, Ba^{2+}, Sr^{2+}, Cs^+, Mg^{2+}, Zn^{2+}, Mn^{2+}, Cu^{2+}, and Hg^{2+}. As shown in Figure 10, only the HPEI-IBAm-AuNPs solution containing Ag^+ ions caused obvious changes in the color (Figure 10A) and absorption spectra (Figure S11) because of the formation of Au-Ag core-shell NPs. The selectivity of this colorimetric sensor can be visualized with the naked eye as shown in Figure 10A. Meanwhile, it can be seen from the UV-Vis absorption spectra (Figure S10) that the $A_{414\ nm}$ value of this colorimetric sensor could be increased significantly to 0.212 upon the addition of Ag^+, and most of the values for other metal ions were only approximately 0.09, except 0.11 of Cu^{2+} and 0.119 of Hg^{2+} (Figure 10B), indicating that the sensor showed great selectivity for Ag^+ detection.

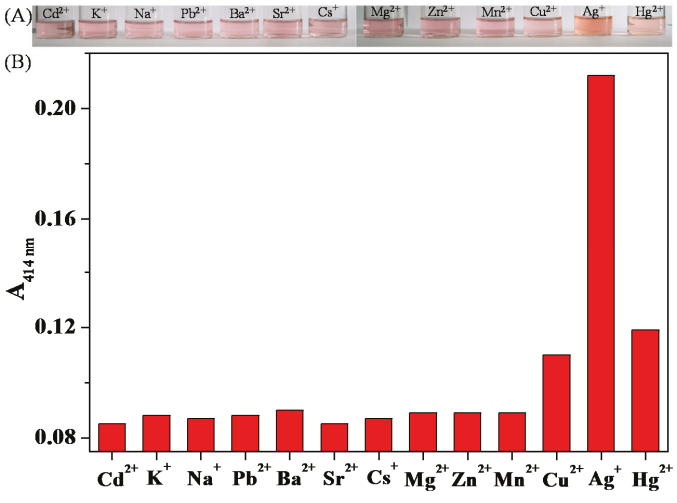

Figure 10. Selectivity of the sensor: (**A**) photographs and (**B**) response ($A_{414\ nm}$) of 0.49 nM HPEI-IBAm-AuNPs solution in the presence of various metal ions at the concentrations of 57.3 μM.

3.5. Ag^+ Detection and Separation in Drinking Water

To further evaluate the applicability of the proposed colorimetric assay, the detection of Ag^+ in drinking water was tested. According to the proposed colorimetric method, no changes in color and UV-Vis spectra were observed in the drinking water sample, indicating that Ag^+ ions were not found. Then, the drinking water samples were spiked with 60, 90, and 120 μM of Ag^+ ions (Table 1 and Figure 11A). The found concentrations based on the linear relationship between $A_{414\,nm}$ (Figure 11E) and Ag^+ concentration were 62.1, 88.4, and 126.3 μM with the recoveries of 98.2%–105.3%, indicating that the proposed colorimetric assay can be used for the detection of Ag^+ in real water samples and has high accuracy. The enrichment and separation of silver by the temperature sensitivity of the HPEI-IBAm were systematically studied. As shown in Figure 11B, the HPEI-IBAm-AuNPs solutions with 60, 90, and 120 μM of Ag^+ became turbid when the ambient temperature was higher than the cloud point (CP) of the system. To achieve the full precipitation of HPEI-IBAm-AuNPs/Ag, the water bath temperature was set to 10 degrees higher than the respective CP of the silver-containing system. Additionally, the HPEI-IBAm-AuNPs/Ag composites can be separated by static stratification (Figure 11C) or centrifugation (Figure 11D). To determine the enriching efficiency of HPEI-IBAm-AuNPs toward Ag^+, the concentration of residual Ag^+ was determined by Inductively Coupled Plasma spectrometer (Table 1). The enriching efficiency of HPEI-IBAm-AuNPs toward Ag is very high (96.1%–97.3%), which is mainly due to the high affinity of AuNPs and amine groups of HPEI-IBAm-AuNPs to silver. All these results suggest that the proposed method based on the colorimetric response and thermoresponsive property of the HPEI-IBAm-AuNPs may be one of the most promising approaches for detecting, enriching, and separating silver (Scheme 1).

Table 1. Results of the Ag^+ recovery and separation experiments performed in drinking water samples.

Added (μM)	Found (μM)	Recovery (%)	Residual Ag (μM)	Enriching efficiency (%)
60	62.1	103.5	1.9	96.8
90	88.4	98.2	3.5	96.1
120	126.3	105.3	3.2	97.3

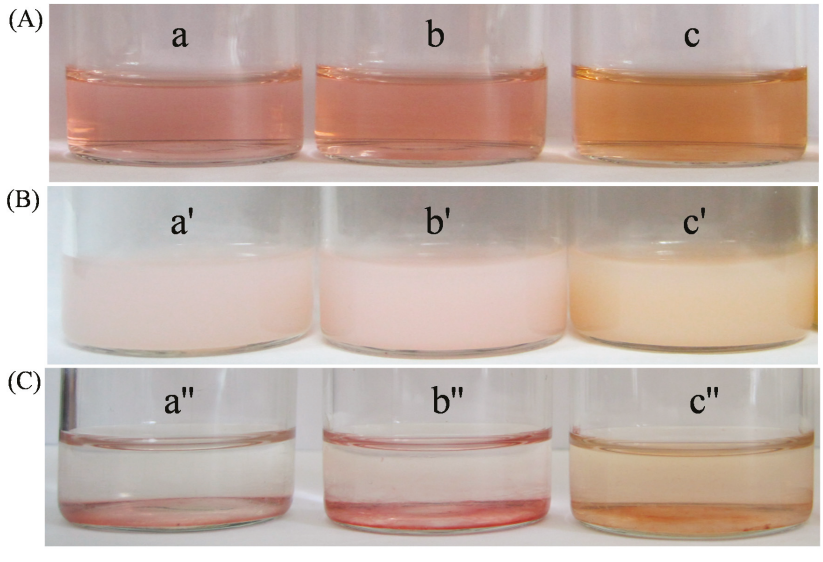

Figure 11. *Cont.*

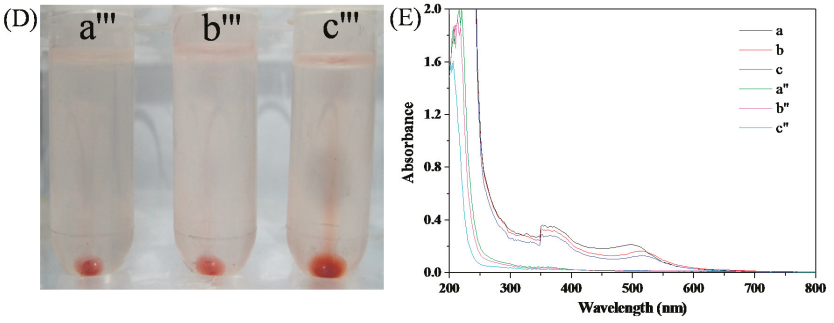

Figure 11. Colorimetric detection and separation of Ag^+ in drinking water: (**A**) photographs of 0.49 nM HPEI-IBAm-AuNPs solution with (a) 60 μM, (b) 90 μM, and (c) 120 μM of Ag^+; (**B**,**C**) represent the changes of 0.49 nM HPEI-IBAm-AuNPs solution with 60, 90, and 120 μM of Ag^+ after keeping in a thermostatted water bath at 50 °C (10 degrees higher than CP) for 5 min and 6 h, respectively; (**D**) represents the change of 0.49 nM HPEI-IBAm-AuNPs solution with (a) 60 μM, (b) 90 μM, and (c) 120 μM of Ag^+ after centrifugation at 50 °C; (**E**) absorption spectra of (**B**,**C**).

4. Conclusions

In summary, an in-situ reaction strategy for the preparation of stable AuNPs has been successfully achieved via a thermal process by using thermoresponsive HPEI-IBAm as templates, reducing agents, and stabilizers without the additional step of introducing a toxic small-molecule reductant. The HPEI-IBAm functionalized AuNPs exhibit excellent thermal stability up to 200 °C, high tolerance of a wide range of pH values (3–13), and high salt resistance. Thermoresponsive HPEI-IBAm not only serves as a green reductant and excellent stabilizer to prepare AuNPs via in-situ formation, but also serves as a trigger agent to cause an obvious color change of HPEI-IBAm-AuNPs solution in the presence of Ag^+, which can be used for the colorimetric detection of Ag^+. This new non-aggregation-based colorimetric sensor with a unique red-to-brown color change showed high stability (maintaining the color lasting without fading) and high selectivity. The colorimetric sensor showed high sensitivity with an extremely low detection limit of 7.22 nM and a good linear relationship in a wide concentration range of 0–2.0 mM (R^2 = 0.9915), which is one of the most sensitive methods for Ag^+ detection and is one of the first reports on Ag^+ detection with the widest range of concentration. Even at low Ag^+ concentrations (5.73 nM-5.73 μM), the sensing response still demonstrated high linearity (R^2 = 0.9957). Moreover, this colorimetric sensor was successfully applied to detect Ag^+ in drinking water. After the sensing detection, the AuNPs/Ag composites can be separated by heating the system above the cloud point of the polymer solution and then by performing static stratification or centrifugation, which can avoid secondary pollutions. Therefore, the proposed colorimetric sensor can not only achieve the detection of Ag^+ with high sensitivity and high selectivity, but also can effectively separate and remove Ag^+, thereby preventing and controlling its pollution to the environment. The HPEI-IBAm functionalized AuNPs can truly realize the integration of green preparation, detection, and separation, which serves the aims of energy saving, environmental protection, and sustainable development, and provides a basis to further develop multifunctional nano-materials.

Supplementary Materials: The following are available online at www.mdpi.com/2073-4360/10/1/42/s1, Figure S1: ^{1}H NMR spectra of HPEI-IBAm (A) and HPEI (B), Figure S2: comparison of FTIR spectra of HPEI-IBAm (A) and HPEI (B), Figure S3: the UV-Vis spectra of the HPEI-IBAm functionalized AuNPs after every evaporation at 110 °C and re-dispersion in Milli-Q water, Figure S4: (A) photographs of (a) the HPEI-IBAm functionalized AuNPs and (b) citrate-capped AuNPs after every evaporation at 110 °C and re-dispersion in Milli-Q water; (B) the maximum absorption peaks of the HPEI-IBAm functionalized AuNPs after each cycle's re-dispersion; (C) the UV-Vis spectra of the citrate-capped AuNPs after each cycle's re-dispersion, Figure S5: the UV-Vis spectra of the HPEI-IBAm functionalized AuNPs after every evaporation at 130 °C and re-dispersion in Milli-Q water, Figure S6: (A) photographs of (a) the HPEI-IBAm functionalized AuNPs and (b) citrate-capped AuNPs

after every evaporation at 200 °C and re-dispersion in Milli-Q water; (B) the UV-Vis spectra of the HPEI-IBAm functionalized AuNPs after each cycle's re-dispersion; (C) the UV-Vis spectra of the citrate-capped AuNPs after each cycle's re-dispersion, Figure S7: the UV-Vis spectra of the HPEI-IBAm functionalized AuNPs under different salt concentrations, Figure S8: the UV-Vis spectra of the citrate-capped AuNPs after 24 h under different salt concentrations, Figure S9: (A) photographs and (B) UV-Vis spectra of (a) 1.2 nM citrate-capped AuNPs after (b) 1 h and (c) 24 h upon the addition of Ag^+, Figure S10: Linear response (A414 nm value of the absorbance at 414 nm) of the colorimetric assay against the Ag+ concentration range of 5.73 nM to 5.73 μM. Figure S11: UV-Vis spectra of 0.49 nM HPEI-IBAm-AuNPs solution in the presence of various metal ions at the concentrations of 57.3 μM, Table S1: colorimetric sensors for Ag^+ detection.

Acknowledgments: This work was financially supported by the National Science Foundation of China (51403097, 21304043), the Natural Science Foundation of Shandong Province (ZR2016FP09), the Project of Shandong Province Higher Educational Science and Technology Program (J16LN04), and the Yantai Key R&D Program (2016ZH063, 2017ZH058, 2017ZH064, 2017ZH059).

Author Contributions: Xunyong Liu and Yi Liu conceived and designed the experiments; Chenxue Zhu, Li Xu, and Yuqing Dai performed the experiments; Yanli Liu contributed analysis tools; Xunyong Liu and Yi Liu wrote the paper.

Conflicts of Interest: The authors declare no conflict of interest.

References

1. Mayer, K.M.; Hafner, J.H. Localized surface plasmon resonance sensors. *Chem. Rev.* **2011**, *111*, 3828–3857. [CrossRef] [PubMed]
2. Saha, K.; Agasti, S.S.; Kim, C.; Li, X.; Rotello, V.M. Gold nanoparticles in chemical and biological sensing. *Chem. Rev.* **2012**, *112*, 2739–2779. [CrossRef] [PubMed]
3. Giljohann, D.A.; Seferos, D.S.; Daniel, W.L.; Massich, M.D.; Patel, P.C.; Mirkin, C.A. Gold nanoparticles for biology and medicine. *Angew. Chem. Int. Ed.* **2010**, *49*, 3280–3294. [CrossRef] [PubMed]
4. Zhou, W.; Gao, X.; Liu, D.; Chen, X. Gold nanoparticles for in vitro diagnostics. *Chem. Rev.* **2015**, *115*, 10575–10636. [CrossRef] [PubMed]
5. Crooks, R.M.; Zhao, M.; Sun, L.; Chechik, V.; Yeung, L.K. Dendrimer-encapsulated metal nanoparticles: Synthesis, characterization, and applications to catalysis. *Acc. Chem. Res.* **2001**, *34*, 181–190. [CrossRef] [PubMed]
6. Min, B.K.; Friend, C.M. Heterogeneous gold-based catalysis for green chemistry: Low-temperature co oxidation and propene oxidation. *Chem. Rev.* **2007**, *107*, 2709–2724. [CrossRef] [PubMed]
7. Liu, Y.; Dai, J.; Xu, L.; Liu, X.; Liu, J.; Li, G. Red to brown to green colorimetric detection of Ag^+ based on the formation of Au-Ag core-shell NPs stabilized by a multi-sulfhydryl functionalized hyperbranched polymer. *Sens. Actuators B* **2016**, *237*, 216–223. [CrossRef]
8. Lou, T.T.; Chen, Z.P.; Wang, Y.Q.; Chen, L.X. Blue-to-red colorimetric sensing strategy for Hg^{2+} and Ag^+ via redox-regulated surface chemistry of gold nanoparticles. *ACS Appl. Mater. Interfaces* **2011**, *3*, 1568–1573. [CrossRef] [PubMed]
9. Lin, C.Y.; Yu, C.J.; Lin, Y.H.; Tseng, W.L. Colorimetric sensing of silver(I) and mercury(II) ions based on an assembly of tween 20-stabilized gold nanoparticles. *Anal. Chem.* **2010**, *82*, 6830–6837. [CrossRef] [PubMed]
10. Liu, Y.; Liu, Y.; Li, Z.; Liu, J.; Xu, L.; Liu, X. An unusual red-to-brown colorimetric sensing method for ultrasensitive silver(I) ion detection based on a non-aggregation of hyperbranched polyethylenimine derivative stabilized gold nanoparticles. *Analyst* **2015**, *140*, 5335–5343. [CrossRef] [PubMed]
11. Cao, G.; Xu, F.; Wang, S.; Xu, K.; Hou, X.; Wu, P. Gold nanoparticle-based colorimetric assay for selenium detection via hydride generation. *Anal. Chem.* **2017**, *89*, 4695–4700. [CrossRef] [PubMed]
12. Ramirez, O.; Bonardd, S.; Saldías, C.; Radic, D.; Leiva, Á. Biobased chitosan nanocomposite films containing gold nanoparticles: Obtainment, characterization, and catalytic activity assessment. *ACS Appl. Mater. Interfaces* **2017**, *9*, 16561–16570. [CrossRef] [PubMed]
13. Wang, X.; Cai, X.; Hu, J.; Shao, N.; Wang, F.; Zhang, Q.; Xiao, J.; Cheng, Y. Glutathione-triggered "off-on" release of anticancer drugs from dendrimer-encapsulated gold nanoparticles. *J. Am. Chem. Soc.* **2013**, *135*, 9805–9810. [CrossRef] [PubMed]
14. Yang, J.; Lee, J.Y.; Ying, J.Y. Phase transfer and its applications in nanotechnology. *Chem. Soc. Rev.* **2011**, *40*, 1672–1696. [CrossRef] [PubMed]

15. Li, X.Y.; Wu, Z.T.; Zhou, X.D.; Hu, J.M. Colorimetric response of peptide modified gold nanoparticles: An original assay for ultrasensitive silver detection. *Biosens. Bioelectron.* **2017**, *92*, 496–501. [CrossRef] [PubMed]
16. Chinwangso, P.; Jamison, A.C.; Lee, T.R. Multidentate adsorbates for self-assembled monolayer films. *Acc. Chem. Res.* **2011**, *44*, 511–519. [CrossRef] [PubMed]
17. Cao, P.F.; Yan, Y.H.; Mangadlao, J.D.; Rong, L.H.; Advincula, R. Star-like copolymer stabilized noble-metal nanoparticle powders. *Nanoscale* **2016**, *8*, 7435–7442. [CrossRef] [PubMed]
18. Cao, P.F.; Rong, L.H.; de Leon, A.; Su, Z.; Advincula, R.C. A supramolecular polyethylenimine-cored carbazole dendritic polymer with dual applications. *Macromolecules* **2015**, *48*, 6801–6809. [CrossRef]
19. Liu, X.Y.; Cheng, F.; Liu, Y.; Li, W.G.; Chen, Y.; Pan, H.; Liu, H.J. Thermoresponsive gold nanoparticles with adjustable lower critical solution temperature as colorimetric sensors for temperature, pH and salt concentration. *J. Mater. Chem.* **2010**, *20*, 278–284. [CrossRef]
20. Liu, Y.; Xu, L.; Liu, J.; Liu, X. Simultaneous enrichment, separation and detection of mercury(II) ions using cloud point extraction and colorimetric sensor based on thermoresponsive hyperbranched polymer-gold nanocomposite. *Anal. Methods* **2015**, *7*, 10151–10161. [CrossRef]
21. Liu, X.Y.; Mu, X.R.; Liu, Y.; Liu, H.J.; Chen, Y.; Cheng, F.; Jiang, S.C. Hyperbranched polymers with thermoresponsive property highly sensitive to ions. *Langmuir* **2012**, *28*, 4867–4876. [CrossRef] [PubMed]
22. Liu, X.Y.; Cheng, F.; Liu, Y.; Liu, H.J.; Chen, Y. Preparation and characterization of novel thermoresponsive gold nanoparticles and their responsive catalysis properties. *J. Mater. Chem.* **2010**, *20*, 360–368. [CrossRef]
23. Zhan, C.; Fu, X.B.; Yao, Y.; Liu, H.J.; Chen, Y. Stimuli-responsive hyperbranched poly(amidoamine)s integrated with thermal and pH sensitivity, reducible degradability and intrinsic photoluminescence. *RSC Adv.* **2017**, *7*, 5863–5871. [CrossRef]
24. Jin, R.; Wu, G.; Li, Z.; Mirkin, C.A.; Schatz, G.C. What controls the melting properties of DNA-linked gold nanoparticle assemblies? *J. Am. Chem. Soc.* **2003**, *125*, 1643–1654. [CrossRef] [PubMed]
25. Shen, M.; Shi, X. Dendrimer-based organic/inorganic hybrid nanoparticles in biomedical applications. *Nanoscale* **2010**, *2*, 1596–1610. [CrossRef] [PubMed]
26. Deng, S.; Locklin, J.; Patton, D.; Baba, A.; Advincula, R.C. Thiophene dendron jacketed poly(amidoamine) dendrimers: Nanoparticle synthesis and adsorption on graphite. *J. Am. Chem. Soc.* **2005**, *127*, 1744–1751. [CrossRef] [PubMed]
27. Kaewtong, C.; Jiang, G.; Ponnapati, R.; Pulpoka, B.; Advincula, R. Redox nanoreactor dendrimer boxes: In situ hybrid gold nanoparticles via terthiophene and carbazole peripheral dendrimer oxidation. *Soft Matter* **2010**, *6*, 5316–5319. [CrossRef]
28. Boisselier, E.; Diallo, A.K.; Salmon, L.; Ornelas, C.; Ruiz, J.; Astruc, D. Encapsulation and stabilization of Gold nanoparticles with "Click" polyethyleneglycol dendrimers. *J. Am. Chem. Soc.* **2010**, *132*, 2729–2742. [CrossRef] [PubMed]
29. Hermes, J.P.; Sander, F.; Peterle, T.; Urbani, R.; Pfohl, T.; Thompson, D.; Mayor, M. Gold nanoparticles stabilized by thioether dendrimers. *Chem. A Eur. J.* **2011**, *17*, 13473–13481. [CrossRef] [PubMed]
30. Alizadeh, A.; Khodaei, M.M.; Hamidi, Z.; Shamsuddin, M.B. Naked-eye colorimetric detection of Cu^{2+} and Ag^{+} ions based on close-packed aggregation of pyridines-functionalized gold nanoparticles. *Sens. Actuators, B* **2014**, *190*, 782–791. [CrossRef]
31. Huang, H.; Chen, S.; Liu, F.; Zhao, Q.; Liao, B.; Yi, S.; Zeng, Y. Multiplex plasmonic sensor for detection of different metal ions based on a single type of gold nanorod. *Anal. Chem.* **2013**, *85*, 2312–2319. [CrossRef] [PubMed]
32. Mulvaney, P. Surface plasmon spectroscopy of nanosized metal particles. *Langmuir* **1996**, *12*, 788–800. [CrossRef]
33. *National Secondary Drinking Water Regulation: EPA 816-F-09-004*; Environmental Protection Agency: Washington, DC, USA, 2009.

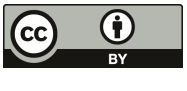

polymers

MDPI

Article

Highly Sensitive Detection of Melamine Based on the Fluorescence Resonance Energy Transfer between Conjugated Polymer Nanoparticles and Gold Nanoparticles

Cui-jiao Zhang [1,2], Zhi-yan Gao [1,2], Qiu-bo Wang [1,2], Xian Zhang [1,2,*], Jin-shui Yao [1,2], Cong-de Qiao [1,2] and Qin-ze Liu [1,2]

[1] School of Materials Science and Engineering, Qilu University of Technology (Shandong Academy of Sciences), Jinan 250353, China; 13256729106@163.com (C.Z.); zhiyangao98@126.com (Z.G.); wangqbqlu18@163.com (Q.W.); yaojsh@qlu.edu.cn (J.Y.); cdqiao@qlu.edu.cn (C.Q.); liuqinze01@163.com (Q.L.)

[2] Shandong Provincial Key Laboratory of Processing and Testing Technology of Glass and Functional Ceramics, Key Laboratory of Amorphous and Polycrystalline Materials, Qilu University of Technology, Jinan 250353, China

* Correspondence: zhangx@qlu.edu.cn; Tel.: +86-531-89631-227

Received: 16 July 2018; Accepted: 2 August 2018; Published: 6 August 2018

Abstract: Adding melamine as additives in food products will lead to many diseases and even death. However, the present techniques of melamine detection require time-consuming steps, complicated procedures and expensive analytical apparatus. The fluorescent assay method was facile and highly sensitive. In this work, a fluorescence resonance energy transfer (FRET) system for melamine detection was constructed based on conjugated polymer nanoparticles (CPNs) and gold nanoparticles (AuNPs). The energy transfer efficiency is up to 82.1%, and the system is highly selective and sensitive to melamine detection with a lower detection limit of 1.7 nmol/L. Moreover, the interaction mechanism was explored. The results showed that the fluorescence of CPNs were firstly quenched by AuNPs, and then restored after adding melamine because of reducing FRET between CPNs and AuNPs. Lastly, the proposed method was carried out for melamine detection in powdered infant formula with satisfactory results.

Keywords: fluorescent assay; fluorescence resonance energy transfer; conjugated polymer nanoparticles; gold nanoparticles; melamine

1. Introduction

As we all know, melamine ($C_3H_6N_6$), an odorless and white heterocycle compound, is widely used in the manufacturing of plastics, laminates, dyes, fabrics, and fertilizers [1,2]. Moreover, it is often added as an additive in food products to increase the amount of protein detection due to its high nitrogen concentration (66% by mass) [3]. However, this will result in kidney stones, urinary system damage and even death [4]. Melamine is ingested beyond the safety limit of 8 μmol/L for infant formula in China and 20 μmol/L in the USA and EU [5]. Therefore, it is quite necessary to develop a cheap, sensitive and reliable method for melamine detection.

Nowadays, many analytical approaches of melamine detection, such as mass spectroscopy (MS) [6], potentiometric [7], gas chromatography mass spectrometry (GC-MS) [8] and electrochemical [9] have been applied. But these methods require expensive and complicated analytical instruments, are time-consuming and require experienced operators, which limit their wide applications in routine analysis.

Fluorescence assays based on FRET have attracted much interest due to significant merits including high sensitivity, simple instruments, operational simplicity and test rapidity, which can be observed when the space distance between the acceptor and the donor is very close (7~10 nm). Many quantum dots (QDs) and organic dyes were recognized as efficient FRET-based melamine donors such as CdTe [10,11], fluorescein [12], rhodamine B [3,13] and so on. However, these materials suffer from high toxicity, poor stability and photobleaching, which lead to irreproducible fluorescence signals for further analysis. Recently, several methods have been reported based on gold nanoparticles (AuNPs) by color changes of the solution to detect melamine [14,15]. Melamine can reduce the stability of AuNPs and result in their aggregation. Meanwhile, the color of AuNPs solution turned to deep blue from wine red. This variation can be lightly observed by the naked eye and UV-Vis absorption measurement [16,17]. Therefore, AuNPs-based colorimetric detection melamine method is rapid and simple [18]. However, interference substances in milk, which compete with melamine during AuNPs binding, often result in a false positive response. To solve this problem, AuNPs have been successfully utilized as the acceptor for the FRET system owing to high extinction coefficients, conductivity, excellent biocompatibility and size-dependent optical properties [19,20]. In addition, CPNs have been developed as fluorescence probes for tumor imaging [21,22], neuroinflammation [23,24] and cell tracking [25]. Compared to organic dyes and traditional QDs, the superiorities of CPNs include easy preparation, extraordinary fluorescence brightness, low toxicity and good biocompatibility [26,27]. For all we know, the melamine detection based on FRET of CPNs and AuNPs has not been reported.

Herein, an efficient "turn-on" fluorescence sensor for melamine detection was designed based on melamine-induced reduction of FRET efficiency between AuNPs and CPNs. The key diagram of our method is displayed in Scheme 1. The fluorescence of CPNs was well quenched when the CPNs nanoparticles were apt to close the surface of AuNPs. However, the aggregation of AuNPs via N-Au interaction after adding melamine would reduce the FRET of CPNs-AuNPs and promote the fluorescence recovery of CPNs. This is because the spectral overlap between the absorption spectrum of AuNPs and the fluorescence emission spectrum of CPNs will alter after adding melamine, and decrease the energy transfer efficiency of CPNs-AuNPs. Furthermore, the above technique has been well used for melamine detection in real milk powder samples.

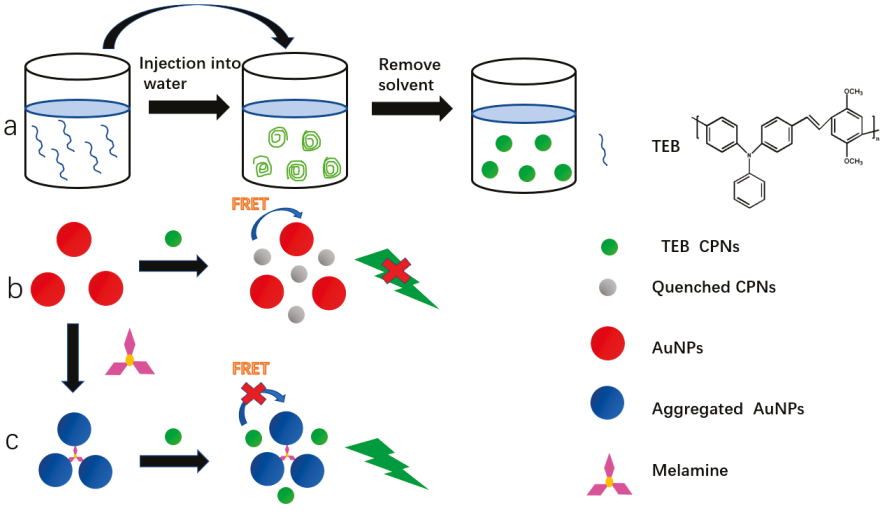

Scheme 1. The mechanism diagram of melamine detection by FRET based on CPNs-AuNPs; (**a**) the preparation process of CPNs; (**b**) the fluorescence of CPNs was quenched by the FRET of CPNs-AuNPs; (**c**) the fluorescence of CPNs was restored after adding melamine.

2. Experimental

2.1. Chemicals and Apparatus

$HAuCl_4 \cdot 4H_2O$ and sodium citrate were gained from Shanghai Chemical Reagent Co. (Shanghai, China). Melamine was obtained from Aladdin Reagent Company (Shanghai, China). L-cysteine, L-histidine, Vitamin C, Glucose, NaOH, $Ca(NO_3)_2 \cdot 4H_2O$, $FeCl_3 \cdot 6H_2O$, KNO_3, Na_2SO_4, $MgCl_2$, NaCl were purchased from Tianjin Chemical Works (Tianjin, China). All chemical reagents were used without further purification. The milk powder was obtained from the local supermarket.

Absorption spectra were measured on UV-2500 spectrophotometer (Shimadzu, Shuzhou, China). Fluorescence measurements were finished with F-7000 FL spectrometer (Hitachi, Tokyo, Japan). Transmission electron microscopy (TEM) were given on a JEM–2100 transmission electron microscope (JEOL Ltd., Musashino, Japan). The zeta potentials and size distribution were estimated by dynamic light scattering (DLS) on a Zetasizer Nano ZS90 (Malvern, Worcestershire, UK).

2.2. Preparation of AuNPs

AuNPs were synthetized via the citrate reduction method described in previous reports [28,29]. Typically, 1 mL aqueous solution of $HAuCl_4$ (1%) and 100 mL ultrapure water were firstly heated to boiling, and sodium citrate solution (1%, 4 mL) was added quickly. The reaction was further refluxed for 20 min, and then stored at 4 °C. The sizes of AuNPs were measured to be about 24 nm by DLS (Figure S1a) and TEM (Figure 4A). The molar concentration of AuNPs was calculated to be approximately 2.96×10^{-9} mol L^{-1} by Lambert-Beer law using the molar extinction coefficient of reported AuNPs in the literature (2.7×10^8 mol^{-1} L cm^{-1} at 520 nm) [16].

2.3. Preparation of CPNs

The Conjugated polymer TEB (Scheme 1) was synthesized according to our previous method [30]. The M_w and M_w/M_n of TEB was 7032 and 1.174, respectively. The nanoparticles of TEB were carried out using the procedure described in the literature [31,32]. As shown in Scheme 1a, TEB were fully dissolved in 10 mL THF to prepare a 20 μg/mL stock solution, and then the solution was rapidly injected into 20 mL of ultrapure water in a sonication bath. After 15 min, THF was removed by rotary evaporation and the solution was concentrated to 10 mL, and then filtered through a 0.22 μm micro-filter. The sizes of CPNs were measured to be about 50.7 nm by DLS (Figure S1c).

2.4. Fluorescence Analysis

Typically, at room temperature, 100 μL CPNs (20 μg/mL) was mixed with as-prepared original AuNPs with different concentrations and incubated for 10 min. Then the emission spectra of solutions were measured.

The AuNPs solution was diluted with ultrapure water to 2.37×10^{-9} mol L^{-1} for further use. The as-prepared AuNPs solution was mixed with different concentrations (0–2 μmol/L) of melamine solution, and the mixture liquid was incubated for 15 min at room temperature. Then, 100 μL CPNs was injected into the above liquid and diluted to 4 μg/mL with PBS (pH = 7). Finally, the above mixture was in a still state for 10 min before the spectral measurement.

2.5. Pretreatment of Real Samples

Milk powder was firstly processed according to the previous reports [11,33]. Briefly, 2 g of milk powder was fully dissolved in 5 mL of acetonitrile and 15 mL of 1% (w/v) trichloroacetic acid. Then the mixed liquid was ultrasonically treated and centrifuged at 10,000 rpm for 15 min. Lastly, the liquid was filtered by a 0.22 μm filter, and further diluted 25-fold to acquire the testing samples.

3. Results and Discussion

3.1. Optical Characteristics of AuNPs and CPNs

The AuNPs were prepared by the reported method [34]. The as-prepared AuNPs was negatively charged with a zeta potential of 8.43 mV (Figure S2a). The absorption and fluorescence emission spectra of AuNPs and CPNs were measured and shown in Figure 1. A broad overlap from 480 to 600 nm between them was found, which implied that the FRET may occur between CPNs (donor) and AuNPs (acceptor). Consequently, the fluorescence intensity of CPNs may be evidently quenched or reduced if CPNs and AuNPs coexist.

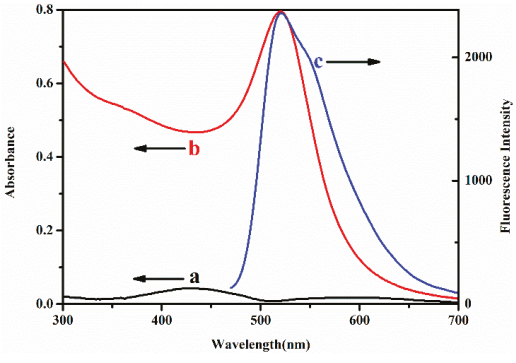

Figure 1. The absorption spectra of the CPNs (a) and AuNPs (b) and fluorescence emission spectrum of CPNs (c).

To identify the above hypothesis, the fluorescence intensities of CPNs were investigated with the increased concentrations of AuNPs (Figure 2). The energy transfer efficiency (E) was measured and gained by the following equation [34]:

$$E = 1 - I/I_0 \quad (1)$$

where I and I_0 are the fluorescence intensity of the donor (CPNs) after and before the addition of acceptor (AuNPs), respectively. E obtained the value of 82.1% according to Equation (1). The fluorescence intensities of CPNs were contravariant to the concentrations of AuNPs. The fluorescence quenching efficiency of CPNs by AuNPs was measured by the Stern–Volmer equation [35]:

$$\frac{F_0}{F} = K_{SV} \times C_Q + 1 \quad (2)$$

where F_0 and F denoted the fluorescence intensity of CPNs before and after the addition of AuNPs, respectively. C_Q is the concentration of AuNPs. The curve of F_0/F to C_Q was linearly fitted and shown in Figure 2b, and the Stern–Volmer equation is described below:

$$\frac{F_0}{F} = 1.635\, C_Q + 1 \quad \left(R^2 = 0.9916\right) \quad (3)$$

K_{SV} was the quenching constant and gained to be 1.635×10^9 $(\text{mol}^{-1}\ \text{L})^{-1}$. This analytical parameter is better than those in previous reports [36,37].

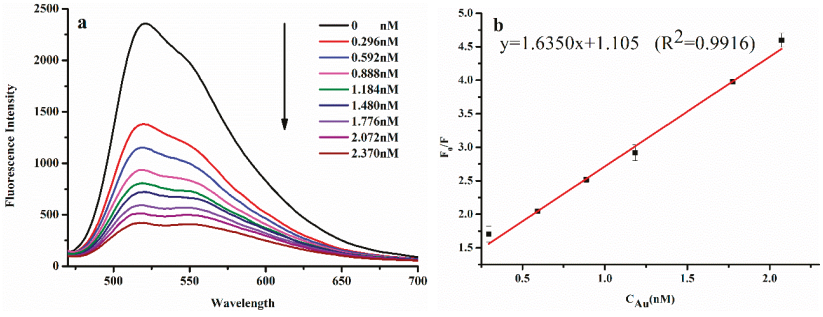

Figure 2. (**a**) Fluorescence emission spectra of CPNs with the increased concentrations of AuNPs; (**b**) the linear fitting plot of F_0/F values at 520 nm versus AuNPs concentrations from 0 to 2.370 nM, CPNs: 0.187 μM.

3.2. Interaction of AuNPs-CPNs with Melamine

The color variation and absorption spectra of AuNPs solutions with the increased concentrations of melamine are shown in Figure 3a,b. The obvious color variations from red to deep blue were found in the concentrations of melamine from 0.4 to 1.6 μM. The characteristic absorption of AuNPs gradually decreased at 522 nm and showed slightly red-shifted. Meanwhile, a longer wavelength absorption band (700 nm) appeared gradually. The possible reason may be that melamine could strongly coordinate to AuNPs by the amine groups, and finally lead to the aggregation and destabilization of dispersed AuNPs [38–40]. Meanwhile, the red-shifted absorption of Au NPs declined the spectral overlap between the emission spectrum from CPNs and the absorption spectrum of AuNPs and reduced *E*.

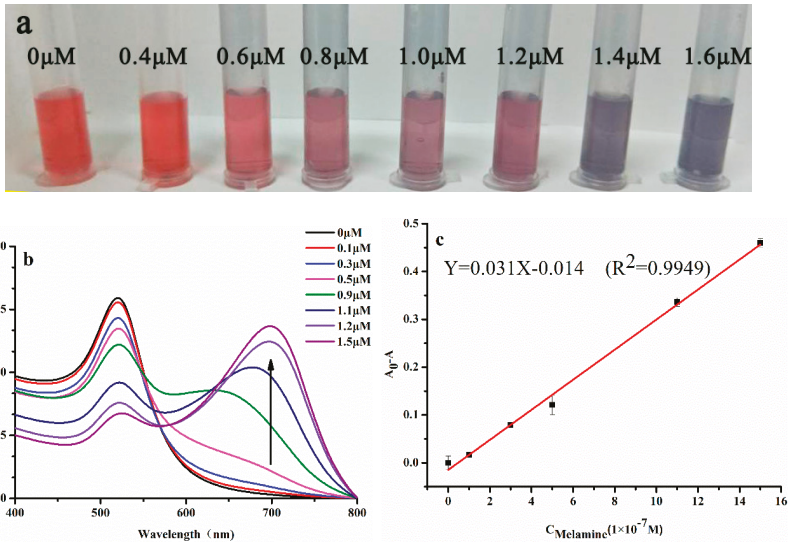

Figure 3. (**a**) The visual color change of the AuNPs with different concentrations of melamine; they were marked on the tubes; (**b**) absorption spectra of CPNs-AuNPs with different concentrations of melamine. AuNPs: 2.37 nM; (**c**) a linear relationship (at 522 nm) between A_0−A and melamine concentrations; A_0 and A are the absorbance in the absence and presence of melamine, respectively.

A good linear relationship between the decreased absorbance at 522 nm and the concentrations of melamine was gained from 0.1–1.5 μmol/L (R^2 = 0.9949, Figure 3c). The relative standard deviation was 0.8% for seven repeated measurements, which illustrated the reliability of the proposed method. The limit of detection ($LOD = 3\delta/K$, where K represents the slope and δ is the standard deviation) was measured to be 6.8 nmol/L. This analytical parameter is better than those in previous reports (Table 1).

Table 1. Comparison of different methods for the determination of melamine.

Method	LOD (μM)	Ref.	Recovery (%)
HPLC	0.79	[41]	97.2–101.2
Turn-off fluorescence CdTe quantum dots	0.31	[11]	103–104
CdTe QDs and Rhodamine B	0.01	[35]	99.2–104
FRET/carbon dots and Au nanoparticles	0.036	[5]	90.5–111.4
FRET between CdTe/CdS QDs and AuNPs	0.03	[2]	90.0–101
Au nanoparticles and Melamine	0.0068	This work (1)	-
FRET/CPNs and Au nanoparticles	0.0017	This work (2)	95.93–100.8

TEM observations could further confirm the aggregation of dispersed AuNPs owing to the addition of melamine. From Figure 4A, the original AuNPs were uniform in size and spherical in shape. After mixing with CPNs, AuNPs were still in a scattered state, indicating that the addition of CPNs did not affect the dispersity of AuNPs (Figure 4D). However, obvious aggregation of AuNPs could be found after adding melamine (Figure 4B). The DLS data also indicated the same conclusion because the average sizes of AuNPs were 24 and 58.8 nm in the absence and presence of melamine (Figure S1a,b), respectively. The results were fully consistent with the spectral variation in Figure 3. Hence, the fluorescence intensity of CPNs could be monitored in the AuNPs-CPNs system by FRET, which afforded a feasible and new strategy for melamine detection. Actually, the addition of melamine led to the aggregation of AuNPs accompanying color change, which have been used for the visual sensing for melamine detection in infants and liquid milk [18]. However, these colorimetric techniques usually displayed lower sensitivity to melamine in comparison with fluorescence analytical methods. It is greatly hopeful to develop a simple way based on the FRET method with the higher sensitivity and the lower detection limit, and fluorescence signals can replace the variation of absorption.

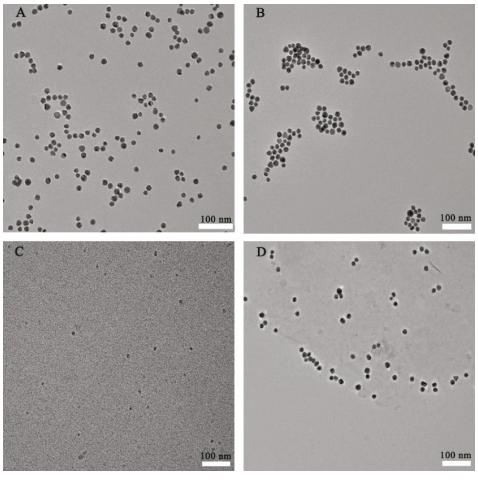

Figure 4. (**A**) TEM images of the original AuNPs; (**B**) TEM images of the AuNPs in the presence of melamine; (**C**) TEM images of the CPNs; (**D**) TEM images of the AuNPs in the presence of CPNs.

3.3. FRET-Based AuNPs-CPNs Emission Response to Melamine

The FRET system of CPNs-AuNPs would be modulated by the concentrations of melamine, and the fluorescence intensity of CPNs would change accordingly because melamine congregated the AuNPs (Scheme 1). The relationship between melamine and the FRET system was further investigated to validate the competition effect between CPNs and melamine. As displayed in Figure 5, it was proved that CPNs and melamine did not directly interact because the absorption and fluorescence intensity of CPNs (curves a and a′ in Figure 5) were identical to the mixture of CPNs and melamine (curves b and b′ in Figure 5). The characteristic absorption of AuNPs displayed no distinct variation before and after adding CPNs (curve c and d in Figure 5a), indicating that CPNs and AuNPs were not directly interacting. In addition, the characteristic absorption of AuNPs-melamine were identical in the absence or presence of CPNs (curves e and f in Figure 5a), which indicated that the aggregation of AuNPs was the result of the addition of melamine. The same conclusion could be got by no change for the average size of AuNPs-melamine before and after adding CPNs (Figure S1b,d). The fluorescence intensity of CPNs-AuNPs was evidently quenched owing to the FRET (curve c′ in Figure 5b) when CPNs and AuNPs were mixed together. Nevertheless, the addition of melamine could distinctly recover the fluorescence of CPNs curve d′ in Figure 5b. In addition, the fluorescence quantum yields (ϕs) of CPNs in the absence and presence of AuNPs and melamine have been calculated using a solution containing coumarin 307 (ϕ = 0.56, in methanol) standard as the reference according to the equation reported [42]. The values of ϕs were listed in Table 2. The change of ϕs was similar to that of fluorescence. With the addition of AuNPs, ϕs of CPNs reduced from 0.22 to 0.0050. However, further adding melamine, ϕs of CPNs were restored. But no obvious variation was found for ϕs of CPN in the presence of melamine.

The present technique for melamine detection was further researched under the optimal conditions. From Figure 6a, the fluorescence emission intensities of AuNPs-CPNs were recovered gradually with the increased concentrations of melamine. The increased fluorescence intensity and melamine concentrations had a fine linear relationship from 5 nmol/L to 1.9 μmol/L (R^2 = 0.9915, Figure 6b). The detection limit was calculated to be 1.7 nmol/L. This analytical parameter is very low in comparison with the reported literatures (Table 1). The relative standard deviation by operating 10 repeated measurements of melamine (1.9 μmol/L) was 1.2%, which illustrated that the fluorescence response of AuNPs-CPNs toward melamine was highly reproducible.

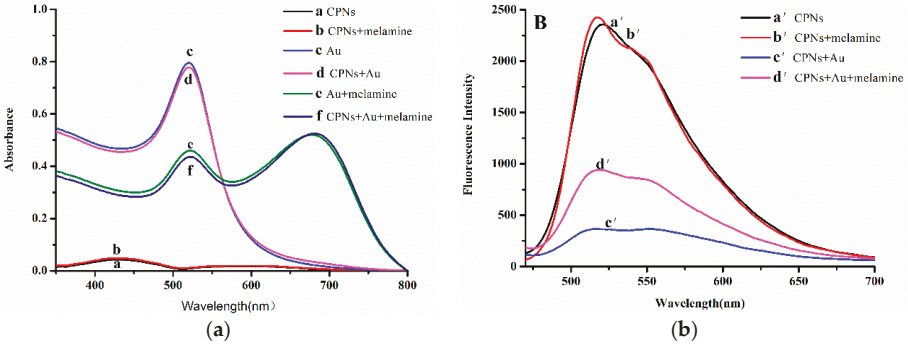

Figure 5. (**a**) Absorption spectra; a: CPNs; b: CPNs and melamine; c: AuNPs; d: AuNPs and CPNs; e: AuNPs and melamine; f: mixture of CPNs, AuNPs and melamine; (**b**) fluorescence spectra; a′: CPNs; b′: CPNs and melamine; c′: AuNPs and CPNs; d′: mixture of CPNs, AuNPs and melamine; CPNs: 0.187 μM; AuNPs: 2.37 nM; melamine: 0.8 μM.

Table 2. The fluorescence quantum yields of CPNs under difference conditions.

Components	Concentration (nM) (CPNs/AuNPs: /Melamine)	ϕ
CPNs	187/0/0	0.22
CPNs +Au NPs (1)	187/1.184/0	0.022
CPNs +Au NPs (2)	187/2.370/0	0.0050
CPNs + AuNPs + melamine (1)	187/2.370/300	0.0086
CPNs + AuNPs + melamine (2)	187/2370/1200	0.016
CPNs + melamine	187/0/1200	0.22

ϕ: Fluorescence quantum yield.

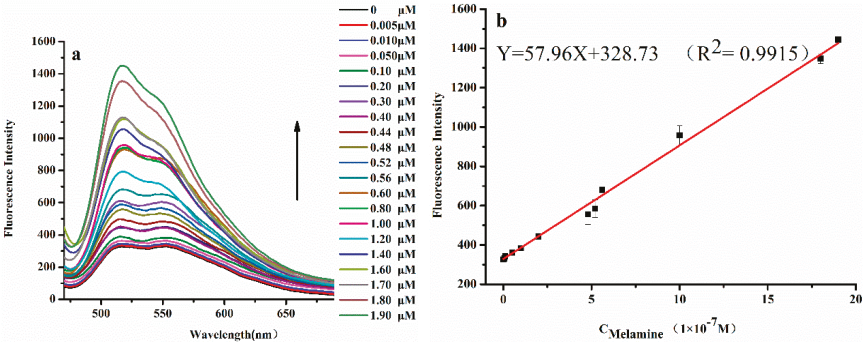

Figure 6. (**a**) Fluorescence emission spectra of CPNs-AuNPs nanosensor with different concentrations of melamine from 0.05 to 19 × 10^{-7} mol/L. CPNs: 0.187 μM. AuNPs: 2.37 nM; (**b**) a linear relationship with respect to the enhanced fluorescence intensities and melamine concentrations.

3.4. Selective Studies and the Application to Real Samples

To evaluate the method used in the specific detection of melamine, the potential interfering substances in real sample and melamine (2 μmol/L), such as Ca^{2+}, Fe^{3+}, Na^{+}, SO_4^{2-}, Cl^{-}, vitamin C, cysteine, histidine and glucose, were examined, respectively. From Figure 7a,b, no obvious interferences were found, which indicated that the AuNPs-CPNs towards melamine detection is highly selective.

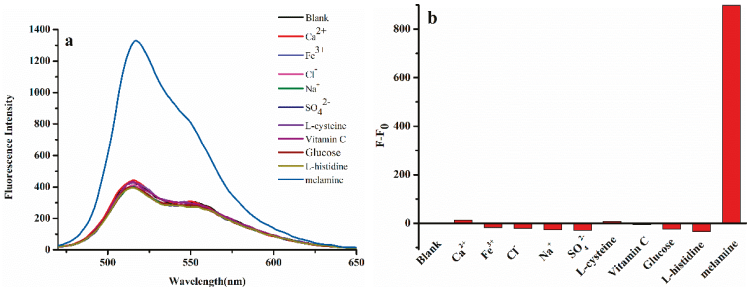

Figure 7. (**a**) Selectivity of the CPNs-AuNPs toward melamine; (**b**) the Bar graph of CPNs-AuNPs selectivity. The concentrations of interferences and melamine were both 2 μM.

To further prove the present method, the amount of melamine was directly spiked into milk powder after sample pretreatment, and the melamine-doped milk samples were further handled by the procedure described in Section 2.4. The analytical results are given in Table 3. The recovered values

of the three milk powder samples varied from 95.93% to 100.8%. These analytical parameters are better than those in previous reports (Table 1), which indicated that the proposed method was suitable for melamine detection in real samples.

Table 3. The application of the proposed method for melamine detection in milk samples spiked with different concentrations of melamine (n = 3, average value of three determinations).

Sample	Amount Added (10^{-7} M)	Amount Founded (10^{-7} M)	Recovery (%)	R.S.D. (%)
1	5.2	5.080	97.74	5.0
2	14	13.430	95.93	4.1
3	18	18.144	100.8	2.7

R.S.D.: relative standard deviation.

4. Conclusions

A new and effective FRET based on the system of CPNs-AuNPs was developed for melamine detection. In the presence of melamine, the FRET between AuNPs and CPNs was gradually inhibited, resulting in the fluorescence recovery of CPNs. Melamine could be detected with a lower detection limit of 1.7 nmol/L under the optimum experimental conditions. Moreover, the proposed technique was used for the detection of melamine in real samples with the satisfactory experimental results.

Supplementary Materials: The following are available online at http://www.mdpi.com/2073-4360/10/8/873/s1.

Author Contributions: X.Z., J.Y., and C.Q. conceived and planned the experiments. C.Z., Z.G. and Q.W. carried out the experiments and contributed to sample preparation. X.Z., J.Y., C.Q., Q.L. and C.Z. contributed to the interpretation of the results. C.Z. took the lead in writing Original Draft Preparation. All authors provided critical feedback and helped shape the research, analysis and manuscript. X.Z. and Q.L. are the project administration and funding acquisition.

Funding: This research was funded by the National Natural Science Foundation of China grant number (51403111, 11774188).

Acknowledgments: This project was supported by the National Natural Science Foundation of China (NSFC 51403111, 11774188). We are particularly grateful to the funding supporting from Qilu University of Technology for talents.

Conflicts of Interest: There is no conflict of interest regarding the publication of this manuscript.

References

1. Du, J.; Wang, Y.; Zhang, W. Gold nanoparticles-based chemiluminescence resonance energy transfer for ultrasensitive detection of melamine. *Spectrochim. Acta A Mol. Biomol. Spectrosc.* **2015**, *149*, 698–702. [CrossRef] [PubMed]
2. Zhao, J.; Wu, H.; Jiang, J.; Zhao, S. Label-free fluorescence turn-on sensing for melamine based on fluorescence resonance energy transfer between CdTe/CdS quantum dots and gold nanoparticles. *RSC Adv.* **2014**, *4*, 61667–61672. [CrossRef]
3. Cao, X.; Shen, F.; Zhang, M.; Guo, J.; Luo, Y.; Xu, J.; Li, Y.; Sun, C. Highly sensitive detection of melamine based on fluorescence resonance energy transfer between rhodamine B and gold nanoparticles. *Dyes Pigm.* **2014**, *111*, 99–107. [CrossRef]
4. Wu, Q.; Long, Q.; Li, H.; Zhang, Y.; Yao, S. An upconversion fluorescence resonance energy transfer nanosensor for one step detection of melamine in raw milk. *Talanta* **2015**, *136*, 47–53. [CrossRef] [PubMed]
5. Dai, H.; Shi, Y.; Wang, Y.; Sun, Y.; Hu, J.; Ni, P.; Li, Z. A carbon dot based biosensor for melamine detection by fluorescence resonance energy transfer. *Sens. Actuators B Chem.* **2014**, *202*, 201–208. [CrossRef]
6. Vaclavik, L.; Rosmus, J.; Popping, B.; Hajslova, J. Rapid determination of melamine and cyanuric acid in milk powder using direct analysis in real time-time-of-flight mass spectrometry. *J. Chromatogr. A* **2010**, *1217*, 4204–4211. [CrossRef] [PubMed]
7. Liang, R.; Zhang, R.; Qin, W. Potentiometric sensor based on molecularly imprinted polymer for determination of melamine in milk. *Sens. Actuators B Chem.* **2009**, *141*, 544–550. [CrossRef]

8. Gao, F.; Ye, Q.; Cui, P.; Zhang, L. Efficient fluorescence energy transfer system between CdTe-doped silica nanoparticles and gold nanoparticles for turn-on fluorescence detection of melamine. *J. Agric. Food Chem.* **2012**, *60*, 4550–4558. [CrossRef] [PubMed]
9. Tsai, T.-H.; Thiagarajan, S.; Chen, S.-M. Detection of melamine in milk powder and human urine. *J. Agric. Food Chem.* **2010**, *58*, 4537–4544. [CrossRef] [PubMed]
10. Xue, M.; Wang, X.; Duan, L.; Gao, W.; Ji, L.; Tang, B. A new nanoprobe based on FRET between functional quantum dots and gold nanoparticles for fluoride anion and its applications for biological imaging. *Biosens. Bioelectron.* **2012**, *36*, 168–173. [CrossRef] [PubMed]
11. Zhang, M.; Cao, X.; Li, H.; Guan, F.; Guo, J.; Shen, F.; Luo, Y.; Sun, C.; Zhang, L. Sensitive fluorescent detection of melamine in raw milk based on the inner filter effect of Au nanoparticles on the fluorescence of CdTe quantum dots. *Food Chem.* **2012**, *135*, 1894–1900. [CrossRef] [PubMed]
12. Chatterjee, S.; Nandi, S.; Bhattacharya, S.C. Fluorescence resonance energy transfer from Fluorescein to Safranine T in solutions and in micellar medium. *J. Photochem. Photobiol. A* **2005**, *173*, 221–227. [CrossRef]
13. Chen, J.; Zheng, A.; Chen, A.; Gao, Y.; He, C.; Kai, X.; Wu, G.; Chen, Y. A functionalized gold nanoparticles and Rhodamine 6G based fluorescent sensor for high sensitive and selective detection of mercury (II) in environmental water samples. *Anal. Chim. Acta* **2007**, *599*, 134–142. [CrossRef] [PubMed]
14. Giovannozzi, A.M.; Rolle, F.; Sega, M.; Abete, M.C.; Marchis, D.; Rossi, A.M. Rapid and sensitive detection of melamine in milk with gold nanoparticles by Surface Enhanced Raman Scattering. *Food Chem.* **2014**, *159*, 250–256. [CrossRef] [PubMed]
15. Chi, H.; Liu, B.; Guan, G.; Zhang, Z.; Han, M.-Y. A simple, reliable and sensitive colorimetric visualization of melamine in milk by unmodified gold nanoparticles. *Analyst* **2010**, *135*, 1070–1075. [CrossRef] [PubMed]
16. Zhao, W.; Brook, M.A.; Li, Y. Design of gold nanoparticle-based colorimetric biosensing assays. *Chembiochem* **2008**, *9*, 2363–2371. [CrossRef] [PubMed]
17. Kumar, N.; Seth, R.; Kumar, H. Colorimetric detection of melamine in milk by citrate-stabilized gold nanoparticles. *Anal. Biochem.* **2014**, *456*, 43–49. [CrossRef] [PubMed]
18. Li, L.; Li, B.; Cheng, D.; Mao, L. Visual detection of melamine in raw milk using gold nanoparticles as colorimetric probe. *Food Chem.* **2010**, *122*, 895–900. [CrossRef]
19. Jana, N.R.; Gearheart, L.; Murphy, C.J. Seeding Growth for Size Control of 5−40 nm Diameter Gold Nanoparticles. *Langmuir* **2001**, *17*, 6782–6786. [CrossRef]
20. Liu, J.; Lu, Y. Fast colorimetric sensing of adenosine and cocaine based on a general sensor design involving aptamers and nanoparticles. *Angew. Chem. Int. Ed.* **2005**, *45*, 90–94. [CrossRef] [PubMed]
21. Lyu, Y.; Fang, Y.; Miao, Q.; Zhen, X.; Ding, D.; Pu, K. Intraparticle Molecular orbital engineering of semiconducting polymer nanoparticles as amplified theranostics for in vivo photoacoustic imaging and photothermal therapy. *ACS Nano* **2016**, *10*, 4472–4481. [CrossRef] [PubMed]
22. Wu, C.; Hansen, S.J.; Hou, Q.; Yu, J.; Zeigler, M.; Jin, Y.; Burnham, D.R.; McNeill, J.D.; Olson, J.M.; Chiu, D.T. Design of highly emissive polymer dot bioconjugates for in vivo tumor targeting. *Angew. Chem. Int. Ed.* **2011**, *123*, 3492–3496. [CrossRef]
23. Zhen, X.; Zhang, C.; Xie, C.; Miao, Q.; Lim, K.L.; Pu, K. Intraparticle energy level alignment of semiconducting polymer nanoparticles to amplify chemiluminescence for ultrasensitive in vivo imaging of reactive oxygen species. *ACS Nano* **2016**, *10*, 6400–6409. [CrossRef] [PubMed]
24. Xie, C.; Uppuyuri, P.K.; Zhen, X.; Pramanik, M.; Pu, K. Self-quenched semiconducting polymer nanoparticles for amplified in vivo photoacoustic imaging. *Biomaterials* **2017**, *119*, 1–8. [CrossRef] [PubMed]
25. Pu, K.; Shuhendler, A.J.; Valta, M.P.; Cui, L.; Saar, M.; Peehl, D.M.; Rao, J. Phosphorylcholine-coated semiconducting polymer nanoparticles as rapid and efficient labeling agents for in vivo cell tracking. *Adv. Healthcare Mater.* **2014**, *3*, 1292–1298. [CrossRef] [PubMed]
26. Geng, J.; Sun, C.; Liu, J.; Liao, L.-D.; Yuan, Y.; Thakor, N.; Wang, J.; Liu, B. Biocompatible conjugated polymer nanoparticles for efficient photothermal tumor therapy. *Small* **2015**, *11*, 1603–1610. [CrossRef] [PubMed]
27. Macneill, C.M.; Coffin, R.C.; Carroll, D.L.; Levi-Polyachenko, N.H. Low band gap donor-acceptor conjugated polymer nanoparticles and their NIR-mediated thermal ablation of cancer cells. *Macromol. Biosci.* **2013**, *13*, 28–34. [CrossRef] [PubMed]
28. Gao, F.; Ye, Q.; Cui, P.; Chen, X.; Li, M.; Wang, L. Selective "turn-on" fluorescent sensing for biothiols based on fluorescence resonance energy transfer between acridine orange and gold nanoparticles. *Anal. Methods* **2011**, *3*, 1180–1185. [CrossRef]

29. Fu, X.; Liu, Y.; Wu, Z.; Zhang, H. Highly Sensitive and Naked Eye Dual-readout Method for L-Cysteine Detection Based on the NSET of Fluorophore Functionalized Gold Nanoparticles. *Bull. Korean Chem. Soc.* **2014**, *35*, 1159–1164. [CrossRef]
30. Zhu, Y.; Zhang, X.; Qin, Y.N.; Liu, Z.E. The Preparation and Fluorescence of Conjugated Polymer Nanoparticles with Triphenylamin Derivatives. *Int. Conf. Mater. Sci. Appl.* **2015**, *3*, 181–185. [CrossRef]
31. Wang, C.; Sun, J.; Mei, H.; Gao, F. Organic semiconductor polymer nanodots as a new kind of off-on fluorescent probe for sulfide. *Microchim. Acta* **2016**, *184*, 445–451. [CrossRef]
32. Wu, C.; Jin, Y.; Schneider, T.; Burnham, D.R.; Smith, P.B.; Chiu, D.T. Ultrabright and Bioorthogonal Labeling of Cellular Targets Using Semiconducting Polymer Dots and Click Chemistry. *Angew. Chem. Int. Ed.* **2010**, *122*, 9626–9630. [CrossRef]
33. Cao, X.; Shen, F.; Zhang, M.; Guo, J.; Luo, Y.; Li, X.; Liu, H.; Sun, C.; Liu, J. Efficient inner filter effect of gold nanoparticles on the fluorescence of CdS quantum dots for sensitive detection of melamine in raw milk. *Food Control* **2013**, *34*, 221–229. [CrossRef]
34. Frens, G. Controlled Nucleation for the Regulation of the Particle Size in Monodisperse Gold Suspensions. *Nat. Phys. Sci.* **1973**, *241*, 20–22. [CrossRef]
35. Tang, G.; Du, L.; Su, X. Detection of melamine based on the fluorescence resonance energy transfer between CdTe QDs and Rhodamine B. *Food Chem.* **2013**, *141*, 4060–4065. [CrossRef] [PubMed]
36. Huang, S.; Wang, L.; Huang, C.; Hu, B.; Su, W.; Xiao, Q. Graphene quantum dot coupled with gold nanoparticle based "off-on" fluorescent probe for sensitive and selective detection of L-cysteine. *Microchim. Acta* **2016**, *183*, 1855–1864. [CrossRef]
37. Guo, L.; Zhong, J.; Wu, J.; Fu, F.; Chen, G.; Chen, Y.; Zheng, X.; Lin, S. Sensitive turn-on fluorescent detection of melamine based on fluorescence resonance energy transfer. *Analyst* **2011**, *136*, 1659–1663. [CrossRef] [PubMed]
38. Wang, H.; Zheng, C.; Dong, T.; Liu, K.; Han, H.; Liang, J. Wavelength Dependence of Fluorescence Quenching of CdTe Quantum Dots by Gold Nanoclusters. *J. Phys. Chem. C* **2013**, *117*, 3011–3018. [CrossRef]
39. Kumar, A.; Mandal, S.; Selvakannan, P.R.; Pasricha, R.; Mandale, A.B.; Sastry, M. Investigation into the Interaction between Surface-Bound Alkylamines and Gold Nanoparticles. *Langmuir* **2003**, *19*, 6277–6282. [CrossRef] [PubMed]
40. Ai, K.; Liu, Y.; Lu, L. Hydrogen-bonding recognition-induced color change of gold nanoparticles for visual detection of melamine in raw milk and infant formula. *J. Am. Chem. Soc.* **2009**, *131*, 9496–9497. [CrossRef] [PubMed]
41. Venkatasami, G.; Sowa, J.R., Jr. A rapid, acetonitrile-free, HPLC method for determination of melamine in infant formula. *Anal. Chim. Acta* **2010**, *665*, 227–230. [CrossRef] [PubMed]
42. Zhang, X.; Li, L.; Liu, Y. Fluorescent detection and imaging of Hg^{2+} using a novel phenanthroline derivative based single- and two-photon excitation. *Mater. Sci. Eng. Carbon* **2016**, *59*, 916–923. [CrossRef] [PubMed]

polymers

MDPI

Article

Thermo-Responsive Fluorescent Polymers with Diverse LCSTs for Ratiometric Temperature Sensing through FRET

Zhaoyang Ding †, Chunfei Wang †, Gang Feng and Xuanjun Zhang *

Faculty of Health Sciences, University of Macau, Macau SAR 999078, China; zhaoyangding@umac.mo (Z.D.); yb67596@umac.mo (C.W.); yb67608@umac.mo (G.F.)

* Correspondence: xuanjunzhang@umac.mo; Tel.: +853-8822-4928

† These authors contributed equally to this work.

Received: 30 January 2018; Accepted: 6 March 2018; Published: 8 March 2018

Abstract: Temperature is a significant parameter to regulate biological reactions and functions inside cells. Sensing the intracellular temperature with a competent method is necessary to understand life science. In this work, an energy-transfer polymeric thermometer was designed for temperature sensing. The thermometer was prepared from two thermo-responsive polymers with different lower critical solution temperatures (LCSTs) of 31.1 °C and 48.6 °C, coupling with blue and red fluorescent molecules, respectively, developed for ratiometric temperature sensing based on the Förster resonance energy transfer (FRET) mechanism. The polymers were synthesized from two monomers, *N*-isopropylacrylamide (NIPA) and *N*-isopropylmethacrylamide (NIPmA), which provided different temperature responses. The fluorescent intensity of each polymer (peaked at 436 and 628 nm, respectively) decreased upon the heating of the polymer aqueous solution. While these two polymer aqueous solutions were mixed, the fluorescent intensity decrease at 436 nm and substantial fluorescence enhancement at 628 nm was observed with the increasing temperature due to FRET effect. The cell imaging of HeLa cells by these thermo-responsive polymers was explored. The difference of LCSTs resulting in ratiometric fluorescence change would have a potential impact on the various biomedical applications.

Keywords: *N*-isopropylacrylamide; *N*-isopropylmethacrylamide; ratiometric temperature sensing; FRET

1. Introduction

Temperature is an essential physiological parameter during all biochemical reactions in living cells. It has a close relationship with cellular functions, such as cell division, gene expression, metabolism, enzyme reaction, and so on [1,2]. In addition, various abnormal medical phenomena, like cancer cell growth, are often accompanied by a temperature increase. Owing to these considerable demands, lots of promising approaches to fluorescent thermometers for cell temperature sensing have been studied [3]. Recently, many works have been developed for this requirement, including small organic dyes [4], quantum dots [5,6], polymers [7–11], and gold nanoclusters [12].

Nowadays, stimuli-responsive polymers have received more attentions for their potential biomedical applications. A variety of stimuli-responsive polymers whose properties change in response to temperature, pH, ionic strength, light, and chemical stress have been investigated [13–17]. Thermo-responsive polymers have been applied in the fields of sensors, catalyst supports, drug carriers, and bio-separation [18–20]. Thermo-responsive polymers based on *N*-isopropylacrylamide (NIPA) were the most common used in these years. These polymers have a lower critical solution temperature (LCST) close to human and most animal's physiological temperature, with good biocompatibility

and low toxicity [21]. Many fluorophores [11,22,23] have already been introduced into NIPA-based polymers to visualize the temperature in living cells as fluorescent thermometer.

Fluorescent temperature sensing is usually based on the fluorescence intensity changes at certain wavelengths instead of fluorescence lifetime owing to its accessibility and prevalence. However, the fluorescence intensity at a single wavelength can be easily affected. Ratiometric fluorescent temperature sensing is more and more popular with potential advantages. For the ratiometric fluorescent temperature sensing based on the fluorescence resonance energy transfer (FRET) mechanism, multi-color fluorescence of NIPA-based polymer temperature sensors were reported [24–27]. In these studies, only one thermo-responsive monomer NIPA was used, which might limit the range of the temperature sensor. When a methyl group is added to NIPA, such as *N*-isopropylmethacrylamide (NIPmA), the LCST of the NIPmA-based polymer was higher at around 45 °C to 50°C [28,29]. The introduction of NIPmA to the NIPA-based temperature sensing system is expected to enlarge the range of the temperature sensing, which should undergo a reversible LCST phase transition between the temperature range from 25 °C to 50°C. With the increasing of temperature, the shrink speed of the NIPA-based polymer was faster than the NIPmA-based polymer, leading to the distance change and FRET change between two polymers as shown in Scheme 1.

To test this hypothesis, we designed a NIPA-based polymer with blue fluorescence molecule (7-[4-(Trifluoromethyl)coumarin]methacrylamide) and a NIPmA-based polymer with red fluorescence molecule (BOBPYBX) synthesized by ourselves to form a novel polymeric ratiometric temperature sensor through FRET by the mixing of these two polymer solutions. We also characterized the effects of the temperature on their fluorescent behavior and exhibiting good performance both in aqueous solution and in the temperature imaging of cells.

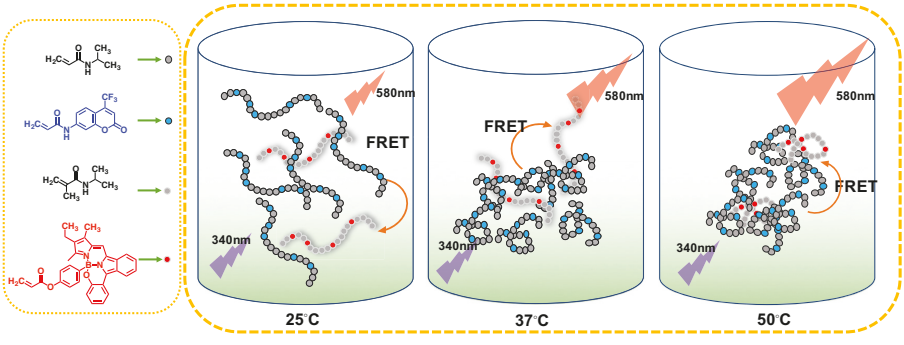

Scheme 1. Fabrication of two thermo-responsive fluorescent polymers with diverse LCSTs.

2. Materials and Methods

2.1. Materials

N-isopropylacrylamide (NIPA), *N*-isopropylmethacrylamide (NIPmA), 7-[4-(trifluoromethyl) coumarin]methacrylamide (TCMA), 2,2′-azobis(isobutyronitrile) (AIBN), 3-mercaptopropionic acid (MPA), 2-hydroxyphenyboronic acid, tetrakis(triphenylphosphine)palladium ($Pd(PPh_3)_4$), Phosphorus(V) oxybromide ($POBr_3$) and phosphorus(V) oxychloride ($POCl_3$) were purchased from Sigma-Aldrich (St. Louis, MO, USA). 1-Isoindolinone, 2,4-dimethyl-3-ethylpyrrole, 4-hydroxyphenylboronic acid, acryloyl chloride, and triethylamine were purchased from Dieckman (Hong Kong) Chemical Industry Company Ltd. (Hong Kong, China). All other reagents and solvents were of analytical grade.

2.2. Synthetic of BOBPYBX

1 as presented in Scheme 2 was synthesized according to previous literatures with modification [30,31]. A solution of $POBr_3$ (20 mmol, 5.73 g) in anhydrous dichloromethane (5 mL) was added dropwise to Dimethylformamide (DMF) (20 mmol, 1.46 g) in anhydrous dichloromethane (15 mL) at 0 °C. The mixture was stirred for 30 min at room temperature. Then a solution of 1-isoindolinone (10 mmol, 1.33 g) in anhydrous dichloromethane (50 mL) was added to the mixture at 0 °C. Subsequently, the reaction mixture was heated at reflux for 6 h. After cooling, the solvent was removed at reduced pressure. Ice water was added, and aqueous NaOH (5 M) was added the mixture to a pH of around 8. A black solid precipitated and the mixture was stirred overnight, then **1** (yield was 84.2%) was collected by filtration.

2 as presented in Scheme 2 and BOBPYOH were synthesized by modifying previous method [32]. To **1** (8.00 mmol, 2 g), to 2-hydroxyphenyboronic acid (17.50 mmol, 2.41 g) and $Pd(PPh_3)_4$ (0.25 mmol, 0.29 g) aqueous Na_2CO_3 (1 M, 20 mL) and dry toluene (50 mL) were added in a Schlenk flask under nitrogen. This reaction mixture was then degassed via three freeze-pump-thaw cycles before filling with nitrogen again. The Schlenk flask was heated to 75 °C for 24 h. After cooling to room temperature, the reaction mixture was washed with water (30 mL × 3). Organic layers were combined, dried over anhydrous Na_2SO_4, and evaporated under vacuum. The crude product was refluxed for 3 h in ethanol (120 mL) containing aqueous NaOH (4 M, 20 mL). The solvent was removed in vacuum. The resultant solid was dissolved in ethyl acetate (100 mL), and neutralized with HCl (3 M). Organic layers were combined, dried under anhydrous Na_2SO_4, filtrated, and concentrated under vacuum, and the residual product was purified by silica gel column chromatography (dichloromethane/ethyl acetate = 1:1) to afford **2** (yield was 75.8%). $POCl_3$ (5.2 mmol, 0.8 g) was added to a dichloromethane solution (15 mL) of 2,4-dimethyl-3-ethylpyrrole (10.4 mmol, 1.28 g) at 0 °C. Then a solution of **2** (5.2 mmol, 1.23 g) in dichloromethane (25 mL) was added dropwise to the reaction mixture at 0 °C. The reaction mixture was stirred at room temperature for 4 h. To this solution, 4-hydroxyphenylboronic acid (52 mmol, 7.17 g) was dissolved in THF and added. Then the reaction mixture was stirred for another 4 h. After evaporation of the solvent, the residual product was purified by silica gel column chromatography (dichloromethane/*n*-hexane = 10:1) to give BOBPYOH (yield was 72.3%). NMR results of BOBPYOH were shown in Figures S1 and S2. ^{1}H NMR (400 MHz, $CDCl_3$) δ = 8.12 (d, *J* = 8.2, 1H), 7.97 (dd, *J* = 7.9, 1.5, 1H), 7.88 (d, *J* = 8.1, 1H), 7.47 (t, *J* = 7.4, 1H), 7.44–7.38 (m, 2H), 7.34 (d, *J* = 7.2, 2H), 7.04 (d, *J* = 8.4, 2H), 7.00–6.94 (m, 1H), 6.54–6.47 (m, 2H), 2.46 (s, 3H), 2.39 (dd, *J* = 7.6, 1.6, 2H), 2.27 (s, 3H), 1.04 (t, *J* = 7.6, 3H). ^{13}C NMR (101 MHz, $CDCl_3$) δ = 157.11, 154.20, 150.96, 143.18, 135.34, 133.23, 133.00, 132.90, 132.10, 130.36, 128.77, 128.43, 126.35, 125.65, 125.38, 123.43, 120.13, 119.65, 119.57, 119.08, 115.92, 114.10, 67.99, 25.62, 17.50, 13.07, 9.59.

BOBPYBX was synthesized by modifying hydroxyl group with acryloyl chloride [33]. To a solution of BOBPYOH (2 mmol, 0.86 g) and triethylamine (3 mmol, 0.3 g) in dichloromethane (20 mL) acryloyl chloride (20 mmol, 1.8 g) was added slowly and stirred for 0.5 h at 0 °C. Then the reaction was stirred further at room temperature for 12 h. The mixture was treated with water and the organic layer was separated. The aqueous layer was extracted with dichloromethane and the combined organic layer was washed with saturated aqueous NH_4Cl, brine, and dried over anhydrous Na_2SO_4. The solvent was removed by rotary evaporation and the residue was purified by silica gel column chromatography (dichloromethane/*n*-hexane = 10:1) to afford BOBPYBX (yield was 35.5%). NMR results of BOBPYBX were shown in Figures S3 and S4. ^{1}H NMR (400 MHz, $CDCl_3$) δ = 8.12 (d, *J* = 8.2, 1H), 7.97 (dd, *J* = 7.9, 1.5, 1H), 7.89 (d, *J* = 8.1, 1H), 7.48 (t, *J* = 7.5, 1H), 7.44–7.38 (m, 2H), 7.34 (dd, *J* = 11.2, 4.0, 1H), 7.28 (d, *J* = 0.9, 1H), 7.20 (d, *J* = 8.4, 2H), 7.02–6.93 (m, 1H), 6.83–6.73 (m, 2H), 6.48 (dd, *J* = 17.3, 1.4, 1H), 6.22 (dd, *J* = 17.3, 10.4, 1H), 5.90 (dd, *J* = 10.4, 1.4, 1H), 2.47 (s, 3H), 2.39 (tt, *J* = 9.2, 4.5, 2H), 2.27 (s, 3H), 1.05 (t, *J* = 7.6, 3H). ^{13}C NMR (101 MHz, $CDCl_3$) δ = 164.68, 156.91, 151.01, 149.31, 143.29, 135.33, 133.43, 133.09, 132.66, 132.03, 131.94, 130.46, 128.74, 128.55, 128.24, 126.39, 125.67, 125.47, 123.47, 120.14, 119.86, 119.81, 119.60, 119.07, 115.97, 17.48, 14.84, 13.05, 9.59.

2.3. Synthesis of Fluorescent Polymers

Two thermo-responsive polymers were named from the monomers, P_{NB} consisted of NIPA and TCMA, and P_{NmR} was NIPmA and BOBPBYX. P_{NB} was prepared using radical polymerization, as shown in Scheme 2. NIPA (1.58 g, 14 mmol) and TCMA (4.3 mg, 0.015 mmol) were dissolved in ethanol (20 mL). AIBN (10 mg, 0.06 mmol) and MPA (50 mg, 0.5 mmol), which act as the radical initiator and the chain transfer agent to control the molecular weight of the polymers, respectively, were added to the solution. The reaction mixture was degassed and reacted in a N_2 atmosphere at 65 °C for 12 h. After the reaction finished, the solvent ethanol was removed by a vacuum dryer and the product was precipitated by *n*-hexane and washed with acetone three times. The solid product was dried under vacuum conditions. The molecular weight of the polymer was determined by gel permeation chromatography (GPC) analysis. P_{NmR} was prepared from NIPmA and BOBPYBX, which was synthesized by ourselves as shown in Scheme 2, according to the above procedure.

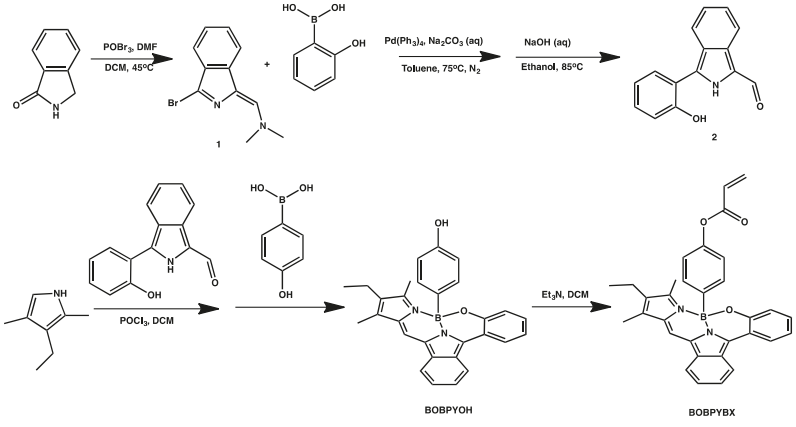

Scheme 2. Synthetic procedure of BOBPYBX.

2.4. Analytical Techniques

GPC was conducted on a Cirrus system (PL-GPC 50, Santa Clara, CA, USA) equipped with a differential refractive index detector. DMF was used as the eluent with a gel column (300 × 650 mm^2) (at 40 °C, the flow rate = 1 mL/min). A Fourier transform infrared spectrometer (FTIR, IRAffinity-1S, Shimadzu, Japan) was used to determinate the structures of the fluorescent polymers. For each sample, each spectrum was obtained by 32 scans with the wavenumber ranging from 400 to 4000 cm^{-1} and resolution was 4 cm^{-1}.

LCSTs of the polymers were determined by measuring the optical transmittance of their aqueous solution (0.5% *w*/*v*). A sample cell with a 1 cm path length was used to measure the transmittance using 500 nm over a range of temperatures from 25 to 50 °C using a UV−Vis spectrophotometer (Shimadzu UV-3600 spectrophotometer, Shimadzu, Japan). The temperature at which the transmittance decreased to half of its initial value was taken as the LCST [34]. Fluorescence spectra (Fluorolg-4 spectrofluorometric) with a temperature controller were performed for the experiments. A quartz cuvette with a 1 cm path length was used. The maximum excitation wavelengths of the fluorescent polymers were as follows (0.5% *w*/*v* aqueous solution): P_{NB} λex = 340 nm; P_{NmR} λex = 580 nm; P_{MIX} λex = 340 nm. The effects temperature on the fluorescence intensity of the polymers were evaluated between 25 and 50 °C.

2.5. Cell Culture

The cervical cancer line HeLa cells were kindly provided by Faculty of Health Sciences, University of Macau. HeLa cells were incubated in DMED (Dubecco's Modified Eagle Medium) medium supplemented with 10% FBS (fetal bovine serum) and 1% penicillin-streptomycin solution. All cells were maintained at 37 °C, in a 5% CO_2 humidified environment.

HeLa cells were seeded into glass-bottomed culture dishes and allowed to adhere for 24 h. After removing the medium, 10 μM polymer solution was added and incubated for 1 h at 37 °C. After the incubation, cells were washed twice by pre-warmed PBS buffer. Fixative solution (Histochoice® Mb Tissue Fixative, Amresco, Dallas, TX, USA) was added for 15 min at room temperature, then washed three with PBS buffer. The samples were observed by Carl Zeiss Confocal LSM710 at 25 °C or 37 °C.

3. Results and Discussion

Two fluorescent polymers were synthesized via radical polymerization. The synthetic scheme and structures of the polymers are shown in Scheme 3. For these two polymers, NIPA and NIPmA, were selected as the backbone of the thermo-responsive fluorescent polymers, to ensure the polymers having enough thermo-responsibility and water-solubility, the NIPA or NIPmA units in polymers were controlled above 98 mol % and less than 1 mol % of the fluorescent monomers were introduced into the polymers. 7-[4-(Trifluoromethyl)coumarin]methacrylamide (blue) and newly-synthesized BOBPYBX (red) were chosen as fluorescent monomers to form the FRET system. The polymers undergo reversible LCSTs phase transition between the temperature range from 25 °C to 50 °C, which covers the physiological temperature of humans and most animals.

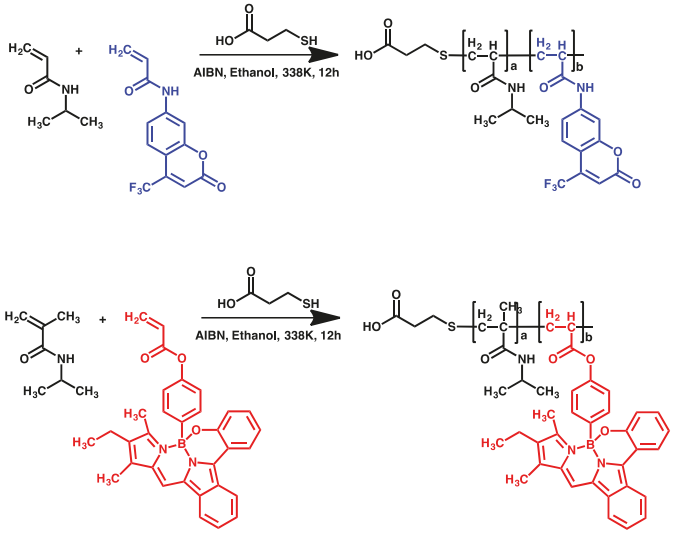

Scheme 3. Syntheses of fluorescent polymers.

The successful synthesis of fluorescent polymers was confirmed by FT-IR and absorption measurement as shown in Figure 1. According to the results, the maximum absorption peaks of P_{NB} and P_{NmR} were 340 nm and 620 nm, respectively. The LCSTs of P_{NB} and P_{NmR} were 31.1 °C and 48.6 °C, which were as expected. The FTIR spectrum of P_{NB} featured the characteristic absorption peaks at 3300–3090 cm^{-1} (secondary amine group), 2980 cm^{-1} (methyl group), 2900 cm^{-1} (methylene group), and 1180–1130 cm^{-1} (trifluoromethyl group), which are attributable to the two monomers. This strongly indicates the successful formation of polymer P_{NB}. The FT-IR spectrum of P_{NmR} also

exhibited the similar result. The fluorescent monomer ratio was so small that did not show very typical peaks in the FT-IR results, however, the absorption spectrum and fluorescent spectrum proved the polymerization was successful. The results of number-averaged and weight-averaged molecular weights were determined by gel permeation chromatography (GPC), as shown in Table 1 and Figures S5 and S6. The oligomeric products were obtained due to the use of chain-transfer agent.

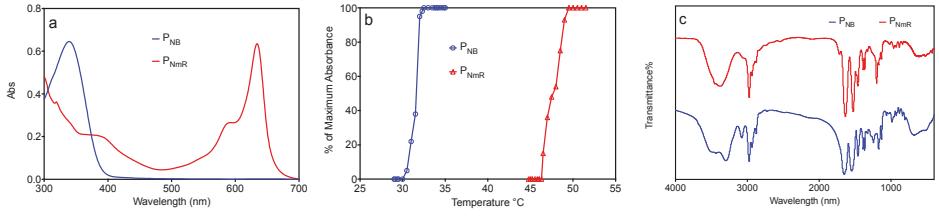

Figure 1. Characterization of fluorescent polymers. (**a**) Absorption spectra of the fluorescent polymers; (**b**) temperature-dependent for the fluorescent polymers in aqueous solution (500 nm, 0.5% *w*/*v*); and (**c**) FT-IR results of the fluorescent polymers.

Table 1. GPC results of fluorescent polymers.

Polymers	M_n	M_w	PDI
P_{NB}	5957	7954	1.33121
P_{NmR}	11,144	16,140	1.44831

M_w: weight average molecular weight; M_n: number average molecular weight; PDI: Polymer dispersity index, PDI = M_w/M_n.

We then investigated the temperature response behavior of the fluorescent polymers. The temperature-dependent fluorescence spectra and optical transmittance of P_{NB} in aqueous solution are shown in Figure 2a. The fluorescent intensity of P_{NB} was found to decrease with increasing of the temperature from 25 °C to 50 °C, and the polymer P_{NmR} showed the similar phenomenon as in Figure 2b. As shown in Figure 2d,e, the fluorescent intensity of both P_{NB} and P_{NmR} had the liner relationship with the temperature from 30 °C to 50 °C. Hydrate form and swollen state of the thermo-responsive polymers were driven by their native properties. The fluorescent monomer displayed higher emission quantum yield in polar media, resulting in the stronger fluorescence intensity with the increase of the temperature. We could, therefore, conclude that the fluorescent intensity responses of these polymers were driven by a combination of the properties of both thermo-responsive monomers and the fluorescent monomers. The LCSTs of P_{NB} and P_{NmR} were 31.1 and 48.6 °C, respectively. Due to these results, ratiometric fluorescent temperature sensing through FRET which is very powerful in analysis and sensing can be achieved by mixing these two polymers, especially between their two LCSTs. We tried several ratios of mixed P_{NB} and P_{NmR}, and the final ratio of P_{NB} and P_{NmR} was set as 20:1. The fluorescence response results were indicated in Figure 2c, a dramatic fluorescence decrease at 436 nm and substantial fluorescence enhancement at 628 nm was observed upon heating. However, the fluorescence enhancement of P_{NmR} was limited in comparison with the result in Figure 2b. The ratio of fluorescent intensity F628 nm/F436 nm had liner relationship with temperature between two LCSTs as shown in Figure 2f. With the increasing of temperature, the shrink speed of P_{NB} was faster than P_{NmR}, leading to the distance change and FRET change between two polymers. The shrink changes and fluorescence changes of the polymers to different temperatures could be directly visualized by the naked eye, and the fluorescence was excited by the light of hand-held UV lamp at 365 nm. For P_{NB} shown in Figure 2g, the polymer solution became turbid from 25 °C to 37 °C and 50 °C, and the fluorescence were all blue emissions. In Figure 2h, P_{NmR} solution was clear at 25 °C and 37 °C, turbid when at 50 °C which was above the

LCST of it and the P_{NmR} solution exhibited dark red emission. P_{MIX} exhibited purple emission at 25 °C, pink and bright pink emission at 37 °C and 50 °C due to FRET effects, as shown in Figure 2i. In the meantime, the P_{MIX} solution became turbid from 25 °C to 37 °C and 50 °C.

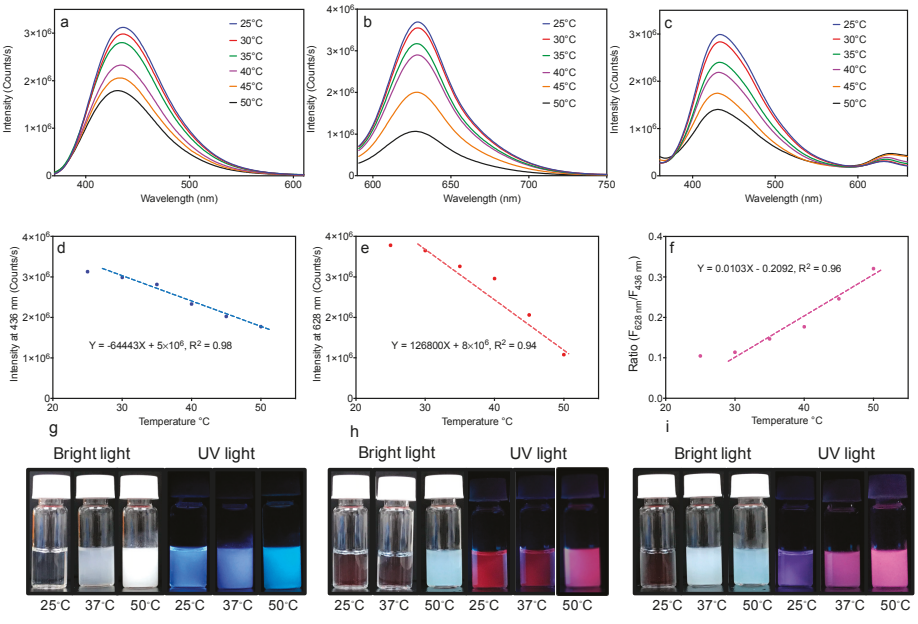

Figure 2. Fluorescence responses of polymers to temperature from 25 °C to 50 °C. (**a**) Fluorescence spectra of P_{NB} upon temperature 25 °C to 50 °C; (**b**) fluorescence spectra of P_{NmR} upon temperature 25 °C to 50 °C; (**c**) fluorescence spectra of P_{MIX} upon temperature 25 °C to 50 °C; (**d**) Linear correlation of P_{NB} between the emission intensity at 436 nm and temperature; (**e**) linear correlation of P_{NmR} between the emission intensity at 628 nm and temperature; (**f**) linear correlation of P_{MIX} between the emission intensity (F628 nm/F436 nm) and temperature; (**g**–**i**) naked eye photographs of the fluorescence change of the polymers P_{NB}, P_{NmR}, and P_{MIX} in aqueous solution (0.5% w/v) at different temperatures, respectively.

In view of the significance of temperature on the biological events within living cells, fluorescent images of HeLa cells incubated with polymers were explored. Figure 3a showed blue emission of cells based on the uptake of P_{NB} and Figure 3b showed a red emission of cells because of the uptake of P_{NmR}. When the cells were incubated with P_{MIX}, both blue and red emissions were observed as shown in Figure 3c,d, and the merge picture showed pink emission. Figure 3c had stronger blue emission and weaker red emission compared with Figure 3d due to the change of observing temperature from 25 °C to 37 °C. The results were consistent with previous fluorescent spectrum data.

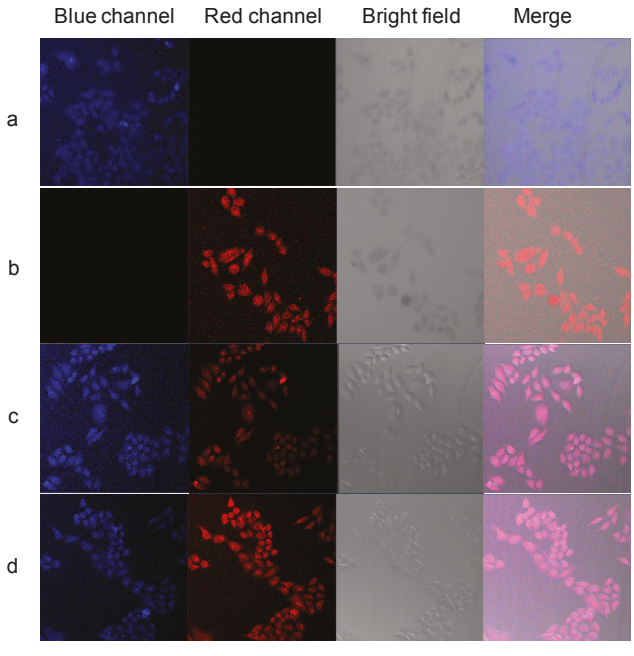

Figure 3. Fluorescent images of HeLa cells incubated with different polymers: (**a**) incubated with P_{NB}; (**b**) incubated with P_{NmR}; and (**c**,**d**) incubated with P_{MIX}; (**a**–**c**) were observed at 25 °C and (**d**) was observed at 37 °C.

4. Conclusions

In summary, two fluorescent polymers, P_{NB} and P_{NmR}, were prepared to form a novel energy-transfer thermometer for ratiometric temperature sensing. They exhibit different LCSTs because of the various thermo-responsive monomers. The temperature sensing system displayed good stability and biocompatibility. The intracellular temperature imaging of living cells by these ratiometric temperature sensing polymers was explored. It is expected that this LCSTs difference showing ratiometric fluorescence change would have a significant impact on the various applications, such as fluorescent temperature sensing and bio-imaging of biological processes at specific organelles.

Supplementary Materials: The following are available online at www.mdpi.com/xxx/s1, Figure S1: ^{1}H NMR of BOBPYOH, Figure S2: ^{13}C NMR of BOBPYOH, Figure S3: ^{1}H NMR of BOBPYOX, Figure S4: ^{13}C NMR of BOBPYOX. Figure S5: GPC result of P_{NB}, Figure S6: GPC result of P_{NmR}.

Acknowledgments: This work was financially supported by Macao Science and Technology Development Fund under Grant No. 052/2015/A2, 082/2016/A2, and the University of Macau research grants under grant Nos. MYRG2016-00058-FHS, MYRG2017-00066-FHS, and SRG2015-00007-FHS.

Author Contributions: Zhaoyang Ding and Xuanjun Zhang conceived and designed the experiments; Zhaoyang Ding, Chunfei Wang, and Gang Feng performed the experiments; and Zhaoyang Ding analyzed the data and wrote the paper.

Conflicts of Interest: The authors declare no conflict of interest.

References

1. Bai, T.; Gu, N. Micro/nanoscale thermometry for cellular thermal sensing. *Small* **2016**, *12*, 4590–4610. [CrossRef] [PubMed]

2. Gota, C.; Okabe, K.; Funatsu, T.; Harada, Y.; Uchiyama, S. Hydrophilic fluorescent nanogel thermometer for intracellular thermometry. *J. Am. Chem. Soc.* **2009**, *131*, 2766–2767. [CrossRef] [PubMed]
3. Wang, X.-D.; Wolfbeis, O.S.; Meier, R.J. Luminescent probes and sensors for temperature. *Chem. Soc. Rev.* **2013**, *42*, 7834–7869. [CrossRef] [PubMed]
4. Uchiyama, S.; Gota, C. Luminescent molecular thermometers for the ratiometric sensing of intracellular temperature. *Rev. Anal. Chem.* **2017**, *36*. [CrossRef]
5. Zhou, J.; Mishra, K.; Bhagat, V.; Joy, A.; Becker, M.L. Thermoresponsive dual emission nanosensor based on quantum dots and dye labeled poly(*N*-isopropylacrylamide). *Polym. Chem.* **2015**, *6*, 2813–2816. [CrossRef]
6. Liu, Y.; Oda, H.; Inoue, Y.; Ishihara, K. Movement of a quantum dot covered with cytocompatible and PH-responsible phospholipid polymer chains under a cellular environment. *Biomacromolecules* **2016**, *17*, 3986–3994. [CrossRef] [PubMed]
7. Hu, X.; Li, Y.; Liu, T.; Zhang, G.; Liu, S. Intracellular cascade fret for temperature imaging of living cells with polymeric ratiometric fluorescent thermometers. *ACS Appl. Mater. Interfaces* **2015**, *7*, 15551–15560. [CrossRef] [PubMed]
8. Chen, Z.; Zhang, K.Y.; Tong, X.; Liu, Y.; Hu, C.; Liu, S.; Yu, Q.; Zhao, Q.; Huang, W. Phosphorescent polymeric thermometers for in vitro and in vivo temperature sensing with minimized background interference. *Adv. Funct. Mater.* **2016**, *26*, 4386–4396. [CrossRef]
9. Kim, J.H.; Jung, Y.; Lee, D.; Jang, W.D. Thermoresponsive polymer and fluorescent dye hybrids for tunable multicolor emission. *Adv. Mater.* **2016**, *28*, 3499–3503. [CrossRef] [PubMed]
10. Li, T.; He, S.; Qu, J.; Wu, H.; Wu, S.; Zhao, Z.; Qin, A.; Hu, R.; Tang, B.Z. Thermoresponsive aie polymers with fine-tuned response temperature. *J. Mater. Chem. C* **2016**, *4*, 2964–2970. [CrossRef]
11. Zhou, H.; Liu, F.; Wang, X.; Yan, H.; Song, J.; Ye, Q.; Tang, B.Z.; Xu, J. Aggregation induced emission based fluorescence PH and temperature sensors: Probing polymer interactions in poly(*N*-isopropyl acrylamide-*co*-tetra(phenyl)ethene acrylate)/poly(methacrylic acid) interpenetrating polymer networks. *J. Mater. Chem. C* **2015**, *3*, 5490–5498. [CrossRef]
12. Maji, S.; Cesur, B.; Zhang, Z.; De Geest, B.G.; Hoogenboom, R. Poly(*N*-isopropylacrylamide) coated gold nanoparticles as colourimetric temperature and salt sensors. *Polym. Chem.* **2016**, *7*, 1705–1710. [CrossRef]
13. Hu, X.; Zhang, Y.; Xie, Z.; Jing, X.; Bellotti, A.; Gu, Z. Stimuli-responsive polymersomes for biomedical applications. *Biomacromolecules* **2017**, *18*, 649–673. [CrossRef] [PubMed]
14. Thambi, T.; Phan, V.H.; Lee, D.S. Stimuli-sensitive injectable hydrogels based on polysaccharides and their biomedical applications. *Macromol. Rapid Commun.* **2016**, *37*, 1881–1896. [CrossRef] [PubMed]
15. Ding, Z.; Cao, X. Affinity precipitation of cellulase using PH-response polymer with cibacron blue F3GA. *Sep. Purif. Technol.* **2013**, *102*, 136–141. [CrossRef]
16. Ding, Z.; Cao, X. Affinity precipitation of human serum albumin using a thermo-response polymer with an L-thyroxin ligand. *BMC Biotechnol.* **2013**, *13*, 109. [CrossRef] [PubMed]
17. Ding, Z.; Kang, L.; Liu, J.; Zhang, X.; Cao, X. Preparation of PH-responsive metal chelate affinity polymer for adsorption and desorption of insulin. *J. Chem. Technol. Biotechnol.* **2017**, *92*, 1590–1595. [CrossRef]
18. Lyon, L.A.; Meng, Z.; Singh, N.; Sorrell, C.D.; St John, A. Thermoresponsive microgel-based materials. *Chem. Soc. Rev.* **2009**, *38*, 865–874. [CrossRef] [PubMed]
19. Weber, C.; Hoogenboom, R.; Schubert, U.S. Temperature responsive bio-compatible polymers based on poly(ethylene oxide) and poly(2-oxazoline)s. *Prog. Polym. Sci.* **2012**, *37*, 686–714. [CrossRef]
20. Wei, M.; Gao, Y.; Li, X.; Serpe, M.J. Stimuli-responsive polymers and their applications. *Polym. Chem.* **2017**, *8*, 127–143. [CrossRef]
21. Roy, D.; Brooks, W.L.A.; Sumerlin, B.S. New directions in thermoresponsive polymers. *Chem. Soc. Rev.* **2013**, *42*, 7214–7243. [CrossRef] [PubMed]
22. Ma, H.; Qi, C.; Cheng, C.; Yang, Z.; Cao, H.; Yang, Z.; Tong, J.; Yao, X.; Lei, Z. Aie-active tetraphenylethylene cross-linked *N*-isopropylacrylamide polymer: A long-term fluorescent cellular tracker. *ACS Appl. Mater. Interfaces* **2016**, *8*, 8341–8348. [CrossRef] [PubMed]
23. Yamada, A.; Hiruta, Y.; Wang, J.; Ayano, E.; Kanazawa, H. Design of environmentally responsive fluorescent polymer probes for cellular imaging. *Biomacromolecules* **2015**, *16*, 2356–2362. [CrossRef] [PubMed]
24. Lee, S.H.; Bui, H.T.; Vales, T.P.; Cho, S.; Kim, H.-J. Multi-color fluorescence of pnipam-based nanogels modulated by dual stimuli-responsive fret processes. *Dyes Pigm.* **2017**, *145*, 216–221. [CrossRef]

25. Qiao, J.; Hwang, Y.-H.; Chen, C.-F.; Qi, L.; Dong, P.; Mu, X.-Y.; Kim, D.-P. Ratiometric fluorescent polymeric thermometer for thermogenesis investigation in living cells. *Anal. Chem.* **2015**, *87*, 10535–10541. [CrossRef] [PubMed]
26. Chen, C.Y.; Chen, C.T. A pnipam-based fluorescent nanothermometer with ratiometric readout. *Chem. Commun.* **2011**, *47*, 994–996. [CrossRef] [PubMed]
27. Yin, J.; Li, C.; Wang, D.; Liu, S. Fret-derived ratiometric fluorescent k^+ sensors fabricated from thermoresponsive poly(*N*-isopropylacrylamide) microgels labeled with crown ether moieties. *J. Phys. Chem. B* **2010**, *114*, 12213–12220. [CrossRef] [PubMed]
28. Hu, J.; Liu, S. Responsive polymers for detection and sensing applications: Current status and future developments. *Macromolecules* **2010**, *43*, 8315–8330. [CrossRef]
29. Iwai, K.; Matsumura, Y.; Uchiyama, S.; de Silva, A.P. Development of fluorescent microgel thermometers based on thermo-responsive polymers and their modulation of sensitivity range. *J. Mater. Chem.* **2005**, *15*, 2796–2800. [CrossRef]
30. Bonnett, R.; McManus, K.A. Approaches to the stepwise synthesis of benzoporphyrins and phthalocyanines. Part 1. Synthesis of *opp*-dibenzoporphyrins (dibenzo [*g*,*q*] porphyrins). *J. Chem. Soc. Perkin Trans. 1* **1996**, 2461–2466. [CrossRef]
31. Diana, P.; Martorana, A.; Barraja, P.; Montalbano, A.; Carbone, A.; Cirrincione, G. Nucleophilic substitutions in the isoindole series as a valuable tool to synthesize derivatives with antitumor activity. *Tetrahedron* **2011**, *67*, 2072–2080. [CrossRef]
32. Chen, N.; Zhang, W.; Chen, S.; Wu, Q.; Yu, C.; Wei, Y.; Xu, Y.; Hao, E.; Jiao, L. Sterically protected N_2O-type benzopyrromethene boron complexes from boronic acids with intense red/near-infrared fluorescence. *Org. Lett.* **2017**, *19*, 2026–2029. [CrossRef] [PubMed]
33. Zhou, B.; Ma, P.; Chen, H.; Wang, C. Amine-accelerated manganese-catalyzed aromatic C–H conjugate addition to α,β-unsaturated carbonyls. *Chem. Commun.* **2014**, *50*, 14558–14561. [CrossRef] [PubMed]
34. Ding, Z.; Zheng, X.; Li, S.; Cao, X. Immobilization of cellulase onto a recyclable thermo-responsive polymer as bioconjugate. *J. Mol. Catal. B Enzym.* **2016**, *128*, 39–45. [CrossRef]

polymers

MDPI

Article

Influence of SiO_2/TiO_2 Nanocomposite on the Optoelectronic Properties of PFO/MEH-PPV-Based OLED Devices

Bandar Ali Al-Asbahi [1,2]

[1] Department of Physics & Astronomy, College of Science, King Saud University, Riyadh 11451, Saudi Arabia; alasbahibandar@gmail.com or balasbahi@ksu.edu.sa; Tel.: +966-114-676-620

[2] Research Chair in Laser Diagnosis of Cancers, College of Science, King Saud University, Riyadh 11451, Saudi Arabia

Received: 26 June 2018; Accepted: 18 July 2018; Published: 20 July 2018

Abstract: The influence of SiO_2/TiO_2 nanocomposites on the performance of organic light-emitting diodes (OLEDs) based on poly(9,9′-di-n-octylfluorenyl-2,7-diyl) (PFO) and various amounts of poly(2-methoxy-5-(2-ethyl-hexyloxy)-1,4-phenylene-vinylene) (MEH-PPV) was investigated. Prior to the fabrication of the OLEDs on indium-tin oxide (ITO) substrates, the hybrids of PFO/MEH-PPV, in the presence and absence of the SiO_2/TiO_2 nanocomposites, were prepared via the solution blending technique. Improvement of the performances of the devices in the presence of the SiO_2/TiO_2 nanocomposites was detected. The existence of the SiO_2/TiO_2 nanocomposites led to better charge carrier injection and, thus, a significant reduction in the turn-on voltage of the devices. The enhancement of MEH-PPV electroluminescence peaks in the hybrids in the presence of SiO_2/TiO_2 nanocomposites is not only a result of the Förster resonance energy transfer, but also of hole-electron recombination, which is of greater significance. Moreover, the existence of the SiO_2/TiO_2 nanocomposites led to a shift of the CIE chromaticity coordinates of the devices.

Keywords: organic light-emitting diodes (OLEDs); PFO/MEH-PPV hybrids; SiO_2/TiO_2 nanocomposite; optoelectronic properties

1. Introduction

There are many advantages that make conjugated polymers attractive as emissive materials in organic light-emitting diode (OLED) devices. Examples of these advantages are low operating voltage, low cost of fabrication, ease of processing and manufacturing, flexibility, capability to build devices with large-area and good solubility in common organic solvents and photothermal stability [1–4]. OLEDs with various colors can be achieved by several techniques, such as: (i) building bilayers in a tandem diode structure [5,6]; (ii) using a single polymer with multiple functional groups [7,8]; (iii) blending of conjugated polymers [9,10]; (iv) mixing polymers with nanostructured materials [11,12], quantum dots [13,14] and small phosphorescent [15,16] or fluorescent [8,17] molecules.

For display applications, polyfluorene (PF) and polyphenylene vinylene (PPV) derivatives have emerged as an attractive class of conjugated polymers because of their good processability and high charge carrier mobility coupled with efficient electroluminescence [18,19]. OLEDs based on hybrids of poly(9,9-di-n-octylfluorenyl-2,7-diyl) (PFO), which acts as a donor material and has a relatively large band gap, and poly(2-methoxy-5-(2-ethyl-hexyloxy)-1,4-phenylene-vinylene) (MEH-PPV), acting as an acceptor material, have attracted research attention [20,21]. By combining two conjugated polymers with contrasting electrical properties, OLEDs based on hybrids of conjugated polymers, as emissive layers, offer numerous advantageous features compared to single component layers, with luminance efficiency being improved by balancing electron and hole injection [22,23]. In spite of these features, hybrid

components require further precautions because a material that emits at a lower energy may also absorb in the range of the spectral emission of another material that emits at a higher energy [9,24], resulting in nonradiative energy transfer processes (Förster resonance energy transfer mechanism) [25,26]. The band intensity of the higher energy emission may be reduced or even eliminated when the nonradiative energy transfer processes is very efficient. Nevertheless, both an increase in the luminous performance and color tuning can be achieved concurrently by the careful choice of the concentration of the lower energy material [9] or by incorporation of suitable nanostructure materials in the hybrids [27,28]. Therefore, it is necessary to understand the emission dynamics of the hybrid materials to interpret the performance of the device.

In a recently-published report, it was demonstrated that the emission intensities of pure SiO_2 and TiO_2 nanoparticles can be enhanced by mixing them to form SiO_2/TiO_2 nanocomposites [29]. This enhancement in the emission intensities can be attributed to the presence of oxygen vacancies and the trapped electrons at the interface of SiO_2/TiO_2 nanocomposite thin films [29]. Therefore, it can be hypothesized that the incorporation of SiO_2/TiO_2 nanocomposites into the hybrids of PFO/MEH-PPV will lead to distinctive enhancement in OLED device performance.

In the current study, the enhancement of OLED performance based on a hybrid of donor (PFO) and various acceptor (MEH-PPV) amounts in the presence and absence of SiO_2/TiO_2 nanocomposites will be characterized in terms of electroluminescence spectra (EL), current-voltage measurements, turn-on voltage and color measurements.

2. Materials and Methods

Both poly(2-methoxy-5-(2-ethyl-hexyloxy)-1,4-phenylene-vinylene) (MEH-PPV, MW = 40,000 g/mol) and poly(9,9′-di-n-octylfluorenyl-2.7-diyl) (PFO, MW = 58,200 g/mol) were purchased from Sigma Aldrich, Saint Louis, MO, USA, and used as received without further purification. The $SiO_2/(20\%TiO_2)$ was prepared as described in a recent report [29]. Prior to fabrication of the thin films, all materials were dissolved in toluene, which was purchased from Fluka (Buchs, Switzerland).

The hybrids of PFO/MEH-PPV with various weight ratios of MEH-PPV (0.1, 0.5, 1.0, 5.0 and 10 wt.%), in the presence and absence of a fixed ratio of 10% $SiO_2/(20\%\ TiO_2)$ nanocomposites, were prepared by the solution blending technique. Before fabrication of the OLEDs, the indium-tin oxide (ITO) substrates (1.2 cm × 2 cm) were treated as reported in recent work [30]. Then, the prepared materials were employed as emissive layers by deposition onto ITO substrates using spin coating (2000 rpm for 20 s), followed by annealing at 120 °C in a vacuum oven to remove the solvent. To deposit an aluminum cathode, the ITO substrates with the emissive layers were moved to an electron beam chamber, where the deposition rate was 2 Å/min at a chamber pressure of 2.5×10^{-6} Pa. For all the OLED devices, the thickness of the fabricated Al cathode was 150 nm, and the active area of each device was 0.076 cm^2.

A Keithley 238 measurement system (Cleveland, OH, USA) was used for I-V measurements, and an HR2000 Ocean Optics Spectrometer (Metric Drive, FL, USA) was used for EL and color measurements.

3. Results and Discussion

3.1. Current-Voltage Measurements

Figure 1 shows the current-voltage (I-V) characteristics of pristine MEH-PPV and PFO/MEH-PPV hybrid-based OLED devices in both the absence and presence of SiO_2/TiO_2 nanocomposites. It can be observed that the current increased in the presence of the SiO_2/TiO_2 nanocomposites, while the turn-on voltage decreased, which demonstrated the improvement of the performance of the OLED device. The higher voltage (>10 V) led to enhancement of the light emissive layer resistivity, and then, the currents rapidly decreased. Nevertheless, the incorporation of SiO_2/TiO_2 nanocomposites resulted in an increase in the current of more than 40-times compared to that measured in their absence.

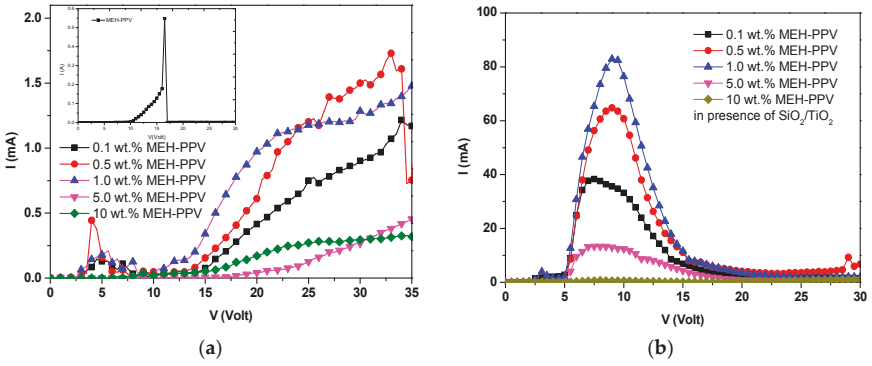

Figure 1. Current-voltage (I-V) measurements of the OLEDs based on hybrids of PFO/MEH-PPV. (**a**) In the absence of SiO_2/TiO_2 nanocomposites; (**b**) in the presence of SiO_2/TiO_2 nanocomposites. The inset shows the I-V curve of the OLEDs based on pristine MEH-PPV.

The higher current can be attributed to a reduction in the resistance and activation energy of the emissive layer [20,31]. The lower turn-on voltage of injection current in the presence of SiO_2/TiO_2 nanocomposites compared to their absence can be attributed to a better charge carrier injection [28,32].

However, the gradual reduction in current upon incrementing the MEH-PPV content (more than 1.0 wt.%) indicated the high resistivity of the devices. Once the content of MEH-PPV exceeded 1 wt.% within the hybrids, more holes and electrons were trapped, and consequently, lower current (and higher resistivity) was observed. This current reduction can be ascribed to MEH-PPV trapping both holes and electrons in PFO and instantaneously holding back their transport. Many reports demonstrate that lower current (and higher resistivity) may cause higher efficiency in exciton confinement and hole-electron recombination, which are crucial for better OLED device performance [33–35].

3.2. Electroluminescence Spectra

Figure 2 presents the EL spectra of OLED devices based on pristine MEH-PPV and PFO/(0.1, 0.5, 1.0, 5.0, 10 wt.%) MEH-PPV hybrids in the absence and presence of SiO_2/TiO_2 nanocomposites. The EL spectra of all OLED devices were dominated by the MEH-PPV emission with a lesser contribution from PFO emission at 440 nm. The profile does not match the behavior observed in the fluorescence spectra (not shown here), where the contribution from the emission of PFO was much more pronounced. In the case of SiO_2/TiO_2 nanocomposites being present, a significant observation in EL spectra can be detected when the content of MEH-PPV exceeded 0.1 wt.%. The peak assigned to the MEH-PPV (740 nm) was enhanced and red-shifted with increasing MEH-PPV content, whereas the peak intensity at 550 nm was decreased. By comparing the EL spectra with the fluorescence spectra in all the OLED devices, the relative EL intensity peak of the PFO diminished significantly upon incrementing the MEH-PPV content. Such significant differences in fluorescence and EL spectra for hybrids of polyfluorene derivatives have been reported [9,36,37]. Moreover, the significant difference between the fluorescence and EL spectra was strong evidence that Förster resonance energy transfer (FRET) was not the only mechanism occurring in the OLED devices during the EL measurements [5]. Whilst fluorescence spectra are created via various types of energy transfer processes or direct excitation, the EL spectra strongly depend on additional factors such as charge transport, charge injection from the electrodes, recombination processes and exciton generation.

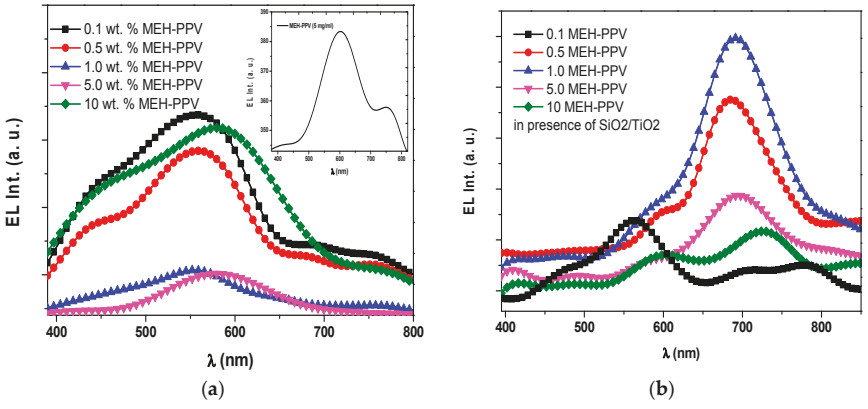

Figure 2. Electroluminescence (EL) spectra of the OLEDs based on PFO/MEH-PPV hybrids at applied voltages corresponding to maximum luminance. (**a**) In the absence of SiO_2/TiO_2 nanocomposites; (**b**) in the presence of SiO_2/TiO_2 nanocomposites. The inset shows the EL spectra of the OLEDs based on pristine MEH-PPV.

A cascade mechanism can be proposed for charge injection in the hybrids that prefers exciton formation in a lower energy gap polymer. The strong relative decrease of the PFO spectrum contribution to the EL spectra for all the OLED devices suggested that after the injection of holes and into the OLED device, either the recombination favorably happened in the MEH-PPV monomers or the excitons were primarily generated in this polymer phase.

Since the HOMO and LUMO of MEH-PPV lay within the range of those of PFO [20,38], it is possible that exciton formation in MEH-PPV occurred through the cascade mechanism. Moreover, due to the position of the MEH-PPV, there was a strong probability that it may have been acting as a trap for the charge carriers and then enhanced charge recombination in this phase. This probability was also evidenced significantly by the reduction in turn-on voltage, as discussed in the section above.

It can be concluded that in the EL spectra, the dominance of the peaks assigned to MEH-PPV in the hybrids was not only the result of FRET, but also arose from hole-electron recombination, which is of greater significance.

3.3. Color Measurements

Figure 3 shows the CIE coordinates of the PFO/0.5 wt.% MEH-PPV-based OLED device in the absence and presence of SiO_2/TiO_2 nanocomposites when the applied voltage was varied from 26–34 V. A blue-shift in the emitted color of the OLEDs was detected with increasing voltage due to phase separation. Many researchers have shown that mixing of two polymers with different emission and charge-transport properties leads to a shift in the color of emission of the OLEDs with varying operating voltage [39,40]. Submicrometer-sized domains with a range of compositions can be caused by phase separation. Subsequently, some of the excited states can be created in the polymer with the higher band gap and then lost to the lower band gap polymer by exciton transfer. The existence of the blue-shifted colors at higher voltages was due to the fact that the electron-hole injection in the higher energy gap required a higher field [40].

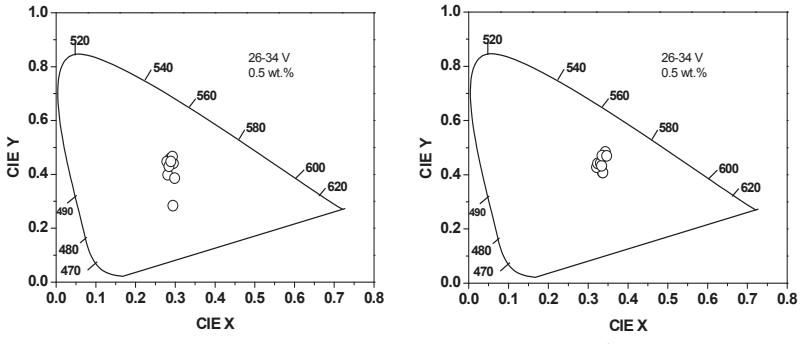

Figure 3. CIE coordinates of the OLEDs based on PFO/MEH-PPV hybrids when the applied voltage was increased from 26–34 V. (**a**) In the absence of SiO_2/TiO_2 nanocomposites, (**b**) in the presence of SiO_2/TiO_2 nanocomposites.

Table 1 summarizes the CIE chromaticity coordinates of the OLEDs based on PFO/MEH-PPV hybrids, with and without SiO_2/TiO_2 nanocomposites, at the applied voltage that caused the highest luminance. The slight shift in CIE coordinate values upon the increment of the MEH-PPV content confirmed that the produced color was stable and consistent with the EL spectra.

Table 1. The CIE chromaticity coordinates delivered by the OLEDs at the applied voltage, which caused highest luminance.

Acceptor Content in the Blend (wt. %)	In the Presence of SiO_2/TiO_2 Nanocomposite			In the Absence of SiO_2/TiO_2 Nanocomposite		
	CIE Coordinates		V (Volt)	CIE Coordinates		V (Volt)
	X	Y		X	Y	
0.1	0.313	0.395	31.5	0.294	0.284	36
0.5	0.337	0.447	30.5	0.298	0.305	34
1	0.333	0.413	29.5	0.285	0.37	39.5
5	0.318	0.279	34	0.374	0.346	34.5
10	0.307	0.226	39.5	0.319	0.243	38

Moreover, the existence of SiO_2/TiO_2 nanocomposites played a crucial role in shifting CIE chromaticity coordinates with respect to those in their absence. This finding is in agreement with the EL spectra (Figure 2), which were red-shifted in the presence of SiO_2/TiO_2 nanocomposites. This shifting can be attributed to efficient Förster resonance energy transfer in the presence of SiO_2/TiO_2 nanocomposites and also to the extension of hole-electron recombination zones [11].

4. Conclusions

The solution blending technique was successfully employed to prepare PFO/MEH-PPV hybrids, in the presence and absence of SiO_2/TiO_2 nanocomposites, which were used as the emissive layer in OLED devices. The incorporation of SiO_2/TiO_2 nanocomposites into the hybrids played a crucial role in enhancing the optoelectronic properties of the devices. The improvement of the performance of the OLED device is demonstrated by the significant reduction in turn-on voltage and the increase in the current of the devices in the presence of SiO_2/TiO_2 nanocomposites compared to those values in their absence. This improvement in the device performance started to reduce when the MEH-PPV content exceeded 1.0 wt.%, even in the presence of the SiO_2/TiO_2 nanocomposites, because MEH-PPV trapped both holes and electrons in the PFO. The shift of EL spectra and CIE coordinates upon addition

of SiO_2/TiO_2 nanocomposites illustrated efficient Förster resonance energy transfer and extension of the recombination zone for holes and electrons in the OLED devices.

Funding: This research received no external funding

Acknowledgments: The author is grateful to the Deanship of Scientific Research, King Saud University, for funding through Vice Deanship of Scientific Research Chairs.

Conflicts of Interest: The author declares that there is no conflict of interest regarding the publication of this paper.

References

1. Assaka, A.M.; Rodrigues, P.C.; De Oliveira, A.R.; Ding, L.; Hu, B.; Karasz, F.E.; Akcelrud, L. Novel fluorine containing polyfluorenes with efficient blue electroluminescence. *Polymer* **2004**, *45*, 7071–7081. [CrossRef]
2. Liu, S.P.; Chan, H.S.; Ng, S.C. Poly[2,7-(9,9-dihexylfluorene)-alt-pyridine] with donor-acceptor architectures: A new series of blue-light-emitting alternating copolymers. *J. Polym. Sci. A Polym. Chem.* **2004**, *42*, 4792–4801. [CrossRef]
3. Jokinen, K.; Bykov, A.; Sliz, R.; Remes, K.; Fabritius, T.; Myllylä, R. Luminescence and spectrum variations caused by thermal annealing in undoped and doped polyfluorene OLEDs. *Solid-State Electron.* **2015**, *103*, 184–189. [CrossRef]
4. Cuerva, C.; Campo, J.A.; Cano, M.; Arredondo, B.; Romero, B.; Otón, E.; Otón, J.M. Bis(pyridylpyrazolate)platinum(ii): A mechanochromic complex useful as a dopant for colour-tunable polymer OLEDs. *New J. Chem.* **2015**, *39*, 8467–8473. [CrossRef]
5. De Azevedo, D.; Freitas, J.N.; Domingues, R.A.; Faleiros, M.M.; Atvars, T.D.Z. Correlation between the PL and EL emissions of polyfluorene-based diodes using bilayers or polymer blends. *Synth. Met.* **2017**, *233*, 28–34. [CrossRef]
6. Zhao, D.; Liu, H.; Miao, Y.; Wang, H.; Zhao, B.; Hao, Y.; Zhu, F.; Xu, B. A red tandem organic light-emitting diode based on organic photovoltaic-type charge generation layer. *Org. Electron.* **2016**, *32*, 1–6. [CrossRef]
7. Nicolai, H.T.; Hof, A.; Blom, P.W. Device Physics of White Polymer Light-Emitting Diodes. *Adv. Funct. Mater.* **2012**, *22*, 2040–2047. [CrossRef]
8. Reineke, S.; Thomschke, M.; Lüssem, B.; Leo, K. White organic light-emitting diodes: Status and perspective. *Rev. Mod. Phys.* **2013**, *85*, 1245. [CrossRef]
9. Quites, F.J.N.; Faria, G.R.C.; Germino, J.C.; Atvars, T.D.Z. Tuning emission colors from blue to green in polymeric light-emitting diodes fabricated using polyfluorene blends. *J. Polym. Chem.* **2014**, *118*, 10380–10390. [CrossRef] [PubMed]
10. Baek, S.J.; Chang, H.J. Fabrication and characterization of white polymer light emitting diodes using PFO: MDMO-PPV. *J. Nanosci. Nanotechnol.* **2012**, *12*, 3606–3610. [CrossRef] [PubMed]
11. Al-Asbahi, B.A.; Jumali, M.H.H.; Yap, C.C.; Salleh, M.M. Influence of TiO_2 nanoparticles on enhancement of optoelectronic properties of PFO-based light emitting diode. *J. Nanomater.* **2013**, *2013*, 561534. [CrossRef]
12. Chen, D.; Liang, J.; Pei, Q. Flexible and stretchable electrodes for next generation polymer electronics: A review. *Sci. China Chem.* **2016**, *59*, 659–671. [CrossRef]
13. Borriello, C.; Prontera, C.; Mansour, S.A.; Aprano, S.; Maglione, M.; Bruno, A.; Luccio, T.D.; Minarini, C. Optoelectronic properties of OLEDs based on CdSe/ZnS quantum dots and F8BT. *Phys. Status Solidi C* **2015**, *12*, 1416–1420. [CrossRef]
14. Kang, B.-H.; You, T.-Y.; Yeom, S.-H.; Kim, K.-J.; Kim, S.-H.; Lee, S.-W.; Yuan, H.; Kwon, D.-H.; Kang, S.-W. Highly efficient white light-emitting diodes based on quantum dots and polymer interface. *IEEE Photon. Technol. Lett.* **2012**, *24*, 1594–1596. [CrossRef]
15. Ikawa, S.; Yagi, S.; Maeda, T.; Nakazumi, H. White polymer light-emitting diodes co-doped with phosphorescent iridium complexes bearing the same cyclometalated ligand. *Phys. Status Solidi C* **2012**, *9*, 2553–2556. [CrossRef]
16. Ouyang, X.; Li, X.-L.; Bai, Y.; Mi, D.; Ge, Z.; Su, S.-J. Highly-efficient hybrid white organic light-emitting diodes based on a high radiative exciton ratio deep-blue emitter with improved concentration of phosphorescent dopant. *RSC Adv.* **2015**, *5*, 32298–32306. [CrossRef]
17. Derue, L.; Olivier, S.; Tondelier, D.; Maindron, T.; Geffroy, B.; Ishow, E. All-solution-processed organic light-emitting diodes based on photostable photo-cross-linkable fluorescent small molecules. *ACS Appl. Mater. Interfaces* **2016**, *8*, 16207–16217. [CrossRef] [PubMed]
18. Amorim, C.; Cavallari, M.; Santos, G.; Fonseca, F.J.; Andrade, A.; Mergulhão, S. Determination of carrier mobility in MEH-PPV thin-films by stationary and transient current techniques. *J. Non-Cryst. Solids.* **2012**, *358*, 484–491. [CrossRef]

19. Scherf, U.; List, E.J. Semiconducting polyfluorenes—Towards reliable structure–property relationships. *Adv. Mater.* **2002**, *14*, 477–487. [CrossRef]
20. Bajpai, M.; Srivastava, R.; Kamalasanan, M.; Tiwari, R.; Chand, S. Charge transport and microstructure in PFO: MEH-PPV polymer blend thin films. *Synth. Met.* **2010**, *160*, 1740–1744. [CrossRef]
21. Chen, H.C.; Wang, C.T.; Liu, C.L.; Liu, Y.C.; Chen, W.C. Full color light-emitting electrospun nanofibers prepared from PFO/MEH-PPV/PMMA ternary blends. *J. Polym. Sci. B Polym. Phys.* **2009**, *47*, 463–470. [CrossRef]
22. Buckley, A.; Rahn, M.; Hill, J.; Cabanillas-Gonzalez, J.; Fox, A.; Bradley, D. Energy transfer dynamics in polyfluorene-based polymer blends. *Chem. Phys. Lett.* **2001**, *339*, 331–336. [CrossRef]
23. Grice, A.; Bradley, D.; Bernius, M.; Inbasekaran, M.; Wu, W.; Woo, E. High brightness and efficiency blue light-emitting polymer diodes. *Appl. Phys. Lett.* **1998**, *73*, 629–631. [CrossRef]
24. Sahoo, H. Förster resonance energy transfer–A spectroscopic nanoruler: Principle and applications. *J. Photochem. Photobiol. C* **2011**, *12*, 20–30. [CrossRef]
25. Főrster, T. 10th Spiers Memorial Lecture. Transfer mechanisms of electronic excitation. *Discuss. Faraday Soc.* **1959**, *27*, 7–17. [CrossRef]
26. Gupta, V.; Bharti, V.; Kumar, M.; Chand, S.; Heeger, A.J. Polymer–Polymer Förster Resonance Energy Transfer Significantly Boosts the Power Conversion Efficiency of Bulk-Heterojunction Solar Cells. *Adv. Mater.* **2015**, *27*, 4398–4404. [CrossRef] [PubMed]
27. Al-Asbahi, B.A.; Jumali, M.H.H.; Yap, C.C.; Salleh, M.M.; AlSalhi, M.S. Inhibition of dark quenching by TiO2 nanoparticles content in novel PFO/fluorol 7GA hybrid: A new role to improve OLED performance. *Chem. Phys. Lett.* **2013**, *570*, 109–112. [CrossRef]
28. Al-Asbahi, B.A.; Haji Jumali, M.H.; AlSalhi, M.S. Enhanced optoelectronic properties of PFO/Fluorol 7GA hybrid light emitting diodes via additions of TiO_2 nanoparticles. *Polymers* **2016**, *8*, 334. [CrossRef]
29. Al-Asbahi, B.A. Influence of anatase titania nanoparticles content on optical and structural properties of amorphous silica. *Mater. Res. Bull.* **2017**, *89*, 286–291. [CrossRef]
30. Al-Asbahi, B.A. Energy transfer mechanism and optoelectronic properties of (PFO/TiO_2)/Fluorol 7GA nanocomposite thin films. *Opt. Mater.* **2017**, *72*, 644–649. [CrossRef]
31. Chang, C.-C.; Hsieh, M.-T.; Chen, J.-F.; Hwang, S.-W.; Chen, C.H. Highly power efficient organic light-emitting diodes with ap-doping layer. *Appl. Phys. Lett.* **2006**, *89*, 253504. [CrossRef]
32. Jumali, M.H.H.; Al-Asbahi, B.A.; Yap, C.C.; Salleh, M.M.; Alsalhi, M.S. Optoelectronic property enhancement of conjugated polymer in poly (9, 9′-di-n-octylfluorenyl-2.7-diyl)/titania nanocomposites. *Thin Solid Films* **2012**, *524*, 257–262. [CrossRef]
33. Zhang, Q.; Chambers, D.K.; Selmic, S. Polymer Light-Emitting Diodes Based on Poly [9, 9-di-(2′-ethylhexyl) fluorenyl-2.7-diyl]. *J. Nanoelectron. Optoe.* **2006**, *1*, 219–223. [CrossRef]
34. Hsieh, S.-N.; Kuo, T.-Y.; Hsu, P.-C.; Wen, T.-C.; Guo, T.-F. Study of polymer blends on polymer light-emitting diodes. *Mater. Chem. Phys.* **2007**, *106*, 70–73. [CrossRef]
35. Al-Asbahi, B.A.; Jumali, M.H.H.; Yap, C.C.; Flaifel, M.H.; Salleh, M.M. Photophysical properties and energy transfer mechanism of PFO/Fluorol 7GA hybrid thin films. *J. Lumin.* **2013**, *142*, 57–65. [CrossRef]
36. De Deus, J.F.; Faria, G.C.; Iamazaki, E.T.; Faria, R.M.; Atvars, T.D.; Akcelrud, L. Polyfluorene based blends for white light emission. *Org. Electron.* **2011**, *12*, 1493–1504. [CrossRef]
37. Voigt, M.; Chappell, J.; Rowson, T.; Cadby, A.; Geoghegan, M.; Jones, R.A.; Lidzey, D.G. The interplay between the optical and electronic properties of light-emitting-diode applicable conjugated polymer blends and their phase-separated morphology. *Org. Electron.* **2005**, *6*, 35–45. [CrossRef]
38. Li, Y.; Cao, Y.; Gao, J.; Wang, D.; Yu, G.; Heeger, A.J. Electrochemical properties of luminescent polymers and polymer light-emitting electrochemical cells. *Synth. Met.* **1999**, *99*, 243–248. [CrossRef]
39. Berggren, M.; Inganäs, O.; Gustafsson, G.; Andersson, M.R.; Hjertberg, T.; Wennerström, O. Controlling colour by voltage in polymer light emitting diodes. *Synth. Met.* **1995**, *71*, 2185–2186. [CrossRef]
40. Berggren, M.; Inganäs, O.; Gustafsson, G.; Rasmusson, J.; Andersson, M.R.; Hjertberg, T.; Wennerström, O. Light-emitting diodes with variable colours from polymer blends. *Nature* **1994**, *372*, 444–446. [CrossRef]

polymers

MDPI

Review

In Situ Synthesis of Hybrid Inorganic–Polymer Nanocomposites

Mohammed M. Adnan [1], Antoine R. M. Dalod [2], Mustafa H. Balci [3], Julia Glaum [1] and Mari-Ann Einarsrud [1,*]

[1] Department of Materials Science and Engineering, Norwegian University of Science and Technology, 7491 Trondheim, Norway; mohammed.m.adnan@ntnu.no (M.M.A.); julia.glaum@ntnu.no (J.G.)
[2] poLight ASA, Kongeveien 77, 3188 Horten, Norway; antoine.dalod@polight.com
[3] Department of Physics, Norwegian University of Science and Technology, 7491 Trondheim, Norway; mustafa.h.balci@ntnu.no
* Correspondence: mari-ann.einarsrud@ntnu.no; Tel.: +47-7359-4002

Received: 14 September 2018; Accepted: 9 October 2018; Published: 11 October 2018

Abstract: Hybrid inorganic–polymer nanocomposites can be employed in diverse applications due to the potential combination of desired properties from both the organic and inorganic components. The use of novel bottom–up in situ synthesis methods for the fabrication of these nanocomposites is advantageous compared to top–down ex situ mixing methods, as it offers increased control over the structure and properties of the material. In this review, the focus will be on the application of the sol–gel process for the synthesis of inorganic oxide nanoparticles in epoxy and polysiloxane matrices. The effect of the synthesis conditions and the reactants used on the inorganic structures formed, the interactions between the polymer chains and the inorganic nanoparticles, and the resulting properties of the nanocomposites are appraised from several studies over the last two decades. Lastly, alternative in situ techniques and the applications of various polymer–inorganic oxide nanocomposites are briefly discussed.

Keywords: nano-hybrids; nanocomposites; sol–gel; in situ synthesis; metal oxides

1. Introduction

Hybrid inorganic–polymer materials have been studied extensively over the last 30 years due to the unique combination of properties that can arise, especially when the inorganic domains possess a dimension in the nanoscale (below 100 nm), forming a nanocomposite [1–6]. The potential combination of the advantages of inorganic materials (e.g., high hardness, high thermal stability, high refractive index, chemical stability, etc.) with those of organic polymers (e.g., processability, flexibility, low weight, etc.) can enable a wide range of applications for these nanocomposites. These range from common plastics reinforcement to abrasion resistant coatings [2,7], flame-retardant materials [8,9], catalysis [10,11], memory devices [12], integral capacitors [13], optical devices [14,15], electrical insulation in microelectronics and nanodielectrics [16–18], fuel cells [19], etc. The defining feature of nanocomposites is the larger interfacial area of the nanoscale inorganic fillers, in comparison to traditional composites. This larger interfacial area results in a considerable volume of interfacial polymer, for a lower filler content, with properties that are unique from the bulk polymer [2,20,21]. The emergence of these new properties can be attributed in part to the interactions between the organic and inorganic components at the interface. Hybrid materials can be divided into two classes, based on the nature and strength of these interactions: In Class I hybrids, there are only weak bonds (e.g., van der Waals, or hydrogen bonds) between the organic and inorganic components, while in Class II hybrids, strong chemical bonds are prevalent at the interfaces [4,7,22]. These interactions are correlated to the size, shape, size distribution, and dispersion state of the nanoparticle fillers.

However, nanoscale materials have a tendency to agglomerate in order to minimize the high surface energy [23,24]. The agglomeration of nanoparticles will reduce the interfacial area and the interactions with the polymers in nanocomposites, thereby negating the potential benefits of using nanoscale fillers. In some cases, agglomeration may even result in the deterioration of material properties and act as defects in the system.

One of the primary challenges in the synthesis of nanocomposites is to ensure a homogeneous dispersion of the inorganic fillers in the polymer matrix. In standard top–down ex situ methods, nanoparticles are pre-synthesized and then mixed into the polymer (blending or intercalation) or a monomer (followed by in situ polymerization) [15,25]. Any agglomerates formed during the synthesis of these nanoparticles (e.g., during flame pyrolysis or precipitation) are difficult to break up during this mixing due to the viscosity of the polymer [26,27]. The resulting inhomogeneity in the nanocomposites can deteriorate the properties of the material. Surface functionalization of the nanoparticles may help to prevent agglomeration of the nanoparticles, or reduce any phase separation due to the incompatibility between the hydrophilic inorganic fillers and the hydrophobic polymer matrix [23,26]. The surface modification can be done using either physical interactions (e.g., surfactants or adsorbed macromolecules) [2,28,29] or chemical interactions (e.g., silane coupling agents or grafted ligands), resulting in Class I and Class II hybrid materials, respectively. However, even with the use of surface-functionalized nanoparticles, it is challenging to achieve a homogeneous dispersion of non-agglomerated nanoparticles in the polymer matrix through conventional ex situ mixing techniques.

An alternative approach to achieve a homogeneous dispersion is the in situ synthesis of inorganic nanoparticles in the polymer matrix, using techniques such as sol–gel chemistry, reverse microemulsion, or hydrothermal/solvothermal synthesis [2,3,7,15,22–24,26,30,31]. These methods typically involve the mixing of precursors with a non-reactive solvent and the monomer/polymer, where the reaction of the precursors initiates the synthesis of particles either before or during polymerization [23,27]. This bottom–up approach to the preparation of nanocomposites can enable increased control over the structure and properties of the nanocomposite by incorporating particle generation, surface modification, and integration into the polymer matrix in one process. Since the nanoparticles are nucleated and grown inside the polymer matrix, the passivating effect of the polymer chain functional groups on the nanoparticles can control particle size and reduce agglomeration [15]. One limitation of such an approach, however, is that the unreacted precursors or byproducts of the in situ reactions may alter the properties of the nanocomposite.

Due to the numerous works published on the in situ preparation of many different nanocomposites, this article aims to familiarize the reader with the sol–gel method for in situ synthesis of inorganic oxides in polymers. SiO_2 (silica) and TiO_2 (titania) are two of the most common inorganic oxide nanofillers used in hybrid materials, and are featured more heavily in this work. A brief synopsis of several other in situ techniques for fabrication of nanocomposites is also provided at the end. In addition to the development of the techniques and strategies used, a discussion of the properties and relevant applications for such nanocomposites is included. For polymer systems, epoxy resins and poly(dimethylsiloxane) are focused on in this review, due to their versatility in multiple areas of application, such as in laminates, structural composites, electrical insulation, and coatings for epoxy [32], and in coatings, optical devices (e.g., LED encapsulation and optical waveguides) and bioactive materials for polydimethylsiloxane (PDMS) [14,33].

2. The Chemistry of In Situ Reactions

2.1. Sol–Gel Process and the Formation of the Inorganic Network

Sol–gel reactions have been used extensively in the preparation of inorganic materials (e.g., glasses and ceramics), and is one of the most common routes for preparing amorphous hybrid networks in situ at low temperatures [2,3,15,27,30,34]. The sol–gel process is well described and consists of two steps: First, the hydrolysis of a molecular precursor (typically a metal alkoxide), followed by a

polycondensation reaction to form the inorganic network (Figure 1). Both reactions can also occur simultaneously once hydrolysis has been initiated. The reactions can be summarized by the following equation, where M represents a metal and R an alkyl group, and X represents H during hydrolysis and M during condensation [35]:

$$M(OR)_n + mXOH \rightarrow [M(OR)_{n-m}\ (OX)_m] + mROH \quad (1)$$

This method is of particular interest in the in situ formation of an inorganic network (e.g., SiO_2, TiO_2, ZnO, Al_2O_3, ZrO_2, etc.) in a polymer matrix, via the swelling of a polymeric host by a solution containing the precursors (e.g., tetraethylorthosilicate (TEOS) and titanium (IV) isopropoxide (TIP)), followed by promotion of the sol–gel reactions [27]. The solvent used is an important parameter for controlling the polymer solubility and preventing liquid–liquid phase separation. Commonly used solvents include alcohols, tetrahydrofuran (THF), and *N*,*N*-dimethylformamide (DMF) [2,22,36].

Several parameters can be adjusted to control the size and morphology of the materials formed by sol–gel processes. The reactivity of the metal alkoxide (which is affected by the type of metal and the steric hindrance of the alkoxy groups) will affect the rate of the hydrolysis reaction, which in turn affects the structure of the metal–oxo networks that form. The hydrolysis is faster when the metal cation has high electrophilicity and high degree of unsaturation ($N - Z$, where N is the coordination number and Z is the oxidation state of the metal) [4]. Transition metal alkoxides (e.g., $M(OR)_4$, where M = Ti, Sn, Zr, Ce, etc.) are therefore typically very reactive (since $N - Z > 0$ typically) [4,22,27], and hydrolyze very easily in the presence of even a small amount of moisture. As a result, inhibitors may be required to prevent precipitates from forming before the condensation reactions can occur, such as chelating agents that stabilize the alkoxide and reduce reactivity (e.g., by increasing steric hindrance). Silicon alkoxides, on the other hand, are less reactive due to their low electrophilicity [4] and require a catalyst to increase the hydrolysis reaction rate [2,22,27]. Acid catalysis promotes the hydrolysis reaction, resulting in the formation of open structures with low fractal dimension [27,30]. Base catalysis, meanwhile, promotes the condensation reaction, leading to colloidal particulate structures [27,30]. Figure 2 shows how pH affects the polymerization behavior of silicon alkoxides.

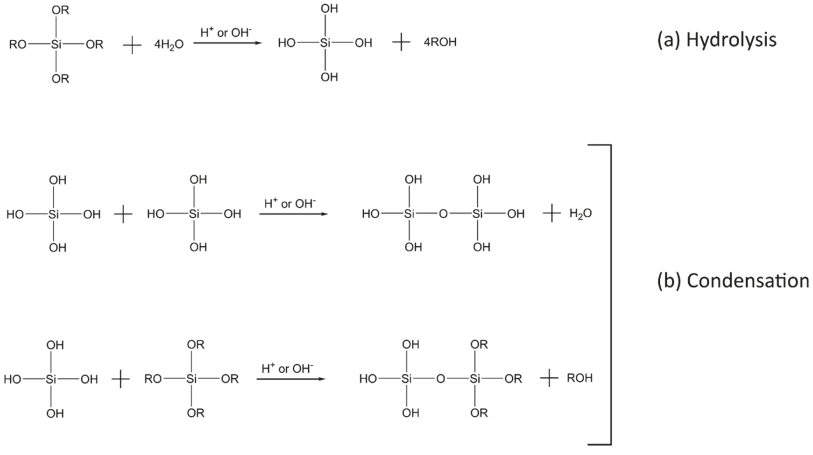

Figure 1. The (**a**) hydrolysis; and (**b**) condensation reactions of a silicon alkoxide precursor ($Si(OR)_4$) in a sol–gel process.

Larger alkoxy groups have greater steric hindrance, resulting in a stabilizing effect that reduces the reactivity of the metal alkoxide. The kinetics of the hydrolysis and condensation reactions are also affected by the temperature, ratio of water to metal alkoxide, type of solvent, etc. [2,30,34]. Control of

the reactivity of metal alkoxides is particularly important when two or more of them must be combined in one polymer system (e.g., in the preparation of nanocomposites with several inorganic oxides as filler), in order to prevent phase separation or precipitation.

In addition, the sol–gel process can also be non-hydrolytic, that is, the process is solvent-free and does not require a water catalyst. The non-hydrolytic sol–gel (NHSG) route usually involves a reaction between a metal precursor and an oxygen donor (e.g., alkoxide, ether, alcohol, carboxylates, etc.) under non-aqueous conditions to form the inorganic oxide [37,38]. The reaction proceeds via a ligand exchange mechanism that is catalyzed by Lewis acids [39]. Due to the difference in reaction mechanism, the reactivity differences for different metals seen earlier in the hydrolytic process may not be the same in this case. The NHSG route offers an alternative in cases where the conventional hydrolytic sol–gel synthesis routes may not be optimal. It is easier to control, as the reactions are slower than for hydrolytic sol–gel [38,39]. Some common reaction pathways in NHSG methods include alkyl halide elimination (reaction between metal chloride and metal alkoxide), ester elimination (reaction between metal alkoxides and acetates), and ether elimination (condensation reaction between metal alkoxides) [38].

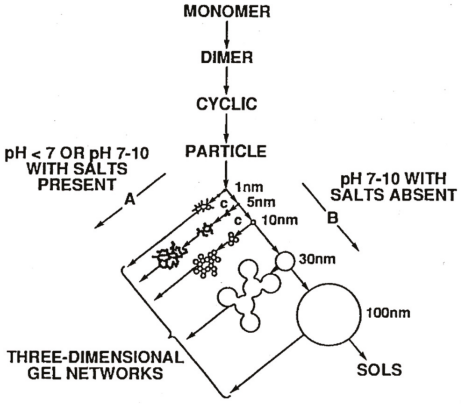

Figure 2. The polymerization behavior of aqueous silica from silicon alkoxide precursors in basic and acidic solutions with and without flocculating salts. Reproduced with permission from Reference [40].

2.2. Formation of the Organic Network and Crosslinks between the Organic and Inorganic Components in Hybrids

The in situ formation of nanoparticles or an inorganic network via sol–gel methods may occur either in the presence of a preformed polymer (that is already polymerized), or by simultaneous formation of both the organic and inorganic networks, forming an interpenetrating polymer network (IPN) [2]. While the inorganic network in hybrids is formed via hydrolysis and condensation reactions, the organic network is formed via polymerization reactions between the monomers, forming macromolecules with repeating units [41,42]. The polymers may be classified into two basic types: Addition and condensation polymers.

Figure 3 shows example reactions in the formation of these two types of polymers. Addition polymers are formed by the linking of monomers without the formation of any byproducts. Addition reactions may be initiated by free radicals, and propagated by the chain radicals (as shown in Figure 3a). Reactions between radicals or radical transfer reactions can terminate radical polymerization. Alternatively, Ziegler–Natta catalysts may also be used in the synthesis of addition polymers [42]. Polyethylene and polypropylene are common examples of addition polymers. Unlike addition polymers, condensation polymers are typically synthesized using difunctional monomers, or different monomers with end groups that can react with each other to form the chain. As a result, a small molecular byproduct (e.g., water, methanol, etc.) may also form (as shown in Figure 3b).

Branches or crosslinks can form if a trifunctional monomer is present in addition. Polyamides and polyesters are two classes of polymers that form via condensation reactions.

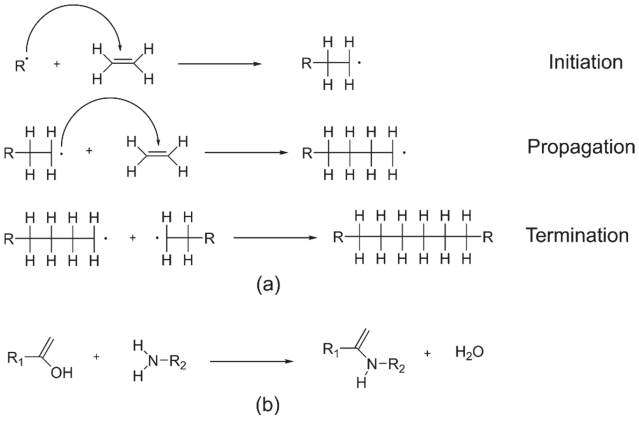

Figure 3. Reactions for the formation of (**a**) addition polymers (showing radical polymerization with one of the possible termination steps); and (**b**) condensation polymers. R· represents a free radical, while R_1 and R_2 represent two different organic groups.

The properties of nanocomposites prepared by the sol–gel process are affected by the size of the particles formed, as well as the interactions between the inorganic and organic components. Strong chemical bonds between the continuous and dispersed phases resulting in the formation of Class II hybrid materials are preferred, since the presence of these bonds will facilitate dispersion and reduce phase separation. However, for these bonds to form, there must be suitable functional groups available on the polymer chains. In some cases, there may be competition for the bonds to form, as these functional groups generally also react with functional groups on other monomers in order to increase the chain length. In other cases, coupling agents may be used to form bridges between the inorganic domains with either the polymer chains or monomer units when there are no suitable functional groups available for bond formation with the inorganic components.

Silane coupling agents (SCAs) are one such example and are often used for modifying the surfaces of filler particles in nanocomposites to increase compatibility between the organic and inorganic components [28,29,43]. These are organosilicon compounds with two different functional groups, typically with the formula $X(CH_2)_nSiR_3$, where X is a functional organic group and R is a hydrolysable group [29,43,44]. The organic group reacts with the polymer matrix and the hydrolysable group reacts with the surface of the inorganic nanoparticles. Commonly used SCAs include 3-aminopropyltriethoxysilane (APTES), 3-glycidyloxypropyltrimethoxysilane (GPTMS), 3-isocyanatopropyltriethoxysilane (IPTES), *n*-decyltriethoxysilane (DTES), and methacryloxypropyltrimethoxysilane (MPTMS) [28,29,45–51]. The SCAs may be introduced to the nanocomposites via several paths, including copolymerization with the monomers and reaction with the preformed polymer or the silicon precursor (or a mixture of the two). Modification of the preformed polymer by the SCA before the sol–gel process is the frequently used approach [2,48–52], allowing polycondensation reactions between the trialkoxysilyl groups on the SCA bonded to the polymer and the metal alkoxide precursor, forming a covalent bond between the two phases.

In addition to SCAs, other coupling agents include carboxylic acids (e.g., oleic acid, tetrafluorobenzoic acid, etc.), polymer/copolymer chains (e.g., poly(ethylene glycol), polymethyl methacrylate, poly(glycidyl methacrylate), etc.), and organophosphorus molecules (e.g., phosphonic acids, aminophenyl phosphate, etc.) [2,28,29,53].

3. Nanocomposite Fabrication via Sol–Gel Processes

A comprehensive overview over all the inorganic–polymer nanocomposites prepared by an in situ sol–gel synthesis is beyond the scope of this review. Therefore, selected examples on the development of epoxy and polydimethylsiloxane (PDMS) nanocomposites prepared using sol–gel processes will be presented. The inorganic components of the nanocomposites from these examples are primarily transition metal oxides (e.g., TiO_2, ZrO_2, etc.) or silica (SiO_2). Table 1 shows a general overview of the various syntheses of nanoparticles in situ in the two different polymer systems. It should be noted that in some of the works referenced, the authors do not specify the inorganic component in the hybrids as nanoparticles, but instead as nanodomains. This is most likely because the inorganic networks formed are so small and polymer-like that they may not qualify as particles with a defined shape (e.g., spheres). This is more prevalent in the works on PDMS nanocomposites, where the hybrids are called, for example, M–O–PDMS (where M is the transition metal) instead of PDMS–M_xO_y nanocomposites. In Table 1, the inorganic components specified are based on the assumption that these inorganic networks will form nanoparticles if they grow to an appreciable size. The chemistry behind the synthesis routes, the effect of various parameters on the inorganic structures formed, as well as the resulting properties of the nanocomposites are reviewed afterwards.

Table 1. Selected examples of the precursors, surface modification and solvents used in the in situ synthesis of metal oxide nanoparticles via sol–gel processes in epoxy and polydimethylsiloxane (PDMS) nanocomposites.

Polymer System	Inorganic Component	Inorganic Precursor	Surface Modification	Solvent	Reference
Epoxy [1]	SiO_2	TEOS	-	-	[54]
			-	Isopropanol	[55–57]
			APTES	Ethanol	[38]
				-	[52]
			GPTMS	-	[51]
			IPTES	-	[48]
				Ethanol	[49]
		TEOS, DPTEOS [2]		-	[58]
		APTES	APTES	DMF	[36]
	SiO_2, TiO_2	TEOS, TEOT [3]	GPTMS	Acetylacetone	[59]
	TiO_2	TIP		-	[60]
		TBO [4]	TCTMTEA [5]	Anhydrous THF	[61]
	SiO_2	TEOS	-	Ionic liquids [6]	[62–64]
PDMS	SiO_2, TiO_2	TEOS, TIP	-	THF and isopropanol	[65]
	TiO_2	TIP	-	Ethanol	[66]
			-	Isopropanol	[14,67]
	SiO_2, TiO_2	TIP, TEOS, MTES [7]	-		[68]
	M_xO_y [8]	$M(OR)_n$ [8]	-	Ethanol	[69–71]
	ZrO_2, TaO_2	ZBO, TE [9]	-	2-ethoxyethanol	[72]
	SiO_2–TiO_2/ZrO_2	TEOS, TIP, ZP [10]	-	Isopropanol	[73]
	M_xO_y [11]	$M(OR)_n$ [11]	-	Ethanol and isopropanol	[74]
	SiO_2	TEOS	-	-	[5,75–80]
			DMDEOS [12]	-	[77]

[1] Molecular weight of the amine curing agent varies (between 230–1970); [2] Diethylphosphatoethyltriethoxysilane; [3] Tetraethylorthotitanate; [4] Titanium (IV) butoxide; [5] Triethoxysilane-capped trimercaptothioethylamine (TMTEA). Acts as both coupling and curing agent; [6] $CH_2CO_2HMImCl$, $C_3H_6CO_2HMImCl$, and$C_7O_3MImMeS$; [7] Methyltriethoxysilane; [8] M = Al, Ti, Ta, Zr, Nb; [9] Zirconium (IV) *n*-butoxide (ZBO), Tantalum (IV) ethoxide (TE); [10] Zirconium propoxide; [11] M = Al, Ge, Sn, Ti, Zr, Nb, Ta; [12] Dimethyldiethoxysilane.

3.1. Epoxy Nanocomposites

Epoxy is a thermosetting polymer and an excellent choice for high performance composite materials when reinforced with SiO_2 due to the resulting strength, toughness, good chemical and heat resistance, and high thermal stability [48,49,51]. Typically, epoxy composites are cured via a condensation reaction with an amine- or anhydride-based curing agent, forming a copolymer. Epoxy nanocomposites containing titania (TiO_2) are also of interest due to the photocatalytic properties imparted to the polymer by the TiO_2, as well as increases in the refractive index [15,60,61]. Due to the challenges with achieving a homogeneous dispersion of nanoparticles when employing a traditional ex situ blending route, there has been an increased focus on the use of in situ sol–gel techniques instead for nanocomposite synthesis. Diglycidyl ether of bisphenol A (DGEBA) is commonly used as the monomer, and poly(oxypropylene diamine), also known as Jeffamine, is often used as the curing agent in these nanocomposites.

For synthesizing nanoparticles in situ in epoxy, most researchers have attempted either a one-step or a two-step procedure, as shown in Figure 4. In the one-step procedure, the precursors and reaction components (epoxy resin, coupling agent, inorganic oxide precursor, curing agent, solvent, catalysts, etc.) are all mixed simultaneously and reacted, before being cast into bulk films. There are several variations of the two-step procedure. In a '*simultaneous*' two-step procedure, the inorganic oxide precursor (TEOS, TIP, etc.) is pre-hydrolyzed in the first step using a catalyst (e.g., *p*-toluenesulfonic acid monohydrate (TSA) or dibutyltin dilaurate (DBTDL)). The second step involves the polymerization of the organic components and the formation of the oxide network simultaneously when the pre-hydrolyzed precursor is mixed with the monomer and curing agent. In a '*sequential*' two-step procedure, the epoxy resin is cured in the first step, before being swollen by the alkoxide, water, catalysts, etc. in the second step. The inorganic oxide network in this case forms in a preformed organic network, as the epoxy is already cured. Finally, there is also the '*chronological*' two-step procedure where an SCA is first added to the epoxy to form modified (silanized) monomer chains. In the next step, the inorganic precursors (alkoxide, water, catalyst, etc.) are added sequentially to form the oxide network before the nanocomposite is cured. Since the coupling agents provide a chemical bond between the organic and inorganic networks, this procedure results in the formation of Class II hybrids. One of the advantages with a two-step procedure is that it offers more control over specific reactions, depending on which variation of the procedure is used, since not all of the reactions are occurring simultaneously, as in the one-step procedure.

3.1.1. Effect of Synthesis Procedure and pH on the Structure and Morphology of Nanocomposites

Matějka et al. prepared epoxy–SiO_2 nanocomposites using a one-step procedure [55–57], a simultaneous two-step procedure [55–57], and a sequential two-step procedure [56,57]. Differences in the structure of the inorganic domains arose based on whether the reaction was carried out in a one-step or two-step procedure. In the one-step procedure, large SiO_2 aggregates (100–300 nm) were observed through scanning electron microscopy (SEM) [57], which was attributed to the reaction being catalyzed by the amine curing agent (a base) due to its molar excess over the acidic catalyst (TSA). Base catalysis promotes the condensation reaction and the formation of colloidal (spherical) particles. Small angle X-ray scattering (SAXS) experiments revealed compact silica structures with high fractal dimension (D_m = 2.7) [55,57]. For hybrids prepared using the two-step simultaneous process, smaller SiO_2 structures were observed (50–100 nm) with a lower fractal dimension (D_m = 1.7), indicating a more open SiO_2 cluster due to the TEOS being pre-hydrolyzed by an acid [55–57]. The choice of catalyst can also affect the morphology—DBTDL was seen to be less effective at hydrolyzing TEOS than TSA, resulting in more compact SiO_2 clusters (D_m = 2.5–2.7) [56,57]. In the two-step sequential process, the distribution of the inorganic phase was not uniform, with a higher SiO_2 concentration on the surface. This was due to the inhomogeneous swelling of the epoxy resin by the TEOS. However, the SiO_2 domains were small (10 nm) and formed an open structure (D_m = 1.9–2.2) due to the acid catalysis of the TEOS hydrolysis [57]. Dynamic mechanical analysis (DMA) showed a larger shear

storage modulus for the in situ epoxy-SiO_2 nanocomposites compared to pure epoxy [57]. However, this reinforcement was dependent on the procedure used for preparation. Acid pre-hydrolysis of TEOS resulted in higher modulus in the nanocomposites, compared to those prepared without pre-hydrolysis (e.g., in the one-step procedure or when the TEOS was pre-hydrolyzed by pH neutral DBTDL catalyst). The sequential two-step procedure with pre-hydrolyzed TEOS possessed the largest storage modulus. In addition, the loss factor (tan δ) also decreased and broadened with the inclusion of SiO_2 in epoxy, with the sequential two-step prepared hybrid showing the largest decrease. The observed reinforcement effects are attributed to increasing interphase interactions in the hybrid systems, resulting in a larger immobilized layer of polymer chains around the nanoparticles [57]. The nanocomposites were determined to have a bicontinuous morphology (the SiO_2 forms a continuous phase in the organic matrix) rather than a particulate composite (with dispersed SiO_2 particles), based on agreement of the data with the two different models [57].

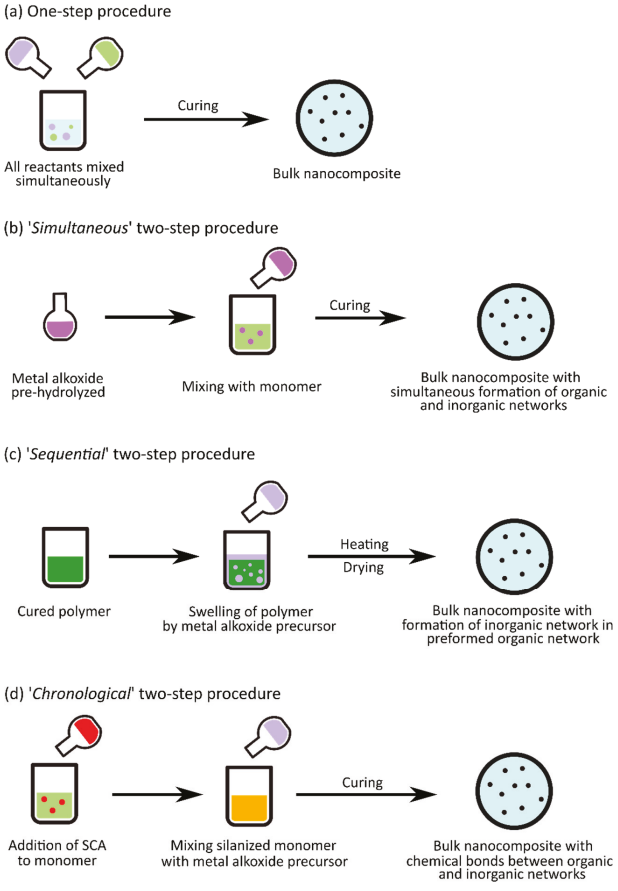

Figure 4. Schematic displaying the general principles of the (**a**) one-step procedure; and the (**b**) '*simultaneous*'; (**c**) '*sequential*'; and (**d**) '*chronological*' two-step procedures used in the in situ synthesis of epoxy nanocomposites. The colors of the various solutions are described as follow: The pure epoxy resins are indicated either by light green (monomer solution), dark green (polymer solution), or orange (monomers modified by silane coupling agents (SCA)), the inorganic oxide precursors are indicated by light purple, or dark purple (pre-hydrolyzed), and the SCAs are indicated by red.

Bauer et al. [54] similarly prepared epoxy–SiO_2 nanocomposites using both a one-step procedure and a two-step sequential procedure, but without any additional catalysts. SAXS data (corroborated by TEM images) showed that the nanocomposites prepared using a one-step procedure had extensive phase mixing (slope of −2 in the Porod region), while those prepared using the two-step sequential procedure (with the pre-cured epoxy) were strongly phase-separated (slope of −4 in the Porod region) [54]. The latter result is contrary to that presented by Matějka et al. [56], where the sequential procedure also led to phase mixing (−2 slope in the Porod region). This difference was attributed by Matějka et al. [56] to differences in the temperature of the synthesis (60 °C instead of 90 °C), with a higher temperature promoting increased grafting between the organic and inorganic networks. Thermogravimetric analysis (TGA) also showed increased thermal stability for the nanocomposites, with the initial mass loss occurring at 20–50 °C higher temperatures than for pure epoxy resin [54]. A decrease in the slope of the thermogravimetric curves (resembling a small plateau) was observed between 400 and 600 °C for pure epoxy resin, corresponding to char formation. This plateau was shifted to higher temperatures for the nanocomposites, with the inorganic network possibly acting as a barrier to the decomposition of the organics. The skeleton-like morphology of the SiO_2 remaining after the organic burn-off indicated the formation of an interpenetrating polymer network (IPN), similar to the bicontinuous morphology suggested by Matějka et al. [57].

3.1.2. The Effect of Silane Coupling Agents

Several works have also employed the 'chronological' two-step procedure in the preparation of epoxy nanocomposites, using SCAs to improve the dispersion of the nanoparticles formed in situ. Figure 5 shows a schematic for a possible outline of the reactions occurring during this procedure between the DGEBA monomer, the coupling agent, and the precursor.

Nazir et al. [52] prepared epoxy–SiO_2 nanocomposites by first modifying the DGEBA monomer with the SCA APTES, followed by sol–gel reaction with TEOS and water and subsequent curing using Jeffamine. Nanocomposites were also prepared without the SCA using the same synthesis procedure, minus the addition of the APTES. TEM images (Figure 6) showed clear differences between the samples (with the same SiO_2 content) prepared with and without the SCA. The nanocomposites without the SCA showed distinct SiO_2 particles, indicating a two-phase morphology, whereas the nanocomposites with the SCA showed less distinct organic and inorganic phases, representing a bicontinuous phase morphology similar to that proposed by Matějka et al. [57]. TGA also showed that the thermal stability, as well as the average energy of activation (E_a) for the degradation, slightly increased for the nanocomposites when APTES was used [52]. However, there was no indication of char formation. Dynamic mechanical thermal analysis (DMTA) showed a higher storage modulus for the nanocomposites in the glassy region. The storage modulus increased with increasing SiO_2 content up to 10 wt % for samples prepared without APTES and up to 15 wt % for samples prepared with APTES (which also showed the highest storage modulus). Further increase in the SiO_2 content led to a decrease in the storage modulus. The glass transition temperature (T_g), given by the position of the loss factor peak, also increased with increasing SiO_2 content (by approximately 4 °C up to 10 wt %) [52]. T_g was observed to be higher for samples prepared with APTES than for those without.

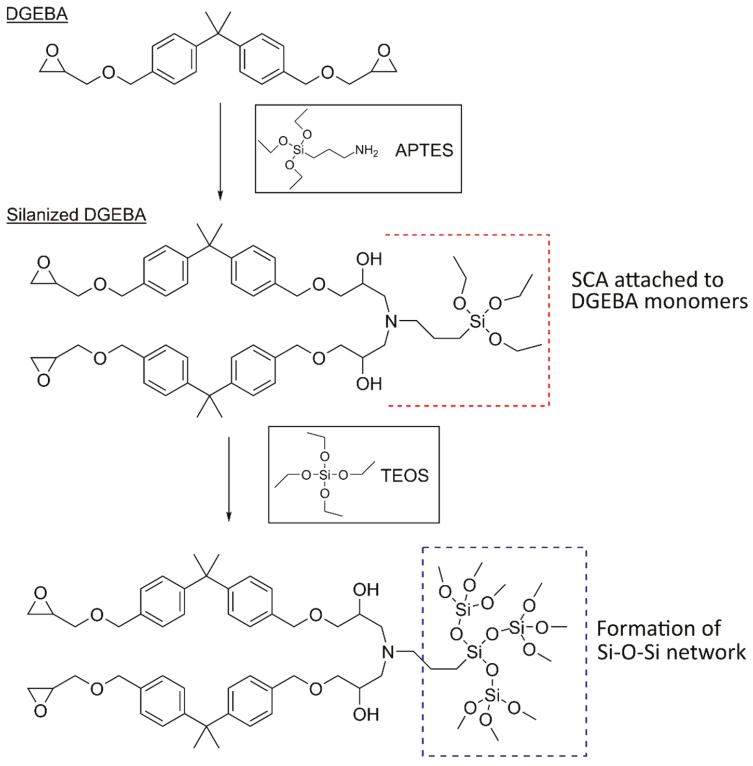

Figure 5. Schematic of the in situ sol–gel reactions possibly occurring in the 'chronological' two-step procedure for the preparation of epoxy–SiO_2 nanocomposites. Diglycidyl ether of bisphenol A (DGEBA) is used as the epoxy monomer, 3-aminopropyltriethoxysilane (APTES) as the coupling agent, and tetraethylorthosilicate (TEOS) as the silica (SiO_2) precursor. The curing step is not shown in this schematic.

Afzal and Siddiqui [51] used a similar procedure to that used by Nazir et al. [52] in the preparation of their epoxy–SiO_2 nanocomposites, the differences being the use of GPTMS as the SCA, a lower pH (2), and a higher temperature for the hydrolysis and condensation reactions (60 °C instead of room temperature). Atomic force microscopy (AFM) was used to investigate the microstructure and surface morphology of the nanocomposites (Figure 7). Inclusion of SiO_2 in epoxy led to increased roughness of the surface. The peaks in Figure 7 represent the SiO_2 nanoparticles and show a homogeneous distribution. At higher SiO_2 loads (above 15 wt %), the SiO_2 begins to agglomerate. The addition of GPTMS resulted in reduced agglomeration and an improved dispersion of the SiO_2. Macroscopic phase separation was only observed above 25 and 30 wt % of SiO_2 for samples treated with and without GPTMS, respectively [51], compared to 20 and 25 wt % for samples treated with and without APTES, respectively [52]. This difference may be attributed to the SCA used, but could also be due to the differences in synthesis conditions. The use of lower pH and higher temperature will promote the hydrolysis of TEOS, resulting in a more network-like open structure, and therefore increased phase mixing. The formation of the silica network was investigated by both Nazir et al. [52] and Afzal and Siddiqui [51], using Fourier transform infrared spectroscopy (FTIR), with the Si–O–Si asymmetric stretching showing an absorption band at 1085 cm^{-1}.

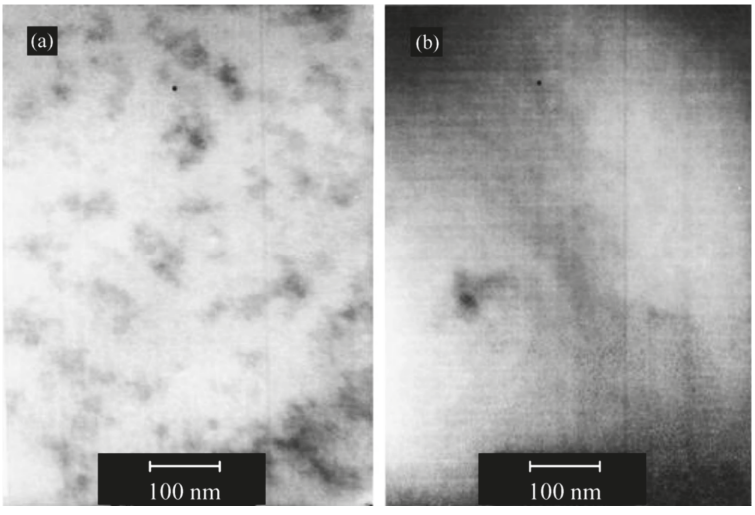

Figure 6. TEM micrographs of epoxy–SiO_2 hybrids with 10 wt % SiO_2: (**a**) Hybrid films prepared without SCAs; and (**b**) hybrid films prepared with APTES. Reproduced with permission from Nazir et al. *Progress in Organic Coatings*; published by Elsevier B.V., 2010.

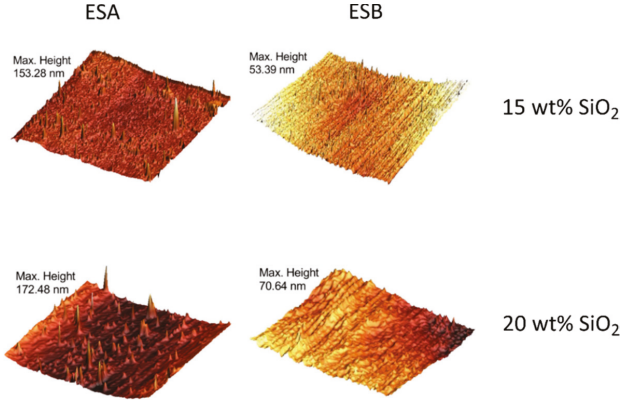

Figure 7. 3D atomic force microscopy (AFM) micrographs showing the surface morphology of epoxy nanocomposites (15 and 20 wt % of SiO_2). The ESA (epoxy silica A) hybrids (**left**) were prepared without 3-glycidyloxypropyltrimethoxysilane (GPTMS), and the ESB (epoxy silica B) hybrids (**right**) were prepared with GPTMS. The peaks represent silica nanoparticles and/or agglomerates, and the SiO_2 is distributed more homogeneously and less agglomerated when GPTMS is used. Reproduced with permission from Afzal and Siddiqi, *Polymer*; published by Elsevier Ltd., Amsterdam, The Netherlands, 2011.

Differential scanning calorimetry (DSC) data corroborated the findings from DMTA by Nazir et al. [52], showing an increased T_g for the epoxy–SiO_2 nanocomposites (by 6 °C up to 10 wt %) compared to pure epoxy [51]. Afzal and Siddiqui attributed the increase in T_g to the loss of mobility of the polymer chains around the SiO_2 nanoparticles, caused by the increased interactions at the interfaces [51]. As with the case of adding APTES, the inclusion of GPTMS also led to a further increase in T_g for the nanocomposites (by 9 °C up to 10 wt %). Excess amount of SiO_2 (above 10 wt %), however, showed a decrease in T_g again (Figure 8), which was suggested to be due to the agglomeration of the nanoparticles, resulting in fewer interactions and fewer immobilized chains [51].

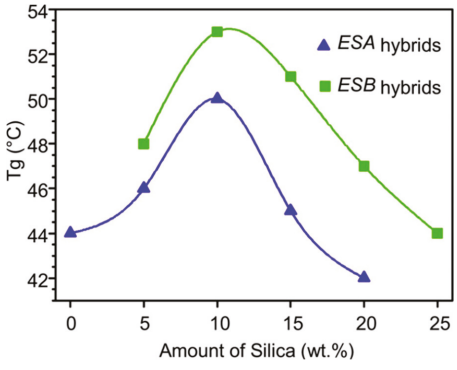

Figure 8. Changes in the glass transition temperature (T_g) with silica content in epoxy nanocomposites. ESA hybrids were not prepared using GPTMS, and ESB hybrids were prepared with GPTMS. Reproduced with permission from Afzal and Siddiqi, *Polymer*; published by Elsevier Ltd., 2011.

Several other works [36,48–50,61] have carried out similar in situ syntheses of epoxy–SiO_2 and epoxy–TiO_2 nanocomposites, using various coupling agents (APTES, IPTES, and triethoxysilane-capped trimercaptothioethylamine (TCTMEA)) and reported similar observations for the changes in properties described above. Guan et al. [61] investigated the optical properties of epoxy–TiO_2 nanocomposite films, and reported over 90% transparency for up to 20 wt % of TiO_2. The refractive index at 632.8 nm also increased from 1.61 (for pure epoxy) to 1.797 (for 65 wt % TiO_2). The tensile strength, impact strength, tensile and flexural moduli, and ductility are improved significantly in in situ prepared epoxy–SiO_2 nanocomposites, compared to pure epoxy [36,48,50]. This toughening of the nanocomposites is attributed to the strong covalent bonds formed at the interfaces between the organic and inorganic networks via the coupling agents, which can withstand external stresses and transfer them to the rigid nanoparticles. However, agglomeration of the nanoparticles in the epoxy can compromise the mechanical properties.

Wu and Hsu [59] prepared epoxy–SiO_2 and epoxy–TiO_2 nanocomposites (both with 10 wt % of inorganic oxide) using TEOS and tetraethylorthosilicate (TEOT), respectively, as the precursors for the inorganic oxides. GPTMS was used as the coupling agent. For the epoxy–SiO_2 nanocomposites, they followed a one-step procedure by mixing all the reactants and adding an acid catalyst (HCl) dropwise while stirring. A similar method was used for the epoxy–TiO_2 nanocomposites, but a mixture of tetraethylorthosilicate (TEOT) and acetylacetone was added dropwise instead of the acid. This was due to the higher reactivity of the TEOT, with the acetylacetone stabilizing the TEOT. Phase separation was observed in samples where GPTMS was not used, whereas the samples prepared with GPTMS were transparent and homogeneous in appearance. TEM images (Figure 9) displayed well-dispersed, non-agglomerated SiO_2 and TiO_2 nanoparticles (22 nm average size) in the epoxy resin. The images, however, show distinct TiO_2 nanoparticles, whereas the SiO_2 nanoparticles are less distinct in contrast and resemble the IPNs reported by Nazir et al. [52] and Bauer et al. [54]. This could be attributed to the controlled hydrolysis of the TEOT, meaning that the condensation rate is higher, leading to the formation of colloidal TiO_2 nanoparticles. Meanwhile, TEOS hydrolysis is catalyzed by the acid, leading to the formation of more polymer-like SiO_2 networks, resulting in the less distinct phase in the TEM image. DSC results confirmed previous observations, with an increase in T_g observed for both types of nanocomposite [59]. TGA results are consistent with other studies for the epoxy–SiO_2 nanocomposites, with an increase in thermal stability compared to the pure epoxy. However, the thermal stability of epoxy–TiO_2 nanocomposites is lower than that of pure epoxy, and is attributed to metal-catalyzed oxidative decomposition pathways [59]. This result is contrary to those reported by Guan et al. [61], where thermal stability increased with increasing TiO_2 content. Char formation was observed between 400 and 500 °C in both studies.

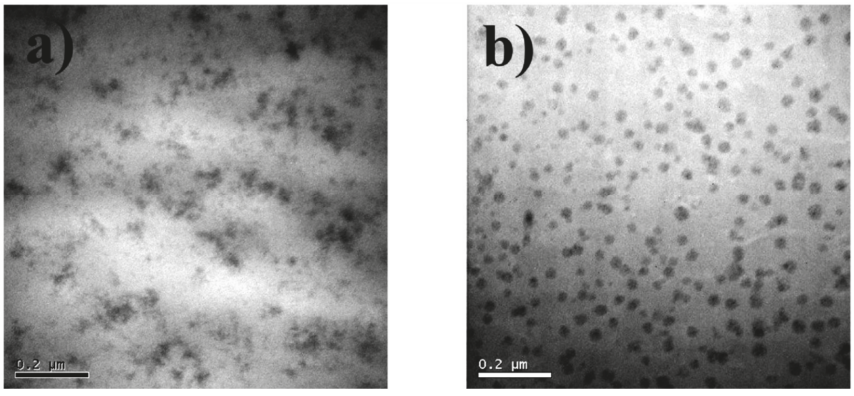

Figure 9. TEM images of the (**a**) epoxy–SiO_2; and (**b**) epoxy–TiO_2 nanocomposites prepared with GPTMS as coupling agent. Reproduced with permission from Wu and Hsu, *The Journal of Physical Chemistry C*; published by American Chemical Society, 2010.

3.1.3. Application of Ionic Liquids in the Synthesis Procedure

Recently, Donato et al. [62–64] used carboxylic and ether ionic liquids (ILs) in both hydrolytic and non-hydrolytic sol–gel processes in the synthesis of epoxy–SiO_2 nanocomposites. Methylimidazolium-based ILs (organic salts with ionic–covalent crystal structures, e.g., $CH_2CO_2HMImCl$, $C_3H_6CO_2HMImCl$, $C_7O_3MImMeS$, etc.) can be applied as replacements for conventional volatile solvents, as catalysts for the sol–gel process, or as silica morphology controllers [62]. Due to their selective interaction features and the ability to self-organize, they can act as molecular templates in the sol–gel synthesis of SiO_2 nanoparticles [63,81], with different ILs resulting in different matrix–filler interface characteristics [62].

Referenced epoxy–SiO_2 nanocomposites prepared without ILs displayed silica aggregates between 100 and 200 nm in size, while those prepared with $C_7O_3MImMeS$ resulted in smaller compact SiO_2 nanodomains (20–50 nm), forming large loose aggregates with D_m = 1.7. However, the use of C_1MImBF_4 instead resulted in large agglomerates (>200 nm) of dense particles, with D_m = 3 and poor dispersion [63]. As a result, the nanocomposites prepared with the MeS–anion IL showed strong interfacial interactions, with an increase in the shear storage modulus and decrease in the loss factor, while those prepared with the BF_4–anion IL showed the opposite (no mechanical reinforcement). However, the nanocomposites prepared with TEOS pre-hydrolyzed using $C_{10}MImBF_4$ and HCl resulted in the most homogeneous morphology, with 10 nm SiO_2 domains, leading to the highest shear storage modulus. This is attributed to the IL cation providing physical crosslinking, as the interfacial interaction is weak due to the immiscibility of the IL and the poly(oxypropylene) chains of the epoxy network [63].

SCAs can also be combined with ILs in the in situ synthesis of epoxy–SiO_2 nanocomposites to tune their mechanical properties. Figure 10 shows a schematic of the various synthesis approaches using ILs and SCAs. The addition of GPTMS in the synthesis led to increased fracture strain and toughness for nanocomposites prepared with both MeS– and BF_4–anion ILs [64]. On the other hand, the tensile strength decreased initially for small amounts of GPTMS, before increasing with the GPTMS content until 20–30% GPTMS, after which it decreased again [64]. However, combination of the IL and GPTMS in the synthesis decreased the tensile moduli of the nanocomposites, which was attributed to a decrease in the crosslinking density in the organic network. Contrary to the findings reported previously in this review, Donato et al. [64] reported a decrease in T_g when GPTMS is used along with ILs.

A non-hydrolytic sol–gel approach was also applied to prepare epoxy–SiO_2 nanocomposites using ILs, with boron trifluoride monoethylamine (BF_3MEA) complex as the solvent [62]. The reaction

in this approach is slower, allowing structure control and avoiding phase separation without the application of a co-solvent [62]. With $C_3H_6CO_2HMImCl$, the epoxy–SiO_2 system displayed small, loosely packed agglomerates (10–100 nm), while without the IL the system showed larger agglomerates (500 nm). Similar to the hydrolytic approach, the use of ILs in the non-hydrolytic sol–gel process also resulted in an increase in the shear storage modulus, fracture strain, toughness, and tensile strength. The non-hydrolytic sol–gel approach with ILs also appears to be better suited for glassy epoxy nanocomposites (formed by using more basic amine curing agents, with lower amine equivalent weight) than for rubbery nanocomposites (formed by using less basic amine curing agents, with higher amine equivalent weight) [62]. This is explained to be due to the catalytic effect of the IL (which is slowed down in the non-hydrolytic approach) and the resulting sensitivity to the basicity of the system when the curing agent is added, but further investigation into the effects of the reaction condition is required for these systems.

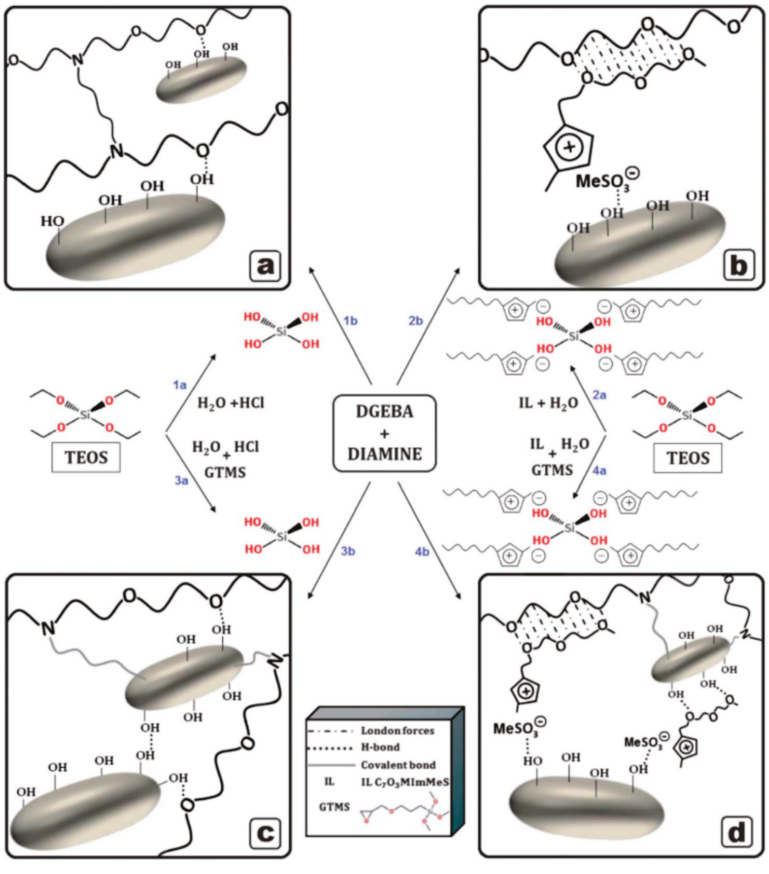

Figure 10. Schematic for various applied synthesis approaches for the preparation of epoxy–SiO_2 nanocomposites (**a**) without ionic liquid (IL) $C_7O_3MImMeS$; (**b**) with IL $C_7O_3MImMeS$; (**c**) with GPTMS; and (**d**) with GPTMS and IL $C_7O_3MImMeS$. GPTMS is labelled as GTMS in the original figure. The gray platelets represent SiO_2 nanoparticles. Reproduced with permission from Donato et al., *Journal of Materials Chemistry*; published by The Royal Society of Chemistry, 2012.

3.2. Polysiloxane Nanocomposites

Polysiloxanes (silicones) are quite prevalent in applications today, for example, in the textile, food, biomedical, aerospace, and electronics industries [82–84]. Polydimethylsiloxane (PDMS) is a homopolymer with the general formula $H_3C[Si(CH_3)_2O]_nSi(CH_3)_3$, where n is the number of repeating units. The PDMS chains can also contain silanol end groups (Si–OH), forming hydroxy-terminated PDMS (PDMS–OH). The use of transition metal oxide fillers for PDMS has recently attracted interest due to the improvements in the optical and mechanical properties of the nanocomposites, opening new possibilities for applications in optical devices [14]. The unique flexible and rubbery properties of PDMS, along with its thermal stability, have also made it suitable for application as thermally stable rubbers and hydrophobic coatings [66,68,72].

Unlike that of epoxy nanocomposites, the synthesis of most PDMS nanocomposites is done without the use of any coupling agents. This is because hydroxy-terminated PDMS precursors (PDMS–OH) already contain silanol end groups, which allows PDMS to participate in the condensation reaction and be integrated into the inorganic network [68]. Coupling agents are therefore not required to improve compatibility between the organic and inorganic components as they are for epoxy nanocomposites, where there are no silanol end groups in the polymer chains. In addition, the selection of solvents and chelating agents is more important in the synthesis of PDMS nanocomposites containing an inorganic network of a transition metal oxide. This is due to the greater reactivity of the transition metal–alkoxide precursors commonly used. This results in the precipitation of colloidal MO_2 particles, where M is the transition metal. Therefore, most sol–gel approaches to these nanocomposites are generally two-step procedures—the metal alkoxide is usually stabilized first by the chelating agent or solvent, and then mixed with the PDMS and the hydrolysis and condensation reactions are initiated.

3.2.1. In Situ Synthesis Procedures Using a Chelating Agent for the Transition Metal Alkoxides

One of the earliest applications of the sol–gel approach in the synthesis of PDMS nanocomposites with a transition metal oxide inorganic network was by Glaser and Wilkes, using a chemically controlled condensation method for PDMS modified by TEOS [65]. TEOS and PDMS were initially mixed with isopropanol or THF as a solvent, and then with glacial acetic acid. The mixture was left overnight in N_2 atmosphere, before TIP was added as the precursor for TiO_2. This pretreatment with a solvent and glacial acetic acid was to prevent the fast hydrolysis of the TIP. The solution was then mold casted and cured to prepare nanocomposite films. The formation of a Ti–O–Ti network in the PDMS–TEOS hybrid resulted in some improvements in the mechanical properties, notably the increased storage modulus after the glass transition, and the stress at break [65].

Yamada et al. [69] investigated the formation behavior of PDMS hybrids prepared using metal alkoxides of Al, Ti, Zr, Nb, and Ta as the inorganic precursors. The ratio of metal alkoxide to PDMS was varied, and the alkoxides were chemically modified using ethyl acetoacetate (EAcAc) to control the hydrolysis of the reactive alkoxides. The EAcAc was first mixed with the metal alkoxides, followed by addition of ethanol, water, and PDMS. After mixing, the solutions were mold casted and cured at 70 °C for 2 days, followed by post curing at 150 °C for 3 days. ^{13}C-NMR and FTIR showed that the EAcAc is bonded to the Al, Ti, and Zr metal alkoxides by substitution of two alkoxy groups, forming a bidentate ligand [69]. For the Ta and Nb alkoxides, however, fewer than 2 alkoxy groups on average were replaced by the EAcAc. Upon addition of water, hydrolysis is initiated and the chelate complex is released. The Al alkoxide, however, formed the strongest chelated complex with EAcAc, and was therefore less subject to the hydrolysis. Chelated complexes are suspected to remain in the hydrolyzed solutions and gels, thus preventing the formation of large inorganic particles. Figure 11 shows an illustration of the formation behavior of these PDMS hybrids when using EAcAc as a chelating agent. The optical properties of these hybrids were also investigated (Figure 12). The refractive indices of the hybrids increased with increasing ratio of metal alkoxide to PDMS (i.e., increasing inorganic content), in the order Al < Zr $\leq$ Ti < Ta $\leq$ Nb for the different metal alkoxides [69]. This sequence is attributed to the fact that, with higher valency cations, the chance to form M–O–Si bonds is larger, leading to a more

densely crosslinked network between PDMS and the metal oxide. The hybrids were transparent in the wavelength region of visible light (400–700 nm), with an absorption edge at 500 nm, thus appearing yellow in color (except for the Ti–O–PDMS hybrid at 650 nm, appearing red instead). The transmittance was reduced to zero in the UV region for all the nanocomposites (below 400 nm). FTIR showed the emergence of a new absorption band around 930 cm^{-1}, which was assigned to the M–O–Si bonds formed by the reaction of the hydrolyzed alkoxides with the Si–OH groups of the PDMS [69].

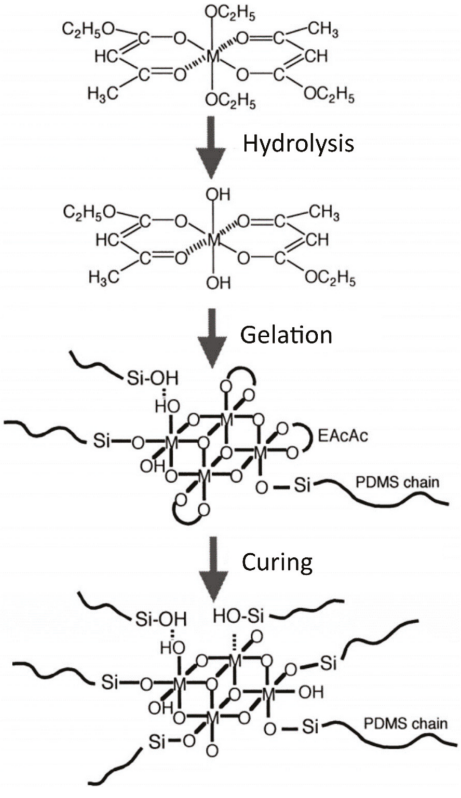

Figure 11. Schematic illustration of the formation of PDMS-based hybrids with metal alkoxide precursors complexed with chelating agent ethyl acetoacetate (EAcAc). Reproduced with permission from Yamada et al. *Journal of Sol–Gel Science and Technology*; published by Kluwer Academic Publishers, 2000.

Shindou et al. [66] prepared PDMS–O–Ti hybrids, using EAcAc as the chelating agent for TIP and ethanol as a solvent. The hybrid films were cured at either 150 °C for 2 h or 300 °C for 6 h. Tapping-mode AFM phase images showed differences in the morphology of the prepared hybrids, depending on the molar ratio of PDMS to TIP and the curing temperature. For the samples cured at 150 °C, low PDMS content (PDMS/TIP < 0.25) showed a continuous phase structure, whereas high PDMS content (PDMS/TIP > 0.35) showed distinct spherical domains of inorganic material (approximately 500–700 nm) in an island-like structure. For the samples cured at 300 °C, however, the images showed homogeneous and featureless surfaces for all PDMS/TIP ratios, indicating homogeneous mixing of the organic and inorganic components in the hybrid [66]. An FTIR absorption band at 960 cm^{-1} disappeared when the sample was heated to 300 °C. This was attributed to a possible coordinate bond between Si and Ti (rather than Si–O–Ti bonds in the hybrid), which is cleaved at

higher temperatures (thus resulting in the disappearance of the band) [66]. The hydrophobicity of the hybrids decreased with decreasing molar ratio of PDMS/TIP, as the contact angle of the films with water was reported to decrease with increasing inorganic content in the hybrids.

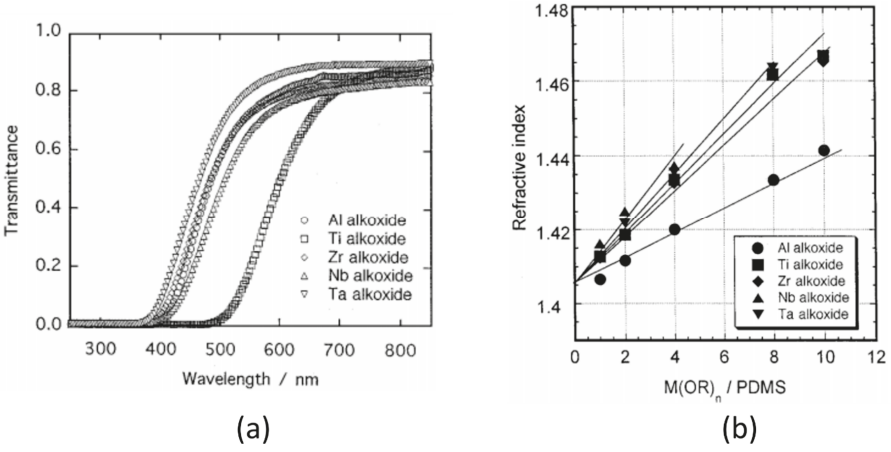

Figure 12. Optical properties of PDMS–O–M hybrids (M = Al, Ti, Zr, Nb or Ta) prepared using M-alkoxides. (**a**) UV-VIS transmittance spectra for hybrids prepared with metal alkoxide to PDMS ratio of 4; (**b**) Change in refractive index with metal alkoxide to PDMS molar ratio for various hybrids. Reproduced with permission from Yamada et al., *Journal of Sol–Gel Science and Technology*; published by Kluwer Academic Publishers, 2000.

Katayama et al. [72] prepared PDMS hybrids using zirconium *n*-butoxide (ZBO) and tantalum ethoxide (TE) as precursors for the inorganic components. EAcAc was again used as a complexing agent, and 2-ethoxyethanol was the solvent. A procedure similar to that used by Yamada et al. [69] was applied in the preparation of the hybrid films. X-ray photon spectroscopy (XPS) revealed information on the chemical bonding state of the inorganic components in the hybrids. Figure 13a shows a comparison of the Zr^{3d} XPS doublet peaks of a PDMS–O–Zr hybrid and ZrO_2. The similarity of the peaks indicates that Zr was most likely present as an oxide in the hybrid, but the higher shift of the binding energy of the doublet peak also shows that the Zr species were bound to a more electron-attractive species (i.e., the siloxane) [72]. This was corroborated by Fourier transforms of the extended X-ray absorption fine structure spectroscopy (EXAFS) (shown in Figure 13b) as the Zr–Zr(Si) peaks in the hybrids were shifted to shorter distances compared to the corresponding peak for ZrO_2. This means that the second neighbors of Zr contained other atoms than Zr [72]. The ZrO_2 nanodomains are then chemically crosslinked to PDMS via Zr–O–Si bonds. High-resolution TEM (HRTEM) images of the hybrids showed inorganic domains of 2–3 nm distributed homogeneously, with the size of the domains increasing with the molar ratio of ZBO/PDMS. Data from SAXS experiments are consistent with the observations from HRTEM. A Guinier analysis indicated a gyration radius of 2.29 nm, which corresponds with the size of the inorganic domains being 2.96 nm, assuming the particles are spherical. FTIR also confirmed the formation of Zr–O–Si bonds between the inorganic domains and the PDMS, with the ZrO_2 nanodomains behaving as crosslinkers for PDMS chains [72]. DMA revealed an increase in the tensile strength and Young's modulus of the hybrids, with a larger increase for the PDMS–O–Zr hybrids than for the PDMS–O–Ta hybrids. The tensile strength and Young's modulus also increased with increasing metal alkoxide to PDMS molar ratio. However, these increases were most prominent at higher temperatures (above 150 °C), which is suspected to be due to increased reaction progress between the PDMS and the hydrolyzed alkoxides. The mechanical properties improved compared to those of PDMS–TEOS hybrid materials. This is suspected to be due to the greater efficiency of the inorganic oxides acting as crosslinkers for PDMS.

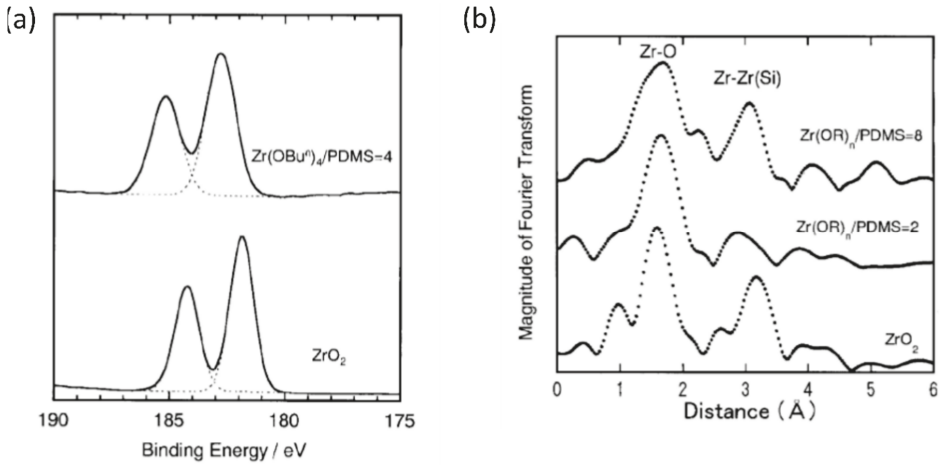

Figure 13. (**a**) Zr^{3d} XPS spectra of a PDMS–ZrO_2 hybrid (ZBO/PDMS molar ratio of 4) and ZrO_2; (**b**) Fourier transforms of extended X-ray absorption fine structure spectroscopy (EXAFS_ spectra for PDMS-ZrO_2 hybrids (ZBO/PDMS ratio of 8 and 2) and ZrO_2. Reproduced with permission from Katayama et al. *Journal of the American Ceramic Society*; published by Wiley–Blackwell, 2002.

Yamada et al. [70,71] also investigated the mechanical properties of PDMS hybrids (prepared using the same procedure described from [69]) earlier, and reported a higher T_g and storage modulus for the hybrids compared to pure PDMS [70]. The inorganic component was also seen to affect the improvements in the mechanical properties, as shown in Figure 14. The storage modulus at room temperature increased in the order of Al < Ti < Ta as the inorganic network became denser. The tensile strength, however, showed slightly different behavior, and increased in the order Al < Ta < Ti. This was attributed to the degree of interaction between the inorganic component and the PDMS, which is dependent on both the strength of the bond as well as the number of bonds forming [71].

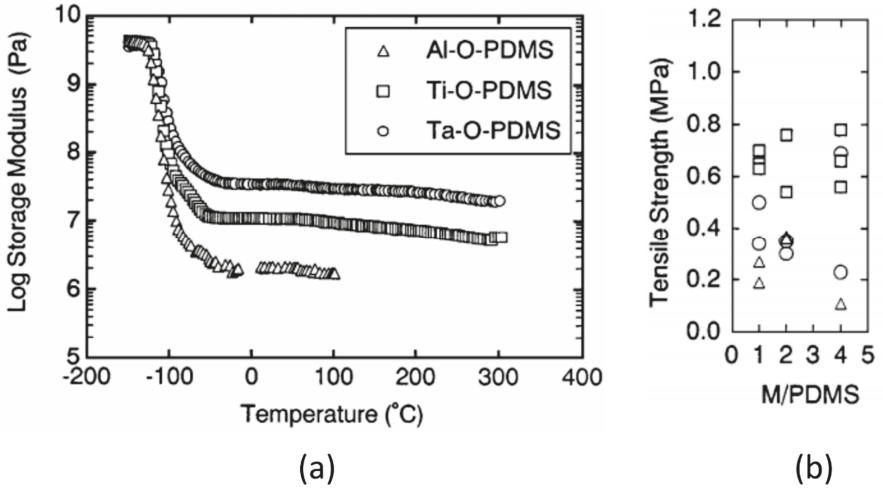

Figure 14. Changes in the (**a**) storage modulus and (**b**) tensile strength, for different PDMS hybrids, as a function of temperature and metal alkoxide to PDMS ratio, respectively. Reproduced with permission from Yamada et al. *Journal of Sol–Gel Science and Technology*; published by Kluwer Academic Publishers, 1998.

3.2.2. In Situ Synthesis Procedures without Chelating Agents

Almeida et al. [73] prepared PDMS–SiO_2–MO_2 hybrids (where M = Ti or Zr) in a slightly different two-step procedure, both with and without a chelating agent. For the samples prepared without a chelating agent, PDMS–OH and the Ti or Zr alkoxides were separately mixed with isopropanol. They were then mixed together simultaneously with TEOS, and the pH was adjusted to 10 or 13. For the samples prepared with a chelating agent, the same procedure was used, but the Ti or Zr alkoxides were mixed with EAcAc instead. After the subsequent curing and heat treatment at 150 °C for 24 h, all the samples were homogeneous and transparent, even those without EAcAc. The lack of precipitation from the transition metal alkoxides in the absence of EAcAc in this case may be attributed to the higher pH, which favors condensation over hydrolysis in the sol–gel reactions, thereby preventing the fast precipitation of TiO_2 or ZrO_2 from the hydrolysis of the alkoxides.

Alternatively, the use of isopropanol in the synthesis may also have been responsible for the reduced hydrolysis rate of the alkoxides. This strategy is used in several other works where PDMS hybrids were prepared without chelating agents. The strategy usually involves the use of an alcohol as a solvent—if the same alcohol is a product of hydrolysis of the metal alkoxide, then the reaction equilibrium is shifted to stabilize the alkoxide [14]. Julian et al. [74] prepared PDMS–O–M nanocomposites using dimethyldiethoxysilane (DMDES) as the PDMS precursor, and metal alkoxides of Al, Ge, Sn, Ti, Zr, Nb, and Ta. Isopropanol or propanol was used as the solvent for the metal alkoxides. The arrangement and length of the siloxane chains were affected by the type of metal alkoxide used in the hybrids, based on results from FTIR and ^{29}Si MAS (magic angle spinning) NMR. In addition, the bands for symmetric Si–O–Si stretching vibration in the Raman spectra were also shifted to lower wavenumber in the hybrids, indicating a more rigid environment for the PDMS chains. The PDMS hybrid system containing Ge most likely consisted of short PDMS chains with a few siloxane units (4–5), while the systems containing Ti, Zr, and Al consisted mostly of long PDMS chains, and those containing Ta, Nb, and Sn had an intermediate structure. The crosslinking effect of the transition metals (via M–O–Si bonds, as evidenced by FTIR) appears to be strongest for Ta- and Nb-containing hybrids, as shown by the largest increases in T_g [74].

More recently, Lu and Mullins [67] used a non-aqueous sol–gel procedure for PDMS–TiO_2 nanocomposites. The hydrolysis of TIP was reduced by mixing with isopropanol before being mixed with PDMS. This procedure was then adapted by Dalod et al. [14] with anhydrous isopropanol instead, and with different viscosities of a PDMS–OH precursor. No chelating agent was used in either of these works. Presence of FTIR bands attributed to Ti–O–Si units and Ti–O–Ti units, as well as the absence of the broad band for –OH groups, confirmed the full reaction of the –OH groups of the PDMS–OH precursor, and the formation of TiO_2 nanodomains crosslinked with PDMS. At high TiO_2 contents, additional bands corresponding to amorphous TiO_2 were observed from Raman spectroscopy, indicating the formation of larger amorphous TiO_2 domains or particles. These TiO_2 domains were calculated to be 3.8 nm on average, based on SAXS measurements. The correlation length between the amorphous inorganic domains decreased with increasing content of TiO_2, indicating that the particles are more densely packed (assuming constant particle size). The contact angle with water decreased with increasing TiO_2 content, showing a reduced hydrophobicity in the hybrids (as seen similarly from the results reported by Shindou et al. [66]). The optical properties of the hybrids were also measured, showing good transparency in the visible range of the spectrum for hybrid films with low TiO_2 content. However, at higher TiO_2 contents, the transparency dropped significantly for the films containing PDMS with 25 and 65 cSt viscosity, due to scattering of light on the rough surface of the samples (Figure 15). The transmittance was also reduced to zero in the UV region (below 320 nm), most likely due to the absorbance of UV by the TiO_2 nanoparticles. With increasing amount of inorganic content, the refractive index increased for the PDMS–TiO_2 hybrid films (Figure 16). The Abbe number decreased with increasing TiO_2 content, showing increased dispersion in the visible region of the light spectrum [14]. The hybrid films were flexible and stiff below and above approximately 5 vol % TiO_2, respectively. This observation was corroborated through dynamic mechanical analysis, where the

shear storage moduli (G') of the hybrid films were measured from 2 to 220 MPa at room temperature, increasing the amount of titanium precursor. At high titania incorporation, the increased fractal dimension as well as the low correlation length (2 nm) measured by SAXS may indicate percolation (titania nanodomains are connected to each other throughout the material), which could explain the drastic increase of G'.

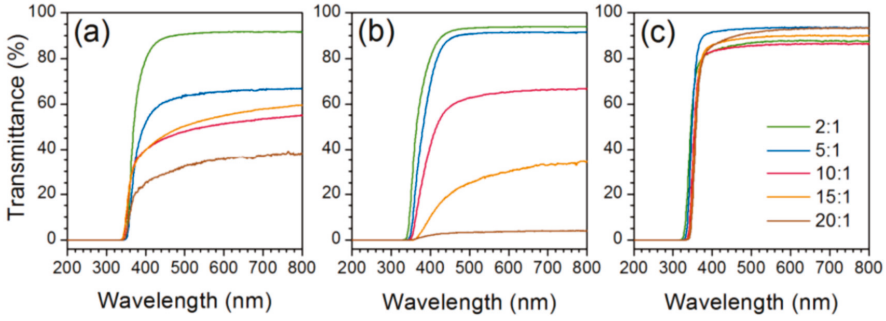

Figure 15. UV-VIS spectra of PDMS–TiO_2 hybrid films for different TIP/PDMS–OH molar ratios (shown in the legend), using PDMS–OH precursors with viscosities of (**a**) 25; (**b**) 65; and (**c**) 750 cSt, corresponding to average molar masses of 2100, 4000, and 20,000 g mol^{-1}, respectively (calculated based on experimental measurements from [85]). Reproduced with permission from Dalod et al. *Nanomaterials*; published by MDPI, 2017.

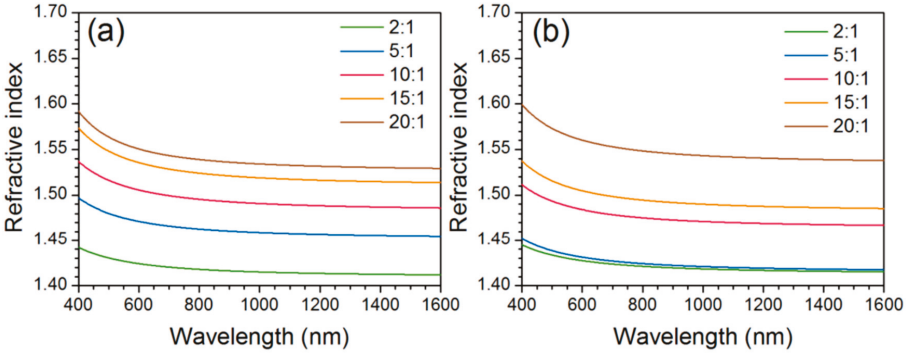

Figure 16. Changes in the refractive indices for PDMS–TiO_2 hybrid films for different TIP/PDMS–OH molar ratios (shown in the legend), using PDMS–OH with viscosities of (**a**) 25 cSt; and (**b**) 65 cSt, corresponding to average molar masses of 2100 and 4000 g mol^{-1}, respectively (calculated based on experimental measurements from [85]). Reproduced with permission from Dalod et al. *Nanomaterials*; published by MDPI, 2017.

3.2.3. PDMS–SiO_2 Nanocomposites by Swelling Techniques

While transition metal-based PDMS hybrids have attracted more interest in recent years due to the possibility to expand their range of applications, silica has traditionally been used to reinforce the mechanical properties of PDMS, particularly to increase the tensile strength, in most commercial applications [2,76]. The swelling technique used for epoxy–SiO_2 nanocomposites by Bauer et al. [54] and Matějka et al. [55] is also often used for the synthesis of PDMS–SiO_2 nanocomposites. Mark and Pan [5] pioneered PDMS–SiO_2 nanocomposites using a sol–gel procedure as early as 1982, with cured PDMS films (from vinyl-terminated and hydroxy-terminated chains) being swollen in TEOS, followed by addition of glacial acetic acid, water, and a phase-transfer catalyst ($(n\text{-Bu})_4PBr$). The hybrids were then extracted in THF and dried under vacuum. The formation of SiO_2 was found to be difficult in the

absence of the catalyst. Stress–strain measurements revealed that the in situ prepared nanocomposites showed increased toughness [5].

Yuan and Mark [77] applied a different double-swelling procedure, where the cured PDMS films were swollen first in TEOS, and then in diethylamine (DEA) as a catalyst. This process was repeated with a different concentration of DEA, resulting in bimodal particle distributions in the nanocomposite. The particle size could be controlled by the concentration of the catalyst, as it affects the rates of the hydrolysis and condensation reactions. TEM and SAXS measurements showed that the SiO_2 particles formed with a lower concentration of DEA were smaller (20–25 nm) than those formed with a higher concentration of DEA (160 nm), which is expected based on the type of catalyst used (DEA is basic, thereby favoring the condensation reactions more). The in situ approach also resulted in improved dispersion quality, compared to a traditional blending with pre-synthesized SiO_2 nanoparticles. Smaller filler particles imparted greater ultimate tensile strength to the nanocomposites, although larger particles improved extensibility more significantly [77]. In addition, several hybrids were prepared in situ with surface modified SiO_2 using dimethyldiethoxysilane (DMDEOS) and vinyl-terminated PDMS precursors. This approach allowed the nanocomposite to remain hydrophobic despite the inclusion of hydrophilic SiO_2 nanofillers. Breiner et al. [78] also showed that the particle size of the SiO_2 filler was dependent on the molecular weight (M_c) of the PDMS chains, with shorter chains (low M_c) resulting in smaller particles due to possible constraining effects.

Dewimille et al. [76] also synthesized PDMS–SiO_2 nanocomposites by swelling cured PDMS films in TEOS, along with either dibutyltin diacetate (DBTDA) or dibutyltin dilaurate (DBTDL) as a catalyst. Hybrid films were also prepared using DEA, similar to Yuan and Mark [77]. From the TEM images, differences in the inorganic structures of the hybrids were observed depending on the type of catalyst used. Particles generated using DEA were larger and more spherical than those generated by DBTDL. SAXS measurements indicated that the DEA-catalyzed systems contained uniformly dense objects with smooth surface fractal dimensions ($D_s = 2$), with the particle radius being calculated to around 15 nm (consistent with TEM images), while the tin-catalyzed systems contained more polymeric inorganic structures instead. This is as expected, since DEA is a more basic catalyst than both DBTDA and DBTDL.

Fragiadakis et al. [75,86] used the same procedure as Dewimille et al. [76] with DBTDA and hydride-terminated PDMS and investigated the glass transition and molecular dynamics of the hybrids. While T_g is not seen to be affected by the SiO_2 content in PDMS, the shape of the step up in heat capacity changes, which indicates contribution of the SiO_2 in the high temperature side. Thermally stimulated depolarization currents (TSDC) were used to characterize the glass transition further, and for the hybrids containing SiO_2 two different α relaxations were present (Figure 17). The first was the primary relaxation associated with the glass transition of the amorphous bulk PDMS (at a temperature which is in good agreement with the DSC measurements), and the second (α_{int} in Figure 17) was assigned to the α relaxation of the PDMS chains in an interfacial layer close to the SiO_2 [75,87]. The double structure of the α-relaxation was attributed to a gradual slowing down of the chain mobility at the interface with the SiO_2 nanoparticles. The range of this interfacial region was calculated to be about 3 nm (based on the dielectric strengths of the two components of the relaxation) [86]. Rajan et al. [79] investigated the optical properties of PDMS–SiO_2 films prepared using the swelling sol–gel approach with either DBTDL/DBTDA catalysts, or with ammonia. UV-VIS transmittance spectra showed over 90% transparency for PDMS–SiO_2 nanocomposites prepared with the neutral catalysts. However, for nanocomposites prepared with ammonia, transparency was lower (70% for 4 wt % SiO_2) and the samples became opaque with higher SiO_2 content (18.5 wt %). This may be attributed to the larger colloidal particles or aggregates that formed under basic conditions during the sol–gel process.

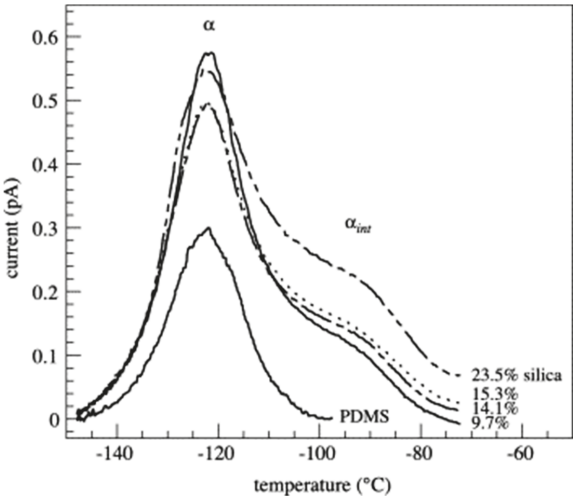

Figure 17. Thermally stimulated depolarization currents (TSDC) thermogram for PDMS and PDMS–SiO_2 nanocomposites in the glass transition region. Reproduced with permission from Fragiadakis et al. *Polymer*; published by Elsevier Ltd., 2005.

4. Alternative Methods for the In Situ Preparation of Nanocomposites

While this review has so far focused on nanocomposites based on the epoxy and PDMS systems to demonstrate syntheses of SiO_2 and transition metal oxide nanoparticles using the sol–gel method, the method is versatile and can be applied to several other polymer systems. SiO_2 and TiO_2 nanoparticles have been successfully synthesized and incorporated in, among other polymeric systems, poly(ethylene oxide), polypropylene, polyimide, and polyaniline, using alkoxide precursors [88–93]. In addition, the sol–gel method can also be combined with other techniques (e.g., electrospinning) to form different structures, such as hybrid nanofibers [94]. The first part of Table 2 shows examples of the various hybrid systems that have been prepared using sol–gel methods. In addition, several other techniques and methods are used for miscellaneous polymer–inorganic nanocomposites. The second part of Table 2 includes selected examples of such cases, where methods that are not based on the sol–gel process are described briefly below to illustrate the chemistry behind the different procedures.

Balci et al. [95] prepared Si nanocrystal organic hybrid films using a single batch solution synthesis. $SiCl_4$ was reduced in a solution of potassium cyclopentadiene, and the resulting Si nanocrystals were surface-terminated using either 1-octanol, oleic acid, acrylic acid, or ethylene glycol. The reaction is based on potassium cyclopentadiene acting as a nucleophile towards the silyl halide, forming Si clusters [96]. The following reaction of $SiCl_4$ on the surface with OH groups of surface capping agent produces HCl [97,98]. In the presence of HCl with excess -OH groups from surface termination groups, H_2O is formed [42]. In addition, a possible side reaction of the cyclopentadiene with the surface termination groups can occur, such as the Diels–Alder reaction with acrylic acid, which results in 5-Norbornene-2-carboxylic acid [99]. The exact nature of the organic network is unknown, and it is suspected that the network is formed by the polymerization of cyclopentadiene into dienophilic oligomers, possibly including polysiloles from the Diels–Alder reaction [100]. Different surface termination groups will have different resulting polymeric structures than the cyclopentadiene group, which will also affect the size distribution of Si nanocrystals and optoelectronic properties of the hybrid film. The mean size of the Si nanocrystals (2–10 nm) was dependent on the type of surface termination, with acrylic acid and 1-octanol causing the largest mean sizes, and ethylene glycol causing the smallest mean sizes. The hybrid films exhibited white light photoluminescence at room temperature when

excited by UV light, which was stable after storage over six months. Ethylene glycol terminated Si nanocrystals showed the largest red shift in photoluminescence.

Table 2. Selected examples of miscellaneous polymer–inorganic nanocomposites prepared using various in situ synthesis procedures. The first part of the table shows nanocomposites prepared using sol–gel techniques, and the second part shows nanocomposites prepared using other in situ approaches.

Polymer	Inorganic Component	Inorganic Precursor	Method	Reference
Poly(ethylene oxide)	SiO_2	TEOS	Sol–gel	[88]
Polypropylene	TiO_2	TBO		[89,90]
	SiO_2	TEOS		[91]
Polyimide	SiO_2			[92]
Polysulfone	TiO_2	TBO		[101]
Poly(vinyl-co-acetate)	SiO_2	TPO [1]		[102]
Polyethylene-octene	SiO_2	$Si(OH)_4$		[103]
Polyaniline	SiO_2	TEOS	Combination of sol–gel and in situ polymerization	[93]
Poly(ethylene terephthalate)	ZnO	ZA [2]	Combination of sol–gel and electrospinning	[94]
	SiO_2	TEOS	Sol–gel	[104]
Nafion	TiO_2	TBO		[105]
Unidentified [3]	Si	$SiCl_4$	Solution-based reduction	[95]
Polystyrene	CdS	CA [4]	In situ precipitation	[106]
Epoxy	TiO_2	TBO	Solvothermal synthesis	[31]
	SiO_2	TEOS	Reverse microemulsion	[107]

[1] Tetrapropoxysilane; [2] Zinc acetate dehydrate; [3] Polymerization of cyclopentadiene into dienophilic oligomers, and possible polysilole, is suspected; [4] Cadmium acetate.

Du et al. [106] incorporated CdS nanoparticles in situ in polystyrene (PS), and showed that the density and size of the CdS nanoparticles can be controlled by altering the sulfonate content in PS. A higher sulfonate content resulted in smaller and more uniform nanoparticles. The microstructure of the PS network, which includes clustering of ionic groups such as SO_3^-, was used to confine the nanoparticles formed. The nanoparticles were synthesized by the reaction between S^{2-} ions released from the decomposition of thioacetamide (TAA) reacted with Cd^{2+} ions from the acetate.

Zhang et al. [31] applied an in situ solvothermal synthesis procedure for preparing epoxy–TiO_2 nanocomposites, using GPTMS as a coupling agent and TBO as the TiO_2 precursor. TBO, ethanol, HCl, and GPTMS were added to DGEBA (preheated to 80 °C), and the homogeneous mixture was transferred to an autoclave. The sealed vessel was then placed in an oven at 100 °C for 3 h. The autogenous pressure inside the vessel increased beyond atmospheric pressure as the temperature is increased, increasing the solubility and reactivity of the reactants, resulting in the hydrolysis and condensation of the TBO. The nanocomposites showed high transparency (above 80% in the visible region of the spectrum) and improved absorbance of UV light (300–420 nm), which increased with increasing TiO_2 content. The films also showed increased hydrophobicity (based on the contact angle with water) when GPTMS was used, indicating successful crosslinks between the nanofiller surface and the polymer chains.

Liu et al. [107] prepared epoxy–SiO_2 nanocomposites using reverse (water in oil) microemulsions, consisting of epoxy resin as the oil phase and an aqueous ammonia solution as the water phase. TEOS was added to the prepared microemulsion and the in situ polymerization of TEOS within

the water phase formed the nanoparticles. In this method, appropriate surfactants should be used to stabilize the microemulsion and control the water solubilization in the oil phase (epoxy). Since ammonia was used in the water phase, the condensation reaction of the TEOS will be catalyzed and should form colloidal particles.

5. Prospects of In Situ Hybrid Materials

Hybrid materials are an attractive choice for applications in multiple areas due to the unique combination of properties that can be achieved from the organic and inorganic components. Proper selection of the polymeric matrix and the inorganic fillers (oxides, metals, sulphides, etc.), and the synthesis routes and conditions can allow one to tailor these properties as required, and design new materials and compounds. Earlier in this work, it has been shown how the in situ generation of inorganic oxide nanoparticles or nanodomains can result in improvements in the mechanical properties (tensile strength, Young's modulus, storage modulus, ductility, etc.), the thermal properties (T_g and thermal stability), as well as the optical properties (transparency and refractive index) for epoxy- and PDMS-based nanocomposites. Several works have shown improvements in other areas as well, such as the dielectric properties, where the nanocomposites were prepared using conventional ex situ methods [18,53,108,109]. Since it is known that ex situ preparation techniques are not optimal for achieving an agglomerate-free and homogeneous dispersion of particles, there is potential room for improving these materials further, using in situ techniques to synthesize the nanocomposites.

Epoxy–SiO_2 nanocomposites have been extensively investigated for applications in electrical insulation, flame-retardant and anticorrosive coatings, encapsulation, adhesives, laminates, aerospace parts, etc. [18,32,51]. Transition metal oxides (TiO_2, Nb_2O_5, Ta_2O_5, ZrO_2, etc.) in epoxy and PDMS have also shown great potential for optical applications (since they can increase the refractive indices for both polymers while maintaining the transparency), such as in lenses, transparent coatings, or LED encapsulation [14]. TiO_2 can also introduce photocatalytic properties to polymer materials and improve resistance to UV degradation. A number of studies have also been carried out on PDMS-based hybrids (with TiO_2, CaO, and SiO_2 as the inorganic component) for use as bioactive materials in the human body to assist bone reparation and formation via apatite formation [33,110,111].

Other polymer nanocomposites can be used similarly in diverse applications. Table 3 shows selected examples of such potential applications of different polymer–oxide nanocomposites. Several polymers (e.g., Nafion, PVA, PVDF, polyimide, etc.) that are commonly applied as membranes in high-temperature proton exchange membrane (PEM) fuel cells have shown improved properties upon the inclusion of oxide fillers [3,112,113]. Improved cell performances have been observed for these nanocomposite membranes at higher temperatures (110–120 °C) and lower relative humidity (80–90%). The use of in situ sol–gel methods in the preparation of these nanocomposites, rather than ex situ casting methods, has led to better dispersion of the nanoparticles and, consequently, a better performance of the material [105]. PEG- and PEO-based nanocomposites may be applied as solid electrolytes for Li–ion batteries, thanks to increased ionic conductivity and thermal stability [88,114]. Poly(ethylene terephthalate) (PET) with ZnO nanofibers prepared through a combination of sol–gel and electrospinning has shown high luminescence capacity, enabling its use in photocatalysts, gas sensors, light emitters, and solar cells [94]. Biopolymers (e.g., chitosan, alginate, etc.) can also be combined with inorganic oxides to form nanocomposites that are used as biosensors and drug-delivery agents [3,115].

Table 3. Selected examples of applications and relevant features for several polymer–inorganic oxide nanocomposites.

Application	Nanocomposite System	Features	Reference
Electrical insulation	Epoxy–SiO_2 Epoxy–TiO_2	Increased dielectric breakdown strength Decreased complex permittivity Increased T_g Increased strength, toughness, ductility	[16,18,108,116–120]
	PE [1]–MgO PE–Al_2O_3	Decreased DC conductivity Increased dielectric breakdown strength Decreased space charge accumulation Decreased complex permittivity	[121–125]
	PI [2]–SiO_2	Decreased electrical conductivity Increased scratch hardness Increased strength	[126]
Fuel cells	Nafion–TiO_2 Nafion–SiO_2	Increased water uptake Decreased resistivity Increased T_g Increased degradation temperature	[105,127,128]
	PVA [3]–SiO_2	Increased liquid retention Increased proton conductivity Higher ion-exchange capacity	[129,130]
	PVDF [4]–Al_2O_3	High proton conductivity High thermal stability Low methanol permeability Increased water uptake	[131]
Coatings	Epoxy–SiO_2	Increased flame retardance High T_g Good thermal stability	[132]
	PDMS–TiO_2–SiO_2	Transparent and hydrophobic Increased hardness	[68]
	Epoxy–SiO_2 Epoxy–Fe_2O_3	Improved corrosion resistance Increased Young's modulus	[133]
	PDMS–PVA–ZnO	Decreased hydrophobicity Reduced contamination by fluorescent biomarkers in biosensors	[134]
	Epoxy–PANI [5]–ZnO	Antifouling and antibacterial properties	[135]
Bioactive materials	PDMS–CaO–SiO_2–TiO_2	Increased Young's modulus High apatite-forming ability High extensibility High strength	[33,111]
	PDMS–CaO–SiO_2	High apatite-forming ability Decreased release of silicon in body fluids Mechanical properties analogous to those of human cancellous bones	[110]
Solid electrolytes	PEO [6]–SiO_2	Increased Li^+ transference number Increased T_g	[88]
	PEG–PU/PAN [7] with TiO_2	Good thermal stability Increased ionic conductivity	[114]
Ultrafiltration	PS[8]–TiO_2	Increased hydrophilicity Increased permeability Increased T_g	[101]
Electromagnetic interference shielding (EMI)	PANI–SiO_2	Increased EMI shielding effectiveness Increased thermal stability	[93]

[1] Polyethylene; [2] Polyimide; [3] Poly(vinyl acetate); [4] Poly(vinylidene fluoride); [5] Polyaniline; [6] Poly(ethylene oxide); [7] Poly(ethylene glycol) –polyurethane/poly(acrylonitrile); [8] Polystyrene.

6. Conclusions

The synthesis of inorganic oxide nanoparticles in situ directly in the polymer matrix is an alternative approach to the preparation of polymer nanocomposites, contrary to nanocomposites processed using traditional ex situ mixing techniques. The use of the sol–gel method in the in situ approach has been shown to be robust and flexible, offering improved control over the morphology of the inorganic structures formed and, therefore, the ability to tailor the properties for desired applications. Perhaps the greatest advantage provided by the sol–gel method is the ability to form Class II hybrid materials with an improved quality of dispersion of the inorganic components. Consequently, improvements are observed in the optical, thermal, and mechanical properties of the nanocomposites, which will broaden the scope of applications for these materials.

In the present review, an appraisal of the sol–gel method for the synthesis of SiO_2 and M_xO_y (where M is a transition metal) nanoparticles in epoxy- and PDMS-based nanocomposites, respectively, has been performed. The nanoparticles are formed via the hydrolysis and subsequent condensation of metal alkoxide precursors inside the monomer resins, followed by the curing of the resins to form the nanocomposite. For the epoxy nanocomposites, the use of surface functionalization (e.g., SCAs or ILs), acid catalysts (e.g., TSA, DBTDL), higher synthesis temperatures, and a two-step procedure with pre-hydrolyzed TEOS have all contributed to smaller and more open nano-SiO_2 structures, with reduced agglomeration and a bicontinuous phase morphology in the nanocomposites. These changes in the structure of the inorganic domains have led to increases in the glass transition temperature, the thermal stability, the mechanical strength, and the storage modulus, and a decrease in the loss factor. For the PDMS nanocomposites, due to the increased reactivity of the transition metal alkoxide precursors, the use of complexing agents (e.g., EAcAc), or an appropriate solvent (e.g., isopropanol) is significant in preventing phase separation or the formation of colloidal MO_2. The formation of MO_2-like nanodomains that are crosslinked with PDMS chains resulted in increased light transmittance, UV absorbance, refractive index, tensile strength, and shear storage modulus in the nanocomposites.

While several alternatives exist for synthesizing inorganic oxide nanoparticles in situ in the polymer, none are more ubiquitous than the sol–gel method, which is applied not only for the two polymer systems focused on in this review, but also for various other polymer–inorganic oxide nanocomposites. The improvements in the properties observed for these hybrid materials make them attractive choices for application in coatings, packaging materials, nanodielectrics, optical devices, and photovoltaics. The next step in the development of these nanocomposites will be to adapt the in situ methods to enable fabrication of the materials at a larger and economic scale, making the leap from the laboratory to the industry.

Author Contributions: Conceptualization, M.-A.E. and M.M.A.; Writing–Original Draft Preparation, M.M.A.; Writing–Review and Editing, M.-A.E., A.R.M.D., M.H.B. and J.G.

Funding: This work is funded by The Research Council of Norway through the project "Stipendiatstillinger til SINTEF Energi AS" (Project No. 259866).

Conflicts of Interest: The authors declare no conflict of interest.

References

1. Camargo, P.H.C.; Satyanarayana, K.G.; Wypych, F. Nanocomposites: Synthesis, Structure, Properties and New Application Opportunities. *Mater. Res.* **2009**, *12*, 1–39. [CrossRef]
2. Zou, H.; Wu, S.; Shen, J. Polymer/Silica Nanocomposites: Preparation, Characterization, Properties, and Applications. *Chem. Rev.* **2008**, *108*, 3893–3957. [CrossRef] [PubMed]
3. Sanchez, C.; Julián, B.; Belleville, P.; Popall, M. Applications of hybrid organic–inorganic nanocomposites. *J. Mater. Chem.* **2005**, *15*, 3559–3592. [CrossRef]
4. Sanchez, C.; Ribot, F. Design of Hybrid Organic-Inorganic Materials Synthesized Via Sol-Gel Chemistry. *New J. Chem.* **1994**, *18*, 1007–1047. [CrossRef]

5. Mark, J.E.; Pan, S.-J. Reinforcement of polydimethylsiloxane networks by in-situ precipitation of silica: A new method for preparation of filled elastomers. *Die Makromol. Chem. Rapid Commun.* **1982**, *3*, 681–685. [CrossRef]
6. Mauritz, K.A.; Jones, C.K. Novel poly(n-butyl methacrylate)/titanium oxide alloys produced by te sol–gel process for titanium alkoxides. *J. Appl. Polym. Sci.* **1990**, *40*, 1401–1420. [CrossRef]
7. Schottner, G. Hybrid Sol-Gel-Derived Polymers: Applications of Multifunctional Materials. *Chem. Mater.* **2001**, *13*, 3422–3435. [CrossRef]
8. Kiliaris, P.; Papaspyrides, C.D. Polymer/layered silicate (clay) nanocomposites: An overview of flame retardancy. *Prog. Polym. Sci.* **2010**, *35*, 902–958. [CrossRef]
9. Chattopadhyay, D.K.; Webster, D.C. Thermal stability and flame retardancy of polyurethanes. *Prog. Polym. Sci.* **2009**, *34*, 1068–1133. [CrossRef]
10. Gallon, B.J.; Kojima, R.W.; Kaner, R.B.; Diaconescu, P.L. Palladium nanoparticles supported on polyaniline nanofibers as a semi-heterogeneous catalyst in water. *Angew. Chem. Int. Ed.* **2007**, *46*, 7251–7254. [CrossRef] [PubMed]
11. Xiong, S.; Wang, Q.; Xia, H. Template synthesis of polyaniline/TiO_2 bilayer microtubes. *Synth. Met.* **2004**, *146*, 37–42. [CrossRef]
12. Leong, W.L.; Lee, P.S.; Lohani, A.; Lam, Y.M.; Chen, T.; Zhang, S.; Dodabalapur, A.; Mhaisalkar, S.G. Non-volatile organic memory applications enabled by in situ synthesis of gold nanoparticles in a self-assembled block copolymer. *Adv. Mater.* **2008**, *20*, 2325–2331. [CrossRef]
13. Pothukuchi, S.; Li, Y.; Wong, C.P. Development of a novel polymer-metal nanocomposite obtained through the route of in situ reduction for integral capacitor application. *J. Appl. Polym. Sci.* **2004**, *93*, 1531–1538. [CrossRef]
14. Dalod, A.; Grendal, O.; Blichfeld, A.; Furtula, V.; Pérez, J.; Henriksen, L.; Grande, T.; Einarsrud, M.-A. Structure and Optical Properties of Titania-PDMS Hybrid Nanocomposites Prepared by In Situ Non-Aqueous Synthesis. *Nanomaterials* **2017**, *7*, 460. [CrossRef] [PubMed]
15. Lü, C.; Yang, B. High refractive index organic–inorganic nanocomposites: Design, synthesis and application. *J. Mater. Chem.* **2009**, *19*, 2884–2901. [CrossRef]
16. Nelson, J.K.; Fothergill, J.C. Internal charge behaviour of nanocomposites. *Nanotechnology* **2004**, *15*, 586–595. [CrossRef]
17. Kochetov, R.; Andritsch, T.; Morshuis, P.H.F.; Smit, J.J. Anomalous Behaviour of the Dielectric Spectroscopy Response of Nanocomposites. *IEEE Trans. Dielectr. Electr. Insul.* **2012**, *19*, 107–117. [CrossRef]
18. Singha, S.; Thomas, M.J. Dielectric properties of epoxy nanocomposites. *IEEE Trans. Dielectr. Electr. Insul.* **2008**, *15*, 12–23. [CrossRef]
19. Lu, X.; Zhang, W.; Wang, C.; Wen, T.-C.; Wei, Y. One-dimensional conducting polymer nanocomposites: Synthesis, properties and applications. *Prog. Polym. Sci.* **2011**, *36*, 671–712. [CrossRef]
20. Nelson, J.K.; Nelson, J.K. *Dielectric Polymer Nanocomposites*; Springer: New York, NY, USA, 2010; ISBN 978-1-4419-1590-0.
21. Hussain, F.; Hojjati, M.; Okamoto, M.; Gorga, R.E. Review article: Polymer-matrix nanocomposites, processing, manufacturing, and application: An overview. *J. Compos. Mater.* **2006**, *40*, 1511–1575. [CrossRef]
22. Judeinstein, P.; Sanchez, C. Hybrid organic–inorganic materials: A land of multidisciplinarity. *J. Mater. Chem.* **1996**, *6*, 511–525. [CrossRef]
23. Caseri, W.R. In situ synthesis of polymer-embedded nanostructures. In *Nanocomposites: In Situ Synthesis of Polymer-Embedded Nanostructures*; Nicolais, L., Catotenuto, G., Eds.; John Wiley and Sons: Hoboken, NJ, USA, 2014; pp. 45–72.
24. Caseri, W.R. Nanocomposites of polymers and inorganic particles: Preparation, structure and properties. *Mater. Sci. Technol.* **2006**, *22*, 807–817. [CrossRef]
25. Jeon, I.Y.; Baek, J.B. Nanocomposites derived from polymers and inorganic nanoparticles. *Materials* **2010**, *3*, 3654–3674. [CrossRef]
26. Althues, H.; Henle, J.; Kaskel, S. Functional inorganic nanofillers for transparent polymers. *Chem. Soc. Rev.* **2007**, *36*, 1454–1465. [CrossRef] [PubMed]
27. Wen, J.; Wilkes, G.L. Organic/Inorganic Hybrid Network Materials by the Sol-Gel Approach. *Chem. Mater.* **1996**, *8*, 1667–1681. [CrossRef]

28. Kango, S.; Kalia, S.; Celli, A.; Njugana, J.; Habibi, Y.; Kumar, R. Surface modification of inorganic nanoparticles for development of organic–inorganic nanocomposites—A review. *Prog. Polym. Sci.* **2013**, *38*, 1232–1261. [CrossRef]
29. Mallakpour, S.; Madani, M. A review of current coupling agents for modification of metal oxide nanoparticles. *Prog. Org. Coat.* **2015**, *86*, 194–207. [CrossRef]
30. Bounor-Legaré, V.; Cassagnau, P. In situ synthesis of organic-inorganic hybrids or nanocomposites from sol-gel chemistry in molten polymers. *Prog. Polym. Sci.* **2014**, *39*, 5050–5056. [CrossRef]
31. Zhang, H.; Qi, R.; Tong, M.; Su, Y.; Huang, M. In Situ Solvothermal Synthesis and Characterization of Transparent Epoxy/TiO_2 Nanocomposites. *J. Appl. Polym. Sci.* **2012**, *125*, 1152–1160. [CrossRef]
32. Gu, H.; Ma, C.; Gu, J.; Guo, J.; Yan, X.; Huang, J.; Zhang, Q.; Guo, Z. An overview of multifunctional epoxy nanocomposites. *J. Mater. Chem. C* **2016**, *4*, 5890–5906. [CrossRef]
33. Chen, Q.; Miyata, N.; Kokubo, T.; Nakamura, T. Bioactivity and mechanical properties of PDMS-modified CaO-SiO_2-TiO_2 hybrids prepared by sol-gel process. *J. Biomed. Mater. Res.* **2000**, *51*, 605–611. [CrossRef]
34. Pomogailo, A.D. Polymer sol-gel synthesis of hybrid nanocomposites. *Colloid J.* **2005**, *67*, 658–677. [CrossRef]
35. Livage, J.; Sanchez, C. Sol-gel chemistry. *J. Non-Cryst. Solids* **1992**, *145*, 11–19. [CrossRef]
36. Yu, W.; Fu, J.; Dong, X.; Chen, L.; Jia, H.; Shi, L. Highly populated and nearly monodispersed nanosilica particles in an organic medium and their epoxy nanocomposites. *ACS Appl. Mater. Interfaces* **2013**, *5*, 8897–8906. [CrossRef] [PubMed]
37. Hay, J.N.; Raval, H.M. Synthesis of organic-inorganic hybrids via the non-hydrolytic sol-gel process. *Chem. Mater.* **2001**, *13*, 3396–3403. [CrossRef]
38. Styskalik, A.; Skoda, D.; Barnes, C.; Pinkas, J. The Power of Non-Hydrolytic Sol-Gel Chemistry: A Review. *Catalysts* **2017**, *7*, 168. [CrossRef]
39. Ogoshi, T.; Chujo, Y. Organic-inorganic polymer hybrids prepared by the sol-gel method. *Compos. Interfaces* **2005**, *11*, 539–566. [CrossRef]
40. Brinker, C.J.; Scherer, G.W. *Sol-Gel Science: The Physics and Chemistry of Sol–Gel Processing*; Academic Press, Inc.: Cambridge, MA, USA, 1990; ISBN 9780080571034.
41. Callister, W.D., Jr.; Rethwisch, D.G.; Balsubramaniam, R. *Callister's Materials Science and Engineering*, 8th ed.; Wiley India: New Delhi, India, 2010.
42. Solomons, G.; Fryhle, C. *Organic Chemistry*, 10th ed.; Wiley: New Delhi, India, 2009; ISBN 0470556595.
43. Plueddemann, E.P. *Silane Coupling Agents*, 2nd ed.; Springer-Verlag US: Boston, MA, USA, 1991; ISBN 978-1-4899-2070-6.
44. Plueddemann, E.P. Adhesion Through Silane Coupling Agents. *J. Adhes.* **1970**, *2*, 184–201. [CrossRef]
45. Mallakpour, S.; Hatami, M. Dispersion of Surface Modified Nanostructure Zinc Oxide in Optically Active Poly(Amide-Imide) Containing Pyromellitoyl-*bis*-L-isoleucine Segments: Nanocomposite Preparation and Morphological Investigation. *Polym. Plast. Technol. Eng.* **2012**, *51*, 1106–1112. [CrossRef]
46. Dalod, A.R.M.; Grendal, O.G.; Skjærvø, S.L.; Inzani, K.; Selbach, S.M.; Henriksen, L.; van Beek, W.; Grande, T.; Einarsrud, M.-A. Controlling Oriented Attachment and in Situ Functionalization of TiO_2 Nanoparticles During Hydrothermal Synthesis with APTES. *J. Phys. Chem. C* **2017**, *121*, 11897–11906. [CrossRef]
47. Dalod, A.R.M.; Henriksen, L.; Grande, T.; Einarsrud, M.-A. Functionalized TiO_2 nanoparticles by single-step hydrothermal synthesis: The role of the silane coupling agents. *Beilstein J. Nanotechnol.* **2017**, *8*, 304–312. [CrossRef] [PubMed]
48. Bi, Y.-T.; Li, Z.-J.; Liang, W. Preparation and characterization of epoxy/SiO_2 nanocomposites by cationic photopolymerization and sol–gel process. *Polym. Adv. Technol.* **2013**, *25*, 173–178. [CrossRef]
49. Yang, C.-F.; Wang, L.-F.; Wu, S.-M.; Su, C.-C. Characterization and Curing Kinetics of Epoxy/Silica Nano-Hybrids. *Materials* **2015**, *8*, 7032–7040. [CrossRef] [PubMed]
50. Jiao, J.; Liu, P.; Cai, Y. One-step synthesis of improved silica/epoxy nanocomposites with inorganic-organic hybrid network. *J. Polym. Res.* **2013**, *20*. [CrossRef]
51. Afzal, A.; Siddiqi, H.M. A comprehensive study of the bicontinuous epoxy-silica hybrid polymers: I. Synthesis, characterization and glass transition. *Polymer* **2011**, *52*, 1345–1355. [CrossRef]
52. Nazir, T.; Afzal, A.; Siddiqi, H.M.; Ahmad, Z.; Dumon, M. Thermally and mechanically superior hybrid epoxy-silica polymer films via sol-gel method. *Prog. Org. Coat.* **2010**, *69*, 100–106. [CrossRef]

53. Siddabattuni, S.; Schuman, T.P.; Dogan, F. Dielectric Properties of Polymer−Particle Nanocomposites Influenced by Electronic Nature of Filler Surfaces. *ACS Appl. Mater. Interfaces* **2013**, *5*, 1917–1927. [CrossRef] [PubMed]
54. Bauer, B.J.; Liu, D.W.; Jackson, C.L.; Barnes, J.D. Epoxy/SiO_2 interpenetrating polymer networks. *Polym. Adv. Technol.* **1996**, *7*, 333–339. [CrossRef]
55. Matějka, L.; Pleštil, J.; Dušek, K. Structure evolution in epoxy–silica hybrids: Sol–gel process. *J. Non-Cryst. Solids* **1998**, *226*, 114–121. [CrossRef]
56. Matějka, L.; Dušek, K.; Pleštil, J.; Kříž, J.; Lednický, F. Formation and structure of the epoxy-silica hybrids. *Polymer* **1999**, *40*, 171–181. [CrossRef]
57. Matejka, L.; Dukh, O.; Kolařík, J. Reinforcement of crosslinked rubbery epoxies by in-situ formed silica. *Polymer* **2000**, *41*, 1449–1459. [CrossRef]
58. Chiang, C.L.; Ma, C.C.M. Synthesis, characterization and thermal properties of novel epoxy containing silicon and phosphorus nanocomposites by sol-gel method. *Eur. Polym. J.* **2002**, *38*, 2219–2224. [CrossRef]
59. Wu, C.C.; Hsu, S.L.C. Preparation of epoxy/silica and epoxy/titania hybrid resists via a sol-gel process for nanoimprint lithography. *J. Phys. Chem. C* **2010**, *114*, 2179–2183. [CrossRef]
60. Sangermano, M.; Malucelli, G.; Amerio, E.; Bongiovanni, R.; Priola, A. Preparation and Characterization of Nanostructured TiO_2/Epoxy Polymeric Films. *Macromol. Mater. Eng.* **2006**, *291*, 517–523. [CrossRef]
61. Guan, C.; Lü, C.L.; Liu, Y.F.; Yang, B. Preparation and characterization of high refractive index thin films of TiO_2/epoxy resin nanocomposites. *J. Appl. Polym. Sci.* **2006**, *102*, 1631–1636. [CrossRef]
62. Donato, R.K.; Perchacz, M.; Ponyrko, S.; Donato, K.Z.; Schrekker, H.S.; Beneš, H.; Matějka, L. Epoxy–silica nanocomposite interphase control using task-specific ionic liquids via hydrolytic and non-hydrolytic sol–gel processes. *RSC Adv.* **2015**, *5*, 91330–91339. [CrossRef]
63. Donato, R.K.; Matějka, L.; Schrekker, H.S.; Pletil, J.; Jigounov, A.; Brus, J.; Slouf, M. The multifunctional role of ionic liquids in the formation of epoxy-silica nanocomposites. *J. Mater. Chem.* **2011**, *21*, 13801–13810. [CrossRef]
64. Donato, R.K.; Donato, K.Z.; Schrekker, H.S.; Matějka, L. Tunable reinforcement of epoxy-silica nanocomposites with ionic liquids. *J. Mater. Chem.* **2012**, *22*, 9939–9948. [CrossRef]
65. Glaser, R.H.; Wilkes, G.L. Structure property behavior of polydimethylsiloxane and poly(tetramethylene oxide) modified TEOS based sol-gel materials. V. Effect of titaniumisopropoxide incorporation. *Polym. Bull.* **1988**, *19*, 51–57. [CrossRef]
66. Shindou, T.; Katayama, S.; Yamada, N.; Kamiya, K. Effect of composition on surface properties of polydimethylsiloxane-based inorganic/organic hybrid films. *J. Sol-Gel Sci. Technol.* **2004**, *30*, 229–237. [CrossRef]
67. Lu, Q.; Mullins, M.E. In situ Synthesis of High Refractive Index PDMS/Metal Oxide Nanocomposites. *MRS Proc.* **2012**, *1400*. [CrossRef]
68. Wu, L.Y.L.; Tan, G.H.; Zeng, X.T.; Li, T.H.; Chen, Z. Synthesis and characterization of transparent hydrophobic sol-gel hard coatings. *J. Sol-Gel Sci. Technol.* **2006**, *38*, 85–89. [CrossRef]
69. Yamada, N.; Yoshinaga, I.; Katayama, S. Formation behavior and optical properties of transparent inorganic-organic hybrids prepared from metal alkoxides and polydimethylsiloxane. *J. Sol-Gel Sci. Technol.* **2000**, *17*, 123–130. [CrossRef]
70. Yamada, N.; Yoshinaga, I.; Katayama, S. Synthesis and dynamic mechanical behaviour of inorganic–organic hybrids containing various inorganic components. *J. Mater. Chem.* **1997**, *7*, 1491–1495. [CrossRef]
71. Yamada, N.; Yoshinaga, I.; Katayama, S. Processing and properties of inorganic-organic hybrids containing various inorganic components. *J. Sol-Gel Sci. Technol.* **1999**, *13*, 445–449. [CrossRef]
72. Katayama, S.; Kubo, Y.; Yamada, N. Characterization and mechanical properties of flexible dimethylsiloxane-based inorganic/organic hybrid sheets. *J. Am. Ceram. Soc.* **2002**, *85*, 1157–1163. [CrossRef]
73. Carlos Almeida, J.; Castro, A.G.B.; Miranda Salvado, I.M.; Margaça, F.M.A.; Vaz Fernandes, M.H. A new approach to the preparation of PDMS–SiO_2 based hybrids—A structural study. *Mater. Lett.* **2014**, *128*, 105–109. [CrossRef]
74. Julián, B.; Gervais, C.; Cordoncillo, E.; Escribano, P.; Babonneau, F.; Sanchez, C. Synthesis and characterization of transparent PDMS-metal-oxo based organic-inorganic nanocomposites. *Chem. Mater.* **2003**, *15*, 3026–3034. [CrossRef]

75. Fragiadakis, D.; Pissis, P.; Bokobza, L. Glass transition and molecular dynamics in poly(dimethylsiloxane)/silica nanocomposites. *Polymer* **2005**, *46*, 6001–6008. [CrossRef]
76. Dewimille, L.; Bresson, B.; Bokobza, L. Synthesis, structure and morphology of poly(dimethylsiloxane) networks filled with in situ generated silica particles. *Polymer* **2005**, *46*, 4135–4143. [CrossRef]
77. Yuan, Q.W.; Mark, J.E. Reinforcement of poly(dimethylsiloxane) networks by blended andin-situgenerated silica fillers having various sizes, size distributions, and modified surfaces. *Macromol. Chem. Phys.* **1999**, *200*, 206–220. [CrossRef]
78. Breiner, J.M.; Mark, J.E.; Beaucage, G. Dependence of silica particle sizes on network chain lengths, silica contents, and catalyst concentrations in in situ-reinforced polysiloxane elastomers. *J. Polym. Sci. Part B Polym. Phys.* **1999**, *37*, 1421–1427. [CrossRef]
79. Rajan, G.S.; Sur, G.S.; Mark, J.E.; Schaefer, D.W.; Beaucage, G. Preparation and characterization of some unusually transparent poly(dimethylsiloxane) nanocomposites. *J. Polym. Sci. Part B Polym. Phys.* **2003**, *41*, 1897–1901. [CrossRef]
80. Zhang, X.; Ye, H.; Xiao, B.; Yan, L.; Lv, H.; Jiang, B. Sol-Gel Preparation of PDMS/Silica Hybrid Antireflective Coatings with Controlled Thickness and Durable Antireflective Performance. *J. Phys. Chem. C* **2010**, *114*, 19979–19983. [CrossRef]
81. Donato, R.K.; Lavorgna, M.; Musto, P.; Donato, K.Z.; Jager, A.; Štěpánek, P.; Schrekker, H.S.; Matějka, L. The role of ether-functionalized ionic liquids in the sol-gel process: Effects on the initial alkoxide hydrolysis steps. *J. Colloid Interface Sci.* **2015**, *447*, 77–84. [CrossRef] [PubMed]
82. Seyferth, D. Dimethyldichlorosilane and the Direct Synthesis of Methylchlorosilanes. The Key to the Silicones Industry. *Organometallics* **2001**, *20*, 4978–4992. [CrossRef]
83. Abbasi, F.; Mirzadeh, H.; Katbab, A.A. Modification of polysiloxane polymers for biomedical applications: A review. *Polym. Int.* **2001**, *50*, 1279–1287. [CrossRef]
84. Kumar, B.V.M.; Kim, Y.W. Processing of polysiloxane-derived porous ceramics: A review. *Sci. Technol. Adv. Mater.* **2010**, *11*. [CrossRef]
85. Kataoka, T.; Ueda, S. Viscosity–molecular weight relationship for polydimethylsiloxane. *J. Polym. Sci. Part B Polym. Lett.* **1966**, *4*, 317–322. [CrossRef]
86. Fragiadakis, D.; Pissis, P.; Bokobza, L. Modified chain dynamics in poly(dimethylsiloxane)/silica nanocomposites. *J. Non-Cryst. Solids* **2006**, *352*, 4969–4972. [CrossRef]
87. Fragiadakis, D.; Pissis, P. Glass transition and segmental dynamics in poly(dimethylsiloxane)/silica nanocomposites studied by various techniques. *J. Non-Cryst. Solids* **2007**, *353*, 4344–4352. [CrossRef]
88. Liu, Y.; Lee, J.Y.; Hong, L. In situ preparation of poly(ethylene oxide)-SiO_2 composite polymer electrolytes. *J. Power Sources* **2004**, *129*, 303–311. [CrossRef]
89. Bahloul, W.; Bounor-Legaré, V.; David, L.; Cassagnau, P. Morphology and viscoelasticity of PP/TiO_2 nanocomposites prepared by in situ sol-gel method. *J. Polym. Sci. Part B Polym. Phys.* **2010**, *48*, 1213–1222. [CrossRef]
90. Bahloul, W.; Oddes, O.; Bounor-Legaré, V.; Mélis, F.; Cassagnau, P.; Vergnes, B. Reactive extrusion processing of polypropylene/TiO_2 nanocomposites by in situ synthesis of the nanofillers: Experiments and modeling. *AIChE J.* **2011**, *57*, 2174–2184. [CrossRef]
91. Jain, S.; Goossens, H.; Picchioni, F.; Magusin, P.; Mezari, B.; Van Duin, M. Synthetic aspects and characterization of polypropylene-silica nanocomposites prepared via solid-state modification and sol-gel reactions. *Polymer* **2005**, *46*, 6666–6681. [CrossRef]
92. Chen, Y.; Iroh, J.O. Synthesis and Characterization of Polymide/Silica Hybrid Composites. *Chem. Mater.* **1999**, *11*, 1218–1222. [CrossRef]
93. González, M.; Soares, B.G.; Magioli, M.; Marins, J.A.; Rieumont, J. Facile method for synthesis of polyaniline/silica hybrid composites by simultaneous sol-gel process and "in situ" polymerization of aniline. *J. Sol-Gel Sci. Technol.* **2012**, *63*, 373–381. [CrossRef]
94. Zhang, J.; Wen, B.; Wang, F.; Ding, Y.; Zhang, S.; Yang, M. In situ synthesis of ZnO nanocrystal/PET hybrid nanofibers via electrospinning. *J. Polym. Sci. Part B Polym. Phys.* **2011**, *49*, 1360–1368. [CrossRef]
95. Balci, M.H.; Aas, L.M.S.; Kildemo, M.; Sæterli, R.; Holmestad, R.; Lindgren, M.; Grande, T.; Einarsrud, M.A. White light emitting silicon nano-crystals-polymeric hybrid films prepared by single batch solution based method. *Thin Solid Films* **2016**, *603*, 126–133. [CrossRef]

96. Fearon, F.W.G.; Young, J.C. Reaction of triphenylsilyl halides with sodium naphthalenide. *J. Chem. Soc. B Phys. Org.* **1971**, 272–276. [CrossRef]
97. Balci, M.H.; Maria, J.; Vullum-Bruer, F.; Lindgren, M.; Grande, T.; Einarsrud, M.A. Synthesis of Monodisperse Silicon Quantum Dots Through a K-Naphthalide Reduction Route. *J. Clust. Sci.* **2012**, *23*, 421–435. [CrossRef]
98. Sletnes, M.; Maria, J.; Grande, T.; Lindgren, M.; Einarsrud, M.A. Octoxy capped Si nanoparticles synthesized by homogeneous reduction of $SiCl_4$ with crown ether alkalide. *Dalt. Trans.* **2014**, *43*, 2127–2133. [CrossRef] [PubMed]
99. Stille, J.K. Diels-alder polymerization. In *Fortschritte Der Hochpolymeren-Forschung*; Springer: Berlin/Heidelberg, Germany, 1961; Volume 3, pp. 48–58. [CrossRef]
100. Sohn, H.; Huddleston, R.R.; Powell, D.R.; West, R.; Oka, K.; Yonghua, X. An electroluminescent polysilole and some dichlorooligosiloles. *J. Am. Chem. Soc.* **1999**, *121*, 2935–2936. [CrossRef]
101. Yang, Y.; Wang, P. Preparation and characterizations of a new PS/TiO_2 hybrid membranes by sol–gel process. *Polymer* **2006**, *47*, 2683–2688. [CrossRef]
102. Bounor-Legaré, V.; Angelloz, C.; Blanc, P.; Cassagnau, P.; Michel, A. A new route for organic-inorganic hybrid material synthesis through reactive processing without solvent. *Polymer* **2004**, *45*, 1485–1493. [CrossRef]
103. Wu, C.S.; Liao, H.T. In situ polymerization of silicic acid in polyethylene-octene elastomer: Properties and characterization of the hybrid nanocomposites. *J. Polym. Sci. Part B Polym. Phys.* **2003**, *41*, 351–359. [CrossRef]
104. He, J.-P.; Li, H.-M.; Wang, X.-Y.; Gao, Y. In situ preparation of poly(ethylene terephthalate)–SiO_2 nanocomposites. *Eur. Polym. J.* **2006**, *42*, 1128–1134. [CrossRef]
105. Amjadi, M.; Rowshanzamir, S.; Peighambardoust, S.J.; Hosseini, M.G. Investigation of physical properties and cell performance of Nafion/TiO_2 nanocomposite membranes for high temperature PEM fuel cells. *Int. J. Hydrogen Energy* **2010**, *35*, 9252–9260. [CrossRef]
106. Du, H.; Xu, G.Q.; Chin, W.S.; Huang, L.; Ji, W. Synthesis, Characterization, and Nonlinear Optical Properties of Hybridized CdS−Polystyrene Nanocomposites. *ACS Chem. Mater.* **2002**, *14*, 4473–4479. [CrossRef]
107. Liu, D.; He, G.; Zeng, X.; Sun, D.; Li, X. Preparation of SiO_2/epoxy nanocomposite via reverse microemulsion in situ polymerization. *Polym. Compos.* **2014**, *35*, 1388–1394. [CrossRef]
108. Bell, M.; Krentz, T.; Nelson, J.K.; Schadler, L.; Wu, K.; Breneman, C.; Zhao, S.; Hillborg, H.; Benicewicz, B. Investigation of dielectric breakdown in silica-epoxy nanocomposites using designed interfaces. *J. Colloid Interface Sci.* **2017**, *495*, 130–139. [CrossRef] [PubMed]
109. Calebrese, C.; Hui, L.; Schadler, L.S.; Nelson, J.K. A Review on the Importance of Nanocomposite Processing to Enhance Electrical Insulation. *IEEE Trans. Dielectr. Electr. Insul.* **2011**, *18*, 938–945. [CrossRef]
110. Kamitakahara, M.; Kawashita, M.; Miyata, N.; Kokubo, T.; Nakamura, T. Bioactivity and Mechanical Properties of Polydimethylsiloxane (PDMS)-CaO-SiO_2 Hybrids with Different PDMS Contents. *J. Sol-Gel Sci. Technol.* **2001**, *21*, 75–81. [CrossRef]
111. Chen, Q.; Miyaji, F.; Kokubo, T.; Nakamura, T. Apatite formation on PDMS-modified CaO-SiO_2-TiO_2 hybrids prepared by sol-gel process. *Biomaterials* **1999**, *20*, 1127–1132. [CrossRef]
112. Bose, S.; Kuila, T.; Nguyen, T.X.H.; Kim, N.H.; Lau, K.; Lee, J.H. Polymer membranes for high temperature proton exchange membrane fuel cell: Recent advances and challenges. *Prog. Polym. Sci.* **2011**, *36*, 813–843. [CrossRef]
113. Tripathi, B.P.; Shahi, V.K. Organic-inorganic nanocomposite polymer electrolyte membranes for fuel cell applications. *Prog. Polym. Sci.* **2011**, *36*, 945–979. [CrossRef]
114. Shah, M.S.A.S.; Basak, P.; Manorama, S.V. Polymer nanocomposites as solid electrolytes: Evaluating ion-polymer and polymer-nanoparticle interactions in PEG-PU/PAN Semi-IPNs and titania systems. *J. Phys. Chem. C* **2010**, *114*, 14281–14289. [CrossRef]
115. Sarkar, S.; Guibal, E.; Quignard, F.; Sengupta, A.K. Polymer-supported metals and metal oxide nanoparticles: Synthesis, characterization, and applications. *J. Nanopart. Res.* **2012**, *14*. [CrossRef]
116. Yeung, C.; Vaughan, A.S. On the Effect of Nanoparticle Surface Chemistry on the Electrical Characteristics of Epoxy-Based Nanocomposites. *Polymers* **2016**, *8*, 126. [CrossRef]
117. Virtanen, S.; Krentz, T.; Nelson, J.K.; Schadler, L.; Bell, M.; Benicewicz, B.; Hillborg, H.; Zhao, S. Dielectric Breakdown Strength of Epoxy Bimodal-polymer-Brush-Grafted Core Functionalized Silica Nanocomposites. *IEEE Trans. Dielectr. Electr. Insul.* **2014**, *21*. [CrossRef]

118. Liang, M.; Wong, K.L. Electrical performance of epoxy resin filled with micro particles and nanoparticles. *Energy Procedia* **2017**, *110*, 162–167. [CrossRef]
119. Goyat, M.S.; Rana, S.; Halder, S.; Ghosh, P.K. Facile fabrication of epoxy-TiO_2 nanocomposites: A critical analysis of TiO_2 impact on mechanical properties and toughening mechanisms. *Ultrason. Sonochem.* **2018**, *40*, 861–873. [CrossRef] [PubMed]
120. Liang, Y.L.; Pearson, R.A. Toughening mechanisms in epoxy–silica nanocomposites (ESNs). *Polymer* **2009**, *50*, 4895–4905. [CrossRef]
121. Roy, M.; Nelson, J.K.; MacCrone, R.K.; Schadler, L.S.; Reed, C.W.; Keefe, R.; Zenger, W. Polymer nanocomposite dielectrics—The role of the interface. *IEEE Trans. Dielectr. Electr. Insul.* **2005**, *12*, 629–642. [CrossRef]
122. Roy, M.; Nelson, J.K.; MacCrone, R.K.; Schadler, L.S. Candidate mechanisms controlling the electrical characteristics of silica/XLPE nanodielectrics. *J. Mater. Sci.* **2007**, *42*, 3789–3799. [CrossRef]
123. Ishimoto, K.; Kanegae, E.; Ohki, Y.; Tanaka, T.; Sekiguchi, Y.; Murata, Y.; Reddy, C. Superiority of dielectric properties of LDPE/MgO nanocomposites over microcomposites. *IEEE Trans. Dielectr. Electr. Insul.* **2009**, *16*, 1735–1742. [CrossRef]
124. Murakami, Y.; Nemoto, M.; Okuzumi, S.; Masuda, S.; Nagao, M. DC Conduction and Electrical Breakdown of MgO/LDPE Nanocomposite. *IEEE Trans. Dielectr. Electr. Insul.* **2008**, *15*, 290–293. [CrossRef]
125. Fleming, R.; Ammala, A.; Casey, P.S.; Lang, S.B. Conductivity and space charge in LDPE containing nano-and micro-sized ZnO particles. *IEEE Trans. Dielectr. Electr. Insul.* **2008**, *15*, 118–126. [CrossRef]
126. Tanaka, T.; Montanari, G.C.; Mulhaupt, R. Polymer Nanocomposites as Dielectrics and Electrical Insulation-perspectives for Processing Technologies, Material Characterization and Future Applications. *IEEE Trans. Dielectr. Electr. Insul.* **2004**, *11*, 763–784. [CrossRef]
127. Adjemian, K.T.; Dominey, R.; Krishnan, L.; Ota, H.; Majsztrik, P.; Zhang, T.; Mann, J.; Kirby, B.; Gatto, L.; Velo-Simpson, M.; et al. Function and characterization of metal oxide-nafion composite membranes for elevated-temperature H_2/O_2 PEM fuel cells. *Chem. Mater.* **2006**, *18*, 2238–2248. [CrossRef]
128. Shao, Z.-G.; Joghee, P.; Hsing, I.-M. Preparation and characterization of hybrid Nafion-silica membrane doped with phosphotungstic acid for high temperature operation of proton exchange membrane fuel cells. *J. Memb. Sci.* **2004**, *229*, 43–51. [CrossRef]
129. Panero, S.; Fiorenza, P.; Navarra, M.A.; Romanowska, J.; Scrosati, B. Silica-Added, Composite Poly(vinyl alcohol) Membranes for Fuel Cell Application. *J. Electrochem. Soc.* **2005**, *152*, A2400. [CrossRef]
130. Nagarale, R.K.; Gohil, G.S.; Shahi, V.K.; Rangarajan, R. Organic-Inorganic Hybrid Membrane: Thermally Stable Cation-Exchange Membrane Prepared by the Sol-Gel Method. *Macromolecules* **2004**, *37*, 10023–10030. [CrossRef]
131. Shen, J.; Xi, J.; Zhu, W.; Chen, L.; Qiu, X. A nanocomposite proton exchange membrane based on PVDF, poly(2-acrylamido-2-methyl propylene sulfonic acid), and nano-Al_2O_3 for direct methanol fuel cells. *J. Power Sources* **2006**, *159*, 894–899. [CrossRef]
132. Liu, Y.-L.; Wu, C.-S.; Chiu, Y.-S.; Ho, W.-H. Preparation, Thermal Properties, and Flame Retardance of Epoxy–Silica Hybrid Resins. *J. Polym. Sci. Part A Polym. Chem.* **2003**, *41*, 2354–2367. [CrossRef]
133. Shi, X.; Nguyen, T.A.; Suo, Z.; Liu, Y.; Avci, R. Effect of nanoparticles on the anticorrosion and mechanical properties of epoxy coating. *Surf. Coat. Technol.* **2009**, *204*, 237–245. [CrossRef]
134. Habouti, S.; Kunstmann-Olsen, C.; Hoyland, J.D.; Rubahn, H.G.; Es-Souni, M. In situ ZnO-PVA nanocomposite coated microfluidic chips for biosensing. *Appl. Phys. A Mater. Sci. Process.* **2014**, *115*, 645–649. [CrossRef]
135. Mostafaei, A.; Nasirpouri, F. Preparation and characterization of a novel conducting nanocomposite blended with epoxy coating for antifouling and antibacterial applications. *J. Coat. Technol. Res.* **2013**, *10*, 679–694. [CrossRef]

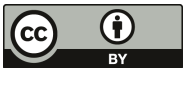

polymers

MDPI

Article

Effect of Morphological Changes due to Increasing Carbon Nanoparticles Content on the Quasi-Static Mechanical Response of Epoxy Resin

Hamed Yazdani Nezhad * and Vijay Kumar Thakur *

Enhanced Composites & Structures Centre, School of Aerospace, Transport & Manufacturing, Cranfield University, Milton Keynes MK9 2BS, UK

* Correspondence: h.yazdani-nezhad@cranfield.ac.uk (H.Y.N.); vijay.kumar@cranfield.ac.uk (V.K.T.); Tel.: +44-(0)1234-750-111 (H.Y.N. & V.K.T.)

Received: 15 September 2018; Accepted: 5 October 2018; Published: 6 October 2018

Abstract: Mechanical failure in epoxy polymer and composites leads them to commonly be referred to as inherently brittle due to the presence of polymerization-induced microcrack and microvoids, which are barriers to high-performance applications, e.g., in aerospace structures. Numerous studies have been carried out on epoxy's strengthening and toughening via nanomaterial reinforcement, e.g., using rubber nanoparticles in the epoxy matrix of new composite aircraft. However, extremely cautious process and functionalization steps must be taken in order to achieve high-quality dispersion and bonding, the development of which is not keeping pace with large structures applications. In this article, we report our studies on the mechanical performance of an epoxy polymer reinforced with graphite carbon nanoparticles (CNPs), and the possible effects arising from a straightforward, rapid stir-mixing technique. The CNPs were embedded in a low viscosity epoxy resin, with the CNP weight percentage (wt %) being varied between 1% and 5%. Simplified stirring embedment was selected in the interests of industrial process facilitation, and functionalization was avoided to reduce the number of parameters involved in the study. Embedment conditions and timing were held constant for all wt %. The CNP filled epoxy resin was then injected into an aluminum mold and cured under vacuum conditions at 80 °C for 12 h. A series of test specimens were then extracted from the mold, and tested under uniaxial quasi-static tension, compression, and nanoindentation. Elementary mechanical properties including failure strain, hardness, strength, and modulus were measured. The mechanical performance was improved by the incorporation of 1 and 2 wt % of CNP but was degraded by 5 wt % CNP, mainly attributed to the morphological change, including re-agglomeration, with the increasing CNP wt %. This change strongly correlated with the mechanical response in the presence of CNP, and was the major governing mechanism leading to both mechanical improvement and degradation.

Keywords: polymers; composites; carbon nanoparticles

1. Introduction

Polymer-based particulate nanocomposites prepared using particulates with small aspect ratios represent one of the emerging classes of composite materials [1–10]. Mechanical properties of nanocomposite materials such as toughness, stiffness, and strength are significantly affected by the interface adhesion amongst the particle and polymer matrix, size/shape of the particle, and its loading [11–15]. These properties are of priority to the main structural analysis [16–18]. Different techniques and manufacturing processes for particulate polymer composites are reviewed in several publications and reports, such as a comprehensive study for calcium carbonate ($CaCO_3$) in [9] and for a number of 2D and 3D layered nanostructures in [19,20] or for dielectric heating purposes [21].

Enhancements in different mechanical properties have been addressed in [9] with the addition of a few weight percentage (wt %) of carbon nanomaterials, e.g., carbon nanotubes, because in thermosetting resins inorganic particles were found to be imperative fillers/reinforcement. It is well-known that with the incorporation of micro/nano-particles, Young's modulus can be enhanced because the rigid inorganic particles commonly exhibit higher stiffness in comparison to the polymer matrices. However, the quality of the bond between nanoparticle and polymer has been proven to play a significant part in the structural strength [9], i.e., interface adhesion among the reinforcing particle–polymer matrix and content of the particle (i.e., loading) are the two most imperative aspects affecting the mechanical properties.

However, a substantial reduction in the fracture toughness of thermoplastic polymers reinforced with rigid particulates in comparison to the as-received polymers has been reported [22]. On the other hand, some studies have also reported on the increment in toughness of thermoplastics such as polypropylene/polyethylene with the incorporation of rigid particles in [4,6]. An increase in impact toughness has also been described in the composites of polyethylene reinforced with $CaCO_3$ particles [4,6,8]. According to [4], nanoparticle incorporation into the polymers results in greater rigidity as well as better yield strength. It has been reported that reinforcement of polypropylene with calcium carbonate particles imparts good strength to the resulting composites at a particular loading. It has also been shown by several authors that the modulus is not affected to a large degree in studies where the mean particle diameter was greater than 100 nm [3,9,23]. These studies were focused on silica/epoxy, aluminum hydroxide filled polypropylene, $CaCO_3$-filled polybenzoxazine, aluminum particle/polyester, and organo-soluble polyimide/silica material systems. Conversely, when the particle size is reduced below 100 nm, there is a clear correlation between particle size and the modulus. Polypropylene/$CaCO_3$ composites containing smaller nanoparticles (21 nm) were shown to exhibit a higher Young's modulus in comparison to the nanoparticles with larger size (39 nm) [2], having characterized the nanoparticles using X-ray diffraction. Thus, it's been suggested that above a critical particle size, no further degrading effect on the modulus of the prepared composites takes place. Furthermore, the magnitude of the critical particle size has been found to be dependent on the type of particle/reinforcement polymer matrix as well as particle/polymer matrix adhesion [24]. In contrast to the effective particle size, treatment for the purpose of increasing the particle-polymer interfacial adhesion exhibits a lesser or negligible effect on the mechanical stiffness. For particulate reinforcement/particle loading (i.e., volume fraction) the composite strength has been found to increase with a decrease in particle size [25], as smaller particles increase the total interfacial surface area. In an interesting work, the effect of the size of the reinforcing particle on the strength of PA6/silica nanocomposites with mean sizes of 12, 25, and 50 nm in [26] was studied and it has been shown that with the incorporation of particles, an increase in strength is observed. In fact, the adhesion quality between the polymer matrix and the reinforcement affects the overall composite strength and toughness. The toughness is also affected by the size of the particle, interfacial adhesion, and particle content level. It is expected that in a ductile medium (e.g., thermoplastics), the inclusion of fillers increases the brittleness of composite if there is limited/no interfacial adhesion. In case of polymer matrices having brittle characteristics (e.g., thermoset epoxy), a reverse phenomenon is expected to occur as the particles introduce a crack arrest mechanism to the brittle medium, thus considerably reducing the brittleness. Moreover, micro-cavitation and micro-debonding can easily occur in such a medium during composite manufacturing or mechanical loading and cracks can coalesce.

Generally speaking, the bond equality is often attributed to process control parameters such as ultrasonication, dispersion, surface functionalization, treatment and mixing techniques. Control over numerous parameters may become an efficiency challenge (in terms of adding extra time and cost) for industrial applications, and as such, industries tend to follow straightforward mixing processes. Also, design against brittle failure (the case of epoxy polymers; this study) in nanocomposites is of critical importance. In a given bulk polymer material, the transition from a brittle to a ductile fracture is significant as the fracture behavior is considerably affected by the internal/external conditions.

Thermoset epoxies are intensely used in structural applications despite the fact their brittleness has necessitated the incorporation of inclusions, e.g., particulate fillers. In the toughness study of nano-filled polymers, plane strain and plane stress driven cracks are superimposed to determine the impact of the incorporation on the modification of the polymer's bulk properties, meaning that if, in the nano-filled polymer, regions with plane stress driven fracture are provoked within the space between nanoparticles, the polymer will tend to yield longer. Thereby, a macroscopic brittle matrix filled by nanoparticles may display localized plastic deformation [27–29]. Accordingly, incorporation of carbon nanoparticles in polymers reduces the polymer resistance to plastic deformation by allowing cavitation and debonding prior to plastic flow. Thus, for a carbon nanoparticle (CNP) filled epoxy, the strength depends on the effective stress transfer among the reinforcing particle and polymer. This is driven by adhesion and therefore geometry-related morphological features can become highly influential. On the other hand, nano-composite stiffness depends on the particle content, not the adhesion. This is attributed to a significantly greater modulus of the particles than the polymer matrix [30]. In this paper, the mechanical response of the bulk of CNP filled epoxy has been studied by focusing on the effects of morphological variation with increasing CNP content. The epoxy has been chosen as the matrix because of its superior mechanical properties; resistance to stresses (e.g., thermal), low viscosity which facilitates the dispersion of reinforcement; low shrinkage, improved adhesion to the targeted substrate, and degradation over time to name only a few [14,17,29]. The study has been performed in two micro- and macro-scales: Bulk and CNP reinforced specimens were manufactured and exposed to tension, compression, and nanoindentation. As the CNP loading content plays a significant role in the determination of the bulk response, mechanical properties (modulus, hardness, strength, and failure strain) were studied with the variation of CNP wt %.

2. Materials and Methods

2.1. Epoxy Resin

The epoxy matrix composite was prepared by first mixing a low viscosity epoxy precursor (Epoxy equivalent weight 117–133 g/eq), with Methyl nadic anhydride (MNA) that acts as a hardener with 2-Dodecenyl succinic anhydride (DDSA). Since the viscosity of the various ingredients differs, it is imperative to mix all the ingredients thoroughly. The mix bundle was stirred for a few hours before adding the curing agent. The epoxy precursor, hardeners, and curing agent were supplied by Sigma-Aldrich, Dorset, UK. 2,4,6-Tri (dimethyl aminomethyl) phenol (DMP-30) was used as the curing agent in this work. According to the epoxy specifications, the viscosity reached 60 cps which is approximately 10 % of the viscosity of conventional resins for composite applications and thus facilitated the CNP incorporation.

The final epoxy mixture was gently injected to molds suitable for the test stages (tensile, compression, and nano-indentation) and was cured at 80 °C for 12 h in a conventional vacuum-assisted heating oven. Higher temperature curing was not used to avoid any possible drawback on the CNP-epoxy interfaces, e.g., the interfacial pre-existing dis-bond due to thermally-induced residual stresses. As per our differential scanning calorimetry (DSC) investigation, the T_g (glass transition temperature) for the final mixture was 77 °C.

2.2. Release Agent

The high-performance solvent-free polymer release agent, Zyvax®Watershield, was applied to the mold surfaces three times for easy mold release. Each time the agent was allowed to dry out on the surfaces for 30 min. The mold was then closed, and the final mixture was injected.

2.3. Curing Agent

A proportion of 1.5–2.0% of DPM-30 was added to the mixture shortly after CNPs were added and stirred for 12 h at room temperature (RT). The 1.5–2% DPM-30 enhances the strength and adds

brittleness to the final mixture according to the supplier's specifications. The temperature of the mixture was not increased before adding the curing agent in order to ensure a slower rate of cross-linking. The final mixture with the CNPs was then stirred under vacuum conditions using a Schlenk line at RT with a magnetic stirrer. The mixture was de-gassed after adding the curing agent, at <5 kPa (0.05 atmospheres).

2.4. Adding Nanoparticle to the Epoxy Mixture

Simple short-step processing methods are highly important for industrial applications as they benefit mass production. A simple mixing method is suggested herein: The epoxy mixture was heated up to 100 °C before the CNPs were added. Heating provides a mixture with a relatively low viscosity that leads to a good CNP dispersion [22]. CNPs, supplied by Sigma-Aldrich with an average size of 50–100 nm (molecular weight of 12.01 g/mol), were then directly added to the mixture, according to the direct addition procedure in [31]. The mixture of the nanoparticles and the epoxy/curing agent bundle was stirred under vacuum conditions, and then allowed to cure after injecting into the mold under 1 kPa (<0.01 atmosphere) vacuum conditions in a vacuum-assisted oven. It has also been shown that the CNP clusters can easily disperse in a low polar epoxy matrix, resulting in a stable dispersion [31]. According to [20,32], one of the current approaches for exfoliation is the exposure of a layered material ultrasonic waves. However, it has further been discussed in [20] that the ultrasonication process (in surfactant/polymer solutions) contributes to the electrostatically/sterically stabilized graphene nanosheets in a solvent. In our heated low viscosity epoxy resin, a well dispersed CNP was expected. Our testing data, to be presented in the following sections, also exhibit consistent trends obtained from nanoindentation and macro-scale mechanical testing, which represent well-dispersed CNPs in the epoxy. Note that re-agglomeration post-stirring was observed; however, due to the comparative nature of this study and the focus on morphological features, it was considered as a constant parameter for all samples.

Based on preliminary trials, the following 30-h procedure (eight stages), detailed in Table 1, was used for the development of a well-dispersed less-agglomerated CNP filled epoxy. The time between stages 4 and 5 can be reduced depending on how long it takes to achieve a satisfactory viscosity for injection purposes.

Table 1. Carbon nanoparticles (CNP) embedment procedure.

Stage	Time (*hh:mm)	Stage Description
1	00:00	One hour stirring epoxy (13 mL), DDSA (8 mL), and MNA (7 mL) at RT
2	01:00	Increase the epoxy mixture temperature to 100 °C Add CNPs Stir the CNP-epoxy mixture at 100 °C for 20 min
3	01:20	Turn off heating Continue stirring for 2 h at **RT under vacuum condition
4	03:20	Add curing agent DMP-30 (2 mL = 15 drops) at RT Stir for 21 h under vacuum conditions using a Schlenk line
5	15:20	Inject the mixture into the mold
6	16:00	Cure the molded mixture using vacuum assisted oven at 80 °C
7	28:00	Take out the mold and let cool down for an hour
8	29:00	Open the mold and take out the specimen

*hh:hour, mm: minute, **DDSA: Dodecenylsuccinic anhydride, MNA: Methyl nadic anhydride, ***RT: room temperature.

2.5. Injection Molding of CNP Filled Epoxy

A mixture of approximately 30 mL epoxy was injected into an aluminum mold. The mold was cleaned using acetone, and dried using compressed air. A Zyvax®liquid sealer was first applied to protect the mold from micro-porosity, followed by application of the Watershield release agent onto

the mold surfaces. Watershield was applied two or three times and was allowed to dry each time for 30 min. The CNP-epoxy mixture was then injected.

2.6. Test Specimens

Three sets of test specimens were extracted from the mold as shown in Figure 1. Tensile specimens (Ø10 mm), compressive specimens (Ø20 mm), leftover material for nanoindentation and SEM investigation. Figure 1 shows the 1 wt % CNP filled epoxy and as-received specimens extracted from the injection mold. Arrows show the direction of uniaxial loads applied using a Tinius-Olsen benchtop machine (Tinius-Olsen, Salfords, UK).

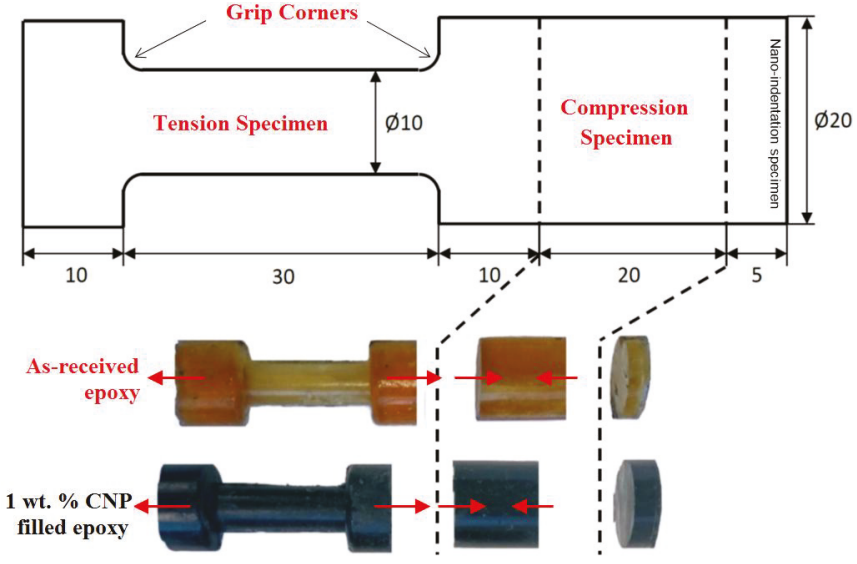

Figure 1. Cylindrical tension, compression and Nanoindentation test specimens extracted from the mold (all dimensions in mm; arrows show loading direction) from CNP filled epoxy composite.

3. Results and Discussion

Initial investigations on the morphology and dispersion of the CNPs in cured specimens were carried out before the mechanical testing.

3.1. Morphology and Composition

A typical site of 2 and 5 wt % CNP filled epoxy specimens is presented in Figure 2. Both samples were gold coated (20 mA, one-round coating) to facilitate electron discharge from the surface of the specimen. The CNPs are observed, mostly, as rod shape fillers dispersed in epoxy, with sizes ranging from 5 to 30 microns, and the two specimens differ in terms of dispersion density.

To ensure the presence of the CNPs observed in the SEM images, a quick survey of the composition was carried out in-situ using the energy dispersive X-ray spectroscopy (EDS) instrument in conjunction with the SEM. EDS data is shown in Figure 3 from three regions of the 5 wt % CNP filled epoxy: Region 1 over an area with no rods, and Regions 2 and 3 over two randomly picked rods. EDS data clearly show the presence of chlorine and Si at the same content level for all regions. The presence of Al is due to the use of the polishing suspension during the preparation of the specimens for SEM. The EDS data from Regions 2 and 3, i.e., rods, show a higher content of carbon and oxygen compared to Region 1. This implies that the observed rods are made of CNP.

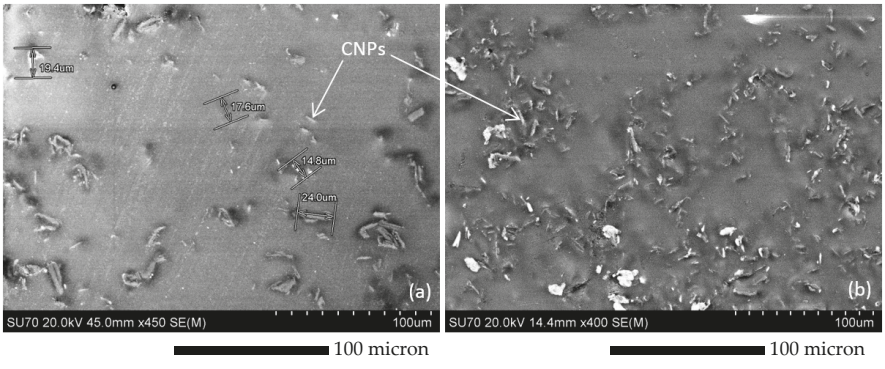

Figure 2. SEM images of (**a**) 2 wt % and (**b**) 5 wt % CNP filled epoxy specimens, showing relatively long rod shape nanoclusters in 2 wt % specimens (~20 micron long) as opposed to relatively short and agglomerated nanoclusters in 5 wt % specimens (~10 micron long).

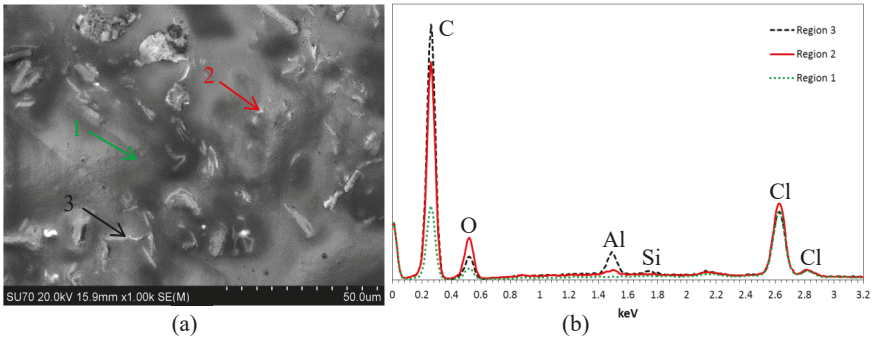

Figure 3. EDS data from 5 wt % CNP filled epoxy, depicting correct identification of rod shape CNP nanoclusters at Regions 2 and 3; (**a**) SEM image, (**b**) EDS data.

3.2. 3D Dispersion

The SEM images presented a CNP dispersion with a 2D architecture. Using the phase contrast imaging capabilities of the advanced computed tomography system, VersaXRM-500 (Xradia, CA, USA) using a high-energy X-ray source (80 kV), high-resolution 3D images of the internal morphology of the nanoparticle embedded epoxy were captured. Impurities such as nanoparticles are observed in yellow (bright spots in black and white), as shown in Figure 4, which show dispersion in 1 wt % CNP embedded epoxy at the center of the specimen, a cylindrical region of Ø2 mm × 2 mm. Voids and air traps appear as dark spots. This indicates a well-dispersed CNP-epoxy structure, achieved through the vacuum-assisted embedment procedure described in Table 1. The primary investigations show that the maximum CNP cluster size is varied between 1–60 microns. The image also indicates a distinct lack of significant air pockets post-cure, a sign of the efficient use of vacuum-assisted injection. Moreover, they show large discrepancies in the size of CNPs for 1 wt % specimens, while small discrepancies for 5 wt % specimen are shown.

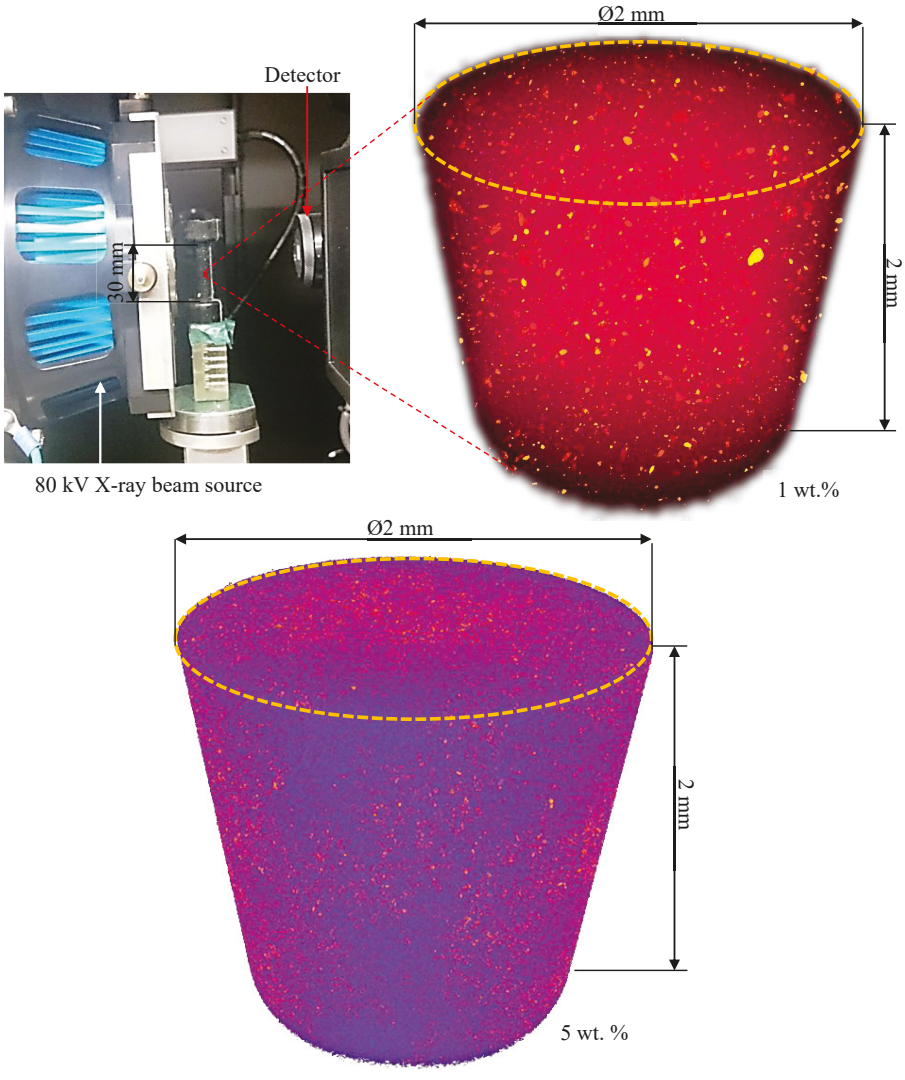

Figure 4. 3D X-ray computed tomography of 1 and 5 wt % CNP embedded epoxy (yellow spots represent CNPs as nanoclusters) at the center of test specimens covering a cylindrical region of Ø2 mm × 2 mm; results for 1 wt % specimens show large discrepancies in the size of CNPs while small discrepancies for 5 wt % specimen.

3.3. Mechanical Testing

3.3.1. Nanoindentation

The nanoindentation experiments were performed using a Nano Indenter G200 supplied by Agilent Technologies (Keysight Technologies, Wokingham, UK). The G200 uses a Nano-Mechanical Actuating Transducer (NMAT) to apply loads and measure displacements during nanoindentation tests. The load is controlled by electromagnetic actuation and the displacement is measured using a capacitance gauge. In order to characterize the specimens, indentation experiments were carried out on the specimens using the dynamic continuous stiffness measurement technique. This technique

allows for continuous measurement of the contact stiffness through the indentation loading. A strain rate target of 0.05/s and a maximum depth of 5 µm was assigned to the indentations, and a Berkovich indenter pyramid tip was used. A total of 20 indentations were carried out randomly over the surface of each sample. Figure 5 shows the modulus and hardness results for the as-received epoxy sample. The results are reasonably consistent with depth for very low scattered data. Averaging the results from the depth of 1 to 5 µm gave mean modulus and hardness values of 3.3 ± 0.01 GPa and 160 ± 5 MPa for the as-received epoxy, respectively.

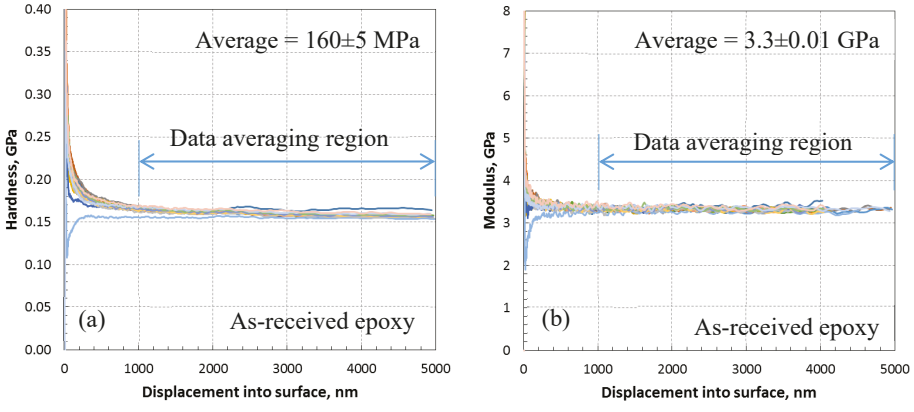

Figure 5. Nanoindentation data of as-received (0 wt % CNP) epoxy; (**a**) variation of hardness with depth showing steady hardness after 1 micron indentation with average hardness of 160 ± 5 MPa, (**b**) variation of modulus with depth showing steady modulus after 1 micron indentation with an average modulus of 3.3 ± 0.01 GPa.

Figure 6 presents the modulus and hardness for the epoxy embedded by 1 wt % CNP. The data for this specimen are very similar to the as-received epoxy with only a slight increase in the mean modulus (3.4 ± 0.2 GPa) and hardness (180 ± 10 MPa), a 3% and 12.5% increase, respectively. This increase is likely due to the presence of CNPs and nanoindentation targeting CNP clusters within two outliers which have been highlighted on the curves. Micrographs of the indentation sites for the outliers 1 and 2 are shown in Figure 7. It is clear that the indentation was carried out very close to what appears to be a large cluster of nanoparticles. The indentation properties for outliner 2 gradually reach the maximum levels at larger indentation depths compared to those of outliner 1, likely due to the presence of a cluster underneath the indenter (not visible in Figure 7). Note that this increase is gradual, and not rapid as it is for the case of fiber-reinforced composites where the indenter comes into contact with fibers in a densely distributed fibrous matrix (see, e.g., [33]). This is expected for the case of 1 wt % and is a sign of a low constraining effect of surrounding nanoparticles as the dispersion density shown in Figure 7 is relatively low.

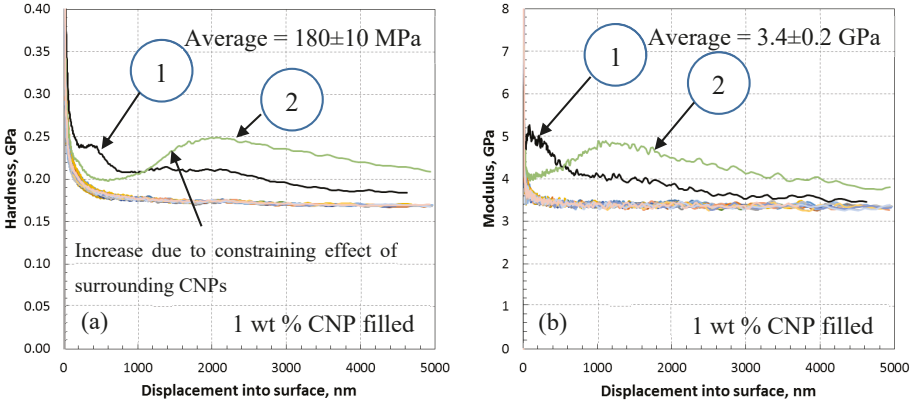

Figure 6. Nanoindentation data of 1 wt % CNP filled epoxy; (**a**) variation of hardness with depth showing non-steady hardness at or near CNPs (outliers 1 and 2 in Figure 7) with an average hardness of 180 ± 10 MPa, (**b**) variation of modulus with depth showing non-steady modulus at or near CNPs (outliers 1 and 2 in Figure 7) with average modulus of 3.4 ± 0.2 GPa.

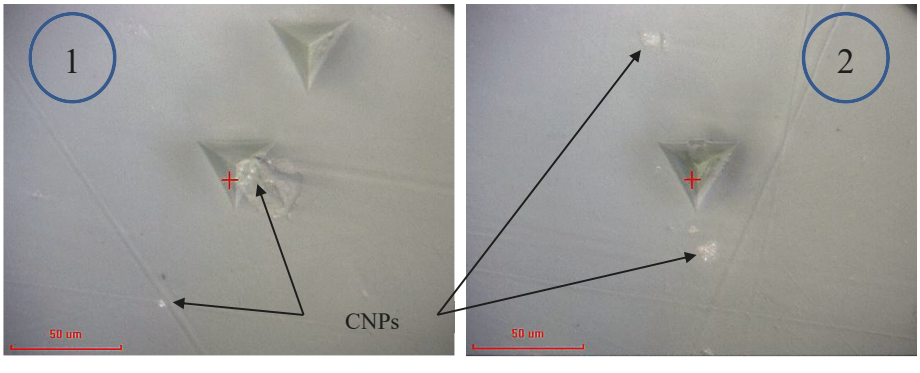

Figure 7. Micrographs of the indentation site of 1 wt % CNP filled epoxy for outliers 1 and 2 in Figure 6, representing indentation at or near CNP clusters.

The modulus and hardness results for 2 wt % CNP filled epoxy are presented in Figure 8, giving mean modulus and hardness values of 3.6 ± 0.3 GPa and 180 ± 20 MPa, respectively. The 2 wt % inclusion of CNP improves the hardness of the as-received epoxy by 12.5%, while the modulus is increased by 8% compared to the as-received epoxy. This is higher than the increase obtained in the 1 wt % inclusion and is thought to be due to the presence of relatively higher CNPs compared to the 1 wt % specimens.

The morphology of the indentation site is provided in Figure 9. As shown, the clusters are densely distributed for this case, as opposed to the 1 wt % case shown in Figure 7, and the agglomeration and shape of the CNP clusters are also different. The figure indicates that a combination of round and rod shape CNPs occurred during the embedment and curing procedure. The rod shape CNPs were formerly observed in the SEM images of the 2 and 5 wt % specimens, see Figure 2.

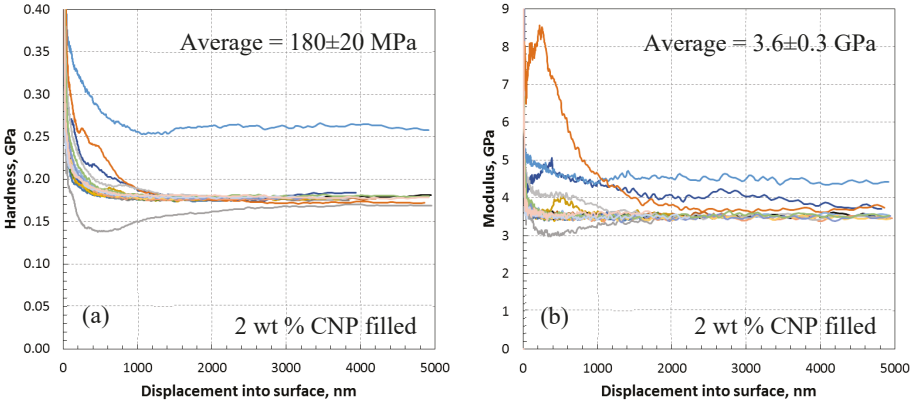

Figure 8. Nanoindentation data of 2 wt % CNP filled epoxy; (**a**) variation of hardness with depth showing non-steady hardness at or near CNPs with average hardness of 180 ± 20 MPa, (**b**) variation of modulus with depth showing non-steady modulus at or near CNPs (Figure 9) with average modulus of 3.6 ± 0.3 GPa.

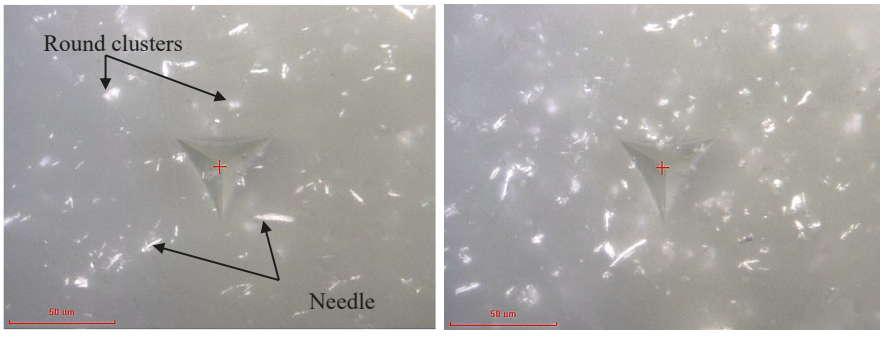

Figure 9. Micrographs of the indentation site of 2 wt % CNP filled epoxy, representing indentation at or near CNP clusters.

Figure 10 presents the modulus and hardness for the epoxy incorporated by 5 wt % CNP showing highly scattered data obtained from the 20 randomly distributed nanoindentation data. Mean modulus and hardness values are 3.4 ± 0.2 GPa and 120 ± 6 MPa, respectively. Compared to the 1 and 2 wt % cases, shown in Figures 6 and 8, no apparent improvement in mean modulus and an apparent reduction in mean hardness is observed. This can be attributed to the morphology and dispersion of CNP. A morphological scan of the indentation site presented in Figure 11 shows that rod-shaped CNPs are presented in greater quantities in the 5 wt % specimen than the 2 wt % one. This introduces a higher stress concentration to the epoxy medium, and therefore results in relatively lower strength observed in the indentation tests.

Micromechanically, stress concentration is higher surrounding a rod-shaped particle as opposed to the concentration surrounding round or elliptical particles, which will lead to a higher stress gradient upon external loading (e.g., compression or tension). Such a stress concentration effect rising from morphological variations from 1 to 5 wt % should have a downgrading effect on relatively large specimens. Further details are provided in Section 3.3.2.

In contrast to the gradual increase seen in the modulus of the 1 wt % case, see Figure 6b, a rapid increase has been observed for several indentations for the 5 wt % case as shown in Figure 10c, and therefore can be inferred as the presence of a higher constraining effect of CNPs in the 5 wt % case.

The indentation and SEM results appear to indicate that the CNPs were not very evenly distributed throughout the material in the scale captured by the nanoindentation (0.2 mm × 0.15 mm); however, based on the 3D X-ray CT data presented in Figure 4, the dispersion is reasonably uniform over a region of 2 mm × 2 mm (covering larger than 100 times the area that the SEM and indentation cover), and considered acceptable for further analysis on a structural scale, i.e., tensile and compressive tests.

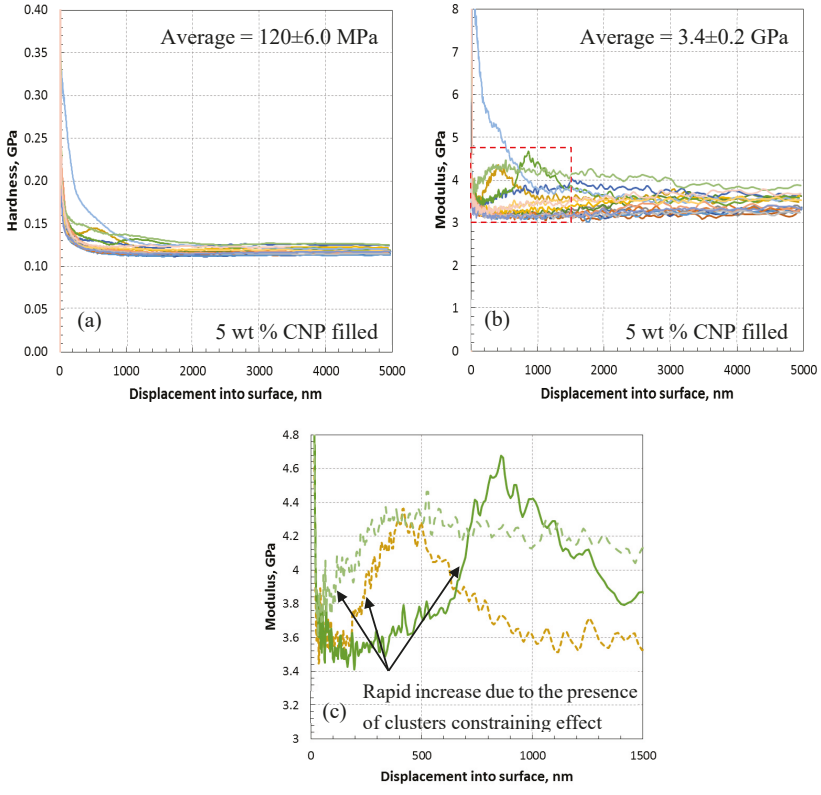

Figure 10. Nanoindentation data of 5 wt % CNP filled epoxy; (**a**) variation of hardness with depth showing steady hardness at or near CNPs (Figure 11) with average hardness of 120 ± 6 MPa, (**b**) variation of modulus with depth showing steady and scattered modulus at or near CNPs (Figure 11) with average modulus of 3.4 ± 0.2 GPa, (**c**) magnified view of dashed-line region from subfigure (**b**).

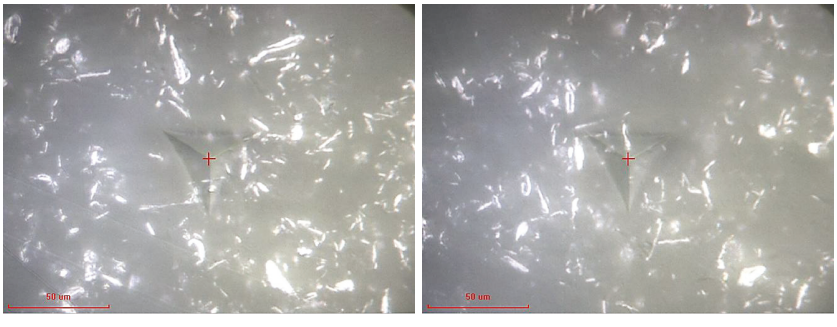

Figure 11. Micrographs of two indentation sites of 5 wt % CNP filled epoxy, representing indentation at or near CNP clusters.

3.3.2. Tension and Compression Test Data

Nanoindentation tests help to realize the local mechanical response of CNPs at the micro-scale, especially surrounding CNPs, in relation to the morphologies that appear in the SEM images. Mechanical testing at the macro-scale using laboratory-scale specimens is required to obtain the properties when numerous CNPs are present. The tension and compression specimens shown in Figure 1 were tested using the uniaxial Tinius testing machine. Both types exhibited a linear elastic behavior until they reach their yield strength point. Young's modulus was obtained from the slope of the linear elastic part of the strain-stress data. The stress values in the tension specimens did not reach the yield point as they failed prematurely at the grip corners, see Figure 1, due to stress concentration, not in the central region. Compression tests were successfully carried out to the point of the ultimate failure and clearly showed the softening and hardening region. Figure 12 presents compression data in the form of force-displacement and stress-strain curves.

For the red dotted lines (0 wt %; as-received epoxy), the discrepancy was the highest between the two testing data immediately after the maximum load and stress were reached. This is attributed to the inherent toughness sensitivity (introduction of microcracks) of epoxy (and not yielding or maximum stresses) to variabilities associated with process parameters control, i.e., uncertainties. Data for the as-received and filled epoxies show a slight improvement in the compressive strength when 1 wt % is incorporated (S_(1 wt %) = 79.86 MPa, S_(0 wt %) = 79.84 MPa). An apparent increase is obtained from 2 wt % CNP inclusion (S_(1 wt %) = 91.13 MPa). This increasing trend is reversed when 5 wt % CNP is incorporated (S_(1 wt %) = 69.40 MPa). The reduction for the 5 wt % is consistent with the tensile and compressive modulus (presented in Table 2) and with the indentation data, see Figure 10. The presence of a relatively high quantity of rod fillers should increase the surface interaction between epoxy and CNPs and thus increase the strength by increasing the sectional area of the interaction surfaces. This expected trend is apparent for the 1 and 2 wt % cases. However, it is degraded in the 5 wt % case, most probably due to the shape of the fillers which imposes a stress concentration at the relatively sharp ends of the fillers, and causes high stress gradients transferring to the surrounding epoxy. This phenomenon is apparent in the SEM images from the tested samples, see Figure 13. Arrows in Figure 13 identify the compression loading direction (vertical) which creates a tilted angle with the direction of microcrack coalescence, an indication of brittle fracture behavior normally occurring in a thermosetting polymer matrix. Therefore, a bi-axial positive deformation occurs across the surface perpendicular to the compression direction and in out-of-plane directions, mainly due to the principle of incompressibility in solid bodies. The deformation in the direction of the applied compression is expectedly negative. According to the SEM images, the stress concentration surrounding nanoparticles causes damage initiation in the brittle medium of the epoxy that propagates in the principle shear plane tilted from the loading direction in the epoxy as the weaker medium. This behavior is the same in the presence of all wt %. However, its effect is more influential in the 5 wt % sample as microcracks occurring surrounding the CNPs are denser and require a lower strain energy to coalesce which leads to macro-cracks and therefore, lower strength compared to the 1 and 2 wt % samples.

The tension and compression test data are summarized in Table 2. The modulus and hardness data from nanoindentation tests are also tabulated for comparison. The increasing trend is seen for all properties with an increasing wt % from 0 to 2. The table also shows a degradation trend for all properties from 2 to 5 wt %. Compressive failure strain at which the compressive strength is reached is approximately identical for all specimens (average 11.47%), except for the 2 wt % case where the failure strain slightly increases to 14%.

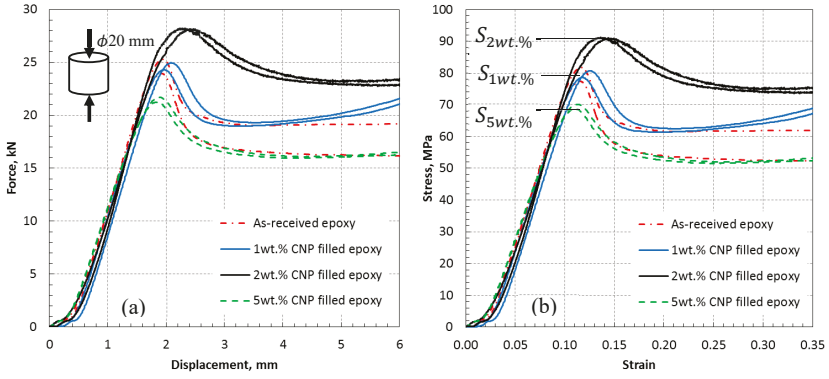

Figure 12. Variation of mechanical response to compression with CNP wt % depicting the maximum threshold at load carrying capacity and maximum stress; (**a**) force versus displacement, (**b**) stress versus strain.

Table 2. Variation of mechanical test data with increasing CNP wt %.

CNP wt %	Tensile Modulus, GPa	Compressive Modulus, GPa	Nanoindentation Compressive Modulus, GPa	Compressive Strength, MPa	Nanoindention Hardness, MPa	Failure Strain, %
0	1.18	0.99	3.3	79.84	160	11.55
1	1.21 ↑ (+3%)	0.99 ↑ (<1%)	3.4 ↑ (+3%)	79.86 ↑ (<1%)	180 ↑ (+13%)	12.15 ↑ (+5%)
2	1.24 ↑ (+5%)	1.03 ↑ (+4%)	3.6 ↑ (+9%)	91.13 ↑ (+14%)	180 ↑ (+13%)	14.00 ↑ (+21%)
5	0.83 ↓ (−30%)	0.84 ↓ (−15%)	3.4 ↑ (+3%)	69.40 ↓ (−13%)	120 ↓ (−25%)	11.10 ↓ (−4%)

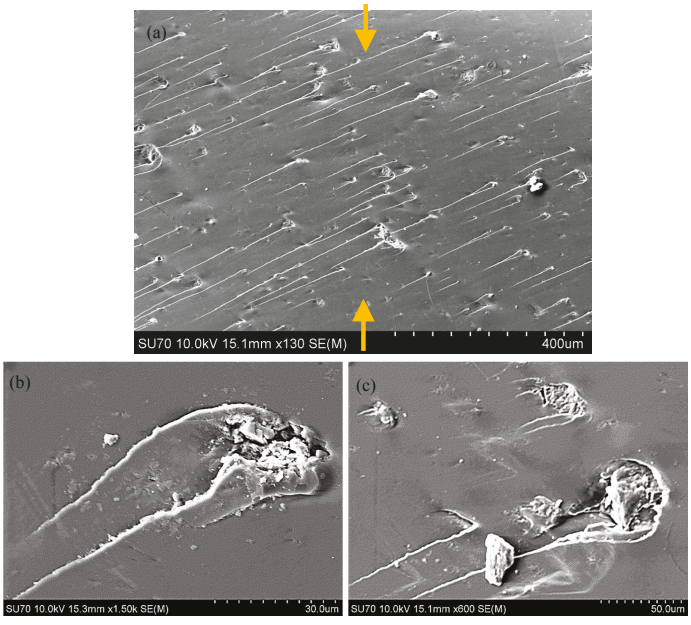

Figure 13. Stress concentration induced microcracks surrounding CNPs in specimens under compression loading; (**a**) microcrack coalesce over a region of 1000 × 700 microns (arrows represent the direction of the compressive load), (**b**,**c**) magnified images of microcracks over regions of 80 × 60 microns.

4. Conclusions

The mechanical performance of the CNP filled epoxy was studied in this work. CNP weight percentage was varied between 1% and 5%, and their mechanical properties were derived on a laboratory-scale under tension and compression, and in micro-scale using nanoindentation. A simple embedment procedure was suggested and was applied for all specimens during processing. All data exhibited an increasing trend in the properties with an increasing CNP content to 2 wt %, and a significant degradation for the 5 wt % incorporation. Studies of the morphological change showed densely dispersed rod CNPs in the 5 wt % specimen, which is believed to be the dominant mechanism for mechanical degradation in the specimen. The effect of loading on re-agglomeration was not studied in this paper. However, it is well-known that the mixing time has a significant effect on the final architecture of the nanoparticles in the cured epoxy. The results for the 2 wt % CNP were promising and showed considerable improvements in all the basic properties. The significant increase in the compressive failure strain for this case (21%) also suggests improvements in energy absorption behavior of the epoxy in the presence of 2 wt % CNP. During the examinations, the materials and embedment procedure were constant. Therefore, adhesion properties can be assumed to be identical for all specimens. Thus, the noted improvement with the 2 wt % CNP can be assumed to be due to the smooth stress transfer between the nanoparticle and epoxy constituents.

Author Contributions: H.Y.Z. and V.K.T. conceived and designed the experiments; H.Y.Z. performed the experiments; V.K.T. analyzed the data and contributed reagents/materials/analysis tools; H.Y.Z. wrote the first draft and V.K.T. finalized the paper.

Funding: This research received no external funding.

Conflicts of Interest: The authors declare no conflict of interest.

References

1. Post, W.; Bose, R.K.; Garcia, S.J.; van der Zwaag, S. Healing of Early Stage Fatigue Damage in Ionomer/Fe_3O_4 Nanoparticle Composites. *Polymers* **2016**, *8*, 436. [CrossRef]
2. Mishra, S.; Sonawane, S.H.; Singh, R.P. Studies on characterization of nano $CaCO_3$ prepared by the in situ deposition technique and its application in PP-nano $CaCO_3$ composites. *J. Polym. Sci. Part B* **2005**, *43*, 107–113. [CrossRef]
3. Lazzeri, A.; Thio, Y.S.; Cohen, R.E. Volume strain measurements on $CaCO_3$/polypropylene particulate composites: The effect of particle size. *J. Appl. Polym. Sci.* **2004**, *91*, 925–935. [CrossRef]
4. Bartczak, Z.; Argon, A.S.; Cohen, R.E.; Weinberg, M. Toughness mechanism in semi-crystalline polymer blends: II. High-density polyethylene toughened with calcium carbonate filler particles. *Polymer* **1999**, *40*, 2347–2365. [CrossRef]
5. Suprapakorn, N.; Dhamrongvaraporn, S.; Ishida, H. Effect of $CaCO_3$ on the mechanical and rheological properties of a ring-opening phenolic resin: Polybenzoxazine. *Polym. Compos.* **1998**, *19*, 126–132. [CrossRef]
6. Qiang, F.; Wang, G.; Liu, C. Polyethylene toughened by $CaCO_3$ particles: The interface behaviour and fracture mechanism in high density polyethylene/$CaCO_3$ blends. *Polymer* **1995**, *36*, 2397–2401. [CrossRef]
7. Fu, Q.; Wang, G. Polyethylene toughened by $CaCO_3$ particles—percolation model of brittle-ductile transition in hdpe/ $CaCO_3$ blends. *Polym. Int.* **1993**, *30*, 309–312. [CrossRef]
8. Fu, Q.; Wang, G.; Shen, J. Polyethylene Toughened by $CaCO_3$ Particle Asterisk - Brittle-Ductile Transition of $CaCO_3$-Toughened Hdpe. *J. Appl. Polym. Sci.* **1993**, *49*, 673–677. [CrossRef]
9. Fu, S.-Y.; Feng, X.-Q.; Lauke, B.; Mai, Y.-W. Effects of particle size, particle/matrix interface adhesion and particle loading on mechanical properties of particulate–polymer composites. *Compos. Part B Eng.* **2008**, *39*, 933–961. [CrossRef]
10. Liu, Z.; Tu, R.; Liao, Q.; Hu, H.; Yang, J.; He, Y.; Bian, H.; Ma, L.; Liu, W. High Thermal Conductivity of Flake Graphite Reinforced Polyethylene Composites Fabricated by the Powder Mixing Method and the Melt-Extruding Process. *Polymers* **2018**, *10*, 693. [CrossRef]

11. Garlof, S.; Mecklenburg, M.; Smazna, D.; Mishra, Y.K.; Adelung, R.; Schulte, K.; Fiedler, B. 3D carbon networks and their polymer composites: Fabrication and electromechanical investigations of neat Aerographite and Aerographite-based PNCs under compressive load. *Carbon* **2017**, *111*, 103–112. [CrossRef]
12. Garlof, S.; Fukuda, T.; Mecklenburg, M.; Smazna, D.; Mishra, Y.K.; Adelung, R.; Schulte, K.; Fiedler, B. Electro-mechanical piezoresistive properties of three dimensionally interconnected carbon aerogel (Aerographite)-epoxy composites. *Compos. Sci. Technol.* **2016**, *134*, 226–233. [CrossRef]
13. Schütt, F.; Signetti, S.; Krüger, H.; Röder, S.; Smazna, D.; Kaps, S.; Gorb, S.N.; Mishra, Y.K.; Pugno, N.M.; Adelung, R. Hierarchical self-entangled carbon nanotube tube networks. *Nat. Commun.* **2017**, *8*, 1215. [CrossRef] [PubMed]
14. Sangermano, M.; Tagliaferro, A.; Foix, D.; Castellino, M.; Celasco, E. In Situ Reduction of Graphene Oxide in an Epoxy Resin Thermally Cured with Amine. *Macromol. Mater. Eng.* **2014**, *299*, 757–763. [CrossRef]
15. Marro Bellot, C.; Olivero, M.; Sangermano, M.; Salvo, M. Towards self-diagnosis composites: Detection of moisture diffusion through epoxy by embedded evanescent wave optical fibre sensors. *Polym. Test.* **2018**, *71*, 248–254. [CrossRef]
16. Sangermano, M.; D'Anna, A.; Marro, C.; Klikovits, N.; Liska, R. UV-activated frontal polymerization of glass fibre reinforced epoxy composites. *Compos. Part B Eng.* **2018**, *143*, 168–171. [CrossRef]
17. Cavasin, M.; Giannis, S.; Salvo, M.; Casalegno, V.; Sangermano, M. Mechanical and thermal characterization of an epoxy foam as thermal layer insulation for a glass fiber reinforced polymer. *J. Appl. Polym. Sci.* **2018**. [CrossRef]
18. Lotfian, S.; Giraudmaillet, C.; Yoosefinejad, A.; Thakur, V.K.; Nezhad, H.Y. Electrospun Piezoelectric Polymer Nanofiber Layers for Enabling in Situ Measurement in High-Performance Composite Laminates. *ACS Omega* **2018**, *3*, 8891–8902. [CrossRef]
19. Coleman, J.N. Liquid Exfoliation of Defect-Free Graphene. *Acc. Chem. Res.* **2013**, *46*, 14–22. [CrossRef] [PubMed]
20. Nicolosi, V.; Chhowalla, M.; Kanatzidis, M.G.; Strano, M.S.; Coleman, J.N. Liquid Exfoliation of Layered Materials. *Science* **2013**, *340*, 1226419. [CrossRef]
21. Mgbemena, C.O.; Li, D.; Lin, M.-F.; Liddel, P.D.; Katnam, K.B.; Thakur, V.K.; Nezhad, H.Y. Accelerated microwave curing of fibre-reinforced thermoset polymer composites for structural applications: A review of scientific challenges. *Compos. Part Appl. Sci. Manuf.* **2018**, *115*, 88–103. [CrossRef]
22. Lauke, B.; Fu, S.-Y. Aspects of fracture toughness modelling of particle filled polymer composites. *Compos. Part B Eng.* **2013**, *45*, 1569–1574. [CrossRef]
23. Singh, R.P.; Zhang, M.; Chan, D. Toughening of a brittle thermosetting polymer: Effects of reinforcement particle size and volume fraction. *J. Mater. Sci.* **2002**, *37*, 781–788. [CrossRef]
24. Omar, M.F.; Akil, H.M.; Ahmad, Z.A. Particle size—Dependent on the static and dynamic compression properties of polypropylene/silica composites. *Mater. Des.* **2013**, *45*, 539–547. [CrossRef]
25. Pukanszky, B. Interfacial Interactions in Particulate Filled Thermoplastics—Mechanism, Strength, Properties. *Makromol. Chem. Macromol. Symp.* **1993**, *70*, 213–223. [CrossRef]
26. Reynaud, E.; Jouen, T.; Gauthier, C.; Vigier, G.; Varlet, J. Nanofillers in polymeric matrix: A study on silica reinforced PA6. *Polymer* **2001**, *42*, 8759–8768. [CrossRef]
27. Nakamura, Y.; Yamaguchi, M.; Okubo, M.; Matsumoto, T. Effect of particle size on the fracture toughness of epoxy resin filled with spherical silica. *Polymer* **1992**, *33*, 3415–3426. [CrossRef]
28. Argon, A.S.; Cohen, R.E. Toughenability of polymers. *Polymer* **2003**, *44*, 6013–6032. [CrossRef]
29. Pappu, A.; Thakur, V.K. Towards sustainable micro and nano composites from fly ash and natural fibers for multifunctional applications. *Vacuum* **2017**, *146*, 375–385. [CrossRef]
30. Muhulet, A.; Miculescu, F.; Voicu, S.I.; Schütt, F.; Thakur, V.K.; Mishra, Y.K. Fundamentals and scopes of doped carbon nanotubes towards energy and biosensing applications. *Mater. Today Energy* **2018**, *9*, 154–186. [CrossRef]
31. Kotsilkova, R.; Fragiadakis, D.; Pissis, P. Reinforcement effect of carbon nanofillers in an epoxy resin system: Rheology, molecular dynamics, and mechanical studies. *J. Polym. Sci. Part B Polym. Phys.* **2005**, *43*, 522–533. [CrossRef]

32. Hernandez, Y.; Nicolosi, V.; Lotya, M.; Blighe, F.M.; Sun, Z.; De, S.; McGovern, I.T.; Holland, B.; Byrne, M.; Gun'Ko, Y.K.; et al. High-yield production of graphene by liquid-phase exfoliation of graphite. *Nat. Nanotechnol.* **2008**, *3*, 563–568. [CrossRef] [PubMed]
33. Hardiman, M.; Vaughan, T.J.; McCarthy, C.T. Fibrous composite matrix characterisation using nanoindentation: The effect of fibre constraint and the evolution from bulk to in-situ matrix properties. *Compos. Part Appl. Sci. Manuf.* **2015**, *68*, 296–303. [CrossRef]

polymers

MDPI

Review

Recent Developments in Graphene/Polymer Nanocomposites for Application in Polymer Solar Cells

Ana Maria Díez-Pascual [1,*], José Antonio Luceño Sánchez [1], Rafael Peña Capilla [2] and Pilar García Díaz [2]

[1] Department of Analytical Chemistry, Physical Chemistry and Chemical Engineering, Faculty of Biology, Environmental Sciences and Chemistry, Alcalá University, 28871 Madrid, Spain; jose.luceno@uah.es
[2] Department of Signal Theory and Communication, Polytechnic High School, Alcalá University, 28871 Madrid, Spain; rafa.pena@uah.es (R.P.C.); pilar.garcia@uah.es (P.G.D.)
* Correspondence: am.diez@uah.es; Tel.: +34-918-856-430

Received: 9 January 2018; Accepted: 21 February 2018; Published: 22 February 2018

Abstract: Graphene (G) and its derivatives, graphene oxide (GO) and reduced graphene oxide (rGO) have enormous potential for energy applications owing to their 2D structure, large specific surface area, high electrical and thermal conductivity, optical transparency, and huge mechanical strength combined with inherent flexibility. The combination of G-based materials with polymers leads to new nanocomposites with enhanced structural and functional properties due to synergistic effects. This review briefly summarizes recent progress in the development of G/polymer nanocomposites for use in polymer solar cells (PSCs). These nanocomposites have been explored as transparent conducting electrodes (TCEs), active layers (ALs) and interfacial layers (IFLs) of PSCs. Photovoltaic parameters, such as the open-circuit voltage (V_{oc}), short-circuit current density (J_{sc}), fill factor (FF) and power-conversion efficiency (PCE) are compared for different device structures. Finally, future perspectives are discussed.

Keywords: nanocomposite; conductive polymer; solar cell; graphene; graphene oxide; power-conversion efficiency; electrode; active layer; interfacial layer

1. Introduction

Organic solar cells (OSCs) have received a lot of attention from both academia and industry in the last three decades since they exhibit important advantages compared to silicon-based devices such as their lightweight nature, flexibility, lower processing costs and lower environmental impact [1,2]. Furthermore, the active layers can be deposited through solution-based methods like spin-coating or printing, which allow massive device fabrication at low temperatures and, consequently, reduce device cost. OSCs are made of electron donor and electron acceptor materials. The material that absorbs the photons from the solar radiation is the donor, in which excited states (or excitons) are created and confined. An exciton is an electron-hole pair bound together by electrostatic interactions, which can be separated into free electron-hole pairs by effective electric fields. The material acquiring the electrons from the dissociated electron-hole pairs is the acceptor.

According to the chemical structures of the active layer components, in particular the electron donor (p-type) semiconductors, OSCs can be further separated into two groups: polymer solar cells (PSCs) and small molecule solar cells. PSCs can also be transparent, which is of value for applications in windows, walls, flexible electronics, and so forth. Their main disadvantages are their low power-conversion efficiency (PCE) and photochemical degradation [3].

PSCs are typically made of an indium tin oxide (ITO) conductive glass followed by a poly(3,4-ethylenedioxythiophene):poly(styrenesulfonate) (PEDOT:PSS) hole-transporting layer, an active layer (i.e., PBDTTT and PCBM), an electron transport layer (i.e., LiF) and, finally, a low work-function metal electrode like Al (Scheme 1). Conversely, in an inverted device, ITO with a buffer layer such as TiOx and ZnO is frequently used as the cathode electrode, and the anode is a high work-function metal like Ag or Au with a hole-transporting layer, i.e., PEDOT:PSS [4].

The nature and order of the layers as well as the nature of the metal electrode play a key role in the performance of the PSC device, hence on its PCE [5]. A bulk heterojunction (BHJ) structure is the most successful PSC architecture formed by blending an electron-rich conjugated polymer as donor and an electron-deficient fullerene as acceptor with a bicontinuous nanoscale interpenetrating network [6].

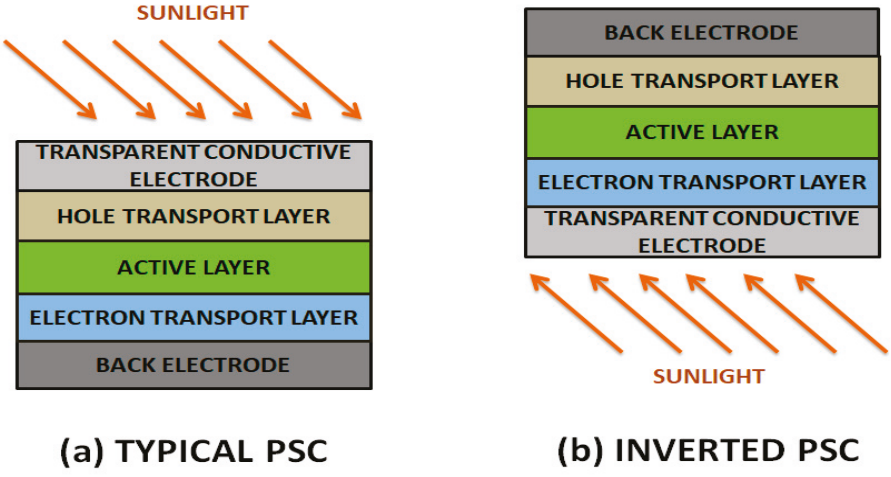

Scheme 1. Schematic representation of a typical (**a**) and inverted (**b**) polymer solar cell (PSC).

Three parameters are typically used to characterize a solar cell: (a) the open-circuit voltage (V_{oc}), the maximum voltage available from a solar cell that occurs at zero current; (b) the short-circuit current density (J_{sc}), the maximum current through the solar cell that occurs when the voltage is zero; (c) the fill factor (FF), which shows the extent to which current-voltage characteristics of the PSC are close to ideal; the optimal theoretical value of FF should be 1. In practice, FF values higher than 0.75 are regarded as very good. The overall performance or power-conversion efficiency (PCE) can be calculated based on these parameters and the incident solar power (P_{in}) [7]. V_{oc} is principally restricted by the difference between the highest occupied molecular orbital (HOMO) of the polymer donor and the lowest free molecular orbital (LUMO) of the fullerene acceptor [8], and J_{sc} is determined by the product of the photoinduced charge-carrier density and the mobility within the organic semiconductors.

Over the last few years, considerable effort has been made to synthesize conjugated polymers and fullerene derivatives for use in BHJ cells [2,6]. They combine the electronic properties of traditional semiconductors and conductors with the ease of processing from solution, are lightweight, and have the mechanical flexibility of plastics. Figure 1 shows the chemical structure of some conjugated polymers widely employed in BHJ PSCs. The characteristic structure of alternating carbon–carbon double bonds is common to all of them, and it is responsible for their electronic properties, low-energy optical transitions, and high-electron affinities. As synthesized conjugated polymers (in a neutral state) are insulators, they become conductive by means of oxidation (*p*-doping) or reduction (*n*-doping).

PEDOT is built from ethylenedioxythiophene (EDOT) monomers. It presents outstanding performance, including good electrochemical properties compared to those of other polythiophenes [9]. It is insoluble in many common solvents and unstable in its neutral state, since it oxidizes quickly in air. To enhance its processability, a polyelectrolyte solution, PSS is typically added, and this results in an aqueous dispersion of PEDOT:PSS, where PEDOT is its oxidized state. PSS acts as the counter ion and keeps the PEDOT chains dispersed in the aqueous medium. Nevertheless, PEDOT:PSS has several drawbacks like high acidity, hygroscopic character and inhomogeneous electrical properties, leading to low durability [10].

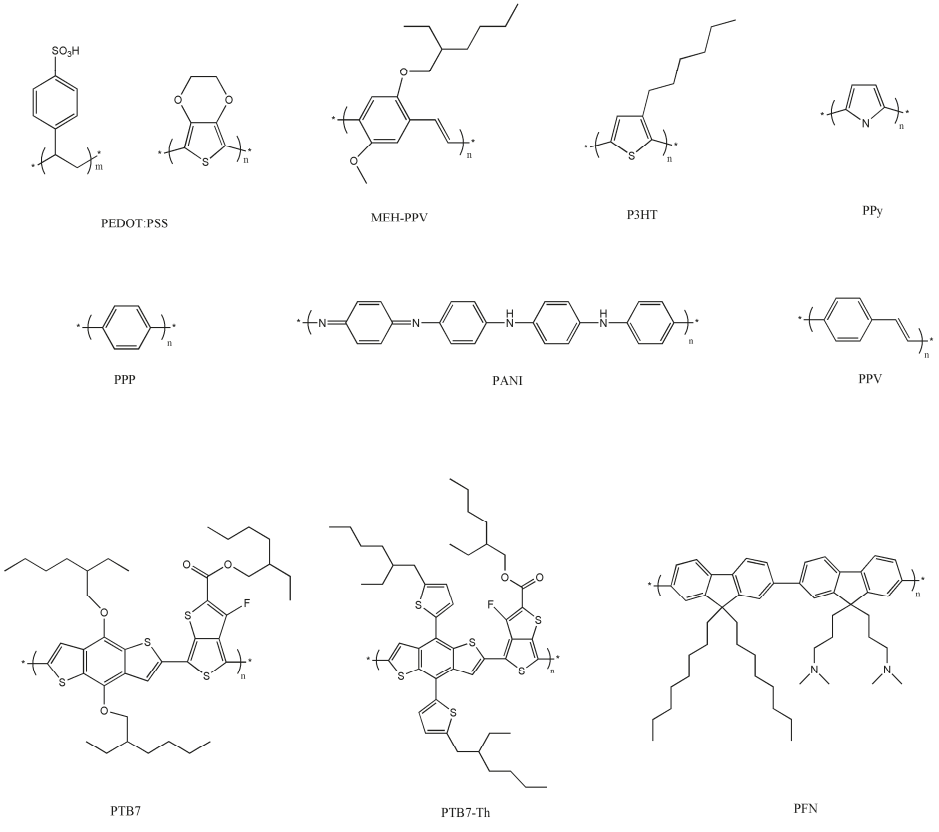

Figure 1. Chemical structure of conjugated polymers typically used in PSCs.

Poly(3-hexylthiophene) (P3HT) is one of the most widely used in photovoltaics due to its interesting electronic properties combined with its ability to self-assemble and to be easily dissolved in organic solvents. Poly(*p*-phenylene vinylene) (PPV) is hardly soluble. Attachment of side-groups to the conjugated backbone, as in poly[2-methoxy-5-(3′,7′-dimethyloctyloxy)-1,4-phenylene vinylene] (MDMO-PPV) or poly[2-methoxy-5-(2′-ethylhexyloxy)-p-phenylene vinylene] (MEH-PPV), significantly enhances the solubility of the polymer. However, PPV and its derivatives suffer from poor absorption and photodegradation [3]. The solubility of polypyrrole (PPy) is also restricted due to the cross-linking of the polymer chains. Neutral PPy is insoluble, though it can swell when exposed to some solvents. Once swelled, PPy can be doped either in acid or basic media and can be dissolved in a few solvents, such as chloroform, dimethyl sulfoxide (DMSO), *N*-Methyl-2-pyrrolidone

(NMP), and tetrahydrofuran (THF). Poly(*p*-phenylene) (PPP) is only soluble in organic solvents, and is important since it is very stable (especially when undoped) and can be used as an electrode. Polyaniline (PANI) is especially attractive as it is relatively inexpensive, wasy to synthesise and environmentally stable. It has a wide range of electrical properties that can be easily controlled by changing its oxidation and protonation state and presents an acid/base doping response [11].

Initially, PSCs based on the BHJ structure used MEH-PPV as electron-donor and fullerene C60 derivatives as electron-acceptor, and were synthesized by spin-coating. However, the efficiency was relatively low (~7.7%) [12]. Over the last few years, the performance of these PSCs has been improved to a great extent, and can achieve PCEs > 9% for single-junction cells [13] and >11% for tandem solar cells [14]. This has been possible with the synthesis of new polymeric donor materials such as polythieno[3,4-*b*]thiophene-*co*-benzodithiophene] (PTB7). This low-bandgap semiconducting polymer has led to some of the highest reported efficiencies for BHJ cells due to its extended absorption into the near infra-red and lower HOMO level [13,15]. Furthermore, it exhibits high solubility in a wide range of solvents, which makes its processing very simple at room temperature, and it is also an excellent candidate for a variety of coating techniques including ink-jet printing, spraying and blade coating. In particular, a highly efficient PSC was obtained with an inverted device structure, where an alcohol-/water-soluble conjugated polymer, poly[(9,9-bis(3′-(*N*,*N*-dimethylamino)propyl)-2,7-fluorene)-alt-2,7-(9,9-dioctylfluorene)] (PFN) was used as the ITO surface modifier, and a blend of [6,6]-phenyl C71-butyric acid methyl ester ($PC_{71}BM$) and PTB7 acted as the photoactive layer. Even an improved performance has been reported for poly[4,8-bis(5-(2-ethylhexyl)thiophen-2-yl)benzo[1,2-*b*:4,5-*b*′]dithiophene-*co*-3-fluorothieno[3,4-b] thiophene-2-carboxylate-2-6-diyl)], commonly known as PTB7-Th or PBDTTT-EFT. This displays lower HOMO/LUMO levels and increased efficiency compared to PTB7 and, more importantly, it is also far more stable. Thus, the PTB7-Th/$PC_{71}BM$ blend has been used as photoactive layer in single junction PSCs [16,17] because of its broadened photoresponse approaching 800 nm. Nonetheless, it has not been possible to further enhance the PCE of these cells since their manufacturing processes are difficult to scale up, and ion diffusion into the polymer layers along with their mechanical brittleness limit their applicability. Therefore, developing new materials with low cost and high stability that can be used as hole-transport layers or electron-transport layers in PSCs is of great interest.

In this regard, the present review summarizes recent progress in the development of graphene (G)/polymer nanocomposites for PSC applications. Due to its unique properties and versatility, G has emerged as a nanomaterial useful for several device parts including transparent conductive electrodes (TCEs), active layers (ALs) and the interfacial layers (IFLs). We will focus on the synthesis of G and its derivatives, graphene oxide (GO) and reduced graphene oxide (rGO), the preparation methods of G/polymer nanocomposites, and the photovoltaic properties of PSCs incorporating these nanocomposites. Although there are a number of reviews about PSCs [1–6], to the best of our knowledge literature reviews dealing with G-based materials for solar-cell applications are scarce [18,19], and none of them focuses on the nanocomposites.

2. Graphene and its Derivatives: Synthesis and Properties

2.1. Synthesis and Properties of Graphene

As is well known, G consists of a flat, atomically thick single layer of sp^2 carbon atoms forming a honeycomb structure (Scheme 2). Due to its 2D nature, its electronic band structure is characterized by a linear dependence of energy on momentum near the Fermi level [20]. G exhibits extraordinary electronic, thermal and mechanical properties [21], very high electron mobility (15,000 cm^2/V s) and a very large surface area (2630 m^2/g) [22]. It presents a thermal conductivity in the range of 3000–6000 W/m K [21], and an electrical conductivity of 9.6×10^7 S/m. Moreover, G is one of the strongest materials on Earth, with an elastic modulus close to 1 TPa [23], an ultimate strength of 130 GPa, and a breaking strength of ~40 N/m [24]. Furthermore, the absorption of a G sheet is

nearly constant, and equal to 2.3% [25]. The combination of these exceptional properties make G an excellent candidate for application in photovoltaic cells. Nonetheless, some issues need to be resolved. In particular, its sheet resistance is very high compared to those of materials currently used as electrodes such as ITO, hence it is important to enhance electronic transport without sacrificing its optical transparency and other properties. Besides, G sheets are flexible and chemically inert, which results in a double application: as an electrode and as a protective layer.

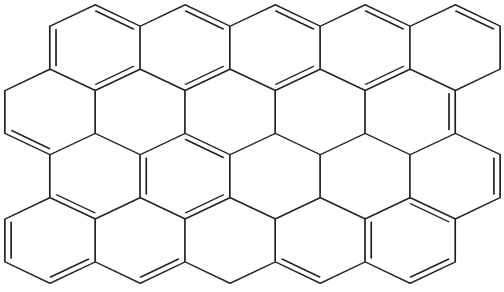

Graphene

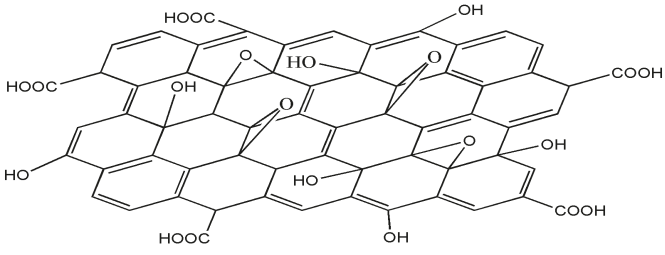

Graphene Oxide

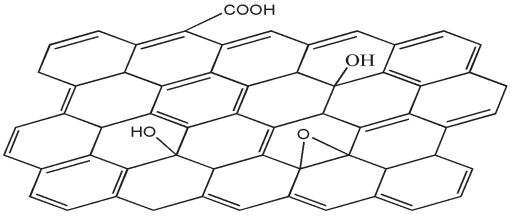

Reduced Graphene Oxide

Scheme 2. Schematic representation of the structure of graphene (G), graphene oxide (GO) and reduced graphene oxide (rGO).

G can be synthesized by several techniques including exfoliation, epitaxial growth, chemical vapor deposition (CVD) and chemical and electrochemical methods. A brief description of these methods along with their feasibility for applications in solar energy devices are shown below.

Mechanical exfoliation was the first method developed to isolate G by peeling it off from graphite flakes using a Scotch tape. This method yields good quality G sheets; however, it is not suitable for mass production.

Epitaxial growth is a substrate-based method, where G is grown on a single-crystal silicon carbide (SiC) by vacuum graphitization (thermal treatment of SiC at ~1300 °C under vacuum). The thickness of G layers can be controlled by adjusting the temperature and time, and the uniformity of the thickness improves with an annealing process [26]. This method is not practical for photovoltaic applications due to its relatively high cost and the strong adhesion of G layers to the substrate.

CVD methods are the most widely used to fabricate G at a large scale, are the simplest, and are cost effective. G is grown directly on a transition metal substrate (Cu, Ni, Pt, Pd, Ru, Ir) by means of saturation of carbon upon exposure to a hydrocarbon gas (i.e., methane) at a high temperature [22]. When the substrate is cooled, the solubility of carbon on the substrate decreases and the carbon precipitates to form mono- to multilayer G sheets. The main disadvantages are the difficult control of the film thickness and the need for relatively expensive substrate materials. G grown on metals seems to be highly suitable for use in transparent electronics.

Chemical-solution processes are inexpensive large-scale production methods to synthesize G for photovoltaic devices [27]. They provide a layered product that can be suitable for transparent electrodes or as dopant in other materials. The main shortcoming of these methods is the insolubility of G. However, the reaction with strong oxidizing agents, such as H_2SO_4, HNO_3, or $KMnO_4$, leads to the attachment of oxygen functional groups to both the basal plane and the edges of G sheets, resulting in the formation of GO (Scheme 2), which is soluble in various solvents, such as water, dimethylformamide (DMF), THF and chloroform [28]. Due to its dispersibility in common organic solvents, GO is highly suitable as a filler in polymeric nanocomposites.

One of the least-used fabrication processes is electrochemical exfoliation, which relies on the penetration of graphite by ions from a solution forced by the applied potential. G obtained by this approach can be dispersed in organic solvents such as DMF, which enables the fabrication of thin films [29]. After reduction via treatment with HNO_3 or under vacuum, layers with good transport and optical properties can be obtained, suitable for the fabrication of transparent electrodes.

2.2. Synthesis and Properties of Graphene Oxide

GO is an oxidized layer of G that contains epoxides, hydroxyls and carbonyls on the basal planes and carboxyls on the edges (Scheme 2). Consequently, some properties of GO differ from those of G: The sp^3 carbon atoms in GO increase interlayer spacing, improving its ability to retain compounds. The attached groups and lattice defects modify the electronic structure of G and serve as strong scattering centers that affect electrical transport. Thus, it presents significantly lower electron mobility, and it is typically insulating, with a sheet resistance of about 10^{12} Ω/sq or higher. It presents aqueous processability, amphiphilicity, surface-functionalization capability, versatility, biocompatibility, and the ability to interact with biological cells and tissues [30]. More importantly, it is highly hydrophilic and can form stable aqueous colloids to facilitate the assembly of macroscopic structures, which is crucial for large-scale uses. Furthermore, it can be deposited on a substrate and later converted into a conductor, hence has great potential for the fabrication of solar cells.

GO can be synthesized using four basic methods [26,30]: Staudenmaier, Hofmann, Brodie and Hummers. The most widely employed, the Hummers´ method, consists of the addition of $KMnO_4$ to a solution of graphite, $NaNO_3$ and H_2SO_4. Many variations of this method have been reported, with improvements constantly being explored to achieve better results and cheaper processes [26,30]. For instance, approaches without using $NaNO_3$ eliminate the evolution of NO_2/N_2O_4 toxic gasses and simplify the disposal of waste water because of the inexistence of Na^+ and NO_3^- ions [31].

GO can also be synthesized from graphite oxide by using sonication, stirring, or a combination of both. Sonication is a time-effective way of fully exfoliating graphite oxide, although it can seriously harm the graphene flakes, reducing their size from microns to nanometres, and even producing

graphene platelets. Mechanical stirring is a less heavy-handed approach, albeit involving longer periods of time.

2.3. Synthesis and Properties of Reduced Graphene Oxide

An interesting property of GO is that it can be partly reduced to graphene-like sheets by eliminating the oxygen-containing groups with the recovery of a conjugated structure (Scheme 2). The reduced GO (rGO) sheets are regarded as functionalized G, chemically modified G or reduced G [32]. The aim is to attain graphene-like materials comparable to the pristine G obtained from direct mechanical exfoliation of graphite both in structure and properties. However, residual functional groups and defects considerably modify the structure of the carbon plane and, therefore, the properties of rGO differ from those of G. In particular, the electrical conductivity of rGO is typically in the range of 10–23 S/cm, much lower than that of G.

rGO can be prepared via the reduction of GO by thermal, chemical or electrical treatments. Thermal annealing consists in the reduction of GO only by heat treatment, via rapid heating (>2000 C/min) [33]. Exfoliation is caused by the abrupt expansion of CO or CO_2 gases evolving into the spaces between graphene sheets during heating. This method cannot be used for GO films on substrates with a low melting point, such as glass and polymers, hence it is not suitable for solar cell applications. Thermal annealing can also be performed by microwave irradiation or via photo-reduction [34], using the energy emitted by a flash lamp or a laser. This process can lead to a much higher degree of reduction of GO, since the lamp/laser can provide higher energy than the thermal annealing, leading to rGO films with higher conductivity (i.e., 256 S/cm [35]), enabling the direct fabrication of electronic devices based on rGO films.

Reduction by chemical reagents is based on their chemical reactions with GO, and can be carried out either at room temperature or applying moderate heat. The reagent more typically used is hydrazine monohydrate ($N_2H_4 \cdot H_2O$), which is added to a GO aqueous dispersion, resulting in agglomerated rGO nanosheets due to the increase in hydrophobicity [36]. However, the toxicity of hydrazine and the possibility of incorporating N to the structure make it inappropriate for large-scale synthesis. Hence, other reducing agents have been proposed, such as $NaBH_4$ [37], hydroiodic acid (HI), and urea.

Electrochemical reduction of GO can be carried out in a usual electrochemical cell using an aqueous buffer solution at room temperature. The reduction does not require chemical agents, and it is induced by the electron exchange between GO and electrodes. This approach seems favorable for electrochemical applications.

3. Preparation of Graphene/Polymer Nanocomposites

A variety of methods have been reported to prepare G/polymer nanocomposites including covalent and non-covalent approaches [24,38].

3.1. Non-Covalent Approaches

Non-covalent strategies include solution mixing, melt-blending and in situ polymerization. The solution technique requires both G material and polymer to be stably dispersed in a common solvent; it involves the dispersion of G in the appropriate solvent, the adsorption of the polymer on to delaminated G sheets in solution, and the elimination of the solvent, resulting in sandwich-like nanocomposites [38]. On the other hand, in the melt-blending process, G or its derivatives are blended into molten polymer matrixes under dramatic shearing. This process is not commonly used, particularly for energy applications. In the in situ polymerization, G is first swollen within the liquid monomer, the initiator is subsequently added and the polymerization begins either by heat or radiation. Nanocomposites with conductive polymers can also be produced via in situ electrochemical polymerization [39], which yields mechanically stable composite films that can be directly used as the electrodes of energy storage devices.

3.2. Covalent Functionalization

In the covalent approach, the polymer chains are grafted on to the G sheets and wrap around them to prevent their aggregation. It can be carried out either via "grafting to" or "grafting from" approaches [40]. In the former, the functional groups of the polymer chains react with those of G or its derivatives to form chemical bonds. For instance, the carboxylic groups of GO can react with hydroxyl or amine groups of a polymer via esterification or amidation reactions [41]. The grafting from consists in the growth of the polymer chains from the surfaces of G sheets, typically via atom-transfer radical polymerization (ATRP).

4. Graphene/Polymer Nanocomposites in Solar Cells

G-based materials have been used in different layers of PSCs including TCEs, ALs and IFLs. The literature on this subject is so extensive that only the most representative examples dealing with polymer/G nanocomposites are described. The most important results are summarized at the end of this section, in Table 1.

4.1. Graphene/Polymer Nanocomposites as Transparent Conductive Electrodes

G and its derivatives have been used as TCEs to replace conventional ITO electrodes in PSCs. A lot of work has been carried out using flexible polymers, such as polyethylene terephthalate (PET) as substrate. In this regard, rGO films synthesized by thermal annealing were deposited on to PET, and the photovoltaic device was fabricated by spin coating the materials on to plasma treated rGO/PET to produce a hydrophilic surface [42]. A maximum PCE of 0.78%, V_{oc} of 0.56 V and J_{SC} of 4.39 mA/cm^2 were attained when using rGO films with a thickness of 16 nm and a transmittance of 65%. Remarkably, the device obtained could withstand up to 1200 bending cycles without sacrificing device performance, whilst traditional cells incorporating ITO normally crack and degrade upon bending due to the brittle nature of ITO. Significantly improved performance (PCE of 3.05%) was obtained by depositing a rGO micromesh obtained via a laser-pattering technique on to PET, ascribed to the superior transparency (59%) and lower sheet resistance (565 Ω/sq) of the rGO micromesh compared to pristine rGO. More importantly, this PSC exhibited a comparable PCE with ITO-based devices (3.82%) and good bending stability [43]. The major drawback of these rGO-based electrodes is their high density of defects that limit device efficiency.

Xu et al. [44] reported the preparation of TCEs based on sulfonated graphene (SG)/PEDOT composites prepared by in situ polymerization (Figure 2). Firstly, SG was prepared from GO in four steps: (1) reduction of GO with $NaBH_4$; (2) sulfonation with the aryl diazonium salt of sulfanilic acid; (3) post-reduction with N_2H_4; (4) functionalization with $NaNO_3$, sulfanilic acid, and azoisobutyronitride (AIBN). Subsequently, SG was dispersed in water followed by the addition of $Fe_2(SO_4)_3$ and the monomer EDOT. The mixture was stirred for 48 h at 50 °C, and then poured into methanol. The excess of EDOT and other impurities were removed through several washing cycles. The composites showed good processability both in water and organic solvents, superior transparency, high thermal conductivity, and thermal stability. A conductivity of 0.2 S/cm and transmittances higher than 80% in the wavelength range of 400–1800 nm were observed for films with thickness of a few nm. This conductivity is much higher than that of a commercial PEDOT:PSS product (10^{-6}–10^{-5} S/cm). Moreover, when a poly(methyl methacrylate) (PMMA) sheet coated with this composite was bent inward, it still retained high electrical conductivity (0.18 S/cm).

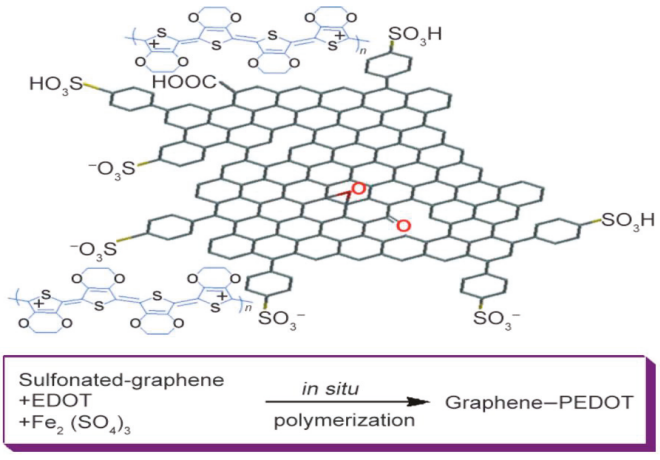

Figure 2. Schematic representation of sulfonated graphene (SG)/poly(3,4-ethylenedioxythiophene): poly(styrenesulfonate) (PEDOT) nanocomposite and its synthesis-reaction conditions. Reprinted from Ref. [44].

A G-based composite electrode was prepared by spin coating a mixed solution of surfactant-functionalized G and PEDOT:PSS [45], with the modified G sheets uniformly distributed in the PEDOT:PSS matrix. The conductivity and transparency of this TCE were comparable to those of an ITO electrode. More importantly, it exhibited high stability (both mechanical and electrical), and it can be bent over 1000 cycles with only a 5% increase in its resistance. However, the presence of the surfactant stabilizer is undesirable from an application point of view. Jo et al. [46] synthesized an aqueous G suspension stabilized by PEDOT:PSS through the chemical reduction of GO in the presence of this polymer, without the need for surfactants. This approach involves strong π–π interactions between rGO sheets and the rigid backbone of PEDOT, and intermolecular electrostatic repulsions between negatively charged PSS bound to the RGO sheets, which impart colloidal stability to the resulting hybrid nanocomposite of rGO/PEDOT. The film exhibited a conductivity of 2.3 kΩ/sq with a transmittance of 80%. Moreover, its conductivity was approximately maintained after 100 bending cycles.

Lima et al. [47] used a GO/PEDOT:PSS nanocomposite as TCE in a cell with structure PET/GO:PEDOT:PSS/F8T2/C_{60}/Al, and a PCE of 1.10% was attained. The nanocomposite was fabricated without the need for any surfactant or dopant, and also played the role of hole-transport material in the device. By changing the GO/PEDOT:PSS ratio, the optical transmittance and sheet resistance of the nanocomposite films was tailored. Furthermore, the films showed good flexibility, without any conductivity reduction after 1000 bending cycles, and the procedure was compatible with large-scale fabrication processes. GO/PEDOT nanocomposites with potential applications as TCEs have also been recently synthesized by the Fenton's reaction [48]. The synthesis was carried out using GO intercalated with $FeCl_3$ and H_2O_2. Then, EDOT monomer was in situ polymerized on to the GO sheets. The resulting composite displayed improved electroactivity and optical properties.

Recently, a 4-layered CVD-doped G treated with PEDOT:PSS was applied as a cathode in inverted PSCs fabricated by spray coating [49]. The active layer was composed of poly[(5,6-difluoro -2,1,3-benzothiadiazol-4,7-diyl)-alt-(3,3‴-di(2-octyldodecyl)2,2′;5′,2″;5″,2‴-quaterthiophen-5,5‴-diyl)] (PffBT4T-2OD) as donor and phenyl-C71-butyric acid methyl ester ($PC_{70}BM$) as acceptor. The resulting device showed a V_{oc} of 0.72 V, J_{sc} of 10.5 mA cm^{-2}, FF of 0.37 and a PCE of 2.8%, respectively, not far from the corresponding values of an ITO-based cell. G-doped PEDOT:PSS nanocomposites have also been prepared by vibration-assisted ultrasonic spray coating [50,51], a single-step, fast, and scalable

process. The resulting films showed a maximum electrical conductivity of 298 S·cm^{-1}, about a 10-fold increase compared to pristine PEDOT:PSS films, with a transparency comparable to that of ITO-coated glasses. This extraordinary improvement was ascribed to the higher carrier mobility and carrier concentration, since G sheets bridge between the PEDOT:PSS rings via strong π–π interactions that act as high-mobility channels. Furthermore, the π–π interactions reduce the number of defect sites in PEDOT:PSS. More importantly, the energy level of G-doped PEDOT:PSS films could be tuned, and they exhibited better stability and superior mechanical properties, including wear resistance and hardness.

Sookhakian et al. [52] modified an ITO electrode with a G/ZnS/PPy ternary nanocomposite. prepared by layer-by-layer electrophoretic deposition. The resulting device showed a V_{oc} of 0.48 V, J_{sc} of 0.42 mA·cm^{-2}, FF of 0.23 and a PCE of 0.92%, respectively, which were higher than those of devices with ZnS- or PPy-modified electrodes. The nanocomposite improved the photovoltaic efficiency because PPy acted as an exceptional sensitizer and hole acceptor, ZnS nanoparticles acted as bridges, whilst G acted as an outstanding conductive collector and transporter.

Liu et al. [53] fabricated semitransparent PSCs based on P3HT: phenyl-C61-butyric acid methyl ester ($PC_{61}BM$) with a CVD-grown single-layer G film doped with Au nanoparticles and PEDOT:PSS as the top electrode and ITO as the bottom electrode (Figure 3a). The use of the doped G electrode led to an increase in conductivity close to 400% compared to pristine G, and a maximum PCE of 2.7% was attained when illuminated from the G side (Figure 3b), which was attributed to the better transmittance of the G electrode. PSCs with higher efficiency are expected to be attained by optimizing the processing conditions and using single-layer G with superior quality.

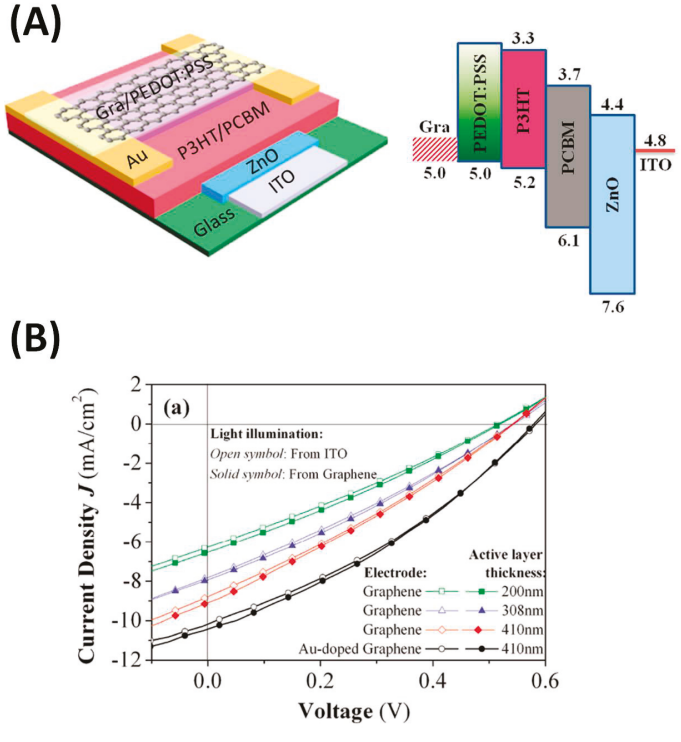

Figure 3. (**A**) Schematic representation and band structure of a PSC with the structure glass/indium tin oxide (ITO)/ZnO/P3HT:PCBM/Au/PEDOT:PSS/G; (**B**) J–V characteristics measured from two sides of the PSC with G top electrode and different active layer thicknesses. Reproduced with permission from Ref. [53].

The same authors [54] fabricated another flexible PSC on polyimide (PI) substrates with multilayer CVD G doped with PEDOT:PSS and Au nanoparticles as top TCE and P3HT:$PC_{61}BM$ as ALs. The device, with an structure of G/Au/PEDOT:PSS/P3HT:PCBM/ZnO/Ag/PI, showed a maximum PCE of ~3.2%, which diminished only by about 8% after 1000 bending cycles, indicating outstanding flexibility and stability. More importantly, it was found that air could not diffuse across the fine space among the G layers, thus providing an excellent packaging effect on flexible solar cells. Multilayer G can act as an environmental barrier and protect the PSCs from air contamination, which simplifies the device fabrication and reduces the associated costs.

Recently, G was prepared via electrochemical exfoliation of graphite [55] using an approach that intercalated sulfate ions (Figure 4). The resulting exfoliated graphene (EG) films were spray deposited on to flexible poly(ethylene 2,6-naphthalate) (PEN), and the composite was applied as anode in PSCs. The device using PTB7:$PC_{71}BM$ as the active layer yielded a PCE of 4.23%, which was kept after 150 bending cycles. This solution processed G-based electrode had a transparency of 70% and a low sheet resistance of 0.52 kΩ/sq, and was mechanically tough, without a change in resistance at different bending angles.

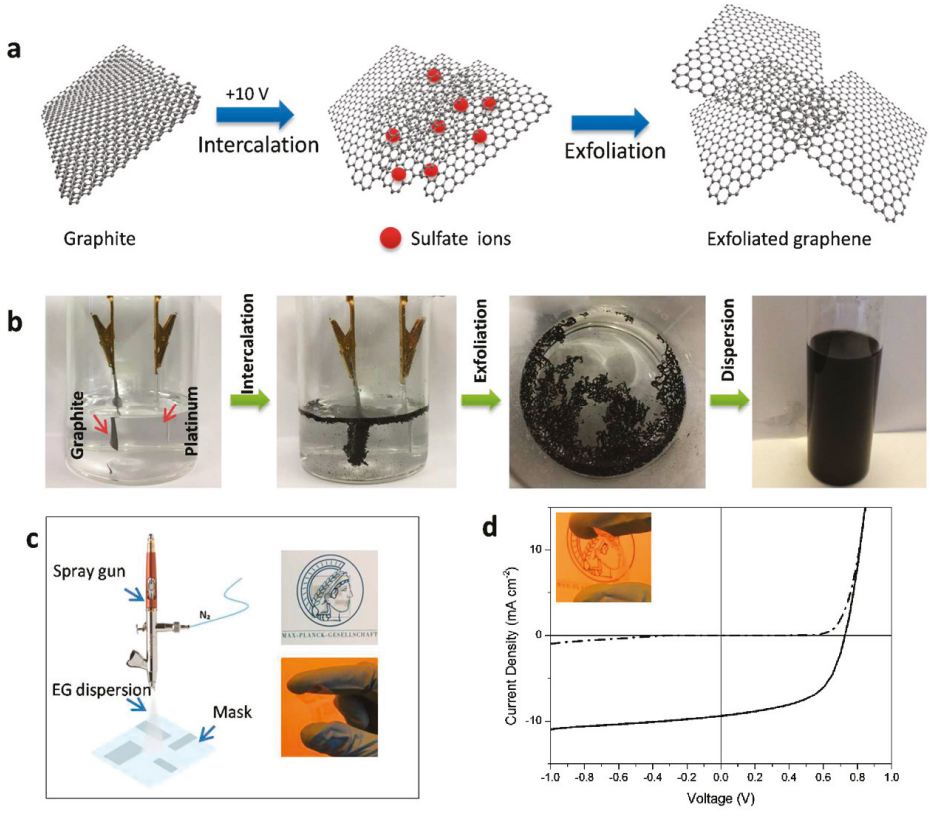

Figure 4. (**a**) Scheme of the electrochemical exfoliation of graphite; (**b**) optical images of the exfoliation process; (**c**) schematic representation of spray deposition of exfoliated graphene (EG) dispersion onto poly(ethylene 2,6-naphthalate) (PEN); (**d**) J–V characteristics of the cell under light (solid line) and dark conditions (dashed line). Reprinted with permission from [55].

An et al. [56] developed another device incorporating a PMMA/G composite as anode. The polymer was spin coated onto highly uniform G prepared by CVD, resulting in a bilayer composite that was further deposited onto a flexible PET substrate. The PMMA improved the adhesion of G onto the substrate, preventing both contamination and crack formation. Based on this novel process, the G sheet resistance was reduced by about 50% at the same transmittance, leading to a device with a configuration of: PET/PMMA-G/MoO_3/PEDOT:PSS/Poly[*N*-9′-heptadecanyl-2,7-carbazole-alt-5,5-(4′,7′-di-2-thienyl-2′,1′,3′-benzothiadiazole)] (PCDTBT):$PC_{70}BM$/Ca/Al that exhibited a V_{oc} of 0.83 V, J_{sc} of 8.88 mA cm^{-2}, FF of 0.45 and a PCE of 3.3%, about 200% higher efficiency than the reference cell without G.

G has also been used as cathode and anode in PSCs. Park et al. [57] developed highly efficient flexible PSCs by modifying the G surface with a PEDOT-block-poly(ethylene glycol) (PEDOT:PEG) copolymer doped with perchlorate (PC) (Figure 5). The G films were fabricated via a low-pressure CVD (LPCVD) method, and comprised three monolayers. They had very good conductivity and transparency (resistivity of 300 Ω/sq and transmittance of 92%), and were applied as the anode in conventional cells and as the cathode in inverted devices [58], reaching PCEs of 6.1% and 7.1%, respectively. Bending tests demonstrated that these G-based devices were strong under mechanical deformation, without significant performance loss after 100 flexing cycles, and showed a maximum V_{oc} of 0.71 V, J_{sc} of 14.8 mA·cm^{-2} and a maximum FF of 57.6%. PSCs with LPCVD G as both anode and cathode have also been fabricated [59]. By using a PMMA-coated G as the bottom film and depositing the top G film onto flexible (PEN) substrates, a PCE of 3.7% was attained.

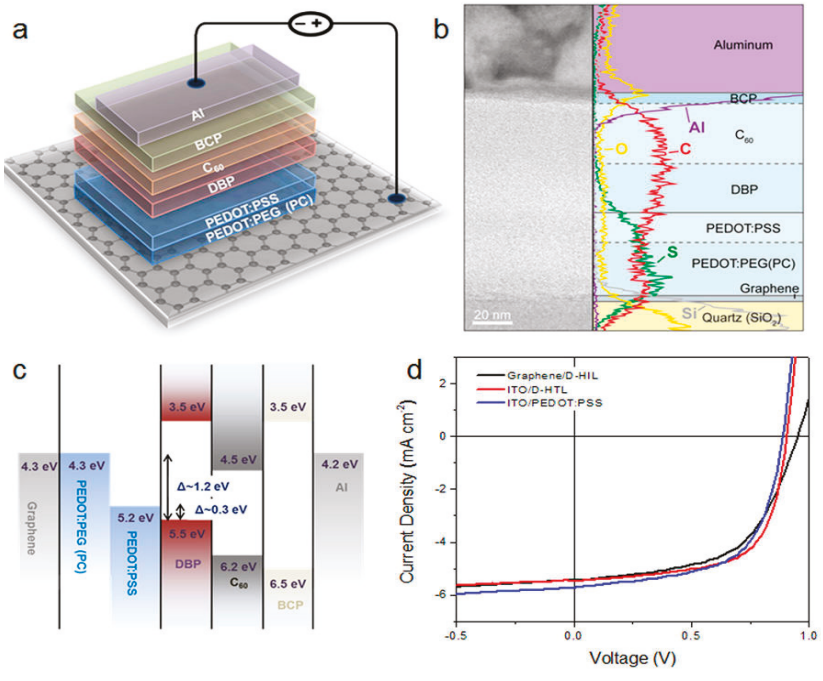

Figure 5. (**a**) Schematic representation of the PSC with G anode and structure G/PEDOT:PEG(PC)/PEDOT:PSS/DBP/C_{60}/BCP/Al; (**b**) cross-sectional transmission electron microscope (TEM) image (left) of the device described in (**a**), with an energy-dispersive line scan on a diagram of the device cross-section (right); (**c**) flat-band energy level diagram of the PSC; (**d**) J–V characteristics of the G-based device compared to ITO reference cells (red and blue lines, respectively). Reproduced with permission from Ref. [57].

4.2. Graphene/Polymer Nanocomposites as Active Layers

Initially, OSCs had an architecture similar to that of conventional solar cells: a single flat semiconductor heterojunction formed by a thin layer of active polymer (donor) and a film of acceptor, sandwiched between two electrodes. The field created in the donor–acceptor interface is responsible for exciton dissociation into free electron-hole pairs. The PCEs of OSCs based on this architecture is very low due to the reduced interface area. This means that only excitons formed very close to the interface (just a few nm) can dissociate into free-charge carriers. Therefore, flat hetorojunction OSCs must be thin, which leads to poor light absortion and low J_{sc}.

Most OSCs developed later with significantly higher PCE where based on the BHJ architecture [6]. In this type of cell, an interpenetrating network with nanoscale phase separation in the active layer (consisting of a polymer donor and a fullerene-derivative acceptor) is formed. The PCE improvement in BHJ solar cells compared to bilayer solar cells is mainly due to the more efficient exciton dissociation enabled by the maximized heterojunction interface and increased charge-carrier collection due to the formation of the interpenetrating network. In this regard, the large specific surface area and 2D structure of G favor the formation of a bicontinuous interpenetrating network of donor and acceptor materials at the nanometer scale.

Liu and coworkers [60] reported the first use of solution-processable G functionalized with phenyl isocyanate as an acceptor and poly(3-octylthiophene) (P3OT) as a donor in PSCs. The device, with an ITO/ PEDOT:PSS/P3OT:G/LIF/Al structure, showed a maximum PCE of 1.4% for a G content of 5 wt % optimized via an annealing process (20 min at 160 °C). The same authors used such functionalized G in a higher concentration (10 wt %) as an acceptor and P3HT as donor in a similar PSC [61], with a maximum PCE of 1.1%, V_{oc} of 0.72 V, J_{sc} of 4.0 mA·cm^{-2} and FF of 0.38 after an annealing treatment at 160 °C for 10 min. The improvement in device performance was explained considering the expansion of the exciton dissociation area due to the faster electron transport through G. However, annealing at higher temperatures (i.e., 210 °C) resulted in a decrease in the PCE (0.57%). An analogous PSC using a P3OT/solution-processable G composite as the active layer was developed by Wang et al. [62]. The device showed a PCE of 1.14%, V_{oc} of 0.67 V, J_{sc} of 4.6 mA·cm^{-2}, and FF of 0.37. Other authors prepared a P3HT/solution processable G/functionalized multiwalled carbon nanotubes (f-MWCNTs) nanocomposite, where P3HT acted as an electron donor, G as an electron acceptor and percolation path for the electrons, and the f-MWCNTs provided percolation paths of holes [63]. The resulting ITO/PEDOT:PSS/P3HT-f-MWCNTs-SPFGraphene/LiF/Al device showed a J_{sc} of 4.7 mA·cm^{-2}, V_{oc} of 0.67 V, FF of 0.32, and a PCE of 1.05%. Nonetheless, the PCE of these cells with solution-processable G is significantly low, and could likely be improved by tuning the G content and processing conditions, since theoretical studies predict an efficiency above 12% for G-based PSCs.

Yu et al. [64] grafted CH_2OH-terminated regioregular P3HT on to the COOH groups of the GO surface via an esterification reaction. The resultant P3HT-grafted GO sheets were found to be soluble in a number of organic solvents, which is advantageous for solution processing. They used P3HT-*g*-GO/C_{60} as the active layer to build a photovoltaic device with the structure ITO/PEDOT:PSS/G-P3HT:C_{60}/Al (Figure 6), showing a PCE of 0.61%, about 200% enhancement compared to the device based on P3HT/C_{60}, since the chemical grafting of P3HT on to G can enhance electron delocalization and light absorption. The same group [65] grafted C_{60} on to the surface of rGO through a lithiation reaction, and the resulting hybrids were used as electron acceptors in the active layer to fabricate BHJ solar cells (device structure: ITO/PEDOT:PSS/C_{60}-rGO:P3HT/Al). A maximum PCE of 1.22%, a J_{sc} of 4.45 mA cm^{-2} and a V_{oc} of 0.56 V were obtained, which are higher than those of many PSCs with non-fullerene electron acceptors, since the rGO–C_{60} hybrid can lead to a more effective electron transport pathway.

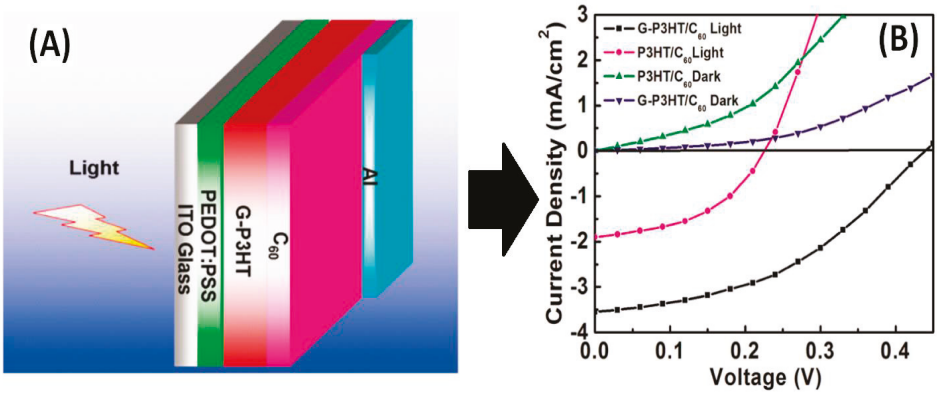

Figure 6. (**A**) Schematic representation of ITO/PEDOT:PSS/G-P3HT:C_{60}/Al PSC; and (**B**) J–V characteristics using P3HT:C_{60} or G-P3HT:C_{60} as the active layer. Reproduced with permission from Ref. [64].

Converting 2D G into 0D quantum dots (GQDs) is a very effective approach to open the band gap of graphene. Furthermore, the GQDs are rich in oxygenated groups and soluble in aqueous and organic solvents, thus enabling further functionalization. GQDs with sizes of 3–5 nm, synthesized via an electrochemical approach, were used as electron-acceptors in a device with the structure of ITO/PEDOT:PSS/P3HT:GQDs/Al [66], leading to a V_{oc} of 0.67 V and a PCE of 1.28%. Aniline-modified GQDs were prepared via a hydrothermal method and used as acceptors in PSCs [67] with P3HT as donor (Figure 7), leading to a PCE of 1.14%. GQDs derived from double-walled carbon nanotubes have also been prepared via a solution-based method and incorporated into an active layer of P3HT:PCBM, leading to a PCE of 5.24% [68]. P3HT:PCBM:GQDs ternary composite represents a novel way to improve the efficiency of PSCs.

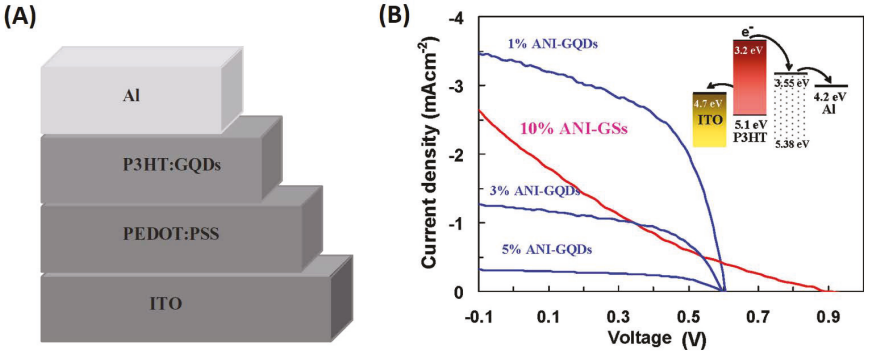

Figure 7. (**A**) Schematic representation; and (**B**) J–V curves of ITO/PEDOT:PSS/P3HT:GQDs/Al device based on aniline-modified GQDs with different GQDs content. Reproduced with permission from Ref. [66,67].

To augment the optical absorptivity and charge-carrier extraction of PSCs, graphene oxide quantum dots (GOQDS) and reduced graphene oxide quantum dots (rGOQDs) have been blended with a PTB7:PC_{71}BM active layer (Figure 8) leading to a device with structure ITO/PEDOT:PSS/GOQDs:PTB7:PC_{71}BM/Al [69]. For rGOQDS, an increase in both J_{sc} and FF was observed due to the

oxygenated functional groups on the surface of the QDs and their improved conductivity, leading to a maximum PCE of 7.6%. Another strategy to increase the band gap of G is doping with heteroatoms [70]. In this regard, PSCs have been developed by incorporating nitrogen-doped rGO in P3HT:PCBM ALs. The highest PCE obtained (4.5%) with this device (ITO/PEDOT:PSS/N-doped graphene:P3HT:PCBM/Al) was about 40% higher than that of a device without G. Overall, the performance of these PSCs with G-based materials is lower than that of conventional cells incorporating C_{60} and its derivatives [2–4]. Additional research should be carried out to control the structure and properties of G and optimize the device fabrication procedure to develop PSCs with higher PCE.

Preliminary studies comparing the performance of G-based and carbon nanotube (CNT)-based PSCs revealed the superiority of those incorporating G. Thus, Lee et al. [71] compared the effect of maleimide-thiophene copolymer-functionalized GO (PTM21-GO) and carbon nanotubes (PTM21-CNTs) on P3HT/PCBM blends for use as active layers in PSCs. The performance was enhanced after incorporating both composites, and the highest PCE (1.70%) was obtained after the addition of 0.3 wt % PTM21-GO. The improved behaviour of the device with GO was attributed to the larger surface-contact area, higher charge-transporting capacity, along with the better dispersive nature after functionalization of the GO sheets compared to the CNTs. Furthermore, the amphiphilic character of GO makes its processability in aqueous solutions easier compared to CNTs that are hydrophobic and insoluble in most of the common solvents.

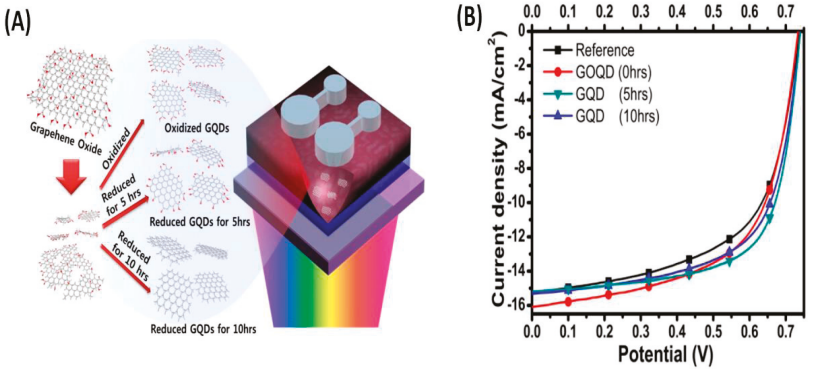

Figure 8. (**A**) Schematic representation of the synthesis of graphene oxide quantum dots (GOQDs) and reduced graphene oxide quantum dots (rGOQDs), where the edge functional groups are controlled by adjusting the thermal reduction time; (**B**) J–V curves of the PSCs with different types of GQDs. Reproduced with permission from Ref. [69].

4.3. Graphene/Polymer Nanocomposites as Interfacial Layers

The IFLs, that is, the hole-transporting layer and electron-transporting layer between the active layer and the anode/or cathode, respectively, strongly condition the performance of PSCs. They are commonly used in order to improve the electrical contacts and enhance charge transport and collection. In addition, IFLs can improve light absorption and radiation distribution in the active layer and enhance performance stability. IFLs reduce charge-carrier recombination in electrodes by selectively allowing the desired carriers to pass through and preventing carriers from reaching the opposite electrodes. This is particularly important in BHJ PSCs, in which the donor and the acceptor semiconductors are randomly distributed in the active layer. Therefore, both semiconductors could be in contact with the anode and cathode, increasing the probability of recombination. IFLs can be designed in order to obtain a low contact resistance at the electrodes, avoiding this requirement to be met at the active layer, which can be designed without that restriction. IFLs also improve light distribution and absorption in PSCs by reducing the reflection of light at interfaces.

G and its derivatives have been used as both types of layers, due to their benefits of superior energy-band structure that results in efficient charge transport and less corrosion for the ITO electrode [18]. A GO/PEDOT:PSS composite was used as the hole transport layer in a PCDTBT:$PC_{71}BM$-based BHJ PSC, leading to a PCE of 4.28%, which is higher compared to devices with either GO or PEDOT:PSS as hole transport layers (PCEs of 2.77 and 3.57%, respectively). In addition, enhanced reproducibility and stability were observed. The improved performance was ascribed to the well-matched work function of GO and PEDOT:PSS that increased charge carriers' mobility and reduced series resistance. Besides, GO could effectively block the electrons due to its large band-gap of ~3.6 eV, leading to an increased shunt resistance [72].

Chuang and Chen [73] developed a PEG-modified Au nanoparticles/GO nanocomposite as the hole-transport layer in a device with the structure: ITO/PEDOT:PSS(Au@PEG–GO)/PBDTTT-CT. PEG improved the solubility of the nanocomposite, so that it was well dispersed in water and several organic solvents. A relatively high PCE of 7.26% was attained. Besides, different spectral-enhancement regions were observed when the nanocomposite was placed at different locations, revealing the different dielectric environments nearby the nanoparticles, which could be useful for improving the broadband absorption of solar irradiation.

Jung et al. [74] synthesized a polyacrylonitrile-grafted rGO nanocomposite (PRGO) that acted as a hole-transport layer in PSCs based on PTB7-Th. The nanocomposite was fabricated via a covalent strategy based on in situ radiation-induced reduction and graft polymerization with acrylonitrile and styryl-functionalized GO. It displayed homogeneous thin-film morphology, good electrical conductivity (0.87 S/cm), high work function (4.87 eV), and exceptional weather stability. This combination of qualities makes it suitable as interfacial material in PSCs in order to improve photovoltaic efficiency and stability. The resulting device showed a PCE of 7.24%, FF of 0.64, J_{sc} of 14.78 mA/cm^2, and V_{oc} of 0.76 V, comparable to those of a PEDOT:PSS-based one: PCE of 7.17%, FF of 0.66, J_{sc} of 13.91 mA/cm^2, and V_{oc} of 0.78 V. More importantly, it exhibited superior durability.

Hu et al. [75] developed a new electron-transport layer based on ZnO nanocrystals dispersed in a G matrix with ethyl cellulose (EC) as a stabilizer. The ZnO@G:EC nanocomposites with different G contents exhibited a relatively smooth morphology (Figure 9), and retained the original structure of G with high conductivity. The device based on P3HT:$PC_{61}BM$, with a structure of: ITO/ZnO@G:EC/P3HT:$PC_{61}BM$/MoO_3/Ag, showed a PCE of 3.9%, about 20% higher than that with bare ZnO nanocrystals. Replacing the active layer by PTB7:$PC_{71}BM$, the PCE raised up to 8.4%. This simple approach can lead to highly conductive electron-transport layers for PSCs.

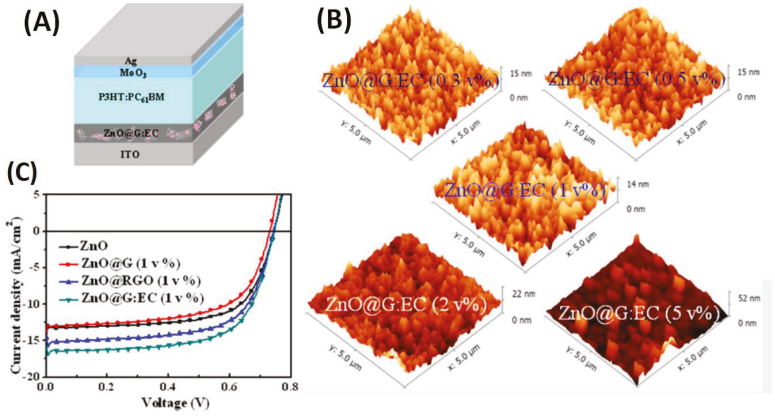

Figure 9. (**A**) Schematic representation of ITO/ZnO@G:EC/P3HT:$PC_{61}BM$/MoO_3/Ag device; (**B**) atomic force microscope (AFM) images of ZnO@G:EC nanocomposites with different G contents; (**C**) J–V curves of PSCs with the different nanocomposites. Reproduced with permission from Ref. [75].

In another study, GO thin films were deposited by spin coating between a P3HT:PCBM active layer and ITO, causing a reduction in the recombination of electrons and holes as well as leakage currents [76]. The deposited GO acted as an effective hole-transport layer, and the best results were obtained for a GO film with a thickness of 2 nm. Thus, the device showed a PCE of 3.5%, a V_{oc} of 0.57 V, J_{sc} of 11.4 mA·cm^{-2} and a FF of 0.54. However, as the thickness of the films increased, the PCE decreased, due to the increased resistance of the hole-transport layer. In addition, spin coating such a thin GO film is extremely difficult. To solve these problems, nanocomposites with single-walled carbon nanotubes (SWCNTs) have been developed. Blending GO with SWCNTs significantly increased the conductivity of the nanocomposite; the device with a GO:SWCNT mass ratio of 1:0.2 exhibited a PCE of 4.1%, a V_{oc} of 0.6 V, J_{sc} of 10.8 mA·cm^{-2}, and FF of 0.63, which are better than those of a PSC with raw GO as the hole-transporting layer. A nanocomposite of few-layer graphene nanosheets and PEDOT:PSS has also been used as a hole-transport layer, leading to an increase in the PCE from 3.1 to 3.7% compared to a conventional device with PEDOT:PSS [77]. In the case of butylamine-modified G/PEDOT:PSS nanocomposite, the PCE raised from 0.42 to 0.74%. Furthermore, when a GO/PEDOT:PSS nanocomposite was applied as the hole-transport layer, a PCE of 1.43 was attained, about 12% higher than the reference cell without GO, ascribed to the enhanced charge-carrier transport due to improved conductivity [78]. Overall, it seems that the addition of G derivatives as additives to PEDOT:PSS improves the performances of PSCs, although the reason for this enhancement is not fully understood yet.

Table 1. Characteristics of PSCs based on G/polymer nanocomposites.

Composite	Device Structure	J_{sc} (mA·cm^{-2})	V_{oc} (V)	FF	PCE (%)	REF
PET/rGO	PET/rGO/PEDOT:PSS/P3HT:PCBM/TiO_2/Al	4.39	0.56	NA	0.78	42
GO:PEDOT:PSS	PET/GO:PEDOT:PSS/F8T2/C60/Al	2.75	0.71	0.52	1.10	47
Au/G/PEDOT:PSS	ITO/ZnO/P3HT:PCBM/PEDOT:PSS/Au/G	10.58	0.59	0.43	2.7	53
G/Au/PEDOT:PSS	G/Au/PEDOT:PSS/P3HT:PCBM/ZnO/Ag/PI	10.6	0.597	0.50	3.17	54
EG/PEDOT:PSS	EG/PEDOT:PSS/PTB7:PC71BM/Ba /Al	6.53	0.707	0.56	4.23	55
PMMA-G	PET/PMMA-G/MoO3/PEDOT:PSS /PCDTBT:PC_{70}BM/Ca/Al	8.88	0.83	0.45	3.3	56
PEN/G	PEN/G/ZnO/PTB7:PC_{71}BM/MoO_3/Ag	14.9	0.71	0.58	6.2	58
P3OT:G	ITO/ PEDOT:PSS/P3OT:G/LiF/Al	4.2	0.92	0.37	1.4	60
P3HT:G	ITO/ PEDOT:PSS/P3HT:G/LiF/Al	4.0	0.72	0.38	1.1	61
P3OT:PCBM–G	ITO/PEDOT:PSS/P3OT:PCBM–G/LiF/Al	4.6	0.67	0.37	1.14	62
P3HT-f-MWCNTs-SPFG	ITO/PEDOT:PSS/P3HT-f-MWCNTs-SPFG/LiF/Al	4.7	0.67	0.32	1.05	63
P3HT-grafted GO	ITO/PEDOT:PSS/G-P3HT:C60/Al	3.5	0.43	0.41	0.61	64
C60-rGO:P3HT	ITO/PEDOT:PSS/C60-rGO:P3HT/Al	4.45	0.56	0.49	1.22	65
P3HT:GQDs	ITO/PEDOT:PSS/P3HT:GQDs/Al	6.33	0.67	0.30	1.28	66
P3HT/ANI-GQDs	ITO/PEDOT:PSS/P3HT/ANI-GQDs/Al	3.51	0.61	0.53	1.14	67
P3HT:PCBM:GQDs	ITO/PEDOT:PSS/P3HT:PCBM:GQDs/LiF/Al	26.46	0.60	0.33	5.24	68
GOQDs:PTB7: PC_{71}BM	ITO/PEDOT:PSS/GOQDs:PTB7: PC_{71}BM/Al	15.2	0.74	0.68	7.6	69
N-dopedG:P3HT:PCBM	ITO/PEDOT:PSS/N-doped G:P3HT:PCBM/Al	14.95	0.59	0.51	4.48	70
PTM21-GO	ITO/PEDOT:PSS/P3HT:PTM21-GO:PCBM/LiF/Al	8.11	0.59	0.30	1.43	71
GO/PEDOT:PSS	ITO/GO/PEDOT:PSS/PCDTBT: PC_{71}BM/Al	10.44	0.82	0.50	4.28	72
Au@PEG–GO	ITO/PEDOT:PSS(Au@PEG–GO) /PBDTTT-CT	16.1	0.75	0.60	7.26	73
PRGO-PTB7-th	NA	14.78	0.76	0.64	7.24	74
ZnO@G:EC	ITO/ZnO@G:EC/P3HT:PC61BM/MoO3/Ag	7.73	0.63	0.73	3.9	75
GO/P3HT:PCBM	ITO/GO/P3HT:PCBM/Al	11.4	0.57	0.54	3.5	76
G:PEDOT:PSS	ITO/FLGs-PEDOT:PSS/PCBM/P3HT/Ca/Al	9.44	0.58	0.55	3.7	77

5. Conclusions and Outlook

G and its derivatives, GO and rGO have emerged as ideal materials for solar-cell applications owing to their 2D structure, outstanding electrical and thermal conductivity, high transparency, flexibility, superior mechanical strength, and very large specific surface area. In order to enhance their processability, chemical and electrochemical properties, and to expand their uses, G-based nanomaterials are frequently blended with polymers. In this regard, G/polymer nanocomposites seem to be useful in a range of device parts including transparent electrodes, active layers and interfacial layers. Nonetheless, while some improvements have already been attained when replacing conventional materials (i.e., ITO, PEDOT:PSS), several issues have to be addressed prior to the use of G-based nanocomposites as a key component in PSCs:

(a) The functionalization and ultrasonication processes applied to G prior to and during the fabrication of polymer nanocomposites leads to a strong reduction in electrical conductivity. Hence, the conductivity of chemically-derived G is considerably lower than that of ideal G. Consequently, G/polymer nanocomposites present poor electrical properties and do not satisfy the requirements for TCEs and counter electrodes in solar cells.

(b) Novel fabrication techniques to synthesize high-quality G thin films with tailored morphology and electronic properties are required, since the performance of G-based PSCs is directly related to the G characteristics: purity, quality, band-gap, structural morphology, etc. In the case of TCEs, solution-processable films with a good balance between high transparency and low sheet resistance are needed. More importantly, techniques that allow the synthesis of G at a large scale and at relatively low cost are highly desirable. Even though a lot of efforts have been made in this direction, the current methods are seriously limited by their low efficiencies, which should be addressed for commercial applications.

(c) The real specific surface area of G-based materials is much lower than the theoretical predictions owing to the strong agglomeration of the G sheets via π–π stacking interactions, and blending with polymers makes the problem even worse. Thus, new approaches to exfoliate the G sheets and keep a large specific surface area when blended with polymers are required. Although significant success has been attained via the addition of stabilizers such as surfactants, these frequently have detrimental effects on final device performance. Hence, novel synthetic routes are sought.

(d) Novel doping or functionalization strategies compatible with the fabrication process of PSCs have to be explored to attain high charge-carrier densities, better stability and tunable energy levels in G-based materials.

(e) The performance of G/polymer nanocomposites in PSCs is well below that reported for traditional materials. Thus, the composition and morphologies of the nanocomposites and the structure of the corresponding PSCs need further optimization. In this regard, developing new types of G-based materials such as GQDs is an interesting alternative. Owing to quantum confinement and the edge effect, the GQDs can exhibit better properties than pristine G, which could allow for the fabrication of PSCs with better PCE.

(f) The toxicity of nanostructured materials is well known [78,79] and the degradation caused by toxicity is of concern. G-based materials may cause cytotoxicity to humans, and this issue should be investigated in detail.

Overall, the research in this area is still in its infancy, and the mechanisms used to explain the observed effects are merely based on assumptions. Nonetheless, it is expected that after extensive research in the field and constant innovative efforts, PSCs incorporating G-based materials could offer a new outlook for the solar-energy industry.

Acknowledgments: Financial support from the Fundación Iberdrola España via a Research Grant in Energy and the Environment 2017 is gratefully acknowledged.

Author Contributions: Ana Maria Diez Pascual designed the manuscript and wrote the paper; Jose Antonio Luceño Sanchez drew the figures. Jose Antonio Luceño Sanchez, Rafael Peña Capilla and Pilar Garcia Diaz contributed to the literature survey; Rafael Peña Capilla and Pilar Garcia Diaz critically reviewed the manuscript.

Conflicts of Interest: The authors declare no conflict of interest.

References

1. Brabec, C.J.; Sariciftci, N.S.; Hummelen, J.C. Plastic solar cells. *Adv. Funct. Mater.* **2001**, *11*, 15–26. [CrossRef]
2. Cheng, Y.-J.; Yang, S.-H.; Hsu, C.-S. Synthesis of conjugated polymers for organic solar cell applications. *Chem. Rev.* **2009**, *109*, 5868–5923. [CrossRef] [PubMed]
3. Jørgensen, M.; Norrman, K.; Krebs, F.C. Stability/degradation of polymer solar cells. *Sol. Energy Mater. Sol. Cells* **2008**, *92*, 686–714. [CrossRef]
4. Thompson, B.C.; Fréchet, J.M. Polymer-Fullerene Composite Solar Cells. *Angew. Chem. Int. Ed. Engl.* **2007**, *47*, 58–77. [CrossRef] [PubMed]
5. Chen, H.-Y.; Hou, J.; Zhang, S.; Liang, Y.; Yang, G.; Yang, Y.; Yu, L.; Wu, Y.; Li, G. Polymer solar cells with enhanced open-circuit voltage and efficiency. *Nat. Photonics* **2009**, *3*, 649–653. [CrossRef]
6. Dennler, G.; Scharber, M.C.; Brabec, C.J. Polymer-fullerene bulk-heterojuntion solar cells. *Adv. Mater.* **2009**, *21*, 1323–1338. [CrossRef]
7. Green, M.A. Solar cell fill factors: General graph and empirical expressions. *Solid State Electron.* **1981**, *24*, 788–789. [CrossRef]
8. Luo, J.; Wu, H.; He, C.; Li, A.; Yang, W.; Cao, Y. Enhanced open-circuit voltage in polymer solar cells. *Appl. Phys. Lett.* **2009**, *95*, 043301. [CrossRef]
9. De Kok, M.M.; Buechel, M.; Vulto, S.I.E.; van de Weijer, P.; Meulenkamp, E.A.; de Winter, S.H.P.M.; Mank, A.J.G.; Vorstenbosch, H.J.M.; Weijtens, C.H.L.; van Elsbergen, V. Modification of PEDOT:PSS as Hole Injection Layer in Polymer LEDs. *Phys. Status Solidi A Appl. Res.* **2004**, *201*, 1342–1359. [CrossRef]
10. Yun, J.-M.; Yeo, J.-S.; Kim, J.; Jeong, H.-G.; Kim, D.-Y.; Noh, Y.-J.; Kim, S.-S.; Ku, B.-C.; Na, S.-I. Solution-processable reduced graphene oxide as a novel alternative to PEDOT:PSS hole transport layers for highly efficient and stable polymer solar cells. *Adv. Mater.* **2011**, *23*, 4923–4928. [CrossRef] [PubMed]
11. Taleghani, H.G.; Aleahmad, M.; Eisazadeh, H. Preparation and Characterization of Polyaniline Nanoparticles Using Various Solutions. *World Appl. Sci. J.* **2009**, *6*, 1607–1611.
12. Walker, B.; Kim, C.; Nguyen, T.Q. Small molecule solution-processed bulk heterojunction Solar Cells. *Chem. Mater.* **2011**, *23*, 470–482. [CrossRef]
13. Das, S.; Keum, J.K.; Browning, J.F.; Gu, G.; Yang, B.; Dyck, O.; Chen, W.; Chen, J.; Ivanov, I.N.; Hong, K.; et al. Correlating high power conversion efficiency of PTB7:PC71BM inverted organic solar cells with nanoscale structures. *Nanoscale* **2015**, *14*, 15576–15583. [CrossRef] [PubMed]
14. You, J.; Dou, L.; Yoshimura, K.; Kato, T.; Ohya, K.; Moriarty, T.; Emery, K.; Chen, C.-C.; Gao, J.; Li, G.; Yang, Y. A polymer tandem solar cell with 10.6% power conversion efficiency. *Nat. Commun.* **2013**, *4*, 1446. [CrossRef] [PubMed]
15. Xue, Z.; Wang, S.; Yang, J.; Zhong, Y.; Qian, M.; Li, C.; Zhang, Z.; Xing, G.; Tao, Y.; Li, Y.; Huang, W. Enhanced power-conversion efficiency in polymer solar cells using an inverted device structure. *Npj Flex. Electron.* **2018**, *2*, 1–7. [CrossRef]
16. Wan, Q.; Guo, X.; Wang, Z.; Li, W.; Guo, B.; Ma, W.; Zhang, M.; Li, Y. 10.8% efficiency polymer solar cells based on PTB-Th and PC71BM via binary solvent additive treatment. *Adv. Funct. Mater.* **2016**, *26*, 6635–6640. [CrossRef]
17. Chen, J.-D.; Cui, C.; Li, Y.-Q.; Zhou, L.; Ou, Q.-D.; Li, C.; Li, Y.; Tang, J.-X. Single junction polymer solar cells exceeding 10% power conversion efficiency. *Adv. Mater.* **2014**, *27*, 1035–1041. [CrossRef] [PubMed]
18. Lin, X.-F.; Zhang, Z.-Y.; Yuan, Z.-K.; Li, J.; Xiao, X.-F.; Hong, W.; Chen, X.-D.; Yu, D.-S. Graphene-based materials for polymer solar cells. *Chin. Chem. Lett.* **2016**, *27*, 1259–1270. [CrossRef]
19. Sun, Y.; Zhang, W.; Chi, H.; Liu, Y.; Hou, C.L.; Fang, D. Recent development of graphene materials applied in polymer solar cell. *Renew. Sustain. Energy Rev.* **2015**, *43*, 973–980. [CrossRef]
20. Wallace, P.R. The band theory of graphite. *Phys. Rev.* **1947**, *71*, 622–634. [CrossRef]

21. Chang, H.; Wu, H. Graphene-Based Nanomaterials: Synthesis, Properties, and Optical and Optoelectronic Applications. *Adv. Funct. Mater.* **2013**, *23*, 1984–1997. [CrossRef]
22. Weiss, N.O.; Zhou, H.; Liao, L.; Liu, Y.; Jiang, S.; Huang, Y.; Duan, X. Graphene: An Emerging Electronic Material. *Adv. Mater.* **2012**, *24*, 5782–5825. [CrossRef] [PubMed]
23. Lee, C.; Wei, X.; Kysar, J.W.; Hone, J. Measurement of the elastic properties and intrinsic strength of monolayer graphene. *Science* **2008**, *321*, 385–388. [CrossRef] [PubMed]
24. Diez-Pascual, A.M.; Gomez-Fatou, M.A.; Ania, F.; Flores, A. Nanoindentation in polymer nanocomposites. *Prog. Mater. Sci.* **2015**, *67*, 1–94. [CrossRef]
25. Nair, R.R.; Grigorenko, A.N.; Novoselov, K.S.; Booth, T.J.; Stauber, T.; Peres, N.M.R.; Geim, A.K. Fine structure constant defines visual transparency of graphene. *Science* **2008**, *320*, 1308. [CrossRef] [PubMed]
26. Zheng, Q.; Kim, J.K. Synthesis, Structure and Properties of Grpahene and Graphene Oxide. In *Graphene for Transparent Conductors. Synthesis, Properties and Applications*; Springer: New York, NY, USA, 2015; pp. 29–94, ISBN 978-1493927685.
27. Wu, J.; Becerril, H.A.; Bao, Z.; Liu, Z.; Chen, Y.; Peumans, P. Organic solar cells with solution processed graphene transparent electrodes. *Appl. Phys. Lett.* **2008**, *92*, 263302. [CrossRef]
28. Díez-Pascual, A.M.; Díez-Vicente, A.L. Poly(Propylene Fumarate)/Polyethylene Glycol-Modified Graphene Oxide Biocomposites for Tissue Engineering. *ACS Appl. Mater. Interfaces* **2016**, *8*, 17902–17914. [CrossRef] [PubMed]
29. Su, C.-Y.; Lu, A.-Y.; Xu, Y.; Chen, F.-R.; Khlobystov, A.N.; Li, L.-J. High-quality thin graphene films from fast electrochemical exfoliation. *ACS Nano* **2011**, *5*, 2332–2339. [CrossRef] [PubMed]
30. Dreyer, D.R.; Park, S.; Bielawski, C.W.; Ruoff, R.S. The Chemistry of Graphene Oxide. *Chem. Soc. Rev.* **2010**, *39*, 228–240. [CrossRef] [PubMed]
31. Chen, J.; Yao, B.; Li, C.; Shi, G. An improved Hummers method for eco-friendly synthesis of graphene oxide. *Carbon* **2013**, *64*, 225–229. [CrossRef]
32. Eda, G.; Chhowalla, M. Chemically derived graphene oxide: towards large-area thin-film electronics and optoelectronics. *Adv. Mater.* **2010**, *22*, 2392–2415. [CrossRef] [PubMed]
33. Pei, S.; Chen, H.-M. The reduction of graphene oxide. *Carbon* **2012**, *50*, 3210–3228. [CrossRef]
34. Cote, L.J.; Cruz-Silva, R.; Huang, J. Flash reduction and patterning of graphene oxide and its polymer composite. *J. Am. Chem. Soc.* **2009**, *131*, 11027–11032. [CrossRef] [PubMed]
35. Zhang, Y.; Guo, L.; Wei, S.; He, Y.; Xia, H.; Chen, Q.; Sun, H.-B.; Xiao, F.-S. Direct imprinting of microcircuits on graphene oxides film by femtosecond laser reduction. *Nano Today* **2010**, *5*, 15–20. [CrossRef]
36. Stankovich, S.; Dikin, D.A.; Dommett, G.H.; Kohlhaas, K.M.; Zimmey, E.J.; Stach, E.A.; Piner, R.D.; Nquyen, S.T.; Ruoff, R.S. Graphene-based composite materials. *Nature* **2006**, *442*, 282–286. [CrossRef] [PubMed]
37. Periasamy, M.; Thirumalaikumar, M. Methods of enhancement of reactivity and selectivity of sodium borohydride for applications in organic chemistry. *J. Organomet. Chem.* **2000**, *609*, 137–151. [CrossRef]
38. Salavagione, H.J.; Díez-Pascual, A.M.; Lázaro, E.; Vera, S.; Gómez-Fatou, M.A. Chemical sensors based on polymer composites with carbon nanotubes and graphene: The role of the polymer. *J. Mater. Chem. A* **2014**, *2*, 14289–14328. [CrossRef]
39. Wang, H.L.; Hao, Q.L.; Xia, X.F.; Wang, Z.J.; Tian, J.; Zhu, J.H.; Tang, C.; Wang, X. In Situ Fabrication of Nanoscale Graphene Oxide/Polyaniline Composite and its Electrochemical Properties. *Adv. Mater. Res.* **2010**, *148–149*, 1547–1550. [CrossRef]
40. Bai, H.; Li, C.; Shi, G. Functional composite materials based on chemically converted graphene. *Adv. Mater.* **2011**, *23*, 1089–1115. [CrossRef] [PubMed]
41. Diez-Pascual, A.M. Tissue Engineering Bionanocomposites based on Poly(propylene fumarate). *Polymers* **2017**, *9*, 260. [CrossRef]
42. Yin, Z.; Sun, S.; Salim, T.; Wu, S.; Huang, X.; He, Q.; Lang, Y.M.; Zhan, H. Organic Photovoltaic Devices Using Highly Flexible Reduced Graphene Oxide Films as Transparent Electrodes. *ACS Nano* **2010**, *4*, 5263–5268. [CrossRef] [PubMed]
43. Konios, D.; Petridis, C.; Kakavelakis, G.; Sygletou, M.; Savva, K.; Stratakis, E.; Kymakis, E. Reduced graphene oxide micromesh electrodes for large area, flexible, organic photovoltaic devices. *Adv. Funct. Mater.* **2015**, *15*, 2213–2221. [CrossRef]

44. Xu, Y.; Wang, Y.; Liang, J.; Huang, Y.; Ma, Y.; Wan, X.; Chen, Y. A hybrid material of graphene and poly (3,4-ethyldioxythiophene) with high conductivity, flexibility, and transparency. *Nano Res.* **2009**, *2*, 343–348. [CrossRef]
45. Chang, H.; Wang, G.; Yang, A.; Tao, X.; Liu, X. A Transparent, Flexible, Low-Temperature, and Solution-Processible Graphene Composite Electrode. *Adv. Funct. Mater.* **2010**, *20*, 2893–2902. [CrossRef]
46. Jo, K.; Lee, T.; Choi, H.J.; Park, J.H.; Lee, D.J.; Lee, D.W.; Kim, B.-S. Stable aqueous dispersion of reduced graphene nanosheets via non-covalent functionalization with conducting polymers and application in transparent electrodes. *Langmuir* **2011**, *27*, 2014–2018. [CrossRef] [PubMed]
47. Lima, L.F.; Matos, C.F.; Gonçalves, L.C.; Salvatierra, R.V.; Cava, C.E.; Zarbin, A.J.G.; Roman, L.S. Water based, solution-processable, transparent and flexible graphene oxide composite as electrodes in organic solar cell application. *J. Phys. D Appl. Phys.* **2016**, *49*, 105106. [CrossRef]
48. Carrasco-Valenzuela, L.; Zaragoza-Contreras, E.A.; Vega-Rios, A. Synthesis of graphene oxide/poly(3,4-ethylenedioxythiophene) composites by Fenton's reagent. *Polymer* **2017**, *130*, 124–134. [CrossRef]
49. La Notte, L.; Bianco, G.V.; Palma, A.L.; Carlo, A.D.; Bruno, G.; Reale, A. Sprayed organic photovoltaic cells and mini-modules based on chemical vapor deposited graphene as transparent conductive electrode. *Carbon* **2018**, *129*, 878–883. [CrossRef]
50. Soltani-kordshuli, F.; Zabihi, F.; Eslamian, M. Graphene-doped PEDOT:PSS nanocomposite thin films fabricated by conventional and substrate vibration-assisted spray coating (SVASC). *JESTECH* **2016**, *19*, 1216–1223. [CrossRef]
51. Chen, Q.; Zabihi, F.; Eslamian, M. Improved functionality of PEDOT:PSS thin films via graphene doping, fabricated by ultrasonic substrate vibration-assisted spray coating. *Synth Met.* **2016**, *222*, 309–317. [CrossRef]
52. Sookhakian, M.; Amin, Y.M.; Baradaran, S.; Tajabadi, M.T.; Golsheikh, A.M.; Basirun, W.J. A layer-by-layer assembled graphene/zinc sulfide/polypyrrole thin-film electrode via electrophoretic deposition for solar cells. *Thin Solid Films* **2014**, *552*, 204–211. [CrossRef]
53. Liu, Z.; Li, J.; Sun, Z.-H.; Tai, G.; Lau, S.-P.; Yan, F. The Application of Highly Doped Single-Layer Graphene as the Top Electrodes of Semitransparent Organic Solar Cells. *ACS Nano* **2012**, *6*, 810–818. [CrossRef] [PubMed]
54. Liu, Z.; Li, J.; Yan, F. Package-Free Flexible Organic Solar Cells with Graphene top Electrodes. *Adv. Mater.* **2013**, *25*, 4296–4301. [CrossRef] [PubMed]
55. Ricciardulli, A.G.; Yang, S.; Feng, X.; Blom, P.W.M. Solution-processable high-quality graphene for organic solar cells. *ACS Appl. Mater. Interfaces* **2017**, *9*, 25412–25417. [CrossRef] [PubMed]
56. An, C.J.; Kim, S.J.; Choi, H.O.; Kim, D.W.; Jang, S.W.; Jin, M.L.; Park, J.-M.; Choi, J.K.; Jung, H.-T. Ultraclean transfer of CVD-grown graphene and its application to flexible organic photovoltaic cells. *J. Mater. Chem. A* **2014**, *2*, 20474–20480. [CrossRef]
57. Park, H.; Chang, S.; Smith, M.; Gradečak, S.; Kong, J. Interface engineering of graphene for universal applications as both cathode and anode in organic photovoltaics. *Sci. Rep.* **2013**, *3*, 1581. [CrossRef] [PubMed]
58. Park, H.; Chang, S.; Zhou, X.; Kong, J.; Palacios, T.; Gradečak, S. Flexible graphene electrode-based organic photovoltaics with record-high efficiency. *Nano Lett.* **2014**, *14*, 5148–5154. [CrossRef] [PubMed]
59. Song, Y.; Chang, S.; Gradečak, S.; Kong, J. Visibly transparent organic solar cells on flexible substrates with all-graphene electrodes. *Adv. Energy Mater.* **2016**, *6*, 1600847. [CrossRef]
60. Liu, Z.; Liu, Q.; Huang, Y.; Ma, Y.; Yin, S.; Zhang, X.; Sun, W.; Chen, Y. Organic Photovoltaic Devices Based on a Novel Acceptor Material: Graphene. *Adv. Mater.* **2008**, *20*, 3924–3930. [CrossRef]
61. Liu, Q.; Liu, Z.; Zhang, X.; Yang, L.; Zhang, N.; Pan, G.; Yin, S.; Chen, Y.; Wei, J. Polymer Photovoltaic Cells Based on Solution-Processable Graphene and P3HT. *Adv. Funct. Mater.* **2009**, *19*, 894–904. [CrossRef]
62. Wang, H.; He, D.; Wang, Y.; Liu, Z.; Wu, H.; Wang, J. Organic Photovoltaic Devices Based on graphene as an electron-acceptor material and P3OT as a donor material. *Phys. Status Solidi A* **2011**, *208*, 2339–2343. [CrossRef]
63. Liu, Z.; He, D.; Wang, Y.; Wu, H.; Wang, J.; Wang, H. Improving photovoltaic properties by incorporating both SPFGraphene and functionalized multiwalled carbon nanotubes. *Sol. Energy Mater. Sol. Cells* **2010**, *94*, 2148–2153. [CrossRef]
64. Yu, D.; Yang, Y.; Durstock, M.; Baek, J.-B.; Dai, L. Soluble P3HT-Grafted Graphene for Efficient Bilayer–Heterojunction Photovoltaic Devices. *ACS Nano* **2010**, *4*, 5633–5640. [CrossRef] [PubMed]

65. Yu, D.; Park, K.; Durstock, M.; Dai, L. Fullerene-Grafted Graphene for Efficient Bulk Heterojunction Polymer Photovoltaic Devices. *J. Phys. Chem. Lett.* **2011**, *2*, 1113–1118. [CrossRef] [PubMed]
66. Li, Y.; Hu, Y.; Zhao, Y.; Shi, G.; Deng, L.; Hou, Y.; Qu, L. An Electrochemical Avenue to Green-Luminescent Graphene Quantum Dots as Potential Electron-Acceptors for Photovoltaics. *Adv. Mater.* **2011**, *8*, 776–780. [CrossRef] [PubMed]
67. Gupta, V.; Chaudhary, N.; Srivastava, R.; Sharma, G.D.; Bhardwaj, R.; Chand, S. Luminescent Graphene Quantum Dots for Organic Photovoltaic Devices. *J. Am. Chem. Soc.* **2011**, *133*, 9960–9963. [CrossRef] [PubMed]
68. Li, F.; Kou, L.; Chen, W.; Wu, C.; Guo, T. Enhancing the short-circuit current and power conversion efficiency of polymer solar cells with graphene quantum dots derived from double-walled carbon nanotubes. *NPG Asia Mater.* **2013**, *5*, e60. [CrossRef]
69. Kim, J.K.; Park, M.J.; Kim, S.J.; Wang, D.H.; Cho, S.P.; Bae, S.; Park, J.H.; Hong, B.H. Balancing Light Absorptivity and Carrier Conductivity of Graphene Quantum Dots for High-Efficiency Bulk Heterojunction Solar Cells. *ACS Nano* **2013**, *7*, 7207–7212. [CrossRef] [PubMed]
70. Jun, G.H.; Jin, S.H.; Lee, B.; Kim, B.H.; Chae, W.-S.; Hong, S.H.; Jeon, S. Enhanced conduction and charge-selectivity by N-doped graphene flakes in the active layer of bulk-heterojunction organic solar cells. *Energy Environ. Sci.* **2013**, *6*, 3000–3006. [CrossRef]
71. Lee, R.-H.; Huang, J.-L.; Chi, C.-H. Conjugated polymer-functionalized graphite oxide sheets thin films for enhanced photovoltaic properties of polymer solar cells. *J. Polym. Sci. B Polym. Phys.* **2013**, *51*, 137–148. [CrossRef]
72. Rafique, S.; Abdullah, S.M.; Shahid, M.M.; Ansari, M.O.; Sulaiman, K. Significantly improved photovoltaic performance in polymer bulk heterojuntion solar cells with graphene oxide/PEDOT:PSS double decked hole transport layer. *Sci. Rep.* **2016**, *7*, 39555. [CrossRef] [PubMed]
73. Chuang, M.-K.; Chen, F.-C. Synergistic Plasmonic Effects of Metal Nanoparticle–Decorated PEGylated Graphene Oxides in Polymer Solar Cells. *ACS Appl. Mater. Interfaces* **2015**, *7*, 7397–7405. [CrossRef] [PubMed]
74. Jung, C.-H.; Noh, Y.-J.; Bae, J.-H.; Yu, J.-H.; Hwang, I.-T.; Shin, J.; Shin, K.; Lee, J.-S.; Choi, J.-H.; Na, S.-I. Polyacrylonitrile-grafted reduced graphene oxide hybrid: An all-round and efficient hole-extraction material for organic and inorganic-organic hybrid photovoltaics. *Nano Energy* **2017**, *31*, 19–27. [CrossRef]
75. Hu, A.; Wang, Q.; Chen, L.; Hu, X.; Zhang, Y.; Wu, Y.; Chen, Y. In Situ Formation of ZnO in Graphene: A Facile Way To Produce a Smooth and Highly Conductive Electron Transport Layer for Polymer Solar Cells. *ACS Appl. Mater. Interfaces* **2015**, *7*, 16078–16085. [CrossRef] [PubMed]
76. Li, S.-S.; Tu, K.-H.; Lin, C.-C.; Chen, C.-W.; Chhowalla, M. Solution-processable graphene oxide as an efficient hole transport layer in polymer solar cells. *ACS Nano* **2010**, *4*, 3169–3174. [CrossRef] [PubMed]
77. Nguyen, D.D.; Tai, N.H.; Chueh, S.Y.; Chen, Y.J.; Kuo, W.S.; Chou, T.W.; Hsu, C.S.; Chen, L.J. Synthesis of ethanol-soluble few-layer graphene nanosheets for flexible and transparent conducting composite films. *Nanotechnology* **2011**, *22*, 295606. [CrossRef] [PubMed]
78. Hu, X.; Zhou, Q. Health and Ecosystem Risks of Graphene. *Chem. Rev.* **2013**, *113*, 3815–3835. [CrossRef] [PubMed]
79. Chng, E.L.K.; Pumera, M. The toxicity of graphene oxides: Dependence on the oxidative methods used. *Chem.–Eur. J.* **2013**, *19*, 8227–8235. [CrossRef] [PubMed]

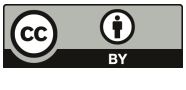

polymers

MDPI

Article

Carrier Transport and Molecular Displacement Modulated dc Electrical Breakdown of Polypropylene Nanocomposites

Daomin Min [1,*], Chenyu Yan [1], Rui Mi [1], Chao Ma [1], Yin Huang [1], Shengtao Li [1,*], Qingzhou Wu [2] and Zhaoliang Xing [3]

[1] State Key Laboratory of Electrical Insulation and Power Equipment, Xi'an Jiaotong University, Xi'an 710049, China; leo-chenyu.yan@stu.xjtu.edu.cn (C.Y.); mr2017@stu.xjtu.edu.cn (R.M.); machao2012@stu.xjtu.edu.cn (C.M.); huangxingyin@stu.xjtu.edu.cn (Y.H.)

[2] Institute of Fluid Physics, China Academy of Engineering Physics, Mianyang 621900, China; wuqingzhou@163.com

[3] State Key Laboratory of Advanced Power Transmission Technology, Global Energy Interconnection Research Institute co. Ltd., Beijing 102209, China; zhaoweimei@sgri.sgcc.com.cn

* Correspondence: forrestmin@xjtu.edu.cn (D.M.); sli@mail.xjtu.edu.cn (S.L.); Tel.: +86-29-8266-3781 (D.M.); +86-29-8266-7849 (S.L.)

Received: 18 September 2018; Accepted: 28 October 2018; Published: 30 October 2018

Abstract: Dielectric energy storage capacitors have advantages such as ultra-high power density, extremely fast charge and discharge speed, long service lifespan and are significant for pulsed power system, smart power grid, and power electronics. Polypropylene (PP) is one of the most widely used dielectric materials for dielectric energy storage capacitors. It is of interest to investigate how to improve its electrical breakdown strength by nanodoping and the influencing mechanism of nanodoping on the electrical breakdown properties of polymer nanocomposites. PP/Al_2O_3 nanocomposite dielectric materials with various weight fraction of nanoparticles are fabricated by melt-blending and hot-pressing methods. Thermally stimulated current, surface potential decay, and dc electrical breakdown experiments show that deep trap properties and associated molecular chain motion are changed by incorporating nanofillers into polymer matrix, resulting in the variations in conductivity and dc electrical breakdown field of nanocomposite dielectrics. Then, a charge transport and molecular displacement modulated electrical breakdown model is utilized to simulate the dc electrical breakdown behavior. It is found that isolated interfacial regions formed in nanocomposite dielectrics at relatively low loadings reduce the effective carrier mobility and strengthen the interaction between molecular chains, hindering the transport of charges and the displacement of molecular chains with occupied deep traps. Accordingly, the electrical breakdown strength is enhanced at relatively low loadings. Interfacial regions may overlap in nanocomposite dielectrics at relatively high loadings so that the effective carrier mobility decreases and the interaction between molecular chains may be weakened. Consequently, the molecular motion is accelerated by electric force, leading to the decrease in electrical breakdown strength. The experiments and simulations reveals that the influence of nanodoping on dc electrical breakdown properties may origin from the changes in the charge transport and molecular displacement characteristics caused by interfacial regions in nanocomposite dielectrics.

Keywords: carrier transport; polypropylene nanocomposite; molecular chain motion; electrical breakdown; electric energy storage

1. Introduction

With the continuous increase in energy consumption and the gradually deterioration of environment caused by using fossil energy, sustainable energy technology becomes more and more important for the energy transformation [1,2]. Energy storage technology is one key issue for the integration of renewable energies such as wind energy and solar energy to power grid [3]. Dielectric energy storage capacitor has the advantages of ultra-high power density, extremely fast charge and discharge speed, environment friendly, long service lifespan, and low manufacturing cost [4], and has a great potential for the application in smart power grid, pulsed power system, and power electronics [4,5]. Capacitors store and release electric energy via polarization and depolarization of dielectric materials, which has no mass diffusion process. Consequently, capacitors can store and release electric energy in a very short period, which means they can provide high power density for power supply system to tune the peak power output [4–6]. Since no chemical reactions involve in the storage and release of electric energy and dielectric materials such as polypropylene (PP), polyester, and polyimide maintain high electrical breakdown strength at relatively high temperatures, dielectric energy storage capacitor has long cycle life and can operate in high temperature circumstance [5–7]. However, the energy density of dielectric energy storage capacitors is very low, limiting its application and miniaturization. It is necessary to develop dielectric materials with high electrical breakdown strength and high dielectric constant to enhance the energy density of dielectric energy storage capacitors [4,5].

Incorporating a small amount of nanofillers into polymers to fabricate nanocomposite materials is an effective approach to enhance their electrical breakdown strength [6,8]. Before the incorporation of nanofillers into polymers, surface modification of nanofillers and/or chemical grafting modification of polymers are usually adopted to improve the bonding strength between nanofillers and the matrices and the dispersion of nanofillers in the matrices [6,8]. Surface modification of nanofillers can decrease their surface energy and improve their compatibility with matrices. Accordingly, surface modified nanofillers can disperse more homogeneously in polymer matrices, and nanocomposites can obtain better electrical performance than neat polymers. The surfaces of MgO, TiO_2, Al_2O_3, and ZnO nanoparticles were modified by γ-methacryloxypropyltrimethoxysilane firstly, and then were separately doped in PP matrix to fabricate nanocomposite dielectric materials [9]. Experimental results revealed that electrical breakdown strengths of all PP nanocomposites increase firstly and then decrease. PP based TiO_2, Al_2O_3, and ZnO nanocomposite dielectric materials show maximum electrical breakdown strengths at nanofiller loading of 1 wt %, while PP/MgO nanocomposite samples has the maximum value at 3 wt % [9]. It was also found that the PP/MgO nanocomposite materials with a loading of 1 wt % has a remarkable enhancement of dc electrical breakdown strength compared with PP matrix [10]. In addition, it was found that PP based silica nanocomposite dielectrics have higher electrical breakdown strengths under both dc and ac ramp voltages [11]. Incorporation of nanoparticles can enhance the electrical breakdown strength of polymer matrix, but the influencing mechanism of nanodoping on electrical breakdown strength remains to be investigated.

Interfacial region models for polymer nanocomposite dielectric materials were proposed based on mesoscopic structure, morphology, molecular motion, crystallization, and electrical properties, and so forth, demonstrating the direction to unravel the mechanism that how nanodoping enhance the electrical breakdown strength of polymer nanocomposites [8,12–16]. For example, Lewis proposed an electric double layer model based on colloidal theory. When nanoparticle loading is relatively low, barriers in electric double layers impede the migration of carriers, leading to the decrease in conductivity and enhancement in electrical breakdown strength. With a further increase in nanoparticle loading, overlapping of interfacial regions appears. This will assist to form conduction path within the bulk of nanocomposites under the applied voltage and accelerate carrier transport, resulting in the increase in conductivity and the decrease in electrical breakdown strength [12,13]. In addition, Tanaka et al. proposed a multi-core model and suggested that interfacial region consists of bonded, bound, and loose layers. Vast deep traps exist in the regions of bonded and bound layers, while shallow traps mainly exist in the region of loose layer [15,16].

Furthermore, Li et al. [14] introduced a multi-region model, which indicated that interfacial region is composed of bonded, transitional, and normal regions. Deep traps mainly are in the bonded and transitional regions, while shallow traps are mainly located in normal region. It can be inferred from the multi-core model [15,16] and multi-region model [14] that when a small amount of nanoparticles are doped, deep traps have dominant effect on electrical breakdown property of nanocomposites. This leads to the decrease in density and energy of carriers as well as conductivity, resulting in an enhancement in electrical breakdown strength. When nanoparticle loading further increases, interfacial regions will start to overlap and the effect brought by shallow traps will be strengthened, resulting in a decrease in electrical breakdown strength.

The increase in energy and/or density of deep traps can suppress charge injection from electrodes. Consequently, the accumulation of space charges is reduced and the distortion of electric field is mitigated, leading to an increase in electrical breakdown strength [8,15–18]. When an electric field of 60 kV mm^{-1} is applied on the sample for 30 min at room temperature, homo space charges accumulate at the regions near electrodes. With an increase in nanofiller loading, accumulation of homo space charges shows a decrease and then is followed by an increase, and distortion of electric field has the similar profile. Thus dc electric field increases firstly and then decreases [19]. Additionally, for PP/Fullerene nanocomposites, when applying an electric field of 60 kV mm^{-1} on the samples, pulsed electro-acoustic (PEA) results indicated that for the sample with a loading of 1 wt %, accumulation of homo space charges within the sample is effectively suppressed and distortion of electric field is mitigated. The sample with this nanofiller loading has higher dc electrical breakdown strength compared with polymeric matrix [20].

In order to investigate the influencing mechanism of nano-doping on electrical breakdown properties of PP nanocomposite dielectric material, PP/Al_2O_3 nanocomposites were fabricated and their trap distribution and dc electrical breakdown properties were measured. The relation between deep trap properties and dc electrical breakdown strength was analyzed. Then, a model considering carrier transport and molecular displacement dynamics was utilized to simulate the dc electrical breakdown behavior of PP nanocomposite dielectric materials.

2. Materials and Methods

2.1. Fabrication of PP/Al_2O_3 Nanocomposite Materials

Semi-crystalline granular PP homopolymer (Borclean™ HC312BF) about 3 mm in diameter was purchased from Borealis, Vienna, Austria. The PP homopolymer has a melt flow rate of 4.4 g/10 min at 190 °C/5 kg, an isotactic index of 96%, and a melting temperature of 161–165 °C. Nano-Al_2O_3 particles about 30 nm in diameter, with purity beyond 99.99% was supplied by Beijing DK nano technology Co., Ltd., China. In addition, γ-methacryloxy propyltrimethoxy silane coupling agent (KH570) was also supplied by Beijing DK nano technology Co., Ltd., China.

Soft agglomeration and hard agglomeration may be formed in inorganic nanparticles in powder state induced by physical forces such as electrostatic force and Van Der Waals force and by bond interaction or chemical effect existing among the particles, respectively. Accordingly, nanoparticles were dried in a vacuum oven at 100 °C for 12 h to eliminate humidity inside. Then, nanoparticles were mixed with ethanol and the mixture was sonicated by an Ultrasonic Oscillator (Xinyi-2400F, Ningbo Xinyi Ultrasonic Instrument Co., Ltd., Ningbo, China) at a frequency of 40 kHz and a power of 100 W for 30 min around room temperature. After that, the mixture was processed by an Ultra-high Pressure Homogenizer (SPCH-18, Stansted Fluid Power, Stansted, UK) at a pressure of 40 MPa at room temperature for 5 times. The treatments by Ultrasonic Oscillator and Ultra-high Pressure Homogenizer can eliminate the agglomerations of nanoparticles.

Surface modification on nanoparticles by γ-methacryloxy propyltrimethoxy silane coupling agent can reduce the electrostatic force and increase the compatibilisation and coupling interaction between nanparticles and PP matrix, which will lead to a more homogeneous dispersion in the polymer matrix. Firstly, 5 g γ-methacryloxy propyltrimethoxy silane coupling agent was hydrolyzed in 10 g deionized

water. Hydrolysis reaction of coupling agent was carried out under 80 °C with a magnetic stirrer until the solution was observed transparent. When the solution was transparent, the hydrolysis reaction was nearly complete. Then, the homogenized mixture was were mixed the hydrolyzed solution of γ-methacryloxy propyltrimethoxy silane coupling agent. The reaction between nanoparticles and coupling agent was carried out under 80 °C, stirring by a Magnetic Stir for 12 h. Thirdly, the mixture was centrifuged by a centrifugal machine (HC-3514, Anhui USTC Zonkia Scientific Instruments Co., Ltd., Hefei, China) at speed of 4000 $rmin^{-1}$ for 10 min, and then ultrasonic processed for 20 min. The cleaning process was repeated for 5 times so that extra coupling agent, reaction accessory product, and impurities can be removed. Subsequently, the mixture was dried under 100 °C for 12 h and grinded prior to use.

After the surface modification by γ-methacryloxy propyltrimethoxy silane coupling agent, nanoparticles were introduced into molten PP matrix and dispersed inside by using a Torque Rheometer (RC-90, HAAKE PolyLab QC, Waltham, MA, USA). During the melt blending process, the temperature of Torque Rheometer was set as 175 °C and rotation speed was 40 r/min. The melting blend time was 10 min. A series of PP nanocomposites with various weight fractions of nano-Al_2O_3 particles, namely, 0.5 wt %, 1 wt % and 2 wt % were prepared. In addition, to ensure the consistency of samples, neat PP samples were also prepared by the same melting method.

Then, sheet samples were prepared through hot-pressing by Plate Vulcanizing machine (YT-LH-20B, Yitong Technology Co., Ltd., Shenzhen, China). After preheating for 15 min without pressure, samples were pressed with a mould under a pressure of 10 MPa at 240 °C for 10 min. Finally, water-cooling process without external pressure was carried out until the samples cool down to room temperature. The average thickness of samples is about 100 μm with a standard deviation of 3.5 μm. The densities are 0.926, 0.930, 0.937, and 0.946 g/m^3 for the samples with loadings of 0 wt %, 0.5 wt %, 1 wt % and 2 wt %, respectively.

2.2. Characterization of PP/Al_2O_3 Nanocomposite Materials

The dispersion quality of Al_2O_3 nanoparticles in PP matrix was investigated by a Scanning Electron Microscope (SEM, GeminiSEM 500, Carl Zeiss AG, Oberkochen, Germany). Dielectric materials were freeze fractured in liquid nitrogen. Then, the cross section of the freeze fractured samples were sputtered with Au by an Ion Sputter (MC1000, Hitachi, Ltd., Tokyo, Japan) as the samples are non-conductive dielectrics. The morphology of fracture surfaces of nanocomposite materials was observed by the SEM with an accelerating voltage of 5 kV.

Thermally stimulated depolarization current (TSDC, Concept 90, Novocontrol technologies, Frankfurt, Germany) measurement was carried out on PP/Al_2O_3 nanocomposite samples to study their trap distribution properties. Before the TSDC measurements, Au electrodes with diameter of 30 mm were sputtered on both sides of samples. Then the sample was put into the vacuum chamber of TSDC apparatus. The sample was heated to 80 °C and then was polarized under an external applied voltage of 250 V for 20 min. After the polarization, the sample was cooled down to −40 °C by liquid nitrogen and then short-circuited for 3 min. Afterwards, the sample was heated with a ramping rate of 2 °C·min^{-1} up to 150 °C. At the same time, depolarization current was measured by a picoammeter (6514B, Keithley, Beaverton, OR, USA).

The conductivity property of nanocomposites were investigated by surface potential decay (SPD) measurement. The experimental process can be divided into surface potential built-up and decay processes. During the surface potential built-up process, a dielectric sample was charged by corona produced by a needle-grid electrode system. The needle and grid electrodes were applied voltages of −13 kV and −3 kV, respectively. Each sample was charged for 3 min. While negative voltage is applied to the needle electrode, high energy electrons emitted from the needle electrode will migrate along electric field and then collide with neutral molecules in the air, generating secondary electrons and positive ions. Then, these electrons can combine with neutral molecules to form negative ions. Under the effect of negative voltage on gird electrode, negative ions move towards dielectric material and transfer electrons to the sample surface. After charging process, the needle-grid electrode system

was moved away and an electrostatic voltmeter probe (3453ST, Trek, Lockport, NY, USA) was moved to the charging position. Surface potentials of samples were measured by a high-voltage electrostatic voltmeter (P0865, Trek, Lockport, NY, USA) for 150 min, and recorded by a Labview® program. All the SPD experiments were carried out at a temperature of 33 °C and a humidity of 49 RH%.

DC electrical breakdown fields of PP/Al_2O_3 nanocomposites were measured by a computer control voltage breakdown testing apparatus (HJC-100kV, Huayang instrumentation Co., Ltd., Yangzhong, China). Sphere-sphere copper electrodes with a diameter of 25 mm were used in dc electrical breakdown experiments. The experiments were performed in transformer oil (25#, China National Petroleum Corporation, Karamay, China) at room temperature (around 33 °C). A ramp dc voltage with a rising rate of 2 kV s^{-1} was applied across the samples until breakdown occurs. The electrical breakdown voltage when the failure took place was recorded by a computer program. For each sample, dc electrical breakdown experiments were repeated for fifteen times.

3. Experimental Results

3.1. Morphology of PP/Al_2O_3 Nanocomposite Materials

Figure 1 depicts the morphology images of fractured surfaces of PP/Al_2O_3 nanocomposite samples with various nanofiller loadings. It is observed from Figure 1a that a monodirectional force trace like a river can be obviously seen on the fracture surface of the sample, and the regions of fracture surface are very smooth. Therefore, fractured surface of neat PP sample reveals a brittle fracture. When a small amount of nanofiller is doped, nanofillers are homogeneously dispersed in the matrix and no agglomeration is observed. With a further increase in nanofiller loading, mean distance between nanoparticles is gradually decreased. ImageJ was introduced to numerically demonstrate the nanoparticle dispersion in the matrix. Mean distance between nanofillers obey Gaussian distribution and are with estimated average values of 623, 435, and 278 nm for PP/Al_2O_3 samples with loadings of 0.5 wt %, 1 wt %, and 2 wt %, respectively. Results indicate that mean distance between nanoparticles gradually decreases with an increase in nanofiller loading.

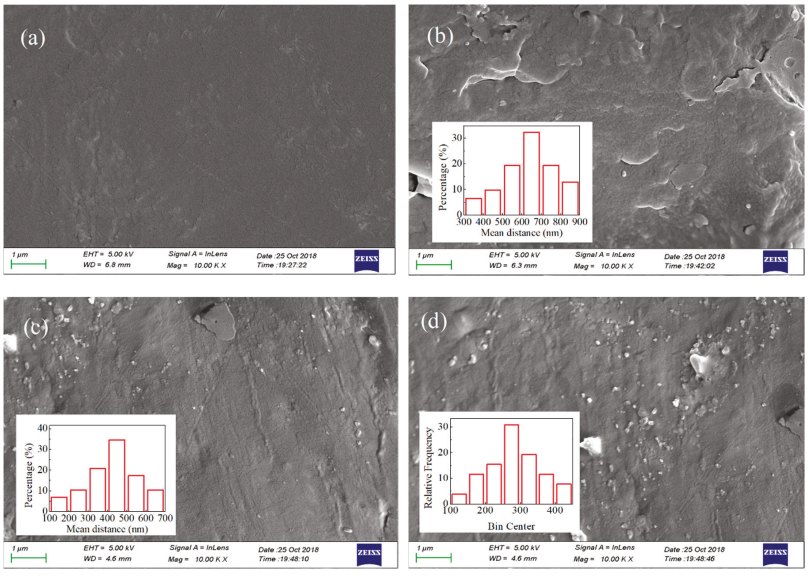

Figure 1. Morphology images of fracture surfaces of PP/Al_2O_3 nanocomposites at various nanofiller loadings, (**a**) 0 wt %, (**b**) 0.5 wt %, (**c**) 1.0 wt %, and (**d**) 2.0 wt %, observed by a high energy SEM.

3.2. Trap Properties for Charge Carriers

The TSDC experimental results of PP/Al_2O_3 nanocomposite dielectric materials are shown in Figure 2a. Two obvious relaxation peaks are observed in TSDC curves for each sample, which are located at temperatures of −10 °C and 125 °C. Another relaxation peak is probably located at around 80 °C. Three peaks from high temperature to low temperature are named as peak α, peak β, and peak γ. It is observed obviously that relaxation peaks α and β of PP nanocomposite dielectric materials are changed by incorporating different loadings of nanoparticles. For example, peak value of α increases in magnitude with an increase in nanofiller loading. In order to extract the trapping parameters of nanocomposite dielectrics, experimental results were analyzed by TSDC equation [21],

$$j_{TSC}(T) = B\exp\left[-\frac{E_a}{k_B T} - \frac{1}{\beta\tau_0}\int_{T_0}^{T}\exp\left(-\frac{E_a}{k_B T}\right)dT\right] \quad (1)$$

Here, $j_{TSC}(T)$ is the TSDC current density in Am^{-2}, B is an undermined factor in Am^{-2}, E_a is the activation energy of relaxation process in eV, τ_0 is the relaxation time constant in s, β is heating rate in K s^{-1}, k_B is the Boltzmann constant, T_0 is the initial temperature of sample at the beginning of heating process in °C, and T is the temperature of sample after heating in °C.

Figure 2a shows that fitting curves with three relaxation processes are in a good agreement with TSDC experiments and the three relaxation peaks are separated. Peak α at about 125 °C is possible to correspond to the traps that can capture carriers. Peak β at around 83 °C may correspond to the traps that can assist the carrier hopping process in dielectrics. Peak γ with relatively low magnitude is observed at around −10 °C, which may reflect the glass transition process. Traps of peak α indicates the deep traps while those of peak β are considered as shallow traps. The energy of deep traps extracted from the TSDC is 0.86 eV for PP/Al_2O_3 sample with various nanofiller loadings, Similar results were found by other researchers. The energies of deep traps in polypropylene/propylene ethylene rubber/ZnO ternary nanocomposites samples with different nanofiller loadings are measured to be 0.84–0.87 eV by TSDC method [22]. It was also found that the trap energies of neat PP, polypropylene/propylene-ethylene copolymer, and polypropylene/ethylene-octene copolymer samples were measured to be around 0.87 eV [19]. In addition, through conduction current measurement trap energy of neat block polypropylene was calculated to be around 0.92 eV [23]. The relaxation time constant τ_0 of relaxation process α changes with the loading, which is 5.79×10^{-9} s at 0 wt %, 1.20×10^{-8} s at 0.5 wt %, 7.10×10^{-9} s at 1.0 wt %, and 6.20×10^{-9} s at 2.0 wt %. Accordingly, the retention times of deep trapped charges, $\tau_{de} = \tau_0 \exp(E_a/k_B T)$, increases firstly and then decreases with an increase in nanofiller loading and are 8.45×10^5, 1.76×10^6, 1.04×10^6, and 9.04×10^5 s for nanocomposite dielectrics at loadings of 0 wt %, 0.5 wt %, 1.0 wt %, and 2.0 wt %, respectively, as show in Figure 2b.

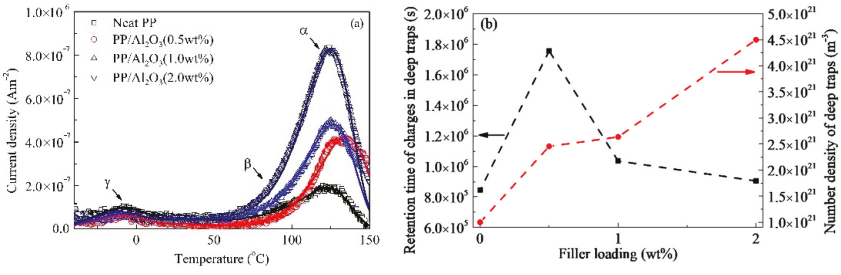

Figure 2. Results of TSDC measurement. (**a**) Comparison of experimental TSDC and fitting results. Symbols represent experimental results and solid lines on symbols are corresponding fitting results calculated by Equation (1). (**b**) Energy and density of deep traps calculated by Equations (1) and (2) as a function of nanofiller loading.

The density of deep traps corresponds to the peak value of relaxation process α and it can be figured out by considering parameter B in Equation (1). It can be described by following equation,

$$N_T(\xi) = N_T(0)B(\xi)/B(0) \quad (2)$$

where ξ is the nanofiller loading. The deep trap density of neat PP, $N_T(0)$, is assumed to be 1×10^{21} m^{-3} [24,25]. In this regard, trap densities are 1.25×10^{21}, 1.59×10^{21}, and 2.81×10^{21} m^{-3} for PP/Al_2O_3 sample with loadings of 0 wt %, 0.5 wt %, 1 wt %, and 2 wt %, respectively. Figure 2b shows the energy and density of deep traps as a function of nanofiller loading. It is indicated that the energy of deep traps increases firstly and then decreases with an increase in nanofiller loading, while the density of deep traps increases monotonically.

3.3. DC Conductivity

Figure 3a shows SPD experimental results of PP/Al_2O_3 nanocomposites. Potential decay rate increases firstly and then is followed by a decrease with an increase in nanofiller loading. For a film polymeric dielectric, the decay of surface potential is dominated by the migration of charge carriers through the material into grounded electrode, so it reflects similar changes in bulk conductivity [26–29]. The bulk conductivity of nanocomposites can be calculated from surface potential measurement results via the following equation [30]:

$$\gamma(\phi_s) = -\frac{d\phi_s(t)}{dt}\frac{\varepsilon_0\varepsilon_r}{\phi_s(t)} \quad (3)$$

Here, φ_s is surface potential in V, t is the decay time in s, ε_0 is the vacuum permittivity in Fm^{-1}, ε_r is the relative permittivity of nanocomposites, and γ is the bulk conductivity in Sm^{-1}.

Figure 3b depicts bulk conductivity of nanocomposite dielectrics as a function of nanofiller loading. The bulk conductivity of neat PP sample is about 4.12×10^{-15} Sm^{-1}. In addition, conductivity has a decrease and then is followed by a monotonic increase with an increase in nanofiller loading. Minimum conductivity reaches 9.43×10^{-16} Sm^{-1} at the nanofiller loading of 0.5 wt %. This trend in PP nanocomposites was also observed by other researchers [9].

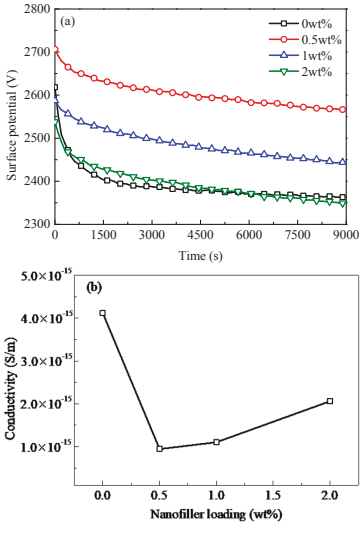

Figure 3. Experimental results of SPD for PP/Al_2O_3 nanocomposites with different nanofiller loadings (**a**) and conductivity calculated by Equation (3) as a function of nanofiller loading (**b**).

3.4. DC Electrical Breakdown Strength of PP Nanocomposites

Electrical breakdown property is generally evaluated by Weibull-distribution. In this work, two-parameter Weibull-distribution can be expressed as [31],

$$P_i = 1 - \exp\left[-(F_{bi}/\alpha)^{\beta}\right], \ (i = 1, 2, \ldots, n) \quad (4)$$

Here, i is the electrical breakdown strength array sorted from the small to large, n represents the testing time for the same sample, P_i is cumulative electrical breakdown probability of the data numbered with i, which is related to i and n, e.g., $P_i = (i - 0.44)/(n + 0.25)$ [31]. Furthermore, F_b is the experimental result of dc electrical breakdown field in kV mm^{-1}, α is characteristic electrical breakdown strength with accumulative probability of 63.2%, and β is shape distribution parameter.

Figure 4 shows the Weibull-distributions of dc electrical breakdown field for PP/Al_2O_3 nanocomposites at various nanofiller loadings. Fitted by Equation (4), characteristic electrical breakdown fields F_b were obtained as shown in Figure 4. DC electrical breakdown field has an increase then is followed by a decrease with an increase in nanofiller loading. The characteristic electrical breakdown fields are 282, 353, 304 and 285 kV mm^{-1} for PP/Al_2O_3 nanocomposites with loading of 0 wt %, 0.5 wt %, 1 wt %, and 2 wt %, respectively. The maximum value of characteristic electrical breakdown field appears around 0.5 wt %. The dc electrical breakdown field of PP/Al_2O_3 nanocomposite material with the loading of 0.5 wt % is 25.2% larger than that of neat PP.

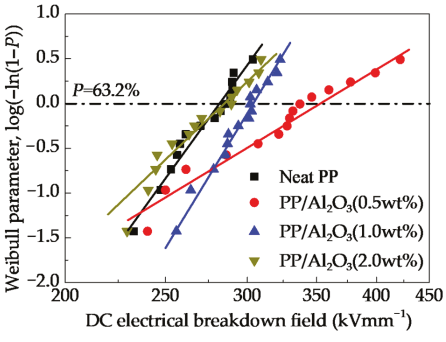

Figure 4. Two-parameter Weibull-distributions of dc electrical breakdown field for PP/Al_2O_3 nanocomposites with various nanofiller loadings. Symbols represent experimental results of dc electrical breakdown and solid lines are calculated results using Equation (4).

3.5. Influence of Trap Properties on dc Conductivity and Electrical Breakdown Strength

Figure 5 shows dc conductivity and electrical breakdown strength of PP/Al_2O_3 nanocomposites as a function of the retention time of deep trapped charges. Conductivity γ decreases with an increase in the retention time of deep trapped charges τ_{de}. According to Arrhenius equation, $\gamma = \gamma_0\tau_{tr}/(\tau_{tr} + \tau_{de})$, the conductivity is proportional to the reciprocal τ_{de}, when τ_{tr} is much smaller than τ_{de} [31]. Here γ_0 is a prefactor of exponential equation and τ_{tr} is the mean time period of mobile charge carriers between two trapping events in s. The retention time of trapped charges at deep trap centers is determined by trap energy and temperature, $\tau_{de} = \tau_0\exp(E_T/k_BT)$ [31,32]. Mobile charges injected from electrodes can be captured by deep traps and the retention time of trapped carriers at deeper traps is longer. This will lead to lower conductivity. As an increase in the retention time of trapped carriers, more charges are trapped at the areas near the interfaces between dielectric material and its electrodes, suppressing the accumulation of space charges and mitigating the distortion of electric field. Accordingly, electrical breakdown strength increases with an increase in the retention time of trapped carriers.

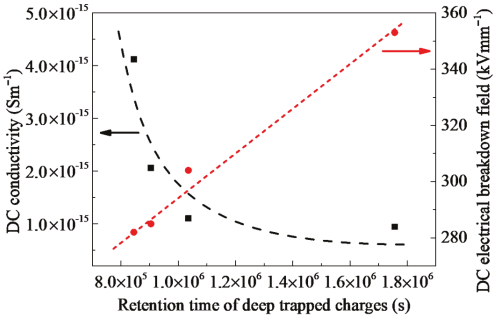

Figure 5. DC conductivity and dc electrical breakdown field of PP/Al_2O_3 nanocomposites as a function of the retention time of deep trapped charges. Symbols represent the experimental results, while dash curves represent the potential types of relations.

Experimental results measured by PEA method indicated that under high electric fields homo space charges can accumulate in the bulk of PP dielectric material [9,19,20,23]. The accumulation of space charges results in the distortion of electric field. The accumulation of homo space charges leads to a decrease in electric fields near the interfaces between the dielectric material and its electrodes and an increase in electric fields in the middle of bulk [9,19,20,23]. It was also reported that the accumulation of space charges increases and electric field distortion is much severer with an increase in the applied electric field [20]. Space charge accumulation and electric field distortion experiments at ultra-high external electric fields demonstrated that electrical breakdown was initiated when the maximum distorted electric field exceeds a threshold value [17,33]. In addition, incorporation of a slight amount nanofillers can suppress the accumulation of space charges in the bulk of material to some extent and electric field distortion can also be mitigated. The comparison of space charge accumulation and dc electrical breakdown results between polyethylene nanocomposites with relatively low nanofiller loadings and neat polyethylene indicated that carrier transport is closely relating to the electrical breakdown property of dielectric material [17,33]. However, excessive increase in nanofiller loading can result in an increase in accumulation of space charges and reinforcement in electric field distortion [8,14]. When nanofiller loading exceeds a threshold value, accumulation of space charges can even be larger than that in neat sample [9]. The quantitative relation between nanodoping and electrical breakdown strength is not fully understood in PP nanocomposites. In the following part, a carrier transport and molecular displacement modulated electrical breakdown model will be used to investigate the influencing mechanism of incorporating nanoparticles into polymers on dc electrical breakdown properties.

4. Modelling Analysis of dc Electrical Breakdown of PP Nanocomposites

4.1. Carrier Transport and Molecular Displacement Modulated Electrical Breakdown Model

As shown in Figure 6, a carrier transport and molecular displacement modulated electrical breakdown (CTMD) model considering five processes, namely charge injection, charge migration, charge trapping/ detrapping, recombination dynamics, and molecular chain motion is introduced to investigate the electrical breakdown property of PP/Al_2O_3 nanocomposite dielectric materials [18,34–37]. The dielectric materials are clamped by two electrodes, and the cathode and anode are at the positions of $x = 0$ and $x = d$, respectively. Here, d is the thickness of sample. A ramp voltage with a rising rate of k_{ramp} is applied to the material, and the external voltage is the product of ramping rate and elapsed time of ramping voltage t, which is also the boundary condition of the CTMD model.

$$V_{appl}(t) = k_{ramp}t \quad (5)$$

Here, V_{appl} is external applied voltage in V, and k_{ramp} is the ramp rate of voltage source in V s^{-1}.

Charges in the bulk can be categorized to two types, mobile charges that move in shallow traps and trapped charges that are captured by deep traps. Charge carriers captured by deep traps will accumulate space charges in dielectric materials. The accumulation of space charges can result in the local distortion of electric field F, which is the minus gradient of electric potential ϕ, namely, $F = -\nabla\phi$. The relation between space charges and electric potential can be solved by Poisson's equation [31],

$$\frac{\partial^2\phi(x,t)}{\partial x^2} = -\frac{e\left[-n_{\text{free(e)}}(x,t) - n_{\text{trap(e)}}(x,t) + n_{\text{free(h)}}(x,t) + n_{\text{trap(h)}}(x,t)\right]}{\varepsilon_0\varepsilon_r} \quad (6)$$

Here, $n_{free(e)}$ and $n_{trap(e)}$ are the number densities of negative mobile and negative trapped charges in m^{-3}, while $n_{free(h)}$ and $n_{trap(h)}$ are the number densities of positive mobile and positive trapped charges in m^{-3} and e is the elementary charge in C. The boundary conditions are $\varphi(0) = 0$ V and $\varphi(d,t) = V_{appl}(t)$.

Negative and positive charge carriers are assumed to be injected from the cathode and anode, respectively, into nanocomposite dielectric materials by modified Schottky thermionic emission [38]. The current densities of carrier injections are determined by effective injection barriers between the dielectric material and its electrodes and electric fields at the interfaces [38].

$$j_{in(e)}(t) = \frac{2\psi^2 e^2 {N_C}^{1/3} v_0 F(0,t)}{k_B T} \exp\left(-\frac{E_{in(e)}}{k_B T}\right) \exp f^{1/2} \quad (7)$$

$$j_{in(h)}(t) = \frac{2\psi^2 e^2 {N_V}^{1/3} v_0 F(d,t)}{k_B T} \exp\left(-\frac{E_{in(h)}}{k_B T}\right) \exp f^{1/2} \quad (8)$$

Here, $j_{in(e)}$ and $j_{in(h)}$ represent the current densities caused by negative charges injected from the cathode and positive charges injected from the anode into the nanocomposite material respectively in A m^{-2}, $E_{in(e)}$ and $E_{in(h)}$ are the effective injection barriers for electrons and holes respectively in eV, N_C and N_V are the density of states in conduction band and valence band respectively, $F(0, t)$ and $F(d, t)$ are the electric fields at the interfaces of $x = 0$ and $x = d$ respectively, and v_0 is the attempt to escape frequency in s^{-1}, which is the reciprocal of relaxation time constant of trapped charges, $v_0 = 1/\tau_0$. Furthermore, the reduced electric field f is determined by coulomb radius, electric field, and temperature, which is $f = eFr_c/k_BT$. Here r_c is the coulomb radius in m, $r_c = e^2/4\pi\varepsilon_0\varepsilon_r k_B T$. Then, the field-dependent parameter ψ can be obtained by $\psi(f) = f^{-1} + f^{-1/2} - f^{-1}(1 + 2f^{1/2})^{1/2}$ [38].

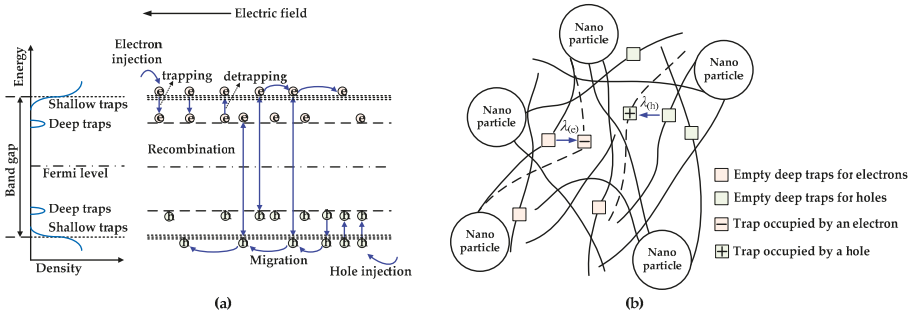

Figure 6. Schematic of carrier transport and molecular displacement modulated electrical breakdown model for polymer nanocomposite dielectric materials. (**a**) Charge injection, migration, trapping, detrapping and recombination dynamics in polymer nanocomposites under external electric field. (**b**) Molecular chains with occupied deep traps move toward electrodes driven by Coulomb force.

As demonstrated in Figure 6a, under the application of electric field, the injected electrons and holes can hop between shallow traps toward the anode and cathode, respectively. The migration of charge carriers can form conduction currents in the bulk of dielectric martials [18,24,34–36],

$$j_{c(e)}(x,t) = en_{free(e)}(x,t)\mu_{0(e)}F(x,t) \quad (9)$$

$$j_{c(h)}(x,t) = en_{free(h)}(x,t)\mu_{0(h)}F(x,t) \quad (10)$$

Here, $j_{c(e)}$ and $j_{c(h)}$ represent the conduction current densities formed by electrons and holes in A m^{-2}, respectively, while $\mu_{0(e)}$ and $\mu_{0(h)}$ are the carrier mobilities of electrons and holes controlled by shallow traps in m^2 V^{-1} s^{-1}, respectively.

Mobile charge carriers may be captured by deep traps during their migration, forming space charges. When trapped charges obtain enough energy, they can be released out of deep traps via thermal activation process. Traps in the CTMD model are assumed to be with single trap energy. Recombination occurs when electrons and holes encounter in the bulk of dielectric materials. Charge migration, trapping, detrapping, and recombination dynamic processes in the bulk obey conservation law and are described by the following four equations [18,24,34–36]:

$$\frac{\partial n_{free(e)}(x,t)}{\partial t} + \frac{1}{e}\frac{\partial j_{c(e)}(x,t)}{\partial t} = -\frac{n_{free(e)}}{\tau_{tr(e)}}\left(1-\frac{n_{trap(e)}}{N_{T(e)}}\right) + \frac{n_{trap(e)}}{\tau_{de(e)}} - R_{e\mu,h\mu}n_{free(e)}n_{free(h)} - R_{e\mu,ht}n_{free(e)}n_{trap(h)} \quad (11)$$

$$\frac{\partial n_{trap(e)}(x,t)}{\partial t} = \frac{n_{free(e)}}{\tau_{tr(e)}}\left(1-\frac{n_{trap(e)}}{eN_{T(e)}}\right) - \frac{n_{trap(e)}}{\tau_{de(e)}} - R_{et,h\mu}n_{trap(e)}n_{free(h)} \quad (12)$$

$$\frac{\partial n_{free(h)}(x,t)}{\partial t} + \frac{1}{e}\frac{\partial j_{c(h)}(x,t)}{\partial t} = -\frac{n_{free(h)}}{\tau_{tr(h)}}\left(1-\frac{n_{trap(h)}}{N_{T(h)}}\right) + \frac{n_{trap(h)}}{\tau_{de(h)}} - R_{e\mu,h\mu}n_{free(e)}n_{free(h)} - R_{et,h\mu}n_{trap(e)}n_{free(h)} \quad (13)$$

$$\frac{\partial n_{trap(h)}(x,t)}{\partial t} = \frac{n_{free(h)}}{\tau_{tr(h)}}\left(1-\frac{n_{trap(h)}}{N_{T(h)}}\right) - \frac{n_{trap(h)}}{\tau_{de(h)}} - R_{e\mu,ht}n_{free(e)}n_{trap(h)} \quad (14)$$

Here, N_T is the density of deep traps in m^{-3}, while $R_{e\mu,h\mu}$, $R_{et,ht}$ and $R_{et,h\mu}$ are the recombination coefficients in $m^3C^{-1}s^{-1}$. Based on the Langevin recombination model [39], recombination coefficient between free electrons and free holes can be expressed as, $R_{e\mu,h\mu} = (\mu_{0(e)} + \mu_{0(h)})/e\varepsilon_0\varepsilon_r$. According to Shockley-Read-Hall model [40,41], trap-assisted recombination coefficients between free electrons and trapped holes and that between trapped-electron and free-hole can be expressed as, $R_{e\mu,ht} = \mu_{0(e)}/e\varepsilon_0\varepsilon_r$ and $R_{et,h\mu} = \mu_{0(h)}/e\varepsilon_0\varepsilon_r$, respectively. The units of $R_{e\mu,h\mu}$, $R_{et,ht}$ and $R_{et,h\mu}$ are all in $m^3C^{-2}s^{-1}$.

Both molecular chains with dipole moment and those with occupied deep traps can move under the external electric field driven by electric forces [37,42,43]. As shown in Figure 6b, molecular chains with deep traps occupied by electrons will move toward the anode, while those with deep traps occupied by holes will move toward the cathode. The displacement of a molecular chain depends on the retention time of charges in trap centers which determines the duration of electric force acted on the molecular chain. The retention time of charges in deep traps is longer than that of charges in shallow traps, accordingly, the electric force acts a longer period on molecular chains with occupied deep traps. The velocity equation for the motion of a molecular chain with trapped charges is expressed as [37,42,43],

$$d\lambda/dt = \mu_{mol}F - \lambda/\tau_{mol} \quad (15)$$

Here, λ is the displacement of a molecular chain in m, while μ_{mol} is the mobility of molecular chains in $m^2V^{-1}s^{-1}$, which is determined by the carrier mobility hopping among shallow traps and the trapping of deep traps, namely $\mu_{mol} = \mu_0\tau_{tr}/(\tau_{tr} + \tau_{de})$. Furthermore, τ_{mol} is the relaxation time constant of molecular chains in s, which equals the retention time of charges in deep traps, $\tau_{mol} = \tau_0\exp(E_T/k_BT)$.

The displacement of molecular chains with occupied deep traps will enlarge the local free volume in nanocomposite dielectric materials. When the energy of electrons gained from electric field in the

enlarged free volume exceeds a threshold value, the energy of deep traps, electrical breakdown would be triggered [34,44]. Since the displacement of a molecular chain with occupied deep traps would determine the electrical breakdown process, in the following numerical simulations we focus on the motion of molecular chains with deep traps.

4.2. Parameters and Numerical Computation Methods

The temperature and thickness of samples are the same as those in experiments, which are 33 °C, and 100 μm, respectively. The relative permittivity is 2.3 measured by broadband frequency spectrometer (Concept 80 Novocontrol, Germany) at a frequency of 1 MHz at room temperature. In addition, the carrier mobilities of electrons and holes controlled by shallow traps both are assumed to be 1×10^{-13} $m^2V^{-1}s^{-1}$ [24,45]. The effective carrier mobility will be modulated by the trapping and detrapping dynamics of deep traps. The energy and density of deep traps and the relaxation time constant of charges in deep traps were characterized by TSDC apparatus for PP/Al_2O_3 nanocomposite dielectric materials and their results shown in Figure 2b are used in simulations. The charge injection from metal electrode into dielectric materials is influenced by surface states such as surface traps and dipoles of dielectrics, which has been evidenced by experiments [32,46] and calculation results of density functional theory [47,48]. It was proposed that charges on metal electrode may transfer to deep surface traps and then are injected into the conduction band via thermal-field activation [47,48]. Consequently, the effective injection barriers for electrons and holes are assumed to be the same as the energy of deep traps, which are 0.86 eV. The trapping coefficients of deep traps which is the reciprocal of mean time period of mobile charge carriers between two trapping events are assumed to be 0.085 s^{-1} [24,45].

Nanocomposite dielectric materials with the thickness of 100 μm is divided into 500 parts, namely, each part Δx is 0.2 μm. The computation time step Δt is set as 1 ms. High order accuracy and stable Runge-Kutta Discontinuous Galerkin method was utilized to solve the charge continuity Equations (11) to (14) [49–51]. Poisson's Equation (6) was solved numerically by Finite Element method. Computed by the CTMD model, dc electrical breakdown strength and distributions of space charges, electric fields, and molecular displacement can be obtained.

4.3. Simulation Results and Discussion

Figure 7a demonstrates the distributions of space charges accumulated in neat PP dielectric materials at various times after the application of a ramp voltage. The cathode and anode are at the positions of $x = 0$ and $x = 100$ μm, respectively. Under high electric fields, homo space charges accumulate near the interfaces between dielectric material and its electrodes. With an increase in time, the voltage applied on samples increases with time at a set ramping rate, namely $V_{appl} = k_{ramp}t_{ramp}$. Charges are injected into the dielectric material continuously, thus homo space charges accumulated monotonically with time. For example, the space charge density near the cathode is 2.6 Cm^{-3} at 5 s, 37.5 Cm^{-3} at 10 s, and 107.6 C m^{-3} at 14 s for neat PP dielectric material. Space charges are gradually decreased from the interfaces near electrodes to the middle of bulk, and a large amount of space charges accumulate at the interfaces near electrodes. Figure 7b shows the distributions of electric fields in neat PP dielectric materials at various times after the application of a ramp voltage. Electric fields tend to be strengthened as a result of an increase in time or applied voltage. The homo space charges accumulated at the interfaces build up an electric field in an inverse direction with applied electric field according to Poisson's equation, resulting in that the electric fields gradually increase from the interfaces between dielectric material and its electrodes to the middle of bulk. Therefore, the electric field near the interfaces are reduced, while electric fields in the middle of the bulk are enhanced. The electric field in the middle of neat PP material is 99.6 kV mm^{-1} at 5 s, 212.2 kV mm^{-1} at 10 s, and 310.6 kV mm^{-1} at 14 s. The simulation results are consistent with experimental results of space charge and electric field distributions in PP dielectric material [9,19,20,23].

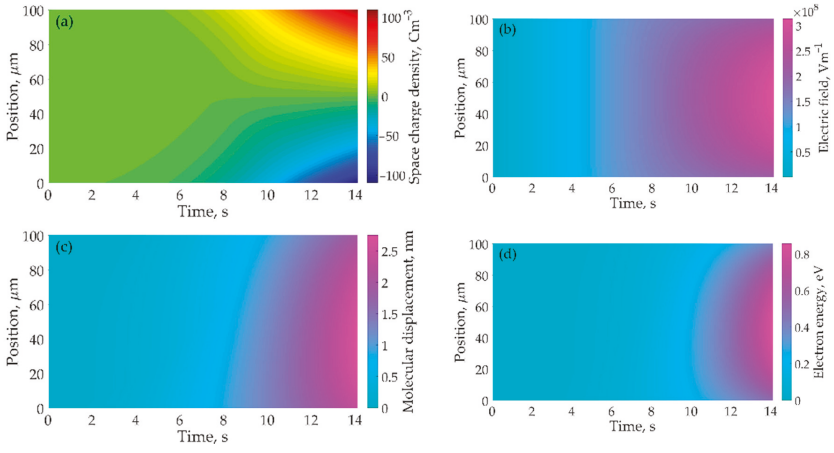

Figure 7. Numerical results of space charge distribution profiles (**a**), electric field distribution profiles (**b**), molecular displacement distribution profiles (**c**), and electron energy distribution profiles (**d**) as a function of time in neat PP dielectric material.

According to the motion dynamics of molecular chains with occupied deep traps, namely Equation (15), molecular displacement increases with increasing the electric field and time as shown in Figure 7c. When the first term in the right part of Equation (15) dominates the motion dynamics of molecular chains, the Equation can be simplified to be $d\lambda/dt = \mu_{mol}F$. If we do not consider the distortion of electric field caused by space charges, we can obtain the time dependent molecular displacement $\lambda = (k_{ramp}\mu_{mol}/2d)t^2$, by replacing F by $k_{ramp}t/d$ and considering the initial condition $\lambda(t = 0) = 0$. It indicates that λ is proportional to the square of time. When the distortion of electric field is considered, we will obtain similar distributions of molecular displacement to those of electric field. The maximum local λ is 0.34 nm at 5 s, 1.33 nm at 10 s, and 2.71 nm at 14 s. As some molecular chains with occupied deep traps move towards electrodes driven by electric force, the free volume around the molecular chains would be enlarged. It is assumed that the length of local free volume equals to the displacement of a molecular chain with occupied deep traps. Mobile charges migrate in the free volume can gain energy from electric field, and their energy w is determined by both the local electric field F and the length of free volume λ, namely $w = eF\lambda$. The distribution of electron energy gain in free volume is shown in Figure 7d. The electron energy gain in the middle of the neat PP material is 0.03 eV at 5 s, 0.27 eV at 10 s, and 0.83 eV at 14 s. When the maximum energy of electrons gained from electric field in a free volume exceeds the energy of deep traps, electrons will transport freely in the dielectric material without trapping. The local current density would be high enough to trigger electrical breakdown inside the material. In addition, the electrical breakdown is initiated at the position with the highest electric field.

Incorporating nanofillers into polymer can form interfacial regions or interaction zones. It has been suggested that these interfacial regions can vary the trap properties, which will change charge transport, the accumulation of space charges, and electrical breakdown properties. Interfacial regions exist between nanoparticles and polymer matrix has been evidenced by the results of differential scanning calorimetry and transmission electron microscopy [52], images of atomic force microscopy and electrostatic force microscopy [53], dielectric spectroscopy [54], and so on. The mesoscopic structure of interfacial regions is influenced by the molecular structure, polarity, cohesion energy of polymers, and by the type, polarity, crystal structure, surface functionalization of nanofillers [8,14]. From the viewpoint of mesoscopic structures, interfacial regions around nanoparticles can generally be divided into several sub-regions, which are bonded, transitional, and normal regions as shown in Figure 8 [14]. When unsaturated bonds, hydrogen bonds, and other organic groups are introduced

on the surface of nanoparticles, strong interaction between nanoparticles and polymeric matrix can be formed via covalent and hydrogen bonds. A tight coupling region or bonded region is generated around nanoparticles with a thickness of about one to several nm. The interaction intensity between nanoparticles and polymer matrix in bonded region is affected by the surface properties and polarity of nanoparticles as well as the characteristic of polymer. The treatment of nanoparticles by silane coupling agent can reinforce the interaction intensity in bonded region. Moreover, a transitional region is formed by regular arranged molecular chains extended from the bonded region to tens of nm. The bonded and transitional regions can change the morphology and crystallinity of polymer nanocomposites. A normal region exists in the area extended from the transitional region to tens of nm, and it has similar properties to polymer matrix [14].

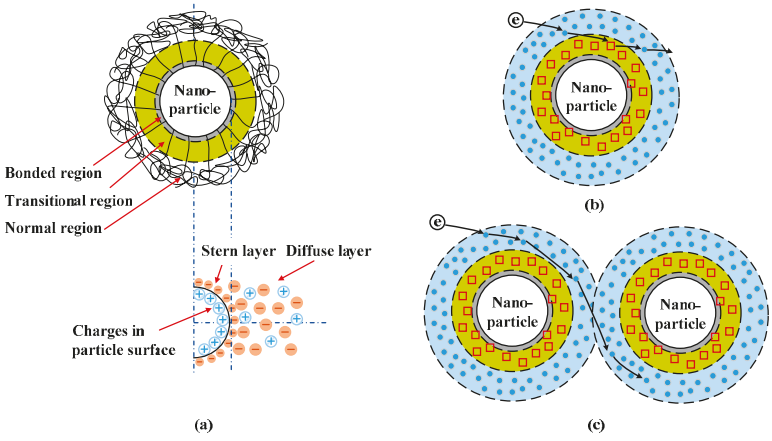

Figure 8. Schematic diagram of interfacial region around nanoparticles in PP/Al_2O_3 nanocomposites; (**a**) multi-region model of interfacial region, (**b**) charge carrier transport through an isolated interfacial region, and (**c**) charge carrier transport through overlapped interfacial regions.

It was suggested that deep traps may be introduced in the bonded and transitional regions and shallow traps may exist in the normal region, as shown in Figure 8b [6,8,14–16]. It was indicated that deep traps dominate the short-term electrical properties of nanocomposites at relatively low nanofiller loadings, while shallow traps play an important role in the long-term electrical properties at relatively high nanofiller loadings [6,8,14–16]. At relatively lower nanofiller loadings, isolated interfacial regions are formed in polymer nanocomposite dielectrics. Deep traps in the bonded and transitional regions can capture mobile charges effectively so that the migration of charge carriers is decelerated. Moreover, deep traps formed in isolated interfacial regions near the surfaces of dielectric materials can hinder the charge injections from electrodes into nanocomposite dielectrics. Figure 9a demonstrates the distribution profiles of space charges accumulated in nanocomposite dielectric materials with nanofiller loadings of 0 wt %, 0.5 wt %, 1 wt %, and 2 wt % at the application time of 14 s (namely V_{appl} = 28 kV). The space charge density decreases firstly and then increases with an increase in nanofiller loading. The space charge density near the interface between dielectric material and anode is 107.0 Cm^{-3} at the loading of 0 wt %, 79.9 Cm^{-3} at 0.5 wt %, 99.6 Cm^{-3} at 1.0 wt %, and 105.2 Cm^{-3} at 2.0 wt %. According to Poisson's Equation (6), the more space charges are accumulated inside dielectric materials, the more severely electric field will be distorted. Figure 9b shows the distributions of electric fields in nanocomposite dielectric materials with nanofiller loadings of 0 wt %, 0.5 wt %, 1 wt %, and 2 wt % at the application voltage of 28 kV. The distortion coefficient that is defined by the maximum electric field divided by the minimum one is 1.49 at the loading of

0 wt %, 1.36 at 0.5 wt %, 1.45 at 1.0 wt %, and 1.48 at 2.0 wt %. The simulated distributions of space charges and electric fields changed by nanodoping is similar to previous findings [9,20].

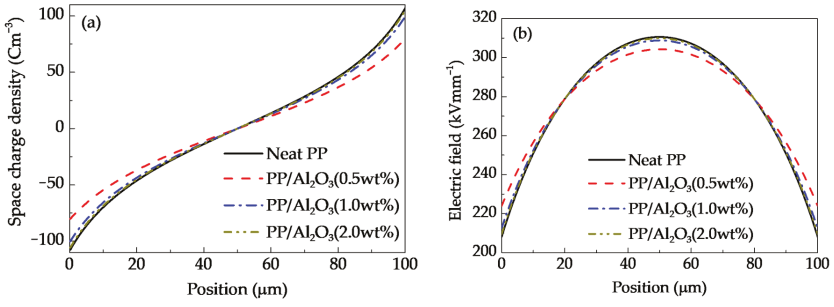

Figure 9. Distributions of space charge density (**a**) and electric field (**b**) at the application time of 14 s (namely V_{appl} = 28 kV) for nanocomposite dielectric materials at various nanofiller loadings.

The molecular chain with occupied deep traps will move under the electric field. Figure 10a shows the distributions of molecular chain displacement in nanocomposite dielectric materials with nanofiller loadings of 0 wt %, 0.5 wt %, 1 wt %, and 2 wt % at elapsed time of 14 s after the application of a ramp voltage. The maximum displacements of molecular chains with occupied deep electron traps are 2.71, 1.29, 2.20, and 2.52 nm in PP nanocomposite dielectric materials with nanofiller loadings of 0 wt %, 0.5 wt %, 1 wt %, and 2 wt % respectively, after applying a ramp voltage for 14 s. The motion of molecular chains with occupied deep traps is modulated by the intermolecular interactions, which is changed by the variation of nanofiller loading [55]. At low nanofiller loadings, the interactions between nanoparticles and polymer matrix increase the friction among molecular chains. Accordingly, the molecular mobility decreases or the relaxation time of molecular chains increases with an increase in nanofiller loading [55], as demonstrated in Figure 6b. When the nanofiller loading exceeds a critic value, the mean distance between two neighbor nanoparticles is very small and a polymer-mediated nanoparticle network will be formed. The molecular chain dynamics may transform from polymer-like to gel-like. The relaxation time of molecular chains decreases with nanofiller loading above a critic value [55]. Consequently, the motion velocity of molecular chains decreases firstly and then increases with the increase in nanofiller loading.

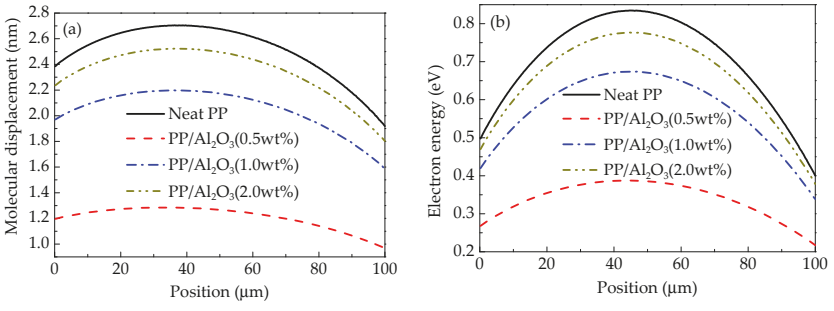

Figure 10. Distributions of molecular displacement (**a**) and electron energy (**b**) at the application time of 14 s (namely V_{appl} = 28 kV) for nanocomposite dielectric materials at various nanofiller loadings.

The molecular chain displacement may result in the increase in the length of free volume in dielectric materials [34,56,57]. It is assumed that the length of free volume is very small in the initial state for PP nanocomposite dielectric materials at room temperature. Therefore, the length of free volume λ is equal to the displacement value of molecular chains under the applied electric field.

The molecular chain displacement or the length of free volume increase with the applied voltage increases. The increases in both local electric field and molecular chain displacement lead to the increase in the energy of electrons gained from electric field in the free volume. Figure 10b shows a comparison of electron energy gain distributions in PP nanocomposite dielectric materials. The energy of electrons gained from electric field in free volume enlarged by molecular chain displacement decreases firstly and then increases with an increase in nanofiller loading. The maximum energies of electrons in PP nanocomposite dielectric materials with nanofiller loadings of 0 wt %, 0.5 wt %, 1 wt %, and 2 wt % after applying a ramp voltage for 14 s are 0.83, 0.39, 0.67, and 0.78 eV respectively.

Figure 11a demonstrates the maximum energy of electrons gained from electric field in free volume enlarged by the displacement of molecular chains of PP nanocomposites at various nanofiller loadings according to the calculations by the CTMD model. Electron energy gain is determined by both electric field and the length of free volume. The electric field in nanocomposites increases with the application time of ramp voltage and the maximum local electric field is enhanced by the accumulation of homo space charges. Moreover, the free volume is enlarged by the displacement of molecular chains with occupied deep traps. In other words, the length of free volume, the integration of the product of electric field and the effective mobility of molecular chain over time, increases with time. The effects of both the enhanced electric field and the enlarged free volume result in the increase in the energy gain of electrons. When the maximum electron energy $w_{\max} = (eF\lambda)_{\max}$ exceeds the trap energy level E_T, mobile charge carriers will migrate in dielectric materials without trapping by deep traps, resulting in the multiplication of local currents and the sudden rise of local temperature. Eventually, electrical breakdown would be triggered [31,44]. Since the motion of molecular chains is restricted by nanoparticles in nanocomposites with relatively lower loadings, the molecular displacement is smaller than that of neat PP as shown in Figure 11b. It indicates that the local free volume is enlarged slower in lightly doped nanocomposites than that in neat PP. Nevertheless, when nanofiller loading is higher than 0.5 wt %, the molecular displacement as well as the local free volume increase with increasing the nanofiller loading. Since dc electrical breakdown is triggered when the maximum electron energy, the product of local free volume and electric field, exceeds a critical value, the maximum electric field at pre-breakdown is inversely proportional to the free volume or molecular displacement as demonstrated in Figure 11b. Therefore, the breakdown electric field increases firstly and then decreases with an increase in nanofiller loading.

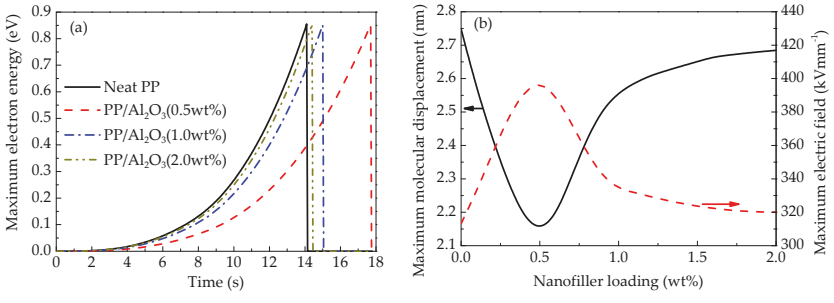

Figure 11. Numerical results of time-dependent maximum electron energy in nanocomposites at various nanofiller loadings (**a**) and maximum molecular displacement and maximum local electric field as a function of nanofiller loading at pre-breakdown (**b**).

Figure 12 shows the comparison of characteristic electrical breakdown strength of experimental and simulation results. It is found that simulation results are in a good agreement with experimental results as shown in Figure 4. The calculated results of dc electrical breakdown strength are 282.1, 358.1, 324.7, and 292.4 kV mm^{-1} for PP/Al_2O_3 nanocomposite dielectric materials with nanofiller loadings of 0 wt %, 0.5 wt %, 1 wt %, and 2 wt %, respectively. It indicates that the CTMD model

consisting dynamics of charge transport and molecular chain displacement can well interpret the nanofiller loading dependent dc electrical breakdown experiments of PP nanocomposite dielectrics.

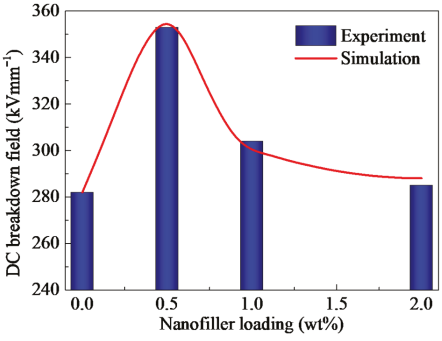

Figure 12. Comparison of experimental and simulation results of dc electrical breakdown field.

5. Conclusions

The influencing mechanism of nanodoping on dc electrical breakdown properties of PP/Al_2O_3 nanocomposite dielectric materials were investigated by experiments and simulations. Nanocomposite dielectric materials with various nanofiller loadings were prepared by melt-blending and hot-pressing methods and nanofillers are homogeneously dispersed in the matrix as indicated in SEM images. Experiments of thermally stimulated current, surface potential decay, and dc electrical breakdown show that incorporating a small amount of nanofillers into polymer matrix increases the retention time of deep trapped charges and hinders the charge transport in nanocomposite dielectrics, resulting in the enhancement of dc electrical breakdown field. Based on the experimental results, a model considering charge transport dynamics and the displacement of molecular chains with occupied deep traps was utilized to simulate the dc electrical breakdown behavior of nanocomposite dielectrics. When the electron energy gain from electric field in free volume enlarged by the molecular displacement exceeds the potential barrier, electrical breakdown would be triggered. It was found that the electrical breakdown field increases firstly and then decreases with an increase in nanofiller loading. At relatively low loadings isolated interfacial regions are formed in nanocomposite dielectrics, resulting in the increases in the retention time of deep trapped charges and the interaction between molecular chains. Accordingly, the transport of charges and the displacement of molecular chains with occupied deep traps are hindered, which can enhance the electrical breakdown strength. At relatively high loadings interfacial regions may overlap in nanocomposite dielectrics so that the retention time of deep trapped charges decreases. The molecular chain dynamics may transform from polymer-like to gel-like and the interaction between molecular chains may be weakened, causing the acceleration of molecular motion driven by electric force and the decrease in electrical breakdown strength. It was concluded that the changes in the charge transport and molecular displacement characteristics affected by nanodoping may be the influencing mechanism of dc electrical breakdown properties of PP nanocomposite dielectrics.

Author Contributions: Conceptualization, D.M.; Formal analysis, R.M.; Funding acquisition, D.M.; Investigation, C.Y., R.M., C.M., Y.H., Q.W. and Z.X.; Methodology, C.Y.; Resources, Q.W. and Z.X.; Supervision, D.M. and S.L.; Writing—Original draft, D.M. and C.Y.; Writing—Review & editing, D.M. and S.L.

Funding: This work was supported by the National Natural Science Foundation of China (grant No. 51507124), the National Basic Research Program of China (grant No. 2015CB251003), the State Key Laboratory of Advanced Power Transmission Technology (grant No. GEIRI-SKL-2018-010), the State Key Laboratory of Power Systems of Tsinghua University (grant No. SKLD16KZ04), the China Postdoctoral Science Foundation (grant No. 2014M552449), and State Grid Corporation of China Science Project (grant No. 522722160001).

Conflicts of Interest: The authors declare no conflict of interest.

References

1. Chu, S.; Cui, Y.; Liu, N. The path towards sustainable energy. *Nat. Mater.* **2016**, *16*, 16–22. [CrossRef] [PubMed]
2. Chu, S.; Majumdar, A. Opportunities and challenges for a sustainable energy future. *Nature* **2012**, *488*, 294–303. [CrossRef] [PubMed]
3. Harsha, P.; Dahleh, M. Optimal management and sizing of energy storage under dynamic pricing for the efficient integration of renewable energy. *IEEE Trans. Power Syst.* **2015**, *30*, 1164–1181. [CrossRef]
4. Chu, B.J.; Zhou, X.; Ren, K.L.; Neese, B.; Lin, M.R.; Wang, Q.; Bauer, F.; Zhang, Q.M. A dielectric polymer with high electric energy density and fast discharge speed. *Science* **2006**, *313*, 333–336. [CrossRef] [PubMed]
5. Huan, T.D.; Boggs, S.; Teyssedre, G.; Laurent, C.; Cakmak, M.; Kumar, S.; Ramprasad, R. Advanced polymeric dielectrics for high energy density applications. *Prog. Mater. Sci.* **2016**, *83*, 236–269. [CrossRef]
6. Huang, X.Y.; Zhi, C.Y. *Polymer Nanocomposites: Electrical and Thermal Properties*; Springer: Basel, Switzerland, 2016; pp. 1–346.
7. Dang, Z.M.; Zhou, T.; Yao, S.H.; Yuan, J.K.; Zha, J.W.; Song, H.T.; Li, J.Y.; Chen, Q.; Yang, W.T.; Bai, J.B. Advanced calcium copper titanate/polyimide functional hybrid films with high dielectric permittivity. *Adv. Mater.* **2009**, *21*, 2077–2082. [CrossRef]
8. Nelson, J.K. *Dielectric Polymer Nanocomposites*; Springer: Spring, NY, USA, 2010; pp. 1–285.
9. Zhou, Y.; Hu, J.; Dang, B.; He, J.L. Effect of different nanoparticles on tuning electrical properites of polypropylene nanocomposites. *IEEE Trans. Dielectr. Electr. Insul.* **2017**, *24*, 1380–1389. [CrossRef]
10. Cao, W.K.; Li, Z.; Sheng, G.H.; Jiang, X.C. Insulating property of polypropylene nanocomposites filled with nano-MgO of different concentration. *IEEE Trans. Dielectr. Electr. Insul.* **2017**, *24*, 1430–1437. [CrossRef]
11. Takala, M.; Ranta, H.; Nevalainen, P.; Pakonen, P.; Pelto, J.; Karttunen, M.; Virtanen, S.; Koivu, V.; Pettersson, M.; Sonerud, B.; et al. Dielectric properties and partial discharge endurance of polypropylene-silica nanocomposite. *IEEE Trans. Dielectr. Electr. Insul.* **2010**, *17*, 1259–1267. [CrossRef]
12. Lewis, T.J. Interfaces are the dominant feature of dielectrics at the nanometric level. *IEEE Trans. Dielectr. Electr. Insul.* **2004**, *11*, 739–753. [CrossRef]
13. Lewis, T.J. Interfaces: Nanometric dielectrics. *J. Phys. D Appl. Phys.* **2005**, *38*, 202–212. [CrossRef]
14. Li, S.; Yin, G.; Chen, G.; Li, J.; Bai, S.; Zhong, L.; Zhang, Y.; Lei, Q.Q. Short-term Breakdown and Long-term Failure in Nanodielectrics: A Review. *IEEE Trans. Dielectr. Electr. Insul.* **2010**, *17*, 1523–1535. [CrossRef]
15. Tanaka, T. Dielectric nanocomposites with insulating properties. *IEEE Trans. Dielectr. Electr. Insul.* **2005**, *12*, 914–928. [CrossRef]
16. Tanaka, T.; Kozako, M.; Fuse, N.; Ohki, Y. Proposal of a multi-core model for polymer nanocomposite dielectrics. *IEEE Trans. Dielectr. Electr. Insul.* **2005**, *12*, 669–681. [CrossRef]
17. Takada, T.; Hayase, Y.; Tanaka, Y.; Okamoto, T. Space Charge Trapping in Electrical Potential Well Caused by Permanent and Induced Dipoles for LDPE/MgO Nanocomposite. *IEEE Trans. Dielectr. Electr. Insul.* **2008**, *15*, 152–160. [CrossRef]
18. Min, D.M.; Wang, W.W.; Li, S.T. Numerical Analysis of Space Charge Accumulation and Conduction Properties in LDPE Nanodielectrics. *IEEE Trans. Dielectr. Electr. Insul.* **2015**, *22*, 1483–1491. [CrossRef]
19. Dang, B.; He, J.L.; Hu, J.; Zhou, Y. Large improvement in trap level and space charge distribution of polypropylene by enhancing the crystalline-amorphous interface effect in blends. *Polym. Int.* **2016**, *65*, 371–379. [CrossRef]
20. Dang, B.; HU, J.; Zhou, Y.; He, J.L. Remarkably improved electrical insulating performances of lightweight polypropylene nanocomposites with fullerene. *J. Phys. D Appl. Phys.* **2017**, *50*, 455303–455308. [CrossRef]
21. Van Turnhout, J. *Electrets*; Springer: Berlin, Germany, 1987; pp. 81–215.
22. Dang, B.; Zhou, Y.; He, J.L.; Hu, J. Relationship between space charge behaviors and trap level distribution in polypropylene/propylene ethylene rubber/ZnO nanocomposites. In Proceedings of the 2016 IEEE Conference on Electrical Insulation and Dielectric Phenomena (CEIDP), Toronto, ON, Canada, 16–19 October 2016; pp. 595–598.
23. Zhang, C.; Zha, J.W.; Yan, H.D.; Li, W.K.; Dang, Z.M. High improvement in trap level density and direct current breakdown strength of block polypropylene by doping with a β-nucleating agent. *Appl. Phys. Lett.* **2018**, *112*, 91902–91905. [CrossRef]

24. Le Roy, S.; Teyssedre, G.; Laurent, C.; Montanari, G.C.; Palmieri, F. Description of charge transport in polyethylene using a fluid model with a constant mobility: Fitting model and experiments. *J. Phys. D Appl. Phys.* **2006**, *39*, 1427–1436. [CrossRef]
25. Teyssèdre, G.; Laurent, C. Charge transport modeling in insulating polymers: From molecular to macroscopic scale. *IEEE Trans. Dielectr. Electr. Insul.* **2005**, *12*, 857–875. [CrossRef]
26. Berlepsch, H.V. Interpretation of surface potential kinetics in HDPE by a trapping model. *J. Phys. D Appl. Phys.* **1985**, *18*, 1155–1170. [CrossRef]
27. Sonnonstine, T.J.; Perlman, M.M. Surface-potential decay in insulators with field-dependent mobility and injection efficiency. *J. Appl. Phys.* **1975**, *46*, 3975–3981. [CrossRef]
28. Wintle, H.J. Surface-Charge Decay in Insulators with Nonconstant Mobility and with Deep Trapping. *J. Appl. Phys.* **1972**, *43*, 2927–2930. [CrossRef]
29. Hoang, A.T.; Pallon, L.; Liu, D.M.; Serdyuk, Y.V.; Gubanski, S.M.; Gedde, U.W. Charge transport in LDPE nanocomposites part I–experimental approach. *Polymers* **2016**, *8*, 87. [CrossRef]
30. Coelho, R.; Aladenize, B.; Cornet, N. On the transient potential in insulators. *IEEE Trans. Dielectr. Electr. Insul.* **2001**, *8*, 760–770. [CrossRef]
31. Dissado, L.A.; Fothergill, J.C. *Electrical Degradation and Breakdown in Polymers*; The Institution of Engineering and Technology: London, UK, 1992; pp. 24–316.
32. Kao, K.C. *Dielectric Phenomena in Solids*; Elsevier: San Diego, CA, USA, 2004; pp. 327–572.
33. Matsui, K.; Tanaka, Y.; Takada, T.; Fukao, T. Space Charge Behavior in Low-density Polyethylene at Pre-breakdown. *IEEE Trans. Dielectr. Electr. Insul.* **2005**, *12*, 406–415. [CrossRef]
34. Min, D.M.; Li, S.T.; Ohki, Y. Numerical Simulation on Molecular Displacement and DC Breakdown of LDPE. *IEEE Trans. Dielectr. Electr. Insul.* **2016**, *23*, 507–516. [CrossRef]
35. Le Roy, S.; Segur, P.; Teyssedre, G.; Laurent, C. Description of Bipolar Charge Transport in Polyethylene Using a Fluid Model with a Constant Mobility: Model Prediction. *J. Phys. D Appl. Phys.* **2004**, *37*, 298–305. [CrossRef]
36. Chen, G.; Zhao, J.; Li, S.; Zhong, L. Origin of thickness dependent dc electrical breakdown in dielectrics. *Appl. Phys. Lett.* **2012**, *100*, 222904. [CrossRef]
37. Lowell, J. Absorption and conduction currents in polymers: A unified model. *J. Phys. D Appl. Phys.* **1990**, *23*, 205–210. [CrossRef]
38. Scott, J.C.; Malliaras, G.G. Charge injection and recombination at the metal-organic interface. *Chem. Phys. Lett.* **1999**, *299*, 115–119. [CrossRef]
39. Van der Holst, J.J.M.; van Oost, F.W.A.; Coehoorn, R.; Bobbert, P.A. Electron-hole recombination in disordered organic semiconductors: Validity of the Langevin formula. *Phys. Rev. B* **2009**, *80*, 235202–235208. [CrossRef]
40. Shockley, W.; Read, W.T. Statistics of the Recombinations of Holes and Electrons. *Phys. Rev.* **1952**, *87*, 835–842. [CrossRef]
41. Kuik, M.; Koster, L.J.A.; Wetzelaer, G.A.H.; Blom, P.W.M. Trap-assisted recombination in disordered organic semiconductors. *Phys. Rev. Lett.* **2011**, *107*, 256805. [CrossRef] [PubMed]
42. Collins, G.; Federici, J.; Imura, Y.; Catalani, L.H. Charge generation, charge transport, and residual charge in the electrospinning of polymers: A review of issues and complications. *J. Appl. Phys.* **2012**, *111*, 44701. [CrossRef]
43. Das-Gupta, D.K. Dielectric and related molecular processes in polymers. *IEEE Trans. Dielectr. Electr. Insul.* **2001**, *8*, 6–14. [CrossRef]
44. Artbauer, J. Electric strength of polymers. *J. Phys. D Appl. Phys.* **1996**, *29*, 446–456. [CrossRef]
45. Boufayed, F.; Teyssedre, G.; Laurent, C.; Le Roy, S.; Dissado, L.A.; Segur, P.; Montanari, G.C. Models of bipolar charge transport in polyethylene. *J. Appl. Phys.* **2006**, *100*, 104105–104110. [CrossRef]
46. Neagu, E.R. A method to measure the electric charge injected/extracted at the metal-dielectric interface. *Appl. Phys. Lett.* **2008**, *92*, 1829041–1829043. [CrossRef]
47. Huzayyin, A.; Boggs, S.; Ramprasad, R. Quantum Mechanical Study of Charge Injection at the Interface of Polyethylene and Platinum. In Proceedings of the 2011 Annual Report Conference on Electrical Insulation and Dielectric Phenomena, Cancun, Mexico, 16–19 October 2011; pp. 800–803.
48. Chen, L.H.; Huan, T.D.; Quintero, Y.C.; Ramprasad, R. Charge injection barriers at metal/polyethylene interfaces. *J. Mater. Sci.* **2016**, *51*, 506–512. [CrossRef]

49. Cockburn, B.; Shu, C.W. Runge-Kutta Discontinuous Galerkin Methods for Convection-Dominated Problems. *J. Sci. Comput.* **2001**, *16*, 173–261. [CrossRef]
50. Gottlieb, S.; Shu, C.W. Total Variation Diminishing Runge-Kutta Schemes. *Math. Comput.* **1998**, *67*, 73–85. [CrossRef]
51. Min, D.M.; Li, S.T. A Comparison of Numerical Methods for Charge Transport Simulation in Insulating Materials. *IEEE Trans. Dielectr. Electr. Insul.* **2013**, *20*, 955–964.
52. Bansal, A.; Yang, H.; Li, C.; Cho, K.; Benicewicz, B.C.; Kumar, S.K.; Schadler, L.S. Quantitative equivalence between polymer nanocomposites and thin polymer films. *Nat. Mater.* **2005**, *4*, 693–698. [CrossRef] [PubMed]
53. Seiler, J.; Kindersberger, J. Insight into the interphase in polymer nanocomposites. *IEEE Trans. Dielectr. Electr. Insul.* **2014**, *21*, 537–547. [CrossRef]
54. Gong, S. Segmental dynamics of polymer melts with spherical nanoparticles. *ACS Macro Lett.* **2014**, *3*, 773–777. [CrossRef]
55. Baeza, G.P.; Dessi, C.; Costanzo, S.; Zhao, D.; Gong, S.; Alegría, A.; Colby, R.H.; Rubinstein, M.; Vlassopoulos, D.; Kumar, S.K. Network dynamics in nanofilled polymers. *Nat. Commun.* **2016**, *7*, 1–6. [CrossRef] [PubMed]
56. Min, D.M.; Li, Y.W.; Yan, C.Y.; Xie, D.R.; Li, S.T.; Wu, Q.Z.; Xing, Z.L. Thickness-Dependent DC Electrical Breakdown of Polyimide Modulated by Charge Transport and Molecular Displacement. *Polymers* **2018**, *10*, 12. [CrossRef]
57. Jones, J.P.; Llewellyn, J.P.; Lewis, T.J. The contribution of field–induced morphological change to the electrical aging and breakdown of polyethylene. *IEEE Trans. Dielectr. Electr. Insul.* **2005**, *12*, 951–966. [CrossRef]

polymers

MDPI

Review

Polyethylene Nanocomposites for Power Cable Insulations

Ilona Pleşa [1,*], Petru V. Noţingher [2], Cristina Stancu [2], Frank Wiesbrock [1] and Sandra Schlögl [1]

[1] Polymer Competence Center Leoben GmbH (PCCL), Roseggerstrasse 12, Leoben 8700, Austria; frank.wiesbrock@pccl.at (F.W.); sandra.schloegl@pccl.at (S.S.)

[2] Faculty of Electrical Engineering, Electrotechnical Material Laboratory, University Politehnica of Bucharest, Splaiul Independentei 313, 060042 Bucharest, Romania; petrunot@elmat.pub.ro (P.V.N.); cstancu@elmat.pub.ro (C.S.)

* Correspondence: ilona.plesa@pccl.at; Tel.: +43-3842-42962-53

Received: 17 October 2018; Accepted: 18 December 2018; Published: 24 December 2018

Abstract: This review represents a comprehensive study of nanocomposites for power cables insulations based on thermoplastic polymers such as polyethylene congeners like LDPE, HDPE and XLPE, which is complemented by original results. Particular focus lies on the structure-property relationships of nanocomposites and the materials' design with the corresponding electrical properties. The critical factors, which contribute to the degradation or improvement of the electrical performance of such cable insulations, are discussed in detail; in particular, properties such as electrical conductivity, relative permittivity, dielectric losses, partial discharges, space charge, electrical and water tree resistance behavior and electric breakdown of such nanocomposites based on thermoplastic polymers are described and referred to the composites' structures. This review is motivated by the fact that the development of polymer nanocomposites for power cables insulation is based on understanding more closely the aging mechanisms and the behavior of nanocomposites under operating stresses.

Keywords: thermoplastic nanocomposite; polyethylene; power cable insulation; electrical property; structure-property relationship

1. Introduction

High-voltage industry undergoes continuous development and modernization of power grid systems in order to yield reliable, cost-effective and environmentally harmless power solutions [1]. Energy power transportation across the seas and inland is targeted to be performed in particular by extruded polymer-based cables. Underground and submarine cables are used since the early stages of electricity transmission and distribution [2]. However, in regions where it is difficult or impossible to implement the overhead transmission network (i.e., densely populated zones or underwater and underground tunnels connections), high-voltage alternate current (HVAC) and high-voltage direct current (HVDC) cable networks are developed to meet the increasing capacity (Figure 1) [1]. In order to increase their levels of operating voltage and to enhance their electrical performance, it is necessary to introduce the next generation of cable insulation materials [3].

Fifty years ago, paper-insulated and oil-impregnated low-voltage (LV), medium-voltage (MV) and high voltage (HV) underground cables were used [4]. An important development took place in the 1960s, when mineral impregnation oil was mixed with small quantities of natural resin or microcrystalline petroleum wax for increasing the viscosity and avoiding the migration of impregnated oil through the cable during the heat evolvement generated by the current. Due to the significant changes in height of cables, another solution was provided by blending synthetic poly(*iso*-butylene)

with microcrystalline wax using special manufacturing techniques for mass-impregnated non-draining cables above 33 kV.

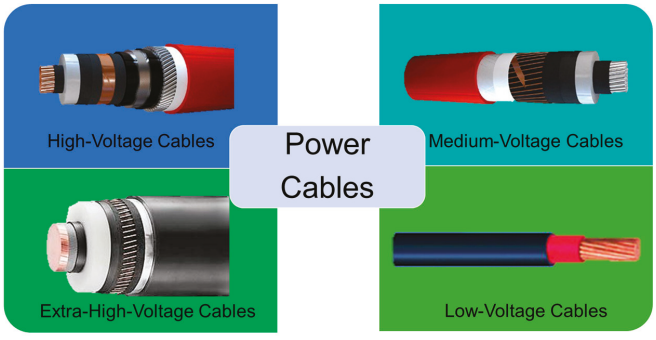

Figure 1. Different types of power cables used for electricity transmission and distribution.

By using polymers such as polyethylene (PE), ethylene-propylene rubber (EPR) or ethylene-propylene-diene-monomer rubber (EPDM), it was possible to obtain high and very high voltage cables (Extra High Voltage Cables EHVC), with a low level of partial discharges, easy maintenance and remarkable longevity. The various process steps for the production of cables containing thermoplast-based insulations are provided in Figure 2.

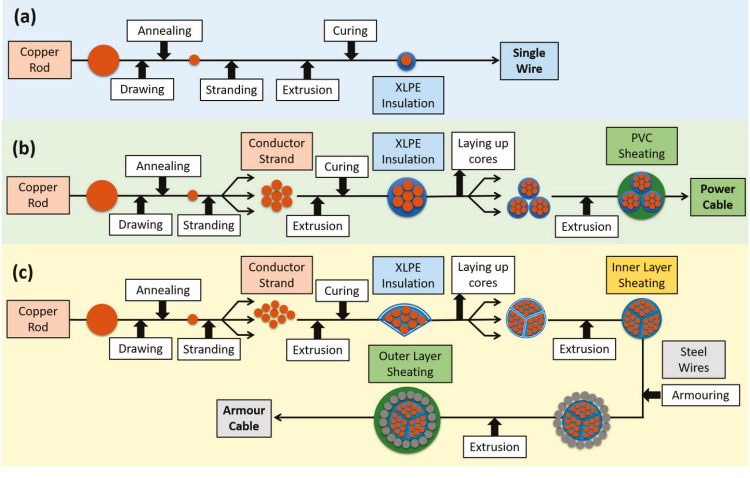

Figure 2. Typical process steps for the production of (**a**) wires, (**b**) power cables and (**c**) armour power cables employing thermoplast-based polymers as insulation. Redrawn and adapted from reference [5].

PE was the most suitable insulation material (comprising low permittivity and high electrical breakdown strength) in the cables production in the late 1960s and early 1970s [4]. However, PE suffers from two major drawbacks: (*i*) the limitation of the maximum operating temperature, which is around 70 °C and (*ii*) the necessity to add antioxidants in order to avoid deterioration of the polymer-based insulation. Taking into consideration these aspects, a new solution was found by crosslinking of PE (yielding XLPE), which improved both, thermal resistance and ageing stability of the material due to the formation of the 3D network. The crosslinking additives such as dicumyl peroxide should not degrade the electrical performance of the crosslinked material [4]. Initially, cables based on XLPE

were manufactured on continuous vulcanization lines, using steam for heating and pressurizing production stages and water under pressure for cooling. Later, it was found that the presence of steam during the crosslinking process introduced a high level of moisture in the cable insulation, resulting in the formation of microvoids in which electrical and/or water trees were developed, resulting in premature breakdown of the insulation. Hence, steam was removed from the production process. A new manufacturing process was developed involving electrical heating and pressurizing with dry nitrogen in a continuous vulcanization line. At that time, water was still used for cooling but was later eliminated from any stage of the process and generally removed as cooling method. Since the 1980s, the failure rates of XLPE cables have decreased significantly by the introduction of these new production techniques [4]. Since then, the development of XLPE for LV, HV and EHV cables with enhanced insulation quality and properties has resulted from the production of materials with fewer impurities as well as the reduction of negative effects generated by the presence of contaminants and by-products of the radical crosslinking. Other approaches involve the introduction of special tree-retardant grades of XLPE, development of colorants for the cable cores, improvement of the compatibility between XLPE and semiconductive materials for cable screens by reduction of the size of carbon black particles and the elimination of ionic contaminants [1,4].

Nowadays, XLPE cables are commonly applied but it becomes more and more difficult to improve the insulation quality, mainly due to high costs involved in the production of purer materials, which stimulates the demand for exploring other possibilities such as polymer-based nanocomposites for obtaining the targeted improvements. While paper-insulated and oil-filled cables for AC and DC applications are very easy to be used, conventional AC-XLPE insulated cables cannot be employed for DC because the electrical conductivity varies with temperature and electric field and, in particular, due to space charge accumulation [4]. For underground power cables insulation, other copolymers of ethylene and propylene (EPR) and terpolymers of ethylene, propylene and a diene component (EPDM) are typically applied [6]. They are highly filled and opaque elastomers due to their chemical and physical properties (e.g., sensitivity to heat, oxidation, ozone and weather, insolubility in many polar solvents, etc.). EPR and EPDM are flexible even at low temperatures (amorphous forms of EPR) and exhibit a certain level of tree retardancy, however at the drawback of some electrical properties (i.e., higher dissipation factor) [6].

Today, on-going research activities aim at the application of new polymer materials with or without nanoparticles (e.g., LDPE/metal oxides nanocomposites containing additional voltage stabilizers), processed by modern methods, which are very promising materials for the future of cables insulation for DC and AC applications.

This publication provides a review of the most important thermoplast-based nanocomposites (i.e., based on LDPE, HDPE, XLPE) used as power cables insulation, starting with their chemical structure, addressing their electrical properties and establishing structure-property-relationships. Particularly for cables insulations based on nanocomposites, the critical factors, which are contributing to the degradation or improvement of the electrical performance under stress, are discussed, with a particular focus on the influence of nanofillers and additives on the electrical properties of the cables' insulation.

2. Critical Challenges of Polymer-Based Nanocomposites in Industrial Applications

The replacement of LDPE (thermoplastic polymer) with XLPE (thermosetting polymer) enhanced the thermomechanical properties of power cable insulations. Due to the crosslinking process, the thermal stability, and, hence, the long-term operation in service, was significantly improved from 70 to 90 °C [7]. XLPE is being able to withstand even short circuit conditions for a few seconds with conductor temperatures over 200 °C [8]. However, in the case of XLPE, the modulus is reduced by several orders of magnitude at operating temperatures between 90 and 100 °C [9]. Power cable insulations with low modulus are prone to irreversible mechanical damage during operation [10]. Currently, conventional XLPE is at the limit of capabilities, both in terms of purity (which influences the electrical properties,

especially the electrical conductivity [11]) and thermal stability (which determines the maximum operating temperature). In order to obtain insulations with higher operating temperatures, which allow higher current densities through conductors, there are two important directions. On the one hand, PE could be replaced by other polymers such as EPR/EPM, PP and copolymers of PE and PP. In particular, the P-Laser cable represents a breakthrough in power cable systems; it is based on the high-performance thermoplastic elastomer HPTE [12]. On the other hand, nanocomposites based on PE or PP and organic or inorganic fillers can be used. Nanoparticles have a larger interfacial area compared to microsized particles, which strongly influences and determines the properties of nanocomposite materials, even at low volume concentration of such fillers (Figure 3) [13–16]. The performance of polymer-based nanocomposites is affected by particle agglomerations since nanoparticles have a strong tendency to aggregate (in particular if polar particles such as silica are dispersed in a non-polar polymer matrix such as PE). In order to avoid agglomeration and to maintain the stability of the nanoparticles within the polymer matrix, they are often surface-functionalized [14,17]. Carefully tailored interfaces of the incorporated nanoparticles enable the preparation of insulating nanocomposites with properties that exceed those of HVDC cables (from 320 to 800 kV), which are applied in industry nowadays.

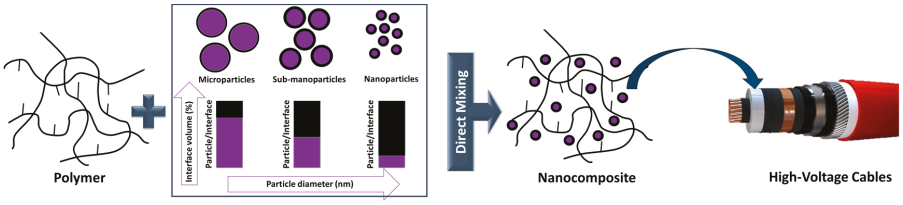

Figure 3. Schematic representation of polymers nanocomposites used for power cable insulation and the influence of the interface on their properties.

Although XLPE technologies are widely adopted and expected to be continuously used in the future [10], the introduction of PE-based nanocomposites for power cables insulation is a solution taken into consideration by many cable manufacturers. For commercial use, nanocomposites have to fulfil several requirements involving improved thermomechanical and electrical properties and sustainable economic and environmental characteristics. For AC cables and their joints, the polymeric materials must exhibit, among other things, low electrical conductivity, tailor-made permittivity and low loss factor, high dielectric breakdown strength, partial discharge resistance, absence of electric and electrochemical treeing, stability at higher operating temperatures, and so forth. In the case of HVDC, the insulating materials must meet two additional essential requirements: (*i*) low variations in electrical conductivity with varying temperature and electric field intensity and (*ii*) low space charge accumulation [7,18].

The experimental studies revealed that the introduction of nanoparticles such as Al_2O_3, SiO_2, TiO_2, MgO, ZnO, carbon black, graphene, graphene oxide and so forth, lead to a significant increase in electrical resistivity (1-2 orders of magnitude [18]) and dielectric rigidity. A reduction of space charge accumulation and an increased resistance to the action of partial discharges as well as electric and water treeing were also observed. In addition to choosing the type and concentration of the particles, the properties of the nanocomposites can be conveniently adjusted by surface modification of the nanoparticles [19]. Generally, the effect of nanoparticles on reducing the electrical conductivity values and space charge accumulation is stronger if their surfaces were covered or treated by, for example, chemical modification. For example, in the case of LDPE nanocomposites with silane-coated Al_2O_3 nanoparticles (50 nm in diameter), the electrical conductivity dropped 50 times to that of LDPE. The greatest reduction in conductivity by two orders of magnitude was achieved by using a treatment with *n*-octyl-bearing silanes [20]. It should be noted that the introduction of nanoparticles in order to improve selected properties might adversely affect other properties of the composites.

For example, the introduction of carbon black CB in LDPE causes a reduction of space charge injection and field distortion but can decrease the DC breakdown strength of the nanocomposite (the dielectric permittivity and dielectric loss remaining adjacent to LDPE without CB) [21].

The maximum value of space charge density accumulated in HVDC insulation must be relatively low in order to ensure higher reliability and long-term life performance [22]. In this case, the maximum electric field must be below the threshold for space charge accumulation [22,23]. In fact, for all the simulations on the behavior of HVDC cables, it was considered that the cables operate below the threshold for space charge accumulation (the cables are space charge free), except for the charge distribution that is the result of a temperature gradient in the insulation [22]. As mentioned above, this can be accomplished by introducing nanostructured materials based on XLPE filled with SiO_2 or MgO nanoparticles [24]. On the other hand, the presence of moisture leads to a deterioration of the electrical properties of polymer-based nanocomposites (in particular, reduced breakdown strength and increased losses) [25–27]. In order to reduce the influence of humidity, a treatment of the nanoparticles can be performed, as shown in literature for MgO nanoparticles [28]. Increasing the moisture resistance of nanoparticles is due to a covalent attachment of functional silanes, which is carried out as an intermediate step after a low-temperature thermal decomposition of $Mg(OH)_2$. It was found that moisture-resistant MgO nanoparticles retained their phase/structure even after extended exposure to humidity and that the addition of these nanoparticles in 1 wt % quantity into a LDPE matrix resulted in a significant increase of the electrical resistivity [28].

The use of PE based nanocomposites for commercially available high-voltage cable insulations is still in its infancy. This is due to, among other things, reduced quantities of nanodielectrics and the fact that the improvements of certain properties of these materials (electrical, thermal properties, etc.) are not always valid for other properties (mechanical properties, etc.) [29]. However, the realization of the first XLPE nanocomposite cables insulation (XLPE with MgO) should be emphasized, namely the $\pm$ 250 kV Hokkaido-Honshu LCC HVDC cable link in 2012 [30–32] and the $\pm$ 400 kV ones, which will be put into operation in a project connecting England and Belgium in 2019 [18]. The effect of MgO on reducing the electrical conductivity is more pronounced than that of SiO_2 because MgO has a higher relative permittivity of ε_r = 9.8 compared to that of SiO_2 of ε_r = 3.9 [18]. It should be noted that the documentation regarding the space charge behavior or mitigation on production-size transmission-class HVDC extruded cables are not yet available [24]. It should be evidenced that a combination of the data availability regarding the applications of nanocomposites and the commercial availability of ultra-clean XLPE enables the future development of HVDC cables with ultra-high voltage rating [33].

In the case of DC cables junctions with two polymer layers, it is also necessary to consider the reduction or even cancellation of superficial charge accumulated in their interfaces. For this purpose, XLPE and nanocomposite layers of EPDM with SiC can be used [34]. It should be noted, however, that the accumulated charge density increases upon the application of voltage and then decreases until cancellation [34]. The introduction of nanoparticles into PE can also lead to an improvement of the thermal conductivity of cable insulation, an important requirement for reducing their thermal ageing. For example, in the case of LDPE and polyhedral oligomeric silesquioxanes (POS) nanocomposites, an increase in thermal conductivity was achieved by approx. 8%, while the dielectric rigidity remained unmodified and the corona discharge resistance increased [35]. In addition, the introduction of boron nitride (BN) particles into LDPE resulted in an increase of the thermal conductivity of up to 1 $W \cdot m^{-1} \cdot K^{-1}$ at a filler loading of 40 wt % [36].

Although a series of PE-based nanocomposites with electrical and/or thermal properties superior to the unfilled polymer have been achieved, the introduction of these new materials into the current production of power cables requires the performance of extensive testing and life modelling to investigate both the space charge trapping properties and the long-term life performance, in order to define suitable levels for the design field and reach cost-effective designs associated with the desired life and reliability levels [22].

3. Polymers for Power Cable Insulations

In the field of MV and HV cables, cable jackets and semiconducting layers, extruded polymers are commonly used. Benefiting from low raw material and processing costs together with high reliability and adequate material performance, polyethylene (PE) and, in particular, crosslinked polyethylene (XLPE) are widely applied [37]. Other polyolefins such as syndiotactic polypropylene (PP) have been reported to exhibit good insulating properties but the high cost of the material hinders widespread application [38]. Along with homopolymers, also blends of different types of polyolefins, copolymers such as ethylene propylene rubber (EPR) and ethylene propylene diene rubber (EPDM) are employed as extrudable dielectric materials. The chemical structures of selected polymers are shown in Figure 4.

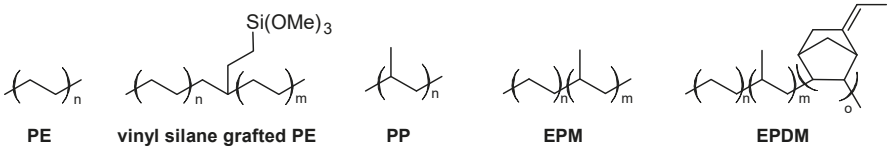

Figure 4. Chemical structure of polymers used as extrudable dielectric materials. PE: polyethylene; PP: polypropylene; EPM: ethylene propylene rubber; EPDM: ethylene propylene diene monomer rubber.

3.1. Power Cable Insulations Based on Polyethylene (PE)

Polyethylene comprises a saturated carbon-carbon backbone and is a typical thermoplast, which means that the polymer melts when heated above its melting point. The type of branching, the crystal structure and the molecular weight of the polymer chains mainly govern the material properties of PE (Figure 5). The most prominent types are low-density polyethylene (LDPE) with a considerable number of short-and long-chain branching, linear low-density PE (LLDPE) with a significant degree of short branches and high-density PE (HDPE) with a low amount of branching. LLDPE and HDPE are produced by coordination polymerization in the presence of selected catalysts (e.g., Ziegler-Natta, Philips, metallocenes), which leads to controlled branching and molecular weight of the polymer chains. In contrast, LDPE is obtained by free-radical polymerization at high pressures and high temperatures without the use of any catalyst, resulting in polymer structures with random short- and long-chain branching. Thus, the material costs of LDPE are much lower than LLDPE or HDPE, which makes it, in conjunction with the low dielectric constant, the low dielectric loss and the high breakdown strength, an ideal candidate for extrudable dielectric materials [39].

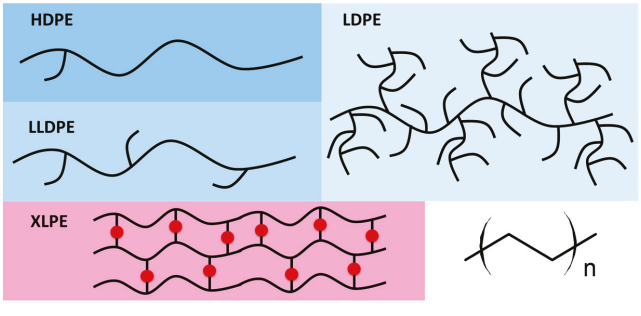

Figure 5. Schematic representation of the structures of varying types of PE.

Previous work has shown that the electrical properties of LDPE such as dielectric strength and space charge formation are influenced by its crystalline structure [40,41]. LDPE is a semi-crystalline polymer typically containing 45–55% crystalline domains in the form of lamellae, which are surrounded by the amorphous bulk phase. The size of the crystalline domains can be controlled by the parameters

of the extrusion process. While high cooling rates result in smaller domains and lower degrees of crystallinity, thermal annealing yields larger domains in conjunction with a higher amount of crystallinity. The annealing and cooling steps of the extruded LDPE insulation are carried out under high pressure and under inert conditions in order to reduce the formation of voids. Particularly in the production of cable insulation, higher crystallinity and smaller domains are favoured as the final product correspondingly shows smaller voids and improved ductility. Along with the crystalline regions, the amorphous bulk has also a distinctive influence on the electrical properties of LDPE. Dissado and Fothergill [42] demonstrated that charge transport mainly occurs within the amorphous regions of LDPE. Khalil [43] has shown that the initial morphology of PE can change during thermal cycling in conjunction with DC conductivity leading to a distinctive increase in conductivity.

The electrical behavior of PE is further influenced by impurities, voids and ageing (e.g., carbonyl moieties formed by oxidation of the polymer chain), which are expected to induce space charge accumulation leading to a local heating that can result in electrical breakdown of the insulation material [42].

3.2. Power Cable Insulations Based on Crosslinked Polyethylene (XLPE)

Aiming at an enhanced thermal and chemical resistivity in combination with improved mechanical properties (in particular at high filler loading) and ageing behavior, LDPE may be crosslinked (XLPE). Due to the crosslinking of the polymer chains, the operational temperature can be increased from 75 to 90 °C. Previous studies [39] report that XLPE is stable at 130 °C during 36 h. However, if the temperature of the conductor reaches 250 °C (e.g., during a short circuit), the XLPE-based insulation degrades within seconds [44].

The most common crosslinking mechanism originates from the addition of radical initiators such as organic peroxides, which undergo homolytic bond cleavage during the extrusion process and initiate radical-induced crosslinking of the polymer chains (Figure 6). Curing with dicumyl peroxide enables safe processing up to 120 °C, while the processing temperature can be increased to 150 °C using 2,5-bis-(*tert*-butylperoxy)-2,5-dimethylhexane. Thermal cleavage of dicumyl peroxide yields several by-products involving methane, acetophenone and cumyl alcohol. The curing of the extruded insulation is usually performed at high pressures in the range of 12–20 bar to avoid the formation of voids from such gaseous by-products. During the production of cables, the XLPE-based insulation is kept in a fan-forced oven at elevated temperature (70 °C) to remove the majority of these by-products (particularly methane, which is highly flammable and forms explosive gas mixtures with air) [39].

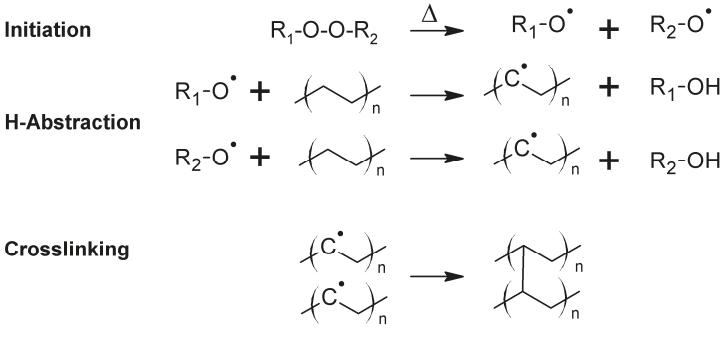

Figure 6. Thermal curing of PE with organic peroxides. Redrawn and adapted from reference [45].

Another well-established approach involves the crosslinking of a chemically modified PE in the presence of a catalyst and moisture after the extrusion process (Figure 7). The chemical functionalization of the PE is carried out by grafting vinyl silanes onto the polymer chain during the extrusion process. Small amounts of an organic peroxide are added to facilitate the grafting process [46]. Modified PE

grades, which are produced by copolymerizing ethylene and 3-vinyltrimethoxysilane, are commercially available [47]. After the extrusion of the modified PE, the cables are stored in a water bath at high temperatures or in a steam chamber to induce the crosslinking reaction. The crosslinking reaction, which involves a hydrolysis reaction followed by a condensation of the generated silanol groups, is catalyzed by dibutyltin dilaurate.

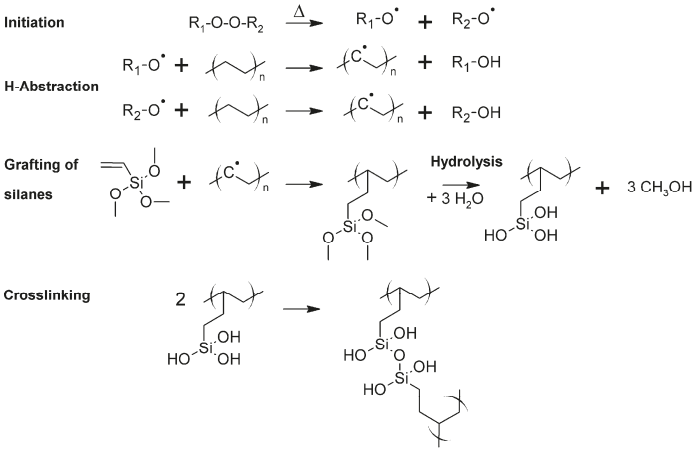

Figure 7. Thermal curing of PE with siloxanes. Redrawn and adapted from reference [48].

In addition, crosslinking of LDPE is also obtained under high energy radiation such as electron beam and gamma radiation generated from a Co^{60} source [49–51]. The crosslinking is based on a free-radical mechanism involving the extraction of a hydrogen atom from the polymer chain by the accelerated electrons or by the electromagnetic wave (Figure 8). Polymer radicals are formed, which recombine under the formation of a covalently bound crosslink site. In order to increase the degree of crosslinking, sensitizers such as acrylates may be added to the polymer. The radiation induced crosslinking is carried out after the extrusion of the insulating layer at ambient conditions. Aiming to avoid a rapid temperature increase during crosslinking, the extruded cables are passed through the electron beam of electron radiation over several cycles until the targeted exposure dose has been reached. In general, crosslinking of PE with high energy radiation has the disadvantage of high processing costs, as special radiation sources at high investment costs are required.

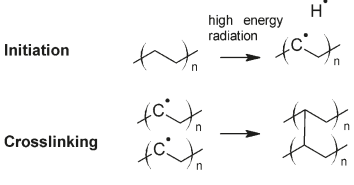

Figure 8. Crosslinking of PE with high energy radiation. Redrawn and adapted from reference [52].

3.3. Power Cable Insulations Based on Other Classes of Polymers

Along with XLPE, ethylene-propylene rubbers have been the most popular dielectric materials in extruded cables over the last decades [39]. They can be divided into two main classes: (*i*) ethylene-propylene rubber (EPM or also EPR) as a copolymer of ethylene and propylene and (*ii*) EPDM as terpolymer, which consists of ethylene, propylene and diene components such as dicyclopentadiene, ethylidene norbornene, and/or vinyl norbornene.

EPR is a fully saturated and nonpolar polymer with high temperature stability and high resistivity towards oxidation and polar solvents. EPR congeners with a low ethylene content are amorphous and easy to process but typically have inferior mechanical properties. In contrast, EPR types with a high ethylene content are semi-crystalline and have improved mechanical properties. Similar to LDPE, EPR may be crosslinked with organic peroxides [53,54].

EPDM has a fully saturated polymer backbone but additionally comprises unsaturated carbon-carbon bonds in the side-chains, which change the reactivity of the polymer in crosslinking reactions. In addition to curing with peroxides, EPDM can be also cured by sulphur vulcanization involving the unsaturated carbon-carbon bonds. While the electrical properties of sulphur- and peroxy-crosslinked EPDM are comparable, it was demonstrated that sulphur-cured EPDM insulations show poor performance after long-term immersion in hot water. In extruded EPM or EPDM insulations, the polymer content is typically in the range of 50%, as a high amount of inorganic fillers (e.g., clay, talc, silica, and alumina) is added to yield smooth surfaces and sufficient mechanical strength of the final insulation.

4. Nanocomposites for Power Cable Insulations

In order to tune the electrical and mechanical properties of extruded polymers, the addition of selected nanosized inorganic and organic fillers has gained increased attraction. These so-called nanocomposites benefit from (*i*) the low weight, (*ii*) the easy processing and (*iii*) shaping of the polymer matrix as well as (*iv*) the salient properties of the incorporated nanoparticles, which are substantially different to their micrometer-scaled counterparts. At a given volume, nanosized fillers have a distinctively larger surface area than microsized ones. As the chemical and physical properties of composites are strongly influenced by the interactions between the filler and the polymer matrix, nanofillers yield different properties than macroscopic particles of the same chemical and morphological composition. This effect is also exploited in the cable industry and numerous studies have been reported on the production, characterization and performance of nanocomposites as dielectrics in cables [14,33,55,56]. The following section gives a short summary describing the types of nanofiller and the preparation of nanocomposites following 'bottom up' and 'top down' processes (Figure 9).

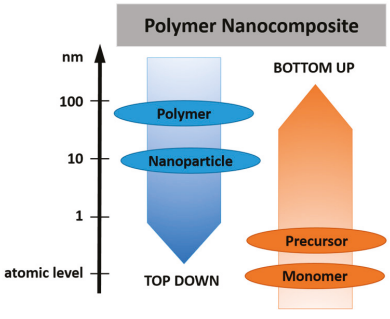

Figure 9. Differences between 'bottom up' and 'top down' processes used in the preparation of polymer nanocomposites.

4.1. Fillers Used in Nanocomposites

It is well known that the high aspect-ratio of nanofillers mainly contributes to their reinforcing efficiency. Depending on the geometry of the particles, three main types of fillers are distinguished (Figure 10): (*i*) (spherical) particles, (*ii*) fibers and (*iii*) platelets [57,58]. In terms of fibers and platelets, the (surficial) area-to-volume ratio is mainly governed by the first term (2/r and 2/t) of the equation, while in nanomaterials, the influence of the second term is negligible. Thus, a change of the

particle geometry from the micro- to nanometre size changes the area-to-volume ratio by three orders of magnitude.

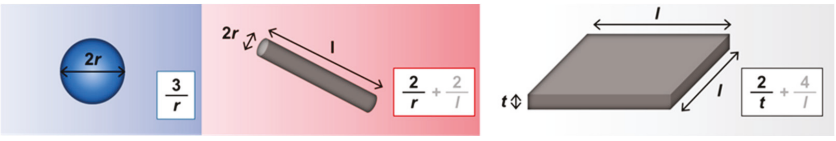

Figure 10. Three main types of nanofillers (from left to right: spherical particles, fibers and platelets), classified by their geometry and area-to-volume ratio. Redrawn and adapted from reference [57].

Along with the geometry, nanofillers may also be classified either by their chemical and morphological structure or by their origin (natural versus synthetic and organic versus inorganic) as shown in Table 1.

The properties of nanocomposites are not only influenced by their geometry and type but also by the dispersion of the filler in the polymer matrix. Nanofillers tend to agglomerate during the preparation of nanocomposites, which compromises the electrical, mechanical and optical properties of the final material [59]. In order to improve the dispersion of the particles in the polymer matrix and to ensure an enhanced bonding between the particles and the polymer matrix, surface modification of the particles is often carried out [60].

Table 1. Examples of different types of nanofillers classified by their origin (Adapted from reference [61]).

Origin		Selected Examples of Nanofillers
natural	animal	silk, wool, hair
	mineral	asbestos
	cellulose	wood, seed, leaf, fruit, stalk, bast
synthetic	inorganic	*oxides:* TiO_2, SiO_2, Al_2O_3, ZnO, MgO, Sb_2O_3 *hydroxides:* $Al(OH)_3$, $Mg(OH)_2$ *metals:* Al, Au, Ag, B, Sn, Cu, steel *silicates:* talc, mica, nanoclay, kaolin *salts:* $CaCO_3$, $BaSO_4$, $CaSO_4$ *carbides:* SiC *nitrides:* AlN, BN
	organic	*carbon based materials:* graphite fibers, nanotubes, carbon black, graphene *natural polymers:* cellulose and wood fibers, cotton, flax, starch *synthetic polymers:* aramid, polyester, polyamide, poly(vinyl alcohol) fibers

4.2. Methods for the Preparation of Nanocomposites

Over the last years, four main routes have been established for the successful incorporation of inorganic nanofillers into a polymer matrix: (*i*) direct mixing of polymer and filler, (*ii*) intercalation based on the exfoliation of, for example, layered silicates, (*iii*) sol-gel processes and (*vi*) in-situ formation of nanofillers in the polymer matrix [59,62,63]. The simplest route involves a direct mixing of the nanoparticles in the polymer, above the glass-transition temperature T_g or the melting point T_m of the polymer (melt-compounding method). Alternatively, the direct mixing can be also carried in a polymer solution (solution-mixing method). After evaporation of the solvent, the fillers are well distributed in the polymer matrix. Direct mixing is a typical top-down process, which means that energy is used (i.e., mixing energy) to transform a bulk material in smaller fragments until a nanocomposite is obtained (Figure 11) [64,65].

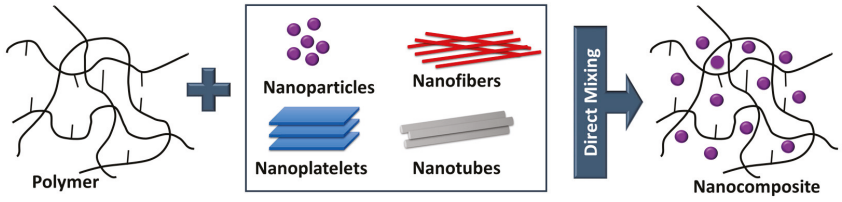

Figure 11. Preparation of nanocomposites by direct mixing.

Another top-down process is the intercalation involving the exfoliation of layered silicates (Figure 12). Three different methods are typically pursued: (*i*) direct intercalation of polymer chains from solution, (*ii*) polymer melt intercalation and (*iii*) intercalation of monomers followed by in-situ polymerization [66].

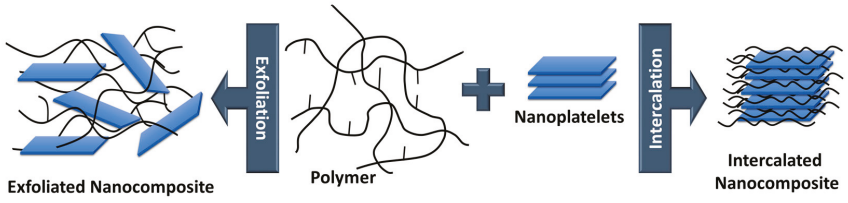

Figure 12. Preparation of nanocomposites by exfoliation and intercalation. Redrawn and adapted from reference [67].

Regarding the direct intercalation of polymer chains from solution, the layered fillers (typically nanoclays) are dispersed into a solvent in which the polymer is soluble [68,69]. The solvent migrates through the layers of the filler to start the exfoliation. After evaporation of the solvent, single clay platelets are well dispersed in the polymer matrix. With respect to melt intercalation, the layered fillers are directly mixed with the polymer melt. Due to shear forces, the exfoliation of the platelets starts and, if the surface polarities of filler and polymer are similar, the polymer chains migrate into the interlayer space. In terms of intercalation of monomers followed by in-situ polymerization, monomers and selected initiators are employed [69]. The monomers intercalate into the layered filler and increase the distance between the layers. Subsequent polymerization of the monomers leads to an exfoliation of the filler and polymer-based nanocomposites are yielded.

The sol-gel process is a prominent example of a bottom-up approach, which involves the building of the targeted material by the assembly of building units (e.g., atom-by-atom or cluster by cluster) [68,70]. The sol-gel process relies on two subsequent reactions steps (Figure 13). In the first step, metal oxides are obtained from the hydrolysis of organic metal alkoxides or esters yielding a colloidal suspension of solid particles in a liquid phase (sol). In a second step, the hydrolyzed intermediates start to condensate forming an interconnected network (gel) between the particles.

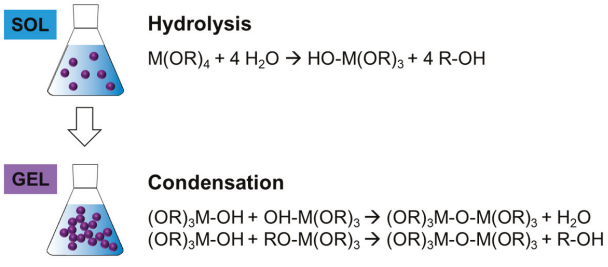

Figure 13. Preparation of nanocomposites by sol-gel processes. Redrawn and adapted from reference [71].

The fourth method involves the in-situ generation of nanoparticles from metal ions by redox reactions, which can be stimuli-triggered by a change of the pH value or by UV light (Figure 14). The in-situ generation of the nanoparticles is usually carried out in conjunction with an in-situ polymerization using colloidal sols with metal ions and monomers. This approach is typically employed to obtain nanocomposites from thermosetting resins such as epoxides or photocurable resins such as acrylates [72–74].

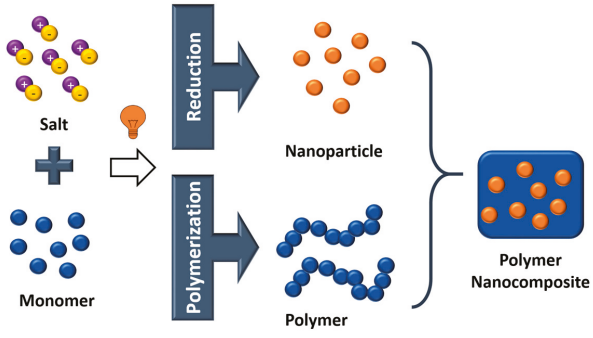

Figure 14. Preparation of nanocomposites by UV-induced in-situ generation of nanoparticles and in-situ polymerization of a photoreactive monomer.

4.3. Surface Modification of Fillers to be Used in Nanocomposites

The homogeneous dispersion of nanosized fillers within the polymer matrix has major influence on the final properties of the nanocomposites [59]. In particular, the surface modification of inorganic particles has become a popular route to avoid agglomeration and cluster formation of nanofillers, since the attachment of functional groups on the particles' surfaces enables the controlled change of polarity and reactivity of the particles' surfaces. A typical example is the surface modification of carbonates or silicates with hydrophobic fatty acids to improve the dispersibility in non-polar polymer matrices such as polyolefins [75]. Besides the dispersibility, the particle-polymer interfaces can be tailored by incorporating functional groups on the fillers' surfaces. As the particle-polymer interface has a crucial influence on the performance of the corresponding nanocomposites, surface modification techniques have gained increased attention for tuning the mechanical and electrical performance of polymer nanocomposites [76–79]. Pallon et al. [80] applied functional silsesquioxane coatings on MgO nanoparticles and incorporated the functional filler in LDPE. They demonstrated that the modified particles were homogenously distributed within the polymer matrix and, by adding only 3 wt % of the surface-treated particles, the volume conductivity was decreased by two orders of magnitude. For the modification of inorganic particles, different strategies are pursued involving (*i*) chemical treatment, (*ii*) grafting reactions and other methods such as (*iii*) adsorption of polymeric dispersants [81].

The typical chemical surface modification reaction proceeds in one step using bifunctional organic compounds with one group that reacts with the nanoparticles' surfaces and a second group, which represents the functionality of the organic shell. One well-established approach is the so-called silanization, in which functional trialkoxysilanes such as 3-aminopropyl triethoxysilane are covalently attached to surficial hydroxyl groups of inorganic particles (e.g., SiO_2, TiO_2, Al_2O_3, ZnO, Fe_3O_4) by condensation reactions (Figure 15) [82,83]. In terms of carbon-based nanofillers such as carbon black, fullerenes, carbon nanotubes or graphene, Diels-Alder reactions can be employed to change the surface characteristics of the particles [84]. If the functional groups of the organic compound are not compatible with the synthetic process, a step-wise procedure may be carried out for the modification of inorganic particles [85].

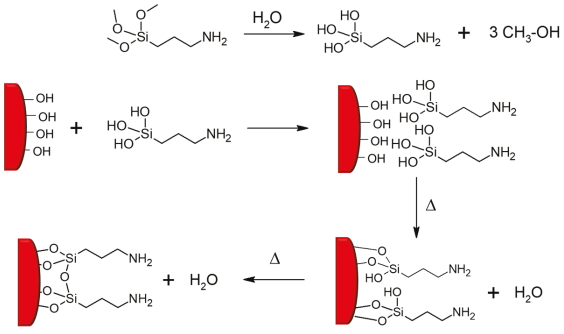

Figure 15. Covalent attachment of functional silanes on nanosized silica. Redrawn and adapted from reference [86].

Grafting reactions represent another route to modify the surface of inorganic particles (Figure 16) [86]. The grafting mechanism involves either (*i*) direct coupling of a polymer chain onto the particle surface ('grafting onto' reactions) or (*ii*) immobilization of a monomer or an initiator on the particle surface, which is followed by a polymerization of reactive monomers ('grafting from' reactions).

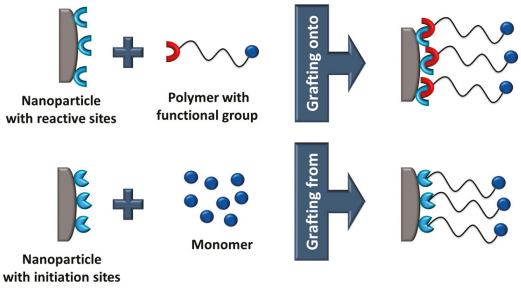

Figure 16. Modification of nanoparticles via (*i*) 'grafting onto' and (*ii*) 'grafting from' reactions.

A convenient method for surface modification of inorganic nanoparticles involves the physical adsorption of polymeric dispersants, which is typically used to enhance the dispersion stability of nanoparticles in solvents [87,88]. The improved dispersion properties mainly rely on the steric repulsive forces between the adsorbed polymer chains and the related increase in surface charges.

5. Electrical Conductivity of Nanocomposites

5.1. General Aspects of Electrical Conduction

Electrical conductivity is an intrinsic property that quantifies the ability of materials to conduct electric current [89,90] and can be classified in three major categories: (*i*) *intrinsic conductivity:* charge carriers are generated based on the chemical structure of the material; (*ii*) *extrinsic conductivity:* charge carriers are generated by impurities, which can be introduced during the fabrication process or by dopants through specific methods; (*iii*) *injection-controlled conductivity:* charge carriers are injected into the material through the interface between the metallic electrodes and the non-metal material.

Regarding insulators, the charge carriers' origins for intrinsic and extrinsic conductivities are not well distinguished; in polymeric insulators, the situation is even less well characterized and understood. Some polymeric materials such as PE can be considered as natural nanodielectric material with contrasting conductive crystallites and resistive amorphous regions of nanometric dimensions [91], as it was described in Section 3 (Figure 17).

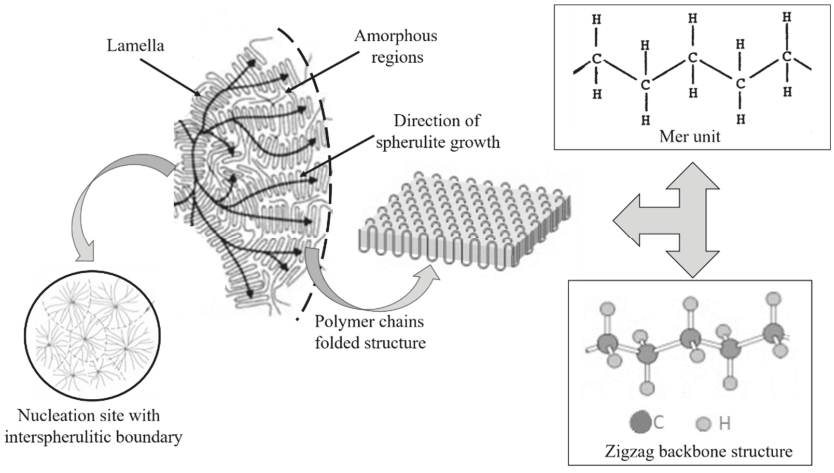

Figure 17. The morphological structure of PE. Redrawn and adapted from reference [92].

In the crystalline phase of PE, intrinsic conduction is improbable due to the large band gap of approx. 8 eV and the corresponding separation of electrons and holes [91]. Excluding any material defects caused by impurities, conduction in PE can only originate from extrinsic charges introduced by the injection process. Hole conduction commonly appears in PE, which suggests that hole injection at the anode occurs more easily compared to the electron injection at the cathode [91]. However, the crystalline regions in PE are surrounded by amorphous regions and the transfer of electrons and holes between them is likely to be hindered. Holes enclosed to the valence band will move along the crystallites' chain paths and will become trapped in the interphase between them and the amorphous regions. However, the transition of holes through this interphase will occur by tunnelling due to a super-exchange between donor and acceptor hole traps [91]. Amorphous regions in PE are considered to have high concentrations of traps introduced by impurities and additives, which may be polarized and maybe even move through them. Hence, extrinsic conduction (ionic transport) is more likely to occur in the amorphous phase [93].

Lewis et al. [91] concluded that the incorporation of oxide nanoparticles in PE causes a strong decrease of the local hole inter-lamella transition rate. They assumed that the tunnelling of holes between lamellae through the amorphous phase in the neighborhood of a particle was strongly influenced by the embedded particle and its surrounding interface. The magnitude of affected transitions, which would lead to macroscopic decrease of mobility and conductivity, would depend on the concentration of nanoparticles embedded within the polymer matrix. In agreement with this conclusion, several experimental results regarding the electrical conductivity of thermoplastic nanocomposites based on polyethylene used as power cables insulation will be presented in the following sections.

5.2. Conductivity of Nanocomposites Based on Polyethylene (PE)

The incorporation of various oxidic nanoparticles (e.g., Al_2O_3, SiO_2, TiO_2, MgO, ZnO, etc.) in PE delivers advantages such as a significant reduction in electrical conductivity for a certain range of nanoparticle concentrations (usually between 0 and 5 wt %). This reduction reflects the ability of the polymer matrix to incorporate the nanoparticles within the inter-lamellae spaces. Above this limit, the excess of nanoparticles is likely to be incorporated in inter-spherulite regions, which does not directly influence the hole conduction from inter-lamellae crystallites [91].

Hoang et al. [94] analyzed the bulk conductivity of LDPE and its nanocomposites with uncoated magnesia (MgO) and alumina (Al_2O_3). The investigations were performed on thin films prepared

by thermal extrusion at 150 °C from a dried powder mixture of LDPE, nanoparticles and antioxidant (0.02 wt % of Irganox 1076). Two types of nanocomposites based on LDPE filled with 1 and 3 wt % of Al_2O_3, as well as five types of LDPE filled with 0.1, 1, 3, 6 and 9 wt % of MgO were prepared. The DC conductivity measurements were carried out at an applied electric field of approximately 30 KV·mm^{-1}, for 11 h. The measurements were conducted at isothermal conditions (room temperature, 40 and 60 °C) by placing the electrode system with the sample inside to a grounded oven (Figure 18a). DC conductivity values were computed from the charging current data registered during 11 h of measurements (Figure 18b). The results on LDPE samples agreed with the data reported in literature [95]. In the case of LDPE/Al_2O_3 samples, the reduction in DC conductivity was proportional with the filler concentration increasing up to 3 wt %. For nanocomposites based on LDPE and MgO, a threshold-like behavior was observed around a nanofiller content of 3 wt % (Figure 18b). If the filler concentration exceeded 3 wt %, further loading with nanoparticles caused a negative effect. This change in the electrical conductivity behavior can be explained by the agglomeration of nanoparticles in the polymer matrix during the manufacturing of the samples [94]. This effect was also reported by Ishimoto et al. [96], Masuda and Murakami et al. [97,98], who described a decrease of electrical conductivity of more than one order of magnitude and a threshold of nanofillers content of approximately 2 wt %.

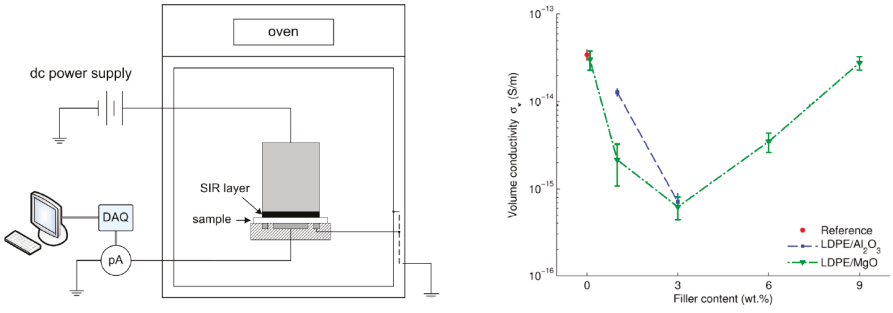

Figure 18. (**a**) Schematic representation of the test setup for DC conductivity measurements; (**b**) Variations of the DC conductivity with the filler concentration of the analysed nanocomposites. Reprinted from reference [94].

Pleşa analyzed the absorption currents and computed the relative DC volume resistivity of nanocomposites based on LDPE with different types of inorganic nanofillers (SiO_2, TiO_2, Al_2O_3) and various concentrations (2, 5 and 10 wt %) [99]. For better compatibility and dispersion of nanoparticles within the polymer, the surface of the nanofillers was treated with maleic anhydride. All measurements were performed at ambient temperature of 27 °C and relative humidity of approx. 50% (Figure 19). Noteworthy, the absorption currents decrease over time as a result of the reduction of the charge carrier's concentration corresponding to bound charges (electric dipoles) and space charge. On the other hand, according to the nanocomposite models presented in literature [100–102], the introduction of nanoparticles into the polymer facilitates an increase in the concentration of the electric dipoles (i.e., especially inside the nanoparticles and/or inside the polymer-nanoparticle interfaces) and also an accumulation of space charge due to the huge area of polymer-nanoparticles interfaces. In this case, polarization and space charge components of absorption currents increase with enhanced concentration of nanofillers, except for LDPE with 2 wt % of nano-TiO_2 that showed lower values compared with all the other types of analyzed materials (Figure 19a,b).

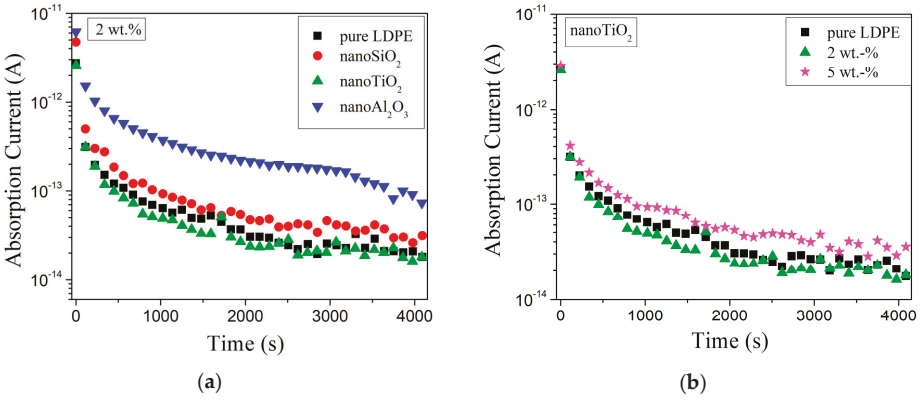

Figure 19. Variations of absorption currents on time for: (**a**) LDPE nanocomposites with 2 wt % of different types of inorganic nanofillers and (**b**) LDPE nanocomposites with 2 and 5 wt % of nano-TiO_2. Reprinted, with permission by the author, from reference [99].

In order to explain the variations of the currents, models of the nanocomposites' structure were used. Starting from the structural models proposed by Tanaka et al. [100] as well as Lewis [103], a new model for nanocomposites based on LDPE with spherical inorganic fillers was developed (Figure 20) [99]. It was considered that the interface was formed by three distinct regions: a bonded first layer, a bound second layer and a loose third layer, with an electric double layer overlapping these three layers. The polymer is in an intimate contact with the nanoparticle surface within the first layer, while the second layer represents an interfacial region. The third layer interacts superficially with the second layer and the properties of this region are supposed to be similar to the polymer matrix.

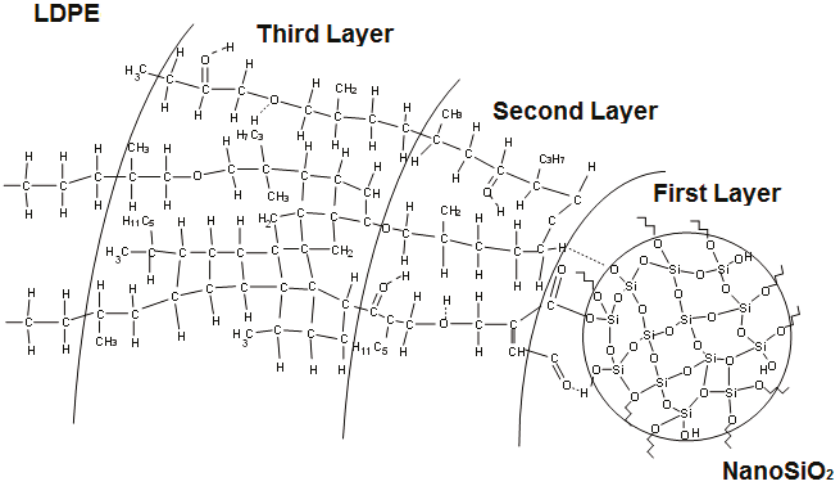

Figure 20. Schematic representation of an interfacial LDPE-nano-SiO_2 structure. Reprinted, with permission by the author, from reference [99].

In case of LDPE nanocomposites with 2 wt % of nano-TiO_2, a decrease of absorption currents compared to unfilled LDPE values was registered (Figure 19a). This behavior could be explained by the presence of crosslinked polymer in the third layer of the polymer-nanoparticle interface, which reduces the mobility of space charges through the material structure and may lead to a decrease of the space

charge component of the absorption current values. Between the end groups of the polyethylene chains from the second layer of the interface and the surface of the functionalized inorganic nanoparticles, hydrogen bridges are formed that reduce the mobility of polymer chains and decrease the polarization component of the absorption current. Tanaka et al. [100] stated that within the intermolecular regions of the interface layers, the introduced traps were distributed as follows: deep traps in the first and second layer and shallow traps in the third layer. By increasing the filler concentration over a certain limit (i.e., >2 wt % in the case of LDPE/nano-TiO_2) inside the polymer matrix, the overlapping zone of filler-polymer interfaces increases, too (i.e., similar with the model presented in Figures 20 and 21a,b). By applying an electric field, the electrical conduction can occur either by charge carriers jumping on the shallow traps from the interfaces, overlapping the neighbor nanoparticles or by tunnelling [99], when the distance between the traps is below the minimum threshold tunnelling, leading, in overall consequence, to an increase in space charge components of the absorption currents (Figure 19b).

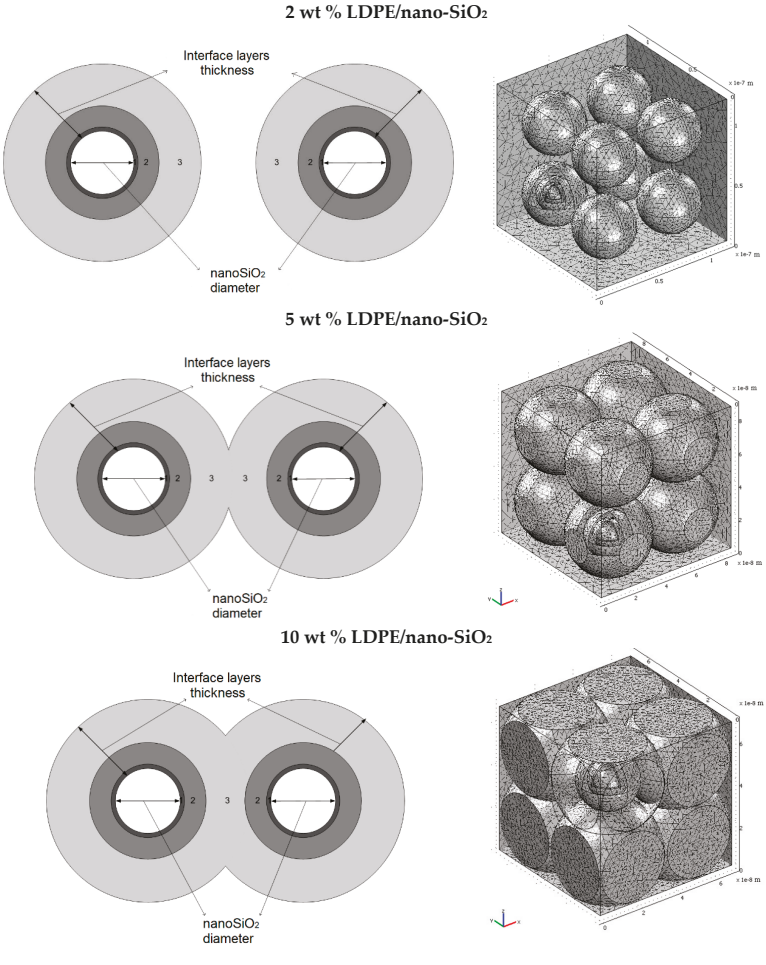

Figure 21. (**a**) Two neighbor nanoparticles within LDPE composites for different filler contents; (**b**) 3D electrostatic model of nanocomposites based on LDPE with nano-SiO_2 in different concentrations. Reprinted, with permission by the author, from reference [99].

The volume resistivity can be calculated according to Equation (1):

$$\rho_v = \frac{S}{d} \cdot \frac{U}{I} \quad (1)$$

in which ρ_v is the volume resistivity (Ω·m), S the electrode surface (m^2), U the applied voltage (V), I the average current after 4000 s starting from the voltage application (A) and d the sample thickness (m). It was observed that the resistivity values depend on the type and concentration of nanoparticles and decrease compared to unfilled LDPE (Table 2). With respect to LDPE with 2 wt % of nano-TiO_2, the DC relative volume resistivity increases by 0.07 percent points compared to unfilled LDPE.

Table 2. DC relative volume resistivity of nanocomposites based on LDPE with 2 (or 5) wt % of different types of inorganic fillers. Adapted with permission by the author from reference [99].

Nanocomposite (Type of Filler)	Filler Content (wt %)	DC Relative Resistivity
Pure LDPE	0	1
LDPE/nano-SiO_2	2	0.54
LDPE/nano-Al_2O_3	2	0.16
LDPE/nano-TiO_2	2	1.07
LDPE/nano-TiO_2	5	0.33

In order to increase the DC electrical properties of XLPE insulation materials, Yan et al. prepared nanocomposites based on XLPE with different loadings of carbon black (CB) by the melt-blending method [104]. The space charge distribution was analyzed together with the dependence of DC electrical conductivity γ on the electric field E at several temperatures T (Figure 22). For low electric fields, a non-linear dependence of γ and E exists, concomitant with a significant increase in conductivity with increasing T. For $E < 20$ kV·mm^{-1}, the electrical conductivity of XLPE/CB is almost constant; however, if the temperature increases over 30 °C, $\gamma(E)$ decreases. This study shows that the presence of CB in XLPE can inhibit the space charge accumulation and the electric field distortion, improving the DC conductivity of XLPE/CB nanocomposites.

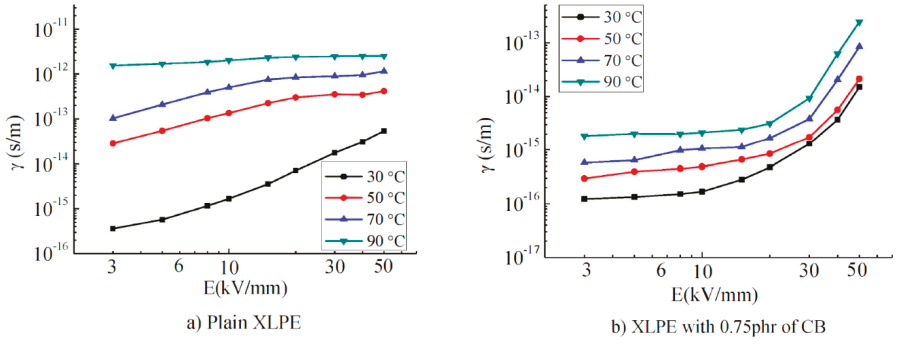

Figure 22. *Cont.*

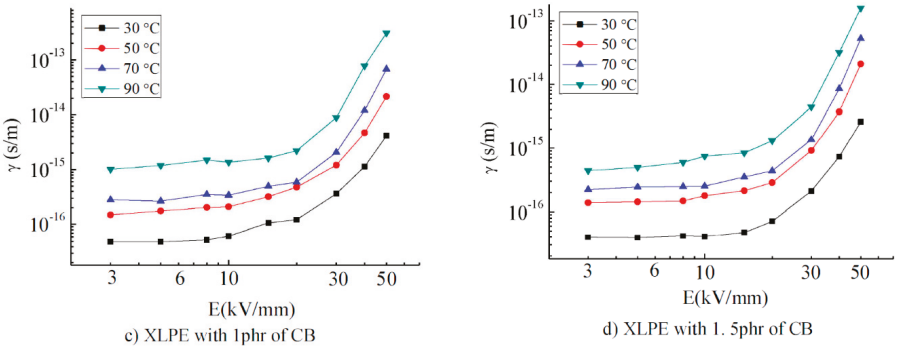

Figure 22. Electrical conductivity [γ(S/m)] variations of XLPE and CB/XLPE nanocomposites at different temperatures. Reprinted, with permission by IEEE, from reference [104].

The correlation of the electrical conductivity with the content of nano-SiO_2 particles in XLPE was analyzed by the CIGRE Working Group D1.24 [105]. It was concluded that the addition of fumed nano-SiO_2 to XLPE reduced the DC conductivity of the nanocomposites. This behavior supports the mechanism describing nanofillers as charge carrier traps; it may be argued that functionalization may strengthen their function. Wang et al. [106] analyzed the electrical resistivity of nanocomposites based on XLPE containing different concentration of nano-TiO_2 (i.e., 1, 3 and 5 wt %). It was found that their volume resistivity was higher compared to pure XLPE and increased with the filler concentration. This behavior was referred to the large number of traps introduced in nanocomposites by the fillers, which capture the charge carriers and prevent the movement of carriers within them. Murata et al. [107] investigated the volume resistivity and space charge distribution in nanocomposites obtained by mixing XLPE with MgO nanofillers. Four types of materials were analyzed: conventional XLPE insulation for AC cables ($XLPE^C$), nanocomposites obtained by mixing $XLPE^C$ with nano-MgO ($XLPE^C$/MgO), a special type of XLPE with a lower degree of crosslinking by-products compared to $XLPE^C$ ($XLPE^S$) and nanocomposites obtained by mixing $XLPE^S$ with nano-MgO ($XLPE^S$/MgO). It was concluded that the presence of by-products (that decrease the volume resistivity) and of nano-MgO (that increases the volume resistivity) acted synergistically within XLPE-based nanocomposites, converting them into excellent materials for DC power cables insulation.

According to the experimental studies presented herein above, two types of PE-based nanocomposites are recommended for power cables, those with low conductivity for insulations (including inorganic particles) and those with increased conductivity for semiconductor layers (including carbon black fillers).

6. Permittivity and Loss Factor of Nanocomposites

6.1. General Aspects of the Complex Dielectric Permittivity

Synthetic polymers are complex molecules comprising a huge number of covalently bound atoms within the macromolecular chains, yielding numerous possible conformations of the individual macromolecular chains in space and time [108]. Due to this large number of conformations, most of the polymers have properties depending on the chain flexibility, the end-to-end vector of the chain, the mean-square dipole moment per molecule and so forth. Correspondingly, their behavior in solution and/or in solid state is analogously complex. Besides systems composed of linear macromolecules, a comprehensive variety of the molecular architectures additionally exists (e.g., branched and hyperbranched polymers, cyclic macromolecules and oligomers, polymers with star-shaped and comb-like structures, copolymers, dendrimers, etc.), which can cause new morphologies in the dense state of these molecules (i.e., phase- or microphase-separated structures).

Since Debye published the theory of dipolar relaxation in 1929 [109], the study of the interaction between electromagnetic radiation and (soft) matter, which is of crucial importance in fundamental and applied science, has been applied to dielectric spectroscopy. This experimental technique is very useful for studying the conformation, the structure and the dynamics of polymers (i.e., dipolar processes) and to evaluate the behavior of polymeric systems over a large range of frequencies and temperatures. Dipolar processes include *very low frequency processes* (i.e., electric charge transport), *Maxwell-Wagner polarization processes* (i.e., charge trapping at interfaces) and *relaxation processes* due to the motion of dipoles groups (i.e., dipole reorientation) [93].

For dielectric spectroscopy studies, one key parameter is the relative complex dielectric permittivity ε^* (Equation (2)) [108]:

$$\varepsilon^*(f) = \varepsilon'(f) - i\varepsilon''(f) \quad (2)$$

in which ε' represents the real part of complex relative permittivity and ε'' the imaginary part of the relative permittivity, the so-called loss part.

The complex relative permittivity is defined as a factor between an outer alternating electric field $\vec{E}(f)$ and the induced electric polarization P of the medium (Equation (3)):

$$\vec{P}(f) = \chi^* \varepsilon_0 \vec{E}(f) \quad (3)$$

in which $\chi^* = \varepsilon^*(f) - 1$ is the complex electric susceptibility of the material and $\varepsilon_0 = 8.85 \cdot 10^{-12}$ F·m^{-1} is the vacuum permittivity.

The complex relative permittivity is a material property depending on frequency, temperature, pressure and structure of the material. According to statistical mechanics, both quantities, namely ε' and ε'', have a physical interpretation: ε' is related to the energy stored reversibly within the material and ε'' is related to the energy dissipated within the material. In dielectric relaxation spectroscopy, the dissipation factor $\tan\delta = \varepsilon''/\varepsilon'$, in which δ is the phase angle between the applied voltage and the resulting electric current, is one parameter for the discussion of the electrical performance of polymer-based materials [108].

The addition of nanoparticles into polymers considerably changes the dielectric behavior due to the formation of interaction zones within the nanocomposites [93]. Correspondingly, there has been a steadily growing interest over the last two decades to analyse these materials, which are referred to as nanodielectrics in this context. In the following section, selected results are presented regarding the permittivity and loss factor of thermoplastic polymer nanocomposites used as power cables insulation (LDPE, XLPE, etc.).

6.2. Permittivity and Loss Factor of Nanocomposites Based on Polyethylene (PE)

A huge number of studies have reported improved dielectric properties of thermoplastic nanocomposites with inorganic nanoparticles compared to the unfilled polymer [69,110–116], which render these nanocomposite materials as interesting candidates for high-voltage applications. The dielectric behavior of thermoplastic nanocomposites systems based on LDPE containing different types and contents of nanofillers have been analysed and presented in the literature.

Pleşa et al. analyzed the behavior of unfilled LDPE and silica-filled LDPE samples [99]. Nanocomposites with different contents of nanofillers ranging from 0 to 10 wt % were prepared and characterized at different temperatures in the range from 300 to 350 K and frequencies from 10^{-2} to 10^6 Hz (Figure 23). The activation energy w_a was estimated, and correlations with the polarization mechanisms were found. The imaginary part of the complex permittivity ε'' was determined as the product of the real part of complex permittivity ε' and the loss factor $\tan\delta$. It was assumed that the conduction losses were substantially lower than the polarization losses by deformation and orientation. In the case of unfilled LDPE (Figure 23a), peaks in the frequency range from 10^1 to 10^3 Hz were

shifted to higher frequencies upon temperature increases. With an increasing concentration of SiO_2 nanoparticles in the polymer matrix (Figure 23b,c), a shift of the ε'' peaks towards lower frequencies as well as their intensification compared to the base polymer were observed. For example, in case of the nanocomposites containing 5 wt % of nanoSiO_2 (Figure 23b), the peaks were in the range of 10^{-1} to 10^{1} Hz. When the concentration of the nanoparticles was increased, the frequency domain into which the peaks shifted increased to 10^{3} Hz in the case of nanocomposites with 10 wt % of nano-SiO_2 (Figure 23c). Hence, the peaks occur at low frequencies in the range of 10^{-1} to 10^{3} Hz, a frequency range in which polarization losses by deformation are neglectable; it was concluded that the losses were caused exclusively by polarization losses from (re-)orientation.

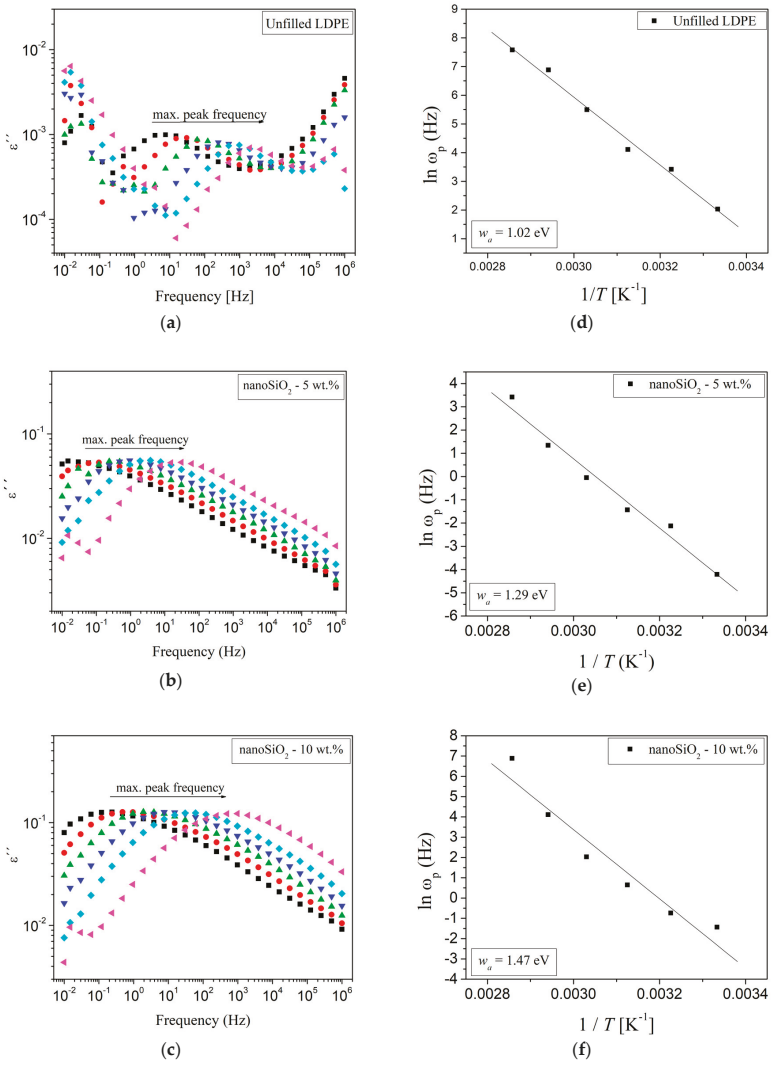

Figure 23. (**a**)–(**c**): Frequency variation of the imaginary part of the relative complex permittivity (ε″) of unfilled LDPE and filled with different concentrations of nano-SiO_2 at (■) 300 K, (●) 310 K, (▲) 320 K, (▼) 330 K, (♦) 340 K, (►) 350 K. (**d**)–(**f**): Dependence of the temperature function (ln $\omega_p(T)$) for unfilled LDPE and filled with different contents of nano-SiO_2. Reprinted, with permission by the author, from reference [99].

According to the Debye model for dipolar relaxation of ideal dielectrics, the imaginary part of the relative complex permittivity ε″ as a function of temperature T is defined by Equation (4):

$$\chi''(\omega) = \chi(0) \cdot f(\omega/\omega_p(T)), \quad (4)$$

in which $\chi(0)$ is a constant and $f(\omega/\omega_p(T))$, which describes the shape of the imaginary part of ε″ is a function of temperature T.

$f(\omega/\omega_p(T))$ can be defined according to Equation (5):

$$\omega_p(T) = A\ \exp(-w_a/kT), \tag{5}$$

in which w_a represents the activation energy corresponding to dipole relaxation, A is a constant and k the Boltzmann constant ($k = 1.38 \cdot 10^{-23}$ J·K^{-1}) [80].

A similar behavior of nanocomposites was reported in literature [117] and the relationship between the frequency and temperature at which the peak occurs was attributed to an Arrhenius-type behavior (Equation (5)). In the case of silica-filled LDPE nanocomposites (see herein above), the activation energy was determined using the Arrhenius-type equation (5) (Figure 23d–f).

The main relaxation in LDPE is α-relaxation attributed to the activation energy of dielectric relaxation (i.e., the orientation energy of the dipoles of the polymer chain and the segments of the polymer chain), which generally occurs at low frequencies. This activation energy is caused by dielectric relaxation and ranges between 1 and 1.5 eV [117]. The estimated activation energies of the silica-filled LDPE nanocomposites correlate well within this interval and increase with the nanoparticles content. If the nanoparticles concentration increases, more and more electrical dipoles will appear in the nanoparticles as well as in the polymer (main) chains and their lateral branches, resulting in more dipoles of the $Si^{\delta+} \rightarrow O^{\delta-}$ and $O^{\delta-} \rightarrow H^{\delta+}$ types within the three layers of the interface (Figure 20 and the model described in Section 5). These bonds are more flexible than the $C^{\delta+} \rightarrow O^{\delta-}$ bonds and involve the movement of large fragments from the PE chain. If the nanoparticle concentration is doubled, the relative permittivity of the LDPE/nano-SiO_2 nanocomposites should 'mathematically' as well increase by the factor of two. However, it has to be considered that the activation energy also increases with a rising concentration of nanoparticles (Figure 23d–f), thus the permittivity of LDPE/nano-SiO_2 nanocomposites is lower. The variation of ε'' as a function of frequency and temperature in the case of nanocomposites of LDPE/SiO_2 indicates the presence of an α-type relaxation process. This is confirmed by the shift of the peaks to higher frequencies with increasing filler concentrations and rising temperatures [108,111,118–120].

Another study by Pleşa et al. on LDPE/10 wt % nano-SiO_2 nanocomposites refers to the influence of moisture absorptionn and temperature treatment of the samples on ε' and tanδ (Figure 24a,b) [99]. The results revealed that the drying step at elevated temperature has a crucial influence on the frequency corresponding to the tanδ peak. In particular at 300 K, the frequency corresponding to the tanδ peak is increased by four orders of magnitude (from approx. 0.2 Hz to 2 kHz) if the sample was kept in hot air before the dielectric measurements were carried out (Figure 24b). This distinctive increase can be explained by the high number of hydroxyl groups ($O^{\delta-} \rightarrow H^{\delta+}$) on the surface of the nanoparticles (Figure 20 and the model described in Section 5). Hence, such types of nanoparticles are highly hydrophilic and contain adsorbed water molecules. These water molecules significantly influence the polarization phenomena even in very low concentrations [118]. Although LDPE is a hydrophobic material, the absorption of water molecules on the surface of SiO_2 nanoparticles is thermodynamically inevitable [121]. By grating LDPE with maleic anhydride MA, hydrogen bridges are formed especially within the first layer of the interface area (Figure 20 and the model described in Section 5) between MA and the nanoparticles, as well as between the nanoparticle and the end groups of the polymer chains from the second layer of the interface. The energy of a hydrogen bond in a water molecule is about 21 KJ·mol^{-1}; by storage of the nanocomposites samples at elevated temperatures before the measurements, the majority of adsorbed water molecules can be removed. Thus, the number of $O^{\delta-} \rightarrow H^{\delta+}$ interactions is significantly decreased. Under these conditions, the energy consumed due the (re-)orientation of dipoles is lower, which corresponds to a decrease of the loss factor and a shift of dielectric relaxation to lower frequencies (Figure 24a,b).

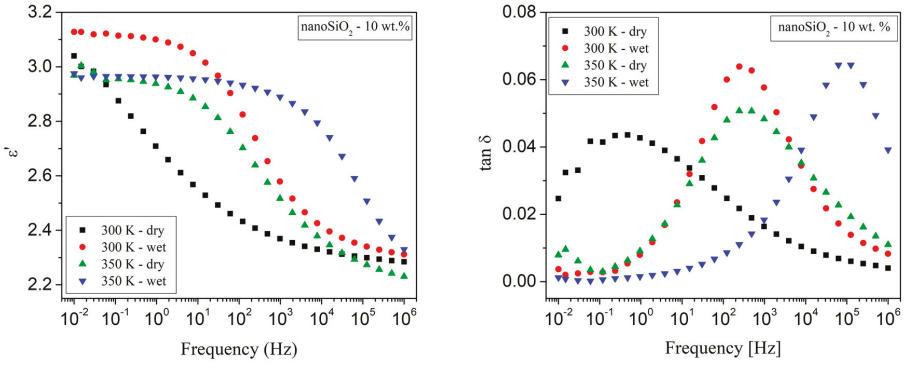

Figure 24. Frequency variation of (**a**) the real part of the complex relative permittivity and (**b**) the loss factor of LDPE/SiO_2 nanocomposites with 10 wt % filler content at 300 and 350 K. Reprinted, with permission by the author, from reference [99].

Nanocomposites based on crosslinked polyethylene XLPE and silica nanoparticles are promising candidates for future power cables insulation due their improved dielectric properties [69,105,110,122,123]. The influence of moisture on the dielectric properties of these nanocomposites, however, has not yet been fully explored. Humidity is well known to be detrimental to dielectrics, reducing the breakdown strength and increasing the losses [25–27].

Hui et al. [124,125] investigated the dielectric behavior of XLPE/silica nanocomposites in humid environments. Compared to the unfilled XLPE, nanocomposites containing silica particles were found to show increased moisture uptake due to filler inclusion. It was assumed that the dielectric behavior of wet XLPE/silica nanocomposites originated from the formation of water shells around the nanoparticles and the change of the inter-particle/cluster distances. The authors investigated unfilled XLPE as well as nanocomposites based on XLPE with unfunctionalized and vinyl silane-functionalized silica fillers (12 nm diameter) in concentrations of 5 and 12.5 wt %, respectively. A part of the samples was stored in humid environment for a month. Figure 25 a,b show the correlation of ε' with the frequency for this set of samples. In the case of 'dry' samples, the permittivity in the low frequency region is very low, which originates from a lack of mobile charges (Figure 25a) [126,127]. For frequencies in the range from 10 to 100 kHz, an increase of the permittivity can be observed, which can be attributed to residual water [126,128,129]. In the case of wet samples (Figure 25b), loss peaks can be observed for nanocomposites with 5 wt % silica nanoparticles at frequencies in the range from 1 to 10^5 Hz, and for unfilled XLPE in the range from 10^3 to 10^5 Hz, which can be attributed to water molecules present in the material. As silica nanoparticles have hydroxyl groups on their surfaces, they are likely sites to bind water; XLPE, on the other hand, is a non-polar material, in which the water molecules are more likely to be present in the amorphous regions, and the movement of dipoles can be inhibited by the structure of the polymer chains. Correspondingly, water present in XLPE triggers delayed dielectric relaxation. For the wet nanocomposites with 12.5 wt % of silica fillers, the significant increase of the real and imaginary permittivity at low frequencies might be explained by quasi-DC behavior [130] due to the ionic charge carriers [127].

When XLPE-based nanocomposites are exposed to humid environments, moisture is likely to dominate their dielectric behavior. Hui et al. observed that nanocomposites based on XLPE with 12.5 wt % silica absorb large amounts of water compared to unfilled XLPE and nanocomposites with 5 wt % of nanoparticles from the same humid environment [124,125]. This observation was assumed to originate from the percolation of water shells due to the higher concentration of nanoparticles and the correspondingly decreasing distance between them.

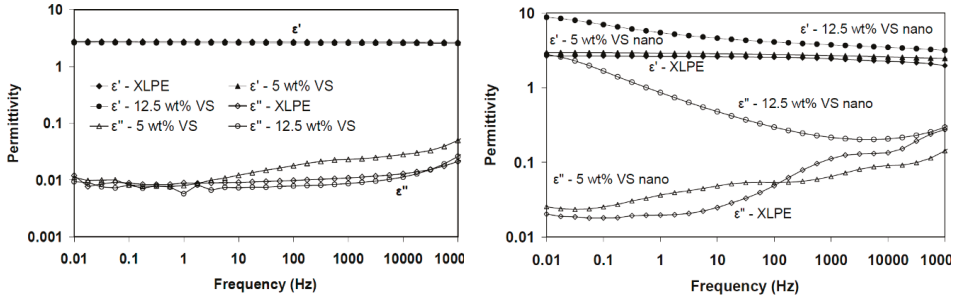

Figure 25. Correlation of permittivity and frequency for (**a**) dry and (**b**) wet samples of unfilled XLPE and nanocomposites filled with 5 and 12.5 wt % of vinyl silane-functionalized silica nanoparticles (storage of the 'wet' samples at 50 °C and 100% r.h.). Reprinted, with permission by IEEE, from reference [124].

Numerous studies on the dielectric behavior of thermoplastic nanocomposites systems based on PE congeners like LDPE, HDPE and XLPE and different types (organic or inorganic) and concentrations of filler, usually between 0 and 10 wt %, were performed until present [14,131]. The most important question to be answered is whether or not the relative permittivity and loss tangent are reduced at the industrially relevant frequencies in nanocomposites, which could transform them into suitable candidates for power cables insulations. In literature, some reported data indicate the reduction of these parameters to certain extent, whilst other publications report the contrary [14]. These results can depend on many factors, such as how the particles were compatibilized or how the fillers were dispersed in the polymer, if the fillers agglomerated or not and so forth. Parameters such as humidity, temperature and so forth, have a significant effect as well.

7. Partial Discharges in Nanocomposites

7.1. Partial Discharges and Measurement Thereof

A partial discharge PD is a localized breakdown of a small portion of a solid or liquid electrical insulation between two conductors under high voltage stresses, which does not bridge the space between the conductors [132]. PDs occur inside cavities, cracks and/or gaseous inclusions inside solid insulations and at conductor-dielectric material interfaces in solid and liquid insulations. PDs with longer lengths deteriorate the insulation characteristics due to erosions of cavity walls by charge carriers, increases of the local temperature, radiation generated by atomic excitation and charge carrier recombination, intensification of the chemical degradation reactions, initiation of new chemical reactions and so forth. [133]. A general overview of erosion processes in thin polymer insulation under partial discharges is presented by Tanaka et al. [134].

The initiation and development of PDs depend on both, the shape and dimension of the cavities as well as the chemical nature and cavity gas pressure. On the other hand, electrical charges deposited by PDs on the cavity surfaces diffuse into the dielectrics (in the areas adjacent to the cavities) and form so-called space charge clouds, which dissipate slowly and change locally the distribution of the electric field.

For the characterization of PDs, several variables are used, such as the PD inception voltage U_i and the PD extinction voltage U_e, the PD pulse repetition frequency n (average number of pulses in one second), the apparent charge q associated to the PD, as well as other derived quantities such as the apparent energy W, the average discharge power P, the average discharge current I, the quadratic rate D and so forth. [135,136]. For the study of the PD's action on solid insulators, different types of set-ups are used, including comparably simple ones (Figure 26) that consist of a rod electrode from a tungsten

wire with rounded tip, which is connected to the high-voltage terminal of an AC supply and a plane electrode of copper or steel that is connected to the ground, respectively to the supply terminal; the plain sample to be analysed is placed between the two electrodes (Figure 26a) [137–139].

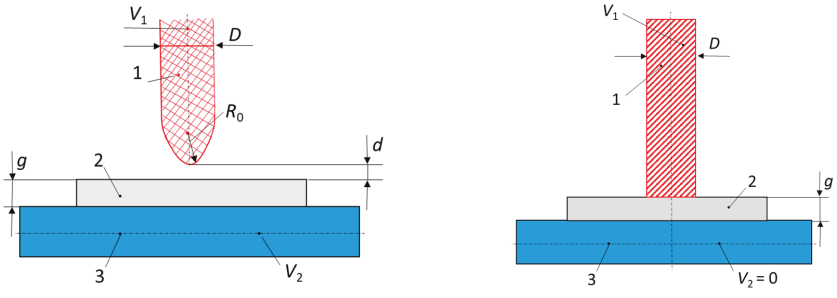

Figure 26. (**a**) Rod-plane electrode configuration for partial degradation tests: 1: Rod electrode; 2: Specimen; 3: Plane electrode; (**b**) Rod-plane electrodes system (similar to IEC Electrode) for surface erosion by PDs.

Charge carriers erode the surface of the sample and the depth of the pits, the compounds formed on the eroded areas and the light emitted by the PD are parameters to quantify a sample's resistance to PDs [139]. Experiments show that the PD initiation voltage decreases for larger cavities, while the maximum lengths, apparent energy and discharge power increase [140,141].

Considering the harmful effect of PDs, in the case of high and very high voltage cables insulation, restrictions are imposed on cavities dimensions and concentrations, such that their apparent charge does not exceed certain limits. For example, for a U_o = 110 kV voltage cable and a crosslinked polyethylene insulation, the apparent charge measured at a voltage of $U = 1.5\ U_o$ should not exceed 10 pC. On the other hand, PDs may occur at high voltage cable joints interfaces manufactured from two distinct insulating layers due to defects introduced during the technological process or during operation (i.e., metallic particles, fibers, cavities and layer depletions) [142].

In order to obtain insulation with the greatest possible resistance to the action of PDs, polymer nanocomposite materials have gained increased attraction. Nanofillers such as MgO, SiO_2, Al_2O_3, rutile, layered silicate systems and so forth, increase the resistance against PDs due to multiple effects including nanoscale segmentation, permittivity difference, coupling agent and nanofiller pile-up [134]. The nanocomposites' behavior to PDs is presented in numerous papers [134]. The majority of the studies focuses on the PD resistance of epoxy resins and polyimide nanocomposites. In the following section, some results are presented for the PD characteristics in PE-based nanocomposites used as power cables insulation.

7.2. Partial Discharges in Nanocomposites Based on Polyethylene (PE)

The CIGRE Working Group D1.24 has conducted different tests in several laboratories from nine countries on the behavior of XLPE and its nanocomposite with fumed silica in an electric field [105]. The authors tested samples based on commercially available XLPE [105] in a set-up consisting of a rod-plane electrode and IEC electrodes systems (Figure 26). Three types of samples were tested: unfilled XLPE (XLPE–H1), nanocomposites filled with 5 wt % of unfunctionalized nano-SiO_2 (XLPE + 5%NS–H2) and nanocomposites with 5 wt % of nano-SiO_2 functionalized with a specific chemical coupling agent, selected to improve the dispersion in polyethylene (XLPE + 5%NS surf–H3). Correlations of the application time of voltage with the pit depth of the eroded area (at 10 kV_{rms}, 250 Hz, 750 h) (Figure 27a), the average erosion speed (Figure 27b) and cross-sectional area of a formed pit (Figure 28a) were determined. It was found that samples with SiO_2 fillers showed a higher resistance

to discharges than those without fillers and that the highest resistance was found in composites with surface-treated fillers (Figure 27a,b and Figure 28a,b). Using the IEC electrodes system (Figure 26b), erosion in an area of 5 mm around the centre of the rod electrode was determined (for 50 h at a voltage of 10 kV_{rms} and 50 Hz) (Figure 28b). The results reveal that XLPE samples with untreated nanofillers show less erosion than the unfilled XLPE samples and that the erosion values for some of the XLPE samples filled with surface-functionalized nanofiller are higher (Figure 28b).

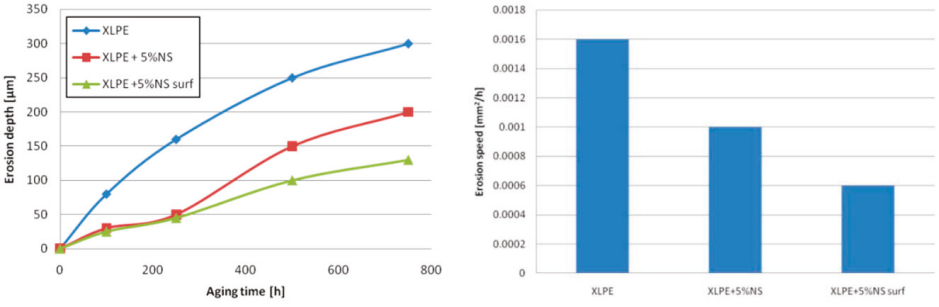

(**a**) (**b**)

Figure 27. (**a**) Variation of the PD erosion pit depth with aging time and (**b**) average erosion speed values of unfilled XLPE, XLPE with 5 wt % of non-functionalized nano-SiO_2 and XLPE with 5 wt % of surface-functionalized nano-SiO_2. Reprinted, with permission by IEEE, from reference [105].

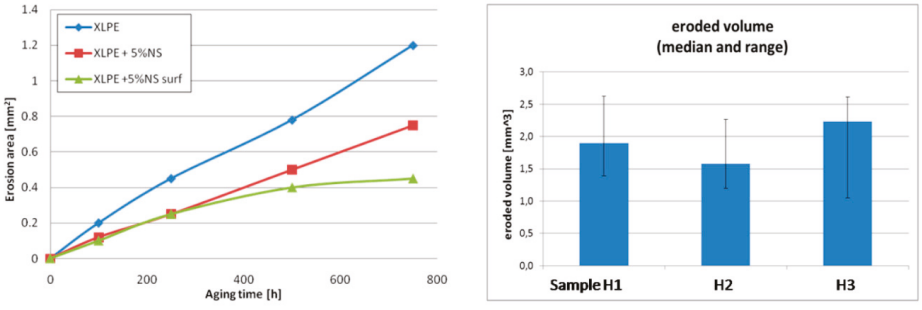

(**a**) (**b**)

Figure 28. (**a**) Correlation of the cross-sectional area of pits with aging time for unfilled XLPE, XLPE with 5 wt % of non-functionalized nano-SiO_2 and XLPE with 5 wt % of surface-functionalized nano-SiO_2 [105]; (**b**) eroded volume by PDs produced with the IEC electrodes system type for unfilled XLPE (H1), XLPE with 5 wt % of non-functionalized nano-SiO_2 (H2) and XLPE with 5 wt % of surface-functionalized nano-SiO_2 (H3). Reprinted, with permission by IEEE, from reference [105].

Using LDPE and fumed silica powder with a mean size of 7 nm, Aulia et al. studied the PD effect on these samples by positive and negative pulse counts using the CIGRE Method II (CM-II) electrode system [143]. The authors observed that the addition of nano-SiO_2 in amounts of up to 4 wt % increased the number of PDs, while even larger concentrations of fillers in the range of 6 to 8 wt % significantly reduced the number of impulses. The same electrodes system (CIGRE Method II) was used by Sami et al. for the study of PD action on two types of PE-based nanocomposites, namely LDPE and HDPE (HDPE/SiO_2 and LDPE/SiO_2), with 0, 1, 2, 4 and 5 wt % of spherical SiO_2 nanoparticles (15 nm in diameter with 99.9% purity and 14 nm in diameter with 99.9% purity) [144]. The authors measured the samples' erosion depth and found that the values increased with an increased content of nanoparticles. It was considered that this behavior could be due to the defects introduced during the fabrication process of the samples [144]. Gao et al. showed that the use of montmorillonite MMT

nanofillers (MMT = $(Na,Ca)_{0.3}(Al,Mg)_2Si_4O_{10}(OH)_2 \cdot n\ H_2O$) with high filling grades of SiO_2 (more than 51 wt %) instead of spherical silica particles also increased the PD resistance of PE [145,146]. Both, the amplitude and the number of PDs were lower in PE/MMT samples than in unfilled PE (under the test condition applied) [145].

The influence of the MgO content on the PE resistance to PDs was analysed by Tanaka et al. [147]. The authors used the rod-to-plane electrode system (Figure 26) for flat samples of LDPE-based nanocomposites containing 0, 1, 5 and 10 wt % of spherical MgO particles with an average diameter of 50 nm. The results showed that the erosion depth of LDPE/MgO samples was significantly lower than that of unfilled LDPE samples (factors of up to 2.8). The authors explained the increase of the PD resistance of LDPE/MgO samples by the multi-core model, considering the fine segmentation of the polymer surface by nanofillers, the morphology formed around the nanofiller nuclei and the degree of bonding between the filler and the polymer [147]. The authors stated that the nanofillers were separated from the base matrix and piled on the surface.

The erosion induced by surface PD on samples of unfilled LDPE and LDPE filled with two types of inorganic nanofillers (quasi-spherical silica nanoparticles and synthetic layered MMT, each in 5 wt % content) was analyzed by Guastavino et al. [148]. The authors described that both types of nanocomposites exhibited longer lifetimes than unfilled LDPE under the same stress conditions.

Chen et al. [149] analyzed the effect of corona discharges on the performance of LDPE samples containing 0.5, 1, 3 and 5 wt % of nano-ZnO. The nanocomposites were exposed to the electric field for different time intervals. It was observed that a reduced content of ZnO nanoparticles lead to improved resistance to corona discharges. After 24 h of 10, 30 and 50 $kV \cdot mm^{-1}$ field application, LDPE/ZnO samples exhibited much lower values of accumulated space charge density than unfilled LDPE. The increase in aging time from 24 to 48 h reduced the volume resistivity and dielectric strength for all types of samples but these reductions were lower for LDPE/ZnO samples. In addition, the increase in the ZnO content caused an increase of the dielectric resistivity and breakdown strength of the samples, with a critical concentration of 5 wt %, at which these values decreased. The results suggested that the addition of nano-ZnO in low contents caused the occurrence of deep traps at the interfaces between nanoparticles and LDPE, in which space charges formed by discharges were accumulated. If the ZnO particle concentration amounted to 5 wt %, electrical resistivity and breakdown strength reached the maximum values after corona aging within the set of samples investigated. Zheng et al. [150] demonstrated that PDs degrade LDPE areas (in LDPE/ZnO nanocomposites) due to the combination of electrons associated with discharges and voids from the material, which generates UV irradiation.

A study of PD levels in HDPE was performed by Yamano and Okada [151] who added azobenzene derivatives such as azobenzene, *p*-nitro-azobenzene, *p*-amino-azobenzene and nitrobenzene-azo-resorcinol in amounts between 0.05 and 0.5 wt % to the polyolefin. The authors found that the level of PDs decreased by up to 20% compared to the samples without additives. It was concluded that this reduction relied on the prevention against secondary electron emission from the void wall due to the excitation of the azobenzene derivatives and prevention of electron detachment from the void wall due to the charge traps in the presence of the azobenzene derivatives [151].

The behavior of nanocomposites based on a blend of natural rubber (0–30 wt %) and LLDPE without or with 5 wt % of nanofillers of alumina trihydrate $Al_2O_3 \cdot 3\ H_2O$ was investigated using the CIGRE method II by Aulia et al. [152]. The results showed that the addition of natural rubber to LLDPE had positive effects on the PD resistance and that LLDPE blends with 20 wt % of natural rubber exhibited the highest PD resistance.

The studies presented in this section confirm that the use of polymer-based nanocomposites with organic or inorganic particles might lead to a reduction in PD degradation in power cable accessories and insulations, contributing to increased cables' lifetimes. The increase in PD resistance of nanocomposites is due, among other things, to the following reasons:

1. Reduction of the polymer free space (preventing the erosion progress starting from PDs);
2. Segmentation of the polymer matrix (hindering the development of PDs);

3. Coupling agents that enhance the bonds between matrices and fillers (hindering the development of PDs);
4. Different values of the electrical permittivity of the matrix and the filler (decreasing the electric field local values and hindering the initiation and the development of PDs);
5. Nanofiller residues piled-up on the surfaces of specimens (hindering the development of PDs).

8. Space Charge in Nanocomposites

8.1. Space Charge Accumulation

Space charge is considered to be an excess of electric charge continuously distributed in a space region (volume or surface) and consists of electrons, holes and ions [153]. In terms of power cables, space charge is generally understood as a separation of free charge in the volume or interface of their insulation components due to: (*i*) carriers generated in the technological processes, (*ii*) space charge injection on the electrodes, (*iii*) the field-assisted thermal ionization of impurities from the insulation and (*iv*) the insulation degradation under the action of (electrical, thermal, mechanical, environmental etc.) stresses during operation [154]. In addition, space charge can accumulate in the case of the electric tree development [155,156] and/or in electrochemical approach (e.g., by water trees) [157–161]. With respect to DC power cable joints with multi-layered insulation, electric charges accumulate at the interfaces of the layers during operation due to the different values of the charge carriers' relaxation time in the adjacent layers τ (Equation (6)):

$$\tau = \varepsilon / \sigma, \tag{6}$$

in which ε represents the permittivity and σ the electrical conductivity of the layer.

Space charge density is measured by different methods such as the piezoelectric-induced pressure wave propagation PIPWP method, the laser-induced pressure propagation LIPP method, the thermal step method TSM method, as well as the pulsed electro-acoustic PEA method [14,154,162,163]. The accumulation in time of the space charge contributes to the local intensification of the electric field, which accelerates the degradation process of the material [133,153]. Although the analysis of the global action of space charge on the insulation is difficult to achieve, it is still necessary to control and to reduce space charge accumulation in high-voltage DC systems [162].

8.2. Space Charge Reduction

Space charge accumulation in polymer cables insulation is closely related to the intensity of the electric field and the concentration of potential pits [111,164], the values of the free volume contained by them [165], the nature and states of the electrodes [154], the insulation dimensions [166] and the temperature gradient [167].

Fillers introduce additional trapping sites at particle interfaces and/or through morphological changes within the polymer matrix that serve to modify the original trap distribution [153]. As a result, the space charge accumulation in polymer nanocomposites changes compared to the unfilled polymers, depending on the nature of the polymer and the nanoparticles characteristics [168–170]. Thus, the volume density of the space charge has lower values [168] and its distribution changes in the case of nanocomposites compared to microcomposites [168,171,172].

Tanaka et al. demonstrated that the space charge inception threshold shifted to lower values for isotactic polypropylene i-PP-based as well as ethylene vinyl acetate EVA-based nanocomposites with nanofillers (from 12 to 4 kV·mm^{-1} for EVA and from 14 to 5 kV·mm^{-1} for PP) [111]. In addition, charges accumulated in the bulk at the field 60 kV·mm^{-1} tended to decrease with increasing addition of nanosized fillers from 2 to 6 wt % (for both, EVA and i-PP). Moreover, the charges dissipated more quickly in nanocomposites compared to microcomposites [153].

8.3. Space Charges in Nanocomposites Based on Polyethylene (PE)

The influence of fumed silica nanoparticles on the space charge accumulation in XLPE for power cable insulations was analyzed by the CIGRE Working Group D1.24 [105]. Three types of samples were used: unfilled XPLE (H1), XLPE with 5 wt % of unfunctionalized nano-SiO_2 (H2) and XLPE with 5 wt % of nano-SiO_2 surface-functionalized with a specific chemical coupling agent, selected to improve the dispersion in polyethylene (H3). The space charge was measured by the pulsed electro-acoustic PEA and the thermal step TS method. The results revealed that the lowest space charge amount occurred in composites with surface-treated nanofillers (Figure 29). The overall results showed that a heterocharge was generated in unfilled XLPE, which was associated with contaminant residues of the crosslinker and natural impurities [105]. Moreover, it was confirmed that nanofillers reduced this heterocharge as the nanoparticles were able to interact with the impurities. Concerning the charge injection, it was demonstrated that homocharges were injected more easily into filled than unfilled XLPE. It was also highlighted that charge packets appeared at very high electric field values [105] and that these charge packets were reduced by the addition of nanoparticles.

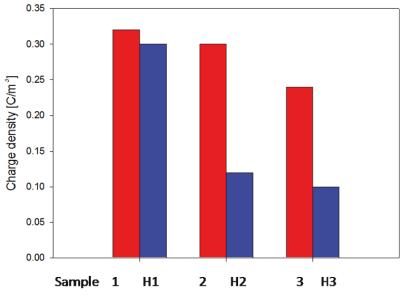

Figure 29. Space charge distribution at 20 kV·mm^{-1} in unfilled and filled XLPE prior to (red bars; samples 1, 2 and 3) and after treatment at 80 °C for 5 d (blue bars; samples H1, H2 and H3). Reprinted, with permission by IEEE, from reference [105].

Lau et al. studied the influence of SiO_2 nanoparticles, both untreated and treated with trimethoxy(propyl)silane, on the space charge formation in nanocomposites based on blends of LDPE (80 wt %) and HDPE (20 wt %) [153]. Space charge measurements were performed via the PEA method on samples subjected to electric fields of 25 and 40 kV·mm^{-1}. The authors revealed that homocharges were separated near both electrodes and that their values increased with rising content of nanofillers. At 40 kV·mm^{-1}, less charge accumulation was observed in samples containing surface-treated nano-SiO_2 compared to composites filled with the same amount of untreated nano-SiO_2 [153]. This behavior was explained by the accumulation of homocharges due to the generation of localized surface states upon the introduction of nanofillers. The influence of the electric field as well as the surface treatment of nano-SiO_2 particles with diameters of 10 to 20 nm on the charge dynamics was studied by Wang et al. [173]. They used trimethoxy(propyl)silane-functionalized and untreated nano-SiO_2 particles. The samples (blends of 80 wt % of LDPE and 20 wt % of XLPE; unfilled or filled with nano-SiO_2) were subjected to DC high fields of 30, 50 and 70 kV·mm^{-1}; the space charge was measured by the PEA method. The authors showed that a lower concentration of silica nanoparticles improved the dynamic space charge and that the composites with surface-treated particles had a better dispersion of the space charge. A reduction of the space charge was obtained in the presence of nanoparticles (especially homocharges) [173].

The influence of TiO_2 on the accumulation of space charges in LDPE was analyzed in two studies [170,172]. Experiments were performed on LDPE samples with different contents of TiO_2 of up to 6 wt %. It was demonstrated that: (*i*) for DC fields of 40 kV·mm^{-1}, the hetero-polar space charge near electrodes was much lower in LDPE/TiO_2 nanocomposites than in pure LDPE; (*ii*) the

space charge inside the nanocomposites was more uniform in the nanocomposites than in pure LDPE (reducing local field strengths) and (*iii*) the space charge decreased after sample breakdown, which was faster in samples containing TiO_2.

Xu et al. studied the influence of polyhedral oligomeric silsesquioxanes POSS nanofillers on the space charge accumulation in LDPE samples [174]. For tests, samples of pure LDPE and LDPE with 1 wt % of *iso*-octyl POSS (IOPOSS), octamethyl POSS (OmPOSS) and octa-*iso*-butyl POSS (OibPOSS) were prepared. In the absence of voltage, the homocharge density was higher in LDPE/OibPOSS and LDPE/OmPOSS samples (for voltages below 5 kV), while the charge injection in LDPE/IoPOSS under 10 kV was the lowest.

The effects of introducing nanosized $BaSrTiO_3$ particles (contents of 2 and 10 wt %) into LDPE on the space charge accumulation in LDPE were studied by Fleming et al. [175,176]. By using 50 nm $BaSrTiO_3$ nanoparticles, the authors prepared flat nanocomposite samples with heights of 150 to 200 μm with aluminium electrodes and subjected them to a DC voltage of 3.1 kV for 1 d at room temperature (r.t.). The results showed that the space charge density was approximately an order of magnitude smaller in the nanocomposite samples compared to unfilled LDPE.

The addition of ZnO nanoparticles in PE leads as well to changes in space charge values. The studies performed by Fleming et al. [95] demonstrated that the ZnO nanoparticles reduced the density of homocharge accumulation close to the electrodes. A study of the ZnO influence on the space charge in LDPE was performed by Tian et al. [177]. Using samples of LDPE with untreated ZnO (average size of 50 nm) at concentrations of 0.1, 0.5, 1, 3, 5, 7 and 10 wt %, the authors determined the space charge density for electric fields of 50 $kV \cdot mm^{-1}$. It was shown that the introduction of ZnO lead to space charge suppression in the nanocomposites due to a significant increase of the trap density.

Murata et al. studied the influence of MgO nanoparticles on the space charge accumulation in LDPE [178]. Flat samples with a thickness of 200 μm were prepared and subjected to DC fields of up to 125 $kV \cdot mm^{-1}$. The authors found that the amount of space charge was reduced in the nanocomposites. Furthermore, the ratio of stress enhancement was reduced by the addition of nanosized MgO-fillers in a certain range of concentrations: At the average stress of 125 $kV \cdot mm^{-1}$, the electric field enhancement ratio of LDPE was reduced by adding 1 wt % of nanosized MgO. However, if the MgO content exceeded 1 wt %, the values of the electric field enhancement ratio did no longer change. Similar findings were presented by Murakami et al. [98]. They observed that the increase in the amount of injected charge depended on the MgO content, which caused a reduction in space charge density values [98]. The space charge formation in LDPE/MgO nanocomposites under DC stress at high temperatures was studied by Taima et al. [179]. LDPE and LDPE/MgO nanocomposite films with a height of 100 μm and a MgO content of 0.2, 0.5, 1.0 and 2.0 wt % were prepared. In order to measure the space charge in DC fields of up to 200 $kV \cdot mm^{-1}$ and at elevated temperatures of up to 60 °C, an improved PEA system was used [180]. The study revealed that: (*i*) the introduction of MgO nanoparticles lead to space charge reduction, (*ii*) the space charge density increased with increasing field and temperature and (*iii*) the local enhancement of the electric field was reduced in LDPE/MgO nanocomposites, particularly at higher concentrations of MgO [180]. Peng et al. studied the space charge in films of 450 μm height based on LLDPE/MgO nanocomposites with a MgO content ranging from 0 to 5 wt % [19]. The samples were subjected to electric fields of 20 and 40 $kV \cdot mm^{-1}$ for 1 h at r.t. and the space charge was measured with a PEA system. The results revealed that, at low nanoparticle loading, the LDPE/MgO interfaces reduced the characteristic trap energy levels and bound charges injected from electrodes. Consequently, a reduction in space charge density in LDPE/MgO nanocomposites was achieved [19].

Research performed by Zheng et al. on LDPE/MgO nanocomposites showed that the space charge distribution improved and the decay rate of space charge increased with rising temperature [181]. The influence of the samples' height and temperature gradient on the space charge accumulation in nanocomposites based on PE was analyzed by Chen et al. [167], Lv et al. [166] and Wu et al. [182]. Chen employed LDPE samples, while Lv was applying XLPE samples with 1 wt % of SiO_2 fillers. In the case of unfilled XLPE samples, a correlation between the space charge distribution and the temperature

gradient was obtained. For the XLPE/SiO_2 nanocomposites, a correlation of the space charge density and the samples' heights was observed: In the case of thin samples, heterocharges accumulated but their density decreased with the increase in samples' heights. XLPE/SiO_2 nanocomposites showed a more pronounced correlation of samples' heights with the heterocharge density than unfilled XLPE under temperature gradients [166]. The influence of the nanoparticles' size on space charge was studied by Wu et al. [183] on samples of LDPE/SiO_2. The concentration of the SiO_2 nanoparticles was kept constant at 2 wt %, while the particle sizes were varied among 7, 12 and 16 nm. The results revealed that the accumulation of space charge in LDPE could be suppressed by nano-SiO_2 and that the nanoparticle content for which this effect was maximal depended on the size of the filler [183]. A similar study on the influence of SiO_2 dimensions on space charge accumulation in LDPE was performed by Yin et al. [170]. The authors used SiO_2 nanoparticles with dimensions of 7 and 16 nm and concentrations of 1, 3 and 5 wt %. It was found that the density of deep traps was significantly reduced after the introduction of nanofillers and that the density of deep traps is lower in nanocomposite filled with 7 nm nanofiller [170].

In the case of DC cables junctions with two distinct polymer layers (i.e., XLPE and EPDM), a layer of space charge is separated at their interfaces whose density depends on the conductivity and electric permittivity values of the polymer layers [133]. Replacing the EPDM layer with one containing SiC particles, the space charge accumulation on the interface gets reduced to significant extent, while the junction performance is improved [34].

9. Electrical Treeing in Nanocomposites

9.1. General Characteristics of Electrical Treeing

Electrical treeing is one of the main causes for failure and damage in electrical power cable insulations [184]. Electrical trees are networks of very thin channels (including gases at high pressures) initiated near insulation and/or electrodes defects, which develop in the insulation during the electrical equipment operation [133,185]. In order to study the electrical treeing and to define the resistance to trees, two methods based on the local electric field intensification are generally used, the needle-plane electrodes method and the electron beam irradiation method. The needle-plane electrodes method is employed particularly for studying the development of electric trees in the bulk of a sample, while the electron beam irradiation method is employed in particular for the study of surface trees [186].

The electric tree channels (Figure 30a) are formed by the local destruction of the material under the synergetic action of the electric field, namely the PDs (from the cavities and channels), the heat and the mechanical stress produced by the electric field and the gases from the channels (yielded from material degradation). The electric trees initiated near the electrodes are called vented trees and they are developed from the electrode to the 'inside' of the material (Figure 30a). In contrast, the trees generated inside the insulation (near cavities, metal inclusions, etc.) have a channels structure developed along the electric field lines on both sides of the defect (electric field concentrator) and are called bow tie trees. Electrical trees have been observed in all polymer classes used for medium- and high-voltage insulation: polyethylene [133], polypropylene [187], silicone rubber [188], ethylene propylene rubber [189], ethylene propylene diene rubber [190], polyimide [191], epoxy resin [192] and so forth. The electric trees obtained in PE with needle-plane electrodes in harmonic fields of 50 Hz are tree-shaped (or branched) for $E < 5.4$ GV·m^{-1}, bush-shaped for E values ranging from 5.4 to 6 GV·m^{-1} and bush-tree-shaped for $E > 6$ GV·m^{-1} (these values decrease with increasing frequency) [42].

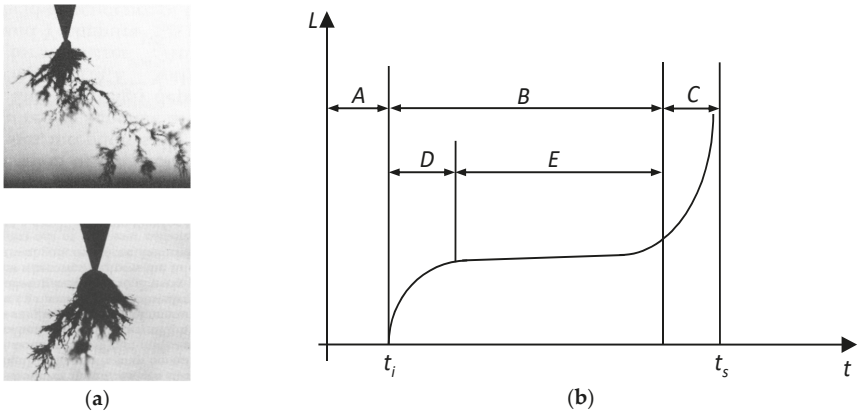

Figure 30. (**a**) Development of vented electric trees in LDPE. (**b**) Schematic representation of the electric tree development: A: inception phase; B: development stage; C: unstoppable growing (prior to breakdown); D: fast growing stage; E: slow propagation region; t_i: initiation time (the time difference between the detection of electrical tree and the voltage application); t_s: breakdown time (the time difference between the breakdown of the specimen and the voltage application). Reprinted, with permission by the author, from reference [133].

The development of electric trees is a discontinuous process, with sudden increases in trees' dimensions (e.g., length *L*) followed by local breakdowns (Figure 30a,b). The involution period of the tree growth is considered as an inception (incubation) period for the occurrence of the 'split' within the initial branch (channel). During this period, PDs extend into the newly formed channels, contributing (by the energy transmitted to their walls) to the increase in diameters (and lengths of the last formed branches) [193]. This evolution is observed for both, tree- and bush-tree shaped congeners, up to the phase C, until the 'accelerated' development phase starts (Figure 30b), in which *L* increases very fast until the thermal breakdown of the specimen has been reached.

Multiple studies of various types of PE for medium and high voltage cables insulations have highlighted the dependence of the electric tree rate development on various factors, such as intensity of the electric field [194], the electric field frequency [193,195,196], chemical characteristics [197] and physical structure of the polymer [198–202], temperature [194], impurities concentration [203], moisture content [204], mechanical stress [155,156,205–207], as well as electrodes characteristics, shapes and dimensions [208,209]. Several new PE compounds containing organic additives (such as polycyclic aromatic compounds or benzophenone derivatives) [203] were obtained, which can capture high-energy electrons and dissipate their energy [210] while forming aromatic anions [42]. Thus, depending on the properties and concentration of the additive, an increase in inception times and a reduction in the propagation rate of the electric trees in PE can be achieved [211]. In order to extend the lifetime of an insulation, composite materials with barriers and surrounding polymer matrix are commonly used in power engineering [212] and many research studies were performed on the development of nanocomposites for increasing electric breakdown resistance [14].

In recent years, a plethora of new polymeric materials has been developed, with improved properties compared to conventional polymers. These include copolymers and especially nanocomposites based on thermoplastic polymers and inorganic fillers [198,213,214]. These improvements depend on several factors, among which the properties of nanoparticles and nanoparticle-induced morphological changes at the nano- or micrometric scale are very important [198]. Based on the multi-core model (Figure 20) [100], an explanation of the increase in electrical treeing resistance of polymer nanocomposites was given [215]: It is considered that the treeing resistance of nanocomposites is due to the control of the acceleration of electron carriers by the diffusion layer

and the multi-core layer. Namely, the electrical treeing resistance depends on the distance between the nanoparticles, the total area of the nanoparticle-polymer interface and, evidently, on the interface characteristics [215,216].

The electric tree growth in polymers can be slowed down by three methods: (*i*) changing the physical structure of the polymer [217], (*ii*) improving the manufacturing process by applying super-clean technology [218] and (*iii*) by adding voltage stabilizers [219]. In the presence of nanoparticles, the tree propagates through the polymer or the interfacial region and forms a zigzag pattern around the nanoparticles, thereby extending the pathway through the composite. Thus, the electrical tree needs more time to pave the way to the opposite electrode [185].

9.2. Electrical Treeing in Nanocomposites Based on Polyethylene (PE)

The increase of the electrical treeing resistance of PE by using organic additives was analyzed by Yamano and Iizuka [216]. The authors studied samples of LDPE, into which different aromatic additives such as naphthalene, anthracene, 9,10-dibromoanthracene, tetracene and pentacene were introduced. It was found that the inception voltage of electric trees U_{iet} depended on the type of the compound added; anthracene was the most effective additive with respect to increasing U_{iet} values.

Alapati et al. [198,220] studied the influence of alumina Al_2O_3 on the electrical treeing resistance, the inception voltage and the propagation rate of electric trees in unfilled LDPE as well as LDPE filled with 1, 3 and 5 wt % of nano-Al_2O_3. The authors observed that the introduction of Al_2O_3 nanoparticles into the polymer lead to an increase of the tree inception voltage with a filler content below 3 wt %. It was also described that the tree growth slowed down and changed in shape, namely from branch to bush, with rising filler loading. Both, the slow propagation of tree growth as well as the reduction in tree inception voltage at increased filler loadings, were attributed to the morphological changes of the nanocomposites. By scanning electron microscopy SEM, it was observed for higher filler loadings that the degree of crystallinity was reduced and the lamellae packing was increased. In addition, LDPE filled with 5 wt % of particles exhibited a high content of disordered spherulitic structures [198]. It should be noted that, for 5 wt % of Al_2O_3 content, the inception voltage of trees decreased. The authors explained this phenomenon by an increase in trap density resulting from the reduction of the critical field required for detrapping [220].

Yamano and Iizuka characterized the behavior of electrical treeing of nanocomposites based on LDPE and Al_2O_3 nanoparticles (0.5 to 9 wt %), phthalocyanine additives (0.5 to 8 wt %), as well as a combination of both fillers [216]. The authors showed that the exclusive addition of Al_2O_3 nanoparticles lead to insignificant increases of the inception voltage of the electric trees U_{iet} only. They concluded that the increase of the U_{iet} (in the presence of Al_2O_3 and phthalocyanine additives) was due to the effects of the π-electron resonance in phthalocyanine and the semi-conductive characteristics of phthalocyanine crystallites [215]. It was also shown that the time interval τ intervened between initiation of the tree in a sample and its breakdown was 10 times higher for the nanocomposites containing Al_2O_3 and phthalocyanine compared to unfilled PE. In samples containing only Al_2O_3 nanoparticles, τ was 3 times higher than in the unfilled polymer, while, in the case of LDPE samples containing phthalocyanines, τ was comparable to the unfilled polymer. The authors explained these results by a better dispersion of Al_2O_3 nanoparticles in the polymer matrix by the addition of phthalocyanines and the increase of the nanoparticle-polymer interface area. It is well-known that phthalocyanine is not soluble in LDPE and, thus, the additive forms small crystals with sizes in the range of 0.1 to several μm in the polymer matrix [221], which distorts the electric field. In order to avoid the effect of limitation in the inception voltage increase, Yamano prepared nanocomposites based on LDPE and Al_2O_3, in which phthalocyanine was replaced by an azobenzene derivative (having π-electron clouds with an absorption band of kinetic energy of the electrons from 2 to 5 eV) [151]. It was shown that for samples containing Al_2O_3 and 2 to 3 wt % of the azobenzene derivative, the initiation voltage of trees was 2.4 times higher compared to samples without additives. The duration of tree initiation increased in the case of samples with additives by approx. 100 times (for a voltage of 15 kV) for samples containing

3 wt % of Al_2O_3 and 2 wt % of the azobenzene derivative as additives. The use of Al_2O_3 also enabled to control the tree growth [221].

Addition of a certain content of montmorillonite MMT to PE improved the electrical treeing resistance of the material. This filler effect depended, among others, on the preparation approach and dispersion degree of MMT in the polymer (Figure 31a) [184]. It was also observed that the shapes of the trees were changed upon the addition of MMT. Tests were carried out on samples with dimensions of 10 × 8 × 3 mm using a needle-plane electrode system (tungsten-needle electrodes with a radius of 3 μm) at a voltage of 7 kV [222]. Branch-shaped trees with 'non-conductive' channels were obtained in unfilled LDPE, while bush-shaped trees with 'conductive' channels were observed in LDPE/MMT nanocomposites. In addition, the results revealed that the tree lengths were shorter by about 60% in LDPE/MMT nanocomposites compared to unfilled LDPE. The influence of the MMT dispersion morphology (isotropy in random arrangement or anisotropy in oriented arrangement) on the development of electric trees in LDPE was studied by Yang et al. [184]. The authors orientated the nanofillers in the matrix by applying an electric field that induced the field-controlled orientation, aggregation and arrangement of the nanoparticles. The sample morphology was influenced by the heating temperature, the type of electric field (AC or DC) and the intensity and application time of the field. It was observed that the applied electric field induced the orientation of the MMT particles parallel to the samples' surfaces, hence achieving a uniform dispersion of MMT in LDPE. When the electric field was set for the tree initiation, the MMT particles were arranged perpendicular with respect to the direction of the electric field, acting as a barrier that inhibited electrical tree initiation (Figure 31a). The MMT barrier interrupted the growth and the original direction of tree growth [184].

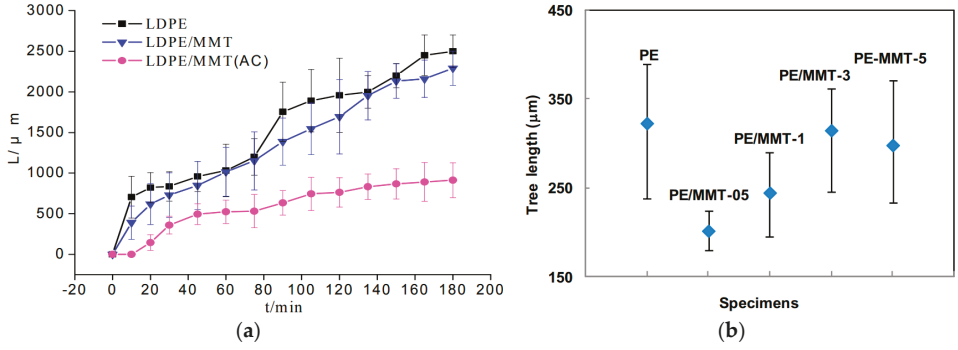

Figure 31. (**a**) Variation in time *t* of electric tree's average lengths *L* developed in unfilled LDPE (LDPE), LDPE with 5 wt % of MMT (LDPE/MMT) and LDPE with 5 wt % of MMT treated in an alternating electric field (LDPE/MMT (AC)). Reprinted, with permission by IEEE, from reference [184]. (**b**) Length dispersion of electrical trees in PE and PE/MMT composites with varying content of MMT: 0 (PE), 0.5 (PE/MMT-0.5), 1 (PE/MMT-1), 3 (PE/MMT-3) and 5 wt % (PE/MMT-5). Reprinted, with permission by IEEE, from reference [223].

In order to improve the electrical tree resistance of cable insulations, PE nanocomposites with nanoMMT layered fillers were prepared by Chi et al. [223]. The authors prepared plate samples with surface-modified MMT in concentrations ranging from 0.5 to 5 wt %. It was shown that the tree length L_{et} in MMT/LDPE samples was reduced, particularly for lower filler concentrations. The lowest values of L_{et} were obtained at a MMT concentration of. 0.5 wt % (Figure 31b) [223]. The development of electric trees in nanocomposites based on LDPE with 10 wt % of fibrous and laminar filosilicate nanofillers such as sepiolite (SEP10), montmorillonite (MMT10) and combined sepiolite and montmorillonite (MMTSEP10) was studied by Guastavino et al. [224,225]. It was found that the treeing inception voltage TIV amounted to 18.8 kV in unfilled LDPE samples. The values significantly decreased to 12.4 kV for SEP 10 and 15.8 kV for MMTSEP10, respectively, and remain practically unchanged at a

value of 18.48 kV for MMT10 samples. It was also observed that the layered MMT platelets have the strongest effect on slowing down the propagation of electrical trees in LDPE nanocomposites [225].

Tiemblo et al. described the initiation and development of electric trees in LDPE with 5 wt % of spherical silica (SPH samples) and organically-modified fibrous phyllosilicate nanoparticles (FIB samples), as well as a modified laminar phyllosilicate montmorillonite (LAM) [226]. The modification of silica nanoparticles and the fibrous phyllosilicate was carried out with grafting strategies using methoxysilanes with *p*-toluenesulfonic acid as the catalyst. The time to inception TTI and the time to breakdown TBD of the samples were measured and the tree growth duration TGD was determined. The results showed that the tree shapes, TTI and TGD depended on the samples' structures and the applied voltage. At voltages below 15 kV, the laminar silicate provided a barrier effect for the propagation of the electric trees as well as the initiation and propagation duration of the electric trees' growth. This phenomenon was explained by the semicrystalline morphology of the nanocomposite upon the addition of LAM. Above 15 kV, however, this type of nanocomposite exhibited TTI values that were higher than those of unfilled LDPE. In agreement with literature data, this observation can be retraced to the interfaces of the large spherulites, which are populated with larger free-volume sites that promote the inception of electrical treeing [226]. The nanocomposites containing silica and the fibrous silicate did not show this barrier effect, as their geometry was either spherical (nano-SiO_2) or fibrillar. Below 15 kV, the fibrous silicate did not influence the tree growth but caused an increase of their initiation time due to the particular semicrystalline morphology. With regard to nano-SiO_2, a reduction in the inception of the tree duration and an increase in the tree propagation rate was observed [226].

The influence of MgO nanoparticles on the development of electric trees in LDPE samples was analyzed by Kurnianto et al. [227]. The authors used plate samples with filler concentrations of 0, 1, 5 and 10 wt %. The tree inception voltage TIV, breakdown voltage BDV, the tree development time t_e and samples breakdown time t_{bd} were measured. It was shown that the MgO nanoparticles acted as barriers for tree initiation and growth. The tree inception voltage increased with increasing filler content from 4.44 kV_{rms} for unfilled LDPE to 5.66 kV_{rms} for samples containing 10 wt % of MgO. Tree development times increased with increasing filler loading from 3.8 min for unfilled LDPE to 10.5 min for samples with 10 wt % of MgO [227]. These results were explained by the fact that MgO particles have a higher affinity for electrons than the polyolefin, which leads to easier electron trapping near the needle electrode. The initiation of some buds of a tree during tree development can be affected by trapping in localized states and local electric fields induced by nanofillers [228]. As a result, the formation of electron avalanches that initiate trees or generate new branches and develop new trees is hindered and the VIT increases. The propagation involves an electron collision with MgO particles, which prevents the development of an electron avalanche [227]. Thus, MgO particles slow down the initiation and the development of the electric trees.

Kawano et al. performed a similar study on the influence of MgO on the initiation and development of electric trees in nanocomposites [229]. The statistical analysis revealed that 63.2% of the respective tree inception voltages were 4.44, 4.60, 4.95 and 5.66 kV_{rms} for LDPE/MgO samples with 0, 1, 5 and 10 wt % of MgO content: The tree inception voltage increased with increasing nanofiller content [229]. Tanaka et al. tested LDPE/MgO samples with filler contents of 1, 2, 5 and 10 wt % at voltage frequencies of 60 and 600 Hz [230]. It was found that the inception voltage tended to decrease slightly if the filler content ranged from 0 to 2 wt % and increased slightly at higher particle concentrations from 2 to 10 wt %. Moreover, the tree length decreased with increasing filler content for less than 2 wt % of nanoparticles. At a filler concentration of 10 wt %, the tree growth is practically suppressed (Table 3) [230]. Using light emission to determine the inception voltage of trees in samples with relatively low contents of MgO nanoparticles, Tanaka et al. showed that the tree inception voltage was increased at a MgO concentration below 1 wt % (Table 4) [231]. It should be noted that the development of electric trees in polyethylene can also be achieved by electron beam irradiation without any applied field. A test performed by Xiao et al. on samples based on LPDE without and

with nano-SiO_2 showed that SiO_2 nanoparticles reduced the tree lengths [232]. Also, the introduction of Buckminster fullerene (C_{60}) or its derivatives such as [6,6]-phenyl-C61-butyric acid methyl ester (PCBM) lead to an increase of the inception field of electric trees by more than 25% [11].

Table 3. Lengths of electrical trees depending on the content of MgO fillers in LDPE/MgO nanocomposite block specimens at 600 Hz. Adapted from reference [230].

MgO content (wt %)	0	1	2	5	8	102
Tree length (μm)	118	76	66	77	62	55

Table 4. Tree inception voltage determined by light emission in LDPE/MgO nanocomposites. Adapted from reference [231].

MgO content (wt %)	0	0.2	0.4	0.5	0.8	1
Tree Inception Voltage (kV_{rms})	2.65	2.73	2.93	3.09	3.13	3.16

10. Water Treeing in Nanocomposites

10.1. General Characteristics

Water trees are diffuse regions that appear inside insulations under the action of the electric field; they consist of water-filled microcavities. Water trees are formed along the electric field lines similar to electric trees. If the water trees start growing on the surface of electrodes, they are called vented trees. This is the case of trees growing in PE insulations of medium and high voltage electrical cables, where the growth starts from semiconductor layers in contact with needle electrodes (Figure 32a) and in plate samples with surface defects (Figure 32c) [133] and so forth. Bow-tie trees (Figure 32b) start growing at defects within the bulk material (impurities, cavities, etc.) and grow into the insulation. The typical characteristic of water tree branches is the formation of spherically shaped microcavities with a radius of 1 to 5 μm with a high density of 10^6 to 10^9 mm^{-3} [233]. Several parameters are used to characterize water treeing, namely the electric field and (inception) voltage, the length at a given time, the maximum length, the average growth rate, the area and the volume occupied by trees, the density of trees and so forth. [163] In water trees, Fe, Al, S, Na, K and C ions were detected in the bow tie trees and Cu, Si, S, K, Ca and Fe ions were detected in vented trees [133,234], as ions that drift with water molecules during the development of water trees and increasing content with the applied voltage [235].

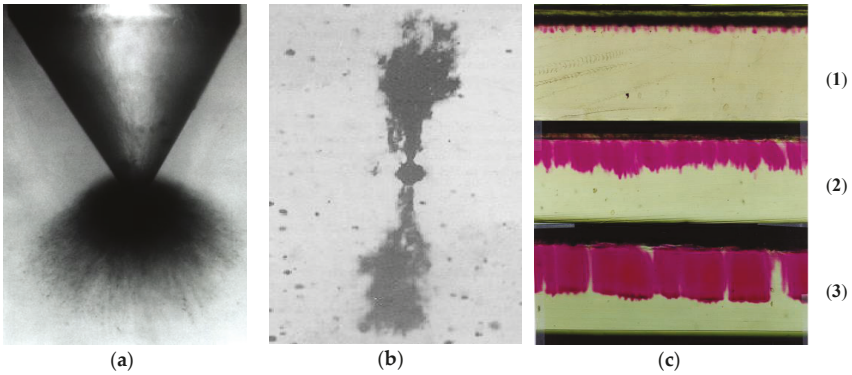

Figure 32. Water trees. (**a**) Vented tree developed at the tip of a needle electrode. (**b**) Bow-tie tree developed starting from an impurity. (**c**) Water trees developed in a laboratory from defects located at the surface of LDPE samples as a function of time t_1 (1) < t_2 (2) < t_3 (3). Reprinted, with permission by the author, from reference [133].

Initiation and water tree growth occur particularly in the lower density regions of insulations (amorphous regions) [236] and are influenced by several factors such as the intensity and frequency of the electric field [42,133], the characteristics and concentration of the salts in the liquid that is in contact with the insulation [237], the concentration of additives [238], the temperature [239,240], the degradation degree of the material [239,241], the quality of the electrode surfaces and semiconductor layers and so forth. [242].

Notingher et al. showed that a critical field strength exists for each material [243]; above that threshold, water trees are formed. Various types of mechanisms have been proposed for the initiation and growth of water trees. Overviews were given by Nunes and Shaw [244], Shaw and Shaw [245], Steennis and Kreuger [236], Dissado and Fothergill [42], Ross [242], Crine [239], Notingher [133] and so forth. It can be concluded that two types of mechanisms seem to play a decisive role in water trees growth: (*i*) mechanisms based on the electrochemical degradation of the insulation and (*ii*) mechanisms based on the mechanical action of the electric forces on the material [246]. A detailed analysis of these mechanisms can be found in references [42] and [133].

Water trees in insulations lead to significant deterioration of the electrical properties and to local increase of the electric field [247]. A reduction of resistivity was observed in various studies by Bahder et al. [248], Tabata et al. [249], Tanaka et al. [250], Steennis et al. [236], Wojtas [251] and so forth. As the water concentration increases in the "tree regions", the permittivity increases correspondingly compared to the material without water trees [252]. The measurements performed by Stucki on samples of PE insulation from cables containing water trees revealed a relative permittivity between 2.7 and 3.6 [253]. Also, dielectric losses increase in insulations deteriorated with water trees. This phenomenon has been studied on samples manufactured in laboratory scale [254] and on insulations of cables in operation [255].

Water tree development reduces the insulation breakdown strength (Figure 33a). If electrical trees are initiated in regions with defects such as cavities, impurities and so forth, these trees will develop around the region of the water trees until the insulation breaks down (Figure 33b). In order to reduce the number and growth rate of water trees, retardants such as organometallic compounds, additives with hydrophilic groups and so forth, are added to polymers, providing, for example, tree-retardant XLPE (TRXLPE) [256–258]. Over the last years, insulations based on various PE-based nanocomposites were manufactured. For the experimental work, two types of models are mainly used, (*i*) the uniform field models [246,259] and (*ii*) divergent field models [246,260,261]. The electrolyte solutions are commonly prepared with NaCl but also other salts such as $AgNO_3$, $CuSO_4$, Fe_2O_3 and so forth, are used; their concentrations being in the range of 0.01 to 10 M [246].

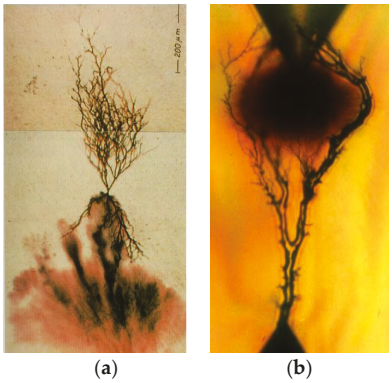

(**a**) (**b**)

Figure 33. Electric trees developed in the presence of water trees. (**a**) The electric tree starts growing from the water tree. (**b**) The electric tree circumvents the water tree. Reprinted, with permission by the author, from reference [133].

10.2. Water Treeing in Nanocomposites Based on Polyethylene (PE)

Series of research studies were performed on samples based on LDPE and XLPE with different types of inorganic nanofillers [240,260,262–265]. Huang et al. studied the effect of nano-SiO_2 particles on the water trees growth in LDPE [262]. LDPE samples without filler (LDPE) were compared with nanocomposites containing 2 wt % of untreated Aerosil 200 nano-SiO_2 (LDPE 200) and with samples containing the same amount of surface-modified nano-SiO_2: For surface modifications, either octyl-trimethoxysilane (LDPE-O) or dimethyldichlorosilane (LDPE-D) were used. For the production of water trees, the authors used plate samples the sandblast surfaces of which were in contact with the electrolyte (1.0 M NaCl solution). A voltage of 5 kV with a frequency of 50 Hz was applied for 45 d and the tree lengths L_{wt} were measured as 827 μm for LDPE, 601 μm for LDPE-D, 573 μm for LDPE-O and 531 μm for LDPE 200. This study revealed that nano-SiO_2 could suppress the water tree growth in PE. In addition, it was shown that hydrophilic SiO_2 comprised a higher efficacy in reducing the rate of water trees growth compared to hydrophobic SiO_2, which can be explained by the alternation of the LDPE morphological structure due to the presence of nano-SiO_2 and by the generation of small spherulites, in which water trees developed faster [266]. Huang et al. [263] conducted a similar study using samples based on LLDPE without fillers and with nano-SiO_2 in 2.5 wt % quantity, the surfaces of which were either untreated (LLDPE-U) or treated with octyl-trimethoxysilane (LLDPE-OCT). After 45 d of sample aging, water trees developed in each sample. It was observed, however, that the water tree growth had lower values in the samples with fillers than in unfilled LLDPE. The authors attributed this behavior to the increase of the number of small spherulites upon the introduction of nanoparticles and the hydrophilic character of the untreated particles. Stress tests with high frequency voltages of 1 kHz using a water needle-plane geometry were performed by Hui et al. on XLPE samples [260]. The authors used plate samples based on XLPE without filler (XLPE) and with nano-SiO_2 fillers in 5 or 12.5 wt % quantity. Two types of nanocomposites were prepared: either with untreated nano-SiO_2 fillers (5UN and 12.5UN) or with vinyl silane-treated nano-SiO_2 fillers (5VS and 12.5VS). Using a NaCl solution with a concentration of 0.5 M, it was confirmed that the morphology of water trees changed by the addition of SiO_2 nanoparticles. In neat XLPE samples, trees grew preferentially from the water needle electrode towards the ground plane, while, in nanocomposites, the water trees had a wider fan-shaped morphology [260]. Furthermore, the nanocomposite with functionalized particles showed a decrease of water tree growth compared to the pristine XLPE (Figure 34). With the increase in the nanoparticle content, water tree development was further restricted. These observations were attributed to the interfacial regions introduced by nanoparticles. In the case of functionalized nanoparticles, more robust interfacial region was argued to be obtained, which further enhanced the resistance to the development of water trees [260].

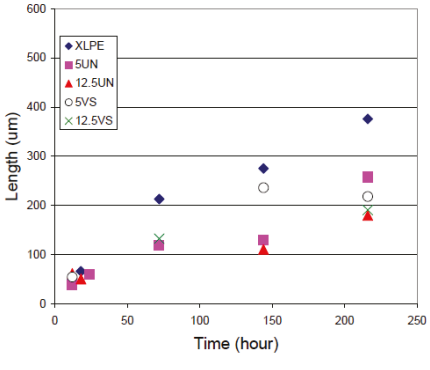

Figure 34. Variation on time of the water tree lengths in unfilled XLPE (XLPE) and composites with untreated nano-SiO_2 fillers (5UN and 12.5UN) or congeners treated with vinyl silanes (5VS and 12.5VS). Reprinted, with permission by IEEE, from reference [260].

The influence of MMT on the development of water trees in XLPE was studied by Li et al. [264]. The authors carried out experiments on plain XLPE samples with a height of 20 mm and nanocomposites with MMT in quantities of 1, 2 and 3 wt %. It was observed that the length of water trees decreased in the nanocomposite samples. This decrease was more pronounced in samples with higher filler contents and ranged from 259 μm in XLPE samples to 107 μm in XLPE/MMT samples with 3 wt % of MMT. This observation was explained by the MMT barrier effect and by the structure of the layered-silicate: The layered structure of MMT was argued to change the electric field distribution and to reduce the pitch of the needle, which slowed down the development of the water trees. The ionic bonds between (defects in) PE and the layered silicate molecules were held responsible for decreasing the relaxation of polymer segments, which reduced the dispersion of the water molecules and slowed down (or even prevented) the formation and growth of water trees [264].

The effect of MgO nanofillers on the water tree retardancy in LDPE and XLPE was characterized by Nagao et al. [240]. The authors used plate samples without and with MgO nanofillers. Water trees were produced in a uniform field, in 1 M of aqueous NaCl solution, an AC voltage of 5 kV_{rms} with a frequency of 400 Hz and temperatures of 313 and 333 K for 46 to 192 h. It was found that the development of water trees in nanocomposites was slowed down and that this effect increased with increasing nano-MgO content. At MgO contents of less than 2 wt %, the density and the length of the trees were lower in MgO/XLPE compared to MgO/LDPE samples.

It can be concluded that the introduction of inorganic nanoparticles into PE results in a slow-down of the water treeing phenomena. However, there are still aspects unclear regarding the explanation of retardant effect in PE, as well as the effect of nanoparticles in other polymers used as power cable insulation (EPR, silicone rubber, etc.).

11. Electrical Breakdown of Nanocomposites

11.1. General Aspects of the Breakdown in Solid Dielectrics

The breakdown of a dielectric occurs at a high concentration of charge carriers such as free electrons in the conduction band and/or holes in the valence band, particularly in the specimen transition in a conductive state [133]. Macroscopically, the breakdown involves a sudden increase in the conduction current passing through an insulator. The minimum value of the electric field strength, at which the breakdown of the dielectric occurs, is called breakdown strength E_{bd} and the minimum voltage applied to the electrodes is called breakdown voltage U_{bd}. The values of dielectric breakdown depend on many factors such as chemical nature of the polymer and its physical structure, the specimen dimensions, the temperature, the frequency, the duration of the applied electric filed, humidity, type and form of electrode and so forth. Depending on the physical processes that cause the breakdown of a solid insulating material, breakdown mechanisms are classified as thermal, electronic, electromechanical, free-volume, by PDs and by treeing (electrical and electrochemical).

Generally, the breakdown strength of the polymer depends on its morphology. In intraspherulitic regions, E_{bd} is higher than in interspherulitic regions and a change in the disorder within the spherulites and/or the interspherulitic region can affect the voltage endurance and, of course, the breakdown strength [13]. Since the nominal voltages of the power cables are increasing (exceeding 500 kV), polymer materials with a higher breakdown strength are required for insulation. The incorporation of inorganic nanofillers into insulation can increase the E_{bd} of the materials, depending on the filler concentration, their shape, size and surface modifications with different agents, material homogeneity, electrical properties of the fillers, sample preparation routes and so forth [267–269].

11.2. Electrical Breakdown in Nanocomposites Based on Polyethylene (PE)

The performance of PE/SiO_2 nanocomposites in high electric fields is presented in numerous papers. A rather detailed experimental study was carried out by CIGRE WG D1.24 [105]. The authors used plate samples of pure XLPE and XLPE with 5 wt % of fumed nano-SiO_2 fillers, either

unfunctionalized or surface-functionalized by a specific chemical coupling agent [105]. Some of the samples were heated at 60 °C in vacuum for 8 d. Three types of cells were used to perform the tests, namely with spherical and cylindrical electrode systems for AC breakdown tests and with needle to plane electrode system for impulse voltage tests. It was observed that (*i*) the addition of nanofillers enhanced the AC breakdown strength, (*ii*) the functionalized nanofillers seemed to cause only a slight increase of E_{bd}, (*iii*) heat treatment seemed to increase the E_{bd} values, and (*iv*) correspondingly, the highest values of E_{bd} were obtained in samples with surface-functionalized nanofillers after heat treatment.

A comparative experimental study on the influence of silica micro- and nanoparticles on breakdown strength and voltage endurance of PE was performed by Roy et al. on plate samples of XLPE and SiO_2/XLPE [13,122,270] (Figure 35). As filler, 5 wt % of nano-SiO_2 were used, either untreated or surface-modified with triethoxyvinylsilane (TES), *N*-(2-aminoethyl) 3-aminopropyl-trimethoxysilane (AEAPS) or hexamethyldisilazane (HMDS). It was shown that (*i*) there was a significant increase in breakdown strength for nanofilled composites compared to unfilled XLPE, (*ii*) the samples with modified nano-SiO_2 had a more significant increase in E_{bd} compared to the untreated ones, (*iii*) the TES nanocomposite samples that were stored at 80 °C exhibited the highest breakdown strength; (*iv*) the breakdown strength had lower values in micro- than in nanocomposites. A similar finding was also reported by Reading and Vaughan [271]. In order to explain the increase of DC breakdown strength and voltage endurance of the nanocomposites compared to the unfilled and microfilled composites, the authors stated that the large number of small particles acted as scattering centres and that the nanoparticles altered the crystalline morphology of XLPE (providing another scattering mechanism). It was suggested that the nanoparticles within the crystalline phase could disturb the continuity of the path provided to the charge carriers, which increased the breakdown strength values. Furthermore, the smaller values of E_{bd} in microcomposites (compared to nanocomposites) were argued to be due to the higher number of defects in microcomposites [272]. In order to explain the existence of higher E_{bd} values in nanocomposites due to surface functionalization of nanoparticles, Roy argued the emergence of 'quasi-conductive' layers [273] in nanocomposites with untreated particles that locally reduce the electric field and do not appear in composites with surface-treated nanoparticles. In addition, polar surface treatments (by, for example, AEAPS and HMDS) have very deep trap sites, which reduce the mobility of charge carriers and increase the breakdown strength [106]. This explanation also takes into account the increase of the interfacial area and the reduction of the free volume in nanocomposites [122,270]. In the case of some polymers, the change in free volume due to the introduction of nanofillers is relatively low and does not excessively affect the breakdown strength [274].

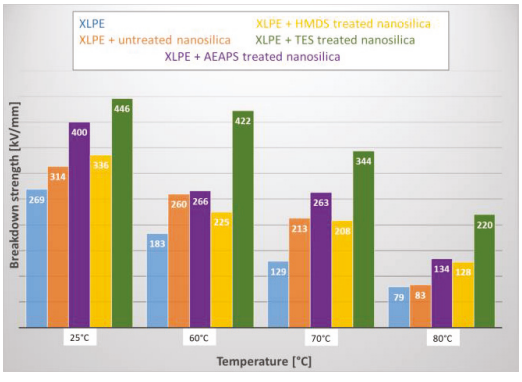

Figure 35. Breakdown strength for different XLPE nanocomposites (KV·mm^{-1}). Redrawn and adapted from reference [13].

Pleşa studied the influence types and contents of inorganic nanoparticles on the performance of plane-shaped LDPE-based nanocomposites in high fields [99]. As inorganic fillers, SiO_2, Al_2O_3 and TiO_2 were used (Figure 36; Table 5). The highest breakdown strength was obtained with LDPE/SiO_2 samples that showed comparable breakdown strength of approx. 40 kV·mm^{-1}, which, however, were lower than those of unfilled LDPE (~ 46 kV·mm^{-1}). In general, the decrease of the breakdown strength in LDPE nanocomposites with inorganic nanoparticles is quite low, which could be correlated with the change in the degree of crystallinity in the nanostructured materials.

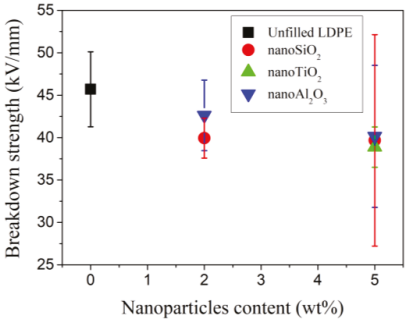

Figure 36. Values of breakdown strength of nanocomposites based on LDPE. Reprinted, with permission by the author, from reference [99].

Table 5. Breakdown strength of LDPE nanocomposites. Reprinted, with permission by the author, from reference [99].

Nanocomposites	Sample Thickness (mm)	U_{bd} (kV)	E_{bd} (kV·mm^{-1})	A (%)
Unfilled LDPE	0.51	23.304	45.694	4.42
LDPE/nano-SiO_2–2 wt %	0.59	23.565	39.941	2.36
LDPE/nano-Al_2O_3–2 wt %	0.55	22.439	42.616	4.16
LDPE/nano-SiO_2–5 wt %	0.55	21.820	39.673	12.46
LDPE/nano-Al_2O_3–5 wt %	0.53	21.273	40.138	8.37
LDPE/nano-TiO_2–5 wt %	0.54	20.995	38.879	2.37

Lau et al. studied the influence of nano-SiO_2 with particle sizes of 10 to 20 nm on the breakdown strength of blends containing 80 wt % LDPE and 20 wt % HDPE [153,275]. Tests on the AC and DC breakdown behavior of PE blends upon the addition of different contents of nanofillers (2, 5 and 10 wt %) and surface modifications (untreated particles and particles surface-treated with trimethoxy(propyl)silane were performed [275]. The addition of 2 and 10 wt % of untreated nano-SiO_2 reduced the DC E_{bd} from 480 (unfilled polymer) to 278 and to 307 kV·mm^{-1}, respectively. In composites with surface-treated nano-SiO_2, the DC breakdown strength was higher than that of composites with untreated nanoparticles. For samples with 2, 5 and 10 wt % of treated nano-SiO_2, the E_{bd} values were 58, 55 and 21 kV·mm^{-1} higher than those with untreated nano-SiO_2. In all cases, E_{bd} of the filled PE was lower than that of the unfilled analogue [275]. The authors explained the reduction of E_{bd} by the accumulation of space, the increase in charge mobility and nanoparticle agglomeration effects [153]. Tests performed in AC showed a slight reduction of E_{bd} values in samples with a filler content of 5 wt % of untreated nano-SiO_2 and a reduction of over 30 kV·mm^{-1} for those containing 10 wt % of filler compared to the unfilled samples [275]. In the case of samples containing surface-treated nano-SiO_2, the AC E_{bd} values were higher than those of non-filled samples, particularly if the nano-SiO_2 content amounted to 10 wt %. In those samples, the sizes of agglomerates were much smaller, which could be the reason for the improved AC breakdown strength [275].

The influence of the matrix structure and the nanofiller content on the breakdown strength of nanocomposites was described by Sami et al. [144]. For the tests, the authors used plate samples with a height of 250 µm based on nanocomposites of the composition HDPE/SiO_2 and LDPE/SiO_2 with 0, 1, 2, 4 and 5 wt % of spherical nanoparticles. The cumulative probability of the electrical failure P was analysed using the two-parameter Weibull function (Figure 37) [276]. E_{bd} increased with increasing nanofiller content, both for LDPE as well as for HDPE nanocomposites. The highest E_{bd} values were obtained for HDPE/SiO_2 with 4 to 5 wt % of nanoparticles [144]. The dielectric strength growth was measured in AC on LDPE/SiO_2 and XLPE/SiO_2 nanocomposites in comparison with the unfilled PE and was reported in additional publications [277,278].

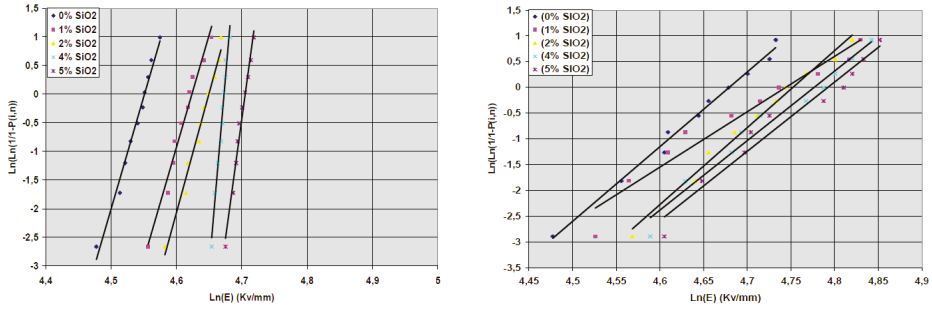

(**a**) (**b**)

Figure 37. Weibull plots of breakdown strength of neat and nanocomposites with varying content of SiO_2 nanoparticles based on (**a**) LDPE and (**b**) HDPE. Reprinted, with permission by IEEE, from reference [144].

The influence of humidity on the breakdown strength of nanocomposites was studied by Hui et al. on XLPE nanocomposites with unfunctionalized (UN) and vinylsilane-functionalized (VS) SiO_2 fillers [123] at loadings of 5 and 12.5 wt % [125]. Multi-recess samples were prepared and exposed to a humid environment of 100% r.h. and 75% r.h. at 50 °C for 14 d. The nanocomposites had a much higher moisture uptake compared to the crosslinked PE resin [125]. The presence of nanoparticles caused an increase of the breakdown strength; under humidity and heat, the E_{bd} values were reduced for all types of samples. In some tests of the nanocomposites, lower E_{bd} values were obtained than in unfilled PE [153,173]. This may be due to the space charge accumulation inside the samples and the local enhancement of the electric field [153].

The change of breakdown strength in samples based on LDPE filled with MMT and MA was presented by Gao et al. [145]. It was shown that the introduction of MMT increased the breakdown strength 1.35 to 1.70 times. The authors explained the increase of E_{bd} of the nanocomposite by the increase of polarity (MA) and the decrease of the free volume (MMT). Both processes intensify the electron scattering and decrease the initiation probability of a breakdown channel. Using nanocomposites based on LDPE and the MMT cloisite 15A in 5 wt % quantity, Guastavino et al. noted an increase of the breakdown strength as well [279]. Green et al. investigated samples of a blend of a high density linear polyethylene HDLPE (10 wt %), a branched low-density polyethylene LDBPE (90 wt %) and a PE/MMT masterbatch MB, which contained 40 wt % of MMT functionalized with dimethyldi(hydrogenated tallow) quaternary amine [280]. The introduction of masterbatch MB led to an increase in dielectric strength from 143 ± 9 MV·m^{-1} (in the absence of MB) to 171 ± 3 MV·m^{-1} (in the case of 20 parts MB) [280]. A very important role in manipulating the breakdown strength is the way how samples were prepared. If the dispersion of MMT nanoparticles into the polymer matrix was inhomogeneous, the values of the breakdown strength were considerably reduced compared to samples with very well dispersed nanocomposites [281,282]. Shah et al. studied the influence of the MMT content on the breakdown strength of nanocomposites based on HDPE [283]. The authors prepared

samples of HDPE with MMT modified by hexadecyl trimethyl ammonium bromide, untreated or treated with 3-aminopropyl triethoxy silane and titanium acetylacetonate in quantities of up to 10 wt %. The results revealed that the breakdown strength of the nanocomposites increased with increasing clay content of up to 5 wt %. If the concentration exceeded 5 wt %, the breakdown strength slightly decreased. The E_{bd} values were also influenced by the type of nanoparticles and amounted to 30 kV·mm^{-1} for unfilled HDPE, 48 kV·mm^{-1} for HDPE with unmodified MMT and 54 kV·mm^{-1} for organoclay nanocomposites [283]. These changes were explained by the fact that exfoliated and intercalated clay platelets altered the electric field repartition and increased the path length for the breakdown.

The use of POSS as filler in LDPE yields composites with breakdown strength different from that of the LDPE matrix. Guo et al. demonstrated that the breakdown strength decreased if octamethyl POSS was applied in 5 wt % quantity, whilst the use of *iso*-octyl POSS in the same amount lead to a decrease of the breakdown strength [284]. The introduction of 0.3 wt % of functionalized graphene within LDPE improved the E_{bd}, while the addition of graphene oxide did not provide any significant change at a content of up to 0.3 wt %.

In a series of papers, the influence of MgO nanofillers on the breakdown strength of PE is detailed. Reddy et al. [285,286] studied the DC breakdown strength of LDPE nanocomposites with small amounts of MgO nanoparticles. Maximum thermal voltage MTV calculations, also known as thermal breakdown voltage, were carried out. The results showed that the values of the MTV increased with nanofiller contents of up to about 5 wt %, for which E_{bd} exhibited a maximum and decreased afterwards. Similar results have been obtained by Tanaka et al. [230], Masuda et al. [97], Murakami et al. [98] and Murata et al. [178]. Peng et al. used plate samples based on LLDPE and MgO nanoparticles surface-modified with (3-aminopropyl) triethoxysilane in concentrations of 0.1, 1, 2 and 5 wt % [19]. The results revealed that, at low nanoparticle loading, the LLDPE/MgO interface produced a large number of shallow traps, which increased the LDPE/MgO interface traps in the nanocomposites. Thus, the number and energy levels of free charges was reduced, enhancing the nanocomposites' breakdown strength. The introduction of 1 wt % of MgO nanoparticles into LLDPE increased the breakdown strength from 346.8 to 380.2 kV·mm^{-1} [19].

The introduction of TiO_2 into PE also increases the breakdown strength. This effect was highlighted by Ma et al. [287] who conducted a study on LDPE-based nanocomposites. The presence of water on the nanoparticle surfaces decreased the E_{bd}: Samples prepared with dried nanoparticles exhibited 50% higher values than those filled with as-received TiO_2 nanoparticles. Samples filled with surface-functionalized TiO_2 showed an approx. 40% increase of E_{bd} [287]. The surface modification was carried out with *N*-(2-aminoethyl) 3-aminopropyl-trimethoxysilane (AEAPS) as a coupling agent.

An experimental study by Tian et al. on plate samples of LDPE filled with untreated ZnO nanoparticles with a mean diameter of 50 nm showed that the breakdown strength of the nanocomposites with a content of less than 1 wt % was higher than those of unfilled PE [177]. If the content was higher than 1 wt %, the E_{bd} values were lower than in unfilled LDPE [177].

From the studies described above, it can be concluded that nanoparticles can influence the breakdown strength of nanocomposites by different mechanisms such as (*i*) serving as heterogeneous nucleation agents (that accelerate the formation of crystalline areas and prohibit the formation of large spherulites), (*ii*) becoming scattering sources for electrons, (*iii*) decreasing the mobility of electrons by forming a large amounts of charge traps, (*iv*) hindering the polymer from the erosion of partial discharge, (*v*) inducing large void defects as well as distorting the local electric field (due of the large permittivity of nanoparticles), (*vi*) forming conductivity pathways and (*vii*) increasing the tunnelling current between nanoparticles.

As was mentioned above, the introduction of inorganic nanofillers into PE leads to the improvement of its electrical properties. On the other hand, some nanoparticles such as SiO_2, ZnO and MgO cause an increase in the aging resistance (respectively, an increase in lifetime) of the nanocomposites compared to unfilled polyethylene [288,289].

12. Conclusions and Outlook

Due to the internationally increasing demands for energy power supply, the development of technologies for long-distance transmission of energy power in direct current has been in the focus of R&D activities, which have addressed research in the area of higher-level voltage cables. Due to high DC voltages in close vicinity to the PE insulations of cables, however, space charges are accumulated, which alter the distribution of the electric field and produce local intensifications that accelerate the degradation processes of the insulations. A solution to counterbalance the occurrence of such phenomena is the introduction of PE-based nanocomposites as insulations of power cables; thermoplast polymer nanocomposites are a promising class of dielectrics as the addition of nanoparticles leads to the improvement of the polymers' basic properties:

- While the introduction of microsized inorganic particles rarely results in an improvement of the electrical properties of composites, the reduction of the particle sizes to the order of nanometres results in improvements of the thermal, mechanical and electrical properties. This is very often due to the interface chemistry and interfacial strength, which increase exponentially in comparison to composites containing microsized particles.
- For the manufacturing of power cables, commonly insulating fillers such as layered silicates, montmorillonite clays, Al_2O_3, TiO_2 and SiO_2 are used; in the case of conducting fillers, graphite platelets and carbon nanotubes are among the most commonly used congeners. Such conducting fillers can improve the mechanical properties of nanocomposites (required in mechanical applications) and electrical conductivity (required for electromagnetic shielding and semiconductor layers of cables). With respect to insulating fillers, layered silicates or clays are in the range of a few nm in thickness and in the range of 100 nm in the other two dimensions, while the sizes of nanoparticles such as SiO_2, TiO_2 and Al_2O_3 are in the range of 30-40 nm.
- The introduction of low contents of nanofillers can increase the resistance to partial discharges (superficial and in the volume of the material), the resistance to electrical trees and water trees, the volume resistivity and the dielectric strength. The comparison of unfilled with nanofilled materials revealed that space charge accumulation phenomena were considerably affected by the presence of nanofillers.
- In the case of nanocomposites, the permittivity is often reduced, and, at low frequencies, it is found to be a 'quasi-DC' feature (large negative slopes in both the real permittivity and tan delta). By using compatibilizers, an increase of the permittivity can be obtained for certain values of the frequency. Depending on the type of compatibilizer, the nanocomposites lifetime can be increased over two orders of magnitude compared to the unfilled polymer.

Although PE-based nanocomposites offer many advantages for usage as insulators in power cables, some issues and short-comings remain to be solved, namely:

- the homogeneous dispersion of the nanoparticles and the characterization of the dispersion phase,
- the online control of the technological processes during commercial manufacturing of nanodielectrics,
- the detailed understanding of the interactions at the interfaces, the charge dynamics and the electrical breakdown behavior of such systems,
- studies of ageing and degradation mechanisms of nanodielectrics (required for their use as cable insulations in submarine applications, superconducting cables, etc.), and
- the detailed understanding of interactions at molecular/atomic level (e.g., the DC current decreases if certain types of nanofillers are added to PI and increases, on the other hand, if layered silicates are dispersed in EVA and PP).

The use of PE-based nanocomposites in industrial applications is also related to the volume of information regarding their behavior under the stress factors of operation. For example,

little knowledge exists regarding the long-term toxicity of nanocomposites and the lifetimes of nanodielectrics. The surface treatment of the nanoscaled fillers is required in order to improve their compatibility with the polymer matrix: The filling grade, particle type, particle size and size distribution, aspect ratio and surface modification jointly alter the properties of the nanocomposites. In summary, the dielectric properties of PE-based nanocomposites show considerable improvements in comparison to unfilled polymers but on-going R&D activities must contribute to the detailed understanding of these phenomena. In order to use PE based nanocomposites for power cables insulation, the following strategies should be considered in the future:

- the mechanisms of doping nanoparticles for improving the characteristics and properties of insulation materials,
- the variations of the electrical conductivity and space charge under the combined action of heat and electrical field,
- the behavior of nanodielectrics to long-term applications in operation (i.e., lifetime estimation to multiple demands),
- the manufacture of recyclable materials for insulation.

Author Contributions: All authors have contributed to the preparation of this manuscript. I.P. and P.V.N. elaborated the plan of the review, wrote the manuscript and designed some figures. C.S. substantially contributed with results and figures to electrical and water treeing subchapters. F.W. provided support for the improvement of manuscript. S.S. was jointly responsible for the sections of the review related to chemistry and materials' structure.

Funding: Funding is provided by the Austrian Government and the State Government of Styria.

Acknowledgments: The research work was performed within the K-Project 'PolyTherm' at the Polymer Competence Center Leoben GmbH (PCCL, Austria) within the framework of the COMET-program of the Federal Ministry for Transport, Innovation and Technology and Federal Ministry for Digital and Economic Affairs with contributions by the University 'Politehnica' of Bucharest. Funding is provided by the Austrian Government and the State Government of Styria.

Conflicts of Interest: The authors declare no conflict of interest.

Abbreviations

AC	alternating current
CB	carbon black
DC	direct current
ε^*	relative complex dielectric permittivity
$\varepsilon'/\varepsilon''$	real/imaginary part of the complex relative permittivity
EHVC	extra high voltage cables
EPDM	ethylene-propylene-diene-monomer rubber
EPR/EPM	ethylene-propylene rubber
EVA	ethylene-vinyl-acetate
HDPE	high-density polyethylene
HV	high-voltage
HVAC	high-voltage alternating current
HVDC	high-voltage direct current
IEC	International Electrotechnical Commission
i-PP	isotactic polypropylene
LDPE	low-density polyethylene
LIPP	laser-induced pressure propagation method
LLDPE	linear low-density polyethylene
LV	low-voltage
MA	maleic anhydride
MMT	montmorillonite

MV	medium-voltage
PD	partial discharge
PE	polyethylene
PEA	pulsed electro-acoustic method
PI	polyimide
POSS	polyhedral oligomeric silsesquioxane
PP	polypropylene
tanδ	dissipation factor
TSM	thermal step method
XLPE	crosslinked polyethylene

References

1. Gubanski, S.M. Insulating materials for next generations of HVAC and HVDC cables. In Proceedings of the IEEE International Conference on High Voltage Engineering and Application (ICHVE), Chengdu, China, 19–22 September 2016; pp. 1–6.
2. Zaccone, E. Chapter 2—Innovative Cables. In *Advanced Technologies for Future Transmission Grids*; Migliavacca, G., Ed.; Springer: London, UK, 2013; pp. 39–84. ISBN 978-1-4471-4548-6.
3. Tanaka, T.; Imai, T. Advances in nanodielectric materials over the past 50 years. *IEEE Electr. Insul. Mag.* **2013**, *29*, 10–23. [CrossRef]
4. Barber, K.; Alexander, G. Insulation of electrical cables over the past 50 years. *IEEE Electr. Insul. Mag.* **2013**, *29*, 27–32. [CrossRef]
5. Taiwan Turnkey-Project Association. Available online: http://www.tpcc.org.tw/wholeplant2/mainchoose/1-4.htm (accessed on 19 March 2018).
6. Jow, J.; Gross, L.; Mendelsohn, A.; Aarts, M.; Kjellqvist, J. Overview of insulating materials system for power cable applications. In Proceedings of the IEEE International Conference on Solid Dielectrics (ICSD), Toulouse, France, 5–9 July 2004; pp. 398–402.
7. Zhou, Y.; Peng, S.; Hu, J.; He, J. Polymeric insulation materials for HVDC cables: DEVELOPMENT, challenges and future perspective. *IEEE Trans. Dielectr. Electr. Insul.* **2017**, *24*, 1308–1318. [CrossRef]
8. Green, C.D.; Vaughan, A.S.; Stevens, G.C.; Pye, A.; Sutton, S.J.; Geussens, T.; Fairhurst, M.J. Thermoplastic cable insulation comprising a blend of isotactic polypropylene and a propylene-ethylene copolymer. *IEEE Trans. Dielectr. Electr. Insul.* **2015**, *22*, 639–648. [CrossRef]
9. Martin, C.P.; Vaughan, A.S.; Sutton, S.J. The thermomechanical behaviour of crosslinked polyethylene cable insulation material. In Proceedings of the Annual Report Conference on Electrical Insulation and Dielectric Phenomena (CEIDP), Albuquerque, NM, USA, 19–22 October 2003; pp. 88–91.
10. Andritsch, T.; Vaughan, A.S.; Stevens, G.C. Novel insulation materials for high voltage cable systems. *IEEE Electr. Insul. Mag.* **2017**, *33*, 27–33. [CrossRef]
11. Jarvid, M.; Johansson, A.; Kroon, R.; Bjuggren, J.M.; Wutzel, H.; Englund, V.; Gubanski, S.; Andersson, M.R.; Müller, C. A new application area for fullerenes: Voltage stabilizers for power cable insulation. *Adv. Mater.* **2014**, *27*, 897–902. [CrossRef] [PubMed]
12. Belli, S.; Perego, G.; Bareggi, A.; Caimi, L.; Donazzi, F.; Zaccone, E. P-Laser: Breakthrough in power cable systems. In Proceedings of the IEEE International Symposium on Electrical Insulation (ISEI), San Diego, CA, USA, 6–9 June 2010; pp. 1–5.
13. Roy, M.; Nelson, J.K.; MacCrone, R.K.; Schadler, L.S. Candidate mechanisms controlling the electrical characteristics of silica/XLPE nanodielectrics. *J. Mater. Sci.* **2007**, *42*, 3789–3799. [CrossRef]
14. Pleşa, I.; Noţingher, P.V.; Schlögl, S.; Sumereder, C.; Muhr, M. Properties of Polymer Composites Used in High-Voltage Applications. *Polymers* **2016**, *8*, 173. [CrossRef]
15. Seiler, J.; Kindersberger, J. Insight into the Interphase in Polymer Nanocomposites. *IEEE Trans. Dielectr. Electr. Insul.* **2014**, *21*, 537–547. [CrossRef]
16. Danikas, M.G. On Two Nanocomposite Models: Differences, Similarities and Interpretational Possibilities Regarding Tsagaropoulos' Model and Tanaka's Model. *J. Electr. Eng.* **2010**, *61*, 241–246. [CrossRef]
17. Reed, C.W. Functionalization of nanocomposite dielectrics. In Proceedings of the IEEE International Symposium on Electrical Insulation (ISEI), San Diego, CA, USA, 6–9 June 2010; pp. 1–4.

18. Li, Z.; Du, B. Polymeric Insulation for High-Voltage DC Extruded Cables: Challenges and Development Directions. *IEEE Electr. Insul. Mag.* **2018**, *34*, 30–43. [CrossRef]
19. Peng, S.; He, J.; Hu, J.; Huang, X.; Jiang, P. Influence of Functionalized MgO Nanoparticles on Electrical Properties of Polyethylene Nanocomposites. *IEEE Trans. Dielectr. Electr. Insul.* **2015**, *22*, 1512–1519. [CrossRef]
20. Liu, D.; Hoang, A.T.; Pourrahimi, A.M.; Pallon, L.K.; Nilsson, F.; Gubanski, S.M.; Olsson, R.T.; Hedenqvist, M.S.; Gedde, U.W. Influence of nanoparticle surface coating on electrical conductivity of LDPE/Al_2O_3 nanocomposites for HVDC cable insulations. *IEEE Trans. Dielectr. Electr. Insul.* **2017**, *24*, 1396–1404. [CrossRef]
21. Luo, S.; Wang, S.; Tu, Y.; Wang, C.; Qin, S. Direct Current Electrical Characteristics of Nano-CB/LDPE Composite. *IEEE Trans. Dielectr. Electr. Insul.* **2017**, *24*, 1390–1395. [CrossRef]
22. Montanari, G.C.; Seri, P.; Lei, X.; Ye, H.; Zhuang, Q.; Morshuis, P.; Stevens, G.; Vaughan, A. Next Generation Polymeric High Voltage Direct Current Cables—A Quantum Leap Needed? *IEEE Electr. Insul. Mag.* **2018**, *34*, 24–31. [CrossRef]
23. Hampton, R.N. Some of the considerations for materials operating under high-voltage, direct current stresses. *IEEE Electr. Insul. Mag.* **2008**, *24*, 5–13. [CrossRef]
24. Reed, C.W. An assessment of material selection for high voltage DC extruded polymer cables. *IEEE Electr. Insul. Mag.* **2017**, *33*, 22–26. [CrossRef]
25. Seifert, J.M.; Karner, H.C. Dielectric diagnostic of moisture induced degradation processes in mineral reinforced high-voltage composite insulation. In Proceedings of the Conference on Electrical Insulation and Dielectric Phenomena (CEIDP), Millbrae, CA, USA, 20–23 October 1996; pp. 825–828.
26. Sumangala, M.G.; Poovamma, P.K.; Dwarakanath, K.; Arunachala Sastry, K.S.; Ratra, M.C. Degradation of electrical properties of organic industrial laminates due to moisture absorption. In Proceedings of the 3rd International Conference on Conduction and Breakdown in Solid Dielectrics (ICSD), Trondheim, Norway, 3–6 July1989; pp. 484–488.
27. Hashizume, T.; Shinoda, C.; Nakamura, K.; Hotta, M.; Tani, T.; Taniguchi, T. A consideration on changes of AC breakdown voltages during an accelerated test of immersed dry-cured XLPE cables. In Proceedings of the 3rd International Conference on Properties and Applications of Dielectric Materials (ICPADM), Tokyo, Japan, 8–12 July 1991; pp. 490–493.
28. Pourrahimi, A.M.; Pallon, L.K.H.; Liu, D.; Hoang, T.A.; Gubanski, S.; Hedenqvist, M.S.; Olsson, R.T.; Gedde, U.W. Polyethylene Nanocomposites for the Next Generation of Ultralow-Transmission-Loss HVDC Cables: Insulation Containing Moisture-Resistant MgO Nanoparticles. *ACS Appl. Mater. Interfaces* **2016**, *8*, 14824–14835. [CrossRef]
29. Cherney, E.A. Nanodielectrics applications-today and tomorrow. *IEEE Electr. Insul. Mag.* **2013**, *29*, 59–65. [CrossRef]
30. Ohki, Y. Development of XLPE-insulated cable for high-voltage dc submarine transmission line (1) [News from Japn]. *IEEE Electr. Insul. Mag.* **2013**, *29*, 65–67. [CrossRef]
31. Ohki, Y. Development of XLPE-insulated cable for high-voltage dc submarine transmission line (2) [News from Japn]. *IEEE Electr. Insul. Mag.* **2013**, *29*, 85–87. [CrossRef]
32. Ohki, Y. Development of an XLPE-insulated cable for LCC-HVDC power lines [News from Japn]. *IEEE Electr. Insul. Mag.* **2018**, *34*, 62–65. [CrossRef]
33. Chen, G.; Hao, M.; Xu, Z.; Vaughan, A.; Cao, J.; Wang, H. Review of high voltage direct current cables. *CSEE J. Power Energy Syst.* **2015**, *1*, 9–21. [CrossRef]
34. Li, J.; Du, B.X.; Kong, X.X.; Li, Z.L. Nonlinear Conductivity and Interface Charge Behaviors between LDPE and EPDM/SiC Composite for HVDC Cable Accessory. *IEEE Trans. Dielectr. Electr. Insul.* **2017**, *24*, 1566–1573. [CrossRef]
35. Guo, M.; Fréchette, M.; Éric, D.; Demarquette, N.R.; Daigle, J.C. Polyethylene/polyhedral oligomeric silsesquioxanes composites: Electrical insulation for high voltage power cables. *IEEE Trans. Dielectr. Electr. Insul.* **2017**, *24*, 798–807. [CrossRef]
36. Du, B.X.; Kong, X.X.; Cui, B.; Li, J. Improved ampacity of buried HVDC cable with high thermal conductivity LDPE/BN insulation. *IEEE Trans. Dielectr. Electr. Insul.* **2017**, *24*, 2667–2676. [CrossRef]
37. Hanley, T.L.; Burford, R.P.; Fleming, R.J.; Barber, K.W. A general review of polymeric insulation for use in HVDC cables. *IEEE Electr. Insul. Mag.* **2003**, *19*, 13–24. [CrossRef]

38. Kim, D.W.; Yoshino, K.; Inoue, T.; Abe, M.; Uchikawa, N. Influence of morphology on electrical properties of syndiotactic polypropylene compared with those of isotactic polypropylene. *Jpn. J. Appl. Phys. Part 1* **1999**, *38*, 3580–3584. [CrossRef]
39. Vahedy, V. Polymer insulated high voltage cables. *IEEE Electr. Insul. Mag.* **2006**, *22*, 13–18. [CrossRef]
40. Kryszewski, M. The effect of modification of supermolecular structure on the properties of polymers. *Pure Appl. Chem.* **1979**, *51*, 2395–2408. [CrossRef]
41. Ueki, M.M.; Zanin, M. Influence of additives on the dielectric strength of high-density polyethylene. *IEEE Trans. Dielectr. Electr. Insul.* **1999**, *6*, 876–881. [CrossRef]
42. Dissado, L.A.; Fothergill, J.C. *Electrical Degradation and Breakdown in Polymers*; Peter Peregrinus Ltd.: London, UK, 1992; pp. 1–620. ISBN 9780863411960.
43. Khalil, M.S. Effect of thermal cycling on dc conductivity and morphology of polyethylene. *Int. J. Polym. Mater.* **1995**, *28*, 179–185. [CrossRef]
44. Tanaka, T.; Greenwood, A. *Advanced Power Cable Technology, Vol. 1—Basic Concepts and Testing*; CRC Press: Boca Raton, FL, USA, 1983; p. 15, ISBN 10 0849351650/ISBN 13 9780849351655.
45. Khonakdar, H.A.; Morshedian, J.; Wagenknecht, U.; Jafari, S.H. An investigation of chemical crosslinking effect on properties of high-density polyethylene. *Polymer* **2003**, *44*, 4301–4309. [CrossRef]
46. Fabris, F.W.; Stedile, F.C.; Mauler, R.S.; Nachtigall, S.M.B. Free radical modification of LDPE with vinyltriethoxysilane. *Eur. Polym. J.* **2004**, *40*, 1119–1126. [CrossRef]
47. Spencer, M.; Parent, J.S.; Whitney, R.A. Composition distribution in poly(ethylene-graft-vinyltrimethoxysilane). *Polymers* **2003**, *44*, 2015–2023. [CrossRef]
48. Melo, R.P.; Aguiar, V.O.; Marques, M.F.V. Silane Crosslinked Polyethylene from Different Commercial PE's: Influence of Comonomer, Catalyst Type and Evaluation of HLPB as Crosslinking Coagent. *Mater. Res.* **2015**, *18*, 313–319. [CrossRef]
49. Ueno, K.; Uda, I.; Tada, S. Radiation-crosslinked polyethylene for wire and cable applications. *Int. J. Radiat. Appl. Instrum. C Radiat. Phys. Chem.* **1991**, *37*, 89–91. [CrossRef]
50. Sasaki, T.; Hosoi, F.; Hagiwara, M.; Araki, K.; Saito, E.; Ishitani, H.; Uesugi, K. Development of radiation crosslinking process for high voltage power cable. *Radiat. Phys. Chem.* **1979**, *14*, 821–830. [CrossRef]
51. Gheysari, D.; Behjat, A. Radiation crosslinking of LDPE and HDPE with 5 and 10 MeV electron beams. *Eur. Polym. J.* **2001**, *37*, 2011–2016. [CrossRef]
52. Svoboda, P. Influence of Branching Density in Ethylene-Octene Copolymers on Electron Beam Crosslinkability. *Polymers* **2015**, *7*, 2522–2534. [CrossRef]
53. Taralli, C.; Tencer, C. *High Voltage EPR Insulation Cable System—Manufacturing and Insulation Relevant Characteristics*; E-CIGRE Paper; CIGRE: Paris, France, 1988.
54. Mazzanti, G.; Montanari, G.C. A comparision between XLPE and EPR as insulation materials for high voltage cables. *IEEE Power Eng. Rev.* **1997**, *12*, 15–28. [CrossRef]
55. David, E.; Fréchette, M. Polymer nanocomposites-major conclusions and achievements reached so far. *IEEE Electr. Insul. Mag.* **2013**, *29*, 29–36. [CrossRef]
56. Calebrese, C.; Hui, L.; Schadler, L.S.; Nelson, J.K. A review on the importance of nanocomposite processing to enhance electrical insulation. *IEEE Trans. Dielectr. Electr. Insul.* **2011**, *18*, 938–945. [CrossRef]
57. Thostenson, E.; Li, C.; Chou, T. Review Nanocomposites in Context. *Compos. Sci. Technol.* **2005**, *65*, 491–516. [CrossRef]
58. Marquis, M.D.; Guillaume, E.; Chivas-Joly, C. Chapter 11, Properties of nanofillers in polymer. In *Nanocomposites and Polymers with Analytical Methods*; InTech: Rijeka, Croatia, 2011; pp. 261–284. ISBN 978-953-307-352-1.
59. Peng, S.; He, J.; Hu, J. Influence of surface modification on electrical properties of polyethylene SiO_2 nanocomposites. In Proceedings of the IEEE 11th International Conference on the Properties and Applications of Dielectric Materials (ICPADM), Sydney, Australia, 19–22 July 2015; pp. 372–375.
60. Hussain, F.; Hojjati, M.; Okamoto, M.; Gorga, R.E. Review article: Polymer-matrix Nanocomposites, Processing, Manufacturing, and Application: An Overview. *J. Compos. Mater.* **2006**, *40*, 1511–1575. [CrossRef]
61. Xanthos, M. Chapter 1, Polymers and polymer composites. In *Functional Fillers for Plastics*, 2nd ed.; Xanthos, M., Ed.; Wiley-VCH Verlag GmbH & Co. KGaA: Weinheim, Germany, 2010; pp. 1–18. ISBN 9783527310548.

62. Pavlidou, S.; Papaspyrides, C.D. A review on polymer-layered silicate nanocomposites. *Prog. Polym. Sci.* **2008**, *33*, 1119–1198. [CrossRef]
63. Jordan, J.; Jacob, K.I.; Tannenbaum, R.; Sharaf, M.A.; Jasiuk, I. Experimental trends in polymer nanocomposites—A review. *Mater. Sci. Eng. A* **2005**, *393*, 1–11. [CrossRef]
64. Roy, M.; Nelson, J.K.; Schadler, L.S.; Zou, C.; Fothergill, J.C. The influence of physical and chemical linkage on the properties of nanocomposites. In Proceedings of the Annual Report Conference on Electrical Insulation and Dielectric Phenomena (CEIDP), Nashville, TN, USA, 16–19 October 2005; pp. 183–186.
65. Reed, C.W. Self-assembly of polymer nanocomposites for dielectrics and HV insulation. In Proceedings of the IEEE International Conference on Solid Dielectrics (ICSD), Winchester, UK, 8–13 July 2007; pp. 397–400.
66. Manias, E.; Touny, A.; Wu, L.; Strawhecker, K.; Lu, B.; Chung, T.C. Polypropylene/montmorillonite nanocomposites. Review of the synthetic routes and materials properties. *Chem. Mater.* **2001**, *13*, 3516–3523. [CrossRef]
67. Tronto, J.; Bordonal, A.C.; Naal, Z.; Valim, J.B. Chapter 1—Conducting Polymers/Layered Double Hydroxides Intercalated Nanocomposites. In *Materials Science—Advanced Topics*; Mastai, Y., Ed.; InTechOpen: London, UK, 2013; pp. 3–31. ISBN 978-953-51-1140-5.
68. Lutz, B.; Kindersberger, J. Influence of absorbed water on volume resistivity of epoxy resin insulators. In Proceedings of the 10th IEEE International Conference on Solid Dielectrics (ICSD), Potsdam, Germany, 4–9 July 2010; pp. 1–4.
69. Smith, R.C.; Liang, C.; Landry, M.; Nelson, J.K.; Schadler, L.S. Studies to unravel some underlying mechanisms in nanodielectrics. In Proceedings of the Annual Report Conference on Electrical Insulation and Dielectric Phenomena (CEIDP), Vancouver, BC, Canada, 14–17 October 2007; pp. 286–289.
70. Patel, R.R.; Gupta, N. Volume Resistivity of Epoxy containing Nano-sized Al_2O_3 fillers. In Proceedings of the Fifteenth National Power Systems Conference (NPSC), Bombay, India, 16–18 December 2008; pp. 361–365.
71. Mera, G.; Gallei, M.; Bernard, S.; Ionescu, E. Ceramic Nanocomposites from Tailor-Made Preceramic Polymers. *Nanomaterials* **2015**, *5*, 468–540. [CrossRef]
72. Sangermano, M.; Yagci, Y.; Rizza, G. In Situ Synthesis of Silver− Epoxy Nanocomposites by Photoinduced Electron Transfer and Cationic Polymerization Processes. *Macromolecules* **2007**, *40*, 8827–8829. [CrossRef]
73. Zhang, H.; Tang, L.C.; Zhang, Z.; Friedrich, K.; Sprenger, S. Fracture behaviours of in situ silica nanoparticle-filled epoxy at different temperatures. *Polymer* **2008**, *49*, 3816–3825. [CrossRef]
74. Yang, F.; Ou, Y.; Yu, Z. Polyamide 6/silica nanocomposites prepared by in situ polymerization. *J. Appl. Polym. Sci.* **1998**, *69*, 355–361. [CrossRef]
75. Papirer, E.; Schultz, J.; Turchi, C. Surface properties of a calcium carbonate filler treated with stearic acid. *Eur. Polym. J.* **1984**, *20*, 1155–1158. [CrossRef]
76. Sahin, M.; Schögl, S.; Kaiser, S.; Kern, W.; Wang, J.; Grützmacher, H. Efficient initiation of radical-mediated thiol-ene chemistry with photoactive silica particles. *J. Polym. Sci. A Polym. Chem.* **2017**, *55*, 894–902. [CrossRef]
77. Roszkowski, P.; Sahin, M.; Ayalur-Karunakaran, S.; Gammer, C.; Schlögl, S.; Kern, W.; Krawczyk, K.K. Synthesis and evaluation of new radical photoinitiators bearing trialkoxysilyl groups for surface immobilization. *Polymer* **2017**, *129*, 207–220. [CrossRef]
78. Sahin, M.; Krawczyk, K.K.; Roszkowski, P.; Wang, J.; Kaynak, B.; Kern, W.; Schlögl, S.; Grützmache, H. Photoactive silica nanoparticles: Influence of surface functionalization on migration and kinetics of radical-induced photopolymerization reactions. *Eur. Polym. J.* **2018**, *98*, 430–438. [CrossRef]
79. Sahin, M.; Schlögl, S.; Kalinka, G.; Wang, J.; Kaynak, B.; Mühlbacher, I.; Ziegler, W.; Kern, W.; Grützmacher, H. Tailoring the interfaces in glass fiber-reinforced photopolymer composites. *Polymer* **2018**, *141*, 221–231. [CrossRef]
80. Pallon, L.K.H.; Hoang, A.T.; Pourrahimi, A.M.; Hedenqvist, M.S.; Nilsson, F.; Gubanski, S.; Gedde, U.W.; Olsson, R.T. The impact of MgO nanoparticle interface in ultra-insulating polyethylene nanocomposites for high voltage DC cables. *J. Mater. Chem. A* **2016**, *4*, 8590–8601. [CrossRef]
81. Kango, S.; Kalia, S.; Celli, A.; Njuguna, J.; Habibi, Y.; Kumar, R. Surface modification of inorganic nanoparticles for development of organic–inorganic nanocomposites—A review. *Prog. Polym. Sci.* **2013**, *38*, 1232–1261. [CrossRef]
82. Shokoohi, S.; Arefazar, A.; Khosrokhavar, R. Silane coupling agents in polymer-based reinforced composites: A review. *J. Reinf. Plast. Compos.* **2008**, *27*, 473–485. [CrossRef]

83. Rong, M.Z.; Zhang, M.Q.; Ruan, W.H. Surface modification of nanoscale fillers for improving properties of polymer nanocomposites: A review. *Mater. Sci. Technol.* **2006**, *22*, 787–796. [CrossRef]
84. Tasdelen, M.A. Diels–Alder "click" reactions: RECENT applications in polymer and material science. *Polym. Chem.* **2011**, *2*, 2133–2145. [CrossRef]
85. Neouze, M.A.; Schubert, U. Surface modification and functionalization of metal and metal oxide nanoparticles by organic ligands. *Chem. Monthly* **2008**, *139*, 183–195. [CrossRef]
86. Jonkheijm, P.; Weinrich, D.; Schröder, H.; Niemeyer, C.M.; Waldmann, H. Chemical Strategies for Generating Protein Biochips. *Angew. Chem.* **2008**, *47*, 9618–9647. [CrossRef] [PubMed]
87. Sato, K.; Kondo, S.; Tsukada, M.; Ishigaki, T.; Kamiya, H. Influence of solid fraction on the optimum molecular weight of polymer dispersants in aqueous TiO_2 nanoparticle suspensions. *J. Am. Ceram. Soc.* **2007**, *90*, 3401–3406. [CrossRef]
88. Nsib, F.; Ayed, N.; Chevalier, Y. Dispersion of hematite suspensions with sodium polymethacrylate dispersants in alkaline medium. *Colloids Surf. A* **2006**, *286*, 17–26. [CrossRef]
89. Kumar, N. Comprehensive Physics XII. In *Unit II: Current Electricity*; Kumar, N., Ed.; Unit II Current Electricity: New Delhi, India, 2003; p. 283. ISBN 978-81-7008-592-8.
90. Kao, K.C. Electrical Conduction and Photoconduction. In *Dielectric Phenomena in Solids with Emphasis on Physical Concepts of Electronic Processes*; Kao, K.C., Ed.; Elsevier Academic Press: San Diego, CA, USA, 2004; pp. 381–514. ISBN 978-0-12-396561-5.
91. Lewis, T.J. Charge transport in polyethylene nano dielectrics. *IEEE Electr. Insul. Mag.* **2014**, *21*, 497–502. [CrossRef]
92. Enriquez, D.J.; Reyes, S.; Cabrera, B.; Cruz, N.; Mendoza, A. Polymer Structures. Available online: https://www.slideshare.net/deschui/polymer-structures-27240126 (accessed on 9 August 2017).
93. Fothergill, J.C. Electrical properties. In *Dielectric Polymer Nanocomposites*; Nelson, J.K., Ed.; Springer: New York, NY, USA, 2010; pp. 197–228. ISBN 978-1-4419-1590-0.
94. Hoang, A.T.; Pallon, L.; Liu, D.; Serdyuk, Y.V.; Gubanski, S.M.; Gedde, U.W. Charge Transport in LDPE Nanocomposites Part I—Experimental Approach. *Polymers* **2016**, *8*, 87. [CrossRef]
95. Fleming, R.J.; Ammala, A.; Lang, S.B.; Casey, P.S. Conductivity and space charge in LDPE containing nano-and micro-sized ZnO particles. *IEEE Trans. Dielectr. Electr. Insul.* **2008**, *15*, 118–126. [CrossRef]
96. Ishimoto, K.; Kanegae, E.; Ohki, Y.; Tanaka, T.; Sekiguchi, Y.; Murata, Y.; Reddy, C.C. Superiority of dielectric properties of LDPE/MgO nanocomposites over microcomposites. *IEEE Trans. Dielectr. Electr. Insul.* **2009**, *16*, 1735–1742. [CrossRef]
97. Masuda, S.; Okuzumi, S.; Kurniant, R.; Murakami, Y.; Nagao, M.; Murata, Y.; Sekiguchi, Y. DC conduction and electrical breakdown of MgO/LDPE nanocomposite. In Proceedings of the Annual Report Conference on Electrical Insulation and Dielectric Phenomena (CEIDP), Vancouver, BC, Canada, 14–17 October 2007; pp. 290–293.
98. Murakami, Y.; Nemoto, M.; Okuzumi, S.; Masuda, S.; Nagao, M.; Hozumi, N.; Sekiguchi, Y. DC conduction and electrical breakdown of MgO/LDPE nanocomposite. *IEEE Trans. Dielectr. Electr. Insul.* **2008**, *15*, 33–39. [CrossRef]
99. Pleşa, I. Influence of Inorganic Fillers on the Dielectric Properties of Polymer Nanocomposites Based on Polyethylene. Ph.D. Thesis, Politehnica University of Bucharest, Bucharest, Romania, 2012.
100. Tanaka, T.; Kozako, M.; Fuse, N.; Ohki, Y. Proposal of a multi-core model for polymer nanocomposite dielectrics. *IEEE Trans. Dielectr. Electr. Insul.* **2005**, *12*, 669–681. [CrossRef]
101. Pleşa, I.; Ciuprina, F.; Notingher, P.V.; Panaitescu, D. Inorganic nanofiller effects on resistivity and absorption currents in LDPE nanocomposites. *Rev. Roum. Sci. Tech.* **2011**, *56*, 277–284.
102. Pleşa, I.; Zaharescu, T. Effects of gamma irradiation on resistivity and absorption currents in nanocomposites based on thermoplastic polymers. In Proceedings of the 8th International Symposium on Advanced Topics in Electrical Engineering (ATEE), Bucharest, Romania, 23–25 May 2013; pp. 1–6.
103. Lewis, T.J. Interfaces: NANOMETRIC dielectrics. *J. Phys. D Appl. Phys.* **2005**, *38*, 202–212. [CrossRef]
104. Yan, Z.; Han, B.; Zhao, H.; Yang, J.; Li, C. Space charge and conductivity characteristics of CB/XLPE nanocomposites. In Proceedings of the International Symposium on Electrical Insulating Materials (ISEIM), Niigata, Japan, 1–5 June 2014; pp. 30–33.

105. Tanaka, T.; Bulinski, A.; Castellon, J.; Frechette, M.; Gubanski, S.; Kindersberger, J.; Montanari, G.C.; Nagao, M.; Morshuis, P.; Tanaka, Y.; et al. Dielectric properties of XLPE/SiO_2 nanocomposites based on CIGRE WG D1.24 cooperative test results. *IEEE Trans. Dielectr. Electr. Insul.* **2011**, *18*, 1482–1517. [CrossRef]
106. Wang, Y.; Xiao, K.; Wang, C.; Yang, L.; Wang, F. Study on dielectric properties of TiO_2/XLPE nanocomposites. In Proceedings of the International Conference on High Voltage Engineering and Application (ICHVE), Chengdu, China, 19–22 September 2016; pp. 1–4.
107. Murata, Y.; Goshowaki, M.; Reddy, C.C.; Sekiguchi, Y.; Hishinuma, N.; Hayase, Y.; Tanaka, Y.; Takada, T. Investigation of space charge distribution and volume resistivity of XLPE/MgO nanocomposite material under DC voltage application. In Proceedings of the International Symposium on Electrical Insulating Materials (ISEIM), Yokkaichi, Japan, 7–11 September 2008; pp. 502–505.
108. Schönhals, A. Dielectric Spectroscopy on Dynamics of Amorphous Polymeric Systems. *Novocontrol Appl. Note Dielectr.* **1998**, *1*, 1–17.
109. Debye, P. Polar molecules. *Chem. Cat.* **1929**, *48*, 1036–1037.
110. Smith, R.C.; Hui, L.; Nelson, J.K.; Schadler, L.S. Interfacial charge behavior in nanodielectrics. In Proceedings of the IEEE Conference on Electrical Insulation and Dielectric Phenomena (CEIDP), Virginia Beach, VA, USA, 18–21 October 2009; pp. 650–653.
111. Tanaka, T. Dielectrics Nanocomposites with Insulating Properties. *IEEE Trans. Dielectr. Electr. Insul.* **2005**, *12*, 914–928. [CrossRef]
112. Ciuprina, F.; Pleşa, I.; Notingher, P.V.; Tudorache, T.; Panaitescu, D. Dielectric Properties of Nanodielectrics with Inorganic Fillers. In Proceedings of the Annual Report Conference on Electrical Insulation and Dielectric Phenomena (CEIDP), Chicoutimi, QC, Canada, 26–29 October 2008; pp. 682–685.
113. Ciuprina, F.; Pleşa, I.; Notingher, P.V.; Zaharescu, T.; Rain, P.; Panaitescu, D. Dielectric properties of LDPE-SiO_2 nanocomposites. In Proceedings of the 10th IEEE International Conference on Solid Dielectrics (ICSD), Potsdam, Germany, 4–9 July 2010; pp. 1–4.
114. Ciuprina, F.; Zaharescu, T.; Jipa, S.; Pleşa, I.; Noţingher, P.V.; Panaitescu, D. Effects of ionizing radiation on the dielectric properties of LDPE-Al_2O_3 nanocomposites. *UPB Sci. Bull. Ser. C* **2010**, *72*, 259–268.
115. Panaitescu, D.; Ciuprina, F.; Iorga, M.; Frone, A.; Radovici, C.; Ghiurea, M.; Sever, S.; Pleşa, I. Effects of SiO_2 and Al_2O_3 nanofillers on polyethylene properties. *J. Appl. Polym. Sci.* **2011**, *122*, 1921–1935. [CrossRef]
116. Ciuprina, F.; Zaharescu, T.; Pleşa, I. Effects of γ-radiation on dielectric properties of LDPE-Al_2O_3 nanocomposites. *Radiat. Phys. Chem.* **2013**, *84*, 145–150. [CrossRef]
117. Shengtao, L.; Guilai, Y.; Fengyan, N.; Suna, B.; Jianying, L.; Tuo, Z. Investigation on the dielectric properties of nano-titanium dioxide—Low density polyethylene composites. In Proceedings of the International Conference on Solid Dielectrics (ICSD), Potsdam, Germany, 4–9 July 2010; pp. 1–4.
118. Zhang, C.; Stevens, G.C. The dielectric response of polar and non-polar nanodielectrics. *IEEE Trans. Dielectr. Electr. Insul.* **2008**, *15*, 606–617. [CrossRef]
119. Jonscher, A.K. *Dielectric Relaxation in Solids*; Chelsea Dielectrics: London, UK, 1983; pp. 1–380, ISBN 0950871109 9780950871103.
120. Comer, A.C.; Kalika, D.S.; Rowe, B.W.; Freeman, B.D.; Paul, D.R. Dynamic relaxation characteristics of Matrimid polyimide. *Polymer* **2009**, *50*, 891–897. [CrossRef]
121. Nguyen, T.; Bentz, D.; Byrd, E. Method for measuring water diffusion in a coating applied to a substrate. *J. Coat. Technol.* **1995**, *67*, 37–46.
122. Roy, M.; Nelson, J.K.; MacCrone, R.K.; Schadler, L.S.; Reed, C.W.; Keefe, R.; Zenger, W. Polymer Nanocomposite Dielectrics—The Role of the Interface. *IEEE Trans. Dielectr. Electr. Insul.* **2005**, *12*, 629–643. [CrossRef]
123. Smith, R.C.; Liang, C.; Landry, M.; Nelson, J.K.; Schadler, L.S. The mechanisms leading to the useful electrical properties of polymer nanodielectrics. *IEEE Trans. Dielectr. Electr. Insul.* **2008**, *15*, 187–196. [CrossRef]
124. Hui, L.; Schadler, L.S.; Nelson, J.K. The Influence of Moisture on the Electrical Properties of Crosslinked Polyethylene/Silica Nanocomposites. *IEEE Trans. Dielectr. Electr. Insul.* **2013**, *20*, 641–653. [CrossRef]
125. Hui, L.; Nelson, J.K.; Schadler, L.S. The influence of moisture on the electrical performance of XLPE/silica nanocomposites. In Proceedings of the 10th IEEE International Conference on Solid Dielectrics (ICSD), Potsdam, Germany, 4–9 July 2010; pp. 1–4.

126. Scarpa, P.C.N.; Bulinski, A.T.; Bamji, S.; Das-Gupta, D.K. Dielectric spectroscopy of AC aged polyethylene in the frequency range of 10^{-5} Hz to 10^{6} Hz. In Proceedings of the Conference on Electrical Insulation and Dielectric Phenomena (CEIDP), Virginia Beach, VA, USA, 22–25 October 1995; pp. 81–84.
127. Kyritsis, A.; Pissis, P.; Grammatikakis, J. Dielectric relaxation spectroscopy in poly(hydroxyethyl acrylates)/water hydrogels. *J. Polym. Sci. Part B Polym. Phys.* **1995**, *33*, 1737–1750. [CrossRef]
128. Medjdoub, A.; Boubakeur, A.; Lebey, T. Dielectric spectroscopy analysis behavior of low density polyethylene. In Proceedings of the Annual Report Conference on Electrical Insulation and Dielectric Phenomena (CEIDP), Chicoutimi, QC, Canada, 26–29 October 2008; pp. 517–520.
129. Scarpa, P.C.N.; Leguenza, E.L.; Das-Gupta, D.K. A study of electrical ageing of cross-linked polyethylene by dielectric spectroscopy. In Proceedings of the 10th International Symposium on Electrets (ISE), Athens, Greece, 22–24 September 1999; pp. 395–398.
130. Fothergil, J.C.; See, K.B.A.; Jour, M.N.A.; Dissado, L.A. Sub-Hertz dielectric spectroscopy. In Proceedings of the International Symposium on Electrical Insulating Materials (ISEIM), Kitakyushu, Japan, 5–9 June 2005; pp. 821–824.
131. David, E.; Castellon, J.; Fréchette, M.; Guo, M.; Helal, E. Dielectric properties of various metallic Oxide/LDPE nanocomposites compounded by different techniques. In Proceedings of the IEEE Electrical Insulation Conference (EIC), Baltimore, MD, USA, 11–14 June 2017; pp. 151–154.
132. Kuffel, E.; Zaengl, W.S.; Kuffel, J. *High Voltage Engineering—Fundamentals*; Newnes: Oxford, UK, 2000; p. 421. ISBN 0-7506-3634-3.
133. Notingher, P.V. *Structure. Properties (Vol. 1). Materials for Electrotechnics*; Politehnica Press: Bucharest, Romania, 2004; pp. 350–403. ISBN 973-8449-81-2/973-8449-81-0.
134. Tanaka, T.; Iizuka, T. Generic PD resistance characteristics of polymer nanocomposites. In Proceedings of the Annual Report Conference on Electrical Insulation and Dielectric Phenomena (CEIDP), West Lafayette, IN, USA, 17–20 October 2010; pp. 1–4.
135. *High-Voltage Test Techniques—Partial Discharge Measurements*, 3rd ed.; IEC 60270; IEC: Geneva, Switzerland, 2002.
136. James, J.; Kulkarni, S.V.; Parekh, B.R. Partial discharge in high voltage equipment-HV cable. In Proceedings of the IEEE 9th International Conference on the Properties and Applications of Dielectric Materials (ICPADM), Harbin, China, 19–23 July 2009; pp. 445–448.
137. Kozako, M.; Fuse, N.; Shibata, K.; Hirai, N.; Ohki, Y.; Okamoto, T.; Tanaka, T. Surface Change of Polyamide Nanocomposite Caused by Partial Discharges. In Proceedings of the Annual Report Conference on Electrical Insulation and Dielectric Phenomena (CEIDP), Albuquerque, NM, USA, 19–22 October 2003; pp. 75–78.
138. Maity, P.; Basu, S.; Parameswaran, V.; Gupta, N. Degradation of Polymer Dielectrics with Nanometeric Metal-oxide Fillers due to Surface Discharges. *IEEE Trans. Dielectr. Electr. Insul.* **2008**, *15*, 52–62. [CrossRef]
139. Tanaka, T.; Ohki, Y.; Ochi, M.; Harada, M.; Imai, T. Enhanced Partial Discharge Resistance of Epoxy/Clay Nanocomposite Prepared by Newly Developed Organic Modification and Solubilization Methods. *IEEE Trans. Dielectr. Electr. Insul.* **2008**, *15*, 81–89. [CrossRef]
140. Wensheng, G.A.O.; Ning, S.U.; Quingduo, Y.I.N. Size effect of partial discharge in solid void defects. In Proceedings of the IEEE 9th International Conference on the Properties and Applications of Dielectric Materials (ICPADM), Harbin, China, 19–23 July 2009; pp. 501–504.
141. Illias, H.A.; Tunio, M.A.; Bakar, A.H.A.; Mokhlis, H.; Chen, G. Partial Discharge Phenomena within an Artificial Void in Cable Insulation Geometry: Experimental Validation and Simulation. *IEEE Trans. Dielectr. Electr. Insul.* **2016**, *23*, 451–459. [CrossRef]
142. Arief, Y.Z.; Ahmad, H.; Hikita, M. Partial discharge characteristics of XLPE cable joint and interfacial phenomena with artificial defects. In Proceedings of the IEEE 2nd International Power and Energy Conference (PECON), Johor Bahru, Malaysia, 1–3 December 2008; pp. 977–982.
143. Aulia, S.; Abdul-Malek, Z.; Arief, Y.Z.; Piah, M.A.M.; Jaafar, M. Partial Discharge Characteristic of Linear Low Density Polyethylene and Silica Nanocomposite. *Appl. Mech. Mater.* **2014**, *554*, 133–136. [CrossRef]
144. Sami, A.; David, E.; Frechette, M.; Savoie, S. Breakdown and Surface Discharge Involving PE/SiO_2 Nanocomposites. In Proceedings of the IEEE International Symposium on Electrical Insulation (ISEI), San Diego, CA, USA, 6–9 June 2010; pp. 1–4.

145. Gao, J.; Zhang, J.; Ji, Q.; Liu, J.; Zhang, M.; Zhang, X. Study on Breakdown and Partial Discharge of Polyethylene/Montmorillonite Nanocomposites. In Proceedings of the International Symposium on Electrical Insulating Materials (ISEIM), Yokkaichi, Japan, 7–11 September 2008; pp. 597–600.
146. Uddin, F. Clays, Nanoclays, and Montmorillonite Minerals. *Metall. Mater. Trans. A* **2008**, *39*, 2804–2814. [CrossRef]
147. Tanaka, T.; Nose, A.; Ohki, Y.; Murata, Y. PD Resistance Evaluation of LDPE/MgO Nanocomposite by a Rod-to-Plane Electrode System. In Proceedings of the 8th International Conference on Properties and Applications of Dielectric Materials (ICPADM), Bali, Indonesia, 26–30 June 2006; pp. 319–322.
148. Guastavino, F.; Dardano, A.; Ratto, A.; Torello, E.; Hoyos, M.; Gomez-Elvira, J.M.; Tiemblo, P. Resistance to surface partial discharges of LDPE nanocomposites. In Proceedings of the Annual Report Conference on Electrical Insulation and Dielectric Phenomena (CEIDP), Vancouver, BC, Canada, 14–17 October 2007; pp. 244–247.
149. Chen, S.; Huang, R.; Peng, Z.; Wang, X.; Cheng, X. The Effect of Nano- ZnO on Withstanding Corona Aging in Low-Density Polyethylene. In Proceedings of the 10th IEEE International Conference on Solid Dielectrics (ICSD), Potsdam, Germany, 4–9 July 2010; pp. 255–258.
150. Zheng, M.B.; Chen, S.Q.; Cheng, X.; Wang, X.; Peng, Z.R. Study on the Similarity of Photo and Corona Aging in Nano-ZnO/LDPE Composite. In Proceedings of the IEEE 9th International Conference on the Properties and Applications of Dielectric Materials (ICPADM), Harbin, China, 19–23 July 2009; pp. 816–819.
151. Yamano, Y.; Okada, M. Reduction of PD in a Void by Additives of Azobenzoic Compound in HDPE Insulating material. *IEEE Trans. Dielectr. Electr. Insul.* **2001**, *8*, 889–896. [CrossRef]
152. Aulia, S.; Ahmad, M.H.; Abdul-Malek, Z.; Arie, Y.Z.; Lau, K.Y.; Novizon, N. Partial Discharge Characteristics in LLDPE-Natural Rubber Blends: Correlating Electrical Quantities with Surface Degradation. *J. Electr. Eng Technol.* **2016**, *11*, 709–718. [CrossRef]
153. Lau, K.Y.; Vaughan, A.S.; Chen, G.; Hosier, I.L.; Holt, A.F.; Ching, K.Y. On the space charge and DC breakdown behavior of polyethylene/silica nanocomposites. *IEEE Trans. Dielectr. Electr. Insul.* **2014**, *21*, 340–351. [CrossRef]
154. Fleming, R.J. Space Charge in Polymers, Particularly Polyethylene. *Braz. J. Phys.* **1999**, *29*, 280–294. [CrossRef]
155. Notingher, P.V. On the Breakdown Mechanism of Inhomogenous Solid Dielectrics. *Rev. Roum. Sci. Tech.* **1979**, *24*, 651–663.
156. Notingher, P.V. Méthodes de calcul de la dureé de rupture dans le systeme pointe-plan. *Rev. Roum. Sci. Tech.* **1986**, *31*, 59–68.
157. Moreau, E.; Mayoux, C.; Laurent, C.; Boudet, A. The Structural Characteristics of Water Trees in Power Cables and Laboratory Specimens. *Trans. Dielectr. Electr. Insul.* **1993**, *28*, 54–64. [CrossRef]
158. Ohki, Y.; Ebinuma, Y.; Katakai, S. Space Charge Formation in Water-treed Insulation. *IEEE Trans. Dielectr. Electr. Insul.* **1998**, *5*, 707–712. [CrossRef]
159. Stancu, C.; Notingher, P.V.; Ciuprina, F.; Notingher, P., Jr.; Agnel, S.; Castellon, J.; Toureille, A. Computation of the Electric Field in Cable Insulation in the Presence of Water Trees and Space Charge. *IEEE Trans. Ind. Appl.* **2009**, *45*, 30–49. [CrossRef]
160. Stancu, C.; Notingher, P.V.; Notingher, P., Jr. Influence of Space Charge Related to Water Trees on the Breakdown Voltage of Power Cable Insulation. *J. Electrostat.* **2013**, *71*, 145–154. [CrossRef]
161. Stancu, C.; Notingher, P.N.; Notingher, P., Jr. Computation of the Electric Field in Aged Underground Medium Voltage Cable Insulation. *IEEE Trans. Dielectr. Electr. Insul.* **2013**, *20*, 1530–1539. [CrossRef]
162. Fothergill, J.C. Ageing, Space Charge and Nanodielectrics: Ten Things We Don't Know About Dielectrics. In Proceedings of the IEEE International Conference on Solid Dielectrics (ICSD), Winchester, UK, 8–13 July 2007; pp. 1–10.
163. Stancu, C. Characterization of Polymeric Insulation Ageing State by Water Tree and Space Charge Measurements. Ph.D. Thesis, Politehnica University of Bucharest (UPB), Bucharest, Romania, Montpellier 2 University 2 (UM2), Montpellier, France, 2008.
164. Ieda, M. Electrical conduction and carrier traps in polymeric materials. *IEEE Trans. Electr. Insul.* **1984**, *EI-19*, 162–178. [CrossRef]
165. Nelson, J.K.; Hu, Y. The Impact of Nanocomposite Formulations on Electrical Voltage Endurance. In Proceedings of the IEEE International Conference on Solid Dielectrics (ICSD), Toulouse, France, 5–9 July 2004; pp. 832–835.

166. Lv, Z.; Wu, K.; Wang, X.; Zhao, X.; Dissado, L.A.; Niu, Y. Thickness dependence of space charge in XLPE and its nanocomposites under temperature gradient. In Proceedings of the IEEE International Conference on Solid Dielectrics (ICSD), Bologna, Italy, 30 June–4 July 2013; pp. 250–253.
167. Chen, X.; Wang, X.; Wu, K.; Peng, Z.R.; Cheng, Y.H.; Tu, D.M. Space charge measurement in LDPE films under temperature gradient and dc stress. *IEEE Trans. Dielectr. Electr. Insul.* **2010**, *17*, 1796–1805. [CrossRef]
168. Nelson, J.K.; Fothergill, J.C.; Dissado, L.A.; Peasgood, W. Towards an understanding of nanometric dielectrics. In Proceedings of the Annual Report Conference on Electrical Insulation and Dielectric Phenomena (CEIDP), Cancun, Mexico, 20–24 October 2002; pp. 295–298.
169. Yin, Y.; Chen, J.; Xiao, D.; Tu, D.; Yin, R.; Qian, H. Effect of Space Charge in Nanocomposite of LDPE/TiO_2. In Proceedings of the IEEE 7th International Conference on Properties and Applications of Dielectric Materials (ICPADM), Nagoya, Japan, 1–5 June 2003; pp. 913–916.
170. Yin, Y.; Wu, J.; Lan, L.; Li, X.; Wang, Q. Effect of nanosilica grain size on the trap density distribution in LDPE/silica nanocomposite. In Proceedings of the IEEE International Conference on Solid Dielectrics (ICSD), Bologna, Italy, 30 June–4 July 2013; pp. 726–729.
171. Nelson, J.K.; Fothergill, J.C. Internal charge behaviour in nanocomposites. *Nanotechnology* **2004**, *15*, 586–595. [CrossRef]
172. Tanaka, T.; Montanari, G.C.; Mülthaupt, R. Polymer Nanocomposites as Dielectrics and Electrical Insulation—Perspectives for Processing Technologies, Material Characterization and Future Applications. *IEEE Trans. Dielectr. Electr. Insul.* **2004**, *11*, 763–784. [CrossRef]
173. Wang, Y.; Chen, G.; Vaughan, A. Space charge dynamics in silica-based polyethylene nanocomposites. In Proceedings of the IEEE Conference on Electrical Insulation and Dielectric Phenomena (CEIDP), Des Moines, IA, USA, 19–22 October 2014; pp. 727–730.
174. Xu, Z.; Guo, M.; Frechette, M.; David, E.; Chen, G. Space charge properties of LDPE-based composites with three types of POSS. In Proceedings of the IEEE Conference on Electrical Insulation and Dielectric Phenomena (CEIDP), Toronto, ON, Canada, 16–19 October 2016; pp. 679–682.
175. Fleming, R.J.; Ammala, A.; Casey, P.S.; Lang, S.B. Conductivity and Space Charge in LDPE/$BaSrTiO_3$ Nanocomposites. In Proceedings of the Annual Report Conference on Electrical Insulation and Dielectric Phenomena (CEIDP), West Lafayette, IN, USA, 17–20 October 2010; pp. 1–4.
176. Fleming, R.J.; Ammala, A.; Casey, P.S.; Lang, S.B. Conductivity and Space Charge in LDPE/$BaSrTiO_3$ Nanocomposites. *IEEE Trans. Dielectr. Electr. Insul.* **2011**, *18*, 15–23. [CrossRef]
177. Tian, F.; Lei, Q.; Wang, X.; Wang, Y. Investigation of electrical properties of LDPE/ZnO nanocomposite dielectrics. *IEEE Trans. Dielectr. Electr. Insul.* **2012**, *19*, 763–769. [CrossRef]
178. Murata, Y.; Murakami, Y.; Nemoto, M.; Sekiguchi, Y.; Inoue, Y.; Kanaoka, M.; Hozumi, N.; Nagao, M. Effects of Nano-sized MgO-filler on Electrical Phenomena under DC Voltage Application in LDPE. In Proceedings of the IEEE Conference on Electrical Insulation and Dielectric Phenomena (CEIDP), Nashville, TN, USA, 16–19 October 2005; pp. 158–161.
179. Taima, J.; Inaoka, K.; Maezawa, T.; Tanaka, Y.; Takada, T.; Murata, Y. Observation of Space Charge Formation in LDPE/MgO Nano-composite under DC Stress at High Temperature. In Proceedings of the IEEE Conference on Electrical Insulation and Dielectric Phenomena (CEIDP), Kansas City, MO, USA, 15–18 October 2006; pp. 302–305.
180. Sato, S.; Yanagisawa, S.; Tanaka, Y.; Takada, T.; Watanabe, R.; Tomita, N. Investigation of Space Charge Behavior in Polyimide film during Elevating Temperature. In Proceedings of the Conference on Electrical Insulation and Dielectric Phenomena (CEIDP), Boulder, CO, USA, 17–20 October 2004; pp. 57–60.
181. Zheng, Y.; Wang, Q.; Yin, Y.; Li, X. Temperature Effect on Space Charge Dynamics in LDPE/MgO Nanocomposite under DC Stress. In Proceedings of the 10th IEEE International Conference on Solid Dielectrics (ICSD), Potsdam, Germany, 4–9 July 2010; pp. 1–4.
182. Wu, K.; Chen, X.; Liu, X.; Wang, X.; Cheng, Y.; Dissado, L.A. Study of the space charge behavior in polyethylene nanocomposites under temperature gradient. In Proceedings of the International Conference on Electrical Insulating Materials (ISEIM), Kyoto, Japan, 6–10 September 2011; pp. 84–87.
183. Wu, J.; Liu, W.; Zheng, Y.; Wang, Q.; Yin, Y. Effect of Nano-additive Size on the Space Charge Behaviour in LDPE/SiO_2 Nanocomposite. In Proceedings of the 10th IEEE International Conference on Solid Dielectrics (ICSD), Potsdam, Germany, 4–9 July 2010; pp. 1–4.

184. Yang, L.; Bai, G.; Liu, Y.; Gu, J.; Li, J.; Zhang, H. Electric Field Inducement of Montmorillonite in LDPE and Properties of Electrical Tree Growing in this Composite. *IEEE Trans. Dielectr. Electr. Insul.* **2015**, *22*, 1684–1693. [CrossRef]
185. Pitsa, D.; Vardakis, G.E.; Danikas, M.G.; Chen, Y. Electrical Tree Simulation and Breakdown in Nanocomposite Polymers: The Role of Nanoparticles. In Proceedings of the IEEE International Conference on Solid Dielectrics (ICSD), Potsdam, Germany, 4–9 July 2010; pp. 1–3.
186. Notingher, P.V. Contributii la Studiul Solicitarilor Materialelor Izolante din Masinile Electrice. Ph.D. Thesis, Politehnica University of Bucharest, Bucharest, Romania, 1983.
187. Holto, J.; Ildstad, E. Electrical Treeing in Extruded Polypropylene High Voltage Cable Insulation. In Proceedings of the International Conference on High Voltage Engineering and Application (ICHVE), New Orleans, LA, USA, 11–14 October 2010; pp. 373–376.
188. Du, B.X.; Ma, Z.L.; Gao, Y. Phenomena and Mechanism of Electrical Tree in Silicone Rubber. In Proceedings of the IEEE 9th International Conference on Properties and Applications of Dielectric Materials (ICPADM), Harbin, China, 19–23 July 2009; pp. 37–40.
189. Guastavino, F.; Dardano, A.; Montanari, G.C.; Testa, L.; Bellucci, F. Electrical Treeing in EVA-Boehmite and EVA-Montmorillonite Nanocomposites. In Proceedings of the IEEE Electrical Insulation Conference (EIC), Montreal, QC, Canada, 31 May–3 June 2009; pp. 382–386.
190. Rouha, N.; Beroual, A. Physico-Chemical Diagnosis of EPDM Electrical Aging by Tree Phenomenon. *IEEE Trans. Dielectr. Electr. Insul.* **2013**, *20*, 1577–1583. [CrossRef]
191. Cui, Y.; Wu, G.; Wu, C.; Luo, Y. Possible Mechanism of Electrical Treeing and Breakdown for Polyimide Nanocomposite Film Used in Inverter-Fed Motor. In Proceedings of the Annual Report Conference on Electrical Insulation and Dielectric Phenomena (CEIDP), West Lafayette, IN, USA, 17–20 October 2010; pp. 1–4.
192. Bahadoorsingh, S.; Rowland, S.M. Investigating the Influence of the Lubricant Coating on Hypodermic Needles on Electrical Tree Characteristics in Epoxy Resin. *IEEE Trans. Dielectr. Electr. Insul.* **2010**, *17*, 701–708. [CrossRef]
193. Dissado, L.A. Understanding Electrical Trees in Solid: From Experiment to Theory. *IEEE Trans. Dielectr. Electr. Insul.* **2002**, *9*, 483–497. [CrossRef]
194. Champion, J.V.; Dodd, S.J.; Vaughan, A.S.; Zhao, Y.; Sutton, S.J. The Effect of Voltage, Temperature and Morphology on Electrical Treeing in Polyethylene Blends. In Proceedings of the 8th International Conference on Dielectric Materials, Measurements and Applications, Edinburgh, UK, 17–21 September 2000; pp. 35–40.
195. Chen, G.; Tham, C.H. Electrical Treeing Characteristics in XLPE Power Cable Insulation in Frequency Range between 20 and 500 Hz. *IEEE Trans. Dielectr. Electr. Insul.* **2009**, *16*, 179–188. [CrossRef]
196. Wang, H.; He, J.; Zhang, X.; Li, Z.; Li, L.; Guan, G. Electrical Tree Inception Characteristics of XLPE Insulation Under Power-Frequency Voltage and Superimposed Impulse Voltage. In Proceedings of the 11th International Symposium on High Voltage Engineering (ISH), London, UK, 27–23 August 1999; pp. 320–323.
197. Champion, J.V.; Dodd, S.J. The effect of material composition and temperature on electrical tree growth in epoxy resins. In Proceedings of the 8th International Conference on Dielectric Materials, Measurements and Applications, Edinburgh, UK, 17–21 September 2000; pp. 30–34.
198. Alapati, S.; Thomas, M.J.; Ajay, K. Effect of morphology on electrical treeing in low density polyethylene nanocomposites. *IET Sci. Meas. Technol.* **2014**, *8*, 60–68. [CrossRef]
199. Cooper, J.M.; Stevens, G.C. The influence of physical properties on electrical treeing in a cross-linked synthetic resin. *J. Phys. D Appl. Phys.* **1990**, *23*, 1528–1535. [CrossRef]
200. Dodd, S.J.; Champion, J.V.; Zhao, Y.; Vaughan, A.S.; Sutton, S.J.; Swingler, S.G. Influence of Morphology on Electrical Treeing in Polyethylene Blends. *IEE Proc.* **2003**, *150*, 58–64. [CrossRef]
201. Harlin, A.; Shuvalov, M.; Ovsienko, V.; Juhanoja, J. Insulation Morphology Effects on the Electrical Treeing Resistance. *IEEE Trans. Dielectr. Electr. Insul.* **2002**, *9*, 401–405. [CrossRef]
202. Hozumi, N.; Ishida, M.; Okamoto, T.; Fukagawa, H. The influence of morphology on electrical tree initiation in polyethylene under ac and impulse voltages. *IEEE Trans. Dielectr. Electr. Insul.* **1990**, *25*, 707–714. [CrossRef]
203. Jarvid, M. Voltage Stabilizers: From Design to Synthesis, Processing and Electrical Characterization. Ph.D. Thesis, Chalmers University of Technology, Gothenburg, Sweden, 2014.

204. Kurnianto, R.; Murakami, Y.; Hozumi, N.; Nagao, M. Characterization of Tree Growth in Filled Resin: The effect of filler and moisture content. *IEEE Trans. Dielectr. Electr. Insul.* **2007**, *14*, 427–435. [CrossRef]
205. Auckland, D.W.; Taha, A.; Varlow, B.R. Correlation of Mechanical Properties with Electrical Treeing Behaviour at Elevated Temperatures. In Proceedings of the Annual Report Conference on Electrical Insulation and Dielectric Phenomena (CEIDP), Pocono Manor, PA, USA, 17–20 October 1993; pp. 636–641.
206. Berg, G.; Sæternes, H.H.; Aakervik, J.; Hvidsten, S. The Effect of Hydrostatic Pressure on Electrical Treeing in Silicone Cable Joints. In Proceedings of the IEEE International Symposium on Electrical Insulation (ISEI), San Juan, PR, USA, 10–13 June 2012; pp. 609–612.
207. Varlow, B.R.; Auckland, D.W. The Influence of Mechanical Factors on Electrical Treeing. *IEEE Trans. Dielectr. Electr. Insul.* **1998**, *5*, 761–765. [CrossRef]
208. Jarvid, E.M.; Johansson, A.B.; Blennow, J.H.M.; Andersson, M.R.; Gubanski, S.M. Evaluation of the Performance of Several Object Types for Electrical Treeing Experiments. *IEEE Trans. Dielectr. Electr. Insul.* **2013**, *20*, 1712–1719. [CrossRef]
209. Vijh, A.K.; Crine, J.-P. Influence of Metallic Electrodes on Electrical Tree Initiation in Polyethylene. *J. Appl. Phys.* **1989**, *65*, 398–399. [CrossRef]
210. Jarvid, M.; Johansson, A.; Englund, V.; Gubanski, S.; Andersson, M.R. Electrical tree inhibition by voltage stabilizers. In Proceedings of the Conference on Electrical Insulation and Dielectric Phenomena (CEIDP), Montreal, QC, Canada, 14–17 October 2012; pp. 605–608.
211. Johansson, A.B. Characterising Resistance to Electrical Treeing in New XLPE-Based Materials for High-Voltage Cables. Ph.D. Thesis, Chalmers University of Technology, Gothenburg, Sweden, 2015.
212. Vogelsang, R.; Farr, T.; Fröhlich, K. The effect of barriers on electrical tree propagation in composite insulation materials. *IEEE Trans. Dielectr. Electr. Insul.* **2006**, *13*, 373–382. [CrossRef]
213. Ding, H.Z.; Varlow, B.R. Effect of nanofillers on electrical treeing in epoxy resin subjected to AC voltage. In Proceedings of the Conference on Electrical Insulation and Dielectric Phenomena (CEIDP), Boulder, CO, USA, 17–20 October 2004; pp. 332–335.
214. Kurnianto, R.; Murakami, Y.; Nagao, M.; Hozumi, N.; Murata, Y. Treeing breakdown in inorganic filler/LDPE nanocomposite material. *IEE J. Trans. Fundam. Mater.* **2007**, *127*, 29–34. [CrossRef]
215. Yamano, Y.; Iizuka, M. Improvement of electrical tree resistance of LDPE by mixed addition of nanoparticles and phthalocyanine. *IEEE Trans. Dielectr. Electr. Insul.* **2011**, *18*, 329–337. [CrossRef]
216. Yamano, Y.; Iizuka, M. Suppression of Electrical Tree Initiation in LDPE by Additives of Polycyclic Compounds. *IEEE Trans. Dielectr. Electr. Insul.* **2009**, *16*, 189–198. [CrossRef]
217. Bahder, G.; Katz, C.; Lawson, J.; Vahlstrom, W. Electrical and electro-chemical treeing effect in polyethylene and crosslinked polyethylene cables. *IEEE Trans. Power APP Syst.* **1974**, *PAS-93*, 977–990. [CrossRef]
218. Khalil, M.S.; Gastli, A. Investigation of the dependence of DC insulation resistivity of ultra-clean polyethylene on temperature and electric field. *IEEE Trans. Power Deliv.* **1999**, *14*, 699–704. [CrossRef]
219. Englund, V.; Huuva, R.; Gubanski, S.M.; Hjertberg, T. Synthesis and Efficiency of Voltage Stabilizers for XLPE Cable Insulation. *IEEE Trans. Dielectr. Electr. Insul.* **2009**, *16*, 1455–1461. [CrossRef]
220. Alapati, S.; Thomas, M.J. Electrical treeing and the associated PD characteristics in LDPE nanocomposites. *IEEE Trans. Dielectr. Electr. Insul.* **2012**, *19*, 697–704. [CrossRef]
221. Yamano, Y. Control of Electrical Tree at Initiation Stage in LDPE by Mixed Addition of Al_2O_3 Nano-particle and Azobenzoic Compound. *IEEE Trans. Dielectr. Electr. Insul.* **2014**, *21*, 209–216. [CrossRef]
222. Zhang, J.; Gao, J.; Liu, J.; Ji, Q.; Zhang, M.; Zhang, X. Studies on Electrical Tree and Partial Discharge Properties of PE/MMT Nanocomposites. In Proceedings of the International Symposium on Electrical Insulating Materials (ISEIM), Yokkaichi, Japan, 7–11 September 2008; pp. 311–314.
223. Chi, X.; Gao, J.; Zhang, X. Electrical Tree Propagating Characteristics of Polyethylene/Nano-Montmorillonite Composites. *IEEE Trans. Dielectr. Electr. Insul.* **2015**, *22*, 1530–1536. [CrossRef]
224. Guastavino, F.; Dardano, A.; Squarcia, S.; Tiemblo, P.; Guzman, J.; Benito, E.; Garcia, N. Electrical treeing in LDPE nanocomposite materials. In Proceedings of the IEEE Conference on Electrical Insulation and Dielectric Phenomena (CEIDP), Virginia Beach, VA, USA, 18–21 October 2009; pp. 697–700.
225. Guastavino, F.; Dardano, A.; Squarcia, S.; Tiemblo, P.; Guzman, J.; Garcia, N. An experimental study about electrical treeing inside LDPE nanocomposites. In Proceedings of the 10th IEEE International Conference on Solid Dielectrics (ICSD), Potsdam, Germany, 4–9 July 2010; pp. 1–4.

226. Tiemblo, P.; Hoyos, M.; Gomez-Elvira, J.M.; Guzman, J.; Garcia, N.; Dardano, A.; Guastavino, F. The Development of Electrical Treeing in LDPE and its Nanocomposites with Spherical Silica and Fibrous and Laminar Silicates. *J. Phys. D Appl. Phys.* **2008**, *41*, 1–8. [CrossRef]
227. Kurnianto, R.; Murakami, Y.; Hozumi, N.; Nagao, M.; Murata, Y. Some Fundamentals on Treeing Breakdown in Inorganic-filler/LDPE Nano-composite Material. In Proceedings of the IEEE Conference on Electrical Insulation and Dielectric Phenomena (CEIDP), Kansas City, MO, USA, 15–18 October 2006; pp. 373–376.
228. Tanaka, T. Buds for Treeing in Epoxy Nanocomposites and their Possible Interaction with Nano Fillers. In Proceedings of the 10th IEEE International Conference on Solid Dielectrics (ICSD), Potsdam, Germany, 4–9 July 2010; pp. 1–4.
229. Kawano, M.; Murakami, Y.; Nagao, M.; Sekiguchi, Y.; Reddy, C.C.; Murata, Y. Treeing Breakdown Phenomena in MgO/LDPE Nanocomposite Material. In Proceedings of the IEEE International Conference on Applications and Dielectric Materials (ICPADM), Harbin, China, 19–23 July 2009; pp. 837–840.
230. Tanaka, T.; Iizuka, T.; Sekiguchi, Y.; Murata, Y.; Ohki, Y. Tree Initiation and Growth in LDPE/MgO Nanocomposites and Roles of Nano Fillers. In Proceedings of the IEEE Conference on Electrical Insulation and Dielectric Phenomena (CEIDP), Virginia Beach, VA, USA, 18–21 October 2009; pp. 646–649.
231. Tanaka, T.; Yokoyama, K.; Ohki, Y.; Murata, Y.; Sekiguchi, Y.; Goshowaki, M. High Field Light Emission in LDPE/MgO Nanocomposite. In Proceedings of the International Symposium on Electrical Insulating Materials (ISEIM), Yokkaichi, Japan, 7–11 September 2008; pp. 506–509.
232. Xiao, C.; Zhang, Y.; Zheng, F.; Xia, J.; Wu, C. Treeing-Like Breakdown in Electron beam Irradiated LDPE with/without Nano- Powder Doping. In Proceedings of the 8th International Conference on Applications and Dielectric Materials (ICPADM), Bali, Indonesia, 26–30 June 2006; pp. 167–170.
233. Chen, J.L.; Filippini, J.C. The Morphology and Behavior of the Water Tree. *IEEE Trans. Electr. Insul.* **1993**, *28*, 271–286. [CrossRef]
234. Stucki, F.; Mueller, K.-B. Properties of Individual Water Trees in VPE Cables. *Elektrizitätswirtschaft* **1993**, *92*, 1732–1736.
235. Meyer, C.T. Water absorption during Water Treeing in Polyethylene. *IEEE Trans. Electr. Insul.* **1983**, *IE-18*, 28–31. [CrossRef]
236. Steennis, E.F.; Kreuger, F.H. Water Treeing in Polyethylene Cables. *IEEE Trans. Electr. Insul.* **1990**, *25*, 989–1028. [CrossRef]
237. Visata, O.I.; Teissedre, G.; Filipinni, J.C.; Notingher, P.V. An Investigation on the Distribution of Ions and Water in Water Trees by FTIR Microspectroscopy. In Proceedings of the IEEE 7th International Conference on Solid Dielectrics (ICSD), Eindhoven, The Netherlands, 25–29 June 2001; pp. 373–376.
238. Chiru, O.; Notingher, P.V.; Jipa, S.; Setnescu, T.; Setnescu, R. Influence of antioxidant content on water trees development. In Proceedings of the 'Electrotechnics '96' Symposium, Bucharest, Romania, 6–7 December 1996; pp. 157–164.
239. Crine, J.-P. Electrical, Chemical and Mechanical Processes in Water Treeing. *IEEE Trans. Dielectr. Electr. Insul.* **1998**, *5*, 681–694. [CrossRef]
240. Nagao, M.; Watanabe, S.; Murakami, Y.; Murata, Y.; Sekiguchi, Y.; Goshowaki, M. Water tree retardation of MgO/LDPE and MgO/XLPE nanocomposites. In Proceedings of the International Symposium on Electrical Insulating Materials, (ISEIM), Yokkaichi, Japan, 7–11 September 2008; pp. 483–486.
241. Notingher, P.V.; Ciuprina, F.; Radu, I.; Filippini, J.C.; Gosse, B.; Jipa, S.; Setnescu, T.; Setnescu, R.; Mihalcea, T. Studies on Water Treeing and Chemiluminescence on Irradiated Polyethylene. In Proceedings of the IEEE International Symposium on Electrical Insulation, Montreal, QC, Canada, 16–19 June 1996; pp. 163–167.
242. Ross, R. Inception and Propagation Mechanisms of Water Treeing. *IEEE Trans. Dielectr. Electr. Insul.* **1998**, *5*, 660–680. [CrossRef]
243. Notingher, P.V.; Ciuprina, F.; Radu, I. The influence of ageing process on the shape and the propagation kinetics of the water trees in needle-plane polyethylene samples. In Proceedings of the IEEE International Conference on Conduction and Breakdown in Solid Dielectrics (ICSD), Västeras, Sweden, 22–25 June 1998; pp. 341–344.
244. Nunes, S.L.; Shaw, M.T. Water Treeing in Polyethylene—A Review of Mechanisms. *IEEE Trans. Electr. Insul.* **1980**, *15*, 437–450. [CrossRef]
245. Shaw, M.T.; Shaw, S.H. Water Treeing in Solid Dielectrics. *IEEE Trans. Electr. Insul.* **1984**, *19*, 419–452. [CrossRef]

246. Visata, O.I. Influence des Arborescences d'eau sur les Propriétés Diélectriques des Polymères. Ph.D. Thesis, Universite Joseph Fourier-Grenoble 1, France et University Politehnica of Bucarest, Bucharest, Romania, 2001.
247. Notingher, P.V.; Radu, I.; Filippini, J.C. Electric Field Calculations in Polymers in the Presence of Water-Trees. In Proceedings of the IEEE 5th International Conference on Conduction and Breakdown in Solid Dielectrics (ICSD), Leicester, UK, 10–13 July 1995; pp. 666–670.
248. Bahder, G.; Eager, G.S.; Lukac, R.G. Influence of Electrochemical Trees on the Electrical Properties of Extruded Polymeric Insulation. In Proceedings of the Annual Report Conference on Electrical Insulation and Dielectric Phenomena (CEIDP), Downingtown, PA, USA, 21–23 October 1974; pp. 289–301.
249. Tabata, T.; Nagai, H.; Fukuda, T.; Iwata, Z. Sulfide Attack and Treeing of Polyethylene Insulated Cables-Cause and Prevention. *IEEE Trans. Power Appar. Syst.* **1972**, *91*, 1354–1360. [CrossRef]
250. Tanaka, T.; Fukuda, T.; Suzuki, S.; Nitta, Y.; Goto, H.; Kubota, K. Water Trees in crosslinked Polyethylene Power Cables. *IEEE Trans. Power Appar. Syst.* **1974**, *PAS-93*, 693–702. [CrossRef]
251. Wojtas, S. Investigations of Polyethylene Insulation Resistivity of Power Cables. In Proceedings of the International Conference on Polymer Insulated Power Cables (Jicable), Paris, France, 21–25 September 1987; pp. 436–440.
252. Radu, I.; Acedo, M.; Notingher, P.; Frutos, F.; Filippini, J.C. A Study on the Dependence of Water Tree Permittivity with Time. In Proceedings of the Annual Report of the Conference on Electrical Insulation and Dielectric Phenomena (ICSD), San Francisco, CA, USA, 20–23 October 1996; pp. 762–765.
253. Stucki, F.; Schönenberger, A. Dielectric Properties on Single Water Trees. In Proceedings of the 4th International Conference on Conduction and Breakdown in Solid Dielectrics (ICSD), Sestri Levante, Italy, 22–25 June 1992; pp. 373–377.
254. Bouzerara, R. Effet de la Température sur la Dégradation du Polyéthylène par le Phénomène d'arborescences d'eau. Ph.D. Thesis, Université Joseph Fourier (UJF), Grenoble, France, 1989.
255. Densley, J. Ageing and diagnostics in extruded insulations for power cables. In Proceedings of the 5th International Conference on Conduction and Breakdown in Solid Dielectrics (ICSD), Leicester, UK, 10–13 July 1995; pp. 1–15.
256. Castellani, L.; Peruzzotti, F.; Zaopo, A.; Cinquemani, P.L.; Foulger, S.; Filippini, J.C.; Lachevre, V. Water Treeing Retardant Materials for Cable Insulators. In Proceedings of the Annual Report Conference on Electrical Insulation and Dielectric Phenomena (CEIDP), Minneapolis, MN, USA, 19–22 October 1997; pp. 1–4.
257. Castellani, L.; Perozzotti, F.; Zaopo, A.; Cinquemani, P.L.; Foulger, S.; Filippini, J.C.; Lachêvre, V. Evaluation of Materials for WTR-insulated Power Cables. *IEEE Trans. Dielectr. Electr. Insul.* **2000**, *7*, 818–824. [CrossRef]
258. Wen, Y.; Foulger, S.H.; Cinquemani, P.L.; Peruzzotti, F.; Zaopo, A. Development and testing of medium voltage power cables with water treeing retardant materials. In Proceedings of the IEEE International Symposium on Electrical Insulation, Arlington, VA, USA, 7–10 June 1998; pp. 534–537.
259. Faremo, H.; Ildstad, E. The EFI test method for accelerated growth of water trees. In Proceedings of the IEEE International Symposium on Electrical Insulation, Toronto, ON, Canada, 3–6 June 1990; pp. 191–194.
260. Hui, L.; Smith, R.; Nelson, J.K.; Schadler, L.S. Electrochemical Treeing in XLPE/silica Nanocomposites. In Proceedings of the IEEE Conference on Electrical Insulation and Dielectric Phenomena (CEIDP), Virginia Beach, VA, USA, 18–21 October 2009; pp. 511–514.
261. Ashcraft, A.C. Treeing Update-Part III: Water Treeing in Polymeric Dielectrics. In Proceedings of the World Electrotechnical Congress, Moscow, Russia, 22 June 1977.
262. Huang, X.; Ma, Z.; Jiang, P.; Kim, C.; Liu, F.; Wang, G.; Zhang, J. Influence of Silica Nanoparticle Surface Treatments on the Water Treeing Characteristics of Low Density Polyethylene. In Proceedings of the IEEE 9th International Conference on Properties and Applications of Dielectric Materials (ICPADM), Harbin, China, 19–23 July 2009; pp. 757–760.
263. Huang, X.; Liu, F.; Jiang, P. Effect of Nanoparticle Surface Treatment on Morphology, Electrical and Water Treeing Behavior of LLDPE Composites. *IEEE Trans. Dielectr. Electr. Insul.* **2010**, *17*, 1697–1704. [CrossRef]
264. Li, X.; Xu, M.; Liu, X.; Xie, D.; Darong, X. Study of Montmorillonite on Morphology and Water Treeing Behavior in Crosslinking Polyethylene. In Proceedings of the International Conference on Electrical Insulating Materials (ISEIM), Kyoto, Japan, 6–10 September 2011; pp. 205–208.

265. Huang, X.Y.; Kim, C.; Jiang, P.K.; Yin, Y.; Li, Z. Influence of aluminum nanoparticle surface treatment on the electrical properties of polyethylene composites. *J. Appl. Phys.* **2009**, *105*, 014105:1–014105:10. [CrossRef]
266. Fan, Z.H.; Yoshimura, N. The influence of crystalline morphology on the growth of water trees in PE. *IEEE Trans. Dielectr. Electr. Insul.* **1996**, *3*, 849–858. [CrossRef]
267. Green, C.; Vaughan, A. Nanodielectrics—How Much Do We Really Understand? *IEEE Electr. Insul. Mag.* **2008**, *24*, 6–16. [CrossRef]
268. Guo, M.; Fréchette, M.; David, E.; Demarquette, N.R. Influence of fabrication techniques on the dielectric properties of PE/POSS polymeric composites. In Proceedings of the IEEE Electrical Insulation Conference (EIC), Montreal, QC, Canada, 19–22 June 2016; pp. 297–300.
269. Huang, X.; Jiang, P.; Tanaka, T. A review of dielectric polymer composites with high thermal conductivity. *IEEE Electr. Insul. Mag.* **2011**, *27*, 8–16. [CrossRef]
270. Roy, M.; Reed, C.W.; MacCrone, R.K.; Schadler, L.S.; Nelson, J.K.; Keefe, R.; Zenger, W. Evidence for the role of the interface in polyolefin nanocomposites. In Proceedings of the International Symposium on Electrical Insulating Materials (ISEIM), Kitakyushu, Japan, 5–9 June 2005; pp. 223–226.
271. Reading, M.; Vaughan, A.S. Comparison of rheological, thermal and electrical properties of poly(ethylene oxide) composites with micro and nano sized silicon dioxide filler. In Proceedings of the 10th IEEE International Conference on Solid Dielectrics (ICSD), Potsdam, Germany, 4–9 July 2010; pp. 1–4.
272. Artbauer, J. Electric strength of polymers. *J. Phys. D Appl. Phys.* **1996**, *29*, 446–456. [CrossRef]
273. Lewis, T.J. Interfaces are the Dominant Feature of Dielectrics at the Nanometric Level. *IEEE Trans. Dielectr. Electr. Insul.* **2004**, *11*, 739–753. [CrossRef]
274. Nelson, J.K.; Huan, Y.; Krentz, T.M.; Schadler, L.S.; Dryzek, J.; Benicewicz, B.C.; Bell, M. Free volume in nanodielectrics. In Proceedings of the IEEE 11th International Conference on the Properties and Applications of Dielectric Materials (ICPADM), Sydney, Australia, 19–22 July 2015; pp. 40–43.
275. Lau, K.Y.; Vaughan, A.S.; Chen, G.; Hosier, I.L. Polyethylene nanodielectrics: The effect of nanosilica and its surface treatment on electrical breakdown strength. In Proceedings of the Annual Report Conference on Electrical Insulation and Dielectric Phenomena (CEIDP), Montreal, QC, Canada, 14–17 October 2012; pp. 21–24.
276. IEEE Std. 930-2004. *IEEE Guide for the Statistical Analysis of Electrical Insulation Breakdown Data*; IEEE: Piscataway, NJ, USA, 2005; pp. 1–41.
277. Virtanen, S.; Vaughan, A.S.; Yang, L.; Saiz, F.; Quirke, N. Dielectric breakdown strength and electrical conductivity of low density polyethylene octylnanosilica composite. In Proceedings of the IEEE Conference on Electrical Insulation and Dielectric Phenomena (CEIDP), Toronto, ON, Canada, 16–19 October 2016; pp. 58–61.
278. Wang, W.; Li, S.; Tang, F.; Li, J. Characteristics on Breakdown Performance of Polyethylene/Silica Dioxide Nanocomposites. In Proceedings of the Annual Report Conference on Electrical Insulation and Dielectric Phenomena (CEIDP), Montreal, QC, Canada, 14–17 October 2012; pp. 521–524.
279. Guastavino, F.; Ratto, A.; Torello, E.; Hoyos, M.; Garcia, N.; Reinecke, H.; Benito, E.; Tiemblo, P. AC electrical strength measurements on LDPE nanocomposites. In Proceedings of the Annual Report Conference on Electrical Insulation and Dielectric Phenomena (CEIDP), Kansas City, MO, USA, 15–18 October 2006; pp. 329–332.
280. Green, C.D.; Vaughan, A.S.; Mitchell, G.R.; Liu, T. Structure Property Relationships in Polyethylene/Montmorillonite Nanodielectrics. *IEEE Trans. Dielectr. Electr. Insul.* **2008**, *15*, 134–143. [CrossRef]
281. Vaughan, A.S.; Green, C.D.; Zhang, Y.; Chen, G. Nanocomposites for high voltage applications: EFFECT of sample preparation on AC breakdown statistics. In Proceedings of the Annual Report Conference on Electrical Insulation and Dielectric Phenomena (CEIDP), Nashville, TN, USA, 16–19 October 2005; pp. 732–735.
282. Vaughan, A.S.; Swingler, S.G.; Zhang, Y. Polyethylene nanodielectrics: The influence of nanoclays on structure formation and dielectric breakdown. *IEEJ Trans. Fundam. Mater.* **2006**, *126*, 1057–1063. [CrossRef]
283. Shah, K.S.; Jain, R.C.; Shrinet, V.; Singh, A.K.; Bharambe, D.P. High Density Polyethylene (HDPE) Clay Nanocomposite for Dielectric Applications. *IEEE Trans. Dielectr. Electr. Insul.* **2009**, *16*, 853–861. [CrossRef]

284. Guo, M.; David, É.; Fréchette, M.; Demarquette, N.R. Low-density polyethylene/polyhedral oligomeric silsesquioxanes composites obtained by extrusion. In Proceedings of the IEEE Conference on Electrical Insulation and Dielectric Phenomena (CEIDP), Toronto, ON, Canada, 16–19 October 2016; pp. 647–650.
285. Reddy, C.C.; Gosyowaki, M.; Murata, Y.; Sekiguchi, Y. Superior thermal breakdown performance of MgO-LDPE nanocomposite materials for HVDC insulation. In Proceedings of the International Symposium on Electrical Insulating Materials (ISEIM), Yokkaichi, Japan, 7–11 September 2008; pp. 661–664.
286. Reddy, C.C.; Ramu, T.S. Polymer Nanocomposites as Insulation for HV DC Cables—Investigations on the Thermal Breakdown. *IEEE Trans. Dielectr. Electr. Insul.* **2008**, *15*, 221–227. [CrossRef]
287. Ma, D.; Siegel, R.W.; Hong, J.-I.; Schadler, L.S.; Mårtensson, E.; Önneby, C. Influence of nanoparticle surfaces on the electrical breakdown strength of nanoparticle-filled low-density polyethylene. *J. Mater. Res.* **2004**, *19*, 857–863. [CrossRef]
288. Wang, Y.; Wang, C.; Zhang, Z.; Xiao, K. Anti-thermal Aging Properties of Low-Density Polyethylene-Based Nanocomposites. *IEEE Trans. Dielectr. Electr. Insul.* **2018**, *25*, 1003–1013. [CrossRef]
289. Esthappan, K.S.; Kuttappan, K.S.; Josepha, R. Effect of titanium dioxide on the thermal ageing of polypropylene. *Polym. Degrad. Stab.* **2012**, *97*, 615–620. [CrossRef]

polymers

MDPI

Article

Adsorption Behavior of Polymer Chain with DifferentTopology Structure at the Polymer-Nanoparticle Interface

Qingliang Song, Yongyun Ji, Shiben Li, Xianghong Wang and Linli He *

Department of Physics, Wenzhou University, Wenzhou 325035, China; qingliangsong1992@163.com (Q.S.); yyji@wzu.edu.cn (Y.J.); shibenli@wzu.edu.cn (S.L.); wxh@wzvtc.edu.cn (X.W.)
* Correspondence: linlihe@wzu.edu.cn; Tel.: +86-577-8668-9068

Received: 18 April 2018; Accepted: 25 May 2018; Published: 28 May 2018

Abstract: The effect of the polymer chain topology structure on the adsorption behavior in the polymer-nanoparticle (NP) interface is investigated by employing coarse-grained molecular dynamics simulations in various polymer-NP interaction and chain stiffness. At a weak polymer-NP interaction, ring chain with a closed topology structure has a slight priority to occupy the interfacial region than linear chain. At a strong polymer-NP interaction, the "middle" adsorption mechanism dominates the polymer local packing in the interface. As the increase of chain stiffness, an interesting transition from ring to linear chain preferential adsorption behavior occurs. The semiflexible linear chain squeezes ring chain out of the interfacial region by forming a helical structure and wrapping tightly the surface of NP. In particular, this selective adsorption behavior becomes more dramatic for the case of rigid-like chain, in which 3D tangent conformation of linear chain is absolutely prior to the 2D plane orbital structure of ring chain. The local packing and competitive adsorption behavior of bidisperse matrix in polymer-NP interface can be explained based on the adsorption mechanism of monodisperse (pure ring or linear) case. These investigations may provide some insights into polymer-NP interfacial adsorption behavior and guide the design of high-performance nanocomposites.

Keywords: chain topology; selective adsorption; polymer-NP interface

1. Introduction

Polymer nanocomposites that consist of mixtures of polymers and organic/inorganic particles are a new member of composite materials, which have been used in a wide variety fields [1]. The macroscopic properties (such as mechanic, electronic, optical, and so forth) of nanocomposites not only depend on the microscopic morphology of constituent nanoparticle (NP) in the polymer matrix [2–6], but also are sensitive to the polymer conformation, especially the local packing at polymer-NP interface. For example, carbon black particles are immersed to increase the strength, viscosity, and durability of rubbers [7,8], and fullerenes are used to enhance the efficiency of polymer-based photovoltaic devices [9].

Nevertheless, it has been proven that the adding of particles into polymeric materials frequently results in agglomeration and phase separation, a uniform dispersion of NPs in polymer matrix is hard to get, owing to the strong interparticle interactions and weak polymer-NP interfacial interaction. Many experimental [10,11], theoretical [12,13], and simulation [14–17] studies have been devoted to investigating this issue. Hooper et al. theoretically pointed out that there are four general categories of polymer-mediated NP organization: contact aggregation due to depletion attraction, segment level tight particle bridging, steric stabilization due to thermodynamically stable "bound polymer layers", and "tele-bridging" where distinct adsorbed layers coexist with longer range bridging [12]. Mackay et al. experimentally demonstrated that thermodynamically stable dispersion of NPs into

a polymeric liquid is enhanced when the radius of gyration of the linear polymer is greater than the NP radius [10]. Liu et al. emphasized that a homogeneous filler dispersion exists just at the intermediate interfacial interaction by computer simulations [14]. In a subsequent study by Singh et al., they analyzed the transitions between different structures in the polymer-NP system caused by the polymer-NP interaction strength and polymer chain length, respectively [15].

On the other hand, some researchers have paid their attention to the polymer conformation behavior in nanocomposites, such as the dimension [11,16,18–20]. However, up to date, there is also controversy as to whether the addition of NPs to a polymer melt causes polymer chains either to expand, shrink or be unperturbed compared to their size in the bulk. For instance, Mackay et al. found that when the radius of gyration of the polymer is larger than the chemically identical NP radius, a 10–20% expansion in deuterated polystyrene (d-PS) chain dimensions occurs by neutron scattering [11]. However, Crawford et al. ensured a spatially uniform dispersion of 13 nm silica NPs miscible in polystyrene melts by neutron scattering, X-ray scattering, and transmission electron microscopy. They found that the polymer size in nanocomposites remains unaltered regardless of the relative size between components and NP loading [16]. From a simulation point of view, Clarke et al. demonstrated that the polymer chains are unperturbed by the presence of repulsive NPs, while it can be stretched and flattened by the attractive NPs with very small size [20]. Yan et al. reviewed the recent progress on the structure, dynamics, and physical properties of PNCs [21]. Besides the investigation on the NP dispersion and polymer conformation, some attentions are also drawn to understanding the local packing [14,22–25] and dynamics [26–29] of polymer matrix at the polymer-NP interface. Chen et al. [22] experimentally observed double glass transition and interfacial immobilized layer in in-Situ-Synthesized PVA/Silica Nanocomposites, and pointed out the interfacial layer is mainly composed of partial segments of different polymer chains, which is further verified by the molecular dynamics simulation of Liu et al. [14]. Vacatello et al. used Monte Carlo (MC) simulations to obtain a general picture of the molecular arrangements in polymer-based nanocomposites, in which the chains are classified as the sequences of interface, bridge and loop segments [24]. Ge et al. [26] investigated the role of polymer topology in the dynamical coupling between NPs and polymers in nanocomposites. Kumar et al. [27] studied the diffusion of nanoparticle in polymer nanocomposites and provided an excellent understanding on the motion of NPs, which the size is smaller than the polymer entanglement mesh size. Besides, Ying et al. [28,29] used molecular dynamics simulation to study the effect of nanoparticle volume fraction on the dynamics of polymer and offered an explanation for understanding the rheological properties of polymer composites.

Obviously, polymer chains around NP exhibit dramatically different interfacial behavior in comparison with the bulk phase. Several groups [30–32] paid their attention on the adsorption mechanism of polymers on flat surfaces. For instance, Cohen-Stuart et al. [30] performed MC simulations for studying the competition between surface adsorption and folding of fibril-forming polypeptides, and their results suggest that a weakly attractive surface can enhance the folding. Sommer et al. [31] used computer simulations on the adsorption of branched and dendritic polymers onto flat surfaces, there is a two-step adsorption scenario on temperature dependence related with strong excluded volume effects.

Nevertheless, there is no general experimental, theoretical, and simulation consensus about the accurate characterization and interpretation of the interfacial region, especially considering the adsorption mechanism of polymer chains with polydispersity close to the surface of NP. We have involved this issue by exploring the interfacial adsorption mechanism by varying the polymer-NP interaction, which may be the main factor in determining the interfacial behavior. Our study further confirmed that one of chain ends prefers to be in contact with NP and shows a perpendicular conformation to the NP surface when the polymer-NP interactions are weak (i.e., endpoint adsorption); while the inner chain monomers wrap NP tightly when the attractive interactions are strong (i.e., middle adsorption) [25]. In order to further characterize the adsorption mechanism and local packing of

bidisperse matrix with different topologies in the polymer-NP interfacial region, we focus on the mixtures of ring and linear polymer chain in nanocomposites.

2. Model and Methods

In our simulation, a standard bead-spring model is used to model polymer chain. Each ring or linear polymer chain consists of n spherical monomers with diameter of σ and mass of m, which are interconnected by the finitely extendable nonlinear elastic (FENE) potential [33]:

$$U_{\mathrm{FENE}}(r) = -\frac{KR_0^2}{2}\ln\left[1-\left(\frac{r}{R_0}\right)^2\right], r < R_0 \tag{1}$$

where r is the distance between the two neighboring monomers. $K = 30\varepsilon/\sigma^2$ is a spring constant and $R_0 = 1.5\sigma$ is a finite extensibility to avoid chain crossing, where σ is the monomer diameter. The stiffness of a polymer chain is described by a bending potential between adjacent bonds:

$$U_{\mathrm{bending}} = k_{\mathrm{b}}(1+\cos\theta) \tag{2}$$

where θ is the angle between two consecutive bonds and the chain stiffness is controlled by varying the value of k_{b}. NP is modeled as a Lennard-Jones (LJ) sphere of radius $R_{\mathrm{n}} = 2.5\sigma$. Mass density of NPs are the same as the polymers, therefore the mass of NP is 125 times of that of a monomer.

Here a truncated and shifted Lennard-Jones (LJ) potential is used to model NP-NP and polymer-NP interactions as well as the nonbonded interactions between all polymer monomers, as follows [34]:

$$U(r) = \begin{cases} 4\varepsilon\left[\left(\frac{\sigma}{r-r_{\mathrm{EV}}}\right)^{12} - \left(\frac{\sigma}{r-r_{\mathrm{EV}}}\right)^{6} + \frac{1}{4}\right] & r - r_{\mathrm{EV}} < r_{\mathrm{cutoff}} \\ 0 & r - r_{\mathrm{EV}} \geq r_{\mathrm{cutoff}} \end{cases} \tag{3}$$

where ε is the LJ potential interaction energy and r_{cutoff} stands for the distance $(r - r_{\mathrm{EV}})$ at which the interaction is truncated and shifted so that the energy and force are zero. In our simulation, we offset the interaction range by r_{EV} to account for the excluded volume effects of different interaction sites. For NP-NP and polymer-NP interactions, r_{EV} equals to $2R_{\mathrm{n}} - \sigma$ and $R_{\mathrm{n}} - \sigma/2$, respectively, while for polymer-polymer interactions, r_{EV} is zero. Here $\varepsilon_{\mathrm{nn}} = \varepsilon_{\mathrm{pp}} = 1.0$ and $r_{\mathrm{cutoff}} = 2^{1/6}\sigma$ in both NP-NP and polymer-polymer interactions with repulsive only part of Equation (3). Meantime, $\varepsilon_{\mathrm{np}}$ is varied to simulate different interfacial interactions with an attractive nature of $r_{\mathrm{cutoff}} = 2.5\sigma$. Here we set ε and σ to be unity for dimensionless simulation.

Our molecular dynamics simulations are performed in a NVT ensemble. The simulation box is set as $35\sigma \times 35\sigma \times 35\sigma$, where periodic boundary conditions are employed in all three directions. NPs with a fixed number of $M = 5$ are embedded at a random position and allowed to move. Here the polymer bulk density is set as $\rho^* = 0.8$ and each polymer chain consists of $n = 30$ monomers. 570 ring chains with $n = 30$ and 570 linear chains with $n = 30$ are mixed in bidisperse case, while 1140 pure ring or linear chains with $n = 30$ are selected in monodisperse case. Additionally, the velocity-verlet algorithm is used to integrate the equation of motions with time step $\Delta t = 0.01\tau$, where the unit of time $\tau = \sqrt{\varepsilon/m\sigma^2}$ and m is the mass unit of a monomer. The desired temperature is set to $T = 1.0$ by using a Langevin thermostat. Rapid annealing from the initial temperature $T = 9$ to $T = 5$ is initially employed, followed by a slow anneal-temper process between $T = 5$ and the desired temperature is performed, to prevent the simulations from trapping into a local minimum energy at a low temperature. All simulations were performed by the open source LAMMPS molecular dynamics package [35].

3. Results and Discussion

To characterize the local packing and competitive adsorption mechanism of bidisperse matrix in the polymer-NP interfacial region, the nanocomposites with the mixture of ring and linear polymer

chain are considered. We change the interaction strength, ε_{np}, from 0.1 to 10.0, representing weak to strong polymer-NP attraction, and the chain stiffness, k_b, from 0 to 50, which corresponds to the flexible, semiflexible, and rigid-like chain, respectively. Then the monodisperse case (pure ring or linear chain) is also analyzed to interpret the intrinsic reason for the competitive adsorption occurred in bidisperse case.

Before the discussion, we first examine the local structure of polymer close to the surface of NP in nanocomposites and define the polymer-NP interfacial region. Take pure linear chain for example, as shown in Figure 1, the polymer-NP pair distribution function $g_{np}(r)$ for various attraction ε_{np} exhibits an evident layering behavior. The obviously high monomer density in "Layer1" (shown in Figure 1) establishes a well defined interface between the polymer and NP, therefore we take the "Layer1" as the polymer-NP interfacial region in the following study. Meanwhile, we present the whole chain in the snapshots of nanocomposites by only one or more monomers per chain located within Layer1. Figure 1 also shows that the polymer density around NP increases with increasing ε_{np} from weak to strong attraction, which is consistent with the studies by Gao et al. [14] and Karatrantos et al. [20].

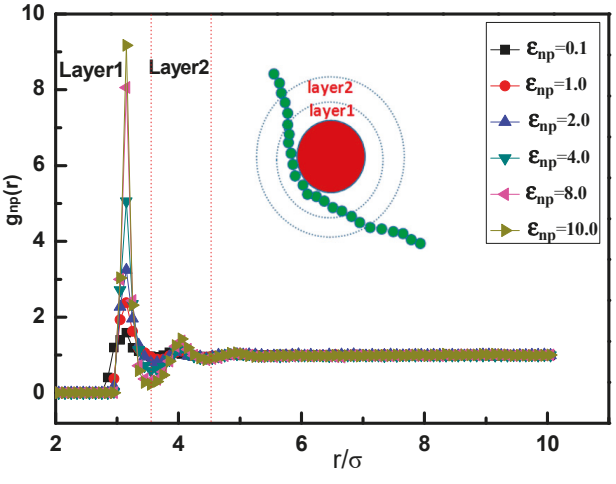

Figure 1. Polymer-nanoparticle (NP) pair distribution function $g_{np}(r)$ in nanocomposites for various attractive interactions ε_{np}.

Then we focus on the bidisperse matrix of the mixture of ring and linear polymer chain with the same amount of monomer. Figure 2 represents an overview of the selective adsorption states that arise upon varying the two main variables, the polymer-NP interaction ε_{np} and chain stiffness k_b. Here "ring chain in majority" in phase diagram indicates that the number of ring chain monomers in polymer-NP interface is more than that of linear chain, while "linear chain in majority" is opposite. The solid line in Figure 2 is used to divided the above two adsorption states. In the case of weak and intermediate attractive interactions ε_{np} such as from 0.1 to 2.0, ring chain always takes precedence over the linear chain regardless of chain stiffness k_b. For the strong attractive interactions, $\varepsilon_{np} > 2.0$ there is a preferential transition from 'ring chain in majority' to 'linear chain in majority' as the chain stiffness k_b increases. From figure, we also can see that the transition point decreases with the increase of k_b. This finding may be related to the different local packing of ring and linear semiflexible chain, which will be discussed detailly in the follow.

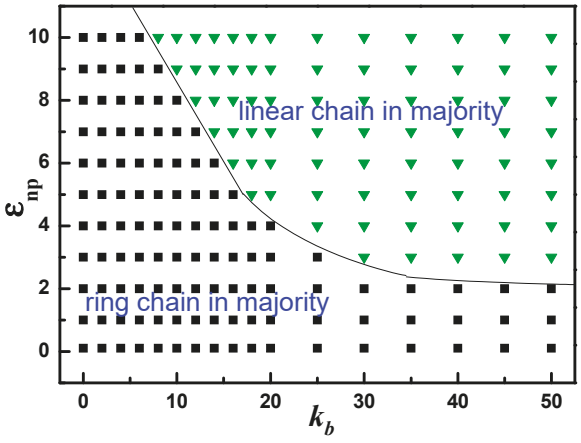

Figure 2. The phase diagram of ring and linear chains adsorbed to polymer-NP interfacial region as a function of polymer-NP interaction ε_{np} and chain stiffness k_b.

To further quantitatively understand the preferential adsorption behavior between ring chains and linear chains in interfacial region, the fractions of ring chain to all monomers in polymer-NP interface f for various interactions are calculated shown in Figure 3. As $\varepsilon_{np} = 1.0$ or 2.0, the value of f is in the range of 0.5 to 0.7, indicating that the ring chain slightly preferentially occupy the interfacial region. As f approximately equals to 0.5, means that the interfacial region shows no selection for ring or linear chains. At the strong polymer-NP interaction, $\varepsilon_{np} = 10.0$, $f > 0.5$ as $0 < k_b \leq 6$, indicating that the ring chain preferentially occupy the interfacial region. Interestingly, the value of f shifts down to be less than 0.5 as k_b increases from 8 to 50. This result suggests the ring chains in interfacial region are quickly replaced by linear chains, as the chain becomes stiffer. The minimum value of f is even close to zero as $k_b \approx 50$, showing an absolute priority for linear chains to occupy the polymer-NP interface.

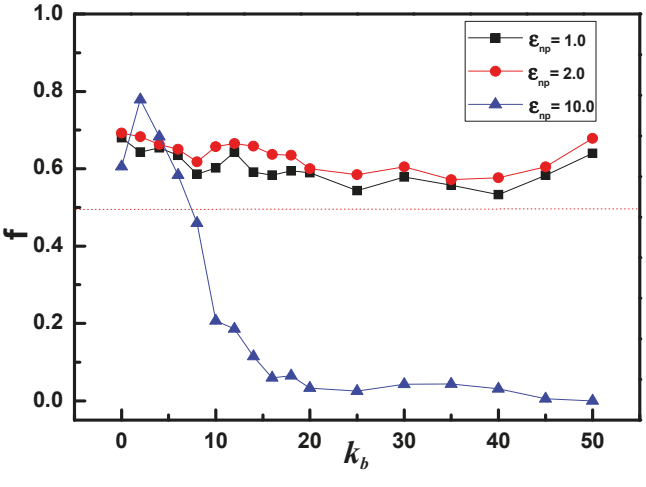

Figure 3. The fraction of ring chain to all chain in polymer-NP interfacial region, as a function of chain stiffness k_b for three attractive interactions.

Meanwhile the polymer-NP pair distribution function $g_{np}(r)$ and its representative snapshots for bidisperse matrix are shown in Figures 4 and 5, respectively. At the weak polymer-NP interactions $\varepsilon_{np} = 1.0$ for $k_b = 0$, 10, and 50, snapshots in Figure 4b display that the interfacial layer is composed of partial segments of ring and linear polymer chains. Ring chains preferentially wet the interfacial layer more than linear chains, in which the peak in $g_{np}(r)$ for ring chain is slightly higher than the peak for linear chain shown in Figure 4a. Similar behavior appears in nanocomposites regardless of the chain stiffness varied from flexible ($k_b = 0$) to semiflexible ($k_b = 10$) and to rigid-like ($k_b = 50$) chain. Some related studies have pointed out that at a weak polymer-NP interaction, polymer chains prefer to performing a "one-endpoint" adsorption behavior, which shows a perpendicular conformation to the NP surface [14,25]. As a result, it can be referred that for weak polymer-NP interaction, ring chains show a higher correlation with NP due to its closed topology structure, and there is no evident chain stiffness dependence.

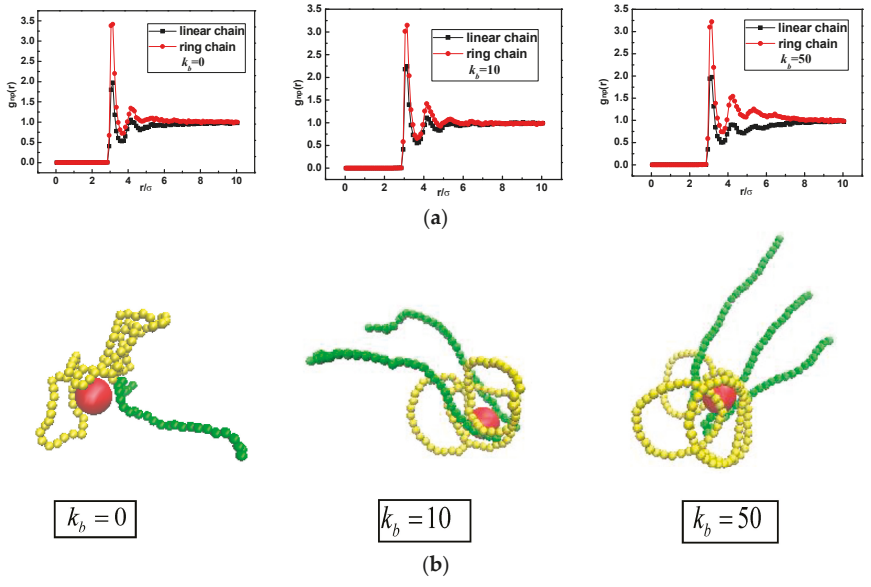

Figure 4. (**a**) Polymer-NP pair distribution function $g_{np}(r)$; (**b**) snapshots of the conformations of nanocomposites with $\varepsilon_{np} = 1.0$. Here ring and linear polymer chain are displayed in yellow and green, respectively.

For the strong polymer-NP interactions $\varepsilon_{np} = 10.0$, our previous study also has given the results that the inner monomers of chains prefer to wrap tightly the surface of NP, which performs a "middle" adsorption behavior [25,36]. Figure 5 shows a ring-to-linear selective adsorption transition with increasing chain stiffness. As $k_b = 0$, i.e., flexible chain, this "middle" adsorption mechanism that the middle monomers of polymer chain tend to cover the surface of NP, drives the ring chains still in majority in comparison with linear chain, due to its closed topology structure. As $k_b = 10$, i.e., semiflexible chain, the middle image in Figure 5b shows that the linear chains favorably wrap around NPs and predominantly crowd the ring chains out of the interfacial region. On the one hand, this phenomenon can be attributed to the fact that the linear semiflexible chains with a proper stiffness are inclined to form a chiral helical structure [37], which is commonly observed in biological environments. For instance, the negatively charged stiff polymer (DNA) wraps around a cationic core particle (protein), in which the packing manner is referred to as a nucleosome-like structure [38–40].

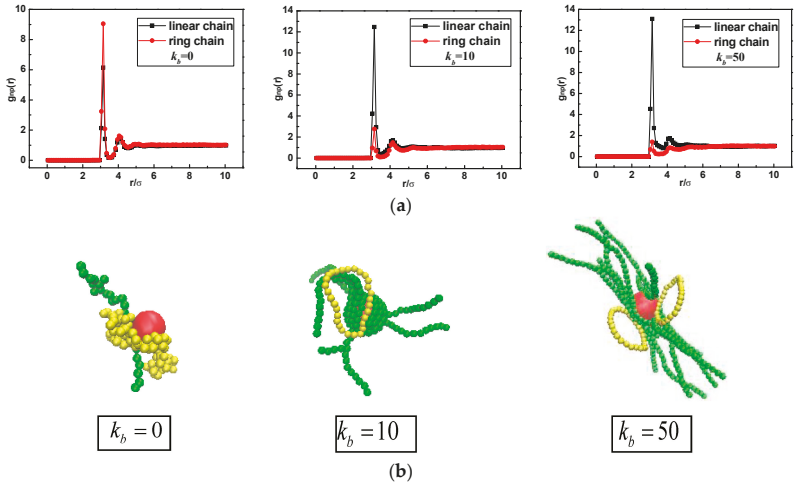

Figure 5. (**a**) Polymer-NP pair distribution function $g_{\mathrm{np}}(r)$; (**b**) snapshots of the conformations of nanocomposites with $\varepsilon_{\mathrm{np}} = 10.0$.

On the other hand, for the ring chain, the entropy gain due to the possible number of states of the chain near to the surface dominates the bending energy cost. As a result, the semiflexible linear chain tends to occupy primarily the interfacial region. With increasing k_{b} = 50, i.e., rigid-like chain, the preferential adsorption behavior by linear chains becomes more pronounced shown in the curve of $g_{\mathrm{np}}(r)$. The spiral linear chain begins to untie and tangentially cover the NP surface with the middle parts of the chain, and little interfacial region is left for the rigid ring, which corresponds to the adsorption state of $f \approx 0$ mentioned in Figure 3.

To interpret the intrinsic reason for the competitive adsorption transition occurred in bidisperse case, we focus on the monodisperse matrix of pure ring or linear chain. At the strong polymer-NP interaction, chain stiffness k_{b} is also increased from 0 to 50. The different polymer conformations for pure linear and ring chain are presented in the snapshots of Figure 6a,b, respectively. For pure linear chain, we can obtain a general picture of local packing of linear chain in polymer-based nanocomposites, in which the linear chain is classified as the sequences of bridge adsorption, chiral helical adsorption, and tangent adsorption. In contrast, the ring chain shows a sequence of conformations of double bridges adsorption, coexistence of double bridges and orbital adsorption, and only orbital adsorption. In fact, this finding provides a direct support for understanding the competitive adsorption transition occurred in bidisperse case.

The schematic diagram shown in Figure 7 offers a clear view for the local packing of monodisperse and bidisperse polymer matrix at the polymer-NP interface. As known by above, the "middle" adsorption mechanism dominates the polymer local packing in the interface under the strong polymer-NP interactions. Let us focus on the cartoons of Figure 7c. As the chain stiffness is weak, i.e., flexible chain, double bridge conformation of ring chain is superior to the single bridge packing of linear chain, illustrating "ring chain in majority" appeared in phase diagram of Figure 2. With the increase of chain stiffness, i.e., semiflexible chain, the helical structure of linear chain is benefit for wrapping the whole surface of NP, and crowding ring chain out of interface region. This finding can reveal the preferential transition from "ring chain in majority" to "linear chain in majority" occurred in phase diagram of Figure 2. Finally, as rigid-like chain, 3D tangent conformation of linear chain is absolute precedence over the 2D orbital plane structure of rigid-like ring, exactly explaining the absolute dominant adsorption state of $f \approx 0$ shown in Figure 3. Our work may provide a theoretical guidance for understanding the forming mechanisms of the conformations differences between linear

chain and ring chain. Rcently, Iwamoto et al. investigated the conformations of ring plystyrenes by SANS and concluded Flory's exponent ν in $R_g = N^{\nu}$ for rings may not be constant but rather show molecular weight dependence due to their topological constraint [41].

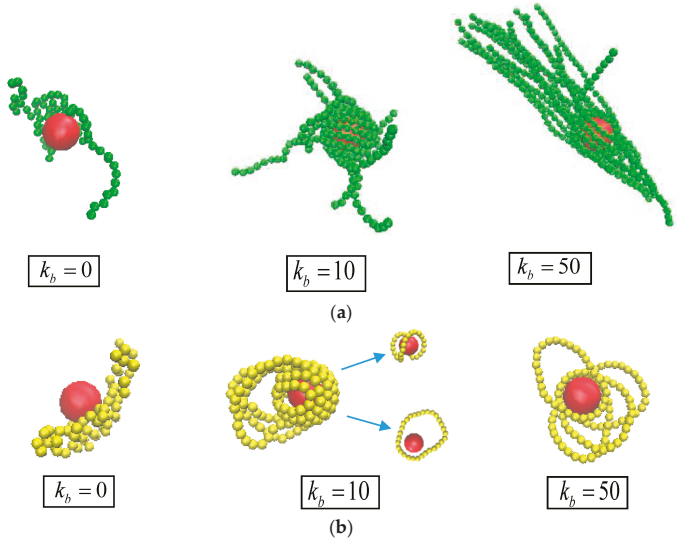

Figure 6. Snapshots of the conformations of nanocomposites at a strong attraction, $\varepsilon_{np} = 10.0$ with k_b = 0, 10, and 50: (**a**) pure linear chain; (**b**) pure ring chain.

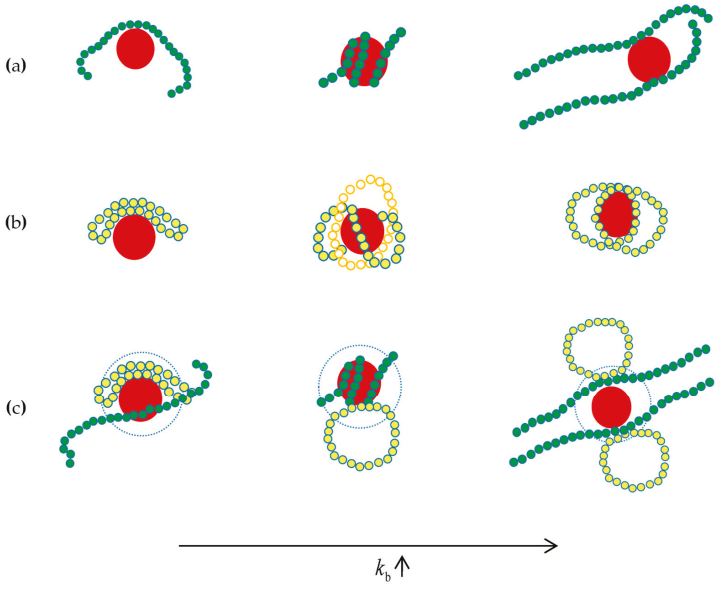

Figure 7. Schematic diagram of nanocomposites conformation at a strong attraction: (**a**) linear chain, (**b**) ring chain, (**c**) mixture of linear chain and ring chain.

4. Conclusions

In conclusion, we investigated the local packing and competitive adsorption behavior of bidisperse matrix with ring and linear polymer chain using coarse-grained molecular dynamics simulations. It is found that for the weak polymer-NP interaction, ring chain are slightly preferred to occupy the interfacial region than linear chain, due to its closed topology structure and regardless of chain stiffness. While for the strong polymer-NP interaction, the "middle" adsorption mechanism dominates the polymer local packing in the interface, and the selective adsorption behavior of bidisperse matrix is sensitive to the chain stiffness. For flexible polymer chain, double bridge conformation of ring chain is superior to the single bridge packing from linear chain, resulting in "ring chain in majority". As increasing chain stiffness, a ring-to-linear selective adsorption transition occurs. The semiflexible linear chain squeezes ring chain out of the interfacial region by forming a helical structure and wrapping tightly the surface of NP, while semiflexible ring chains still have the configurations of double bridge or 2D plane orbit. Further increasing stiffness to rigid-like chain, "linear chain in majority" selective adsorption behavior becomes more dramatic, in which 3D tangent conformation of linear chain is absolutely prior to the 2D plane orbital structure of ring chain. In addition, the monodisperse of pure ring or linear chain is also considered to explain the ring-to-linear selective adsorption transition with increasing chain stiffness. Besides, other topology structure e.g., star-like or dendritic chain will be the next step toward this issue that the effect of topology structure on adsorption behavior occurred at the polymer–NP interface.

Author Contributions: Q.S. performed the simulations; Q.S. and L.H. analyzed the data; Q.S. and L.H. wrote the paper; Y.J., S.L. and X.W. offered the tutorials and suggestions.

Acknowledgments: This research was supported by the Program of National Natural Science Foundation of China (Nos. 21674082 and 21474076).

Conflicts of Interest: The authors declare no conflict of interest.

References

1. Usuki, A.; Kojima, Y.; Kawasumi, M.; Okada, A.; Fukushima, Y.; Kurauchi, T.; Kamigaito, O. Synthesis of nylon 6-clay hybrid. *J. Mater. Res.* **1993**, *8*, 1179–1184. [CrossRef]
2. Delcambre, S.P.; Riggleman, R.A.; de Pablo, J.J.; Nealey, P.F. Mechanical properties of antiplasticized polymer nanostructures. *Soft Matter* **2010**, *6*, 2475–2483. [CrossRef]
3. Zhu, J.; Uhl, F.M.; Morgan, A.B.; Wilkie, C.A. Studies on the Mechanism by Which the Formation of Nanocomposites Enhances Thermal Stability. *Chem. Mater.* **2001**, *13*, 4649–4654. [CrossRef]
4. Caseri, W. Nanocomposites of polymers and metals or semiconductors: Historical background and optical properties. *Macromol. Rapid Commun.* **2000**, *21*, 705–722. [CrossRef]
5. Zuev, V.V.; Ivanova, Y.G. Mechanical and electrical properties of polyamide-6-based nanocomposites reinforced by fulleroid fillers. *Polym. Eng. Sci.* **2012**, *52*, 1206–1211. [CrossRef]
6. Roca, A.G.; Marco, J.F.; Morales, M.d.P.; Serna, C.J. Effect of Nature and Particle Size on Properties of Uniform Magnetite and Maghemite Nanoparticles. *J. Phys. Chem. C* **2007**, *111*, 18577–18584. [CrossRef]
7. Gregor, H.; Thomas, A.V.; Gert, H. Universal properties in the dynamical deformation of filled rubbers. *J. Phys. Condens. Matter* **1996**, *8*, L409–L412.
8. Mackay, M.E.; Dao, T.T.; Tuteja, A.; Ho, D.L.; Van Horn, B.; Kim, H.C.; Hawker, C.J. Nanoscale effects leading to non-Einstein-like decrease in viscosity. *Nat. Mater.* **2003**, *2*, 762–766. [CrossRef] [PubMed]
9. Sariciftci, N.S.; Smilowitz, L.; Heeger, A.J.; Wudl, F. Photoinduced Electron Transfer from a Conducting Polymer to Buckminsterfullerene. *Science* **1992**, *258*, 1474–1476. [CrossRef] [PubMed]
10. Mackay, M.E.; Tuteja, A.; Duxbury, P.M.; Hawker, C.; Van Horn, B.; Guan, Z.; Chen, G.; Krishnan, R.S. General Strategies for Nanoparticle Dispersion. *Science* **2006**, *311*, 1740–1743. [CrossRef] [PubMed]
11. Tuteja, A.; Duxbury, P.M.; Mackay, M.E. Polymer Chain Swelling Induced by Dispersed Nanoparticles. *Phys. Rev. Lett.* **2008**, *100*, 077801. [CrossRef] [PubMed]
12. Hooper, J.B.; Schweizer, K.S. Contact Aggregation, Bridging, and Steric Stabilization in Dense Polymer-Particle Mixtures. *Macromolecules* **2005**, *38*, 8858–8869. [CrossRef]

13. Hooper, J.B.; Schweizer, K.S. Theory of Phase Separation in Polymer Nanocomposites. *Macromolecules* **2006**, *39*, 5133–5142. [CrossRef]
14. Liu, J.; Gao, Y.Y.; Cao, D.P.; Zhang, L.Q.; Guo, Z.H. Nanoparticle Dispersion and Aggregation in Polymer Nanocomposites: Insights from Molecular Dynamics Simulation. *Langmuir* **2011**, *27*, 7926–7933. [CrossRef] [PubMed]
15. Patra, T.K.; Singh, J.K. Coarse-grain molecular dynamics simulations of nanoparticle-polymer melt: Dispersion vs. agglomeration. *J. Chem. Phys.* **2013**, *138*, 144901. [CrossRef] [PubMed]
16. Crawford, M.K.; Smalley, R.J.; Cohen, G.; Hogan, B.; Wood, B.; Kumar, S.K.; Melnichenko, Y.B.; He, L.; Guise, W.; Hammouda, B. Chain Conformation in Polymer Nanocomposites with Uniformly Dispersed Nanoparticles. *Phys. Rev. Lett.* **2013**, *110*, 196001. [CrossRef] [PubMed]
17. Hou, G.Y.; Tao, W.; Liu, J.; Gao, Y.Y.; Zhang, L.Q.; Li, Y. Tailoring the dispersion of nanoparticles and the mechanical behavior of polymer nanocomposites by designing the chain architecture. *Phys. Chem. Chem. Phys.* **2017**, *19*, 32024–32037. [CrossRef] [PubMed]
18. Allegra, G.; Raos, G.; Vacatello, M. Theories and simulations of polymer-based nanocomposites: From chain statistics to reinforcement. *Prog. Polym. Sci.* **2008**, *33*, 683–731. [CrossRef]
19. Vacatello, M. Chain Dimensions in Filled Polymers: An Intriguing Problem. *Macromolecules* **2002**, *35*, 8191–8193. [CrossRef]
20. Karatrantos, A.; Clarke, N.; Composto, R.J.; Winey, K.I. Polymer conformations in polymer nanocomposites containing spherical nanoparticles. *Soft Matter.* **2015**, *11*, 382–388. [CrossRef] [PubMed]
21. Yan, L.T.; Xie, X.M. Computational modeling and simulation of nanoparticle self-assembly in polymeric systems: Structures, properties and external field effects. *Prog. Polym. Sci.* **2013**, *38*, 369–405. [CrossRef]
22. Chen, L.; Zheng, K.; Tian, X.Y.; Hu, K.; Wang, R.X.; Liu, C.; Li, Y.; Cui, P. Double Glass Transitions and Interfacial Immobilized Layer in in-Situ-Synthesized Poly(vinyl alcohol)/Silica Nanocomposites. *Macromolecules* **2010**, *43*, 1076–1082. [CrossRef]
23. Barbier, D.; Brown, D.; Grillet, A.C.; Neyertz, S. Interface between end-functionalized PEO oligomers and a silica nanoparticle studied by molecular dynamics simulations. *Macromolecules* **2004**, *37*, 4695–4710. [CrossRef]
24. Vacatello, M. Molecular Arrangements in Polymer-Based Nanocomposites. *Macromol. Theory Simul.* **2002**, *11*, 757–765. [CrossRef]
25. He, L.L.; Zhang, D.; Zhang, L.X. Selective adsorption behavior of polymer at the polymer-nanoparticle interface. *J. Polym. Sci. B* **2016**, *54*, 1829–1837. [CrossRef]
26. Ge, T.; Kalathi, J.T.; Halverson, J.D.; Grest, G.S.; Rubinstein, M. Nanoparticle Motion in Entangled Melts of Linear and Nonconcatenated Ring Polymers. *Macromolecules* **2017**, *50*, 1749–1754. [CrossRef] [PubMed]
27. Kalathi, J.T.; Yamamoto, U.; Schweizer, K.S.; Grest, G.S.; Kumar, S.K. Nanoparticle Diffusion in Polymer Nanocomposites. *Phys. Rev. Lett.* **2014**, *112*, 108301. [CrossRef] [PubMed]
28. Li, Y.; Kröger, M.; Liu, W.K. Nanoparticle Effect on the Dynamics of Polymer Chains and Their Entanglement Network. *Phys. Rev. Lett.* **2012**, *109*, 118001. [CrossRef] [PubMed]
29. Li, Y.; Kroger, M.; Liu, W.K. Dynamic structure of unentangled polymer chains in the vicinity of non-attractive nanoparticles. *Soft Matter* **2014**, *10*, 1723–1737. [CrossRef] [PubMed]
30. Ni, R.; Kleijn, J.M.; Abeln, S.; Cohen-Stuart, M.A.; Bolhuis, P.G. Competition between surface adsorption and folding of fibril-forming polypeptides. *Phys. Rev. E* **2015**, *91*, 022711. [CrossRef] [PubMed]
31. Sommer, J.U.; Kłos, J.S.; Mironova, O.N. Adsorption of branched and dendritic polymers onto flat surfaces: A Monte Carlo study. *J. Chem. Phys.* **2013**, *139*, 244903. [CrossRef] [PubMed]
32. Wang, Y.; Shu, X.; Liu, J.; Ran, Q. Conformational properties and the entropic barrier in the "head-on" adsorption of a single polymer chain towards a flat surface. *Soft Matter.* **2018**, *14*, 2077–2083. [CrossRef] [PubMed]
33. Kremer, K.; Grest, G.S. Dynamics of entangled linear polymer melts: A molecular-dynamics simulation. *J. Chem. Phys.* **1990**, *8*, 5057–5086. [CrossRef]
34. Smith, J.S.; Bedrov, D.; Smith, G.D. A molecular dynamics simulation study of nanoparticle interactions in a model polymer-nanoparticle composite. *Compos. Sci. Technol.* **2003**, *63*, 1599–1605. [CrossRef]
35. Plimpton, S. Fast Parallel Algorithms for Short-Range Molecular Dynamics. *J. Comput. Phys.* **1995**, *117*, 1–19. [CrossRef]

36. Doxastakis, M.; Chen, Y.L.; Guzmán, O.; de Pablo, J.J. Polymer-particle mixtures: Depletion and packing effects. *J. Chem. Phys.* **2004**, *120*, 9335–9342. [CrossRef] [PubMed]
37. Jain, S.; Goossens, J.G.P.; Peters, G.W.M.; van Duin, M.; Lemstra, P.J. Strong decrease in viscosity of nanoparticle-filled polymer melts through selective adsorption. *Soft Matter* **2008**, *4*, 1848–1854. [CrossRef]
38. Sakaue, T.; Yoshikawa, K.; Yoshimura, S.H.; Takeyasu, K. Histone Core Slips along DNA and Prefers Positioning at the Chain End. *Phys. Rev. Lett.* **2001**, *87*, 078105. [CrossRef] [PubMed]
39. Kornberg, R.D.; Lorch, Y. Twenty-Five Years of the Nucleosome, Fundamental Particle of the Eukaryote Chromosome. *Cell* **1999**, *98*, 285–294. [CrossRef]
40. Kunze, K.K.; Netz, R.R. Salt-Induced DNA-Histone Complexation. *Phys. Rev. Lett.* **2000**, *85*, 4389–4392. [CrossRef] [PubMed]
41. Iwamoto, T.; Doi, Y.; Kinoshita, K.; Ohta, Y.; Takano, A.; Takahashi, Y.; Nagao, M.; Matsushita, Y. Conformations of Ring Polystyrenes in Bulk Studied by SANS. *Macromolecules* **2018**, *51*, 1539–1548. [CrossRef]

polymers

MDPI

Review

Nanoparticle-Hydrogel Composites: From Molecular Interactions to Macroscopic Behavior

Corinna Dannert, Bjørn Torger Stokke and Rita S. Dias *

Department of Physics, NTNU- Norwegian University of Science and Technology, NO-7491 Trondheim, Norway; corinnad@stud.ntnu.no (C.D.); Bjorn.Stokke@ntnu.no (B.T.S.)

* Correspondence: rita.dias@ntnu.no; Tel.: +47-735-934-22

Received: 22 November 2018; Accepted: 27 January 2019; Published: 6 February 2019

Abstract: Hydrogels are materials used in a variety of applications, ranging from tissue engineering to drug delivery. The incorporation of nanoparticles to yield composite hydrogels has gained substantial momentum over the years since these afford tailor-making and extend material mechanical properties far beyond those achievable through molecular design of the network component. Here, we review different procedures that have been used to integrate nanoparticles into hydrogels; the types of interactions acting between polymers and nanoparticles; and how these underpin the improved mechanical and optical properties of the gels, including the self-healing ability of these composite gels, as well as serving as the basis for future development. In a less explored approach, hydrogels have been used as dispersants of nanomaterials, allowing a larger exposure of the surface of the nanomaterial and thus a better performance in catalytic and sensor applications. Furthermore, the reporting capacity of integrated nanoparticles in hydrogels to assess hydrogel properties, such as equilibrium swelling and elasticity, is highlighted.

Keywords: hybrid hydrogels; nanoparticles; nanosheets; clays; polymers; adhesion

1. Introduction

Hydrogels are three-dimensional cross-linked polymer networks that absorb a large amount of water when placed in aqueous solution [1]. Hydrogels are thus soft and wet materials with characteristic features of both solids, in terms of well-defined shapes, and liquids, in the large amount of free water and potentially soluble molecules that can diffuse in and out of the gels. Based on the possibility to tune the properties of hydrogels over a wide parameter space and the fact that a broad range of polymer constituents are available, these soft materials have been developed for applications such as super-absorbent polymers, contact lenses, tissue engineering, biotechnological devices, and drug delivery systems [2–11]. Biomedical applications have been particularly powered by the possibility of synthesizing polymer networks with swelling/deswelling properties sensitive to stimuli such as temperature, pH, light, or specific biomarkers.

Large efforts have been dedicated to improving the mechanical properties beyond those of one component hydrogel networks. One such strategy is (i) the synthesis of topological gels where the network strands are interlocked by topological restrictions as realized by a slide-ring (e.g., figure-of-eight cross-links) maintaining proximity of the network strands [12–15]. These slide-ring, topological hydrogels are distinct from chemical gels cross-linked by covalent bonds between polymer chains, or physical gels where the network is established by intermolecular interactions, such as Coulomb forces or hydrophobic interactions. Other strategies comprise (ii) the development of double-network hydrogels [16] and (iii) the addition of clays and nanoparticles (NPs) to polymer solutions that act (at least partially) as cross-linkers [17]. The latter strategy, in particular, allows the formation of composite gels that are mechanically stronger due to the integration of entities supporting dissipative mechanisms [18], but also shows self-healing properties [19].

The incorporation of NPs into hydrogels has also been explored for purposes other than tailor-making and improving the mechanical and optical properties of hydrogels. For example, hydrogel particles can be made magnetic by the incorporation of magnetic NPs, thus facilitating separation and recycling processes [20]; stimuli-sensitive hydrogels loaded with enzymes or NPs containing drugs have been developed for drug delivery applications [21]; and NPs can also be included in hydrogels for studying their swelling properties [22,23].

In this work, we briefly review different synthesis pathways that have been employed to prepare NP-hydrogel networks, and outline the impact of NPs in improving various properties of the nanocomposites as compared to conventional materials. Furthermore, we present applications that are unique to nanocomposites. As a basic reference framework for the discussion, we summarize the free energy of hydrogels, including the relevant molecular parameters. Thus, the free energy of a hydrogel ΔF_{gel} is conventionally described in three additive contributions, reflecting deformation, ΔF_{el}; mixing of the polymer with the solvent, ΔF_{mix}; and a term arising from the charged nature of polymers affecting the ionic balance between the hydrogel and the immersing solution. In a simple form, these terms are given as:

$$\Delta F_{el} + \Delta F_{mix} + \Delta F_{ion} = \frac{\upsilon k_B T}{2}\left(\lambda_1^2 + \lambda_2^2 + \lambda_3^2 - 3\right) + \frac{k_B T}{v_s}(v_s c \ln \varphi_2 + \chi \varphi_2) + \Delta F_{ion} \quad (1)$$

where υ is the molar number of elastic active polymer chains in the gel; k_B is the Boltzmann constant; T is the absolute temperature; λ_I, with I = 1, 2, and 3, represents the deformation ratio in the three orthogonal axis directions; v_s is the volume per solvent molecule; c is the nominal solvent concentration (number of solvent molecules per unit volume of the polymer); φ_2 is the volume fraction of the polymer phase; and χ is the Flory-Huggins interaction parameter. There are also extensions of this expression which include a more detailed account of reference states, as detailed in Ref. [24]. Equation (1) provides a basis for linking the understanding of mechanical properties (e.g., deformation at a constant swelling volume), such as shear modulus G defined from the proportionality between the shear stress t and shear γ:

$$\frac{d\Delta F_{el}}{d\gamma} = G\gamma; \text{ where } \gamma = \lambda_1 - \lambda_1^{-1} \quad (2)$$

Calculating G from Equation (1) yields $G = \upsilon k_B T$, thus providing a direct interpretation of how changes in υ, as can be experienced in NP–hydrogel networks, affect the mechanical properties. Equation (1) also provides the basis for the interpretation of how molecular parameters affect the swelling equilibrium of hydrogel (e.g., minimum free energy as adjusted through changes in φ_2 and stretching of the network chains). Conventionally, the swelling pressure is used for the description of free hydrogel swelling equilibrium, where the last term gives rise to the osmotic pressure term representing the Donnan equilibrium. This term has also been elaborated to include molecular parameters of the network and the valence of the electrolytes, as described in Ref. [25]. A recent review by Creton [18] gives an overview of different networks and gels and their properties, as well as recent advances in fine tuning the behavior of these networks.

2. Design of Nanoparticle–Hydrogel Composites

NP-hydrogel composites can be roughly divided into two classes, depending on the dimensions of the system.

2.1. Nano- and Micro-Gel Composites

The first class refers to systems composed of one or a few NPs, where typically, a (small) hydrogel serves as a coat to the NP, giving a core-shell type of structure (Figure 1). Such systems have a large application potential. Nanogels can be prepared from proteins (e.g., collagen and fibrin) and other naturally-derived polymers, such as DNA, chitosan, hyaluronic acid (HA), and alginate [26,27], and have a large loading capacity for cargo ranging from inorganic NPs to biomacromolecules, such as

enzymes and nucleic acids, as well as hydrophobic drugs, which makes them desirable for drug delivery applications [28–31]. As depicted in Figure 1, the soft polymer coat that surrounds the NP (cargo) makes these systems less likely to aggregate, due to the steric repulsions between particles, and provides protection to the encapsulated biological molecules from degradation and elimination, assuring a longer circulation time of active biological content [29,32]. Nanogels prepared from stimuli responsive polymers can be used for controlled delivery of the cargo, by exploring their swelling properties [1]. For example, the pH-triggered swelling of nanogels has been suggested to improve the uptake of nuclear acting drugs (chemotherapy) via the endocytic pathway due to the swelling of the nanogels in the acidic lysosomal compartments and consequent release of the drugs. These ultimately diffuse into the cell nucleus, which was not observed to occur using nanogels that do not possess the pH-sensitive moiety [33]. In a different and elegant design, the triggered release of the cargo was achieved by using gels with bonds that are either easily hydrolysable or cleaved by ubiquitous enzymes like esterases, or by enzymes that are over-expressed in the target cells [34]. Temperature, light, and magnetic-responsive nanogel composites have been explored for applications within drug delivery, as soft robots, sensors, and vehicles for capture and delivery [35]. Magnetic-responsive nanogel composites in particular are also popular in imaging and diagnostics, as reviewed in [36]. Systems composed of small dimension gels surrounding an NP core can also be used as an intermediate step in the formation of hydrogel shells with liquid cores, achieved by the dissolution of the NP core [37].

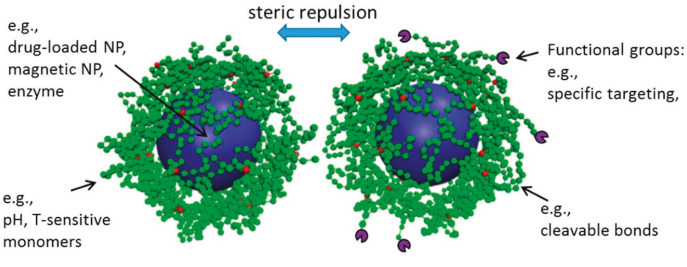

Figure 1. Nanoparticle—nanogel complexes depicting steric repulsions between the adsorbed polymers chains, and possible functionalization of the polymers in the nanogels. Snapshots were adapted from Nicholas Christiansen's master thesis, August 2018, NTNU.

The approaches reported so far within this class of materials are valuable, but at the same time mostly of an empirical character that can be exploited as a qualitative basis for design guidelines. Further progress to a priori support the design of NP-loaded hydrogels with a predetermined drug loading capacity (given e.g., basic information on hydrophilic/hydrophobic nature), and, e.g., tailor-made circulation time, is currently awaiting.

2.2. Macroscopic Hydrogel Composites

The second class of NP–hydrogel composites gathers larger hydrogel entities, e.g., μm–cm dimensions, where NPs are incorporated at various concentrations, depending on the particular enhancement of functionality or application. Similar to the micro-/nanogel class, the macroscopic hydrogel composites can be classified according to the dominating type of interaction of the NP with the network chains, e.g., covalent or non-covalent, as well as their combination with polymer networks being either chemical, physical, or topological.

Independently of the class, the incorporation of NPs in hydrogels can be achieved by applying different routes. NPs can be added to: (a) pre-formed hydrogels; (b) polymers solutions that are subsequently gelled, either using the NPs as cross-linkers or independently of their presence; or (c) monomer solutions prior to co-cross-linking polymerization, in the presence of the NPs. It is also possible to grow the NPs from precursors that are incorporated in the polymer network using strategies (a) and (b) (Figure 2).

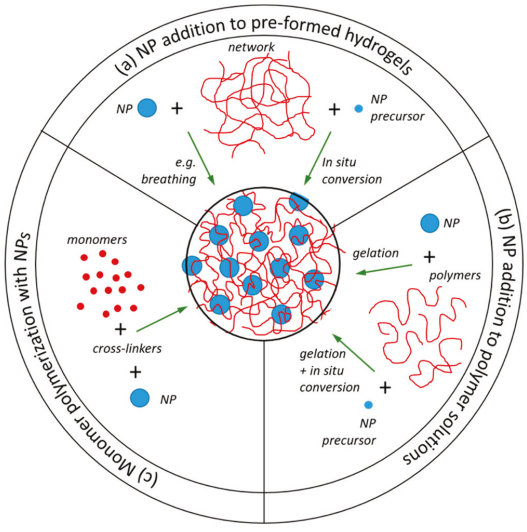

Figure 2. Approaches used for preparing nanoparticle—hydrogel composites: (**a**) NP addition to pre-formed hydrogels; (**b**) NP addition to polymer solutions and (**c**) Monomer polymerization in the presence of NPs. See text for details.

2.3. Nanoparticle Addition to Pre-Formed Hydrogels

NP addition to pre-formed gels can be further divided into the synthesis of NPs using the polymer networks as scaffolds (in situ conversion) and the addition of pre-formed NPs to hydrogels (Figure 2a). The former has been particularly popular for the synthesis of metal NP-doped microgels for applications such as catalysts [38], biosensors [39], engineering optical devices materials and device architectures [40], the development of antimicrobial materials [41], and other biomedical applications [42]. The microgel structure can, in principle, be used for growing an NP in each of the polymer voids (whose size can thus be controlled by the cross-linking density). Components other than the NPs can also be loaded in the gels (such as drugs or small proteins), in which case the NPs can be used, e.g., to control drug burst release [43]. In addition, the composition of the polymer network can be explored so that the microgel is responsive to stimuli like temperature, light, or pH [44]. The methodology was first described by Antonietti and co-authors, where gold and iron oxide colloids with "non-classical shapes" were synthesized within polystyrene sulfonate microgels. Three typical morphologies were obtained, depending on the reduction rate and reducing agent: small and spherical colloids, long threads, and "nanonuggets" (algae-like). The shape of the NPs could be further controlled by the cross-linking density of the gels, where a larger cross-linking density resulted in thinner structures and more spherical colloids. These systems are based on the electrostatic attractions between the metal ions and the oppositely charged polymers in the network. Better control of the NP density within the gel can be achieved by incorporating chemical groups in the polymer network that have affinity to the NP precursors (nucleation groups). It has been shown that it is possible to control the size, morphology, and stability of the NPs by adjusting the concentration of the nucleation groups in the hydrogel side chains [45].

Pardo-Yissar and co-authors explored the cyclic deswelling and swelling of polymer networks in a poor and good solvent, acetone and aqueous suspension of NPs, respectively, to incorporate pre-formed Au NPs on polyacrylamide films, in what they name a "breathing" mechanism [46]. Such a procedure was chosen since the polymer film could not be formed in the presence of the NPs, due to NP aggregation. It is suggested that during the breathing out cycle, when the gels are placed in acetone and de-swell, the NPs remain inside the gels due to the collapse and physical entanglements

of the polymer chains and hydrogen bonding between the monomers and the citrate surface of the NPs. The authors reported an increased NP concentration inside the gel with each breathing cycle and that the NPs were well-distributed within the film [46]. However, it was not clear if such systems are stable in aqueous solution, where NP leaching from the hydrogel may occur with time. A different procedure was adopted to co-assemble colloidal Au with poly(*N*-isopropylacrylamide) (PNIPAm) microgel, based on the centrifugation of the microgel particles with the NPs, followed by removal of the supernatant and redispersion of the Au particles through the microgel pellet by gentle heating, agitation, and sonication cycles [47]. The resulting composite could be further manipulated by light exposure where the Au plasmon absorption was explored to induce local heating, thus triggering local deswelling within the PNIPAm microgels.

Albeit apparently working, further fundamental insight on the breathing process for the incorporation of NPs can potentially be obtained by determination of the mesh size of the network at various conditions of cycling, and how the mesh size is controlled by the molecular parameters. Such a strategy could provide more fundamental knowledge to the design of NP–hydrogel composites with respect to adjustment of the size of NPs relative to the mesh size of the network, and thereby also control the efficiency of the incorporation process, as well as the leaching of NPs.

2.4. NP Addition to Polymer Solutions Prior to Network Formation

The synthesis routes described so far, in situ formation of NPs in a preformed hydrogel network and mixing pre-synthesized NPs into polymeric networks, are widely employed for the preparation of iron oxide NP—hydrogel composites. Other strategies comprise the blending of pre-formed NPs with polymeric chains prior to cross-linking of the polymer chains, or mixing the polymer chains with iron salts for the formation of both NPs and a network during the cross-linking step (Figure 2b). Within the former, different procedures have been developed. One can simply exploit the addition of NPs to polymer solutions, followed by polymer gelation. In Ref. [20], for example, chitosan/poly(vinyl alcohol) (PVA)/Fe_3O_4 hybrid gel particles were prepared using an instantaneous gelation method where aqueous solutions of the three components were first mixed, followed by dripping of the solution through a needle into a sodium hydroxide bath. Such hybrid gel particles were developed as low-cost recyclable biomaterials for the removal of dyes from aqueous solution, where the inclusion of the magnetic NPs allows the separation and recycling of the gel particles using magnetic fields. The mechanism with which the NPs are kept within the gel was not elucidated in the work. Liu and co-workers explored variations in pH to assemble polyhedral oligomeric silsesquioxane (POSS)/carboxymethyl cellulose (CMC) hybrid hydrogels [48]. They started with the NPs in a solution at high pH, where the surface NH_2 groups were not protonated, to avoid electrostatic interactions between the particles and the COO^- groups in CMC and the concomitant formation of a precipitate. After mixing the POSS with the CMC, the hydrolysis of added D-(+)-gluconic acid δ-lactone slowly reduced the pH, which, according to the authors, induced the formation of the hybrid network through the formation of hydrogen bonds between POSS-NH_2 and CMC. It is unclear if hydrogen bonds are indeed the driving force for the association of CMC with POSS-NH_2 (see discussion in Section 3). The presence of charged COO^- groups in the polymer chains is expected to facilitate the protonation of the NH_2 groups in the POSS and vice-versa, as the pH is decreased. Indeed, the pKa of such groups has been found to change significantly in the presence of oppositely charged macromolecules, and can possess a charge for wider ranges of pH values than the pure substances (Figure 3) [49]. Recent work instead suggests that the formation of a polymer network may still be due to electrostatic interactions between the CMC and the POSS NPs, but by starting with weakly charged NPs and changing the pH so they slowly obtain more charge, the polymer chains will likely interact with and bridge several NPs, creating a network, instead of strongly interacting with one (or few) NP(s), which leads to the formation of neutralized large complexes (precipitate) [50].

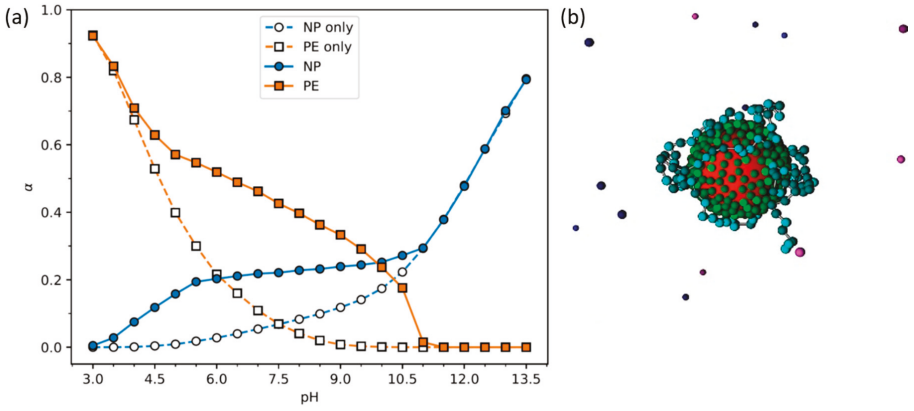

Figure 3. (**a**) Titration curves for a 120-monomer long polyelectrolyte (PE) (orange) and NP (blue) with pH sensitive groups both separately (dashed lines) and in a mixture (solid lines), given as the fractional charge (α) as a function of pH, obtained from Monte Carlo simulations. The difference between the dashed and solid lines shows that the fractional charge of the individual components increases in the presence of the oppositely charged NP or polymer. (**b**) Representative snapshot of adsorbed PE onto the NP. The PE is described as a sequence of hard-spheres (in green) connected by harmonic bonds. The NP is modeled as a hard-sphere with 20 Å with a density of 4.8 surface sites per nm^2 (in blue). Dark monomers and surface groups correspond to neutral groups, and particles with bright colors refer to charged groups. The pKa of the monomers and NP surface groups was set to 7.0 and 6.8, respectively. Purple and black particles are the counterions of the PE and NP, respectively. For details on the calculation method and model, see Refs [49,50]. Data and figures by Morten Stornes.

Poly(sodium acrylate) (PANa) grafted with monomeric groups with a low critical solution temperature behavior in water (N-isopropylacrylamide, NIPAm) was mixed with SiO_2 NPs to form hybrid networks [51]. Despite the electrostatic repulsions between the PANa backbone and the silica NPs, the formation of hybrid networks with viscoelastic properties comparable to those of covalently cross-linked gels was observed. It was proposed that the NIPAm side chains interact specifically with the silica NPs, via the formation of hydrogen bonds between the alkylene oxide units and the silanol groups, respectively, with the NPs serving as cross-links of the polymer network for the NIPAm grafted PANa. PANa chains grafted with poly(ethylene oxide-co-propylene oxide) (PPO) side chains did not show the same interaction strength with the NPs.

It is challenging to prepare homogeneous hybrid gels with large polymer fractions simply by blending the components if the interactions between the polymer and NPs are too strong, as these tend to associate strongly, leading to heterogenous materials [52]. In such cases, a viable approach for the synthesis of hydrogel NP composites is polymerization of the polymer network, from the monomers, in the presence of the NPs, with or without a chemical cross-linker (see Section 2.5).

In a different strategy, Pasqi and co-authors describe the synthesis of composite hydrogels containing CMC polymer chains and TiO_2 NPs functionalized with amine groups, thus supporting covalent binding of the NPs to the hydrogel network. The NPs served as cross-linkers in the hydrogel, allowing for the mechanical advantages of hybrid gels, but without some of the disadvantages, such as the leaching of NPs from the network, a common problem in hybrid networks where the NPs are only physically embedded in the polymer network, making these ideal to applications within, for example, tissue engineering [53]. A similar procedure has been followed to synthesize gelatin/Ag [54], pectin/hydroxyethyl methacrylate/TiO_2 [55], and chitosan/Au [56] hydrogel composites, among others. In addition to the increased stability of the formulation, with respect to the release of NPs from the networks, such "click-hydrogels", where the NPs are covalently bond to the polymer network, have the advantage of multivalency, where many polymer chains can be linked to a single NP, which

increases factor ν in Equation (1), as opposed to the most common tetra-functionality of the cross-links in chemical gels. On the other hand, the presence of covalent bonds between the NPs and the polymer network restricts, to a large extent, the extensibility and self-healing potential of the hybrid material, when compared to hybrid hydrogels where the NPs are not covalently bound to the polymer network.

As mentioned, it is also possible to mix metal salts and polymer solutions for the simultaneous formation of NPs and cross-links within the hydrogel matrix. This is described as the best method to obtain monodisperse NPs and a good colloidal stability, while exploring the advantage of a one-pot strategy [57]. This methodology has been used to produce hybrid gels with different compositions, e.g., PVA/PNIPAm/Fe_3O_4 obtained upon the mixing of PVA (or PVA and PNIPAm) polymers with iron salts, followed by the drop-wise addition of this solution into an ammonia solution [58], or polysaccharide-grafted poly(*N*,*N*-dimethylacrylamide) (PDMAm)/iron oxide particles, prepared using a similar procedure [57].

2.5. Monomer Polymerization in the Presence of Nanoparticles

The polymerization of monomers into a network in the presence of pre-made NPs (schematically depicted in Figure 2c) is probably the most common procedure to incorporate NPs into polymer networks. This strategy was pioneered by Haraguchi and co-workers [17,19,59], using a free radical polymerization of NIPAm or *N*,*N*-dimethylacrylamide (DMAm) in the presence of clays. It is suggested that the polymerization starts at the (large) surface of the clay (diameter of 20 to 30 nm and thickness of 1 nm), evolves throughout the solution, and leads to a network where the clay particles act as cross-links [60]. These gels are physical composite hydrogels due to the nature of the interaction between the polymers and NP and the lack of an added cross-linker. This methodology has been extended to prepare composite hydrogels made of modified clay particles or of spherical silica or titanium oxide NPs, both in the presence and absence of cross-linker agents, with the intention of improving the mechanical properties of the gels. Many of these examples can be found listed in Section 4.

In addition to inorganic clay and metal nanoparticles, this approach has also been explored in the preparation of hydrogel composites containing metal-oxide nanometer-scale sheets (nanosheets, NSs). As recently reviewed [61], NSs are two-dimensional nanomaterials possessing very large aspect ratios, and a range of unique chemical, physical, electronic, and optical properties. Of special interest are NSs such as titanium oxide or graphitic carbon nitride (g-CN), which, in addition to serving as reinforcing fillers and introducing function in the hydrogels (see Section 5.4), can trigger the in situ radical polymerization of acrylamide monomers and derivatives, by radiation with ultraviolet light and the concomitant production of hydroxyl radicals [62]. Such photo-initiated free-radical polymerization leads to the formation of hydrogels even in the absence of cross-linkers, but adding cross-linkers significantly increases the mechanical strength of the gels [63].

In an example involving biological polymers and nanomaterials, Serizawa and co-workers have found that macromolecular crowding induced by water-soluble polymers allows the enzymatic synthesis of cellulose-based nanoribbon hydrogels and suppression of cellulose NS formation and concomitant precipitation [64]. Such suppression is believed to be due to an increase in the effective viscosity of the synthesis media and/or depletion stabilization of the colloidal products [64,65]. In a recent publication [65], the same group extended this concept to form nanocomposite hydrogels by polymerizing cellulose-derived monomers, with cellulose nanocrystals (CNCs) acting as crowding agents. A reported self-assembled peptide/g-CN hydrogel, developed as a light-responsive scaffold material, is an interesting example of a nanocomposite hydrogel where non-covalent interactions are explored to both polymerize the peptide monomers (monomer—monomer interactions) and induce cross-link formation (monomer—NSs interactions) [66].

3. Overall Mechanism and Forces Involved in Hybrid Composite Formation

NP—hydrogel systems have received much interest in the past decades, fueled by recent novel applications (see Sections 5 and 6). The interactions between the polymer network and the NP surface have not been studied to the same extent and, in many of the systems, are poorly understood. Considering that the improvement of the mechanical properties of the gel systems arises from the interaction of these with the surface of the NPs, understanding the interactions at play in these systems is fundamental for tailor-making such materials.

The general consensus is that NPs act as multifunctional cross-linkers for the polymer network; that is, two or more polymer chains in the network bind to one NP, and the polymer chains, in turn, bridge two or more NPs. The formation of composite networks necessarily relies on the affinity between the polymer monomers and the surface of the NPs. The adsorption of the monomers should be at least comparable to the thermal energy ($\sim k_B T$), since the polymer loses conformational entropy upon adsorption to the particle surface. On the other hand, the interaction strength between the polymer monomers and the NP surface does not need to be very large: the ability of the polymer to form multiple links, due to its conformational entropy and thus ability to adopt different conformations, dictates a strong enough interaction to restrict the infinite swelling (dissolution) of the network when placed in excess water, or the gluing of two gels mediated by NPs [67]. This concept has been further expanded by using polymer chains with dendritic end groups possessing positively charged groups. Both the large number of adhesion points and the amine groups guarantee a strong interaction with negatively charged clay surfaces [68]. Block polymers with positively charged end blocks also contribute to the formation of strong clay-hydrogel composites [69]. This mechanism underpins the improved mechanical qualities of the composite gels, described in Section 4. In addition, when the gel is under tension, some monomers and/or polymers will desorb from the NPs, dissipating the tension and retarding failure. Furthermore, such breaking in the cross-linking is reversible since the same or other neighboring strands can in turn adsorb to the NPs, replacing the detached link [70]. This mechanism also supports the self-healing capability that numerous composite NP-hydrogels show.

Gluing hydrogels and tissue using NPs is interesting from an application point of view, but also allows a direct assessment of the adhesion forces between the hydrogels mediated by the particles. Indications of the importance of the interactions between the polymer network and the NPs arise from studies where adhesion forces between PDMAm hydrogels glued using colloidal mesoporous silica NPs were found to increase when increasing the specific surface area of the particles, achieved by increasing the pore diameter and volume of the synthesized particles [71]. Further, the particles with the largest pore diameter could absorb the largest amount of polymer at a given concentration. Additionally, it was also shown that the amount of adsorbed polymer on NPs (suspended in aqueous solution) correlated well with the gel-gel adhesion energy. Interestingly, the zeta potential of the particles decreased (from -18.5 to -35.7 mV) when increasing the specific surface area (from 219 to 514 m^2/g), but this fact was not explored or discussed in the work [71].

Another indication that the macroscopic gel—gel adhesion is mediated by polymer—particle adsorption is based on studies where the cross-linking density of the glued hydrogels is varied. A larger concentration of cross-links leads to more constrained polymer chains and weaker adsorption energies. Furthermore, more swollen networks show weaker adhesion [67]. This is also supported by models that suggest that the energy landscape of the system is strongly dependent on the elastic properties of the gels [72]. These studies further indicate that NP dispersions can be used to assemble hydrogels, without affecting the rigidity of the material [67,72,73].

The chemistry of the NP surface and the composition of the hydrogel are important parameters in the adhesion of NPs to the polymer network and can be explored to increase the strength of the interaction and thus adhesion. One possibility is to include moieties supporting electrostatic interactions between NPs and the network. Such interactions are long ranged and the possibility of tuning their strength with variations in ionic strength and pH makes this a popular route in some applications [74,75]. The adsorption of neutral polymers onto surfaces, on the other hand, often relies

on specific and short-range interactions. Poly(ethylene oxide) (PEO), for example, is a commercial polymer that can be used as a dispersant for latex and a flocculant for clays and silica particles. In fact, the ability of polymers to stabilize colloidal suspensions against flocculation, which is of large importance in the formulation of, for example, paints and cosmetics, has fueled the study of polymer adsorption onto particles and surfaces since the 50s [76–78].

Clays and silica NPs are recurrent compounds in nanocomposite hydrogels and it was established early on that PNIPAm and PDMAm showed relatively strong interactions with the NPs (and thus a good adsorption ability), while PVA and PAAm did not [79–81]. It is commonly described that hydrogen bonds established between the polymer moieties and the silanol (Si–OH) groups on the surface of the silica particles are the driving force of the adsorption of neutral polymers to the surface. Indeed, it was shown, using infrared spectroscopy, that DMA forms hydrogen bonds with the surface groups on the silica surface in the absence of water (in chloroform), which is to be expected [79]. Nevertheless, and as stated by Rubio and Kitchener, "In an aqueous medium, however, such bonding must be reduced by competition from water molecules." [82]. These authors also mention, citing another work, that the non-adsorption of PVA could be due to the difficulty in displacing water from the silanol groups.

Perrin and co-authors [80] studied the structure and dynamics of polymers near a silica surface using a coarse-grained model. The model used, based on the Martini force field, describes groups of atoms using beads (two for the monomer backbone and two for each the side chains of the monomer) with different degrees of polarity. In addition, beads can be defined as hydrogen bond donors and/or acceptors. The only non-bounded interactions included in the simulations were represented by a modified Lennard-Jones potential. The work focused on two polymers with slightly different compositions, PDMAm and PAAm, which were found to interact and not interact, respectively, with silica NPs using lap adhesion tests [67]. The interaction energy between the model silica surface and the used solvent model was found to be very slightly larger than that of silica—PDMAm and significantly larger than that of silica—PAAm side chain monomers. On the other hand, snapshots of the systems (Figure 4) show that even for PDMAm, the polymer coverage of the surface is not very large, with an apparent larger fractional occupation of solvent molecules near the surface of silica. This was especially obvious in the PAAm systems, where the polymer occupation at the surface decreased. Without discussing it much, but highlighting the fundamental role of the solvent in the absorption mechanism, Perrin and co-authors conclude that the strongest solvation of the PAAm dictates the lack of adsorption at the silica surface. These results suggest that entropic effects, rather than the direct H-bonds between polymers and particles, are the driving force for polymer adsorption onto NPs. Naturally, when the polymers do adsorb, hydrogen bonds between the monomers and surface groups can be easily formed. It is interesting to note that PDMAm, which has been shown to interact with silica NPs, has two methyl groups in each monomer, which makes it a more hydrophobic polymer than PAAm. Rubio and Kitchener studied the adsorption of high molecular weight PEO onto various forms of silica. They suggest that (i) isolated silanol groups are probably the principal adsorption sites, (ii) the adsorption of PEO is favored if the regions between the sites are hydrophobic, and (iii) the adsorption of PEO is disfavored if the regions between the adsorption sites are hydrated and (iv) particularly disfavored if the surface is appreciably ionized [82], although other work has showed no appreciable difference in PEO adsorption to silica within the pH range 2.5–10, where one would expect some variation in the ionization of the NPs [83]. Regarding point (ii), other evidence pointing to the significance of the hydrophobic interactions is the fact that a "salting-out" effect was observed in these systems; that is, the addition of 20 mM of salt led to an increase in the strength of the interaction. Conclusion (iv) arises from studies showing that the adsorption of PVA onto silica surfaces was higher at pH 3.6 than at pH 9, justified by the presence of more undissociated silanol groups to form hydrogen bonds with the polymer chains [84]. While this is a good argument, it is also suggested in Ref. [82] that the presence of ionized groups at the silica surface decreases the hydrophobicity of the surface

(weakening the interaction if this is, at least partially, hydrophobic in nature), or that the presence of condensed counterions could prevent PEO from approaching the surface.

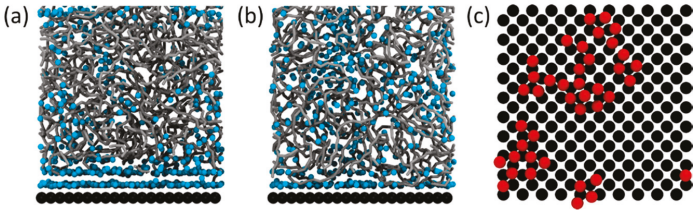

Figure 4. Snapshots of molecular dynamic simulations depicting solvated polymers (in gray) near a silica surface (in dark). Panels (**a**) and (**b**) refer to PAAm and PDMAm, respectively. Panel (**c**) shows the top view of the absorbed PDMAm monomers. Reprinted with permission from Perrin, E.; Schoen, M.; Coudert, F.; Boutin, A. Structure and Dynamics of Solvated Polymers near a Silica Surface: On the Different Roles Played by *Solvent Journal of Physical Chemistry B* **2018**, 122, 4573–4582. Copyright (2018) American Chemical Society.

In a recent article, an off-lattice model taking into account the excluded volume of polymers and ions is used to describe the adsorption of PVP on a silica surface. Interestingly, the predictions from the model were found to be in good agreement with experiments when both a hydrogen bonding-based interaction (based on a Lennard-Jones potential that could have been used to describe van der Waals interactions) and excluded volume effects between ions and (neutral) polymer chains were included. The effect of the latter was discussed to be two-fold: the direct competition between the polymer and the ions for surface adsorption and consequent decrease in the polymer adsorption [85], and/or an improved titration of the silanol groups enhanced by counterion condensation and, concomitantly, less opportunities for these groups to form hydrogen bonds with silica [86].

In a recent publication, Sato and co-authors probed the importance of van der Waals forces for the interactions between silica NPs and PAAm and PDMAm gels, by varying the Hamaker constant, *A*, achieved by changing the refractive index of the medium using ethylene glycol [87]. They observed that for sufficiently high concentrations of ethylene glycol, where PAAm and PDMAm have similar *A* values, the quantity of particles adsorbed onto each gel is similar. Hydrogen bonding and hydrophobic interactions were dismissed since the silica surface was well-hydrated and both the polymers and silica surface were hydrophilic. In their opinion, the driving force for NP adsorption on hydrogels is van der Waals interactions, at least under conditions where chemical and electrostatic adsorption are negligible.

It is clear that polymers possessing carboxyl or ether oxygen groups in their composition will form hydrogen bonds with hydroxyl groups at surfaces, and that the strength of these interactions depends on the chemistry of the groups. It is, however, not clear if this is the driving force of association or if instead van der Waals forces predominate. Additionally, entropic effects derived from a preference of the hydration waters on the particle surface and/or the polymer to be in bulk rather than associated, should not be disregarded in these systems.

While this discussion has predominantly focused on interactions between polymer network chains and clay particles or silica NPs, similar arguments can be used in equivalent systems. He and co-authors [88] describe the formation of intermolecular hydrogen bonds between g-CN NSs and sodium alginate chains, based on infra-red spectroscopy, showing a broadening and shift of the peaks corresponding to the O–H stretching vibration in g-CN NSs, and pointing out studies of sodium alginate with graphene oxides (GOs) with different surface functionalization on the formation of (dry) films [89]. Graphene NSs have attracted much interest due to their high specific surface area, electron transport, and mechanical properties [90]. As mentioned below, these materials are prone to aggregation in aqueous solution and large efforts have been devoted to increasing their

stability in solution. This can be achieved by surface modifications, such as the introduction of charged surface groups, leading to stabilization through electrostatic repulsions or the adsorption of polymers and stabilization through steric repulsions. In ref. [89], it is found (not surprisingly) that (the negatively charged) alginate interacts more strongly with positively charged GOs than with GOs with modifications that introduce negatively charged surface groups. Furthermore, infrared spectroscopy was used to identify the groups involved in alginate –GO interactions, in dry films, which were attributed to intermolecular hydrogen bonds. Nanocomposite hydrogels have also been prepared using GO and PVA solutions [91]. Interestingly, the authors describe the hydrogel structure as networks of GO NSs with the PVA acting as a physical cross-linking agent, as opposed to the most commonly described polymer network with nanomaterials acting as cross-linking sites. The PVA is stated to function as a cross-linking agent since the GO NSs can interact weakly in pure solution. Additionally, in these systems, hydrogen bonding between the hydroxyl, epoxy, and carboxyl groups at the surface of the GO sheets and the hydroxyl-rich PVA chains is considered to be the dominant force, again based on the characterization of dry samples [92].

It is worth mentioning that the predominant role of hydrogen-bonding in cellulose association in water, and the interaction of cellulose with non-ionic polymers in aqueous solution, has recently been challenged [93–95].

As mentioned above, it is possible to make use of the photo-initiation abilities of g-CN NSs to trigger the in situ radical polymerization of acrylamide monomers and derivatives [62,96]. Since radicals can be generated at the surface of the g-CN NSs, it is suggested that polymerization starts at the surface of the NSs, which also acts as anchoring points for the monomer, i.e., the polymers are effectively covalently bound to the surface of the NSs. The formation of strong hydrogels without the addition of external cross-linkers is, according to the authors, a clear indication of the formation of covalent bonds between the NSs and the polymer network [97]. In addition, control experiments where the NSs were physically embedded in the hydrogel via redox initiation in the dark (no photo-initiation) created a hydrogel that was still stronger than the (PDMAm hydrogel) control, due to the filler reinforcement effect of the NSs, but weaker than the gels where the polymer is bound to the NSs. Still considering g-CN NSs, an interesting self-assembled peptide/g-CN hydrogel nanocomposite was recently reported where both the peptide polymerization (monomer-monomer interaction) and interaction between peptide monomers and NSs were driven by non-covalent π-π interactions between the aromatic rings in the monomers and the aromatic rings of the monomers and the graphitic structure of the NSs, respectively [66].

A recent article by Liu and co-authors [98] has highlighted the need for careful structural and mechanistic studies within the NP–hydrogel nanocomposite field. While studying the effect of the size and shape of silica NPs on biological tissue (pig liver) adhesion, the authors came across an unexpected effect of NaOH or KOH bases in the tissue gluing process. It was found that the synthesized NPs achieved tissue adhesion that was similar to that obtained using commercial Ludox silica NPs (SM-30) [67] only after exposing the NPs to a concentrated base solution. Such treatment caused the etching of the NP surface, changing the particle size and shape into "poorly defined clusters of spherical particles", and changing the surface charge of the NPs from negative to nearly neutral [98]. Surprisingly, much stronger tissue adhesion was achieved by simply adding a drop of strong base solution to two liver surfaces that were pressed together without the addition of NPs. It is suggested that the strong base changes or damages (possibly denaturates) the surface proteins of the pig liver, which enhances protein-protein interactions and improves the adhesion of the tissue. In this respect, and according to the authors, the presence of the silica NPs is unnecessary or even a hindrance to the adhesion process.

In fact, SM-30 has been shown to glue hydrogels made of PDMAm [67], in a system where it is not clear how a strong base would affect the hydrogel–hydrogel interactions. In addition, PDMAm polymers were shown to adsorb to silica particles (including Ludox) [71]. Furthermore, Stöber silica

NP solutions [73] and colloidal mesoporous silica NPs [71] have been shown to glue rat skin and enhance wound healing, apparently without the aid of a strong base.

While the proposed base-induced protein denaturation mechanism is a rather interesting one and certainly worthy of further studies, it does not seem to be the only one at play. Having in mind, in particular, the studies involving ex vivo (pig [98] and calf liver [67]) and in vivo (rat skin [73]) systems, one may also have to consider tissue composition specificity, as well as the presence of components that may only be present in living tissue, while developing NPs for tissue adhesion and discussing the relevant interactions at play.

4. Nanoparticles for Improving Hydrogel Properties

4.1. Optical Properties

Typically, gels are transparent and flexible at a low cross-linker content and become opaque and fragile at a high cross-link density [99]. This has been attributed to the development of structural inhomogeneities [100]. A decrease in transmittance can also be obtained by variations in temperature when gels are composed of temperature-responsive polymers. For example, PNIPAm polymers exhibit a coil-to-globule transition for temperatures above the lower critical solution temperature, which leads to changes in gel transmittance [59]. It is therefore important to have enough information about the behavior of the polymers at different temperatures and pHs in order to be able to establish whether the transmittance varies because of the cross-link density or other factors [101].

Assuming that gel transmittance is decreased upon the formation of heterogeneous domains, the observed larger transmittance of nanocomposite hydrogels suggests that the cross-links in nanocomposite gels are more uniformly distributed [59] and that only a very small amount of the NPs form oligomers or bigger clusters [102]. Oligomers and bigger clusters, in addition to heterogeneity, can lead to an increase in diffusive scattering, which decreases the transparency [103]. Accordingly, the optical behavior of, for example, cellulose-based hydrogels with silicate NPs, was observed to be highly dependent on the concentration of NPs in the network [103,104], which was explained by both an increase in cross-link density and an increase in NP aggregates [103]. On the other hand, Haraguchi et al. [59] reported that PNIPAm–clay nanocomposites show a constant transparency for clay NP concentrations up to 60 wt % (against polymer) (see Figure 4 in Ref. [59]), which could indicate that gel transmittance is independent of clay concentration. It is most likely, however, that all nanocomposite hydrogels show a decrease of transparency above a certain critical concentration of NPs, which was simply not reached in the study by Haraguchi and co-workers. The NP concentration where the decrease in transmittance is observed will depend on the properties of the NPs and on the intermolecular interactions between NPs and between NPs and the polymers in the gel.

Depending on the composition, the transmittance of nanocomposite gels may also be sensitive to pH variations. For example, Ahmed and co-authors [105] showed that nanocomposite hydrogels obtained from sodium silicates/colloidal silica mixtures, developed for bacterial encapsulation, lost transparency when lowering the pH from 7 to 5 (as well as the ability to gel) when using Ludox silica particles, while sodium silicate NPs showed the opposite trend, with samples becoming more opaque when the pH was increased from 5 to 6. The authors concluded that the transparency variations were related to NP aggregation upon pH variation and that by varying the pH and NP concentration, whose increase resulted in an increase in optical density, it was possible to synthesize gels with a similar transparency for a wide range of silicate concentrations [105].

In addition to temperature, NP concentration, and pH, swelling and de-swelling can affect gel transmittance. Yang et al. [106] showed that some NP–hydrogel composites turned white on de-swelling, ending up at 0% transmittance. However, in general, nanocomposite hydrogels are highly translucent materials [103] and can exhibit a transmittance above 90% even for high concentrations of NPs [59,107], depending on the general composition, pH, and temperature of the solution. Overall, hydrogel composites show a higher transparency than chemically cross-linked gels due to less

structural inhomogeneities that arise when chemical cross-links are formed inhomogeneously during polymerization [108].

4.2. Mechanical Properties

The mechanical properties of hydrogel composites can depend strongly on the concentration of NPs, but tend to behave differently from covalently cross-linked gels [52]. In addition, the length of the polymer chains also plays an important role in the mechanical properties of the hydrogels; the longer and more flexible the polymer chains between the cross-linking points (NPs) are, the greater the flexibility of the nanocomposite hydrogel [109]. This is also true for covalently cross-linked gels; however, the number of cross-links is much higher than in hydrogel composites [109]. Due to this, the chain length between cross-links is generally larger in nanocomposite gels than in covalently cross-linked gels composed of the same polymers [109]. In the following, we discuss the impact of NP integration in hydrogels on the mechanical properties of the resulting materials, with an emphasis on stress-strain behavior, including the elastic and storage moduli, and stress relaxation.

4.2.1. Stress-Strain Behavior

In contrast to covalently cross-linked hydrogels, nanocomposite hydrogels typically exhibit an improved behavior in response to stress. Multiple studies have shown that NP–hydrogel networks can withstand high degrees of deformation, such as elongation, bending, compression, and tearing [110–112].

Nanocomposite hydrogels have been shown to exhibit an increase of both shear storage modulus (G') [59,68,74,103,112–115] and Young's modulus (E) [52,59,102,103,105,107,109,114–116] in comparison to covalently cross-linked hydrogels with a similar polymer composition prepared with some form of cross-linking agent (for example N,N'-methylenebis(acrylamide)) [59,109]. However, as previously mentioned, the covalently cross-linked gels generally have a higher cross-linking density [109], which might justify, at least partially, the different behavior of the materials. It was shown that increasing the concentration of NPs can lead to an increase in shear storage modulus and Young's modulus for low NP concentrations, followed by a plateau [59,102–105,109,111,112,117,118]. This was also the case with PAAm hydrogels reinforced with graphene NSs [119].

Recently, magnetic fields have been used to orient stacked titanate (IV) NSs and form anisotropic composites. These were shown to resist compressibility applied orthogonally to the oriented NSs while undergoing deformation under parallel shear forces. The resistance to compressibility in these systems arises from electrostatic repulsions between the NSs [62]. Additionally, g-CN NSs have recently become a popular inorganic hydrogel filler, where the mechanical properties are also dominated by the electrostatic repulsion between the NSs, as shown by the increase in the shear storage modulus of the hydrogels upon the decrease (more negative) of the zeta potential of the nanosheets [97].

Figure 5 summarizes reported elastic moduli as a function of NP concentration for different nanocomposite hydrogels. They all show an increase of the Young's modulus with NP concentration [17,52,59,109], even if they are composed of different polymers and/or NPs. It is important to note in Figure 5 that the definition of NP concentration is different for the silica and the clay NPs. All in all, the nanocomposite hydrogels depicted here show a comparable increase in elastic modulus. At variance, the elastic modulus of HA/silica NP hydrogels was shown to decrease above a certain NP concentration (2%), which did not occur with chemically cross-linked HA gels (using divinyl sulfone as a cross-linker) [102].

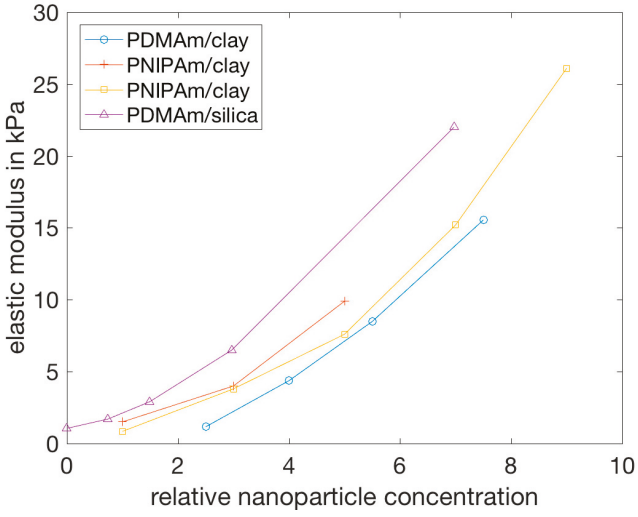

Figure 5. Elastic moduli for different nanocomposite hydrogels. Replotted using data from PDMAm/clay [109] (blue dots), PNIPAm/clay [17,59] (yellow squares and red crosses), and PDMAm/silica [52] (purple triangles). The concentration of clay particles is $C_{Clay} = (100)\left(\frac{m_{Clay}}{M_{Clay}}\right)$, with m_{Clay} representing the weight of clay per 1000 mL of water and M_{clay} representing the molecular mass of clay [17,59,109]. The silica NP concentration is the weight ratio between silica and DMA [52]. The amount of polymer in the samples varied from approximately 1.5 g to 6 g.

The storage modulus increases steadily as the concentration of NPs increases [59,74,113,118], showing up to a hundred-fold increase [74], until the gel reaches a critical strain region. Above this region, the storage modulus decreases rapidly, indicating that the gel collapses into a quasi-liquid state [68]. In addition, nanocomposite hydrogels can exhibit a significant strain rate dependence [49]. The important property of the nanocomposite hydrogels that leads to the increase of the storage modulus, below the critical NP concentration, is the lack of cross-links formed by covalent bonds [74].

Such response to stress indicates that:

- The NPs of the examined samples were integrated in the hydrogel networks, forming physical cross-links that cause the nanocomposite hydrogel to behave as an elastic gel with high extensibility [74,104,113];
- When the concentration of NPs increases, the resulting interactions between them become more important than the NP-polymer interactions, leading to an increase in the stiffness of the network and thus decreasing maximum elongation at break [52,103].

The elongation at break was shown to be greater for hydrogel composites than for covalently cross-linked hydrogels prepared with the same monomers and with a comparable cross-linking density [59,103,104,109,111,116,118]. While typical covalently cross-linked gels break at an elongation of approximately 50%, regardless of cross-link density [84,89], nanocomposite hydrogels could be extended to about 1000%, or more, before breaking [52,107,111,114,116], which shows an improved mechanical behavior when compared to covalently cross-linked hydrogels. Figure 6 shows the elongation at break from three different studies and clearly depicts how the elongation at break shows a tendency to decrease with increasing clay concentration, at least up to a certain NP concentration. It is unclear from the presented data points if two of the systems show a minimum in the elongation at break, or if they reach a plateau. An important observation is that the data for the PNIPAm/clay nanocomposite hydrogels, representing gels prepared (apparently) under the same conditions, do

not show the same behavior, which suggests that environmental factors during the preparation or characterization of the hydrogels, such as temperature, might have an effect on the mechanical properties of the nanocomposite hydrogels. In another study, however, PVA-clay hydrogels have been shown to exhibit a drastic increase in the elongation at break as the clay concentration increased, within the studied concentrations [117]. In general, all these NP–hydrogel composites gels exhibit very high elongations at break, above 1000%, for low clay concentrations [17,59,109].

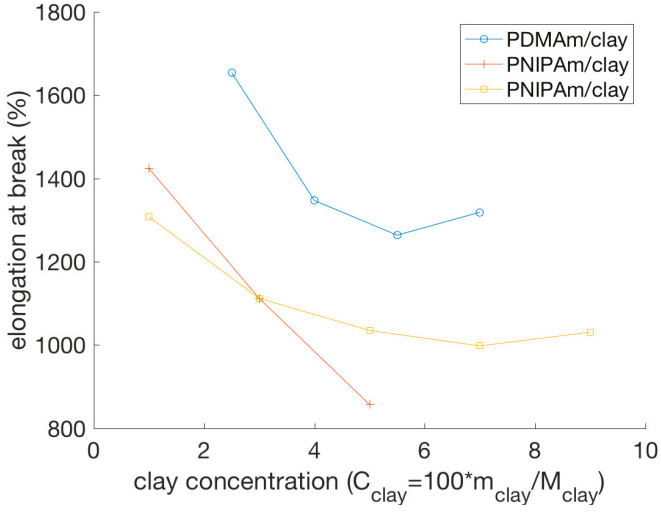

Figure 6. Elongation at break of nanocomposite hydrogels. Data from Haraguchi et al. [17,59,109] of elongations at break for PDMAm and clay hydrogels [109] (blue circles), PNIPAm and clay hydrogels [17] (red crosses), and PNIPAm and clay hydrogels [59] (yellow squares) replotted as a function of clay concentration C_{clay}.

Some nanocomposite hydrogels can even be elongated at a sufficient length to form a knot without displaying damage or breaking in the process [59]. Also, the shape recovery after elongation can be almost 100% [59,111,112,116].

In summary, the incorporation of NPs into hydrogels can improve the elastic and storage moduli and increase the elongation at break, with the enhanced mechanical properties being attributed to the physical cross-links between NPs and polymer chains [52,104].

4.2.2. Stress Relaxation

Nanocomposite hydrogels also exhibit a different stress relaxation than chemically cross-linked hydrogels. Following a sufficiently long waiting time after exposing a macroscopic sample of these materials to stress, the stress relaxes and reaches a plateau without further change [52]. This process strongly depends on the concentration of NPs in the gel [52], which suggests that the interactions between these and the polymers play a key role in it. This hypothesis was supported by the finding that stress relaxation also depends on the type of cross-links in the gel [101]. In nanocomposite hydrogels, stress relaxation occurs mainly through dissipative mechanisms of breaking and reforming cross-links between NPs and polymers [101], while in covalently cross-linked gels, stress relaxation occurs mainly through the migration of water [103]. Thus, the nature of NP-hydrogel interactions in nanocomposite hydrogels is the cause for this stress relaxation behavior.

5. Novel Functionalities

5.1. Self-Healing Hydrogels

Polymer gels with self-healing abilities can regenerate, similarly to living matter, in response to damages in the polymer network and formation of cracks [120]. This repair should occur both autonomously and spontaneously [110] and can be achieved through different approaches. One of these approaches consists of using NPs as network cross-linkers.

Table 1 shows an overview of some recent studies where self-healing nanocomposite hydrogels were synthesized and studied.

Haraguchi and co-authors [110] developed a self-healing gel by synthesizing a nanocomposite gel composed of PDMAm or PNIPAm and inorganic, hydrophilic, synthetic hectorite clay NPs. Mechanical damage, i.e., knife cuts, healed autonomously, without the use of healing agents (Figure 7), just by keeping the cut surfaces in contact at ambient or slightly elevated temperatures [110]. The same behavior was also observed for other types of gels [68], suggesting it is not specific to polymer networks of a particular composition. The self-healing behavior can be attributed to the nature of the nanocomposite hydrogel. At the freshly cut surface of such a gel, long polymer chains, for example, PDMAm chains, that are adsorbed onto the surface of hydrophilic inorganic clay NPs inside the gel at one end have the ability to interact with clay particles on the other gel surface [110]. Thus, by adjoining two cut surfaces, the chains of each surface will diffuse into the network of the other surface and bridge neighboring clays, thus gluing the two gel surfaces together [110].

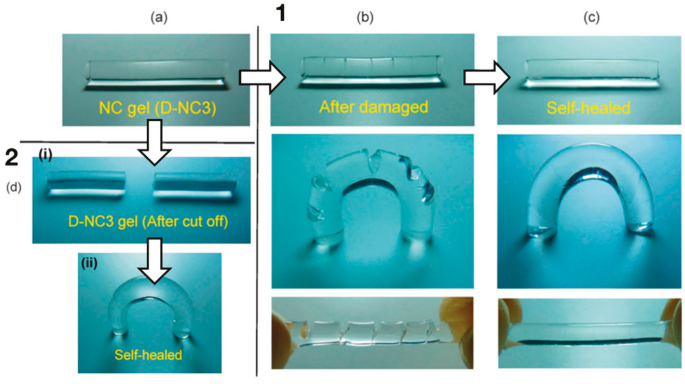

Figure 7. Self-healing nanocomposite hydrogel composed of PDMAm and hectorite clay NPs (D-NC3). The nanocomposite hydrogels were (1) damaged or (2) cut off using a knife and then healed by keeping the cut surfaces in contact at 37 °C for varying times, ranging from 48 to 100 h. Reprinted with permission from Haraguchi, K.; Uyama, K.; Tanimoto, H. Self-healing in Nanocomposite Hydrogels. *Macromolecular Rapid Communications* **2011**, *32*, 1253–1258. Copyright (2011) John Wiley and Sons.

For many nanocomposite gels, the time the two cut surfaces have to be in contact in order for self-healing to occur strongly depends on the temperature [107,110,118,121–125]. Haraguchi et al. [110] showed that at a temperature of 37 °C, the self-healing was completed, with a 100% recovery of tensile strength, after 48 h, see Figure 8. Factors that increase polymer diffusion, such as higher temperatures or a longer contact time, also increased the rate of self-healing, since the polymer chains at each surface have to diffuse into the opposite surface to create new bonds and thus glue the two surfaces together [107,110,118,125]. For example, for composite hydrogels made of PDMAm and hectorite, it took only 30 min for full self-healing at 80 °C [110]. On the other hand, self-healing hardly occurred at high temperatures for PNIPAm/hectorite hydrogels, due to the coil-globule transition of PNIPAm chains at 32 °C [110]. This shows that self-healing is dependent on the composition of the hydrogels, which needs to be considered in the development of nanocomposite hydrogels.

Table 1. Selected recent studies on self-healing nanocomposite hydrogels with different compositions.

Polymer/Nanoparticle Materials	Self-Healing Test	Self-Healing Efficiency	Reference
Hydroxyapatite/calcium-containing silicate glass (bioactive glass)	Compression tests were performed using a Zwick Roell Z2.5 instrument	Complete recovery of mechanical properties	[126]
Poly(*N*,*N*-dimethylacrylamide) or poly(*N*-isopropylacrylamide)/Hectorite clay	Keeping surfaces in contact at ambient/elevated temperatures	Complete recovery of mechanical properties after 10 h	[110]
Bisphosphonated hyaluronan/calcium phosphate	Keeping surfaces in contact for short time (min 5 s)	Almost complete recovery of mechanical properties (98%)	[74]
Carboxybetaine methacrylamide and 2-hydroxyethyl methacrylate/Laponite clay	Keeping surfaces in contact for 5 min, ambient temperature	Mechanically stable and resistant to handling	[112]
Monomer acrylamide copolymerized with *N*-isopropylacrylamide/hectorite clay	Keeping surfaces in contact for 4 days at 20 °C or 4 h at 80 °C	Possessed ultrahigh extensibility and up to 90% strength recovery	[107]
Sodium polyacrylate polymer particles and hyperbranched bis-MPA polyester-64-hydroxyl/reduced graphene oxide	Contact with gentle pressure for 30 s	Nearly full restoration of the electrical conductivity	[127]
Poly(*N*,*N*-dimethylacrylamide)/graphene oxide-hectorite clay	Keeping the cut surfaces in contact and irradiated with a NIR laser under ambient condition	After healing for 2–3 min, strength recovery of ~96%	[128]
Poly(acrylic acid)/graphene oxide	Contact at 45 °C for 48 h	Almost full recovery of mechanical properties	[118]
Poly(acrylamide)/exfoliated montmorillonite layers	Gels were dried and reswollen at room temperature, and then merged into a single bar	Fracturing did not occur at interface	[116]
Poly(acrylamide)/Laponite	Contact at 80 °C for 24 h	Healing efficiency to up to 50%	[121]
Poly(aspartamide)(GABA/DOPA/EA)/graphene oxide	Fractured gel pieced held in contact	Healing interface strong enough to be stretched without fracturing	[129]
2-acrylamido-2-methyl propane sulfonic acid and acrylamide/zirconium hydroxide	Contact for 5 min-24 h at room temperature	healing efficiency of up to 86% (in strain efficiency)	[122]
Poly(ethylene glycol)/cellulose nanocrystals	Contact at 90 °C for a varying contact time under nitrogen	Up to 78% healing efficiency	[123]
Poly(acrylic acid)/iron ions and 2,2,6,6-tetramethylpiperidine-1-oxyl radical oxidized cellulose nanofibrils (additional cross-linker)	Contact immediately without applied stress for the prescribed contact time 25 °C	Healing interface strong enough to sustain self-supporting, bending, and lifting weights (350 g)	[111]
linear polyurethane chains/maleimide functionalized graphene oxide NPs	Contact at different temperatures for different times	Up to 99% healing efficiency, complete healing at 120 °C after 10 min	[29]
Poly(acrylamide)/Graphene oxide NPs	Contact for different times and different water content	Healing efficiency of up to 92.3%	[115]
Poly(*N*,*N*-dimethyl acrylamide)-gum arabic/TiO_2	Contact at different temperatures for different times	Healing interface could withstand various deformations such as bending, tying and subsequent elongation. Gels healed at room temperature broke easily at interface	[124]
Poly (2-acrylamido-2-methyl-1-propanesulfonic acid)/Laponite clay and *N*,*N*′-methylenebis (acrylamide) (additional cross-linker)	Contact at 50 °C for 24 h	Fracturing occurred at healing interface, the original network structure could not be completely recovered	[114]

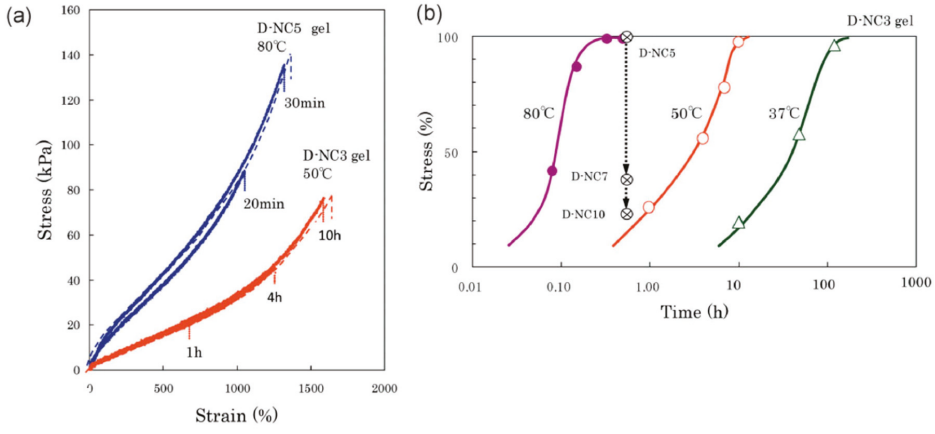

Figure 8. Tensile mechanical properties of self-healed PDMAm/synthetic hectorite nanocomposite hydrogels (D-NCn, where n indicates increasing concentration of hectorite) shown in Figure 7. (**a**) Stress-strain curves of the original and the self-healed gels before (dashed lines) and after (solid lines) cutting. (**b**) Effects of self-healing conditions (time and temperature) on the recovery of tensile strength of self-healed gels. Reprinted with permission from Haraguchi, K.; Uyama, K.; Tanimoto, H. Self-healing in Nanocomposite Hydrogels *Macromolecular Rapid Communications* **2011**, 32, 1253–1258. Copyright (2011) John Wiley and Sons.

The ability of the gels to self-heal decreases with an increasing concentration of clay NPs (C_{Clay}) [110]. In gels with very high C_{Clay}, self-healing becomes very difficult due to the short lengths of the chains bridging the NPs [110]. However, if the length of the polymer chain bridging two NPs is too large, the healing time increases, since the free ends of the polymer chains need a longer time to diffuse and find another NP [125]. Self-healing did not only reestablish the tensile strength after contact for a short duration, but it was also long lasting. It could also be achieved after a relatively long waiting time after the cut, particularly for gels with long polymer chains, since long chains at the cut surfaces have a lower probability of interacting with the clay NPs within the same surface [110]. However, if the chains are short enough to bind to the same surface, the cut surfaces only adhere when they are freshly cut [68].

Nejadnik and co-authors [74] showed that self-healing does not only occur in synthetic hydrogels, but also in gels consisting of bisphosphonated hyaluronan (HABP) and calcium phosphate (CaP) NPs. In their work, it was reported that the HABP/CaP hydrogel displayed fast self-healing behavior, with the joining of two cut surfaces occurring in less than 5 s [74]. The healing occurred, as in other nanocomposite hydrogels, because the interactions between the CaP NPs and grafted bisphosphonate groups of hyaluronan are non-covalent and can thus be restored within a limited contact duration. The rapid nature of the self-healing process was attributed to the fact that the interactions (not discussed) were stronger than other less specific non-covalent interactions in other nanocomposite hydrogels [74].

Interestingly, nanocomposite hydrogels with different compositions could be combined by cutting and healing. By joining the cut surfaces of two different gels at ambient temperatures, the two gels could be combined and did not detach with alternating swelling and de-swelling treatments [110].

To summarize, it is possible for nanocomposite hydrogels consisting of long-chained polymers and inorganic NPs to show self-healing behavior. When cut, the polymers at a surface are able to diffuse into the network of the other surface and form new bonds with the NPs there. Because these bonds are non-covalent, they are easily formed and broken, which is essential for the self-healing process.

5.2. Adhesive Materials

Another novel functionality of nanocomposite hydrogels is related to (a few) reports on the adhesion of plastic, glass, and tissue induced by hydrogels of particular compositions [130]. It is suggested that the non-covalent interactions between the NPs and polymer chains are responsible for the adhesion and, since these can be broken and reformed autonomously, adhesion can also be reversible [130]. Wu and co-authors [131] showed that nanocomposite hydrogels consisting of poly(ethylene glycol) and synthetic silica Laponite platelets have improved adhesion properties compared to hydrogels without the Laponite NPs. The improved adhesion was attributed to the increased flexibility of the nanocomposite hydrogels, which leads to better stress dissipation [131]. Furthermore, the adhesive strength is largest for lower NP concentrations, and it decreases as the cross-linking density increases. A study by Gahawar et al. [132] showed similar results, with poly(ethylene glycol) and Laponite nanocomposite hydrogels showing the ability to adhere to osteoblast cells. This demonstrates that nanocomposite hydrogels could be used for a wide range of biomedical applications, especially in the field of wound closure [132]. Unfortunately, Laponite platelets have been shown to be cytotoxic, even at low concentrations [133], suggesting that they are not biocompatible as of yet.

5.3. Nanoparticles for Gluing Hydrogels

Conventional adhesives often consist of polymers, since they both dissipate energy under stress and are flexible enough to establish good contact between surfaces. However, it is difficult to glue together hydrogels using polymers, which makes the assembly of gels or tissues very challenging. Inspired by the mechanism of nanocomposite hydrogel formation, Rose and co-authors glued PDMAm hydrogels and liver tissue using silica NPs, in a process named (nano)bridging, where NPs can adsorb to the polymer network or macromolecules in the tissue and act as connectors between the two surfaces [67,73]. If the NPs have diameters comparable to the network mesh size, multiple polymer chains can be absorbed to the same particle, creating an adhesive layer, with the polymers in the gel acting as bridges between NPs. When the adhesion site is strained, some monomers detach from the NPs, thus releasing the tension. These detached segments can easily reattach, or a neighboring strand can be adsorbed to replace the detached segments. This effect leads to an adhesive junction that can withstand high tensions without fracturing. In fact, the adhesion site was stronger than the gel network itself, so fracturing did not occur at the adhesion site [67].

The position of the NP between the two gels or tissues is found to be dependent on elastic and capillary forces, which in turn varies with NP size and the rigidity of the gel or tissue [72]. It is suggested, using a combination of molecular dynamics simulations and theoretical calculations, that nanobridging is enhanced when using large NPs on hard gels. More specifically, the size of the NPs should be large enough to avoid penetration into the network and diffusion from the interface [72].

5.4. Hydrogels for Improved Nanoparticle Performance

Many of the applications of nanocomposite hydrogels are based on the improved functionalities of the hydrogels due to the presence of the NPs. However, some recent studies have instead explored hydrogels as a mean to improve the properties and functionalities of NPs. Of special interest here are the ultrathin 2D nanomaterials, NSs.

As recently reviewed [61], the discovery of mechanically exfoliated graphene [90] has led to an enormous research effort in the fields of condensed matter physics, material science, and nanotechnology, fueled by the exceptional properties of these 2D nanomaterials. One of the characteristics that makes these materials unique, the very large specific surface area, makes them attractive to applications in catalysis and sensing. A challenge that is often faced in these systems is NSs aggregation and poor solution stability, induced by the relatively strong van der Waals

interactions between the NSs. In fact, these forces have been explored for the assembly of van der Waals heterostructures, where NSs with different compositions are layered to form novel materials [134,135].

When used as fillers, the poor solution stability of the nanomaterials will affect the mechanical performance of the hydrogels, as discussed above. When the application is related to the large surface area of the materials, which is especially appealing in applications within catalysis and sensing, the aggregation of the NSs will necessarily result in a decrease in the efficiency of the system. We will here mention work performed with g-CN as an illustrative example. The g-CN group of materials has gathered significant interest in the past years due to its photocatalytic activity in the visible range. Besides its good light harvesting and catalytic properties, g-CN is relatively easy and cheap to synthesize, and much research has been conducted for tuning the properties of this class of materials. The two-dimensional structure of g-CN facilitates the hybridization with other components, e.g., graphene, and other modifications such as metal doping and sensitization with organic dyes have been attempted, according to the desired application [136]. g-CNs are particularly appealing for environmental applications involving air purification, water disinfection and decontamination, and waste remediation (see ref. [136] and references within). The ideal performance relies on the adsorption of the hazardous pollutants by the large surface area of the NSs and the photo-degradation of the pollutant, which allows the reutilization of the photocatalyst. Jiang and co-authors have recently described the synthesis of a polyaniline/g-CN composite hydrogel for application in organic pollutant removal [96]. Such a system, as opposed to the more traditional structures of the catalysts (tubes, sheets, and wires), allows for a larger accessibility of the surface area and concomitant facilitated adsorption and concentration of the pollutant (methylene blue) into the hydrogel, followed by the in situ oxidization of the pollutant via photocatalysis. In addition to enhancing the accessibility of the NSs to the organic dyes, and thus the photocatalytic performance of the NSs, due to the improved dispersion of the NSs within the polymer network, the separation from the media and reuse of such photoactive hydrogels should be more easily achieved than the nanometer-sized g-CN material on its own. Another advantage of using hydrogels as a matrix for NPs dispersion is the possibility to mold the hydrogels to the shape that best suits a particular application, as demonstrated using PDMAm/g-CN hydrogel nanocomposites [63]. In the same work, the selectivity of the hydrogel nanocomposite to different pollutants was tested, with the capture of positively charged dyes being particularly efficient, due to the negatively charged surface groups of g-CN.

Another interesting example of the applications of hydrogel nanocomposites is found in ref. [88], where He and co-authors describe the assembly of g-CN into tailored 3D architectures, for broadband solar wastewater remediation. While the resulting product was an aerogel membrane, thus outside the scope of this review, the described (woodpile) structures were obtained by 3D printing the g-CN NSs (building blocks) mixed with sodium alginate, for stabilizing the g-CNs and achieving a good rheological (shear thinning) behavior for the extrusion (printing) process. Furthermore, after the printing process, the 3D-printed structures were submerged in a Ca^{2+} solution to induce the gelation of the alginate chains and concomitant formation of rigid and robust structures that were, in the last step, dried to form the aerogels. Thus, the formation of highly ordered g-CN/sodium alginate hydrogel nanocomposites was an intermediate step in the formation of these promising materials.

While very exciting [137], the field of 2D materials also brings a number of challenges. The poor stability of NSs in solution and structural decomposition/degradation can potentially be improved using hydrogels as coatings and/or dispersion medium, as well as hybridization with other materials. Common to other mentioned nanomaterials is the challenging task of synthesising materials with the criteria required for industry and commercialization, in terms of production yield, quantity, and quality. This is especially important in ultrathin 2D nanomaterials, where the physico-chemical properties highly depend on their structural features.

6. Nanoparticles as Tools for Studying and Monitoring Hydrogel Properties

In addition to functionalities in modulating the connectivity of the polymer part of hydrogels, including NPs in hydrogels can also be used as a means to monitor their properties. Thus, the combination of particularities of the NPs and observation by various means, mainly optical, provides information on changes in equilibrium swelling, local deformation, and elasticity. These approaches require careful selection of the properties and concentration of the NPs to support the selected observation method.

6.1. Crystalline Colloidal Arrays in Hydrogels

Firstly, monitoring changes in the swelling volume, based on Bragg's diffraction principle from a lattice of embedded NPs (Figure 9a), requires the inclusion of the NPs in the polymer network with a lattice-like organization. In addition to the crystalline colloid (NP) array (CCA) considered here, inverse opal assemblies and holograms can also be embedded in hydrogels for monitoring their properties [22,138]. The formation of NP arrays embedded in hydrogels to form a sufficiently regular 3D pattern for the Bragg diffraction, exploits electrostatic driven, inter-particle (repulsive) interactions between monodisperse, equally charged NPs. At a sufficiently large concentration, these types of particles adopt periodic nanostructures suitable for characterization by diffraction. The nature of the NPs and the concentration offer a handle to control the particular lattice type, e.g., body centered cubic (BCC) crystals are reported to be favorable using small NPs (diameter < 80 nm) at low concentrations (<3%), whereas face centered cubic lattices are the more prevalent minimum energy organization for larger NPs (diameter > 100 nm) in more concentrated dispersions (>8%), as recently summarized [22]. The integration of the NP lattice in the hydrogel can be realized using procedures as outlined above.

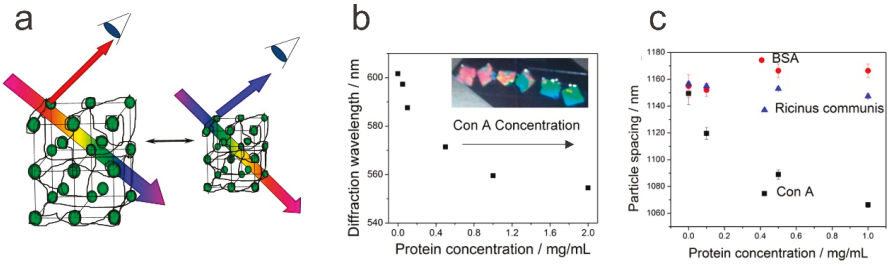

Figure 9. Integration of NP to aid characterization capability of the hydrogels by colloidal crystals embedded in hydrogels. (**a**) The change in the refracted wavelength from 3D crystalline colloidal arrays embedded in hydrogels yields a shift in color when the hydrogel changes its equilibrium swelling state due to various stimuli and molecular details of the responsive network component. Adapted with permission from Cai, Z., et al. Two-Dimensional Photonic Crystal Chemical and Biomolecular Sensors. *Analytical Chemistry* **2015**, *87*, 5013–5025. Copyright (2015) American Chemical Society. (**b**) Changes in diffracted wavelength from a 2D-colloidal crystal mannose hydrogel of AAm, AAc, and mannose side chains as a function of Con A concentration in 0.1 M NaCl aqueous solutions that contain 1 mM Ca^{2+} and 0.5 mM Mn^{2+}. (**c**) Calculated colloidal particle spacing for the same 2D colloidal crystal mannose hydrogel as in panel (b) versus the concentration of Con A, Ricinus communis, and BSA. Adapted with permission from Zhang, J.-T., et al. Two-Dimensional Photonic Crystal Sensors for Visual Detection of Lectin Concanavalin A. *Analytical Chemistry* **2014**, *86*, 9036–9041. Copyright (2014) American Chemical Society.

Provided that periodic nanostructures can be realized in the hydrogels, the reflected wavelength from periodically ordered colloids within hydrogels displays a maximum, as obtained from combining the well-known relations of Bragg's and Snell's law [139]:

$$\lambda_{\max} = 1.633\left(\frac{D}{m}\right)\left(\frac{V}{V_0}\right)^{1/3}\sqrt{{n_a}^2 - \sin^2\theta} \quad (3)$$

where D is the diameter of the embedded NP, m is the order of the Bragg diffraction, and (V/V_0) is the volumetric swelling ratio of the hydrogel. The refractive index n_a in this equation refers to the average of the NP—hydrogel system. This approach provides a quantitative relation between a spectroscopically determined parameter and the extent of swelling as governed by the thermodynamics of the specimen for the actual environmental conditions, as can be deduced from Equation (1).

The application of hydrogel-integrated CCA for the determination of analyte concentration through its effect on the swelling state, and determined based on diffraction from the CCA part, can be grouped into the size of the analyte, e.g., ions, molecules, and macromolecules. CCA embedded in hydrogels for the detection of ions includes, e.g., Pb^{2+} [140–142], Hg^{2+} [142,143], and Cd^{2+} [144], which are all examples motivated by the need for the detection of toxic concentrations of heavy metal ions. In addition to the CCA part facilitating the readout process, the hydrogel constructs also need to include recognition moieties with high selectivity and sensitivity to support detection in an interesting analyte concentration range. Concerning the sensitivity and selectivity of the molecular groups incorporated into the hydrogel networks, it is interesting to compare the work by Jana and co-workers [143] exploiting the mercury inhibition of immobilized urease as the recognition and transducing principle with the work by Ye and co-workers [142] that uses an aptamer sequence recognizing mercury. In the former, the authors exploit the de-swelling of a partly anionic polyacrylamide network with the immobilized urease in the presence of urea, with the mechanism of de-swelling being the charge screening of the anionic network due to the product of the enzymatic degradation of urea, ions HCO_3^-, and NH_4^+. The presence of mercury inhibits the catalytic activity of the enzyme, thus displaying a smaller de-swelling effect. For a NP–hydrogel CCA composite including 360 μmol/mL urease and 0.3 mol/mL carboxylate groups within the hydrogel, a sensitivity of 1 ppb mercury in water was reported, which is below the maximum contamination level stated by EPA, USA, for safe drinking water [23]. Jana and co-workers obtained a similar sensitivity in the recorded wavelength shift for the Hg^{2+} induced swelling (as low as 10 nM) for the aptamer grafted hydrogel. Moreover, they reported that the response was highly selective for Hg^{2+} as compared to other possible ions, among which data were provided for Pb^{2+}, Ag^+, Mn^{2+}, Zn^{2+}, Mg^{2+}, Ca^{2+}, Al^{3+}, Ba^{2+}, Fe^{3+}, Cu^{2+}, and Cr^{3+}. In addition to the aptamer and enzyme strategy, the incorporation of crown ethers in the CCA embedded hydrogels is a widely adopted strategy. This was introduced in the early work of CCA embedded hydrogels by Asher by exploiting a crown ether (4-acryloylaminobenzo-18-crown-6 (AAB18C6)) sensitive to lead, barium, and potassium. The binding of the various ions with specific affinity transforms the crown ether to a charged group, thus inducing swelling of the hydrogel construct. The ionic selectivity and specificity of the crown ethers then underpin the similar properties of the CCA embedded hydrogel swelling properties. The recent review by Lowe and co-workers [23] and references therein provide a more extensive summary of crown ethers and their ionic selectivity as employed as recognition moieties in responsive hydrogels combined with optical readout strategies.

Shifting from CCA hydrogel composites sensitive to ions to materials being able to recognize small molecules, we again find various strategies being employed that integrate and transform the recognition and further processing to a swelling effect readily recorded as shifts in the reflection. Examples of molecules being detected by this approach include, e.g., glucose [145,146], urea [147], ethanol [148], creatinine [149], or ammonia [150]. For glucose, phenylboronic acid (PBA) groups are introduced in the hydrogel network and the CCA embedded hydrogel becomes sensitive to this analyte (and other bearing cis-hydroxyls) in a concentration-dependent manner. Asher demonstrated that this system diffracted light in the visible range, thus ensuring a visible perception of changes in glucose

concentrations. A simple observation of a color change in the mirror, provided that such functional material is embedded in a contact lens, and comparison to a color scale calibrated in blood sugar level, is suggested to be beneficial for the health of diabetic patients [145,151]. Later work in this field also includes the improvement of glucose selectivity in the recognition process by modification of the original recognition moiety [146]. While the recognition of glucose induces changes in the swelling of the hydrogel component either by a cross-linking or χ-parameter change of the hydrogel, the specific swelling response to other small molecules can either exploit the same principles, or expand these to, for example, enzymatic or ionic stimuli [22,138].

For CCA embedded in hydrogels designed for the recognition of macromolecules based on, e.g., complementarity in the ssDNA sequence [152], biotin [153], or proteins [154], these groups of materials additionally need to consider transport of the analyte more explicitly compared to the constructs directed towards the smaller analytes. This is due to the general issue on the impact of polymer networks structure (mesh size) on the transport properties of the analytes [155]. Reducing the potential impact of constraining the analyte transport, e.g., by increasing the water content, can inversely affect the mechanical stability of the composite. In the report by Asher and co-workers [154], the reduction in the diffracted wavelength due to reduced proximity between the colloidal particles in the presence of ConA (Figure 9b,c) is driven by the multifunctional binding of mannose to the Con A, thus deswelling the hydrogel in a Con A concentration-dependent manner.

Most of the studies employing CCA within hydrogels explore these constructs as a recognition and transducing element where the hydrogel hosts the recognition functionality by the integration of various functional groups and the transducing principle is based on the associated changes in the equilibrium swelling. The CCA part is embedded to facilitate an optical readout, and also to offer the means for direct perception of changes by the human eye. The approaches mostly focus on the direct correlation between the analyte concentrations and the change in the peak of the wavelength. However, the distribution of the wavelength of the reflected light appears to be much less explored as a basis for understanding hydrogels.

6.2. Traction Force Microscopy

While observations of the positional changes within the CCA array embedded in hydrogels are based on the collective behavior of the assumed homogeneous changes in the swelling volume within the illuminated domain, embedding NPs at a lower concentration combined with scattering or optical imaging and subsequent image analysis offer alternative means for the characterization of hydrogels. The image analysis strategy typically establishes trajectories of the embedded particles within the hydrogels, by the simultaneous monitoring of many particles. The incorporation of fluorescent beads facilitates the determination of local deformation of the elastic matrix by connecting sequential positions of the beads from time laps imaging. This information is also conventionally converted to stress fields based on the calibrated elastic modulus of the hydrogel matrix (assuming homogeneous mechanical properties). This group of observations is mostly applied to hydrogels at an equilibrated cross-link density. Typically, the hydrogels are subjected to an applied force, and the approach provides maps of deformation and rate of deformation of the hydrogels. Here, the NP concentration is generally much lower than for the CCA approach, since the initial regular (lattice) organization is not required. Instead, the requirement is that the concentration of the NPs is sufficiently low to allow unique identification of the trajectory of the individual particles between subsequent images.

In an early example of such a strategy by Dembo and Wang [156], fluorescent latex beads (200 nm) were included at the volume ratio 1:125 relative to a stock solution of 10 wt % acrylamide (AAm) pre-gel used to prepare a covalent anchored AAm gel to a glass surface. The AAm thin film was surface functionalized with collagen or fibronectin [157] and used for determination of deformation as induced by fibroblasts adhering and locomoting on the AAm substrate. The approach enabled the identification of a suggested frontal towing action of the migrating cell, as deduced from changes in traction forces recorded by the deformed substrate preceding observed changes in the direction of

the migration. Following this, and earlier reports on the balancing force exerted by a biological entity on an elastic surface [158], the approach of mapping localized positions/forces within a hydrogel include, e.g., characterization in three dimensions [159–161] and characterization using super-resolution optical microscopy to reveal dimensional changes at a 50 nm resolution [157,162]. Colin-York and coworkers described the steps involved in realizing high resolution traction force mapping by combining image processing of STED micrographs of a mechanically calibrated hydrogel with embedded nanoparticles [157] (Figure 10). Adherent HeLa cells with fluorescently labelled components in the focal adhesion points (paxillin-EGFP) were grown on a fibronectin coated AAm hydrogel with an elastic modulus of 40 kPa. Analysis of the displacement of embedded fluorescent nanoparticles following the release of the cell anchoring, and thereby the force exerted from the cells on the AAm using methods analogous to particle imaging velocimetry, yields maps of the traction force exerted on the matrix (Figure 10d). The use of STED for the imaging process yields better resolved force maps as compared to the application of conventional confocal imaging. Another recent example is the detailed mapping of human mesenchymal cells inducing local degradation of a 3D network comprised of PEG, including peptide segments susceptible to cell secreted matrix metalloproteinases (MMPs) [163]. The deformation and stress fields in this case displayed a combination of localized stress/deformation changes due to both the displacement of network parts and the cutting of elastically active network chains.

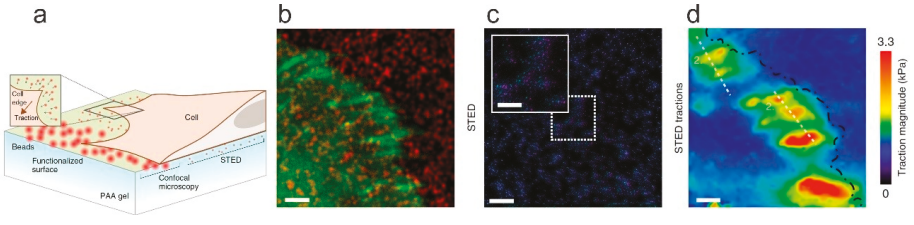

Figure 10. Illustration of traction force microscopy as realized by integrating fluorescent NPs in an elastic matrix (polyacrylamide) and spatio-temporally monitoring their position using either confocal or high resolution (stimulated emission depletion) microscopy to map out deformation and local forces exerted by growing cells on the substrate (**a**) and the process illustrated to map the traction magnitude exerted by growing HeLa cells on an acrylamide gel (**b**–**d**) using STED-Traction Force Microscopy (STFM). The change in the location of the embedded nanoparticles due to the release of traction from the HeLa cells (**c**) and calculated map of traction magnitude on the hydrogel (d) over the same region of interest as shown in (**b**). The scale bar is 2 μm (**b**–**d**). The paxillin in the focal adhesion points of HeLa was labelled with EGFP and 40 nm red fluorescent beads were embedded in the AAm hydrogel (**b**). STED imaging of the positions of the fluorescent beads embedded in the gel under the cell shifted from before (cyan) to after (magenta) treatment with trypsin-EDTA to relax the traction force (**c**) and used as a basis for the analysis of the traction force (**d**). Adapted with permission from Colin-York, H., Eggeling, C.; Fritzsche, M. Dissection of mechanical force in living cells by super-resolved traction force microscopy. *Nature Protocols* **2017**, *12*, 783–796. Copyright (2017) Springer Nature.

6.3. Micro-Rheology

From a hydrogel material perspective, traction force microscopy is devoted to exploitation of the linear, equilibrium elastic properties of the matrices. At variance, NPs embedded in viscoelastic media have, for a long time, been supporting the determination of micro-rheological properties over frequency ranges that, in many cases, also extend the range easily accessible by macro-rheology [164–167]. There is a range of micro-rheological approaches available, and generally one can group them into passive micro-rheology, where the determination of movement of NPs due to thermal energy forms the basis for extraction of the (localized) rheological moduli, or active micro-rheology, where the probe is actively driven by some external field coupling to the NP, e.g., optical trapping [168,169]. Despite the advocated strongholds of micro-rheology in terms of, e.g., extended frequency range accessible and

small sample volume requirements, the main body of applications appears to be within viscoelastic materials possessing terminal relaxations and not that extensively in, e.g., hydrogels displaying (apparent) equilibrium elastic properties on a time scale extending beyond minutes. A couple of examples include the reported nearly frequency-independent complex modulus of AAm hydrogels in the frequency range ω from 0.1 to 100 s^{-1} for polymer concentrations from 10 to 5 wt %, while a stronger frequency dependence was observed below 4 wt % AAm [164] (Figure 11). These features were deduced from data collected in the single scattering limit. Examples of data obtained using this strategy (Figure 11b) illustrate reasonable agreement with bulk rheology data and that data can be collected over an extended frequency range, e.g., exceeding six orders of magnitude, thus providing mechanical spectra with regions containing signatures of various dominating relaxations. Moreover, the small volume requirements for the scattering-based approach as compared to bulk rheology are considered an advantage.

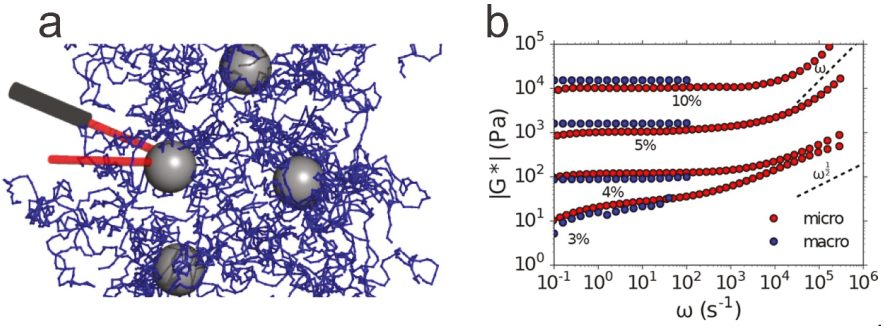

Figure 11. Dynamic light scattering of NPs embedded in hydrogels conducted in backscattering model records information related to the Brownian motion of the NP (**a**), which is further processed to extract rheological signatures of the polymer network. Comparison between micro-rheology data deduced from backscattering mode (micro-rheology) and conventional macroscopic rheology (macro) on cross-linked AAm hydrogels with mass concentrations from 3% to 10% (**b**). The rheological data are presented as the magnitude of the complex shear modulus versus the angular frequency, $|G^*(\omega)|$. Reprinted with permission from Krajina, B., et al., Dynamic Light Scattering Microrheology Reveals Multiscale Viscoelasticity of Polymer Gels and Precious Biological Materials. *ACS Central Science*, 2017. **3**(12): p. 1294–1303. Copyright (2017) American Chemical Society.

7. General Comments and Outlook

Some disadvantages of NP-hydrogel nanocomposites have been pointed out throughout the text, but we will revise them here while pointing out other drawbacks and challenges, as well as an outlook for further developments.

Despite the large interest and potential novel applications of this class of materials, NP-hydrogel nanocomposites still face some challenges before they can be used in real applications. One such challenge is the synthesis of the materials with the criteria required for industry and commercialization. This entails different levels of fabrication, ranging from the synthesis of the nanomaterials and hydrogels to the assembly of the nanocomposites, which also depends on the chosen route for the nanocomposite synthesis. As mentioned, the properties of nanomaterials, particularly the ultrathin 2D NSs, are strongly dependent on the physico-chemical properties of their structural features and the control of such properties for the relatively large-scale synthesis that is required for commercialization is challenging. The controlled preparation of the composites, namely the homogeneous distribution of NPs and NSs in hydrogels (currently achieved by resorting to electrostatics), constitutes another challenge, as well as the formation of anisotropic nanocomposites with controlled structures, or simply the synthesis of micro-gel composites with a defined size and a good batch-to-batch reproducibility.

Regarding the latter, flow chemistry, where reactions are performed in channels in a continuous stream rather than in a flask, arises as a promising tool for improving the synthesis of such materials [170]. Regarding macroscopic hydrogel composites, processing techniques such as 3D printing should provide good opportunities for developing hydrogel composites with controlled structures either as final materials or as intermediate steps in the production of aerogels.

The large availability of materials (both polymers and nanomaterials) dictates that the number of possible combinations is enormous, as can be testified by the large amount of publications in the last couple of decades. In many of these, the components are mixed in different proportions and, generally, the mechanical properties of the final material are tested. There is often a lack of discussion on the mechanisms involved in the formation of the hydrogel composite materials and the reason for the improved (or not) mechanical properties. A better understanding of the interactions at play will allow the design of nanocomposite hydrogels with the best properties for the particular applications, whether that entails a more efficient incorporation of the NPs, a better mechanical performance, and a long-term stability of the nanocomposite material; the hydrophilic/hydrophobic nature of the material for improved drug loading capacity and controlled release; or the precise control of shape variations induced by external stimuli, to name a few. Furthermore, the need for optimization of the material for a specific function offers further opportunities for the development of yet new nanomaterials and polymers that can be combined in a range of exciting possibilities. It is thus fundamental to develop new and/or improve existing multi length-scale methodologies for predicting the properties of the materials based on the individual components, as a guide for experimental development. This would allow a more efficient design of materials. Just recently, Lamberti, Barba and coworkers [171] provided an overview of the coupling between solvent diffusion, viscous relaxation time, and a so-called process time, and based on the ranking and differences in these, classified the typical dominant dynamic behavior of hydrogels in terms of viscoelastic and poro-elastic relaxation. Inclusion of NP into the hydrogel can be expected to offer an additional strategy to the network parameters of the hydrogels to tailor-make the dynamic properties of NP-hydrogel composites, which so far, have not been widely explored. Inclusion of high aspect ratio NP in this context may potentially provide strategies for soft materials design with anisotropic dynamic properties.

Another practical aspect to consider when looking into NP-hydrogel composite materials for particular applications is their stability in time regarding durability and fatigue behavior. As reviewed by Creton [18], this is a topic that is seldom discussed within the field of hydrogels, and while the presence of nanomaterials has the potential to improve these properties, these need to be properly assessed. Furthermore, the leaching of nanomaterial from the nanocomposite with time will likely affect the stability and performance of the material, and may also induce environmental toxicity. This may also be the case during the manufacture and disposal of the nanocomposite materials. The cytotoxicity of the material is another practical concern that currently limits the application of such materials in biomedicine and biomimetic materials.

The continuous development of new techniques will allow a better quantitative and predictive knowledge of these materials and the opening of novel and exciting applications.

8. Conclusions

NP–hydrogel systems have received much interest in the past decades, fueled by recent suggested applications. Several different ways have been proposed to synthesize nanocomposite hydrogels, ranging from adding NPs to existing hydrogel networks to simultaneously synthesizing NPs and hydrogel in a one pot reaction. It is also possible to coat the NPs with nanogels, which have been explored for, for example, drug delivery applications.

The formation of nanocomposite hydrogels relies on non-covalent attractive interactions between the NPs and the macromolecule network. Thus, an understanding of the intermolecular interactions at play between the surface of the NPs and the macromolecular network is of paramount importance in the development of systems with desirable qualities. The interactions between NPs and polymers can

be electrostatic (if charged groups are present) or based on van der Waals forces. The hydrophobic effect may play a significant role in the adsorption of polymers to surfaces, if the monomers are, e.g., methylated. Many studies suggest that hydrogen bonding is the driving force for association, but this might not be very relevant for hydrogels in water.

The individual interactions between NPs and monomers do not necessarily have to be very strong, but the large number of interaction points can lead to a strong adhesion. Due to the non-covalent nature of the interaction between the polymers and NPs, nanocomposite hydrogels can exhibit self-healing abilities, where fractures or cuts can be healed autonomously by reforming bonds across surfaces. Following this same principle, NPs can be used to glue two hydrogels by forming bonds with the polymers in each network and thus bridging the two surfaces. Furthermore, tension and stress can more easily be dissipated, as the non-covalent bonds can break and reform when strained. Therefore, many nanocomposite hydrogels have superior mechanical properties in comparison to pure hydrogels. Taking the opposite perspective, hydrogels have been used to disperse NSs in aqueous solution and to aid the assembly of aerogels with defined 3D structures and photocatalytic activity. This, in turn, increases the accessibility of the large specific surface area of the 2D materials to diverse solutes, thus improving the performance of the nanomaterial. Overall, the composition and characteristics of both NPs/NSs and polymers are important parameters in the synthesis, physico-chemical properties, and application potential of nanocomposite hydrogels. While there is a large number of available polymers and nanomaterials, and the potential to prepare many more, there is a need for accompanying theoretical and modelling studies, as well as the development of new experimental techniques, for a multiscale characterization of the material and a quantitative and predictive understanding of the structure and behavior. This will hopefully contribute to more efficient synthesis processes with better control of the final product and the concomitant expansion of possible applications.

NPs incorporated in hydrogel networks can be used as tools for monitoring hydrogel properties. For example, swelling equilibrium can be monitored by following Bragg's diffraction from a lattice of embedded NPs arrays. Also, traction force microscopy can give insight into the forces generated by living matter through mapping of the local response of adherent NP-hydrogel composites. The latter strategy affords the characterization of localized forces, primarily in adhesion processes, that are very challenging to determine using alternative strategies.

Author Contributions: All three authors contributed to the drafting, writing, and proof-reading of the manuscript.

Funding: This work was supported by the Norwegian University of Science and Technology.

Acknowledgments: Morten Stornes and Nicholas Christiansen are acknowledged for fruitful discussions.

Conflicts of Interest: The authors declare no conflict of interest.

References

1. Barbucci, R. (Ed.) *Hydrogels Biological Properties and Applications*; Springer: Milan, Italy, 2010.
2. Bohidar, H.B.; Dubin, P.; Osade, Y. (Eds.) *Polymer Gels: Fundamentals and Applications*; Oxford University Press: Oxford, UK, 2003.
3. Huglin, M.R. *Hydrogels in Medicine and Pharmacy*; Peppas, N.A., Ed.; CRC Press Inc.: Boca Raton, FL, USA, 1986.
4. Wichterle, O. *Soft Contact Lenses*; Ruben, M., Ed.; Wiley: New York, NY, USA, 1978; pp. 3–5.
5. Haider, M.; Megeed, Z.; Ghandehari, H. Genetically engineered polymers: Status and prospects for controlled release. *J. Controlled Release* **2004**, *95*, 1–26. [CrossRef] [PubMed]
6. Jeong, B.; Gutowska, A. Lessons from nature: Stimuli-responsive polymers and their biomedical applications. *Trends Biotech.* **2002**, *20*, 305–311. [CrossRef]
7. Langer, R.; Tirrell, D.A. Designing materials for biology and medicine. *Nature* **2004**, *428*, 487–492. [CrossRef] [PubMed]
8. Megeed, Z.; Cappello, J.; Ghandehari, H. Genetically engineered silk-elastinlike protein polymers for controlled drug delivery. *Adv. Drug Deliv. Rev.* **2002**, *54*, 1075–1091. [CrossRef]

9. Chacko, R.T.; Ventura, J.; Zhuang, J.M.; Thayumanavan, S. Polymer nanogels: A versatile nanoscopic drug delivery platform. *Adv. Drug Deliv. Rev.* **2012**, *64*, 836–851. [CrossRef] [PubMed]
10. Stuart, M.A.C.; Huck, W.T.S.; Genzer, J.; Muller, M.; Ober, C.; Stamm, M.; Sukhorukov, G.B.; Szleifer, I.; Tsukruk, V.V.; Urban, M.; et al. Emerging applications of stimuli-responsive polymer materials. *Nat. Mater.* **2010**, *9*, 101–113. [CrossRef] [PubMed]
11. Merino, S.; Martín, C.; Kostarelos, K.; Prato, M.; Vázquez, E. Nanocomposite Hydrogels: 3D Polymer-Nanoparticle Synergies for On-Demand Drug Delivery. *ACS Nano* **2015**, *9*, 4686–4697. [CrossRef] [PubMed]
12. Okumura, Y.; Ito, K. The polyrotaxane gel: A topological gel by figure-of-eight cross-links. *Adv. Mater.* **2001**, *13*, 485–487. [CrossRef]
13. Karino, T.; Shibayama, M.; Ito, K. Slide-ring gel: Topological gel with freely movable cross-links. *Phys. B Condens. Matter* **2006**, *385*, 692–696. [CrossRef]
14. Ito, K. Novel cross-linking concept of polymer network: Synthesis, structure, and properties of slide-ring gels with freely movable junctions. *Polym. J.* **2007**, *39*, 489. [CrossRef]
15. Bin Imran, A.; Esaki, K.; Gotoh, H.; Seki, T.; Ito, K.; Sakai, Y.; Takeoka, Y. Extremely stretchable thermosensitive hydrogels by introducing slide-ring polyrotaxane cross-linkers and ionic groups into the polymer network. *Nat. Commun.* **2014**, *5*. [CrossRef] [PubMed]
16. Gong, J.P.; Katsuyama, Y.; Kurokawa, T.; Osada, Y. Double-network hydrogels with extremely high mechanical strength. *Adv. Mater.* **2003**, *15*, 1155–1158. [CrossRef]
17. Haraguchi, K.; Takehisa, T. Nanocomposite hydrogels: A unique organic-inorganic network structure with extraordinary mechanical, optical, and swelling/de-swelling properties. *Adv. Mater.* **2002**, *14*, 1120–1124. [CrossRef]
18. Creton, C. 50th Anniversary Perspective: Networks and Gels: Soft but Dynamic and Tough. *Macromolecules* **2017**, *50*, 8297–8316. [CrossRef]
19. Haraguchi, K. Nanocomposite hydrogels. *Curr. Opin. Solid State Mater. Sci.* **2007**, *11*, 47–54. [CrossRef]
20. Zhu, H.Y.; Fu, Y.Q.; Jiang, R.; Yao, J.; Xiao, L.; Zeng, G.M. Novel magnetic chitosan/poly(vinyl alcohol) hydrogel beads: Preparation, characterization and application for adsorption of dye from aqueous solution. *Bioresour. Technol.* **2012**, *105*, 24–30. [CrossRef] [PubMed]
21. Gaharwar, A.K.; Peppas, N.A.; Khademhosseini, A. Nanocomposite hydrogels for biomedical applications. *Biotechnol. Bioeng.* **2014**, *111*, 441–453. [CrossRef]
22. Jung, S.; Kaar, J.L.; Stoykovich, M.P. Design and functionalization of responsive hydrogels for photonic crystal biosensors. *Mol. Syst. Des. Eng.* **2016**, *1*, 225–241. [CrossRef]
23. Yetisen, A.K.; Naydenova, I.; Vasconcellos, F.D.; Blyth, J.; Lower, C.R. Holographic Sensors: Three-Dimensional Analyte-Sensitive Nanostructures and Their Applications. *Chem. Rev.* **2014**, *114*, 10654–10696. [CrossRef]
24. Quesada-Perez, M.; Maroto-Centeno, J.; Forcada, J.; Hidalgo-Alvarez, R. Gel swelling theories: The classical formalism and recent approaches. *Soft Matter* **2011**, *7*, 10536–10547. [CrossRef]
25. Schröder, U.P.; Oppermann, W. Properties of polyelectrolyte gels. In *Physical Properties of Polymeric Gels*; Wiley: Chichester, West Sussex, England, 1996; pp. 19–38.
26. Hoare, T.R.; Kohane, D.S. Hydrogels in drug delivery: Progress and challenges. *Polymer* **2008**, *49*, 1993–2007. [CrossRef]
27. Ahmed, E.M. Hydrogel: Preparation, characterization, and applications: A review. *J. Adv. Res.* **2015**, *6*, 105–121. [CrossRef] [PubMed]
28. Raemdonck, K.; Demeester, J.; De Smedt, S. Advanced nanogel engineering for drug delivery. *Soft Matter* **2009**, *5*, 707–715. [CrossRef]
29. Lin, C.H.; Sheng, D.K.; Liu, X.D.; Xu, S.B.; Ji, F.; Dong, L.; Zhou, Y.; Yang, Y.M. A self-healable nanocomposite based on dual-crosslinked Graphene Oxide/Polyurethane. *Polymer* **2017**, *127*, 241–250. [CrossRef]
30. Qiao, Z.Y.; Zhang, R.; Du, F.S.; Liang, D.H.; Li, Z.C. Multi-responsive nanogels containing motifs of ortho ester, oligo(ethylene glycol) and disulfide linkage as carriers of hydrophobic anti-cancer drugs. *J. Controlled Release* **2011**, *152*, 57–66. [CrossRef] [PubMed]
31. Beloqui, A.; Kobitski, A.Y.; Nienhaus, G.U.; Delaittre, G. A simple route to highly active single-enzyme nanogels. *Chem. Sci.* **2018**, *9*, 1006–1013. [CrossRef] [PubMed]

32. Kabanov, A.V.; Vinogradov, S.V. Nanogels as Pharmaceutical Carriers: Finite Networks of Infinite Capabilities. *Angew. Chem.* **2009**, *48*, 5418–5429. [CrossRef] [PubMed]
33. Oishi, M.; Hayashi, H.; Michihiro, I.D.; Nagasaki, Y. Endosomal release and intracellular delivery of anticancer drugs using pH-sensitive PEGylated nanogels. *J. Mater. Chem.* **2007**, *17*, 3720–3725. [CrossRef]
34. Nazli, C.; Demirer, G.S.; Yar, Y.; Acar, H.Y.; Kizilel, S. Targeted delivery of doxorubicin into tumor cells via MMP-sensitive PEG hydrogel-coated magnetic iron oxide nanoparticles (MIONPs). *Colloids Surf. B* **2014**, *122*, 674–683. [CrossRef]
35. Chen, T.; Hou, K.; Ren, Q.Y.; Chen, G.Y.; Wei, P.L.; Zhu, M.F. Nanoparticle-Polymer Synergies in Nanocomposite Hydrogels: From Design to Application. *Macromol. Rapid Commun.* **2018**, *39*. [CrossRef]
36. Ma, Y.K.; Ge, Y.X.; Li, L.B. Advancement of multifunctional hybrid nanogel systems: Construction and application in drug co-delivery and imaging technique. *Mater. Sci. Eng. C* **2017**, *71*, 1281–1292. [CrossRef] [PubMed]
37. Gao, H.F.; Yang, W.L.; Min, K.; Zha, L.S.; Wang, C.C.; Fu, S.K. Thermosensitive poly (*N*-isopropylacrylamide) nanocapsules with controlled permeability. *Polymer* **2005**, *46*, 1087–1093. [CrossRef]
38. Palioura, D.; Armes, S.P.; Anastasiadis, S.H.; Vamvakaki, M. Metal nanocrystals incorporated within pH-responsive microgel particles. *Langmuir* **2007**, *23*, 5761–5768. [CrossRef] [PubMed]
39. Kim, M.; Kwon, J.E.; Lee, K.; Koh, W.-G. Signal-amplifying nanoparticle/hydrogel hybrid microarray biosensor for metal-enhanced fluorescence detection of organophosphorus compounds. *Biofabrication* **2018**, *10*, 035002. [CrossRef] [PubMed]
40. Hsu, S.W.; Rodarte, A.L.; Som, M.; Arya, G.; Tao, A.R. Colloidal Plasmonic Nanocomposites: From Fabrication to Optical Function. *Chem. Rev.* **2018**, *118*, 3100–3120. [CrossRef] [PubMed]
41. Wahid, F.; Zhong, C.; Wang, H.S.; Hu, X.H.; Chu, L.Q. Recent Advances in Antimicrobial Hydrogels Containing Metal Ions and Metals/Metal Oxide Nanoparticles. *Polymers* **2017**, *9*, 636. [CrossRef]
42. Strong, L.E.; West, J.L. Thermally responsive polymer-nanoparticle composites for biomedical applications. *Wiley Interdiscip. Rev.-Nanomed. Nanobiotech.* **2011**, *3*, 307–317. [CrossRef]
43. Hezaveh, H.; Muhamad, II. Effect of MgO nanofillers on burst release reduction from hydrogel nanocomposites. *J. Mater. Sci.* **2013**, *24*, 1443–1453. [CrossRef]
44. Zhang, J.G.; Xu, S.Q.; Kumacheva, E. Polymer microgels: Reactors for semiconductor, metal, and magnetic nanoparticles. *J. Am. Chem. Soc.* **2004**, *126*, 7908–7914. [CrossRef]
45. Wang, C.; Flynn, N.T.; Langer, R. Controlled structure and properties of thermoresponsive nanoparticle-hydrogel composites. *Adv. Mater.* **2004**, *16*, 1074–1079. [CrossRef]
46. Pardo-Yissar, V.; Gabai, R.; Shipway, A.N.; Bourenko, T.; Willner, I. Gold nanoparticle/hydrogel composites with solvent-switchable electronic properties. *Adv. Mater.* **2001**, *13*, 1320–1323. [CrossRef]
47. Jones, C.D.; Lyon, L.A. Photothermal patterning of microgel/gold nanoparticle composite colloidal crystals. *J. Am. Chem. Soc.* **2003**, *125*, 460–465. [CrossRef] [PubMed]
48. Liu, H.X.; Huang, S.J.; Li, X.J.; Zhang, L.H.; Tan, Y.Y.; Wei, C.; Lv, J. Facile fabrication of novel polyhedral oligomeric silsesquioxane/carboxymethyl cellulose hybrid hydrogel based on supermolecular interactions. *Mater. Lett.* **2013**, *90*, 142–144. [CrossRef]
49. Stornes, M.; Linse, P.; Dias, R.S. Monte Carlo Simulations of Complexation between Weak Polyelectrolytes and a Charged Nanoparticle. Influence of Polyelectrolyte Chain Length and Concentration. *Macromolecules* **2017**, *50*, 5978–5988. [CrossRef]
50. Stornes, M.; Shrestha, B.; Dias, R.S. pH-Dependent Polyelectrolyte Bridging of Charged Nanoparticles. *J. Phys. Chem. B* **2018**, *122*, 10237–10246. [CrossRef] [PubMed]
51. Portehault, D.; Petit, L.; Pantoustier, N.; Ducouret, G.; Lafuma, F.; Hourdet, D. Hybrid thickeners in aqueous media. *Colloids Surf. A* **2006**, *278*, 26–32. [CrossRef]
52. Carlsson, L.; Rose, S.; Hourdet, D.; Marcellan, A. Nano-hybrid self-crosslinked PDMA/silica hydrogels. *Soft Matter* **2010**, *6*, 3619–3631. [CrossRef]
53. Pasqui, D.; Atrei, A.; Giani, G.; De Cagna, M.; Barbucci, R. Metal oxide nanoparticles as cross-linkers in polymeric hybrid hydrogels. *Mater. Lett.* **2011**, *65*, 392–395. [CrossRef]
54. Garcia-Astrain, C.; Chen, C.; Buron, M.; Palomares, T.; Eceiza, A.; Fruk, L.; Corcuera, M.A.; Gabilondo, N. Biocompatible Hydrogel Nanocomposite with Covalently Embedded Silver Nanoparticles. *Biomacromolecules* **2015**, *16*, 1301–1310. [CrossRef]

55. da Silva, E.P.; Guilherme, M.R.; Garcia, F.P.; Nakamura, C.V.; Cardozo, L.; Alonso, C.G.; Rubira, A.F.; Kunita, M.H. Drug release profile and reduction in the in vitro burst release from pectin/HEMA hydrogel nanocomposites crosslinked with titania. *RSC Adv.* **2016**, *6*, 19060–19068. [CrossRef]
56. Garcia-Astrain, C.; Hernandez, R.; Guaresti, O.; Fruk, L.; Mijangos, C.; Eceiza, A.; Gabilondo, N. Click Crosslinked Chitosan/Gold Nanocomposite Hydrogels. *Macromol. Mater. Eng.* **2016**, *301*, 1295–1300. [CrossRef]
57. Bardajee, G.R.; Hooshyar, Z.; Asli, M.J.; Shahidi, F.E.; Dianatnejad, N. Synthesis of a novel supermagnetic iron oxide nanocomposite hydrogel based on graft copolymerization of poly((2-dimethylamino)ethyl methacrylate) onto salep for controlled release of drug. *Mater. Sci. Eng. C* **2014**, *36*, 277–286. [CrossRef] [PubMed]
58. Zhou, L.; He, B.Z.; Zhang, F. Facile One-Pot Synthesis of Iron Oxide Nanoparticles Cross-linked Magnetic Poly(vinyl alcohol) Gel Beads for Drug Delivery. *ACS Appl. Mater. Interfaces* **2012**, *4*, 192–199. [CrossRef] [PubMed]
59. Haraguchi, K.; Takehisa, T.; Fan, S. Effects of clay content on the properties of nanocomposite hydrogels composed of poly(*N*-isopropylacrylamide) and clay. *Macromolecules* **2002**, *35*, 10162–10171. [CrossRef]
60. Miyazaki, S.; Karino, T.; Endo, H.; Haraguchi, K.; Shibayama, M. Clay concentration dependence of microstructure in deformed poly(*N*-isopropylacrylamide)-clay nanocomposite gels. *Macromolecules* **2006**, *39*, 8112–8120. [CrossRef]
61. Tan, C.L.; Cao, X.H.; Wu, X.J.; He, Q.Y.; Yang, J.; Zhang, X.; Chen, J.Z.; Zhao, W.; Han, S.K.; Nam, G.H.; et al. Recent Advances in Ultrathin Two-Dimensional Nanomaterials. *Chem. Rev.* **2017**, *117*, 6225–6331. [CrossRef] [PubMed]
62. Liu, M.J.; Ishida, Y.; Ebina, Y.; Sasaki, T.; Hikima, T.; Takata, M.; Aida, T. An anisotropic hydrogel with electrostatic repulsion between cofacially aligned nanosheets. *Nature* **2015**, *517*, 68–72. [CrossRef]
63. Sun, J.W.; Schmidt, B.; Wang, X.; Shalom, M. Self-Standing Carbon Nitride-Based Hydrogels with High Photocatalytic Activity. *ACS Appl. Mater. Interfaces* **2017**, *9*, 2029–2034. [CrossRef]
64. Hata, Y.; Kojima, T.; Koizumi, T.; Okura, H.; Sakai, T.; Sawada, T.; Serizawa, T. Enzymatic Synthesis of Cellulose Oligomer Hydrogels Composed of Crystalline Nanoribbon Networks under Macromolecular Crowding Conditions. *ACS Macro Lett.* **2017**, *6*, 165–170. [CrossRef]
65. Hata, Y.; Sawada, T.; Serizawa, T. Effect of solution viscosity on the production of nanoribbon network hydrogels composed of enzymatically synthesized cellulose oligomers under macromolecular crowding conditions. *Polym. J.* **2017**, *49*, 575–581. [CrossRef]
66. Ko, J.W.; Choi, W.S.; Kim, J.; Kuk, S.K.; Lee, S.H.; Park, C.B. Self-Assembled Peptide-Carbon Nitride Hydrogel as a Light-Responsive Scaffold Material. *Biomacromolecules* **2017**, *18*, 3551–3556. [CrossRef] [PubMed]
67. Rose, S.; Prevoteau, A.; Elziere, P.; Hourdet, D.; Marcellan, A.; Leibler, L. Nanoparticle solutions as adhesives for gels and biological tissues. *Nature* **2014**, *505*, 382–385. [CrossRef] [PubMed]
68. Wang, Q.; Mynar, J.L.; Yoshida, M.; Lee, E.; Lee, M.; Okuro, K.; Kinbara, K.; Aida, T. High-water-content mouldable hydrogels by mixing clay and a dendritic molecular binder. *Nature* **2010**, *463*, 339–343. [CrossRef] [PubMed]
69. Tamesue, S.; Ohtani, M.; Yamada, K.; Ishida, Y.; Spruell, J.M.; Lynd, N.A.; Hawker, C.J.; Aida, T. Linear versus Dendritic Molecular Binders for Hydrogel Network Formation with Clay Nanosheets: Studies with ABA Triblock Copolyethers Carrying Guanidinium Ion Pendants. *J. Am. Chem. Soc.* **2013**, *135*, 15650–15655. [CrossRef] [PubMed]
70. Montarnal, D.; Capelot, M.; Tournilhac, F.; Leibler, L. Silica-Like Malleable Materials from Permanent Organic Networks. *Science* **2011**, *334*, 965–968. [CrossRef] [PubMed]
71. Kim, J.H.; Kim, H.; Choi, Y.; Lee, D.S.; Kim, J.; Yi, G.R. Colloidal Mesoporous Silica Nanoparticles as Strong Adhesives for Hydrogels and Biological Tissues. *ACS Appl. Mater. Interfaces* **2017**, *9*, 31469–31477. [CrossRef] [PubMed]
72. Cao, Z.; Dobrynin, A. Nanoparticles as Adhesives for Soft Polymeric Materials. *Macromolecules* **2016**, *49*, 3586–3592. [CrossRef]
73. Meddahi-Pelle, A.; Legrand, A.; Marcellan, A.; Louedec, L.; Letourneur, D.; Leibler, L. Organ Repair, Hemostasis, and In Vivo Bonding of Medical Devices by Aqueous Solutions of Nanoparticles. *Angew. Chem.* **2014**, *53*, 6369–6373. [CrossRef]

74. Nejadnik, M.R.; Yang, X.; Bongio, M.; Alghamdi, H.S.; Van den Beucken, J.; Huysmans, M.C.; Jansen, J.A.; Hilborn, J.; Ossipov, D.; Leeuwenburgh, S.C.G. Self-healing hybrid nanocomposites consisting of bisphosphonated hyaluronan and calcium phosphate nanoparticles. *Biomaterials* **2014**, *35*, 6918–6929. [CrossRef]
75. Abe, H.; Hara, Y.; Maeda, S.; Hashimoto, S. Adhesion of Gels by Silica Particle. *J. Phys. Chem. B* **2014**, *118*, 2518–2522. [CrossRef]
76. Napper, D. *Polymeric Stabilization of Colloidal Particles*; Academic Press: London, UK, 1983.
77. Ottewill, R.H. Stability and Instability in Disperse Systems. *J. Colloid Interface Sci.* **1977**, *58*, 357–373. [CrossRef]
78. Overbeek, J.T.G. Recent Developments in Understanding of Colloid Stability. *J. Colloid Interface Sci.* **1977**, *58*, 408–422. [CrossRef]
79. Amiel, C.; Sebille, B. FTIR Study of Copolymer Adsorption on Silica. *J. Colloid Interface Sci.* **1992**, *149*, 481–492. [CrossRef]
80. Perrin, E.; Schoen, M.; Coudert, F.; Boutin, A. Structure and Dynamics of Solvated Polymers near a Silica Surface: On the Different Roles Played by Solvent. *J. Phys. Chem. B* **2018**, *122*, 4573–4582. [CrossRef] [PubMed]
81. Greenland, D.J. Interactions between organic polymers and inorganic soil particles. In *Proceeding Symposium on Fundamentals of Soil Conditioning*; De Boodt, M., Ed.; State University of Ghent: Ghent, Belgium, 1972; pp. 897–914.
82. Rubio, J.; Kitchener, J.A. Mechanism of Adsorption of Poly(Ethylene Oxide) Flocculant on Silica. *J. Colloid Interface Sci.* **1976**, *57*, 132–142. [CrossRef]
83. Mathur, S.; Moudgil, B.M. Adsorption mechanism(s) of poly (ethylene oxide) on oxide surfaces. *J. Colloid Interface Sci.* **1997**, *196*, 92–98. [CrossRef]
84. Tadros, T.F. The interaction of cetyltrimethylammonium bromide and sodium dodecylbenzene sulfonate with polyvinyl alcohol. adsorption of the polymer—Surfactant complexes on silica. *I. Colloid Interface Sci.* **1974**, *46*, 528–540. [CrossRef]
85. Postmus, B.; Leermakers, F.; Stuart, M. Self-consistent field modeling of poly(ethylene oxide) adsorption onto silica: The multiple roles of electrolytes. *Langmuir* **2008**, *24*, 1930–1942. [CrossRef] [PubMed]
86. Spruijt, E.; Biesheuvel, P.; de Vos, W. Adsorption of charged and neutral polymer chains on silica surfaces: The role of electrostatics, volume exclusion, and hydrogen bonding. *Phys. Rev. E* **2015**, *91*, 012601. [CrossRef] [PubMed]
87. Sato, N.; Aoyama, Y.; Yamanaka, J.; Toyotama, A.; Okuzono, T.J. Particle Adsorption on Hydrogel Surfaces in Aqueous Media due to van der Waals Attraction. *Sci. Rep.* **2017**, *7*, 6099. [CrossRef] [PubMed]
88. He, P.S.; Tang, X.W.; Chen, L.; Xie, P.W.; He, L.; Zhou, H.; Zhang, D.; Fan, T.X. Patterned Carbon Nitride-Based Hybrid Aerogel Membranes via 3D Printing for Broadband Solar Wastewater Remediation. *Adv. Funct. Mat.* **2018**, *28*, 1801121. [CrossRef]
89. Nie, L.; Liu, C.H.; Wang, J.; Shuai, Y.; Cui, X.Y.; Liu, L. Effects of surface functionalized graphene oxide on the behavior of sodium alginate. *Carbohydr. Polym.* **2015**, *117*, 616–623. [CrossRef] [PubMed]
90. Novoselov, K.S.; Geim, A.K.; Morozov, S.V.; Jiang, D.; Zhang, Y.; Dubonos, S.V.; Grigorieva, I.V.; Firsov, A.A. Electric field effect in atomically thin carbon films. *Science* **2004**, *306*, 666–669. [CrossRef] [PubMed]
91. Bai, H.; Li, C.; Wang, X.L.; Shi, G.Q. A pH-sensitive graphene oxide composite hydrogel. *Chem. Commun.* **2010**, *46*, 2376–2378. [CrossRef]
92. Liu, L.Q.; Barber, A.H.; Nuriel, S.; Wagner, H.D. Mechanical properties of functionalized single-walled carbon-nanotube/poly(vinyl alcohol) nanocomposites. *Adv. Funct. Mater.* **2005**, *15*, 975–980. [CrossRef]
93. Reid, M.; Villalobos, M.; Cranston, E. The role of hydrogen bonding in non-ionic polymer adsorption to cellulose nanocrystals and silica colloids. *Curr. Opin. Colloid Interface Sci.* **2017**, *29*, 76–82. [CrossRef]
94. Lindman, B.; Karlstrom, G.; Stigsson, L. On the mechanism of dissolution of cellulose. *J. Mol. Liq.* **2010**, *156*, 76–81. [CrossRef]
95. Medronho, B.; Romano, A.; Miguel, M.; Stigsson, L.; Lindman, B. Rationalizing cellulose (in)solubility: Reviewing basic physicochemical aspects and role of hydrophobic interactions. *Cellulose* **2012**, *19*, 581–587. [CrossRef]

96. Jiang, W.J.; Luo, W.J.; Zong, R.L.; Yao, W.Q.; Li, Z.P.; Zhu, Y.F. Polyaniline/Carbon Nitride Nanosheets Composite Hydrogel: A Separation-Free and High-Efficient Photocatalyst with 3D Hierarchical Structure. *Small* **2016**, *12*, 4370–4378. [CrossRef]
97. Kumru, B.; Shalom, M.; Antonietti, M.; Schmidt, B. Reinforced Hydrogels via Carbon Nitride Initiated Polymerization. *Macromolecules* **2017**, *50*, 1862–1869. [CrossRef]
98. Liu, H.; Peng, Y.; Yang, C.; Wang, M. Silica Nanoparticles as Adhesives for Biological Tissues? Re-Examining the Effect of Particles Size, Particle Shape, and the Unexpected Role of Base. *Part. Part. Syst. Charact.* **2017**, *34*. [CrossRef]
99. Mallam, S.; Horkay, F.; Hecht, A.M.; Geissler, E. Scattering and Swelling Properties of Inhomogeneous Polyacrylamide Gels. *Macromolecules* **1989**, *22*, 3356–3361. [CrossRef]
100. Okajima, T.; Harada, I.; Nishio, K.; Hirotsu, S. Discontinuous crossover between fast and slow kinetics at the volume phase transition in poly-N-isopropylacrylamide gels. *Jpn. J. Appl. Phys. 2* **2000**, *39*, L875–L877. [CrossRef]
101. Zhao, X.; Huebsch, N.; Mooney, D.; Suo, Z. Stress-relaxation behavior in gels with ionic and covalent crosslinks. *J. Appl. Phys.* **2010**, *107*. [CrossRef] [PubMed]
102. Valles-Lluch, A.; Poveda-Reyes, S.; Amoros, P.; Beltran, D.; Pradas, M.M. Hyaluronic Acid-Silica Nanohybrid Gels. *Biomacromolecules* **2013**, *14*, 4217–4225. [CrossRef] [PubMed]
103. Boonmahitthisud, A.; Nakajima, L.; Nguyen, K.D.; Kobayashi, T. Composite effect of silica nanoparticle on the mechanical properties of cellulose-based hydrogels derived from cottonseed hulls. *J. Appl. Polym. Sci.* **2017**, *134*, 44557. [CrossRef]
104. Du, J.; Wu, R.L.; Liu, H.H.; Nie, X.D.; Li, H.L.; Xu, S.M.; Wang, J.D. Synthesis of Amphoteric Nanocomposite Hydrogels with Ultrahigh Tensibility. *Polym. Compos.* **2015**, *36*, 538–544. [CrossRef]
105. Ben Ahmed, N.; Ronsin, O.; Mouton, L.; Sicard, C.; Yepremian, C.; Baumberger, T.; Brayner, R.; Coradin, T. The physics and chemistry of silica-in-silicates nanocomposite hydrogels and their phycocompatibility. *J. Mater. Chem. B* **2017**, *5*, 2931–2940. [CrossRef]
106. Yang, C.C.; Xue, R.; Zhang, Q.S.; Yang, S.L.; Liu, P.F.; Chen, L.; Wang, K.; Zhang, X.Y.; Wei, Y. Nanoclay cross-linked semi-IPN silk sericin/poly(NIPAm/LMSH) nanocomposite hydrogel: An outstanding antibacterial wound dressing. *Mater. Sci. Eng. C* **2017**, *81*, 303–313. [CrossRef]
107. Wang, T.; Zheng, S.; Sun, W.; Liu, X.; Fu, S.; Tong, Z. Notch insensitive and self-healing PNIPAm-PAM-clay nanocomposite hydrogels. *Soft Matter* **2014**, *10*, 3506–3512. [CrossRef]
108. Shibayama, M.; Karino, T.; Miyazaki, S.; Okabe, S.; Takehisa, T.; Haraguchi, K. Small-angle neutron scattering study on uniaxially stretched poly(N-isopropylacrylamide)-clay nanocomposite gels. *Macromolecules* **2005**, *38*, 10772–10781. [CrossRef]
109. Haraguchi, K.; Farnworth, R.; Ohbayashi, A.; Takehisa, T. Compositional effects on mechanical properties of nanocomposite hydrogels composed of poly(*N*,*N*-dimethylacrylamide) and clay. *Macromolecules* **2003**, *36*, 5732–5741. [CrossRef]
110. Haraguchi, K.; Uyama, K.; Tanimoto, H. Self-healing in Nanocomposite Hydrogels. *Macromol. Rapid Commun.* **2011**, *32*, 1253–1258. [CrossRef] [PubMed]
111. Shao, C.; Chang, H.; Wang, M.; Xu, F.; Yang, J. High-Strength, Tough, and Self-Healing Nanocomposite Physical Hydrogels Based on the Synergistic Effects of Dynamic Hydrogen Bond and Dual Coordination Bonds. *ACS Appl. Mater. Interfaces* **2017**, *9*, 28305–28318. [CrossRef] [PubMed]
112. Kostina, N.; Sharifi, S.; Pereira, A.; Michalek, J.; Grijpma, D.; Rodriguez-Emmenegger, C. Novel antifouling self-healing poly(carboxybetaine methacrylamide-co-HEMA) nanocomposite hydrogels with superior mechanical properties. *J. Mat. Chem. B* **2013**, *1*, 5644–5650. [CrossRef]
113. Jeong, S.H.; Koh, Y.H.; Kim, S.W.; Park, J.U.; Kim, H.E.; Song, J. Strong and Biostable Hyaluronic Acid-Calcium Phosphate Nanocomposite Hydrogel via in Situ Precipitation Process. *Biomacromolecules* **2016**, *17*, 841–851. [CrossRef] [PubMed]
114. Su, E.; Okay, O. Hybrid cross-linked poly(2-acrylamido-2-methyl-1-propanesulfonic acid) hydrogels with tunable viscoelastic, mechanical and self-healing properties. *React. Funct. Polym.* **2018**, *123*, 70–79. [CrossRef]
115. Pan, C.; Liu, L.; Chen, Q.; Zhang, Q.; Guo, G. Tough, Stretchable, Compressive Novel Polymer/Graphene Oxide Nanocomposite Hydrogels with Excellent Self-Healing Performance. *ACS Appl. Mater. Interfaces* **2017**, *9*, 38052–38061. [CrossRef]

116. Gao, G.; Du, G.; Sun, Y.; Fu, J. Self-Healable, Tough, and Ultrastretchable Nanocomposite Hydrogels Based on Reversible Polyacrylamide/Montmorillonite Adsorption. *ACS Appl. Mater. Interfaces* **2015**, *7*, 5029–5037. [CrossRef]
117. Kokabi, M.; Sirousazar, M.; Hassan, Z.M. PVA-clay nanocomposite hydrogels for wound dressing. *Eur. Polym. J.* **2007**, *43*, 773–781. [CrossRef]
118. Zhong, M.; Liu, Y.; Xie, X. Self-healable, super tough graphene oxide-poly(acrylic acid) nanocomposite hydrogels facilitated by dual cross-linking effects through dynamic ionic interactions. *J. Mater. Chem. B* **2015**, *3*, 4001–4008. [CrossRef]
119. Gonzalez-Dominguez, J.M.; Martin, C.; Dura, O.J.; Merino, S.; Vazquez, E. Smart Hybrid Graphene Hydrogels: A Study of the Different Responses to Mechanical Stretching Stimulus. *ACS Appl. Mater. Interfaces* **2018**, *10*, 1987–1995. [CrossRef] [PubMed]
120. Binder, W.H. *Self-Healing Polymers: From Principles to Applications*; Wiley-VCH: Weinheim, Germany, 2013; p. 446.
121. Yang, J.; Zhu, L.; Yan, X.; Wei, D.; Qin, G.; Liu, B.; Liu, S.; Chen, Q. Hybrid nanocomposite hydrogels with high strength and excellent self-recovery performance. *RSC Adv.* **2016**, *6*, 59131–59140. [CrossRef]
122. Jiang, H.; Zhang, G.; Feng, X.; Liu, H.; Li, F.; Wang, M.; Li, H. Room-temperature self-healing tough nanocomposite hydrogel crosslinked by zirconium hydroxide nanoparticles. *Compos. Sci. Tech.* **2017**, *140*, 54–62. [CrossRef]
123. Shao, C.; Wang, M.; Chang, H.; Xu, F.; Yang, J. A Self-Healing Cellulose Nanocrystal-Poly(ethylene glycol) Nanocomposite Hydrogel via Diels-Alder Click Reaction. *ACS Sustain. Chem. Eng.* **2017**, *5*, 6167–6174. [CrossRef]
124. Wu, D.; Xu, J.; Chen, Y.; Yi, M.; Wang, Q. Gum Arabic: A promising candidate for the construction of physical hydrogels exhibiting highly stretchable, self-healing and tensility reinforcing performances. *Carbohydr. Polym.* **2018**, *181*, 167–174. [CrossRef] [PubMed]
125. Wang, Q.; Gao, Z.; Yu, K. Interfacial self-healing of nanocomposite hydrogels: Theory and experiment. *J. Mech. Phys. Solids* **2017**, *109*, 288–306. [CrossRef]
126. Diba, M.; An, J.; Schmidt, S.; Hembury, M.; Ossipov, D.; Boccaccini, A.; Leeuwenburgh, S. Exploiting Bisphosphonate-Bioactive-Glass Interactions for the Development of Self-Healing and Bioactive Composite Hydrogels. *Macromol. Rapid Commun.* **2016**, *37*, 1952–1959. [CrossRef]
127. Peng, R.; Yu, Y.; Chen, S.; Yang, Y.; Tang, Y. Conductive nanocomposite hydrogels with self-healing property. *RSC Adv.* **2014**, *4*, 35149–35155. [CrossRef]
128. Zhang, E.; Wang, T.; Zhao, L.; Sun, W.; Liu, X.; Tong, Z. Fast Self-Healing of Graphene Oxide-Hectorite Clay-Poly(*N*,*N*-dimethylacrylamide) Hybrid Hydrogels Realized by Near-Infrared Irradiation. *ACS Appl. Mater. Interfaces* **2014**, *6*, 22855–22861. [CrossRef]
129. Wang, B.; Jeon, Y.; Park, H.; Kim, J. Self-healable mussel-mimetic nanocomposite hydrogel based on catechol-containing polyaspartamide and graphene oxide. *Mater. Sci. Eng. C* **2016**, *69*, 160–170. [CrossRef] [PubMed]
130. Peak, C.W.; Wilker, J.J.; Schmidt, G. A review on tough and sticky hydrogels. *Colloid Polym. Sci.* **2013**, *291*, 2031–2047. [CrossRef]
131. Wu, C.J.; Wilker, J.J.; Schmidt, G. Robust and Adhesive Hydrogels from Cross-Linked Poly(ethylene glycol) and Silicate for Biomedical Use. *Macromol. Biosci.* **2013**, *13*, 59–66. [CrossRef] [PubMed]
132. Gaharwar, A.K.; Rivera, C.P.; Wu, C.J.; Schmidt, G. Transparent, elastomeric and tough hydrogels from poly(ethylene glycol) and silicate nanoparticles. *Acta Biomater.* **2011**, *7*, 4139–4148. [CrossRef] [PubMed]
133. Xie, F.; Boyer, C.; Gaborit, V.; Rouillon, T.; Guicheux, J.; Tassin, J.F.; Geoffroy, V.; Rethore, G.; Weiss, P. A Cellulose/Laponite Interpenetrated Polymer Network (IPN) Hydrogel: Controllable Double-Network Structure with High Modulus. *Polymers* **2018**, *10*, 634. [CrossRef]
134. Geim, A.K.; Grigorieva, I.V. Van der Waals heterostructures. *Nature* **2013**, *499*, 419–425. [CrossRef] [PubMed]
135. Frisenda, R.; Navarro-Moratalla, E.; Gant, P.; De Lara, D.; Jarillo-Herrero, P.; Gorbachev, R.; Castellanos-Gomez, A. Recent progress in the assembly of nanodevices and van der Waals heterostructures by deterministic placement of 2D materials. *Chem. Soc. Rev.* **2018**, *47*, 53–68. [CrossRef]
136. Zhao, Z.W.; Sun, Y.J.; Dong, F. Graphitic carbon nitride based nanocomposites: A review. *Nanoscale* **2015**, *7*, 15–37. [CrossRef]

137. Ong, W.J.; Tan, L.L.; Ng, Y.H.; Yong, S.T.; Chai, S.P. Graphitic Carbon Nitride (g-C3N4)-Based Photocatalysts for Artificial Photosynthesis and Environmental Remediation: Are We a Step Closer to Achieving Sustainability? *Chem. Rev.* **2016**, *116*, 7159–7329. [CrossRef]
138. Yetisen, A.K.; Butt, H.; Volpatti, L.R.; Pavlichenko, I.; Humar, M.; Kwok, S.J.J.; Koo, H.; Kim, K.S.; Naydenova, I.; Khademhosseini, A.; et al. Photonic hydrogel sensors. *Biotechnol. Adv.* **2016**, *34*, 250–271. [CrossRef]
139. Saito, H.; Takeoka, Y.; Watanabe, M. Simple and precision design of porous gel as a visible indicator for ionic species and concentration. *Chem. Commun.* **2003**, 2126–2127. [CrossRef]
140. Kamenjicki, M.; Asher, S.A. Epoxide functionalized polymerized crystalline colloidal arrays. *Sens. Actuators B* **2005**, *106*, 373–377. [CrossRef]
141. Holtz, J.H.; Asher, S.A. Polymerized colloidal crystal hydrogel films as intelligent chemical sensing materials. *Nature* **1997**, *389*, 829–832. [CrossRef]
142. Ye, B.F.; Zhao, Y.J.; Cheng, Y.; Li, T.T.; Xie, Z.Y.; Zhao, X.W.; Gu, Z.Z. Colorimetric photonic hydrogel aptasensor for the screening of heavy metal ions. *Nanoscale* **2012**, *4*, 5998–6003. [CrossRef]
143. Arunbabu, D.; Sannigrahi, A.; Jana, T. Photonic crystal hydrogel material for the sensing of toxic mercury ions (Hg^{2+}) in water. *Soft Matter* **2011**, *7*, 2592–2599. [CrossRef]
144. Lin, F.Y.; Yu, L.P. Thiourea functionalized hydrogel photonic crystal sensor for Cd2+ detection. *Anal. Methods* **2012**, *4*, 2838–2845. [CrossRef]
145. Muscatello, M.M.W.; Stunja, L.E.; Asher, S.A. Polymerized Crystalline Colloidal Array Sensing of High Glucose Concentrations. *Anal. Chem.* **2009**, *81*, 4978–4986. [CrossRef]
146. Zhang, C.J.; Cano, G.G.; Braun, P.V. Linear and Fast Hydrogel Glucose Sensor Materials Enabled by Volume Resetting Agents. *Adv. Mater.* **2014**, *26*, 5678–5683. [CrossRef] [PubMed]
147. Zeng, F.; Wu, S.Z.; Sun, Z.W.; Xi, H.Y.; Li, R.F.; Hou, Z.L. Urea sensing materials via solidified crystalline colloidal arrays. *Sens. Actuators B* **2002**, *81*, 273–276. [CrossRef]
148. Chen, C.; Zhu, Y.H.; Bao, H.; Shen, J.H.; Jiang, H.L.; Peng, L.M.; Yang, X.L.; Li, C.Z.; Chen, G.R. Ethanol-assisted multi-sensitive poly(vinyl alcohol) photonic crystal sensor. *Chem. Commun.* **2011**, *47*, 5530–5532. [CrossRef]
149. Sharma, A.C.; Jana, T.; Kesavamoorthy, R.; Shi, L.J.; Virji, M.A.; Finegold, D.N.; Asher, S.A. A general photonic crystal sensing motif: Creatinine in bodily fluids. *J. Am. Chem. Soc.* **2004**, *126*, 2971–2977. [CrossRef] [PubMed]
150. Kimble, K.W.; Walker, J.P.; Finegold, D.N.; Asher, S.A. Progress toward the development of a point-of-care photonic crystal ammonia sensor. *Anal. Bioanal. Chem.* **2006**, *385*, 678–685. [CrossRef]
151. Alexeev, V.L.; Das, S.; Finegold, D.N.; Asher, S.A. Photonic crystal glucose-sensing material for noninvasive monitoring of glucose in tear fluid. *Clin. Chem.* **2004**, *50*, 2353–2360. [CrossRef]
152. MacConaghy, K.I.; Chadly, D.M.; Stoykovich, M.P.; Kaar, J.L. Label-free detection of missense mutations and methylation differences in the p53 gene using optically diffracting hydrogels. *Analyst* **2015**, *140*, 6354–6362. [CrossRef] [PubMed]
153. Zhang, J.T.; Chao, X.; Liu, X.Y.; Asher, S.A. Two-dimensional array Debye ring diffraction protein recognition sensing. *Chem. Commun.* **2013**, *49*, 6337–6339. [CrossRef] [PubMed]
154. Zhang, J.T.; Cai, Z.Y.; Kwak, D.H.; Liu, X.Y.; Asher, S.A. Two-Dimensional Photonic Crystal Sensors for Visual Detection of Lectin Concanavalin A. *Anal. Chem.* **2014**, *86*, 9036–9041. [CrossRef] [PubMed]
155. Amsden, B. Solute diffusion within hydrogels. Mechanisms and models. *Macromolecules* **1998**, *31*, 8382–8395. [CrossRef]
156. Dembo, M.; Wang, Y.L. Stresses at the cell-to-substrate interface during locomotion of fibroblasts. *Biophys. J.* **1999**, *76*, 2307–2316. [CrossRef]
157. Colin-York, H.; Eggeling, C.; Fritzsche, M. Dissection of mechanical force in living cells by super-resolved traction force microscopy. *Nat. Protocols* **2017**, *12*, 783–796. [CrossRef]
158. Harris, A.K.; Wild, P.; Stopak, D. Silicone rubber substrata: A new wrinkle in the study of cell locomotion. *Science* **1980**, *208*, 177–179. [CrossRef]
159. Miller, J.S.; Shen, C.J.; Legant, W.R.; Baranski, J.D.; Blakely, B.L.; Chen, C.S. Bioactive hydrogels made from step-growth derived PEG-peptide macromers. *Biomaterials* **2010**, *31*, 3736–3743. [CrossRef] [PubMed]
160. Legant, W.R.; Miller, J.S.; Blakely, B.L.; Cohen, D.M.; Genin, G.M.; Chen, C.S. Measurement of mechanical tractions exerted by cells in three-dimensional matrices. *Nat. Methods* **2010**, *7*, 969–971. [CrossRef] [PubMed]

161. Koch, T.M.; Munster, S.; Bonakdar, N.; Butler, J.P.; Fabry, B. 3D Traction Forces in Cancer Cell Invasion. *PLoS ONE* **2012**, *7*, e33476. [CrossRef] [PubMed]
162. Colin-York, H.; Shrestha, D.; Felce, J.H.; Waithe, D.; Moeendarbary, E.; Davis, S.J.; Eggeling, C.; Fritzsche, M. Super-Resolved Traction Force Microscopy (STFM). *Nano Lett.* **2016**, *16*, 2633–2638. [CrossRef] [PubMed]
163. Schultz, K.M.; Kyburz, K.A.; Anseth, K.S. Measuring dynamic cell-material interactions and remodeling during 3D human mesenchymal stem cell migration in hydrogels. *Proc. Natl. Acad. Sci. USA* **2015**, *112*, E3757–E3764. [CrossRef] [PubMed]
164. Krajina, B.A.; Tropini, C.; Zhu, A.; DiGiacomo, P.; Sonnenburg, J.L.; Heilshorn, S.C.; Spakowitz, A.J. Dynamic Light Scattering Microrheology Reveals Multiscale Viscoelasticity of Polymer Gels and Precious Biological Materials. *ACS Cent. Sci.* **2017**, *3*, 1294–1303. [CrossRef] [PubMed]
165. Khan, M.; Mason, T.G. Local collective motion analysis for multiprobe dynamic imaging and microrheology. *J. Phys. Cond. Matter* **2016**, *28*. [CrossRef]
166. Squires, T.M.; Mason, T.G. Fluid Mechanics of Microrheology. *Ann. Rev. Fluid Mech.* **2010**, *42*, 413–438. [CrossRef]
167. Crocker, J.C.; Valentine, M.T.; Weeks, E.R.; Gisler, T.; Kaplan, P.D.; Yodh, A.G.; Weitz, D.A. Two-point microrheology of inhomogeneous soft materials. *Phys. Rev. Lett.* **2000**, *85*, 888–891. [CrossRef]
168. Yao, A.; Tassieri, M.; Padgett, M.; Cooper, J. Microrheology with optical tweezers. *Lab Chip* **2009**, *9*, 2568–2575. [CrossRef]
169. Robertson-Anderson, R.M. Optical Tweezers Microrheology: From the Basics to Advanced Techniques and Applications. *ACS Macro Lett.* **2018**, *7*, 968–975. [CrossRef]
170. Plutschack, M.B.; Pieber, B.; Gilmore, K.; Seeberger, P.H. The Hitchhiker's Guide to Flow Chemistry(II). *Chem. Rev.* **2017**, *117*, 11796–11893. [CrossRef] [PubMed]
171. Caccavo, D.; Cascone, S.; Lamberti, G.; Barba, A. Hydrogels: Experimental characterization and mathematical modelling of their mechanical and diffusive behaviour. *Chem. Soc. Rev.* **2018**, *47*, 2357–2373. [CrossRef] [PubMed]

MDPI
St. Alban-Anlage 66
4052 Basel
Switzerland
Tel. +41 61 683 77 34
Fax +41 61 302 89 18
www.mdpi.com

Polymers Editorial Office
E-mail: polymers@mdpi.com
www.mdpi.com/journal/polymers

MDPI
St. Alban-Anlage 66
4052 Basel
Switzerland

Tel: +41 61 683 77 34
Fax: +41 61 302 89 18

www.mdpi.com

ISBN 978-3-03921-284-2